Photons micro-ondes, mesure et informatique quantique

par

Baptiste Royer

Thèse présentée au département de physique
en vue de l'obtention du grade de docteur ès science (Ph.D.)

FACULTÉ des SCIENCES
UNIVERSITÉ de SHERBROOKE

Sherbrooke, Québec, Canada, 13 août 2019

Le 8 juin 2019

le jury a accepté la thèse de M. Baptiste Royer dans sa version finale.

Membres du jury

Professeur Alexandre Blais
Directeur de recherche
Département de physique

Professeur Jeffrey Quilliam
Membre interne
Département de physique

Professeur Yasunobu Nakamura
Membre externe
University of Tokyo

Professeur David Poulin
Président rapporteur
Département de physique

À ma famille

Sommaire

Les circuits supraconducteurs constituent aujourd'hui une architecture prometteuse vers la réalisation d'un ordinateur quantique universel. Cependant, avant qu'un tel ordinateur voie le jour, plusieurs défis doivent être surmontés autant au niveau matériel que logiciel. Les circuits supraconducteurs forment aussi une architecture intéressante pour la réalisation d'expériences fondamentales en optique quantique grâce aux jonctions Josephson qui permettent aux photons micro-ondes d'interagir directement entre eux. Dans cette thèse, j'ai abordé certains des grands défis du domaine des circuits supraconducteurs dans le contexte de l'informatique quantique et de l'optique quantique micro-onde.

Je me suis tout d'abord intéressé à la détection de photons micro-ondes uniques (chapitre 3). Avec mes collaborateurs, nous avons ainsi proposé deux méthodes pour réaliser un détecteur de photons uniques à grande efficacité quantique. Une de ces méthodes se base sur un ensemble de qubits supraconducteurs (section 3.2), tandis que l'autre promet une large bande de détection en se basant sur un métamatériau unidimensionnel (section 3.3). La réalisation expérimentale de ces propositions permettrait d'ajouter une pièce importante dans la boîte à outils de l'optique quantique micro-onde. Je me suis ensuite penché sur la correction d'erreurs dans les qubits supraconducteurs (section 4). Plus précisément, j'ai développé un circuit expérimentalement compact permettant de mesurer les propriétés d'un ensemble de qubits, une opération essentielle pour les techniques de correction d'erreurs quantiques. Finalement, j'ai consacré une partie de mon doctorat à modéliser des expériences effectuées dans le groupe d'Andreas Wallraff à l'ETH Zürich (chapitre 5). Nous avons ainsi réalisé trois expériences basées sur un couplage variable de type Raman entre un qubit supraconducteur et un résonateur micro-onde. Dans la première expérience, nous avons réalisé le premier transfert d'état quantique déterministe entre deux qubits supraconducteurs distants (section 5.2). Nous avons ensuite amélioré cette expérience en utilisant un code de détection d'erreur pour transférer l'information quantique de manière plus robuste entre les deux qubits (section 5.3). Ces expériences représentent une étape importante vers la réalisation d'une architecture modulaire de l'ordinateur quantique. Finalement, nous avons développé une méthode pour rapidement initialiser des qubits supraconducteurs

dans leur état fondamental (section 5.4), une opération essentielle de l'ordinateur quantique.

Mot-clés : Photons micro-ondes, détecteur de photons uniques, trajectoires quantiques, mesure homodyne, mesure de parité, intrication à distance, transfert d'état quantique, initialisation de qubit

Remerciements

Tout d'abord, un grand merci à Alexandre pour son temps. Merci de m'avoir enseigné tant de choses. Merci de m'avoir donné l'opportunité de travailler avec autant de gens talentueux. Merci de m'avoir permis de voyager et de rencontrer tant de gens intelligents et intéressants.

Un merci spécial à Kevin et Arne qui ont patiemment répondu à mes questions. Merci à tous les membres du groupe, Shruti, Agustìn, Nicolas, Nicolàs, Bright, Jérôme, Alexandre, Christian, Samuel, Jonathan, Lucas, Mathieu, Udson, Alexandru, Catherine, Camille, Jaya, Ivan. Merci pour les innombrables discussions et pour les bons temps ces dernières années. J'aimerais aussi remercier mes collègues à l'étranger pour leur travail exceptionnel. Merci à Philipp, Paul et Sebastian de l'ETH. Merci à John Mark à l'UC Berkeley. Merci à Jack et Bharath du MIT. J'espère pouvoir continuer à travailler avec chacun d'eux. J'aimerais aussi remercier le CRSNG, Calcul Québec et Calcul Canada pour leur soutien financier.

Évidemment, merci à mes parents Alain et Cécile pour m'avoir donné le goût d'apprendre et pour leur support constant. Merci à mes sœurs Christelle, Sandrine et Marguerite pour leur soutien indéfectible. Un grand merci à Noémie qui me soutient tous les jours. Finalement, un grand merci à mes amis Samuel, Samuel, Samuel, Édouard, Karl, Maxime, Francis, Jonathan pour les jeux, l'escalade, les bières, les cafés, les combos, le soccer et tant d'autres choses qui ont animés ces dernières années.

Table des matières

Liste des figures

Liste des tableaux

Chapitre 1

Introduction

Depuis les premières démonstrations de contrôle cohérent d'états quantiques basés sur les jonctions Josephson [1, 2, 3], le domaine des circuits supraconducteurs a connu un essor considérable. Ce développement rapide peut s'expliquer en partie par la promesse de plusieurs applications pour ces circuits, la principale étant la réalisation d'un ordinateur quantique. L'architecture d'électrodynamique quantique en circuit [4, 5] apparaît en effet comme un candidat prometteur pour la réalisation d'un ordinateur quantique grâce aux longs temps de cohérence et au contrôle rapide des qubits supraconducteurs [6]. En plus de l'informatique quantique, les circuits supraconducteurs constituent aussi une plateforme attrayante pour les expériences d'optique quantique où, contrairement aux photons dans les longueurs d'onde visibles, il est facile de faire interagir les photons micro-ondes entre eux grâce à la nonlinéarité des jonctions Josephson [7, 8, 9, 10]. Les circuits supraconducteurs trouvent aussi des applications en cosmologie avec, par exemple, la recherche de matière noire [11, 12, 13]. En effet, certains modèles théoriques prédisent une interaction faible entre la matière noire et le champ électromagnétique, menant à une émission de photons micro-ondes qui est en principe détectable.

Du point de vue d'un théoricien, le domaine des circuits supraconducteurs constitue un terrain de jeu extraordinaire. À quelques exceptions près, les techniques analytiques et numériques actuelles permettent de modéliser avec précision les expériences réalisées en laboratoire. Ainsi, à la manière des blocs LEGO^{TM}, il est possible d'agencer des éléments de circuits et de prédire les propriétés du résultat

avec un grand degré de confiance. Une grande partie de cette thèse, soit les chapitres 3 et 4, se situe dans ce contexte. Mes travaux de doctorat m'ont ainsi amené à étudier divers agencements de circuits dans le but d'ajouter de nouvelles fonctionnalités dans la boîte à outils des circuits supraconducteurs. À cause du caractère intrinsèquement quantique de ces systèmes, ce type de travail requiert de prendre en compte plusieurs aspects fondamentaux de la mécanique quantique.

Le premier défi sur lequel je me suis penché est celui de la détection de photons micro-ondes uniques, plus particulièrement dans la gamme de fréquences 5-10 GHz. Dans les longueurs d'onde visibles et proches infrarouges, le développement de détecteurs de photons uniques a permis de réaliser de nombreuses expériences en informatique quantique [14] et en cryptographie quantique [15]. Cependant, l'utilisation de ces mêmes détecteurs dans les micro-ondes est impossible due à la grande différence d'énergie entre les longueurs d'onde visibles et les micro-ondes, et le développement de nouvelles méthodes est nécessaire. Une piste possible pour la détection de photons micro-ondes uniques est de s'inspirer de la mesure de qubits supraconducteurs [4], une opération similaire dont la fidélité excède aujourd'hui 99% [16]. Comme je le montre en détail au chapitre 3, la détection de photons micro-ondes uniques est cependant plus difficile à implémenter que la mesure de qubits, en partie à cause de la nécessité de capturer les photons avant de les détecter, et en partie à cause de phénomènes fondamentaux reliés à la mesure en mécanique quantique.

On peut imaginer beaucoup d'applications pour un détecteur de photons micro-ondes uniques. Une première option serait de s'inspirer de l'optique quantique dans les longueurs d'onde visibles [17] et de réaliser des expériences par exemple l'échantillonnage de bosons (*boson sampling*) [18] en prenant avantage des éléments propres aux micro-ondes. Un détecteur de photons serait également utile pour mesurer des qubits supraconducteurs [19, 20] dans certaines situations où la mesure dispersive ne peut pas être utilisée [21, 9] ou encore pour mesurer des propriétés globales de qubits [22]. Un détecteur de photons trouverait aussi des applications en métrologie [23], dans la recherche de matière noire [24], dans la caractérisation de statistique de photons de systèmes mésoscopiques [25] ou encore dans la réalisation d'une architecture modulaire de l'ordinateur quantique [26, 27, 28]. En fin de compte, avec la mesure homodyne permettant déjà la mesure des quadratures du champ

électromagnétique [29], l'existence d'un détecteur de photons uniques à grande efficacité compléterait la boîte à outils des détecteurs en optique quantique micro-onde.

Avant mes travaux de doctorat, quelques propositions pour un détecteur de photons micro-ondes avaient été avancées [30, 31, 32, 33, 34, 35, 36], avec seulement quelques résultats expérimentaux [37, 38, 39]. C'est dans ce contexte que j'ai, avec mes collaborateurs, développé deux nouvelles propositions, tentant de développer des circuits à la fois réalistes et performants. Le premier dispositif [40], présenté à la section 3.2 et plus simple à réaliser, se base sur l'absorption d'un photon dans un ensemble de qubits supraconducteurs. En mesurant de façon continue cet ensemble, je montre qu'il est possible de mesurer des photons micro-ondes avec une grande efficacité, mais sur une étroite bande de fréquence. La deuxième proposition, présentée à la section 3.3 et plus complexe à fabriquer, promet de détecter des photons micro-ondes avec une grande efficacité sur une large bande de fréquences. Cette proposition se base sur l'absorption d'un photon dans un métamatériau constitué de plusieurs milliers de jonctions Josephson.

Un deuxième défi sur lequel je me suis penché est celui de l'implémentation pratique de codes de corrections d'erreurs quantiques. Comme mentionné plus haut, une des motivations principales derrière le développement des circuits supraconducteurs est la perspective d'un ordinateur quantique. Bien qu'un pan de la recherche actuelle soit dirigé vers l'utilisation et le développement de processeurs quantiques à échelle intermédiaire [41], il semble clair que cette approche n'est pas extensible (*scalable*). En particulier, un plus grand processeur implique une plus grande probabilité d'erreur, ce qui impose une limite naturelle sur la taille des processeurs quantiques. Heureusement, il est possible de corriger ces erreurs en encodant l'information logique de manière redondante dans un ensemble de qubits physiques [42, 43, 44, 45]. Le prix à payer pour cette protection est un surcoût expérimental significatif et l'implémentation pratique de ces codes de correction d'erreur reste un défi de taille. En particulier, ces codes de correction nécessitent de mesurer les propriétés de sous-ensembles de qubits, une opération connue sous le nom de « mesure de parité ». À partir du résultat de cette mesure, il est possible de déterminer lorsqu'une erreur survient et ainsi permet de la corriger. Étant donné que cette opération de mesure doit être effectuée à intervalles réguliers, il est crucial

qu'elle soit rapide avec une fidélité approchant l'unité.

L'approche standard pour la mesure de parité est d'utiliser un qubit ancillaire préparé dans son état fondamental [46, 47, 48, 49, 50, 51, 52]. En utilisant une série de portes logiques à deux qubits, il est possible d'encoder la valeur de parité des qubits de données dans l'état de ce qubit ancillaire qui est ensuite mesuré. Cette approche nécessite une surcharge expérimentale considérable, car chaque stabilisateur requiert l'addition d'un qubit. Chaque porte à deux qubits allonge aussi le temps de mesure, en plus de potentiellement introduire des erreurs.

Une autre approche à la mesure de parité est de mesurer directement les propriétés d'un ensemble de qubits couplés au même mode de mesure [53, 54, 55, 56, 57, 22, 58], typiquement un résonateur micro-onde. En évitant l'ajout d'un qubit ancillaire et l'utilisation de portes à deux qubits, cette approche est expérimentalement plus compacte et typiquement plus rapide. Le défi avec ce type de méthode est de mesurer *seulement* la parité des qubits et éviter d'induire un déphasage parasite dû à la mesure. Au chapitre 4, j'introduis une méthode pour surmonter cette difficulté en utilisant un résonateur nonlinéaire avec un pilotage paramétrique [59]. En apparence très différents, la mesure de parité et la détection de photons sont deux sujets fortement reliés par le concept de mesure dans les circuits supraconducteurs.

La dernière partie de cette thèse, présentée au chapitre 5, concerne les travaux que j'ai effectués en collaboration avec le groupe d'Andreas Wallraff à l'ETH Zürich. Pour ces travaux, mon rôle n'a pas été de développer de nouveaux circuits, mais plutôt d'offrir un support théorique afin de mieux comprendre et de modéliser les expériences suisses.

La première expérience que nous avons réalisée est l'intrication sur demande de deux qubits supraconducteurs distants [60]. Une approche possible à la réalisation d'un ordinateur quantique est l'architecture modulaire, où plusieurs processeurs quantiques sont reliés en réseau pour accomplir un calcul [26, 27, 61]. L'avantage de cette approche est que plusieurs petits processeurs pourraient être plus faciles à fabriquer qu'un seul grand processeur. Par contre, pour connecter ces processeurs quantiques, il est nécessaire d'établir un lien quantique entre eux, c'est-à-dire un canal de communication où il est possible de transférer un état quantique ou générer de l'intrication. Avec mes collègues de l'ETH Zürich, nous avons démontré ces deux

opérations entre deux qubits supraconducteurs en se basant sur le transfert d'un photon micro-onde unique [62]. Cette expérience est donc une étape importante vers la réalisation d'une architecture modulaire de l'ordinateur quantique.

La principale source d'erreur pour ce montage expérimental est la perte de photons dans le transfert entre les deux nœuds. Plus généralement, le transfert parfait de micro-ondes sur de longues distances semble difficile à réaliser considérant que l'air atténue les micro-ondes et qu'il semble difficile de fabriquer de longs guides d'ondes supraconducteurs. Le développement de codes de correction d'erreurs pour le transfert d'état est donc une autre étape importante vers l'architecture modulaire de l'ordinateur quantique. Dans la deuxième expérience que nous avons réalisée, nous avons démontré un protocole de transfert robuste contre la perte de photons [63] en utilisant un encodage en temps plutôt qu'en état de Fock. Avec cet encodage, il est possible de détecter lorsqu'un photon est perdu en cours de route, et on peut ainsi recommencer l'expérience jusqu'à ce qu'il y ait un transfert complet. Dans cette situation, la perte de photons n'a aucun effet sur la fidélité de l'état final, et diminue plutôt le taux de succès du transfert d'état.

La troisième expérience que nous avons réalisée est orientée vers un objectif différent des deux précédentes. Une des conditions pour effectuer un calcul quantique est de connaître l'état initial des qubits [64] et, de plus, plusieurs protocoles de correction d'erreurs quantiques requièrent un flot constant de qubits ancillaires préparés dans leur état fondamental. L'initialisation de qubits est donc une opération cruciale de l'ordinateur quantique. Une procédure pour initialiser des qubits est de les mesurer puis d'appliquer une opération de rétroaction conditionnelle au résultat obtenu [65, 66, 67, 68, 69]. Cette approche, en plus de nécessiter un circuit de rétroaction, est limitée par la fidélité de lecture et par la fuite vers les niveaux supérieurs du qubit qu'elle peut occasionner [70, 71, 68]. En utilisant un montage expérimental similaire à celui employé pour l'intrication à distance, nous avons démontré une méthode rapide et sans rétroaction pour initialiser des qubits [72]. Un avantage de cette méthode est qu'elle utilise le même circuit que pour la mesure de qubits, la rendant compatible avec la plupart des processeurs quantiques supraconducteurs actuels.

Avant de présenter les travaux originaux introduits plus haut, je commence par

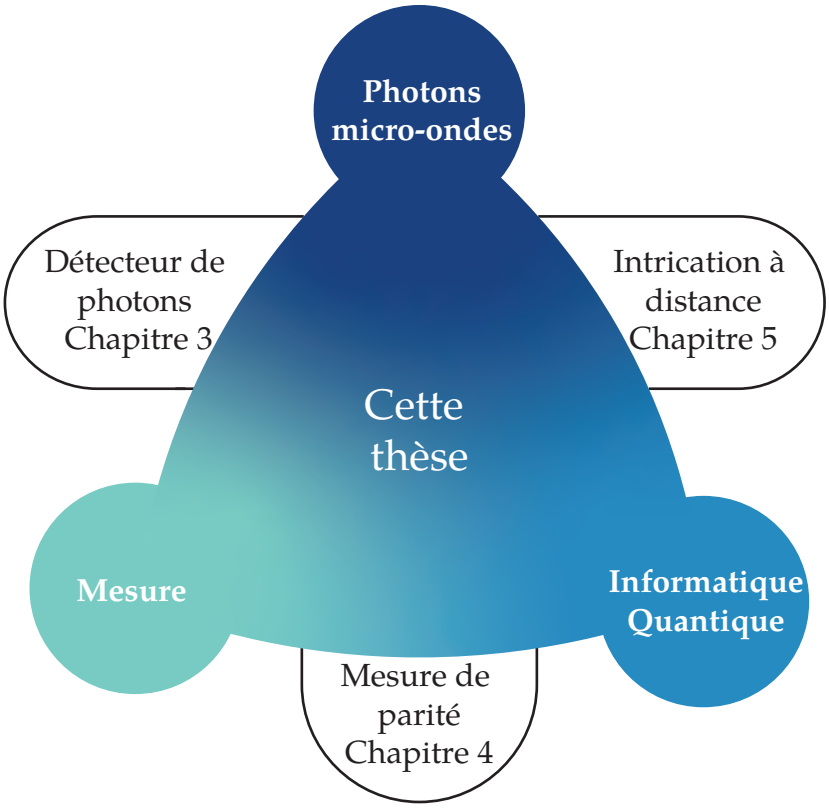

FIGURE 1.1 – Les trois chapitres de résultats cette thèse peuvent être divisés par les sujets abordés, soit les photons micro-ondes uniques (marine), la mesure en physique quantique (turquoise) et l'informatique quantique (bleu).

un chapitre de théorie rappelant les concepts nécessaires à la compréhension des chapitres 3, 4 et 5. Plus précisément, la section 2.1 traite des circuits supraconducteurs et la section 2.2 aborde plus généralement les systèmes ouverts en mécanique quantique. Je continue ensuite par les chapitres 3, 4 et 5, qui peuvent être relié thématiquement comme illustré sur la 1.1. Je finis par une courte conclusion au chapitre 6.

Chapitre 2

Théorie

Dans ce chapitre j'introduis les éléments de théorie utiles aux prochains chapitres. Le tableau 2.1 résume plusieurs conventions d'écriture que j'utilise dans cette thèse.

2.1 Circuits supraconducteurs

Dans cette section, je rappelle certaines notions importantes pour la modélisation des circuits supraconducteurs. Pour une introduction plus complète à ce sujet, je réfère le lecteur aux notes de Girvin [73] et aux notes de Vool et Devoret [74].

2.1.1 Qubits supraconducteurs

La plupart de mes résultats peuvent être appliqués à plusieurs types de qubits supraconducteurs. Ici, je me concentre uniquement sur le transmon [75], dont le circuit est présenté à la figure 2.1. On décrit les circuits supraconducteurs à partir des variables de charge, $\hat{n}$, et flux, $\hat{\phi} = \int_{-\infty}^{t} dt' \hat{v}(t)$, de nœud [74], où $\hat{v}$ est la différence

$\hbar = 1$	J'utilise un système d'unités tel que $\hbar = 1$ afin de simplifier les équations.
ρ	L'utilisation de cette lettre grecque est réservée aux matrices de densité.
$\hat{O}$	Les opérateurs sont généralement coiffés d'un accent circonflexe, à l'exception de ρ.
$\hat{a}$	De façon générale, cet opérateur est utilisé pour décrire un mode de cavité.
$\hat{b}$	De façon générale, cet opérateur est utilisé pour décrire un mode de transmon.
$\mathcal{O}$	Les lettres majuscules calligraphiques « mathcal » sont réservées aux superopérateurs.

TABLEAU 2.1 – Différentes conventions d'écriture utilisées dans cette thèse.

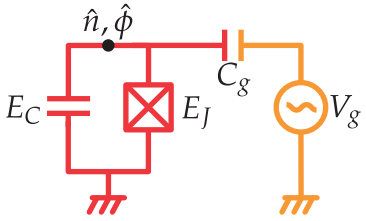

FIGURE 2.1 – Le circuit du transmon (rouge) consiste en une capacité et une jonction Josephson en parallèle et se caractérise par un ratio $E_J/E_C \gtrsim 50$. L'énergie Josephson E_J peut être rendue ajustable en remplaçant la jonction Josephson par un SQUID (*Superconducting quantum interference device* [76]) avec un flux ajustable [75]. On peut contrôler le transmon par une source de micro-ondes, V_g (orange).

de voltage sur la jonction. À partir de ces variables, l'Hamiltonien du circuit de la figure 2.1 est donné par

$$\hat{H} = 4E_C(\hat{n} - n_g)^2 - E_J \cos\left(\frac{\hat{\phi}}{\phi_0}\right), \tag{2.1}$$

où $E_C = e^2/2C$ est l'énergie de charge de la capacité C, E_J est l'énergie de la jonction Josephson, $\phi_0 = \hbar/2e$ est le quantum de flux réduit et n_g est le décalage classique de charge sur l'îlot supraconducteur mesuré en unités de charge de paire de Cooper $2e$. Ce décalage est induit par un couplage capacitif entre l'îlot du transmon et son environnement, représenté en orange sur la figure 2.1. Le régime transmon est défini

par un grand ratio $E_J/E_C \gtrsim 50$ et permet en pratique d'éliminer la dépendance des niveaux d'énergie par rapport à n_g [75]. En général, seuls quelques niveaux du transmon participent à la dynamique. Dans cette thèse, les transmons sont utilisés comme des systèmes à deux niveaux (qubits) ou trois niveaux (qutrits) selon le contexte.

Il est utile de décrire le transmon comme un oscillateur anharmonique en utilisant des opérateurs d'échelle $\hat{b}, \hat{b}^\dagger$ respectant les relations de commutation usuelles $[\hat{b}, \hat{b}^\dagger] = 1$. Le lien entre les variables de charge et de flux et les opérateurs d'échelle est donné par

$$\begin{aligned} \hat{\phi} &= \phi_0 \left(\frac{8E_C}{E_J}\right)^{1/4} \frac{(\hat{b} + \hat{b}^\dagger)}{\sqrt{2}}, \\ \hat{n} &= -i \left(\frac{E_J}{8E_C}\right)^{1/4} \frac{(\hat{b} - \hat{b}^\dagger)}{\sqrt{2}}. \end{aligned} \tag{2.2}$$

Avec ces définitions et en négligeant les termes oscillants à hautes fréquences (approximation séculaire), l'équation 2.1 se réduit à l'Hamiltonien d'un oscillateur Duffing [77],

$$\hat{H}_{\text{Transmon}} = \omega_q \hat{b}^\dagger \hat{b} + \frac{\alpha_q}{2} \hat{b}^\dagger \hat{b}^\dagger \hat{b} \hat{b}, \tag{2.3}$$

où $\omega_q \approx \sqrt{8E_J E_C} - E_C$ dénote la fréquence et $\alpha_q \approx -E_C$ l'anharmonicité du transmon. Comme illustré sur la figure 2.2, on appelle les premiers niveaux d'un transmon «g» de l'anglais *ground* et «e» de l'anglais *excited*. Faute de meilleurs noms, le second état excité est appelé «f» dans la littérature. Lorsque le transmon est utilisé comme un qubit et lorsque la fuite vers les niveaux supérieurs est négligeable, on approxime l'équation 2.3 par $\hat{H} = \omega_q \hat{\sigma}_z/2$, le lien entre les opérateurs $\hat{b}, \hat{b}^\dagger$ et les les matrices de Pauli étant donné par $\hat{\sigma}_z = 2\hat{b}^\dagger \hat{b} - 1$, $\hat{\sigma}_x = \hat{b} + \hat{b}^\dagger$ et $\hat{\sigma}_y = -i(\hat{b} - \hat{b}^\dagger)$ [1].

Pour contrôler le transmon, une ligne à transmission est couplée capacitivement à l'îlot supraconducteur, comme illustré en noir sur la figure 2.1. On modélise l'application d'un pulse micro-onde à une fréquence ω_d en ajoutant un terme à l'équation 2.3, $\hat{H} = \hat{H}_{\text{Transmon}} + \epsilon(t)\cos(\omega_d t + \varphi)(\hat{b} + \hat{b}^\dagger)$ où $\epsilon(t)$ est proportionnel à l'amplitude de l'onde. Afin de simplifier la modélisation de ces impulsions de contrôle, on se place dans un référentiel tournant à la fréquence ω_d et on utilise une

1. Cette définition de $\hat{\sigma}_z$ diffère d'un facteur -1 par rapport à la définition habituellement utilisée en informatique quantique [78].

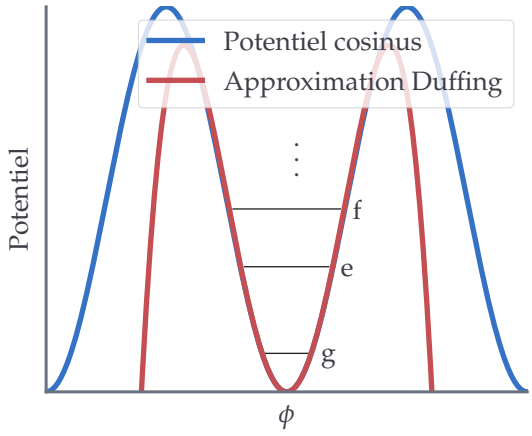

FIGURE 2.2 – La courbe en bleu montre le potentiel complet de la jonction Josephson. En général, seuls les premiers niveaux $n \lesssim 3$ du transmon participent à la dynamique et une approximation quartique du potentiel est suffisante, $\cos(x) \approx 1 - x^2/2 + x^4/24$.

approximation séculaire (*RWA*),

$$\hat{H} = \Delta_d \hat{b}^\dagger \hat{b} + \frac{\alpha_q}{2} \hat{b}^\dagger \hat{b}^\dagger \hat{b} \hat{b} + \frac{\epsilon(t)}{2} (\hat{b}\, e^{i\varphi} + \hat{b}^\dagger\, e^{-i\varphi}), \tag{2.4}$$

où $\Delta_d = \omega_q - \omega_d$. En choisissant $\omega_d = \omega_q$, il est possible d'effectuer une inversion de population (pulse pi) entre les niveaux $g \leftrightarrow e$. En choisissant plutôt $\omega_d = \omega_q - \alpha_q$, on effectue plutôt une inversion entre les états $e \leftrightarrow f$. De plus, la phase φ permet de choisir l'angle de rotation, $\hat{\sigma}_x$ ou $\hat{\sigma}_y$. Une technique maintenant répandue dans le domaine et connue sous le nom de DRAG (*Derivative Removal by Adiabatic Gate*) permet d'agir uniquement sur les niveaux désirés et d'éviter la fuite vers les niveaux indésirables en choisissant astucieusement l'amplitude de l'onde $\epsilon(t)$ [79].

2.1.2 Électrodynamique quantique en circuit

Une des grandes avancées du domaine des qubits supraconducteurs a été l'introduction de l'électrodynamique quantique en circuit (EDQc) [4, 5], où un qubit supraconducteur est couplé à un oscillateur harmonique. La figure 2.3 montre un circuit typique de l'EDQc, où un transmon est couplé capacitivement à un résona-

teur LC de fréquence ω_r. Notons que dans cette thèse, j'utilise les mots oscillateur, résonateur et cavité de façon interchangeable étant donné que leurs descriptions mathématiques sont équivalentes. Le couplage capacitif montré à la figure 2.3 mène

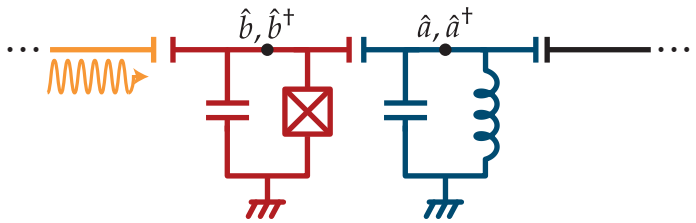

FIGURE 2.3 – Circuit typique pour un qubit transmon dans l'architecture EDQc. Une capacité couple le circuit LC (bleu) et le transmon (rouge). Le transmon est piloté par un second port capacitif (orange) et le résonateur est couplé à une ligne à transmission (noir) permettant la mesure du transmon.

à un couplage g de type Rabi se réduisant au modèle Jaynes-Cummings [80] dans l'approximation séculaire,

$$\hat{H}_{\mathrm{JC}} = \omega_q \hat{b}^\dagger \hat{b} + \frac{\alpha_q}{2} \hat{b}^\dagger \hat{b}^\dagger \hat{b} \hat{b} + \omega_r \hat{a}^\dagger \hat{a} + g(\hat{a}\hat{b}^\dagger + \hat{b}\hat{a}^\dagger), \tag{2.5}$$

où les opérateurs $\hat{a}, \hat{a}^\dagger$ sont les opérateurs d'échelle ($[\hat{a}, \hat{a}^\dagger] = 1$) créant et annihilant des excitations du résonateur, respectivement. Les qubits supraconducteurs sont habituellement opérés dans le régime dispersif avec un grand désaccord en fréquence entre le qubit et le résonateur, $|g/\Delta| \ll 1$, $\Delta = \omega_q - \omega_r$. Dans ce régime, le système est bien décrit par l'Hamiltonien dispersif

$$\hat{H}_{\mathrm{Disp}} = \omega_q \hat{b}^\dagger \hat{b} + \frac{\alpha_q}{2} \hat{b}^\dagger \hat{b}^\dagger \hat{b} \hat{b} + \omega_r \hat{a}^\dagger \hat{a} + \chi \hat{a}^\dagger \hat{a} \hat{b}^\dagger \hat{b}, \tag{2.6}$$

où le couplage dispersif est donné par [2]

$$\chi = 2\left(\frac{g^2}{\Delta} - \frac{g^2}{\Delta + \alpha_q}\right). \tag{2.7}$$

Notons que l'Hamiltonien 2.6 représente un léger abus de notation. En effet, les opérateurs $\hat{a}, \hat{b}$ de l'équation 2.6 font référence aux modes propres habillés du Ha-

2. Notons que cette définition de χ diffère d'un facteur 2 par rapport à certaines définitions utilisées dans la littérature [4].

miltonien 2.5, alors que les opérateurs $\hat{a}, \hat{b}$ de l'Hamiltonien 2.5 représentent les modes locaux illustrés sur la figure 2.3. Une conséquence de cet habillage est l'effet Purcell [81, 82], c'est-à-dire la dissipation du mode propre transmon, $\hat{b}$, due à la dissipation du résonateur dans le guide d'onde de mesure (en noir sur la figure 2.3). Ce type de dissipation peut être minimisé en modifiant l'environnement électromagnétique du résonateur, par exemple en ajoutant un résonateur supplémentaire appelé filtre Purcell [83].

L'architecture d'EDQc permet la lecture du transmon en tirant avantage du fait que l'état du qubit change la fréquence de résonance du résonateur de ω_r lorsque le qubit est dans l'état $|g\rangle$ à $\omega_r + \chi$ lorsque le qubit est dans l'état $|e\rangle$. La fréquence de résonance du résonateur, et donc l'état du qubit, peut être mesurée en envoyant une onde de pilotage à une fréquence $\omega_r + \chi/2$ au résonateur et en mesurant la phase de l'onde réfléchie [3]. Typiquement, ce type de mesure est optimisé pour la lecture des deux premiers niveaux du transmon, mais il est aussi possible d'utiliser l'interaction dispersive, équation 2.6, pour réaliser une mesure ternaire distinguant les états g, e et f [84, 60].

2.1.3 Représentations en espace de phase

Les simulations numériques de systèmes d'EDQc sont généralement effectuées dans une base de Fock en tronquant l'espace d'Hilbert. Cependant, il existe plusieurs autres méthodes héritées de l'optique quantique [29] pour décrire l'état des variables quantiques continues représentant les résonateurs micro-ondes. Les représentations en espace de phase constituent une manière graphiquement élégante de représenter ces états quantiques et, dans certains cas, permettent d'effectuer des calculs analytiques.

À partir des opérateurs d'échelle on définit les quadratures du champ $\hat{X} = (\hat{a} + \hat{a}^\dagger)$ et $\hat{Y} = -i(\hat{a} - \hat{a}^\dagger)$ [4], qui sont proportionnelles aux parties réelles et imaginaires de l'opérateur $\hat{a}$. On peut ainsi exprimer les états cohérents $|\alpha\rangle$, états propres de $\hat{a}$, à partir de leur quadrature $\alpha = \langle \hat{a} \rangle = \left\langle \hat{X} + i\hat{Y} \right\rangle /2 = (X + iY)/2$.

3. La mesure de l'état du qubit peut aussi se faire en envoyant une onde de pilotage à la fréquence ω_r ou $\omega_r + \chi$ et en mesurant l'amplitude de l'onde réfléchie.

4. On trouve aussi les conventions $\hat{X}/2$ et $\hat{X}/\sqrt{2}$.

La première représentation en espace de phase que j'utilise est la fonction Husimi Q [85],

$$Q(\alpha) = \frac{1}{\pi} \langle \alpha | \rho | \alpha \rangle . \tag{2.8}$$

Comme le montre l'équation 2.8, la fonction $Q : \mathbb{C} \to \mathbb{R}$ évaluée au point α représente le recouvrement entre une matrice de densité ρ et l'état cohérent $|\alpha\rangle$. Le préfacteur $1/\pi$ sert de normalisation afin que $\int d^2\alpha \, Q(\alpha) = 1$. La fonction Q est particulièrement utile comme représentation graphique : la figure 2.4a représente un exemple de fonction Q pour un état cohérent $\alpha = 2 + 2i$. Afin de simplifier cette représentation, on utilise souvent des schémas approximatifs comme celui de la figure 2.4b. D'un point de vue opérationnel, la fonction Q est reliée à la densité de probabilité pour une mesure hétérodyne des quadratures X, Y (la mesure hétérodyne est discutée plus en détails à la section 2.2.5).

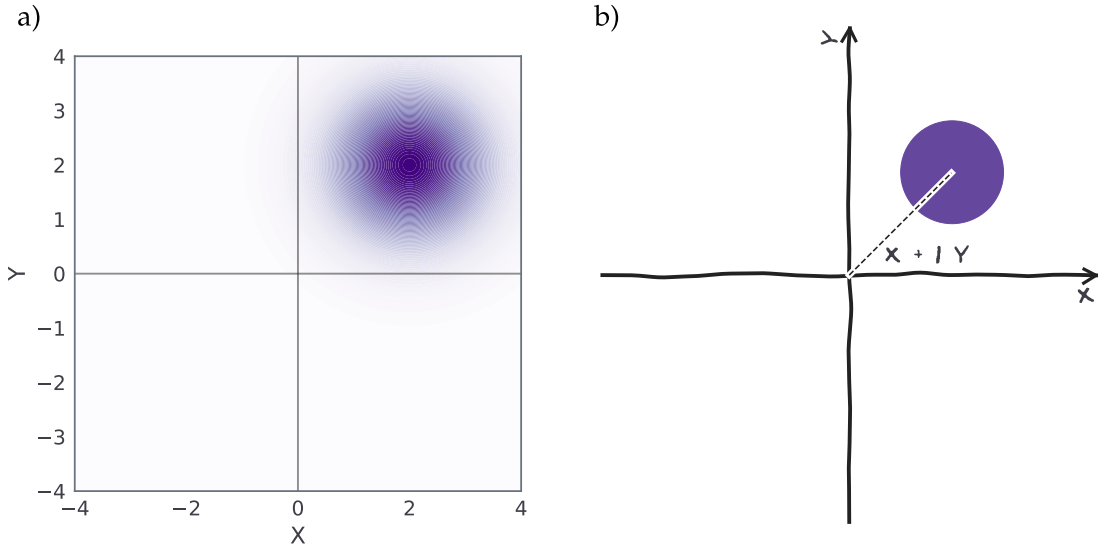

FIGURE 2.4 – Deux représentations de la fonction Q pour un même état cohérent $\alpha = 2 + 2i$. Le panneau a) est une représentation exacte tandis que b) est un sketch.

La deuxième représentation que j'utilise est la fonction P positive,

$$\rho = \int d^2\alpha d^2\beta \, P(\alpha, \beta) \frac{|\alpha\rangle\langle\beta^*|}{\langle\beta^*|\alpha\rangle} \tag{2.9}$$

La fonction P positive n'est pas très utile comme représentation graphique, car

plusieurs états simples n'ont pas de fonction P analytique. Par exemple, la fonction P positive pour un état cohérent est donnée par un delta de Dirac, $\rho = |\alpha_*\rangle\langle\alpha_*| \leftrightarrow P(\alpha, \beta) = \delta^2(\alpha - \alpha_*)\delta^2(\beta - \alpha_*)$. Par contre, la fonction P positive est utile pour des calculs analytiques, entre autres car elle permet d'évaluer des valeurs moyennes pour des opérateurs en ordre normal,

$$\left\langle \hat{a}^{\dagger m} \hat{a}^n \right\rangle = \int d^2\alpha d^2\beta \, \alpha^m \beta^n P(\alpha, \beta). \tag{2.10}$$

2.1.4 Électrodynamique quantique en guide d'onde

Comme expliqué à la section 2.1.2, l'électrodynamique quantique en circuit décrit la situation ou des qubits, ou plus généralement des modes non linéaires, sont couplés à un mode bosonique. L'électrodynamique quantique en guide d'onde (EDQg) décrit plutôt ce qui se passe lorsque plusieurs modes électromagnétiques sont couplés à un guide d'onde, c'est-à-dire à un continuum de modes bosoniques [21, 86, 9]. Deux configurations typiques d'EDQg sont illustrées à la figure 2.5. Dans cette section, je présente une introduction aux concepts pertinents à cette thèse et réfère le lecteur aux travaux de Lalumière *et al.* [86, 87] pour plus de détails.

Une situation standard d'EDQg est décrite par un Hamiltonien en trois parties,

$$\hat{H} = \hat{H}_q + \hat{H}_g + \hat{H}_{\text{int}}, \tag{2.11}$$

où $\hat{H}_q$ est l'Hamiltonien des transmons, $\hat{H}_g$ celui du guide d'onde et $\hat{H}_{\text{int}}$ l'interaction entre les deux. Dans la situation d'EDQg de base, l'Hamiltonien pour un ensemble de N transmons est simplement donné par

$$\hat{H} = \sum_{j=1}^{N} \omega_{q,j} \hat{b}_j^\dagger \hat{b}_j, \tag{2.12}$$

où l'indice j sert à différencier les différents transmons. Le guide d'onde, quant à lui, est décrit par un continuum de modes

$$\hat{H}_g = \int_0^\infty d\omega \, \omega \left[\hat{a}_D^\dagger(\omega) \hat{a}_D(\omega) + \hat{a}_G^\dagger(\omega) \hat{a}_G(\omega) \right], \tag{2.13}$$

où l'opérateur de champ $\hat{a}_D^\dagger(\omega)$ ($\hat{a}_G^\dagger(\omega)$) crée une excitation délocalisée de fréquence ω se propageant vers la droite (gauche). On considère une relation de dispersion linéaire, $\omega = v|k|$, avec v la vitesse de la lumière dans le guide d'onde.

Typiquement, la présence d'un tel continuum de modes mène à de la dissipation dans un bain Markovien et est peu intéressante. Cependant, dû au caractère unidimensionnel du guide d'onde, des effets collectifs apparaissent lorsque les ondes émises par les différents modes interfèrent entre elles [88]. Dans l'approximation séculaire, cette interaction est décrite par l'Hamiltonien

$$\hat{H}_{\text{int}} = \sum_j \int d\omega \, \sqrt{v\kappa_j} \left[\hat{a}_D(\omega) \hat{b}_j^\dagger \, \mathrm{e}^{-i\omega x_j/v} + \hat{a}_G(\omega) \hat{b}_j^\dagger \, \mathrm{e}^{i\omega x_j/v} \right] + c.h., \tag{2.14}$$

où x_j est la position du j-ième transmon dans le guide d'onde. Par convention, on calcule les distances par rapport au premier transmon, $x_1 \equiv 0$. De plus, je suppose ici que le couplage avec le guide d'onde et la fréquence des différents modes est uniforme, $\kappa_j = \kappa$ et $\omega_{q,j} = \omega_q \forall j$. L'objectif du formalisme d'EDQg est d'éliminer le guide d'onde du problème et de décrire seulement le comportement effectif des transmons.

Un premier cas de figure, illustré sur la figure 2.5a), est celui où deux transmons, sont couplés à un guide d'onde côte à côte $x_2 = 0$. Dans cette configuration, l'interaction avec le guide d'onde est donnée par

$$\hat{H}_{\text{int}} = \sqrt{v\kappa} \int d\omega \, (\hat{b}_1^\dagger + \hat{b}_2^\dagger) \left[\hat{a}_D(\omega) + \hat{a}_G(\omega) \right] + (\hat{b}_1 + \hat{b}_2) \left[\hat{a}_D^\dagger(\omega) + \hat{a}_G^\dagger(\omega) \right]. \tag{2.15}$$

À partir de cet Hamiltonien, on déduit que ce n'est plus les modes individuels des transmons, $\hat{b}_1$ ou $\hat{b}_2$, qui interagissent avec le guide d'onde, mais plutôt le mode collectif (normalisé) $\hat{b}_+ = (\hat{b}_1 + \hat{b}_2)/\sqrt{2}$. De manière plus intuitive, l'émission d'un photon par les deux modes interfère constructivement seulement si la phase entre ces deux modes est positive. En d'autres mots, seul l'état $|B\rangle = (|ge\rangle + |eg\rangle)/\sqrt{2}$ peut émettre ou absorber un photon dans le guide d'onde (en supposant la présence d'une seule excitation). À l'inverse, si la phase entre les deux modes est négative, $|D\rangle = (|ge\rangle - |eg\rangle)/\sqrt{2}$, il y a une interférence destructive, ce qui empêche l'émission et l'absorption de photons. En absence de déphasage, on a donc un état super-radiant, $|B\rangle$, et un état sombre métastable, $|D\rangle$.

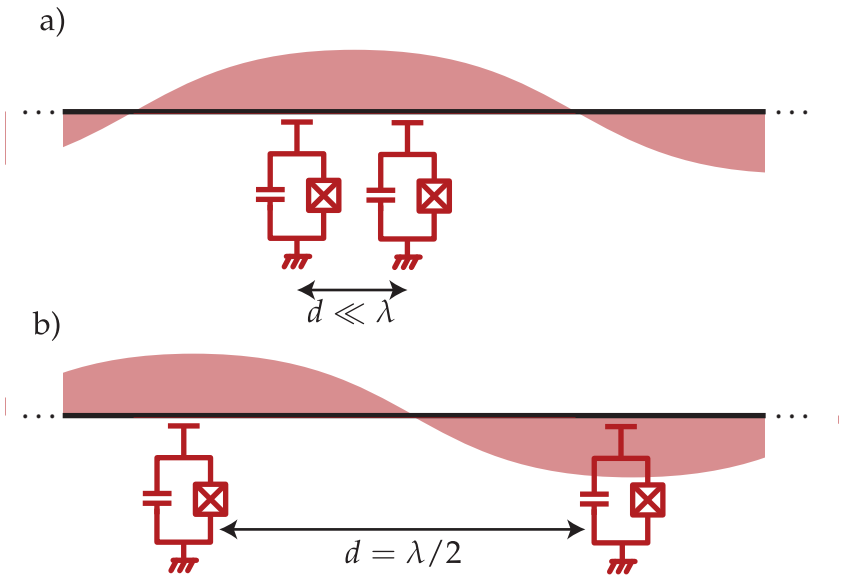

FIGURE 2.5 – Schémas de deux situations typiques en électrodynamique quantique en guide d'onde : deux transmons (rouge) sont couplés à un guide d'onde (noir) et émettent des photons de longueur d'onde $\lambda = 2\pi v/\omega_q$ (rouge pâle). Dans les deux cas, l'interférence dans le guide d'onde mène à un phénomène de dissipation collective, c'est-à-dire à la formation d'un état super-radiant et d'un état sombre métastable. a) Les deux transmons sont séparés par une distance $d \ll \lambda$. b) Les deux transmons sont séparés par une distance $d = \lambda/2$.

Dans le cas général ou N modes sont couplés côte à côte au même guide d'onde, le mode superradiant est donné par la superposition symétrique de tous les modes, $\hat{b}_+ = \sum \hat{b}_i/\sqrt{N}$, et le taux de dissipation de ce mode est multiplié par N, $\kappa_+ = N\kappa$. Un corolaire de ceci est que, dans le sous-espace à une excitation, tous les états orthogonaux à $\hat{b}_+ |0\rangle$ sont sombres (découplés du guide d'onde).

Un deuxième cas de figure, illustré sur la figure 2.5b), est celui où deux modes sont séparés par une distance correspondant à une moitié de longueur d'onde, $d = \lambda/2 \Rightarrow x_2 = \pi v/\omega_q$. Dans cette situation, les photons émis par les deux modes interfèrent constructivement si la phase est négative, $|B\rangle = (|ge\rangle - |eg\rangle)/\sqrt{2}$, et destructivement si la phase est positive, $|D\rangle = (|ge\rangle + |eg\rangle)/\sqrt{2}$. La situation illustrée à la figure 2.5b est donc similaire à celle illustrée à la figure 2.5a avec les états superradiants et sous-radiants inversés. L'opérateur de saut relié à cette situation est donné par $\hat{L} = \sqrt{2\kappa}\hat{b}_-$, avec $\hat{b}_- = (\hat{b}_1 - \hat{b}_2)/\sqrt{2}$.

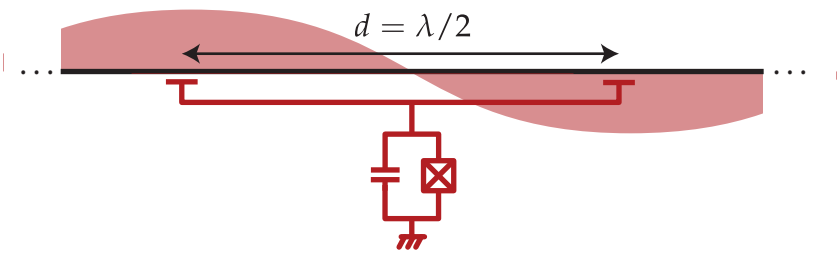

FIGURE 2.6 – Configuration particulière où, par interférence destructive, un transmon est effectivement découplé du guide d'onde.

Finalement, considérons la situation de mode géant illustrée sur la figure 2.6, où un seul mode $\hat{b}_1$ est couplé à deux positions différentes séparées par une distance $d = \lambda/2$. En suivant un résonnement similaire à la configuration 2.5b), l'émission à ces deux endroits interfère de manière destructive, ce qui découple effectivement le guide d'onde et le mode en question, $\hat{b}_- = (\hat{b}_1 - \hat{b}_1)/\sqrt{2} = 0$ [89].

Notons que lorsque deux systèmes sont couplés à une distance $d \neq n\pi/2$ avec $n \in \mathbb{N}$, une interaction cohérente apparait dans l'Hamiltonien. Étant donné que je ne fais pas référence davantage à ce phénomène dans cette thèse, je réfère le lecteur aux références [86, 9] pour plus de détails sur cette interaction. Finalement, étant donné la grande vitesse des photons micro-ondes ($v \sim c/3$), le temps de propagation entre différents systèmes ($d/v \sim 1$ cm$/v \sim 0.1$ ns) est généralement négligeable lorsqu'on le compare au temps de relaxation des systèmes en question ($1/\kappa \sim 1/(2\pi \times 5\,\text{MHz}) \sim 30$ ns) [90]. Conséquemment, on ne tient pas compte du délai de propagation entre les différents modes.

2.2 Systèmes quantiques ouverts

Lors de la modélisation de différents circuits supraconducteurs, il est important de prendre en compte le couplage avec l'extérieur, par exemple pour modéliser la mesure de ces systèmes. Dans cette section je passe brièvement en revue les outils utilisés pour modéliser les systèmes ouverts en mécanique quantique.

2.2.1 Équation maîtresse

On utilise en général l'équation maîtresse sous sa forme Linbladienne [91] pour simuler l'évolution des systèmes quantiques ouverts,

$$\dot{\rho} = -i[\hat{H}, \rho] + \sum_j \mathcal{D}[\hat{L}_j]\rho, \tag{2.16}$$

où $\hat{H}$ est l'Hamiltonien du système quantique, $\{\hat{L}_j\}$ sont un ensemble d'opérateurs de saut et $\mathcal{D}[\hat{L}_j]\bullet = \hat{L}_j \bullet \hat{L}_j^\dagger - \{\hat{L}_j^\dagger \hat{L}_j, \bullet\}/2$ dénote le superopérateur de dissipation. Le premier terme de l'équation 2.16 est équivalent à l'équation de Schrödinger et c'est le deuxième terme qui représente le couplage avec des systèmes extérieurs. À l'intérieur du superopérateur de dissipation, on distingue la contribution des sauts quantiques discrets $\hat{L} \bullet \hat{L}^\dagger$ du terme de normalisation, $\{\hat{L}^\dagger \hat{L}, \bullet\}/2$. Par exemple, dans le cas où un résonateur est couplé à une ligne à transmission, l'opérateur de saut est donné par $\hat{L} = \sqrt{\kappa}\hat{a}$ et le premier terme du superopérateur $\mathcal{D}$ représente la perte discrète d'un photon par saut quantique, alors que le deuxième terme représente la perte d'énergie déterministe à un taux κ du résonateur dans la ligne à transmission. Le tableau 2.2 liste plusieurs opérateurs de sauts correspondant à des couplages standards en EDQc.

Notons qu'une condition nécessaire et suffisante pour que l'équation 2.16 soit valide est que les bains soient markoviens, c'est-à-dire sans mémoire des états précédents. Cette condition est généralement respectée pour des systèmes EDQc.

Finalement, on peut aussi préciser la notion d'états sombres introduits à la section 2.1.4. Dans le contexte de l'équation maîtresse 2.16, un état $|\psi\rangle$ est sombre si

$$\hat{L}_i |\psi\rangle = 0 \; \forall \; i. \tag{2.17}$$

Pour la situation illustrée à la figure 2.5a), cette condition se traduit par $\hat{b}_+ |\psi\rangle = 0 \Rightarrow |\psi\rangle = (|eg\rangle - |ge\rangle)/\sqrt{2}$.

$\sqrt{\kappa}\hat{a}$	Dissipation d'un résonateur. On distingue parfois les pertes externes κ_{ext} vers un bain contrôlé tel qu'une ligne à transmission et les pertes internes κ_{int} vers un bain non contrôlé tel que le substrat des échantillons.
$\sqrt{\gamma}\hat{b}$	Temps de vie fini des transmons, $\gamma = \frac{1}{T_1}$.
$\sqrt{\gamma_\phi}\hat{b}^\dagger\hat{b}$	Déphasage pur des transmons, $\gamma_\phi = \frac{1}{T_2} - \frac{1}{2T_1}$.
$\sqrt{\gamma}\hat{\sigma}_-$	Temps de vie fini des qubits, $\gamma = \frac{1}{T_1}$.
$\sqrt{\frac{\gamma_\phi}{2}}\hat{\sigma}_z$	Déphasage pur des qubits, $\gamma_\phi = \frac{1}{T_2} - \frac{1}{2T_1}$.

TABLEAU 2.2 – Différents opérateurs de sauts, $\hat{L}$, typiquement utilisés en EDQc.

2.2.2 Représentations de canaux quantiques

L'équation maîtresse 2.16 permet de calculer comment un état initial évolue dans le temps vers un état final ρ_f. On utilise en général la fidélité d'état pour comparer la matrice de densité finale obtenue avec une autre matrice de densité ρ_0 [78],

$$\mathcal{F}_s(\rho_f, \rho_0) = \text{Tr}\left[\sqrt{\sqrt{\rho_0}\rho_f\sqrt{\rho_0}}\right]. \tag{2.18}$$

On veut aussi comparer des opérations (ou canaux) quantiques dans leur ensemble sans supposer d'état initial particulier. Il existe plusieurs représentations pour un canal quantique $\mathcal{E}$, telles que les opérateurs de Kraus, la représentation Stinespring et la représentation en superopérateur. Ici, j'utilise surtout la matrice de procédé χ (*process matrix*),

$$\mathcal{E}(\rho) = \sum_{mn} \chi_{mn}\hat{\sigma}_m\rho\hat{\sigma}_n, \tag{2.19}$$

où les $\hat{\sigma}_i$ forment une base d'opérateurs. Dans cette thèse, j'applique cette représentation à des opérations de qubits en choisissant la base des matrices Pauli avec la convention $\hat{\sigma}_0 = \hat{\mathbb{I}}$ et $\hat{\sigma}_2 = -i\hat{\sigma}_y$. On peut déterminer la matrice de procédé χ à partir de l'équation maîtresse en calculant l'évolution d'un ensemble complet d'états [78].

Il existe plusieurs méthodes pour comparer deux canaux quantiques. La fidélité de procédé (*process fidelity*) correspond à la norme d'Hilbert-Schmidt entre deux

matrices de procédé χ_1 et χ_2,

$$\mathcal{F}_p(\mathcal{E}_1, \mathcal{E}_2) = \mathrm{Tr}[\chi_1 \chi_2]. \tag{2.20}$$

Une autre méthode populaire pour comparer un canal quantique avec une opération unitaire $\hat{U}$ est la fidélité moyenne de porte (*average gate fidelity*), ici définie par rapport à une évolution unitaire,

$$\mathcal{F}_{\mathrm{av}}(\mathcal{E}, \hat{U}) = \int d\psi \, \langle\psi| \, \hat{U}^\dagger \mathcal{E} \left(|\psi\rangle\langle\psi| \right) \hat{U} \, |\psi\rangle \, . \tag{2.21}$$

Cette mesure correspond au recouvrement entre l'état après l'évolution idéale $\hat{U}$ et l'évolution donnée par $\mathcal{E}$, moyennée sur tous les états initiaux.

Afin de prendre en compte la fuite vers les niveaux supérieurs des transmons, la simulation d'opérations logiques sur des qubits est souvent faite en considérant plus que deux niveaux dans l'équation maîtresse 2.16. Pour calculer la fidélité de procédé ou la fidélité moyenne de porte, on utilise une base complète d'états initiaux seulement pour le sous-espace des qubits et on projette à la fin de l'évolution sur ce même sous-espace. Ainsi, la trace de la matrice de procédé, théoriquement égale à 1 pour un canal CPTP (*Completely-Positive, Trace-Preserving*) [78], fournit des renseignements sur la fuite vers des niveaux supérieurs.

2.2.3 Théorie entrée-sortie

Comme son nom l'indique, la théorie d'entrée-sortie (*input-output*) donne un formalisme qui permet de relier entre eux les champs d'entrée, les champs de sortie et les variables internes d'un système quantique [29]. La figure 2.7 représente graphiquement la situation décrite par l'équation centrale de cette théorie,

$$\hat{a}_{\mathrm{out}} = \hat{L} + \hat{a}_{\mathrm{in}}, \tag{2.22}$$

où $\hat{a}_{\mathrm{in/out}}$ dénotent les champs d'entrée/sortie respectant les relations de commutation $[\hat{a}_{\mathrm{in/out}}(t), \hat{a}^\dagger_{\mathrm{in/out}}(t')] = \delta(t - t')$. L'opérateur de saut $\hat{L}$ est le même que celui apparaissant dans l'équation maîtresse 2.16 et l'équation 2.22 est linéaire, car dans

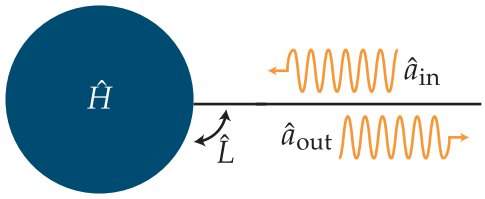

FIGURE 2.7 – La relation d'entrée-sortie 2.22 décrit les conditions frontière entre un système quantique décrit par un Hamiltonien $\hat{H}$ (rond bleu) et un bain unidimensionnel (guide d'onde représenté par une ligne noire). L'opérateur couplant le système quantique et ce bain est donné par $\hat{L}$, un opérateur ayant les dimensions de $\hat{H}$ et les dimensions d'un champ, $[\hat{L}] = \sqrt{\text{Hz}}$.

la grande majorité des cas le couplage entre le système quantique et le bain est de forme bilinéaire.

En pratique, on ne mesure jamais directement les observables de systèmes d'EDQc. On mesure toujours des champs de sortie et c'est la relation 2.22 qui permet de relier les mesures effectuées aux observables d'intérêts telles que l'état d'un qubit.

2.2.4 Systèmes en cascade

Il arrive régulièrement des situations où deux systèmes quantiques sont reliés en cascade, c'est-à-dire que le champ de sortie de l'un correspond au champ d'entrée de l'autre [92, 93]. La figure 2.8 présente de manière schématique cette situation, où le champ d'entrée (sortie) du j-ième système est noté par $\hat{a}_{j,\text{in}}$ ($\hat{a}_{j,\text{out}}$). Bien souvent, la transmission des signaux quantiques entre les deux systèmes est imparfaite, par exemple dû à l'ajout d'un circulateur. Ces pertes sont modélisées par un séparateur de faisceau (*beamsplitter*) hypothétique transmettant une fraction ν des photons entre les deux systèmes quantiques, $\hat{a}_{2,\text{in}} = \sqrt{\nu}\hat{a}_{1,\text{out}}$ [5].

On peut simuler cette situation en cascade à l'aide de l'équation maîtresse 2.16 en ajoutant un terme à l'Hamiltonien des systèmes 1 et 2 et en utilisant un terme de

5. Plus rigoureusement, on doit prendre en compte le bruit du vide, $\hat{a}_{2,\text{in}} = \sqrt{\nu}\hat{a}_{1,\text{out}} + \sqrt{1-\nu}\hat{h}_{\text{in}}$, afin de conserver les bonnes relations de commutation.

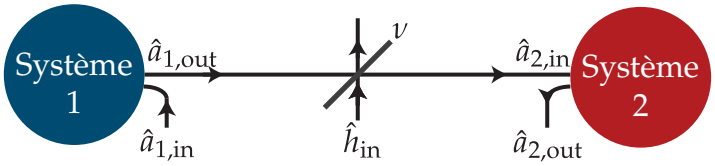

FIGURE 2.8 – Le champ de sortie du système 1 correspond au champ d'entrée du système 2. La perte de photons dans le transfert entre les deux systèmes quantiques est modélisée par un séparateur de faisceau de transparence ν, $\hat{a}_{2,\text{in}} = \sqrt{\nu}\hat{a}_{1,\text{out}}$.

dissipation collectif,

$$\hat{H}_{\text{cascade}} = \hat{H}_1 + \hat{H}_2 - i\frac{\sqrt{\nu\kappa_1\kappa_2}}{2}(\hat{a}_1\hat{a}_2^\dagger - \hat{a}_1^\dagger\hat{a}_2), \tag{2.23}$$

$$\begin{aligned}\hat{L}_{\text{cascade},1} &= \sqrt{(1-\nu)\kappa_1}\hat{a}_1,\\ \hat{L}_{\text{cascade},2} &= \sqrt{\nu\kappa_1}\hat{a}_1 + \sqrt{\kappa_2}\hat{a}_2,\end{aligned} \tag{2.24}$$

où $\hat{H}_j$ est l'Hamiltonien du j-ième système et $\hat{L}_j = \sqrt{\kappa_j}\hat{a}_j$ le terme de saut du j-ième système. On retrouve l'équation maîtresse de deux systèmes indépendants lorsque la transmission du canal est nulle, $\nu \to 0$.

Notons qu'ici aucune approximation n'est faite par rapport au délai de propagation τ entre les deux systèmes. En effet, même lorsque ce délai n'est pas négligeable, il est possible de redéfinir la variable de temps du deuxième système, $t \to t + \tau$. Dans cette situation, un seul temps est utilisé pour décrire le système combiné, mais il est important de retenir que $\rho_2(t+\tau) = \text{Tr}_1[\rho(t)]$. De plus, cette redéfinition est possible seulement parce qu'aucune information ne se propage depuis le deuxième système jusqu'au premier, évitant tout phénomène de rétroaction.

2.2.5 Mesure homodyne

Un type de mesure commun en EDQc est la mesure homodyne, mesurant une quadrature du champ de sortie, $\hat{X}_{\text{out},\varphi} = \hat{a}_{\text{out}}\,e^{i\varphi} + \hat{a}_{\text{out}}^\dagger\,e^{-i\varphi}$ [29]. Grâce à la relation d'entrée-sortie 2.22, il est facile de relier cette quadrature aux observables du système

quantique en observation. De plus, la phase φ peut être choisie de façon arbitraire en ajustant la phase d'une onde de référence appelée oscillateur local.

Étant donné que les signaux typiques en EDQc sont de très faible amplitude, il est essentiel de les amplifier avant de les mesurer. Les amplificateurs actuels ne sont pas parfaits et ajoutent du bruit dans le signal en plus de les amplifier [94]. On caractérise la quantité de bruit ajouté par l'efficacité de mesure homodyne, $0 \leq \eta_{\text{hom}} \leq 1$, et l'observable mesurée est en pratique donné par

$$\hat{M} = \sqrt{\eta_{\text{hom}}}(\hat{a}_{\text{out}}\, e^{i\varphi} + \hat{a}^{\dagger}_{\text{out}}\, e^{-i\varphi}). \tag{2.25}$$

La mesure hétérodyne est similaire à la mesure homodyne, à la différence que les deux quadratures du champ électromagnétique sont mesurées simultanément,

$$\begin{aligned} \hat{M}_1 &= \sqrt{\frac{\eta_{\text{hom}}}{2}}(\hat{a}_{\text{out}}\, e^{i\varphi} + \hat{a}^{\dagger}_{\text{out}}\, e^{-i\varphi}) + \frac{\hat{h}_{\text{in}}}{\sqrt{2}}, \\ \hat{M}_2 &= \sqrt{\frac{\eta_{\text{hom}}}{2}}(\hat{a}_{\text{out}}\, e^{i(\varphi+\pi)} + \hat{a}^{\dagger}_{\text{out}}\, e^{-i(\varphi+\pi)}) - \frac{\hat{h}_{\text{in}}}{\sqrt{2}}, \end{aligned} \tag{2.26}$$

où $\hat{h}_{\text{in}}$ est un opérateur de champ pour le bruit du vide. Les lois de la mécanique quantique interdissent en principe la mesure simultanée des deux quadratures du champ. La mesure hétérodyne permet d'y arriver en séparant premièrement le signal en deux, par exemple à l'aide d'un séparateur de faisceau 50/50, puis en réalisant une mesure homodyne sur chacun des signaux de sortie en choisissant deux angles de mesures distincts, φ et $\varphi + \pi$. Le prix à payer pour ceci est un signal plus faible (le facteur $1/\sqrt{2}$) et l'ajout de bruit du vide ($\hat{h}_{\text{in}}$) provenant du deuxième port d'entrée du séparateur de faisceau.

2.2.6 Trajectoires quantiques

Le fait d'effectuer une mesure en mécanique quantique mène à l'effondrement de la fonction d'onde. Plus généralement, pour une mesure décrite par un POVM (*Positive-Operator Valued Measure*) [78], $\{\hat{M}_j\}$, la matrice de densité ρ' décrivant l'état

minimalement perturbé [6] après la mesure de l'opérateur $\hat{M}_j$ est donnée par

$$\rho' = \frac{\hat{M}_j \rho \hat{M}_j^\dagger}{\mathrm{Tr}[\hat{M}_j \rho \hat{M}_j^\dagger]}, \tag{2.27}$$

Dans le cas d'une mesure continue, par exemple la mesure homodyne décrite dans la section précédente, cette mise à jour doit se faire de manière continue. Dans le cas typique où l'on mesure le champ de sortie d'un résonateur, l'équation 2.27 prend la forme d'une équation maîtresse stochastique [29],

$$d\rho_c = -i[\hat{H}, \rho_c]dt + \sum_j \gamma_j \mathcal{D}[\hat{L}_j]\rho_c \, dt + \sqrt{\kappa \eta_{\mathrm{hom}}}\mathcal{H}[\hat{a}\, e^{i\varphi}]\rho_c \, dW, \tag{2.28}$$

où l'effet de la mesure est inclus dans le superopérateur $\mathcal{H}[\hat{a}\, e^{i\varphi}]\bullet = \hat{a}\, e^{i\varphi} \bullet + \bullet \hat{a}^\dagger e^{-i\varphi} - \mathrm{Tr}[\hat{a}\, e^{i\varphi} \bullet + \bullet \hat{a}^\dagger e^{-i\varphi}]\bullet$ et la variable aléatoire dW représente les fluctuations du champ quantique de sortie. Mathématiquement, cette variable est décrite par un processus de Wiener, c'est-à-dire une variable aléatoire caractérisée par une moyenne d'ensemble $E[dW] = 0$ et une variance $E[dW^2] = dt$. Le résultat de la mesure homodyne dans cette situation est donné par

$$j_{\mathrm{hom}}(t) = \sqrt{\kappa \eta_{\mathrm{hom}}} \langle \hat{X}_\varphi \rangle + \xi(t), \tag{2.29}$$

où on note la quadrature de mesure $\hat{X}_\varphi = \hat{a}\, e^{i\varphi} + \hat{a}^\dagger e^{-i\varphi}$ et le bruit du vide $\xi(t) = dW/dt$. Afin d'extraire une valeur s à partir de $j_{\mathrm{hom}}(t)$, on utilise un filtre f,

$$s = \int dt\, f(t) j_{\mathrm{hom}}(t), \tag{2.30}$$

où la forme du filtre est optimisée selon l'information à extraire.

L'équation maîtresse stochastique 2.28 permet ainsi de simuler *une* réalisation d'une expérience donnée, alors que l'équation maîtresse standard 2.16 donne seulement accès aux moyennes d'ensemble. Dans l'équation 2.28, on distingue l'état quantique conditionné sur la mesure homodyne, ρ_c, de l'état utilisé dans l'équation maîtresse standard, ρ, qu'on peut retrouver à l'aide d'une moyenne d'ensemble,

6. Dans le cas complètement général, l'appareil de mesure peut générer une évolution selon un canal quantique $\mathcal{E}_i$ dépendant de la mesure et l'état final après la mesure est donné par $\rho'' = \mathcal{E}_i(\rho')$, où ρ' est calculé à partir de l'équation 2.27.

$\rho = E[\rho_c]$. On retrouve l'équation maîtresse standard 2.16, à partir de l'équation maîtresse stochastique de la même façon, $E[\dot{\rho}_c] = \dot{\rho}$.

Notons que la forme de l'équation 2.28 est valable seulement pour une mesure homodyne. Une mesure différente du champ de sortie, par exemple avec un détecteur de photon ou une mesure hétérodyne, mène à une rétroaction différente sur le système quantique et conséquemment une équation maîtresse stochastique différente [95].

Chapitre 3

Détection de photons micro-ondes uniques

3.1 Contexte général

Avant de discuter plus en détail la physique des détecteurs de photons, il est utile de préciser la notion de photon micro-onde itinérant. Dans cette thèse, j'étudie des circuits généralement réalisés en aluminium, un matériau qui possède une température critique (T_C) de 1,2 K $\sim$ 25 GHz [96]. Pour des températures expérimentales typiques de 15 mK $\sim$ 300 MHz, la population de quasi-particules peut donc généralement être négligée et seulement les paires de Cooper peuvent être excitées. [1], ce qui implique que les excitations se propagent sans dissipation. De plus, la force de Coulomb implique que les champs électriques sous la fréquence plasma ne peuvent pas pénétrer l'aluminium et les oscillations plasma sont donc absentes. Conséquemment, pour un morceau d'aluminium isolé, tous les degrés de liberté sont gelés dans leur état fondamental [73]. Lorsqu'on inclut des plans de masse et des capacités, des modes collectifs acoustiques apparaissent dans les fréquences micro-ondes d'intérêt (1 - 10 GHz) avec une dispersion linéaire $\omega = vk$ [87], où ω est la fréquence angulaire, v la vitesse de propagation et k le vecteur d'onde. Ces modes

1. Des expériences récentes semblent montrer qu'à basse température les quasi-particules ne suivent pas un équilibre thermique et leur présence est une source de décohérence non négligeable pour les qubits supraconducteurs [97, 98, 99, 100]. Dans cette thèse j'ignore ce type d'effet.

collectifs sont les photons micro-ondes itinérants. Due aux dimensions des circuits étudiés dans cette thèse (typiquement 10 μm $\times$ 100 nm $\times$ 1 - 1000 cm), on peut considérer que ces photons se propagent dans un médium à une seule dimension $k \in \mathbb{R}$. Ce caractère unidimensionnel est crucial, car il permet, entre autres, d'éviter tous les problèmes d'ajustement de mode (*mode matching*) habituellement présents pour les photons optiques se propageant dans l'air. Pour donner des ordres de grandeur, la vitesse typique des photons considérés dans cette thèse est d'environ $v \sim c/3$ avec c la vitesse de la lumière dans le vide, ce qui correspond à une longueur d'onde $\lambda \sim 2$ cm pour un photon de 5 GHz.

Ayant mieux cerné ce en quoi consiste les photons micro-ondes itinérants, je me penche maintenant sur la première partie originale de cette thèse, c'est-à-dire la conception de dispositifs permettant de mesurer ces photons. Je distingue ici les photons localisés, c'est-à-dire ceux d'un mode de résonateur, et les photons itinérants se propageant dans une ligne à transmission. Cette distinction est importante, car les défis à relever pour mesurer l'un ou l'autre sont différents. La mesure de photons localisés a d'ailleurs déjà été réalisée dans des systèmes d'EDQc [101, 102, 103], alors que la mesure de photons itinérants reste un problème ouvert (ou l'était lorsque j'ai commencé à travailler sur ce sujet).

L'approche que nous avons poursuivie pour aborder ce défi est la suivante. Afin de mesurer un photon itinérant, l'information contenue dans un état de Fock, $|0\rangle$ ou $|1\rangle$, est convertie vers un état cohérent, $|\alpha_0\rangle$ ou $|\alpha_1\rangle$. La mesure homodyne introduite à la section 2.2.5 permet ensuite de distinguer ces deux états cohérents et donc de mesurer la présence ou l'absence du photon. Un mode étant dans un état classique ($|\alpha_{0/1}\rangle$) permettant de distinguer deux états quantiques ($|0/1\rangle$) est généralement appelé un mode pointeur [104], en analogie avec un appareil de mesure analogique possédant une aiguille pointant vers une valeur particulière. Comme illustré à la figure 3.1, on a donc un schéma général de détection de photon décomposé en trois étapes :

1. Absorption du photon dans le mode de capture B [2],

2. Dans la figure 3.1, le photon est représenté par une fonction d'onde en exponentielle décroissante. C'est la forme du photon utilisée dans l'article de la section 3.2.2. Ce choix est motivé par le fait que c'est la forme la plus facile à réaliser expérimentalement en excitant un qubit et en le laissant relaxer naturellement.

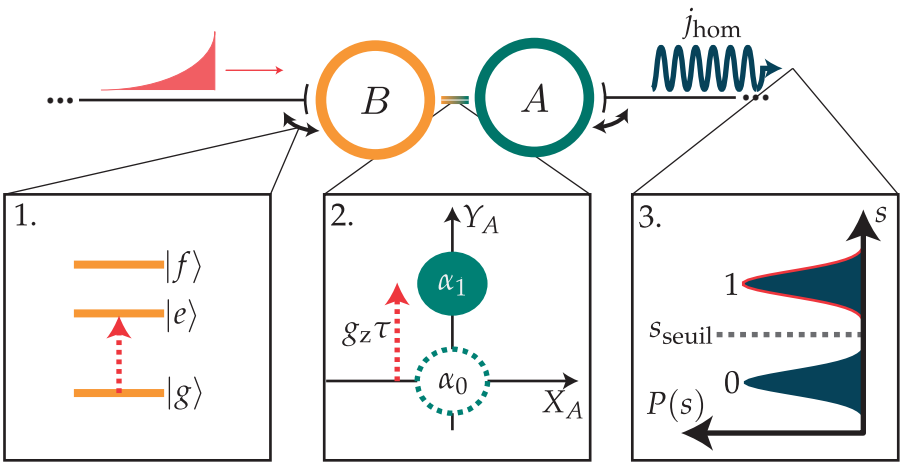

FIGURE 3.1 – 1. Le photon de signal (rouge) est absorbé par le mode de capture B (orange) qui passe de l'état $|g\rangle$ à l'état $|e\rangle$. 2. La présence d'une excitation dans le mode B induit un déplacement dans l'état cohérent du mode pointeur A, $|\alpha_0\rangle \rightarrow |\alpha_1\rangle$. 3. Le champ de sortie est envoyé à une mesure homodyne qui est filtrée et donne une valeur s qui permet de déterminer si un photon est présent lorsqu'elle dépasse une valeur seuil s_{seuil} (pointillé gris). La probabilité d'obtenir une certaine valeur $P(s)$ est, dans le cas idéal, séparée en deux distributions distinctes.

2. Interaction pendant un temps τ avec le mode pointeur A menant à une séparation d'états cohérents $|\alpha_{0/1}\rangle$,
3. Mesure homodyne du champ de sortie du mode pointeur A.

Les différentes étapes énumérées plus haut représentent une aide conceptuelle et non pas nécessairement une séquence d'étapes distinctes. De plus, la mesure homodyne étant un élément standard des expériences d'EDQc à ce jour, j'apporte des solutions seulement pour les deux premières étapes. Je note par $\hat{b}$ l'opérateur d'échelle du mode de capture B ($[\hat{b}, \hat{b}^\dagger] = 1$) et par $\hat{a}$ celui du mode pointeur A ($[\hat{a}, \hat{a}^\dagger] = 1$).

Considérons d'abord une interaction entre le mode pointeur A et le mode d'absorption B de la forme

$$\hat{H} = g_z \hat{b}^\dagger \hat{b} (\hat{a} + \hat{a}^\dagger). \tag{3.1}$$

L'Hamiltonien 3.1 représente un cas d'école de mesure quantique, où l'observable qu'on désire mesurer, $\hat{b}^\dagger \hat{b}$, est couplée au générateur de déplacement d'un mode

pointeur, $\hat{a} + \hat{a}^\dagger$. Après un temps d'interaction τ, la quadrature $\hat{Y}$ du mode pointeur est déplacée de $g_z\tau$, comme illustré sur la figure 3.1. Ainsi, pour un déplacement plus grand que les fluctuations du vide, $g_z\tau > 1$, il est possible de distinguer la présence d'un photon dans le mode B. Dans la situation illustrée à la figure 3.1, on considère que le mode de capture B est couplé au guide d'onde de signal avec une amplitude κ_B, fixant ainsi le temps d'interaction avec le mode A à $\tau = 1/\kappa_B$. Afin de maximiser le déplacement dans le mode pointeur, le régime de paramètre optimal est donc donné par $g_z/\kappa_B \gg 1$.

Le problème se complique lorsqu'on considère le problème d'absorption (étape 1). En effet, l'effet Zénon quantique stipule qu'un système mesuré constamment est bloqué dans son état initial [105, 106, 107]. Plus précisément, lorsque l'intervalle de temps entre chaque mesure est plus court que la vitesse d'évolution du système quantique, les projections répétées vers le sous-espace initial gèlent le système dans son système initial. Dans la situation illustrée à la figure 3.1, on peut considérer que le nombre d'excitations du système B est mesuré à un taux g_z par le système A et la transition entre l'état $|g\rangle$ et $|e\rangle$ se fait dans un temps donné par $1/\kappa_B$. Afin de minimiser la rétroaction de la mesure due à l'effet Zénon quantique [3], le régime de paramètre optimal est donc $g_z/\kappa_B \ll 1$, ce qui est incompatible avec l'étape 2 décrite plus haut. De façon équivalente, on peut voir cette rétroaction de la mesure comme induisant des fluctuations dans la fréquence de résonance du mode de capture B, $\omega_B \rightarrow \hat{\omega}_B = \omega_B + g_z\hat{X}$. Dû aux fluctuations du vide, on peut considérer que la bande d'absorption du mode B est, à chaque instant, centrée sur une valeur aléatoire entre $\omega_B \pm g_z/2$ (voir figure 1b de la section 3.2.2). Lorsque ces fluctuations sont plus grandes que la largeur de bande κ_B, ce phénomène empêche un photon signal d'être absorbé par le mode de capture B.

Considérant conjointement les étapes 1 et 2 illustrées à la figure 3.1, ce schéma mène à un cul-de-sac paramétrique et de nouvelles solutions sont nécessaires. J'ai travaillé sur deux méthodes permettant de surmonter les défis mentionnés plus haut : les deux articles qui en résultent sont présentés aux sections 3.2 et 3.3. Le premier

3. Ici, l'utilisation du terme effet Zénon quantique n'est pas complètement adéquate. En effet, cette rétroaction est présente même dans le cas où le mode pointeur est fermé, c'est-à-dire où le mode pointeur a un facteur de qualité infini. On peut alors se demander si cette situation hypothétique, où aucune information ne quitte le mode pointeur, constitue une situation de mesure quantique. Dans l'article, nous avons choisi d'utiliser un terme plus faible : effet de *type* Zénon (*Zeno-like effect*).

d'entre eux propose d'utiliser un ensemble fini d'absorbeur pour capturer un photon, je réfère à cet article comme étant la version discrète du détecteur de photons. Le deuxième article propose plutôt d'absorber le photon dans un métamatériau, qu'on modélise par un continuum de modes d'absorption. J'utilise le terme de détecteur continu pour référer à cette version.

3.1.1 Caractéristiques d'un détecteur de photons

Avant de présenter nos propositions pour la réalisation de détecteurs de photons, j'introduis les différentes caractéristiques servant à les décrire.

Efficacité et bruit de comptage (*dark counts*)
L'efficacité η est définie comme la probabilité que le dispositif détecte un photon en supposant qu'un photon est envoyé [17],

$$\eta = P(1|1). \tag{3.2}$$

Pour calculer cette quantité numériquement, je simule des N trajectoires quantiques où un photon est envoyé au détecteur. À partir du signal homodyne filtré de sortie, s, chaque trajectoire est analysée et classifiée comme évènement de détection lorsque $s > s_{\text{seuil}}$, où s_{seuil} est une valeur seuil fixée au préalable. L'efficacité est ensuite donnée par le ratio entre le nombre de trajectoires classifiées comme évènement de détection et le nombre total de trajectoires, $\eta = N_1/N$. Expérimentalement, cette méthode requiert de pouvoir envoyer un photon unique au détecteur.

Le taux de bruit de comptage Γ_{sombre} est défini comme le taux auquel le détecteur annonce un évènement de détection sans photon de signal,

$$\Gamma_{\text{sombre}} = P(1|0)/\tau_m, \tag{3.3}$$

où τ_m est un temps de mesure caractéristique du détecteur. Ce taux peut être calculé de manière similaire à l'efficacité en n'envoyant aucun photon de signal au détecteur.

Une autre méthode pour mesurer l'efficacité d'un détecteur de photons uniques est d'utiliser des impulsions cohérentes comme signal et de varier le nombre moyen

de photons $\bar{n}$ compris dans ces états cohérents [31]. Ainsi, il est possible d'extraire la relation $P(1|\bar{n})$, à partir de laquelle on calcule l'efficacité, $\eta = \lim_{\bar{n}\to 0} \partial P(1|\bar{n})/\partial\bar{n}$. La limite à faible nombre de photons sert à éviter les potentiels effets de saturation dus à la présence de $n \geq 2$ photons dans l'impulsion cohérente. Avec cette méthode, le taux de bruit de comptage est donné par $P(1|\bar{n} = 0)/\tau_m$. Telle que calculée avec cette méthode, l'efficacité est strictement plus faible que lorsqu'elle est calculée avec l'équation 3.2, car elle soustrait la contribution des faux positifs, $P(1|0)$, à l'efficacité. Cette méthode est plus facile à implémenter expérimentalement, car elle ne requiert pas de source à photons uniques. Par contre, elle requiert une calibration précise du nombre moyen de photons $\bar{n}$ incidents au détecteur.

Dans les travaux qui suivent, la définition 3.2 est utilisée à cause de sa simplicité et de sa signification opérationnelle. Cependant, il est important de souligner que cette valeur prend du sens seulement si elle mentionné avec Γ_{sombre}, ou alors si le bruit de comptage est très faible, $\Gamma_{\text{sombre}} \to 0$. Dans le cas contraire, il est facile de tricher pour obtenir une $\eta = 1$ en choisissant $s_{\text{seuil}} \to -\infty$, une situation où le détecteur est complètement inutile.

Fidélité

La fidélité de la mesure est une mesure pertinente lorsque le détecteur donne une réponse binaire, 0 ou 1. Par exemple, on pourrait être intéressé de distinguer la présence ou l'absence d'un photon dans un intervalle de temps donné. L'efficacité est, à l'inverse, plus adaptée pour caractériser un détecteur opérant en mode continu. On définit la fidélité de la mesure, $\mathcal{F}$, comme la probabilité que le résultat annoncé par le détecteur corresponde à l'état mesuré [108, 33, 34],

$$\mathcal{F} = \frac{1}{2}\left(1 + \eta - P(1|0)\right), \tag{3.4}$$

en supposant que $P(0) = P(1) = 1/2$.

Une autre définition de la fidélité utilisée dans la littérature est donnée par $\mathcal{F} = 1 - P(1|0) - P(0|1)$ [16, 109]. Cette définition, strictement inférieure à celle donnée par l'équation 3.4, correspond à la moyenne des corrélations entre le résultat annoncé et l'état mesuré lorsqu'on identifie l'état sans photons 0 à la valeur numérique -1.

Non-démolition quantique

On définit un détecteur de photons non-démolition quantique (NDQ) comme un dispositif préservant le photon après un évènement de détection. Plus précisément, on appelle NDQ un détecteur qui préserve la fonction d'onde du photon détecté.

Résolution en temps

Dans cette thèse, je me suis intéressé à développer des détecteurs de photons qui permettent non seulement de déterminer la présence d'un photon unique, mais aussi le temps t auquel le photon arrive au détecteur. Cette caractéristique est utile dans une situation où l'émission de photons micro-ondes se fait de façon aléatoire, par exemple lorsque cette émission résulte d'une interaction avec la matière noire [24]. De plus, lorsque le temps d'émission est connu, ce type de détecteur permet de reconstruire la fonction d'onde des photons à partir d'histogrammes de temps de détection (voir figure 4 de l'article 3.2.2). À l'inverse, plusieurs détecteurs de photons sont ouverts pendant un intervalle de temps fini et ne révèlent qu'un seul bit d'information : la présence ou non d'un photon dans cet intervalle de temps. Ce type de détecteur [109, 110, 111] est approprié pour des applications en communications quantiques, où le temps d'arrivée des photons est généralement prédéterminé [4]. On peut ajouter que l'effet Zénon quantique n'est présent que pour les détecteurs à la fois résolus en temps et NDQ, imposant une limite intrinsèque à cette catégorie de détecteur.

Réponse du détecteur à n photons

Un détecteur de photon unique devrait évidemment détecter la présence d'un photon unique. Cependant, plusieurs différences existent lorsqu'on considère plusieurs photons dans le signal d'entrée. Le premier type de détecteur, et le plus difficile à réaliser, est le détecteur résolu en nombre qui permet de distinguer la présence de n photons. Le deuxième type de détecteur détecte plutôt la parité du nombre de photons, n modulo 2. Ce type de détecteur est utile, par exemple, pour créer des états de chats [112] s'il est NDQ en plus. Le troisième type de détecteur à seuil annonce un évènement de détection dès que le signal d'entrée contient plus de photons qu'une valeur seuil, $n \geq n_{\text{seuil}}$, où typiquement $n_{\text{seuil}} = 1$.

4. Les communications quantiques se basant sur un encodage temporel sont aussi incluses dans cette catégorie ; le temps d'arrivée d'un photon peut alors prendre plusieurs valeurs différentes. Crucialement, les fenêtres de détection possibles sont prédéterminés et il est possible de réinitialiser le détecteur entre chacune d'elles.

Plusieurs autres caractéristiques sont utilisées pour décrire les détecteurs de photons [17]. On peut mentionner par exemple le temps de récupération (*dead time*) après un évènement de détection et l'incertitude en temps (*timing jitter*) pour les détecteurs résolus en temps. La largeur de bande est aussi une caractéristique importante. Notamment, le détecteur proposé à la section 3.3.2 est le seul promettant une largeur de bande de l'ordre du GHz.

Le tableau 3.1 synthétise les différentes propositions théoriques et réalisation expérimentales pour des détecteurs de photons, les comparants sur certaines des caractéristiques introduites plus haut. Les travaux présentés dans cette thèse sont en violet, les autres travaux théoriques en blanc et les réalisations expérimentales en vert. J'ai tenté de ramener les performances de chacun de ces articles aux définitions données par les équations 3.2 et 3.3. Cependant, étant donné la disparité des définitions et méthodes de mesure utilisées, cette comparaison ne devrait pas être prise au pied de la lettre. Par exemple, certains articles théoriques négligent les imperfections expérimentales et rapportent une efficacité parfaite, $\eta = 1$. Finalement, la largeur de bande est absente de ce tableau, car peu d'articles décrivent précisément cette caractéristique. Les articles sont placés en ordre chronologique de publication.

	η (%)	Γ_{sombre} μs^{-1}	NDQ	Résolution en temps
Romero *et al.* (2009) [30]	100	0	✘	✘
Helmer *et al.* (2009) [31]	31*		✓	✓
Chen *et al.* (2011) [37]	70**		✘	✘
Peropadre *et al.* (2011) [32]	100		✘	✘
Koshino *et al.* (2013) [33]			✘	✘
Sathyamoorthy *et al.* (2014) [34]	90		✓	✓
Fan *et al.* (2014) [35]	90		✓	✓
Koshino *et al.* (2016) [36]	90	0.007	✘	✓
Inomata *et al.* (2016) [39]	66*	0.037	✘	✘
Narla *et al.* (2016) [38]	40	0.025	✓	✓
Kyriienko *et al.* (2016) [113]	95	0.09	✘	✘
Oelsner *et al.* (2017) [20]			✘	✓
Wong *et al.* (2017) [114]	98		✘	✘
Leppäkangas *et al.* (2018) [115]	90	0.63	✘	✓
Kono *et al.* (2018) [110]	84*	0.02	✓	✘
Besse *et al.* (2018) [109]	84	0.24	✓	✘
Royer *et al.* (2018) [40]	92	0.004	✓	✓
Opremcak *et al.* (2018) [116]		0.003	✘	✘
Lescanne *et al.* (2019) [111]	58	0.001	✓	✘
Grimsmo *et al.* (2019) XX	99		✓	✓

* : Méthode d'états cohérents
** : Efficacité définie comme $P(1|0)(1 - P(0|1))$

TABLEAU 3.1 – Comparaison entre différents détecteurs de photons uniques dans les micro-ondes. Les travaux présentés dans cette thèse sont en violet et les travaux expérimentaux sont en vert. Étant donné les grandes variations dans les métriques utilisées et les ressources nécessaires à l'implémentation de ces dispositifs, la comparaison entre ces différentes méthodes ne devrait pas être prise de façon trop littérale. Certaines cases sont laissées vides lorsque l'information contenue dans les articles est insuffisante.

3.2 Détecteur de photons micro-ondes uniques, version discrète

3.2.1 Contexte

Nous avons vu à la section précédente que le modèle d'absorption à un mode de la figure 3.1 mène à une dichotomie paramétrique où l'on cherche à obtenir simultanément $g/\kappa_B \gg 1$ (grand déplacement) et $g/\kappa_B \ll 1$ (faible rétroaction). Afin de résoudre ce problème, une solution est d'augmenter le temps d'interaction τ entre le mode pointeur A et le mode de capture B sans augmenter l'effet de rétroaction de la mesure. Dans le contexte de la figure 3.1, cela se traduit par la recherche d'une configuration où $\tau \gg 1/\kappa_B$. Dans cet article, je considère que la largeur de bande du détecteur, κ_B, reste fixe.

Une première méthode est d'utiliser un système de type Λ comme illustré sur la figure 3.2, où un photon incident génère une transition entre deux états $|g\rangle$ et $|e\rangle$. L'idée centrale ici est un mécanisme de dissipation supplémentaire $\kappa_{e\to m}$ depuis l'état $|e\rangle$ vers un état métastable $|m\rangle$ [30, 32, 37, 117, 118, 39, 113, 114, 20, 116, 115, 111]. Il est en suite possible de mesurer la population de l'état $|m\rangle$ sans les limitations du schéma 3.1, car le temps d'interaction avec le mode pointeur τ est donné par le temps de vie de l'état $|m\rangle$ [5]. Il existe différentes versions de cette proposition, mais une difficulté récurrence est de respecter la condition d'ajustement d'impédance, $\kappa_B = \kappa_{e\to m}$.

La méthode développée durant ma thèse se base sur un phénomène différent et exploite plutôt un ensemble d'absorbeurs pour capturer le photon incident. Comme il avait déjà été remarqué par Fan *et al.* [119], le simple fait d'augmenter le nombre d'absorbeur ne mène pas à une situation plus avantageuse que celle illustrée à la figure 3.1. En effet, pour un ensemble homogène d'absorbeurs, seul l'état superradiant collectif se couple au signal (voir section 2.1.4), une situation formellement équivalente au schéma 3.1, et donc héritant des mêmes problèmes. L'idée centrale présentée dans l'article 3.2.2 est d'utiliser un ensemble *inhomogène* d'absorbeurs,

5. J'ai omis le mode pointeur de la figure 3.2, car dans certains cas l'état m est un état classique pouvant être mesuré directement [37, 20, 116].

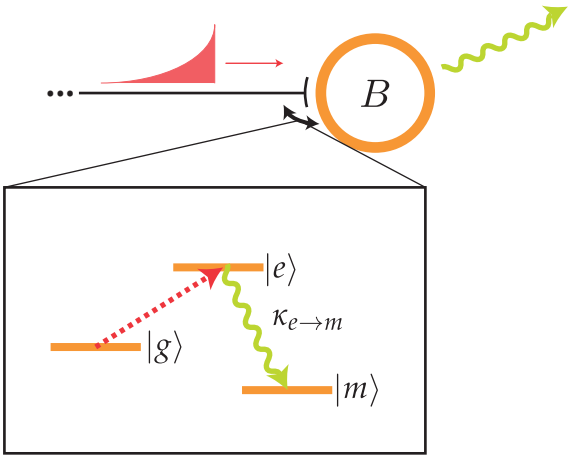

FIGURE 3.2 – 1. Le photon de signal (rouge) est absorbé par le mode de capture B (orange) qui passe de l'état $|g\rangle$ à l'état $|e\rangle$. Un mécanisme de dissipation engendre une transition irréversible de l'état $|e\rangle$ vers l'état $|m\rangle$ (vert pâle). La présence du photon de signal est donc détectée en mesurant la population de l'état $|m\rangle$. Ce type de détecteur peut être rendu NDQ lorsque le processus de dissipation $\kappa_{e\to m}$ est effectué dans un canal contrôlé.

où il est possible de stocker temporairement un photon de signal dans les états sombres [6].

Dans ce design, il n'y a pas de processus menant à la destruction du photon signal et, après l'absorption, le photon est réémis dans le guide d'onde. Suivant cette intuition, une méthode pour caractériser le temps de capture est de regarder la fonction d'onde du photon réémis par l'ensemble d'absorbeurs où le délai dû au stockage dans les états sombres apparaît clairement. Ce phénomène est illustré à la figure 3.3 pour différents nombres d'absorbeurs. Pour ce graphique, la fonction d'onde du photon d'entrée (gris) est donnée par $\left\langle \hat{b}^\dagger_{\text{in}} \hat{b}_{\text{in}}(t) \right\rangle = \kappa_C \, \mathrm{e}^{-\kappa_C t} (\kappa_C t)^2/2$, avec une largeur de bande du photon beaucoup plus petite que la largeur de bande du détecteur, $\kappa_C = \kappa_B/10$. Le temps $\kappa_B t = 0$ correspond au moment où le photon arrive au détecteur et on trace la fonction d'onde du photon après réflexion sur l'ensemble d'absorbeurs pour $N = 2$ (jaune), $N = 4$ (vert pâle), $N = 6$ (vert foncé) [7].

6. Techniquement, ces états ne sont plus parfaitement sombres et le terme quasi sombre serait plus approprié. Afin de simplifier le texte, j'utilise le terme sombre quand même.

7. Le cas $N = 6$ est absent de l'article

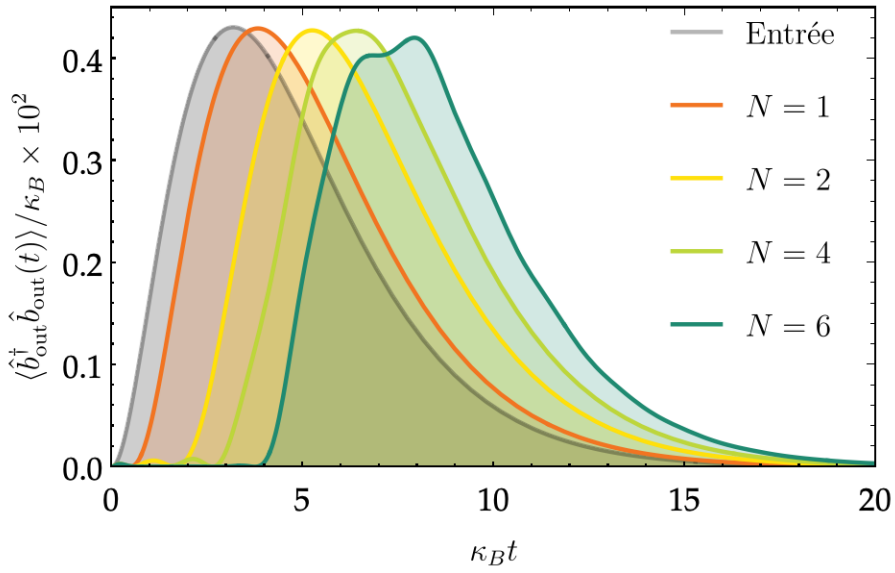

FIGURE 3.3 – Fonction d'onde du photon signal après réflexion sur l'absorbeur (courbes colorées). La courbe grise indique la fonction d'onde du photon avant l'absorption par le détecteur. Le décalage entre la courbe grise et les courbes colorées indique un temps de capture du photon dans le détecteur.

Pour un seul absorbeur (orange), $N = 1$, le photon est réfléchi après un temps $\tau \approx 1/\kappa_B$ et il est clair que ce délai augmente avec N.

Ce type de physique a déjà été étudié avec comme but la réalisation de mémoires photoniques. Pour un faible nombre d'absorbeurs, une augmentation du temps de capture a été observée avec des magnons [120]. Les ensembles de spins représentent aussi une réalisation pratique de cette idée aux fréquences optiques et dans la limite d'un très grand nombre d'absorbeurs [121, 122, 123, 124, 125, 126, 127, 128, 129].

Un élément essentiel du détecteur de photon présenté ici est l'implémentation d'un Hamiltonien généralisant l'équation 3.1, soit

$$\hat{H} = g_z \sum_{i=1}^{N} \hat{b}_i^\dagger \hat{b}_i (\hat{a} + \hat{a}^\dagger), \tag{3.5}$$

où le déplacement du mode pointeur A est proportionnel au nombre *total* de photons dans l'ensemble d'absorbeurs. Cet Hamiltonien permet de surmonter les limitations imposées par l'effet Zénon quantique, car la rétroaction de la mesure affecte seule-

ment l'absorption par l'état super-radiant couplé au guide d'onde de signal, alors que le résonateur mesure le nombre de photons dans tous les états de l'ensemble.

Finalement, il est intéressant de mentionner que les détecteurs NDQ peuvent être placés en cascade pour améliorer l'efficacité totale [34, 35]. Dans ce type de configuration, la fidélité de la mesure augmente avec le nombre de détecteurs au prix d'une plus grande complexité expérimentale. Notamment, ces configurations requièrent l'utilisation de circulateurs entre chacun des détecteurs, ce qui rend cette approche peu attrayante.

3.2.2 Article

L'idée d'utiliser le couplage longitudinal pour la détection de photons uniques a été avancée par Jérôme Bourrassa et Nicolas Didier suite à leur papier traitant de la mesure de qubit utilisant un couplage longitudinal [130]. J'ai rapidement repris le projet et, avec Arne Grimsmo, nous avons étudié l'effet de rétroaction de la mesure sur l'efficacité du détecteur. J'ai ensuite développé la méthode des états sombres qui permet d'augmenter le temps d'interaction entre le mode de capture et le mode pointeur, faisant la plupart des calculs analytiques et des simulations présentées dans l'article. Alexandre Choquette-Poitevin a participé aux simulations numériques visant à optimiser les paramètres du détecteur durant son stage à l'été 2017 et Alexandre Blais a supervisé le tout. J'ai écrit le manuscrit avec l'aide de tous les auteurs. Le matériel supplémentaire pour cet article se trouve en annexe B.1.

Erratum
Dans le paragraphe en bas à droite de la page 3, les références aux figures devraient toutes lire figure 3 et non figure 4.

Baptiste Royer, Arne L. Grimsmo, Alexandre Choquette-Poitevin et Alexandre Blais. Itinerant microwave photon detector. *Phys. Rev. Lett.* **120**, 203602 (2018)

Itinerant Microwave Photon Detector

Baptiste Royer,[1,*] Arne L. Grimsmo,[1,2] Alexandre Choquette-Poitevin,[1] and Alexandre Blais[1,3]
[1]Institut quantique and Département de Physique, Université de Sherbrooke, 2500 boulevard de l'Université, Sherbrooke, Québec J1K 2R1, Canada
[2]Centre for Engineered Quantum Systems, School of Physics, The University of Sydney, Sydney, New South Wales 2006, Australia
[3]Canadian Institute for Advanced Research, Toronto, Ontario M5G 1Z8, Canada

(Received 24 October 2017; published 16 May 2018)

The realization of a high-efficiency microwave single photon detector is a long-standing problem in the field of microwave quantum optics. Here, we propose a quantum nondemolition, high-efficiency photon detector that can readily be implemented in present state-of-the-art circuit quantum electrodynamics. This scheme works in a continuous fashion, gaining information about the photon arrival time as well as about its presence. The key insight that allows us to circumvent the usual limitations imposed by measurement backaction is the use of long-lived dark states in a small ensemble of inhomogeneous artificial atoms to increase the interaction time between the photon and the measurement device. Using realistic system parameters, we show that large detection fidelities are possible.

DOI: 10.1103/PhysRevLett.120.203602

Introduction.—While the detection of localized microwave photons has been realized experimentally [1–3], high-efficiency detection of single *itinerant* microwave photons remains an elusive task [4]. Such detectors are increasingly sought after due to their applications in quantum information processing [5–7], microwave quantum optics [8], quantum radars [9–11], and even the detection of dark matter axions [12].

In recent years, a large number of microwave photon detector proposals have been put forward [13–21], and some proof-of-principle experiments have been performed [7,22–24]. For their operation, many of these proposals rely on *a priori* information about the photon arrival time [7,14,15,17,24,25], limiting their applicability. In this Letter, we are rather interested in continuous detectors, where the arrival time of a photon can be inferred *a posteriori* [13,16,18–23]. Moreover, we also focus on nondestructive detection of photons [4,13,19,25]. This property proves to be useful in a number of applications, such as quantum networks [5,6] and the study of quantum measurement [26]. A challenge in designing continuous single photon detectors is set by the quantum Zeno effect, which loosely states that the more strongly a quantum system is measured the less likely it is to change its state [27–29]. Any nonheralded photon detection scheme based on absorbing the photon into a medium thus faces the problem that strong continuous measurement reduces the absorption efficiency and thus the photon detection efficiency [13].

In this Letter, we introduce a nondestructive and continuous microwave photon detector that circumvents this measurement backaction problem with minimal device complexity, without requiring any active control pulses, and avoiding the use of nonreciprocal elements [19,20]. In essence, our proposal relies on absorbing a signal photon in a medium made of an ensemble of inhomogeneous artificial atoms, where the presence of long-lived dark states allows us to increase the effective lifetime of photons inside this composite absorber without lowering its bandwidth. We show that high detection efficiencies can be obtained by weakly and continuously monitoring the ensemble excitation number. We also present a simple circuit-QED design implementing this idea [30,31], where an ensemble of transmon qubits [32] are continuously measured through standard dispersive measurement.

Single-absorber detector.—Before introducing our proposal based on an ensemble of artificial atoms, we first study a simple single-absorber model and motivate our solution by explaining how the quantum efficiency of such a scheme is fundamentally limited due to quantum mechanical backaction effects. This simple model is illustrated in Fig. 1(a), where a signal photon (red) traveling along an input waveguide is absorbed into a single "absorber" mode B (orange) at a rate κ_B. This first mode is coupled to a second "measurement" harmonic mode A (green) which decays at a rate κ_A into an output port continuously measured using a standard homodyne measurement chain (not shown). In this toy model, we assume that the two modes are coupled by the longitudinal interaction ($\hbar = 1$),

$$\hat{H}_I = g_z \hat{b}^\dagger \hat{b} (\hat{a} + \hat{a}^\dagger), \tag{1}$$

where $\hat{a}$ and $\hat{b}$ are the annihilation operators of modes A and B, respectively. This interaction implements a textbook photon number measurement: the measured observable $\hat{b}^\dagger \hat{b}$ is coupled to the generator of displacement of a pointer

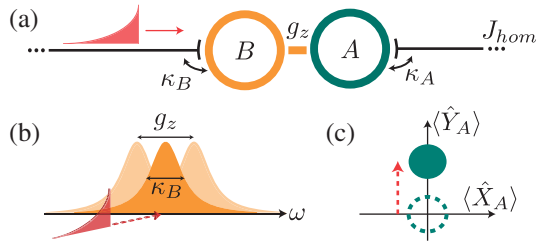

FIG. 1. (a) Sketch of a single absorber model for photon detection. A signal photon (red) is absorbed in a mode B and induces a coherent state displacement in a harmonic mode A which is measured using homodyne measurement. (b) Coupling between A and B induces fluctuations in the absorption spectrum of mode B, preventing the absorption of incoming photons. (c) Illustration of phase space for mode A as a photon is absorbed in B.

state $\hat{X}_A = \hat{a} + \hat{a}^\dagger$. As schematically illustrated in Fig. 1(c), the homodyne measurement of the orthogonal quadrature $\hat{Y}_A = -i(\hat{a} - \hat{a}^\dagger)$ allows us to precisely measure the photon number *inside* the absorber mode B without destroying the photon.

In order to induce a displacement in mode A, a signal photon however needs to first enter mode B, an unlikely process at large coupling strengths g_z. Indeed, as schematically illustrated in Fig. 1(b), $\hat{H}_I$ induces quantum fluctuations of the absorber's frequency which can prevent it from absorbing the arriving photon. This quantum fluctuation-induced spectral mismatch can be interpreted as a quantum Zeno-like effect since the width of these fluctuations directly relates to the measurement strength through g_z [29]. In order to minimize this unwanted measurement backaction, the width of these fluctuations, compared with the absorber's linewidth g_z/κ_B, should ideally be minimized. On the other hand, the displacement of the measurement mode A, which is given roughly by g_z/κ_B as well, should be maximized to improve the detection efficiency [33]. The optimal quantum efficiency of this toy model is obtained by balancing these two conflicting requirements. Numerically, we find an optimal operating point at $g_z/\kappa_B = 1$, the smallest coupling strength for which the induced displacement is distinguishable from vacuum noise $\langle\hat{Y}_A^2\rangle_{\text{vacuum}} = 1$.

Numerical Simulations.—To model the signal photon arriving at the detector, a source mode C is introduced, with a frequency matching the absorber mode B, $\omega_C = \omega_B$. To minimize reflection, we take the signal photon linewidth to be much smaller than the absorber's linewidth, $\kappa_C/\kappa_B = 0.1$. Following the experiments of Refs. [34,35], this mode is initialized with one excitation leading to a signal photon emission with an exponentially decaying waveform.

The quantum efficiency of this simple photon detector is calculated by simulating multiple realizations of the above scenario and computing the corresponding homodyne current out of the measurement mode A. This is realized by numerically integrating the stochastic master equation [26],

$$d\rho = \mathcal{L}\rho dt + \sqrt{\eta_h\kappa_A}\mathcal{H}[-i\hat{a}]\rho dW,$$
$$\hat{H} = \hat{H}_I - \frac{i\sqrt{\kappa_B\kappa_C}}{2}(\hat{c}\hat{b}^\dagger - \hat{c}^\dagger\hat{b}), \tag{2}$$

where $\hat{c}$ is the annihilation operator of the source mode C and $\mathcal{L}\bullet$ is the Linbladian superoperator $\mathcal{L}\bullet = -i[\hat{H}, \bullet] + \sum_j \mathcal{D}[\hat{L}_j]\bullet$ with $\hat{L}_1 = \sqrt{\kappa_A}\hat{a}$, $\hat{L}_2 = \sqrt{\kappa_B}\hat{b} + \sqrt{\kappa_C}\hat{c}$. The combination of the term coupling $\hat{c}$ and $\hat{b}$ in $\hat{H}$ and of the composite decay operator $\hat{L}_2$ assures that the output of mode C is cascaded to the input of mode B [36,37]. Moreover, η_h is the homodyne measurement chain efficiency, $\mathcal{D}[\hat{L}]\bullet = \hat{L}\bullet\hat{L}^\dagger - \frac{1}{2}\{\hat{L}^\dagger\hat{L}, \bullet\}$ is the dissipation superoperator, and $\mathcal{H}[\hat{a}]\bullet = \hat{a}\bullet + \bullet\hat{a}^\dagger - \langle\hat{a} + \hat{a}^\dagger\rangle\bullet$ is the homodyne measurement backaction superoperator. The Wiener process dW is a random variable with the statistical properties $E[dW] = 0$ and $E[dW^2] = dt$, where $E[\bullet]$ denotes an ensemble average. For each trajectory, the resulting homodyne current is given by $J_{\text{hom}}(t) = \sqrt{\eta_h\kappa_A}\langle\hat{Y}_A\rangle + dW/dt$ [26]. Here and below, we use $N_{\text{traj}} = 2000$ trajectories and, to focus solely on the characteristics of the photodetector itself, assume a perfect homodyne detection chain $\eta_h = 1$.

For each homodyne current realization, we consider a photon is detected if the convolution of the signal with a filter, $\bar{J}_{\text{hom}}(t) = J_{\text{hom}}(t) \circ f(t)$, exceeds a threshold value Y_{thr}. To give more weight to times where the signal is, on average, larger, we use $f(t) \propto \langle\hat{Y}_A(t)\rangle_{\text{ME}}$ computed by solving the standard unconditional master equation [20]. The quantum efficiency $\eta = N_{\text{click}}/N_{\text{traj}}$ is then computed, where N_{click} is the number of trajectories where a photon is detected [38]. Although with this model no prior information about the photon arrival time is needed, if this information is available, the measurement can be restricted to a time window of length τ_m. In that case, a better metric is the measurement fidelity $\mathcal{F} = \frac{1}{2}(\eta + 1 - \Gamma_{\text{dark}} \times \tau_m)$ [17,19], where Γ_{dark} is the dark count rate, i.e., the rate at which the detector "clicks" without a signal photon. To maximize the detector repetition rate, τ_m is set to the smallest value that maximizes the fidelity.

For the single absorber model with $g_z/\kappa_B = 1$ and $\kappa_A/\kappa_B = 0.2$, we obtain an efficiency of 79% with $\Gamma_{\text{dark}}/\kappa_B = 1.4 \times 10^{-3}$ and a fidelity of $\mathcal{F} = 82\%$ for a time window of $\kappa_B\tau_m = 125$. The detector dead time after a detection event is given by the reset time of the measurement mode A back to vacuum. This corresponds to several decay times $1/\kappa_A$ or, alternatively, can be sped up by using active reset approaches [39–41].

This scheme is similar to previously studied models [13,20,42], and although it leads to relatively large

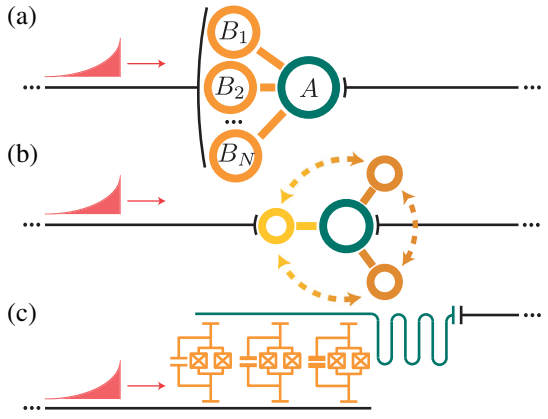

FIG. 2. (a) Absorber B is replaced by an ensemble of inhomogeneous modes coupled at the same point of the input waveguide. (b) Redrawing of (a) in the bright and dark states basis for $N = 3$. (c) Possible circuit-QED implementation for $N = 3$. Tunable transmon qubits acting as absorbers are coupled capacitively on one side to an input transmission line and on the other side to a measurement resonator.

detection fidelities, the resulting displacement of mode A is small, $\langle \hat{Y}_A \rangle \sim g_z/\kappa_B = 1$. In this situation, adding an imperfect homodyne measurement chain $\eta_h < 1$ leads to a significant reduction of the quantum efficiency.

Absorption into an ensemble.—As already pointed out, the key issue with using a single absorber is that both the total displacement of the measurement mode A and the measurement backaction on B scale with g_z/κ_B. This stems from the fact that the time spent in a simple resonant system is given by the inverse of its bandwidth. In order to increase the quantum efficiency, we thus present a scheme where the interaction time with the photon is increased while keeping the ratio g_z/κ_B constant.

As schematically illustrated in Fig. 2(a), we first replace the single absorber by a small ensemble of $N \lesssim 5$ artificial atoms, and second, we inhomogeneously detune each atom with respect to the average ensemble frequency. By connecting these absorbers approximately to the same point of the input waveguide [43], symmetry imposes that the absorbers state, after the absorption of a photon, should be invariant under permutation. The only state satisfying this condition is the all-symmetric superposition of excitation in the absorbers $\hat{b}_+ = 1/\sqrt{N}\sum_i \hat{b}_i$, which we refer to as the bright state [44,45]. Other nonsymmetric states, which we call dark states, completely decouple from the waveguide and are long lived. We, furthermore, design the coupling to the measurement mode A such that the measured observable is $\hat{N}_B = \sum_i \hat{b}_i^\dagger \hat{b}_i$, the total photon number in the ensemble. In this case, the ideal interaction picture Hamiltonian becomes

$$\hat{H}_I^E = g_z \hat{N}_B \hat{X}_A + \sum_{i=1}^{N} \Delta_i \hat{b}_i^\dagger \hat{b}_i, \tag{3}$$

where $\Delta_i = \omega_{Bi} - \omega_B \lesssim \kappa_B$ is the ith atom detuning with respect to the average ensemble frequency $\omega_B = \sum_i \omega_{Bi}/N$, and the first term represents the direct generalization of Eq. (1) for an ensemble of atoms.

In this model, a signal photon is absorbed in the collective bright state $\hat{b}_+$ at a rate scaling linearly with N. Without loss of generality and to fix the effective collective absorption rate of the absorbers at κ_B, we choose the bare linewidth of the atoms to be $\kappa_{Bi} = \kappa_B/N$. In the case where the atoms are on resonance $\Delta_i = 0 \ \forall \ i$, the bright and dark subspaces are uncoupled, and the model becomes equivalent to the single absorber model illustrated in Fig. 1(a) [46].

On the other hand, nonhomogeneous detunings $\Delta_i \neq \Delta_j$ lead to coupling of the bright and dark subspaces. If this coupling is carefully adjusted, a signal photon can be absorbed into the bright state, transferred to a long-lived dark state, and after some time τ_{trap}, return to the bright state where it is re-emitted. Figure 2(b) illustrates this process schematically with the bright state (yellow) being coupled to $N - 1$ dark states (dark orange). In practice, this process is optimized by having equally spaced detunings. Crucially, changing the detunings affects neither the coupling strength g_z nor the effective linewidth κ_B, leaving the measurement backaction unaffected. On the other hand, the total displacement induced in the measurement mode A is changed from g_z/κ_B to roughly $g_z \times (1/\kappa_B + \tau_{\text{trap}})$. As a result, by increasing τ_{trap} and reducing g_z, we can thus, as desired, significantly increase the quantum efficiency by simultaneously increasing the induced displacement and reducing the measurement backaction. In practice, τ_{trap} can be made longer by increasing the number of dark states where the photon can get trapped (i.e., increasing N) and optimizing the detunings $\vec{\Delta}$ accordingly [47]. In the large N limit, the mechanism leading to τ_{trap} is reminiscent of photon memories using inhomogeneous spin ensembles [49–52].

We perform full stochastic master equation simulations using Eq. (2) with the replacements $\hat{b} \to \hat{b}_+$, $\hat{H}_I \to \hat{H}_I^E$ and show the increase in measurement fidelity $\mathcal{F}$ as a function of ensemble size in Fig. 3(a). As shown in Fig. 4(b), for $N = 4$, a quantum efficiency of $\eta = 92\%$ is obtained at a low estimated dark count rate $\Gamma_{\text{dark}}/\kappa_B = 7 \times 10^{-6}$. For a time window of $\kappa_B \tau_m = 126$, this translates to the measurement fidelity of $\mathcal{F} = 96\%$ observed in Fig. 4(a). As illustrated in Fig. 4(b), the threshold Y_{thr} can be varied to trade a higher dark count rate for a higher efficiency or the converse. Here, Γ_{dark} is computed from trajectories with no signal photon (full lines) and, where it is too small to be precisely calculated from trajectories, estimated from time correlations in the filtered signal from vacuum (colored dashed lines) [47].

Importantly, due to the increased interaction time, the measured homodyne signal increases with N and, for $N = 4$, is already much larger than vacuum noise. As a

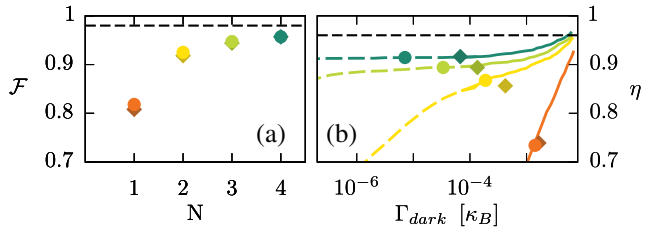

FIG. 3. (a) Fidelity as a function of the number of absorbers. The circles are calculated using the ideal model with $\kappa_A/\kappa_B = 0.2$, $g_z^{(1)}/\kappa_B = 1$, $g_z^{(2)}/\kappa_B = 0.6$, $g_z^{(3)}/\kappa_B = 0.5$, and $g_z^{(4)}/\kappa_B = 0.4$ with the detunings $\vec{\Delta}^{(2)}/\kappa_B = (0.55, -0.55)$, $\vec{\Delta}^{(3)}/\kappa_B = (0.7, -0.7, 0)$, and $\vec{\Delta}^{(4)}/\kappa_B = (0.7, -0.7, 0.23, -0.23)$. The diamonds are calculated using realistic parameters for a transmon ensemble dispersively coupled to a resonator with $\kappa_B/2\pi = 10$ MHz, $g_z/\chi = 10$, and T_1, $T_2 = 30$ μs. (b) Detector efficiency as a function of the dark count rate. Solid lines correspond to statistics extracted from trajectories, while for the dashed lines Γ_{dark} was estimated using an analytical formula. The lines were calculated for the ideal model, and the points indicate where the fidelity is maximized. The black dashed line in (a) and (b) correspond the upper bound $\eta_{\max}$ imposed by the photon shape used here.

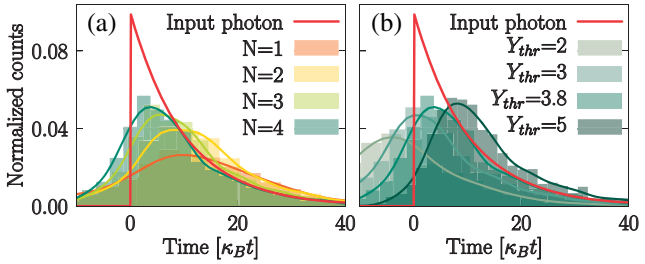

FIG. 4. (a) Normalized number of detection events as a function of time for (a) different number of absorbers in the ideal model Eq. (3) and for (b) different thresholds for $N = 4$. In both (a) and (b), the input photon shape (red) is shown for comparison and an arbitrary time offset has been substracted from the homodyne signal.

result, the detector becomes increasingly robust to potential imperfections in the homodyne detection chain ($\eta_h < 1$). We, moreover, expect the quantum efficiency to continue increasing as the number of absorbers is raised above 4. For $N \geq 5$, the required Hilbert space size for numerical simulations is impractically large. Nevertheless, at $N = 4$, the performance is already close to an expected maximum of $\eta_{\max} \sim 96\%$ indicated by the black dashed line in Figs. 3(a) and 3(b). This upper bound is due to high frequency components of the signal photon that are directly reflected from the absorber and thus do not lead to a detectable signal in mode A [47]. This upper bound value is linked to the choice of both detector and signal photon parameters and could be improved upon further optimization.

Since our proposal is continuous, the time τ_c at which the homodyne signal crosses the threshold reveals information about the photon arrival time. Figure 4 shows histograms of the normalized number of counts for τ_c, as recorded from trajectories where a photon is detected. In Fig. 4(a), the number of absorbers is varied, and the signal threshold Y_{thr} is set to optimize the fidelity (see Fig. 3). On the other hand, in Fig. 4(b), we set $N = 4$ and vary the threshold. In both Figs. 4(a) and 4(b), the input photon shape (red) is shown for comparison. As the threshold increases, the distribution of crossing times narrows and the precision on the photon arrival time therefore increases. As mentioned above, increasing N leads to larger homodyne signals. Hence, adding more absorbers allows us to increase the threshold which, in turn, improves the arrival time precision. Moreover, since $1/\kappa_C$ is the longest timescale in these simulations, at $N = 4$ the photon shape can be resolved from the histogram. The mismatch between the distribution and the red line near $\kappa_B t = 0$ is due to the sharp, high frequency feature of the input photon that is reflected from the absorbers without detection.

Physical implementation.—A possible implementation of this model, based on dispersive coupling of transmon qubits, is illustrated in Fig. 2(c). Here, an ensemble of superconducting transmon qubits is capacitively coupled on one side to a transmission line and on the other side to a measurement resonator (mode A) with coupling strength g. We take a large detuning between the qubits center frequency ω_B and the resonator frequency $\omega_r - \omega_B \gg \kappa_A, \kappa_B, g$ and use the standard dispersive approximation [47]. The absorption of a signal photon by the qubits induces a shift in the resonator frequency which is detected by continuously probing the resonator with a coherent drive corresponding to a field amplitude α [30]. In this situation, we find that the system of Fig. 2(c) is well described by the displaced dispersive Hamiltonian [47],

$$\hat{H}_\chi^D = g_z \hat{N}_B \hat{X}_A + \sum_{i=1}^{N} \Delta_i \hat{b}_i^\dagger \hat{b}_i + 2\chi \hat{N}_B \hat{a}^\dagger \hat{a} + \Delta_+ \hat{b}_+^\dagger \hat{b}_+, \quad (4)$$

where χ is the usual transmon dispersive shift [32,47], $g_z = 2\chi\alpha$, and Δ_+ results from a combination of the resonator-induced Lamb shift and spurious qubit-qubit coupling [47]. The first two terms correspond exactly to the ideal model Hamiltonian Eq. (3), while the two additional last terms are small and imposed by this specific implementation.

As the diamonds in Fig. 3 show, at $\alpha = 5$, the two additional terms in Eq. (4) have a minimal impact on the quantum efficiency. Moreover, it is possible to mitigate the detrimental effect of a small Δ_+ by adjusting the detunings $\vec{\Delta}$.

As an example, choosing realistic parameters $N = 4$, $\kappa_B/2\pi = 10$ MHz, $\kappa_A/2\pi = 2$ MHz, $\chi/2\pi = 0.4$ MHz, $\alpha = 5$, and $\vec{\Delta}/2\pi = (6.6, -7.4, 2.3, -2.3)$ MHz and using current transmon decoherence times T_1, $T_2 = 30$ μs [53],

we obtain $\eta = 92\%$ with $\Gamma_{\mathrm{dark}} = 4.2 \times 10^{-3}\ \mu\mathrm{s}^{-1}$. Given a time window of $\tau_m = 2\ \mu$s, this corresponds to a large measurement fidelity of $F = 96\%$.

Conclusion.—We have presented a high-efficiency, nondestructive scheme for itinerant microwave photon detection where no prior information about the photon arrival time is needed. This scheme is based on the continuous measurement of the photon number in an ensemble of inhomogeneous artificial atoms where the photon can be stored for long times due to the existence of long-lived dark states. We also presented a realistic physical implementation of this idea using an ensemble of transmon qubits dispersively coupled to a single resonator. Using only four transmons, we estimate that fidelities as high as 96% are attainable for the photon shape considered, and we expect that adding more transmons will improve this fidelity even further. Since the output signal is proportional to the total number of photons, the same model could be used as a photon-number resolving detector. Future work will investigate this possibility.

We thank Jérôme Bourassa and Nicolas Didier for suggesting this project, Stéphane Virally for useful discussions, and Jean-Claude Besse for comments on the manuscript. Part of this work was supported by the Army Research Office under Grant No. W911NF-14-1-0078 and the Natural Sciences and Engineering Research Council of Canada (NSERC). This research was undertaken thanks in part to funding from the Canada First Research Excellence Fund and the Vanier Canada Graduate Scholarships.

*baptiste.royer@usherbrooke.ca

[1] S. Gleyzes, S. Kuhr, C. Guerlin, J. Bernu, S. Deleglise, U. Busk Hoff, M. Brune, J.-M. Raimond, and S. Haroche, Nature (London) **446**, 297 (2007).
[2] B. R. Johnson, M. D. Reed, A. A. Houck, D. I. Schuster, L. S. Bishop, E. Ginossar, J. M. Gambetta, L. DiCarlo, L. Frunzio, S. M. Girvin, and R. J. Schoelkopf, Nat. Phys. **6**, 663 (2010).
[3] D. I. Schuster, A. A. Houck, J. A. Schreier, A. Wallraff, J. M. Gambetta, A. Blais, L. Frunzio, J. Majer, B. Johnson, M. H. Devoret, S. M. Girvin, and R. J. Schoelkopf, Nature (London) **445**, 515 (2007).
[4] S. R. Sathyamoorthy, T. M. Stace, and G. Johansson, C.R. Phys. **17**, 756 (2016).
[5] N. Gisin and R. Thew, Nat. Photonics **1**, 165 (2007).
[6] H. J. Kimble, Nature (London) **453**, 1023 (2008).
[7] A. Narla, S. Shankar, M. Hatridge, Z. Leghtas, K. M. Sliwa, E. Zalys-Geller, S. O. Mundhada, W. Pfaff, L. Frunzio, R. J. Schoelkopf, and M. H. Devoret, Phys. Rev. X **6**, 031036 (2016).
[8] C. Gardiner and P. Zoller, *Quantum Noise: A Handbook of Markovian and Non-Markovian Quantum Stochastic Methods with Applications to Quantum Optics*, Springer Series in Synergetics (Springer, New York, 2004).
[9] S. Lloyd, Science **321**, 1463 (2008).
[10] S.-H. Tan, B. I. Erkmen, V. Giovannetti, S. Guha, S. Lloyd, L. Maccone, S. Pirandola, and J. H. Shapiro, Phys. Rev. Lett. **101**, 253601 (2008).
[11] S. Guha and B. I. Erkmen, Phys. Rev. A **80**, 052310 (2009).
[12] S. K. Lamoreaux, K. A. van Bibber, K. W. Lehnert, and G. Carosi, Phys. Rev. D **88**, 035020 (2013).
[13] F. Helmer, M. Mariantoni, E. Solano, and F. Marquardt, Phys. Rev. A **79**, 052115 (2009).
[14] G. Romero, J. J. García-Ripoll, and E. Solano, Phys. Rev. Lett. **102**, 173602 (2009).
[15] C. H. Wong and M. G. Vavilov, Phys. Rev. A **95**, 012325 (2017).
[16] O. Kyriienko and A. S. Sørensen, Phys. Rev. Lett. **117**, 140503 (2016).
[17] K. Koshino, K. Inomata, T. Yamamoto, and Y. Nakamura, Phys. Rev. Lett. **111**, 153601 (2013).
[18] K. Koshino, Z. Lin, K. Inomata, T. Yamamoto, and Y. Nakamura, Phys. Rev. A **93**, 023824 (2016).
[19] S. R. Sathyamoorthy, L. Tornberg, A. F. Kockum, B. Q. Baragiola, J. Combes, C. M. Wilson, T. M. Stace, and G. Johansson, Phys. Rev. Lett. **112**, 093601 (2014).
[20] B. Fan, G. Johansson, J. Combes, G. J. Milburn, and T. M. Stace, Phys. Rev. B **90**, 035132 (2014).
[21] J. Leppäkangas, M. Marthaler, D. Hazra, S. Jebari, G. Johansson, and M. Hofheinz, Phys. Rev. A **97**, 013855 (2018).
[22] Y.-F. Chen, D. Hover, S. Sendelbach, L. Maurer, S. T. Merkel, E. J. Pritchett, F. K. Wilhelm, and R. McDermott, Phys. Rev. Lett. **107**, 217401 (2011).
[23] G. Oelsner, C. K. Andersen, M. Rehák, M. Schmelz, S. Anders, M. Grajcar, U. Hübner, K. Mølmer, and E. Il'ichev, Phys. Rev. Applied **7**, 014012 (2017).
[24] K. Inomata, Z. Lin, K. Koshino, W. D. Oliver, J.-S. Tsai, T. Yamamoto, and Y. Nakamura, Nat. Commun. **7**, 12303 (2016).
[25] A. Reiserer, S. Ritter, and G. Rempe, Science **342**, 1349 (2013).
[26] H. Wiseman and G. Milburn, *Quantum Measurement and Control* (Cambridge University Press, Cambridge, England, 2010).
[27] B. Misra and E. C. G. Sudarshan, J. Math. Phys. (N.Y.) **18**, 756 (1977).
[28] K. Kraus, Found. Phys. **11**, 547 (1981).
[29] P. Facchi and S. Pascazio, Phys. Rev. Lett. **89**, 080401 (2002).
[30] A. Blais, R.-S. Huang, A. Wallraff, S. M. Girvin, and R. J. Schoelkopf, Phys. Rev. A **69**, 062320 (2004).
[31] A. Wallraff, D. I. Schuster, A. Blais, L. Frunzio, R. S. Huang, J. Majer, S. Kumar, S. M. Girvin, and R. J. Schoelkopf, Nature (London) **431**, 162 (2004).
[32] J. Koch, T. M. Yu, J. Gambetta, A. A. Houck, D. I. Schuster, J. Majer, A. Blais, M. H. Devoret, S. M. Girvin, and R. J. Schoelkopf, Phys. Rev. A **76**, 042319 (2007).
[33] The displacement $\sim g_z/\kappa_B$ corresponds to the interaction strength multiplied by the typical photon lifetime inside B.
[34] A. A. Houck, D. I. Schuster, J. M. Gambetta, J. A. Schreier, B. R. Johnson, J. M. Chow, L. Frunzio, J. Majer, M. H. Devoret, S. M. Girvin, and R. J. Schoelkopf, Nature (London) **449**, 328 (2007).
[35] D. Bozyigit, C. Lang, L. Steffen, J. M. Fink, C. Eichler, M. Baur, R. Bianchetti, P. J. Leek, S. Filipp, M. P. da Silva, A. Blais, and A. Wallraff, Nat. Phys. **7**, 154 (2011).

[36] C. W. Gardiner, Phys. Rev. Lett. **70**, 2269 (1993).
[37] H. J. Carmichael, Phys. Rev. Lett. **70**, 2273 (1993).
[38] R. H. Hadfield, Nat. Photonics **3**, 696 (2009).
[39] D. T. McClure, H. Paik, L. S. Bishop, M. Steffen, J. M. Chow, and J. M. Gambetta, Phys. Rev. Applied **5**, 011001 (2016).
[40] C. C. Bultink, M. A. Rol, T. E. O'Brien, X. Fu, B. C. S. Dikken, C. Dickel, R. F. L. Vermeulen, J. C. de Sterke, A. Bruno, R. N. Schouten, and L. DiCarlo, Phys. Rev. Applied **6**, 034008 (2016).
[41] S. Boutin, C. K. Andersen, J. Venkatraman, A. J. Ferris, and A. Blais, Phys. Rev. A **96**, 042315 (2017).
[42] G. J. Milburn and S. Basiri-Esfahani, Proc. R. Soc. A **471**, 20150208 (2015).
[43] In practice, the distance d between the artificial atoms should be much smaller than their wavelength $d \ll 2\pi v_0/\omega_B$, with v_0 the speed of light in the waveguide and ω_B the atoms frequency.
[44] K. Lalumière, B. C. Sanders, A. F. van Loo, A. Fedorov, A. Wallraff, and A. Blais, Phys. Rev. A **88**, 043806 (2013).
[45] A. F. van Loo, A. Fedorov, K. Lalumière, B. C. Sanders, A. Blais, and A. Wallraff, Science **342**, 1494 (2013).
[46] B. Fan, A. F. Kockum, J. Combes, G. Johansson, I.-c. Hoi, C. M. Wilson, P. Delsing, G. J. Milburn, and T. M. Stace, Phys. Rev. Lett. **110**, 053601 (2013).
[47] See Supplemental Material at http://link.aps.org/supplemental/10.1103/PhysRevLett.120.203602 for more details on the analytical expressions and the simulations, which includes Ref. [48].
[48] U. Vool and M. Devoret, Int. J. Circuit Theory Appl. **45**, 897 (2017).
[49] Z. Kurucz, J. H. Wesenberg, and K. Mølmer, Phys. Rev. A **83**, 053852 (2011).
[50] I. Diniz, S. Portolan, R. Ferreira, J. M. Gérard, P. Bertet, and A. Auffèves, Phys. Rev. A **84**, 063810 (2011).
[51] Y. Kubo, I. Diniz, A. Dewes, V. Jacques, A. Dréau, J.-F. Roch, A. Auffeves, D. Vion, D. Esteve, and P. Bertet, Phys. Rev. A **85**, 012333 (2012).
[52] B. Julsgaard, C. Grezes, P. Bertet, and K. Mølmer, Phys. Rev. Lett. **110**, 250503 (2013).
[53] D. C. McKay, S. Filipp, A. Mezzacapo, E. Magesan, J. M. Chow, and J. M. Gambetta, Phys. Rev. Applied **6**, 064007 (2016).

3.2.3 Compléments de résultats

Conception de l'expérience à UC Berkeley

Suite à la publication de cet article, nos collègues à l'université de Berkeley en Californie ont travaillé à la réalisation pratique du détecteur. Dans ce contexte, nous avons développé le schéma illustré à la figure 3.4b. Bien qu'identique en esprit au schéma présenté dans l'article original, ce nouveau design permet de contourner plusieurs problèmes expérimentaux de façon astucieuse. J'explique donc les différences entre le schéma de la figure 3.4b et le schéma 3.4a (figure recopiée du matériel supplémentaire, voir annexe B.1), autre que le nombre de transmons augmenté de 3 à 4.

Premièrement, les transmons ont été disposés avec une distance de $d = \lambda/2$ entre eux au lieu de $d \ll \lambda$. D'un point de vue pratique, cela permet d'éloigner physiquement les transmons de minimiser le couplage capacitif parasitique pouvant apparaître lorsque les transmons sont trop près les uns des autres. D'un point de vue conceptuel, ce changement ne fait que changer la symétrie de l'état super-radiant depuis $\hat{b}_B \propto \hat{b}_1 + \hat{b}_2 + \hat{b}_3 + \hat{b}_4$ vers $\hat{b}_B \propto \hat{b}_1 - \hat{b}_2 + \hat{b}_3 - \hat{b}_4$, où $\hat{b}_j$ est l'opérateur d'échelle du j-ième transmon et $\hat{b}_B$ est l'opérateur d'échelle du mode super-radiant. Cela ne change en rien la physique en jeu.

Une deuxième différence avec le schéma original, illustré à la figure 3.4a, est le couplage des transmons avec le résonateur de mesure. Dans l'article original, ce couplage est considéré comme homogène, $g_i = g \,\forall\, i$. Sur le schéma de la figure 3.4, le résonateur de mesure est un résonateur $\lambda/2$ et l'amplitude du champ électrique a un signe inversé aux deux extrémités. Conséquemment, le couplage des deux premiers transmons a un signe inverse par rapport aux deux derniers, $g_1 = g_2 = -g_3 = -g_4$. Un premier avantage de cette configuration est l'apparente symétrie du dispositif qui permet une meilleure homogénéité dans les couplages. Un deuxième avantage concerne le décalage de Lamb induit par ce résonateur de mesure. En effet, la nature du couplage entre les transmons et le résonateur de mesure induit une interaction directe entre chaque paire de transmons. Cette interaction transmon-transmon peut être vu de façon équivalente comme un décalage de Lamb du mode collectif couplé au résonateur de mesure, ici donné proportionnel à $\hat{b}_1 + \hat{b}_2 - \hat{b}_3 - \hat{b}_4$. Dans l'article

original, je note l'amplitude de ce décalage par Δ_+, voir équation 4. Des simulations numériques semblent suggérer qu'un décalage de Lamb sur un des états sombres dégrade moins l'efficacité quantique qu'un décalage de Lamb sur l'état super-radiant. Dans la limite d'un grand décalage de Lamb $\Delta_+ \gg \kappa_B$, la configuration considérée dans l'article original est réduite à la configuration à un seul mode de capture (figure 3.1), $N \to 1$. À l'inverse, avec le schéma amélioré 3.4b, un grand décalage de Lamb induit seulement la perte effective d'un mode sombre, $N \to N - 1$.

Une troisième amélioration par rapport au schéma original de la figure S3 est l'absence d'un filtre sur la ligne de mesure. L'objectif de ce filtre est d'éviter qu'une trop grande partie du signal de mesure soit dissipée dans le guide d'onde signal [8]. En effet, il est inévitable que le résonateur de mesure soit couplé indirectement au guide d'onde de signal par les transmons. La méthode proposée dans l'article original pour réduire cette dissipation est d'ajouter un filtre réduisant la densité de modes du guide d'onde du signal à la fréquence ω_r. Dans le schéma amélioré 3.4b, la distance de $\lambda/2$ entre les transmons agit comme un filtre naturel qui empêche la dissipation du résonateur de mesure dans le guide d'onde de signal par interférence destructive. Étant donné que les transmons et le résonateur ne sont pas à la même fréquence, la distance calculée de $\lambda/2$ pour les transmons ne correspond pas à exactement $\lambda/2$ pour le résonateur. Cependant, la différence est suffisamment petite pour garder un effet d'interférence destructive significatif.

Finalement, une quatrième différence est la terminaison du guide d'onde de signal. Sur la figure 3.4b, l'ajout d'une longueur de $\lambda/4$ à la fin de ce guide d'onde permet une meilleure symétrie dans le design et, conséquemment, un couplage plus uniforme des transmons au guide d'onde. La terminaison de ce guide d'onde en circuit ouvert induit une phase de π entre l'onde incidente et l'onde réfléchie. La phase totale entre les ondes émises par les transmons vers la droite et l'onde réfléchie est donc de 2π, car la distance de $\lambda/4$ entre les transmons et la terminaison induit une phase de $\pi/2 \times 2$ (aller et retour).

La figure 3.4c montre une photo d'un échantillon correspondant au schéma 3.4b et des résultats préliminaires obtenus à partir de cet échantillon semblent indiquer que le détecteur fonctionne.

8. Ce type de dissipation est parfois appelé effet Purcell inverse.

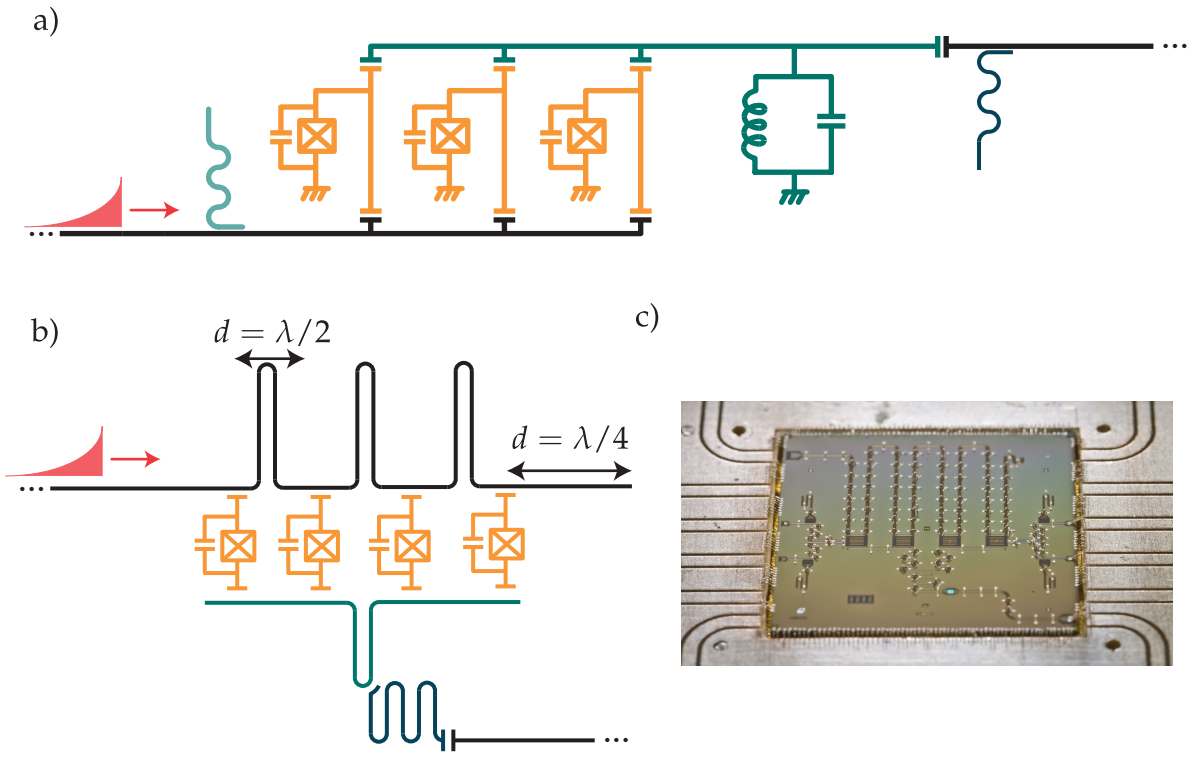

FIGURE 3.4 – Différences entre le schéma original (a) adapté de la figure S3 du matériel supplémentaire (section B.1) et le design fabriqué à Berkeley (b et c). a,b) Un photon (rouge) se propage vers un ensemble de transmons (orange). Le résonateur de mesure $\lambda/2$ (vert) est choisi à une fréquence désaccordée des transmons, $\omega_r - \omega_q \approx 2\pi \times 1$ GHz. Un filtre Purcell (bleu) diminue la dissipation des transmons dans le guide d'onde de mesure. a) La distance entre les transmons est de $d \ll \lambda$. b) La distance entre les transmons est de $d = \lambda/2$. Le photon et les distances inter-transmons ne sont pas à l'échelle. c) Photo du détecteur fabriqué à UC Berkeley, gracieuseté de John Mark Kreikebaum.

3.2.4 Avenues de recherche

Il serait d'intéressant d'observer la réponse du détecteur sous un signal contenant plus d'un photon pour déterminer si le nombre de photons peut être résolu. Une partie de ce projet serait évidemment de réaliser des simulations avec plus d'un photon dans le signal. Une autre partie serait de classifier correctement les signaux de mesures et une option pourrait être d'utiliser des outils d'apprentissage machine pour réaliser cette tâche [108]. Finalement le développement de nouvelles méthodes

de caractérisation pour ce type de détecteur sont nécessaires, car les métriques introduites à la section 3.1.1 ne s'appliquent qu'à des signaux de photons uniques. Une piste de solution pourrait être l'utilisation de la tomographie de détecteur [131, 132, 50].

Une deuxième avenue intéressante serait d'explorer les applications potentielles d'un détecteur résolut en temps, et plus particulièrement les possibilités qu'offrent un tel détecteur dans les photons micro-ondes par rapport aux photons optiques. Par exemple, on pourrait imaginer des expériences contenant à la fois une mesure homodyne et un détecteur de photons. Une autre option serait de réduire volontairement l'amplitude du couplage g_z et d'étudier l'effet d'une mesure faible du nombre de photons dans divers scénarios.

Finalement, une direction de recherche naturelle est d'étudier la dynamique du détecteur dans la limite d'un très grand nombre d'absorbeurs, $N \to \infty$. D'une certaine façon, c'est ce dont traite l'article de la prochaine section.

3.3 Détecteur de photons micro-ondes uniques, version continue

3.3.1 Contexte

Une limitation importante du détecteur présenté dans la section précédente et de tous les détecteurs de photons proposés jusqu'à présent est leur étroite largeur de bande. En effet, tous ces détecteurs se basent sur l'absorption d'un photon dans un mode de capture avec un grand facteur de qualité. La largeur de bande de ce mode, κ_B, impose donc une limite naturelle à la largeur de bande du détecteur.

Afin d'obtenir un long temps d'interaction entre le photon et le mode de mesure, une solution alternative est d'absorber ce photon dans un métamatériau unidimensionnel de longueur z avec une relation de dispersion linéaire, $\omega = v|k|$. Ainsi, le temps d'interaction avec le photon n'est plus donné par le facteur de qualité d'un mode localisé, mais plutôt par le temps de vol du photon dans le métamatériau,

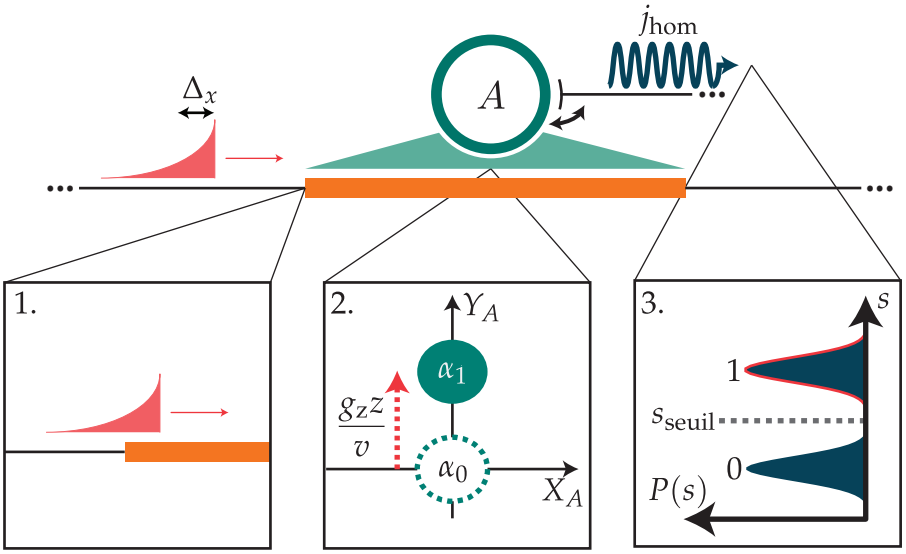

FIGURE 3.5 – 1. Un photon d'étendue spaciale Δ_x (rouge) se propage et est absorbé par un métamatériau (orange) de longueur z couplé sur toute sa longueur à un mode de mesure A (vert). 2. La présence du photon dans le métamatériau génère un déplacement dans le mode de mesure A. 3. Une mesure homodyne du champ de sortie permet de distinguer la présence du photon.

$\tau = z/v$. Un grand temps d'interaction avec le mode de mesure, et conséquemment un grand déplacement de l'état cohérent $g_z z/v \gg 1$, est obtenu en rallongeant le métamatériau.

La différence entre la version discrète du détecteur (section 3.2.2) et cette version continue est conceptuellement similaire à la différence entre les amplificateurs paramétriques Josephson (*JPA*) [133, 134, 135, 136, 137, 138, 139, 140] basés sur des modes localisés et les amplificateurs paramétriques Josephson à ondes progressives (*JTWPA*) [141] basés sur des métamatériaux avec une non linéarité distribuée sur une grande distance.

Le fonctionnement général du détecteur continu est illustré à la figure 3.5 où on considère que le couplage entre le métamatériau et le mode de mesure est donné

par la généralisation naturelle du Hamiltonien 3.5,

$$\hat{H} = g_z \int_{-z/2}^{z/2} dx\, \hat{b}_x^\dagger \hat{b}_x (\hat{a} + \hat{a}^\dagger), \tag{3.6}$$

avec $\hat{b}_x$ l'opérateur de champ annihilant un photon à la position x du guide d'onde, $[\hat{b}_x, \hat{b}_{x'}^\dagger] = \delta(x - x')$. De manière similaire à la situation décrite par l'Hamiltonien 3.5, le mode de mesure est sensible au nombre *total* de photons dans le métamatériau. Le fait que le métamatériau interagisse avec un seul mode géant A est aussi un élément crucial. En effet, il a été démontré qu'il est impossible d'obtenir un déplacement appréciable pour un mode de mesure à partir d'une interaction cross-Kerr strictement locale [142, 143, 144, 119].

Comme pour le détecteur discret présenté à la section précédente, la présence du mode de mesure A induit une rétroaction due à la mesure du métamatériau et impose une limite supérieure sur l'amplitude du couplage g_z. Lorsque le photon est absorbé dans un mode avec un grand facteur de qualité (figure 3.1), on a vu que la variable quantifiant la rétroaction de la mesure est donnée par g_z/κ_B. On peut alors se demander comment se traduit cette variable pour le détecteur continu. L'intuition pour répondre à cette question est que le mode de mesure A identifie non seulement la présence du photon, mais aussi sa position à l'intérieur du métamatériau. En raison du principe d'incertitude d'Heisenberg, une mesure de la position implique une rétroaction sur la quantité de mouvement.

Considérons un point localisé x du métamatériau. Ce point interagit avec le mode de mesure pendant un temps $\tau_x = \Delta_x/v = (v/\sigma)/v = 1/\sigma$, où Δ_x est l'étendue spatiale du photon incident et σ cette étendue convertie en unité de fréquence. En considérant que la précision de la mesure est approximativement donnée par le déplacement de l'état cohérent dans le mode de mesure, on obtient que la variable caractérisant la rétroaction de la mesure est donnée par $g_z\tau_x = g_z/\sigma$. Pour le détecteur continu, l'amplitude du couplage longitudinal g_z impose donc une limite *inférieure* sur la largeur de bande des photons qu'il est possible de détecter, ou de manière équivalente une limite supérieure sur l'étendue spaciale des photons détectables. Contrairement au détecteur discret, la limite supérieure pour la largeur de bande du détecteur continu n'est pas donnée par des raisons fondamentales, mais plutôt les caractéristiques du métamatériau comme la bande de fréquence Ω

sur laquelle la relation de dispersion est linéaire, $\omega = v|k|$.

On peut aussi interpréter la rétroaction de la mesure pour le détecteur discret (section précédente) dans le contexte du principe d'incertitude d'Heisenberg entre position et quantité de mouvement. En effet, le détecteur discret illustré sur la figure 3.1 mesure non seulement la présence du photon, mais aussi sa position à un point localisé donné par le mode d'absorption B. En considérant que le temps d'interaction avec le point localisé B est donné par $1/\kappa_B$, on retrouve la condition $g_z/\kappa_B \ll 1$ pour minimiser l'effet de la rétroaction.

Pour une ligne à transmission avec une relation de dispersion linéaire, $\omega = v|k|$, les états propres sont des ondes planes se déplaçant vers la droite ($k > 0$) ou la gauche ($k < 0$), voir équation 2.13. Suivant ce résultat, il est utile de décomposer les opérateurs de champ spatiaux en modes se déplaçant en directions inverses, $\hat{b}_x = (\hat{b}_{D,x} + \hat{b}_{G,x})/\sqrt{2}$. Cette décomposition est naturelle lorsqu'on exprime l'opérateur de champ spatial en fonction de sa transformée de Fourier qui correspond aux modes propres de l'Hamiltonien,

$$\begin{aligned}
\hat{b}_x &= \frac{1}{\sqrt{2\pi}} \int_{-\infty}^{\infty} dk \sqrt{\frac{\hbar Z}{2|k|}} \hat{b}_k \, \mathrm{e}^{ikx} \\
&= \frac{1}{\sqrt{2\pi}} \int_{0}^{\infty} dk \sqrt{\frac{\hbar Z}{2|k|}} \hat{b}_k \, \mathrm{e}^{ikx} + \frac{1}{\sqrt{2\pi}} \int_{-\infty}^{0} dk \sqrt{\frac{\hbar Z}{2|k|}} \hat{b}_k \, \mathrm{e}^{ikx} \\
&\equiv \frac{\hat{b}_{D,x} + \hat{b}_{G,x}}{\sqrt{2}},
\end{aligned} \tag{3.7}$$

où Z est l'impédance de la ligne à transmission. Alors que pour une ligne à transmission standard les modes $\hat{b}_{v,x}$ sont découplés, on remarque que ce n'est pas le cas dans l'Hamiltonien 3.6 et une réflexion du photon est possible due à la mesure,

$$\hat{b}_x^\dagger \hat{b}_x \propto \hat{b}_{D,x}^\dagger \hat{b}_{D,x} + \hat{b}_{G,x}^\dagger \hat{b}_{G,x} + \hat{b}_{G,x}^\dagger \hat{b}_{D,x} + \hat{b}_{G,x}^\dagger \hat{b}_{D,x}. \tag{3.8}$$

On montre dans l'article que le processus de réflexion, $\hat{b}_{G,x}^\dagger \hat{b}_{D,x}$, est très peu probable. L'intuition ici est qu'une réflexion du photon induit un grand changement dans son impulsion qui doit être compensée par l'interaction. Dans le régime où l'amplitude de l'interaction est faible devant la fréquence du photon, $g_z/\omega \ll 1$, ce processus peut être négligé et on peut se restreindre à la dynamique des modes se propageant

dans une seule direction, $\hat{b}_x^\dagger \hat{b}_x \approx \hat{b}_{D,x}^\dagger \hat{b}_{D,x}/2$.

3.3.2 Article

L'idée d'utiliser un métamatériau pour réaliser un détecteur de photon a germé naturellement des travaux d'Arne Grimsmo sur les JTWPA [145] et de nos travaux présentés à la section précédente. En plus des nombreuses discussions sur la conception des différents aspects de ce détecteur, ma contribution pour cet article a été d'obtenir une équation maîtresse effective pour le système émetteur-résonateur en utilisant le formalisme d'intégrale de chemin Keldysh [146, 147]. À ma connaissance, c'est la première fois que le formalisme Keldysh est utilisé dans un tel contexte.

Arne L. Grimsmo, Baptiste Royer, John Mark Kreikebaum, Kevin O'Brien, Irfan Siddiqi et Alexandre Blais. Quantum metamaterial for nondestructive microwave photon counting. In preparation, (2019)

Quantum metamaterial for nondestructive microwave photon counting

Arne L. Grimsmo*[1,2], Baptiste Royer[1], John Mark Kreikebaum, Kevin O'Brien, Irfan Siddiqi, Alexandre Blais[1,3]

[1] Institut quantique and Départment de Physique, Université de Sherbrooke, Sherbrooke, Québec, Canada J1K 2R1

[2] Centre for Engineered Quantum Systems, School of Physics, The University of Sydney, Sydney, NSW 2006, Australia

[3] Canadian Institute for Advanced Research, Toronto, Canada

Detecting traveling photons is an essential primitive for many quantum information processing tasks, but it remains challenging at microwave frequencies. We introduce a single-photon detector design operating in the microwave domain, based on a weakly nonlinear metamaterial built from a large number of coupled Josephson junctions. The combination of weak nonlinearity and the large spatial extent of this detector circumvents well-known obstacles limiting approaches based on a localized Kerr medium. Using numerical many-body simulations we show that the single-photon detection fidelity increases with the length of the metamaterial to approach one at experimentally realistic lengths. Moreover, this weakly nonlinear metamaterial allows for a remarkably large detection bandwidth. In stark contrast to conventional photon detectors operating in the optical domain, the photon is not destroyed by the detection and the photon wavepacket is left only minimally disturbed. This detector design offers new possibilities for quantum information processing, quantum optics and metrology in the microwave frequency domain.

Introduction

In contrast to infrared, optical or ultraviolet frequencies where single-photon detectors are a cornerstone of experimental quantum optics, the realization of a detector with similar performance at microwave frequencies is far more challenging (*1–13*). The interest in realizing such a detector is intimately linked to the emergence of engineered quantum systems whose natural domain of operations is the microwave frequency range, including superconducting quantum circuits, spin ensembles, and spin or charge degrees of freedom in semiconductor quantum dots. The continuing improvement in coherence and control over these quantum devices offers a wide range of new applications for microwave single-photon detection, such as photon-based quantum computing (*14*), modular quantum computing architectures (*15*), high-precision sensing (*16*), and the detection of dark matter axion (*17*).

For this reason, a number of theoretical proposals and experimental demonstrations of microwave single-photon detectors have recently emerged. These schemes can broadly be divided into two categories: Time-gated schemes where accurate information about the photon's arrival time is needed a priori (*2, 6, 7, 10, 11, 13*), and detectors that operate continuously in time and attempt to accurately record the photon arrival time (*1, 3–5, 8, 9, 12, 13*). In this work, we are concerned with the last category which is simultaneously the most challenging to realize and finds the widest range of applications.

Depending on the intended application, there are several metrics characterizing the usefulness of single-photon detectors. Not only is high single-photon detection fidelity required for most quantum information applications, but large bandwidth, fast detection and short dead times are also desirable (*18*). Moreover, the ability to resolve photon number and nondestructive photon counting are of fundamental interest and offers new possibilities for quantum measurement and control. Although some theoretical proposals and proof-of-concept experiments do well on a subset of these characteristics, a detector design that performs well across all desiderata in the microwave frequency range is still lacking. In particular, detectors that promise high detection fidelity typically suffer from narrow detection bandwidths (*5, 6, 12*), and even in theoretical simulations previous proposals for continuous-time detectors have performance bounds below unit detection fidelity (*1, 3–5, 8, 9, 12*).

In this article, we introduce the Josephson Traveling-Wave Photodetector for which we predict remarkably high detection fidelities without sacrificing detector bandwidth. This detector exploits a weakly nonlinear, one-dimensional metamaterial designed to respond to the presence of a single photon. The nonlinearity is provided by a large number of coupled Josephson junctions. Because the detector response does not rely on any resonant interaction, a large detection bandwidth in the range of hundreds of MHz is feasible. The detection and reset times are predicted to be in the μs range for typical parameters. Moreover, the signal-to-noise ratio (SNR) grows linearly with the length of the metamaterial which can be made large, leading to single-photon detection fidelities approaching unity. By interrogating the nonlinear medium with a giant probe—a probe system that couples to the medium over a spatial extent that is large compared to the length of the signal photons—this approach bypasses previous no-go results for photon counting based on localized cross-Kerr interaction (*19–22*).

Results

Many proposals for itinerant microwave photon detection rely on capturing the incoming photon in a localized absorber mode that is interrogated using homodyne or heterodyne detection (*1, 3–5, 12, 13*). A first challenge associated with this approach is linked to a version of the quan-

*Corresponding author. Email: arne.grimsmo@sydney.edu.au

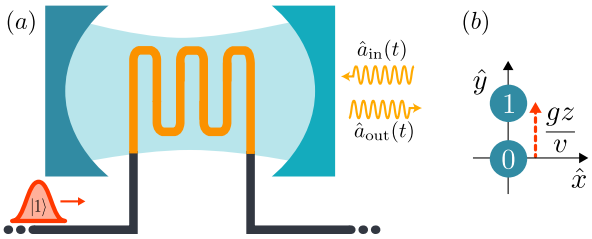

Figure 1: a) Sketch of the JTWPD. Standard transmission lines (black) are coupled to both ends of a one-dimensional metamaterial (orange) of length z and linear dispersion relation, $\omega = vk$. A cross-Kerr interaction χ between the metamaterial and the giant probe mode (blue) leads to a phase shift in the strong measurement tone (yellow) while the signal photon (red) travels through the metamaterial. b) Phase space picture of the probe mode. With respect to the idle coherent state $|\alpha\rangle$, the presence of a signal photon displaces the states by gz/v, with $g = \chi\alpha$.

tum Zeno-effect: continuously and strongly monitoring the absorber will prevent the incoming photon from being absorbed (*1, 12*). This manifests itself as photon backscattering and limits the detector's quantum efficiency. Even in the absence of continuous monitoring, another difficulty concerns the tradeoff between efficiency and bandwidth. Indeed, a large detector response to a single photon requires a sufficiently long interaction time with the photon. In principle, this can be achieved by making the absorber mode long-lived. However, as the mode linewidth is inversely proportional to the photon lifetime, this imposes a serious constraint on the detector bandwidth.

Our solution to overcome these obstacles is illustrated schematically in Fig. 1: In place of a localized absorber, we use a long and weakly nonlinear metamaterial. Backscattering is avoided by using a nonlinearity that is locally weak, yet a large response is made possible by having a long photon time-of-flight through the metamaterial. The presence of a photon is recorded using a continuously monitored probe mode that is nonlinearly coupled to the metamaterial along the full extent of its length. Thanks to this nonlinear cross-Kerr coupling, in the presence of the measurement tone $\hat{a}_{\rm in}(t)$, a single photon in the metamaterial induces a displacement of the output field $\hat{a}_{\rm out}(t)$ relative to its idle state. While the interaction between the metamaterial and the probe mode is locally too weak to cause any noticeable change in $\hat{a}_{\rm out}(t)$, the displacement accumulates as the photon travels through the metamaterial leading to a large enough signal to be recorded using homodyne detection. Inspired by the Josephson traveling wave amplifier (*23*), the nonlinearity in our proposal is provided by a chain of Josephson junctions and we therefore refer to this detector as a Josephson Traveling-Wave Photodetector (JTWPD).

JTWPD design and working principle As illustrated in Fig. 2, the backbone of the metamaterial is a waveguide of length z (orange) realized as a linear chain of capacitively coupled LC-oscillators. The oscillators are coupled via an array of Josephson junctions to a readout resonator acting as a giant probe (blue). With the metamaterial coupled at $x = \pm z/2$ to an impedance matched linear transmission line, the interaction time between the photon and the giant probe is $\tau = z/v$ where v is the speed of light in the metamaterial. Rather than working in this transmission mode, the interaction time can be doubled by terminating the metamaterial at $x = +z/2$ with an open where the photon wavepacket is reflected. To simplify the analysis, we consider the transmission mode but results for the reflection mode can be obtained simply by doubling τ.

The full detector Hamiltonian can be expressed as $\hat{H} = \hat{H}_0 + \hat{H}_r + \hat{H}_{\rm int}$, where $\hat{H}_0$ contains the linear part of the waveguide including the metamaterial as well as the input and output linear waveguides, $\hat{H}_r$ is the probe resonator Hamiltonian and $\hat{H}_{\rm int}$ describes the nonlinear coupling between the probe and the metamaterial. As shown in the Supplementary Materials, in the continuum limit where the size a of a unit cell of the metamaterial is small with respect to the extent of the photon wavepacket, $\hat{H}_0$ takes the form

$$\hat{H}_0 = \sum_{\nu=\pm} \int_\Omega d\omega \hbar\omega \hat{b}^\dagger_{\nu\omega} \hat{b}_{\nu\omega}. \tag{1}$$

In this expression, $\hat{b}^\dagger_{\pm\omega}$ creates a delocalized right/left-moving photon with energy $\hbar\omega$ and satisfies the canonical commutation relation $[\hat{b}_{\nu\omega}, \hat{b}^\dagger_{\mu\omega'}] = \delta_{\nu\mu}\delta(\omega - \omega')$. The subscript Ω in Eq. (1) is used to indicate that we only consider the band of frequencies around which the metamaterial's dispersion relation is linear. Moreover, the probe resonator Hamiltonian $\hat{H}_r$ can be written in a displaced and rotating frame with respect to the coherent drive field as

$$\hat{H}'_r = \frac{\hbar K}{2} \hat{a}^{\dagger 2} \hat{a}^2, \tag{2}$$

where K is a self-Kerr nonlinearity induced by the coupling junctions and whose expression is given in Eq. (13) of the Materials and Methods.

Finally, the junctions also lead to cross-Kerr coupling between the array of oscillators and the probe mode. As mentioned above, this coupling is chosen to be locally weak such that the nonlinearity is only activated by the presence of a strong coherent drive $\hat{a}_{\rm in}(t)$ on the probe. In this limit, the nonlinear interaction Hamiltonian $\hat{H}_{\rm int}$ in the same rotating and displaced frame is given by

$$\begin{aligned} \hat{H}'_{\rm int} = \hbar \sum_{\nu\mu} \int_{-z/2}^{z/2} dx \chi(x) \hat{b}^\dagger_\nu(x) \hat{b}_\mu(x) \left(\hat{a}^\dagger \hat{a} + \alpha^2\right) \\ + \hbar \sum_{\nu\mu} \int_{-z/2}^{z/2} dx g(x) \hat{b}^\dagger_\nu(x) \hat{b}_\mu(x) \left(\hat{a}^\dagger + \hat{a}\right), \end{aligned} \tag{3}$$

where we have defined the x-dependent photon annihilation operators

$$\hat{b}_\nu(x) = \sqrt{\frac{\bar{\omega}}{2\pi v}} \int_\Omega \frac{d\omega}{\sqrt{\omega}} \hat{b}_{\nu\omega} e^{\nu i\omega x/v}, \tag{4}$$

with $\bar{\omega}$ a nominal center frequency for the incoming photon and which is introduced here for later convenience. The parameter $\chi(x)$ is a dispersive shift per unit length given in Eq. (20), while $g(x) = \alpha\chi(x)$ with α the displacement of the probe resonator field under the strong drive $\hat{a}_{\rm in}$. The expression for α, which we take to be real without loss of generality, can be found in Eq. (18) of the Materials and Methods.

As can be seen from the second term of Eq. (3) which dominates for small $\chi(x)$ and large α, the combined effect

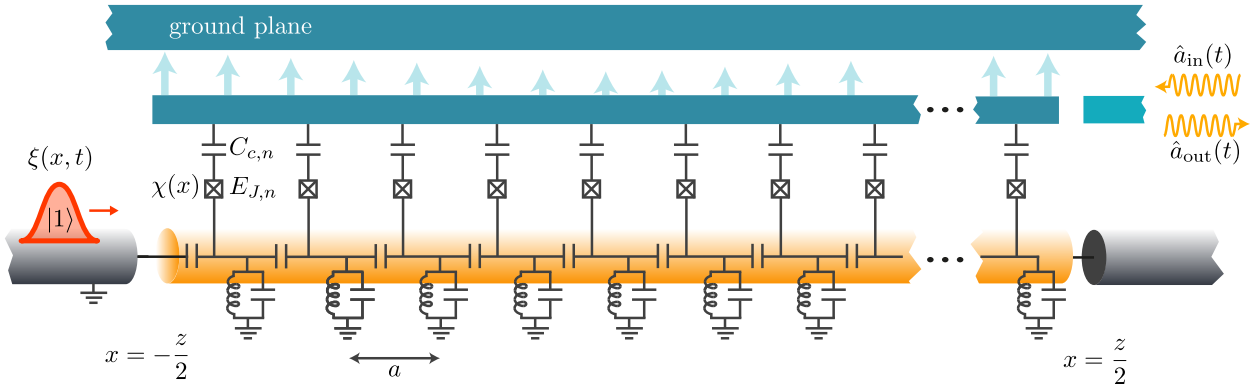

Figure 2: Schematic representation of the JTWPD. The probe resonator with ground plane on top and the center conductor below (blue), as well as a readout port on the right, acts as a giant probe. The light blue arrows illustrate the fundamental mode function of a $\lambda/2$ resonator. This probe is coupled via a position dependent cross-Kerr interaction $\chi(x)$, mediated by an array of Josephson junctions, to a metamaterial waveguide (orange). The metamaterial is coupled to impedance matched input/output transmission lines at $x=-z/2$ and $x=z/2$ (grey). An incoming photon of Gaussian shape $\xi(x,t)$ is illustrated (red).

of the cross-Kerr coupling and the strong drive results in a longitudinal-like interaction between the metamaterial and the probe mode (*24*). This corresponds to a photon-number dependent displacement of the probe field relative to the idle state displacement α, which accumulates when a photon travels along the metamaterial. By continuously monitoring the output field of the probe mode, a photon is registered when the integrated homodyne signal exceeds a predetermined threshold. This approach shares similarities with the photodetector design introduced in Ref. (*12*), with the important distinction that here the photon is probed *in-flight* as it travels through the metamaterial rather than after interaction with a localized absorber mode. As will become clear later, this leads to a large detection bandwidth.

As discussed below and in the Supplementary Materials, a crucial feature of this detector is that although the detection bandwidth is large, the metamaterial is engineered such as to have frequency cutoffs. The low-frequency cutoff avoids the detector from being overwhelmed by low-frequency thermal photons. Moreover, decay of the probe mode via the metamaterial to the input and output waveguides is minimized by choosing the probe mode resonance frequency to be outside of the metamaterial's bandwidth. In this situation, the metameterial effectively acts as a Purcell filter for the probe mode, thereby avoiding degradation of the probe mode quality factor.

Backaction and detector noise In the JTWPD, backaction on the incoming photon's wavevector, and therefore photon backscattering, is minimized by working with a giant probe which, optimally, does not acquire information about the photon's position. Focusing first on the ideal case where the probe mode self-Kerr nonlinearity K and the dispersive shift $\chi(x)$ can be ignored, we clarify the dominant noise process for the probe resonator and the associated backaction on the photon by deriving a perturbative master equation for the probe. In the subsequent section, we turn to full numerical analysis including the effect of the nonlinearities K and $\chi(x)$.

Considering the ideal case for the moment and ignoring the spatial dependence of $g(x)$, the interaction Hamiltonian takes the simple longitudinal-coupling form

$$\hat{H}_{\rm ideal}=\hbar g\sum_{\nu\mu}\int_{-z/2}^{z/2}dx\hat{b}_\nu^\dagger(x)\hat{b}_\mu(x)\left(\hat{a}^\dagger+\hat{a}\right). \tag{5}$$

The incoming photon is modeled by an emitter system with annihilation operator $\hat{c}$, $[\hat{c},\hat{c}^\dagger]=1$, located at $x_0<-z/2$ and initialized in Fock state $|1\rangle$. The decay rate $\kappa_c(t)$ of the emitter to the transmission line is chosen such as to have a Gaussian wavepacket with center frequency $\bar{\omega}$ and full width at half maximum (FWHM) γ propagating towards the detector [see Eq. (21) of Materials and Methods]. Using Keldysh path integrals, we trace out the waveguide to find a perturbative master equation for the joint emitter-probe system. As discussed in the Materials and Methods, to second order in the interaction, this master equation takes a remarkably simple form

$$\begin{aligned}\dot{\hat{\rho}}=&-i\left[gn_{\rm det}(t)(\hat{a}+\hat{a}^\dagger),\hat{\rho}_c\right]+\Gamma(t)\mathcal{D}[\hat{a}+\hat{a}^\dagger]\hat{\rho}_c\\&+\kappa_c(t)\mathcal{D}[\hat{c}]\hat{\rho}+\kappa_a\mathcal{D}[\hat{a}]\hat{\rho}.\end{aligned} \tag{6}$$

In this expression, $\mathcal{D}[\hat{o}]\bullet=\hat{o}\bullet\hat{o}^\dagger-1/2\{\hat{o}^\dagger\hat{o},\bullet\}$ is the usual Lindblad-form dissipator and we have defined $\hat{\rho}_c(t)=\hat{c}\hat{\rho}(t)\hat{c}^\dagger/\langle\hat{c}^\dagger\hat{c}\rangle(t)$,

$$n_{\rm det}(t)=\frac{1}{v}\int_{-z/2}^{z/2}dx\left|\xi\left(x,t\right)\right|^2, \tag{7}$$

$$\Gamma(t)=\frac{4g^2}{\kappa_a v}\int_{-z/2}^{z/2}dx\left[1-e^{-\frac{\kappa_a}{2v}\left(x+\frac{z}{2}\right)}\right]\left|\xi\left(x,t\right)\right|^2, \tag{8}$$

with $\xi(x,t)=\xi(t-x/v)$ the incoming photon envelop and $n_{\rm det}(t)$ the fraction of the photon that is in the metamaterial at time t. A term of order $g/\bar{\omega}$ describing backscattering of the photon into the left-moving field has been dropped from Eq. (6). With $\bar{\omega}$ the carrier frequency of the incoming photon, this contribution is negligible.

With $\hat{\rho}_c$ the state of the system *conditioned* on a photon having been emitted, the first term of Eq. (6) has an intuitive interpretation that is consistent with the

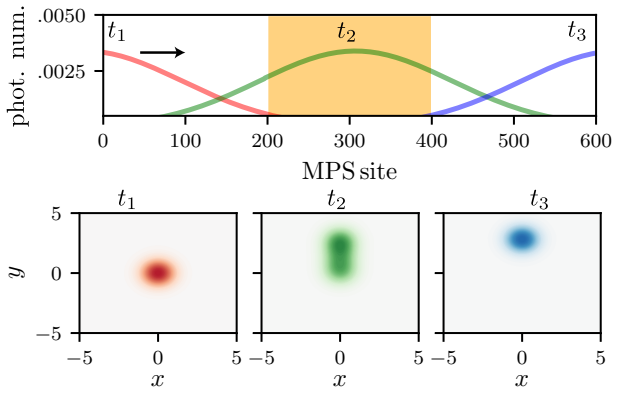

Figure 3: The top panel shows snapshots of the photon number population along the MPS sites at three different times t_1 (red), t_2 (green) and t_3 (blue). The white region corresponds to the linear waveguide and the orange region to the metamaterial with its coupling to the probe resonator. The lower three panels show the Wigner function $W(x, y)$ of the intracavity probe field at the three respective times. When the photon is only partially inside the metamaterial, the probe is in a superposition of displaced states (middle lower panel). Parameters are $\kappa_a = \chi(x) = K = 0$, $g\tau = 2$ and $\gamma\tau = 2$.

form of $\hat{H}_{\text{ideal}}$: The probe resonator is conditionally displaced by a drive equal to the longitudinal coupling amplitude times the photon fraction in the metamaterial, $g \times n_{\text{det}}(t)$. Indeed, while the x-quadrature of the probe, $\hat{x} = (\hat{a}^\dagger + \hat{a})/\sqrt{2}$, is a constant of motion under Eq. (6), the y-quadrature, $\hat{y} = i(\hat{a}^\dagger - \hat{a})/\sqrt{2}$, is not. Moreover, the second term of Eq. (6), proportional to the rate $\Gamma(t)$, is the dominant process contributing to noise also along the y-quadrature. The origin of the noise term can be understood as follows. When the photon first enters the detector and is only partially inside the metamaterial, the probe mode field evolves to a superposition of being displaced to different average values of $\hat{y}$, leading to enhanced fluctuations in this quadrature. This effect can be seen clearly in the numerical results of Fig. 3, which are described in more detail below. Finally, the last line of Eq. (6) describes the usual decay of the emitter and probe at respective rates $\kappa_c(t)$ and κ_a.

As the increased fluctuations in the y-quadrature arise due to uncertainty in the photon's position, a spatially longer photon is expected to lead to larger fluctuations. A homodyne measurement of the probe's y-quadrature will collapse the superposition of displaced states and thus lead to a backaction effect localizing the photon and randomizing its wavevector. This effect can be minimized by decreasing the interaction strength g while keeping gz/v constant by increasing z. In other words, backaction can be minimized by increasing the detector length relative to the spatial extent of the photon. This intuitive reasoning is confirmed by numerical results in the next section.

Numerical Matrix Product State simulations We now turn to numerical simulations of the JTWPD including the self- and cross-Kerr nonlinearities K and χ that were dropped from the above discussion. To go beyond the perturbative results of Eq. (6), it is no longer possible to integrate out the waveguide degrees of freedom. A brute-force numerical integration of the dynamics is, however, intractable, as the JTWPD is an open quantum many-body system with thousands of modes. We overcome this by using a numerical approach where the systems is represented as a stochastically evolving Matrix Product State (MPS) conditioned on the homodyne measurement record of the probe output field.

Our approach is based on trotterizing the time evolution and discretizing the photon waveguide, including the nonlinear metamaterial, along the x axis. Building upon and extending recent developments of MPS in the context of waveguide QED (*25, 26*), this leads to a picture where the waveguide is represented by a "conveyor belt" of harmonic oscillators (referred to as MPS sites below) interacting with the probe resonator (see Materials and Methods). Measurement backaction under continuous homodyne detection of the probe resonator is included by representing the state as a quantum trajectory conditioned on the measurement record (*27*). With our approach this is simulated using a stochastic MPS algorithm. Further details on this numerical technique can be found in Materials and Methods and the Supplementary Materials.

As in the previous section, we consider a Gaussian photon wavepacket with FWHM γ propagating towards the detector by an emitter initialized in the state $|1\rangle$ localized to the left of the detector. The interaction strength is quantified by the dimensionless quantity $g\tau$ where $\tau = z/v$ is the interaction time as before, and the photon width by the dimensionless quantity $\gamma\tau$. Example snapshots of the photon number distribution along the MPS sites at three different times $t_1 < t_2 < t_3$ are shown in Fig. 3, along with the corresponding Wigner functions of the probe mode field. Because of the impedance match and negligible backaction, the photon wavepacket travels without deformation along the MPS sites.

We start by comparing numerical results from MPS simulations to the perturbative master equation obtained in Eq. (6). To help in directly comparing the simulation results, we first consider the idealized situation where $\chi(x) = K = 0$. In Fig. 4, we show the average probe resonator displacement $\langle\hat{y}\rangle$ whose integrated value is linked to the detector signal and the noise $\langle\Delta\hat{y}^2\rangle$ as a function of time. To verify the prediction that fluctuations in $\hat{y}$ increase for spatially longer photons, we compare Gaussian wavepackets of different spectral widths γ. Recall that a *smaller* $\gamma\tau$ implies a *longer* photon relative to the detector length. The solid lines in Fig. 4 are obtained using MPS simulations with $\gamma\tau = 2$ (blue), 4 (orange), 6 (green) and 10 (bright purple). The dotted lines are obtained from Eq. (6) for the same parameters. The agreement between the approximate analytical results and the full non-perturbative MPS results is remarkable.

In panels (c, d) of Fig. 4 we use a spatially varying $g(x)$, and we consequently only show MPS results in these panels. In practice, the probe will be realized from a resonator whose vacuum fluctuations vary in space. To confirm the robustness of the detector to this variation, Fig. 4 (b, c) shows $\langle\hat{y}\rangle$ and $\langle\Delta\hat{y}^2\rangle$ versus time as obtained from MPS simulations for $g(x) = 2\bar{g}\cos^2(2\pi x/z) + \mu(x)$. The cosine models the dependence on the mode function of a $\lambda/2$ resonator while $\mu(x)$ is added to take into account potential random variations in the coupling strength which we take

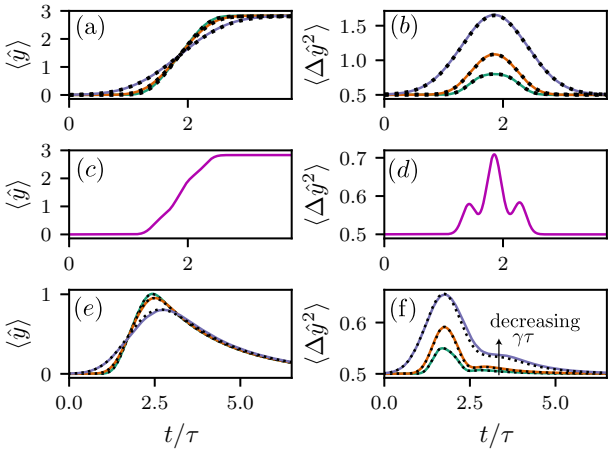

Figure 4: Time evolution of the intra-cavity probe displacement $\langle\hat{y}\rangle$ $[(a,c,e)]$ and fluctuations $\langle\Delta\hat{y}^2\rangle$ $[(b,d,f)]$, in the idealized case $\chi(x) = K = 0$. Top row: $\kappa_a = 0$ and $g\tau = 2$. Middle row: $\kappa_a = 0$ and spatially varying $g(x)$ with average value $\bar{g}\tau = 2$. Bottom row: $\kappa_a\tau = 1.0$ and $g\tau = 2$. The solid lines correspond to MPS simulations with different photon widths $\gamma\tau = 2$ (blue), 4 (orange), 6 (green) and 10 (bright purple), while the dotted lines are from integrating Eq. (6).

here to be as large as 10%. Moreover, to show the effect of a non-uniform $g(x)$ more clearly, we use $\gamma\tau = 10$ corresponding to spatially shorter photons than in the other panels. Although additional structures can now be seen, the long-time average displacement remains unchanged confirming that the detector is robust against spatial variations of the metamaterial-probe coupling.

Panels (e, f) of Fig. 4 show results fo $\kappa_a > 0$. In this situation the MPS evolves stochastically with each trajectory resulting in a measured current $J_{\rm hom}(t) = \sqrt{\kappa_a}\langle\hat{y}\rangle_{\rm traj} + \xi(t)$, where $\xi(t) = dW_t/dt$ with dW_t a Wiener process representing white noise (*27*). We compare $\langle\hat{y}\rangle$ and $\langle\Delta\hat{y}^2\rangle$ averaged over one thousand stochastic trajectories to the results obtained by integrating the Keldysh master equation Eq. (6). The agreement is excellent for large $\gamma\tau$, but small deviations are observed when this parameter is decreased. We attribute this to terms of higher than second order in the interaction Hamiltonian, which are neglected in Eq. (6). The exponential decay of $\langle\hat{y}\rangle$ at long time observed in panel (e) simply results from the finite damping rate κ_a. Indeed, the photon-induced displacement stops once the photon has travelled past the metamaterial at which point the probe mode relaxes back to its idle state.

For a given trajectory, we infer that a photon is detected if the homodyne current convolved with a filter (*4*)

$$\bar{J}_{\rm hom}(t) = \int_0^{\tau_m} dt' J_{\rm hom}(t') f(t'-t). \tag{9}$$

is larger than a threshold $y_{\rm thr}$, i.e. $\max_t \bar{J}_{\rm hom}(t) > y_{\rm thr}$. The filter $f(t) \propto \langle\hat{y}(t)\rangle$ is obtained from averaging over a large number of trajectories and is chosen such as to give more weight to times where the signal is on average larger. We maximize t over the time window $[-\tau_m, \tau_m]$ and chose the threshold to optimize between quantum efficiency and dark counts. The quantum efficiency η is defined as the probability of detecting a photon given that

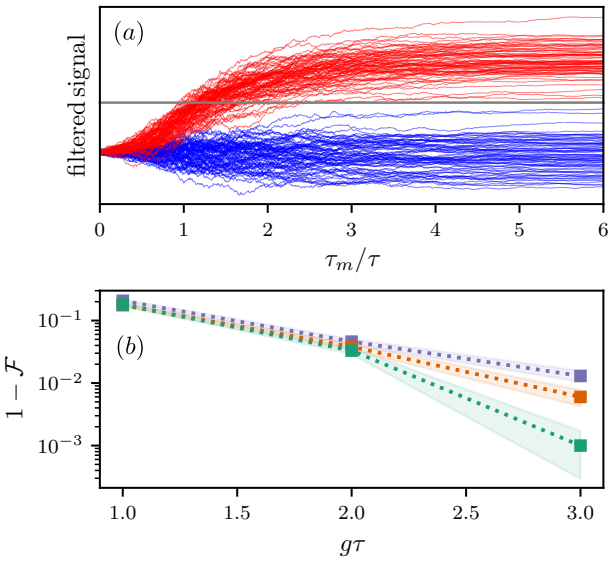

Figure 5: (a) 75 filtered homodyne currents (arbitrary units) for $g\tau = 3$, $\kappa_a\tau = 1.0$, $|K|/\kappa_a = 10^{-2}$ and $g/\chi = 5$. Red traces are obtained with an incoming Gaussian photon of unitless width $\gamma\tau = 6$, and blue traces for vacuum. The horizontal gray line is the threshold chosen to maximize the assignment fidelity. (b) Infidelity versus $g\tau$ for $\gamma\tau = 2$ (blue), 4 (orange), and 6 (green), found by averaging over $N_{\rm traj} = 2000$ trajectories. Other parameters as in (a). The shaded regions indicate the standard error $\pm\sqrt{\mathcal{F}(1-\mathcal{F})/N_{\rm traj}}$.

one was present. From the above procedure, it can be estimated as $\eta = N_{\rm click|1}/N_{\rm traj|1}$, with $N_{\rm click|1}$ the number of reported "clicks" and $N_{\rm traj|1}$ the number of simulated trajectories with a photon. On the other hand, the dark count probability is estimated similarly as the fraction of reported clicks $p_D = N_{\rm click|0}/N_{\rm traj|0}$ in a simulation with no incoming photon. In these simulations, the dark count rate is set by the threshold and the vacuum fluctuations of the probe resonator. A number that incorporates both η and p_D, and is thus a good measure of the performance of a photodetector, is the assignment fidelity (*4*)

$$\mathcal{F} = \frac{1}{2}\left(\eta + 1 - p_D\right). \tag{10}$$

In practice, if the arrival time of the photon is known to lie within some time window, one can optimize t in Eq. (9) over this window in a post-processing step (*12*). In our numerical simulations, the arrival time is known such that this optimization is not necessary and we can therefore simply evaluate $\bar{J}_{\rm hom}(t)$ at $t = 0$.

Fig. 5 shows 75 typical filtered output records, $\bar{J}_{\rm hom}(t = 0)$, as a function of the measurement window τ_m. These results are obtained from stochastic MPS simulations with $\gamma\tau = 6$, $g\tau = 3$, $\kappa_a\tau = 1.0$, and include self- and cross-Kerr couplings with $|K|/\kappa_a = 10^{-2}$ and $g/\chi = 5$. The red traces correspond to simulations where a photon was present, while the blue traces are for incoming vacuum. The horizontal gray line is the threshold chosen to optimize the assignment fidelity. At $\tau_m/\tau \gtrsim 3$, most traces are correctly identified. Panel (b) shows the assignment fidelity for $\gamma\tau = 2$ (blue), 4 (orange) and 6 (green) as as function of $g\tau$ but fixed $g/\chi = 5$. The measurement time

τ_m is chosen sufficiently large to maximize $\mathcal{F}$. As expected from Fig. 4, the fidelity is reduced for smaller $\gamma\tau$ because spatially longer photons (smaller $\gamma\tau$) lead to more noise in the measurement.

A remarkable feature of Fig. 5 is the clear trend of the assignment fidelity approaching unity with increasing $g\tau$. This number can be increased at fixed interaction strength g by increasing the detector length. In the next section we show that values of $g\tau$ in the range 1–3 used in Fig. 5 are within reach for experimentally realistic parameters and metamaterial lengths.

JTWPD design parameters The JTWPD shares similarities with the Josephson Traveling Wave Parametric Amplifier (JTWPA) (*23*). State of the art JTWPAs consists of a metamaterial with $N_{\rm cells} \simeq 2000$–$3000$ unit cells, each comprised of a large Josephson junction and a shunt capacitance to ground. In addition, LC oscillators used to engineer the dispersion relation are placed every few unit cells. We envision a JTWPD with a similar number of unit cells, with a modest increase in complexity for each unit cell. The most significant design difference is that in the JTWPD every unit cell is coupled to the same probe resonator. In practice, this resonator can be a coplanar waveguide resonator or a 3D cavity.

As shown in the Supplementary Materials, the number of unit cells necessary to reach a given value of $g\tau$ can be expressed as

$$N_{\rm cells} = \frac{1}{2}\left(\frac{|g\tau|}{\alpha}\frac{R_K}{8\pi Z_{\rm tml}}\right)^2 \frac{\bar{\omega}^2}{|K|E_J/\hbar}. \qquad (11)$$

where we neglect spatial dependence of the parameters for simplicity. In contrast to the simulation results, we assume here that the detector is operated in reflection mode, effectively halving the number of unit cells needed for a given value of τ. In this expression $R_K = h/e^2$ is the quantum of resistance, $Z_{\rm tml}$ the characteristic impedance of the metamaterial, and E_J the junction Josephson energy.

Recall that the parameter $K < 0$ appearing in Eq. (11) is the Kerr nonlinearity of the resonator resulting from the Josephson junctions used to couple the probe to the metameterial [see Eq. (13)]. However, the total Kerr nonlinearity of the resonator $K_{\rm tot} = K + K_s$ can be adjusted by introducing another nonlinear element such as transmon in the straddling regime (*28*) or a SNAIL (*29*) to the probe. Following this approach, we can allow for a detector with a larger negative $K < 0$ contributing to reducing $N_{\rm cells}$, yet still have a total Kerr nonlinearity $K_{\rm tot} \simeq 0$ to avoid nonlinear response of the probe mode. Very similar ideas have recently been used to cancel unwanted cross-Kerr nonlinearities of order 200 kHz (*30*).

Fig. 6 shows $N_{\rm cells}$ as a function of the probe self-Kerr K to reach $g\tau$ in the range 1–3, for a photon center frequency of $\bar{\omega}/(2\pi) = 5$ GHz. In these plots we use a junction critical current $I_c = E_J/\phi_0 = 5\,\mu$A, which is similar to junctions used in JTWPAs (*23*), and the other parameters are $\alpha = 5$ and $Z_{\rm tml} = 50\,\Omega$. Crucially, it is possible to reach $g\tau$ in the range 1–3, as in our numerical simulations above, using $N_{\rm cells} \sim 2000$–3000 without needing an excessively large $|K|$. Alternatively, the same value of $g\tau$ can be reached for a smaller $|K|$ by increasing the transmission line characteristic impedance, $Z_{\rm tml}$, as is clear from Eq. (11). Impedance matching with $50\,\Omega$ input and output transmission lines can then be achieved using low loss impedance transformers. As discussed in more detail in the Supplementary Materials, the self-Kerr can be tuned by varying the small coupling capacitance C_c between the junctions and the probe resonator, with typical values in the 1–10 fF range.

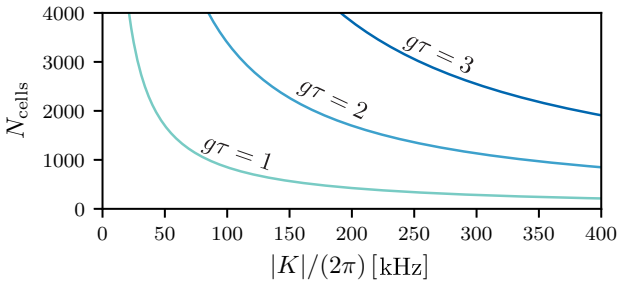

Figure 6: Number of unit cells needed to reach $g\tau$ in the range 1–3 as a function of probe resonator Kerr nonlinearity $|K|$, for $\alpha = 5$, $\bar{\omega}/(2\pi) = 5$ GHz, $I_c = 5\,\mu$A and $Z_{\rm tml} = 50\,\Omega$. The total Kerr non-linearity of the resonator $K_{\rm tot} = K + K_s$ can be tuned close to zero using, *e.g.*, a transmon in the straddling regime.

The speed of light in the metamaterial is set by $v/a = (C_0/C_{\rm nn})\omega_0$, where ω_0 is the resonance frequency of the LC oscillators in the array, C_0 the total capacitance of the LC and $C_{\rm nn}$ the nearest neighbor coupling between LCs (see Supplementary Materials). With $C_{\rm nn}/C_0 = 0.1$ and $\omega_0/(2\pi) = 5$ GHz we thus get an interaction time $\tau = 2z/v = 1.3\,\mu$s for $N_{\rm cells} = 2000$ as a representative example. To have $\kappa_a\tau = 1$ as in the simulations above, this then suggests a probe decay rate in the range $\kappa_a/2\pi \simeq 0.1$ MHz. We note that larger values of $\kappa_a\tau$ might also be of interest, but we found this regime too demanding for numerical simulations due to the prohibitively small time steps needed. Based on the numerical results in the previous section, the detection time is of the order $\tau_m \simeq 3\tau$, and thus expected to be in the μs range for this choice of τ. The detector reset time is naturally of the order $1/\kappa_a$ and thus in the 10 μs range, but can likely be made faster using active reset protocols. To avoid significant backaction effects, the photon's spectral width must not be too small as we have shown in the preceding sections. A value for the dimensionless photon width of $\gamma\tau = 2$ corresponds to a FWHM of $\gamma/(2\pi) = 0.25$ MHz, for the value $\tau = 1\,\mu$s. We emphasize that the detection fidelity increases with increasing γ, and from our numerical results we thus expect photons of spectral width in the MHz range or larger to be detectable with very high fidelity. The bandwidth of the detector is, on the other hand, set by appropriately choosing the LC oscillators of the metamaterial. The LC array has an approximately linear dispersion relation in a band around the resonance frequency ω_0, with frequency cuttoffs at $\omega_0 \pm (C_{\rm nn}/C_0)\omega_0$. For example, with $\omega_0/2\pi \simeq 5$ GHz and $C_{\rm nn} \sim 0.1C_0$, the JTWPD can reach bandwidths in the several hundreds of MHz range. Depending on intended application, it might not be necessary to engineer such a large bandwidth and the coupling capacitance can be chosen smaller, for example to reduce the rate of thermal photons incident on the detector.

Discussion

Previous work have questioned whether cross-Kerr interaction can be used for high-fidelity single photon counting (*22*), seemingly in contradiction with our results. There is, however, a fundamental difference between our proposal and the approach of Ref. (*22*). There, a number of nonlinear absorbers *independently* couple to a traveling control field. This is similar to an alternative version of our proposal where each unit cell of the metematerial couples to an independent probe resonator. More generally, we can consider a situation where we partition the N unit cells of the detector into M blocks, with each block coupled to an independent readout probe resonator. With $M = N$ we have a setup similar to Ref. (*22*), while $M = 1$ corresponds to the JTWPD. However, as shown in Materials and Methods, such a setup gives a $\sqrt{M}$ *reduction* in the probe resonator's displacement. Our proposal thus has an $\sqrt{N}$ improvement in the SNR scaling. This improvement comes from using what we referred to in the introduction as a giant probe, i.e. a probe resonator that has a significant length compared to the photon. This contrasts with conventional circuit QED-based photodectors relying on point-like probe systems. Interestingly, such a setup does not have any obvious analog in the optical domain, demonstrating the potential of using metamaterials based on superconducting quantum circuits to explore fundamentally new domains of quantum optics.

In summary, we have introduced the JTWPD, a microwave photodetector based on a weakly nonlinear metamaterial coupled to a giant probe. This detector is unconditional in the sense that no a priori information about the photon arrival time or detailed knowledge of the photon shape is needed for its operation. Detection fidelities approaching unity, corresponding to detector efficiency approaching one and dark count rates approaching zero, are predicted for metamaterial length that are compatible with state-of-the-art experiments. Moreover, because the JTWPD does not rely on absorption in a resonant mode, large detection bandwidths are possible.

A remarkable feature of the JTWPD, which distinguishes this detector from photodetectors operating in the optical regime, is the nondestructive nature of the interaction. Together with the large bandwith and high detection fidelity, this opens new possibilities for single-photon measurement and control, including feedback of photons after measurement, weak single-photon measurement, and cascading photon detection with other measurement schemes or coherent interactions.

Materials and Methods

Kerr nonlinearity of the probe resonator The self- and cross-Kerr shifts of the probe resonator induced by the nonlinear coupling to the waveguide can be found using a black-box quantization approach (*31*). As shown in the Supplementary Materials, the probe resonator Hamiltonian can be written as

$$\hat{H}_r = \hbar\omega_r \hat{a}^\dagger \hat{a} + \frac{\hbar K}{2}\hat{a}^{\dagger 2}\hat{a}^2 + \hbar\left(i\varepsilon e^{-i\omega_d t}\hat{a}^\dagger + \text{H.c.}\right), \quad (12)$$

with $\hat{a}$ the annihilation operator for the probe mode satisfying $[\hat{a}, \hat{a}^\dagger] = 1$. The resonator frequency ω_r includes significant frequency shifts due to the Josephson junction couplers. Moreover, the Kerr-nonlinearity K takes the form

$$\hbar K = -\sum_n E_{J,n}\frac{8\pi^2 Z_r^2}{R_K^2}|u(x_k)|^4 \quad (13)$$

with $E_{J,n}$ the Josephson energy of the nth junction, $\phi_0 = \hbar/2e$ the reduced flux quantum and $R_K = h/e^2$ the quantum of resistance. Furthermore, Z_r is the characteristic impedance of the probe resonator and $u(x_n)$ is a dressed resonator mode function evaluated at the location x_n of the nth junction, such that $\sqrt{Z_r}u(x_n)$ is the zero-point fluctuations of the probe resonator biasing the nth junction (*31*). The last term of $\hat{H}_r$ describes a resonator drive with amplitude ε and frequency ω_d. Taking damping of the probe resonator into account, the dynamics of the system is described by the master equation

$$\dot{\rho} = -\frac{i}{\hbar}[\hat{H}_r, \rho] + \kappa_a \mathcal{D}[\hat{a}]\rho. \quad (14)$$

Moving to a frame rotating at the drive frequency and then displacing the field such that $\hat{a} \to \hat{a} + \alpha$, $\hat{H}_r$ takes the form

$$\hat{H}_r'/\hbar = (\delta + 2K|\alpha|^2)\hat{a}^\dagger\hat{a} + \frac{K}{2}\hat{a}^{\dagger 2}\hat{a}^2, \quad (15)$$

where $\delta = \omega_r - \omega_d$ and with α chosen such as to satisfy the steady-state equation

$$(\delta + K|\alpha|^2)\alpha - \frac{i\kappa_a}{2}\alpha + i\varepsilon = 0. \quad (16)$$

To drive the probe mode on resonance despite the Kerr nonlinearity, we chose ω_d such that $\delta = -2K|\alpha|^2$. With this choice, the transformed probe Hamiltonian reduces to

$$\hat{H}_r' = \hbar K/2\hat{a}^{\dagger 2}\hat{a}^2 \quad (17)$$

while the nonlinear equation for α becomes

$$K|\alpha|^2\alpha + \frac{i\kappa_a}{2}\alpha = i\varepsilon. \quad (18)$$

For $K|\alpha|^2 \ll \kappa_a$, the solution is approximately $\alpha = 2\varepsilon/\kappa_a$ and the steady-state of the resonator is to a good approximation the coherent state $|\alpha\rangle$. As discussed further in the Supplementary Materials, in the opposite limit, the steady-state becomes non-Gaussian something which can reduce the signal-to-noise ratio of the detector. To remain in the linear regime for sizeable α, we take $|K|/\kappa_a$ to be small.

Waveguide-probe cross-Kerr coupling In the laboratory frame, the cross-Kerr interaction between the probe resonator and the waveguide takes the form

$$\hat{H}_{\text{int}} = \hbar\sum_{\nu\mu}\int_{-z/2}^{z/2} dx\chi(x)\hat{b}_\nu^\dagger(x)\hat{b}_\mu(x)\hat{a}^\dagger\hat{a}, \quad (19)$$

to fourth order in the Josephson junction potentials and where $\nu = \pm$ refers to the direction of propagation of the photon. In this expression, we have defined the dispersive shift per unit length

$$\hbar\chi(x_n) = -\frac{vE_{J,n}}{a\bar{\omega}}\frac{(4\pi)^2 Z_m Z_{\text{tml}}}{R_K^2}|u(x_n)|^2, \quad (20)$$

with $\bar{\omega}$ the photon center frequency introduced for later convenience, $Z_{\rm tml}$ the characteristic impedance of the transmission line at frequency $\bar{\omega}$, and we recall that a is the unit cell length. Because we are only interested in small photon number in the waveguide, we have safely dropped fast-rotating terms and higher-order terms in $\hat{b}_{\nu\omega}$ from Eq. (19). Moving to the rotating and displaced frame introduced for the probe resonator above, Eq. (19) leads to Eq. (3) where $g(x) = \alpha\chi(x)$ with α given by Eq. (18) and where we take α to be real without loss of generality.

The integral in $\hat{H}_{\rm int}$ should be interpreted as a Riemann sum, and the continuum limit is valid as long as all relevant wavelengths are much longer than a. Moreover, the expression for $\hat{b}_\nu(x)$ in Eq. (4) and $\chi(x)$ in Eq. (20) are derived under the assumption that dispersion is negligible over a relevant frequency band around $\bar{\omega}$, where the photon number is non-zero. In other words, we are working under the assumption that the incoming photon is sufficiently narrow. Nevertheless, we expect that photons with large spread of frequency components compared to previous proposals can be detected.

Effective Keldysh master equation We describe the main steps of the derivation leading to Eq. (6) and refer the reader to the Supplementary Materials for more details. We model the incoming photon using an emitter located at position x_0 to the left of the metamaterial and of annihilation operator $\hat{c}$. After initializing the emitter in the state $|1\rangle$, the emitter decay rate, $\kappa_c(t)$, is chosen such as to model the desired single-photon wavepacket. Here, we choose a Gaussian wavepacket $\xi(t)$ of variance σ^2

$$\xi(t) = \left(\frac{2\sigma^2}{\pi}\right)^{1/4} e^{-i\bar{\omega}t} e^{-\sigma^2(t+x_0/v)^2}, \tag{21}$$

by using

$$\kappa_c(t) = \sqrt{\frac{8\sigma^2}{\pi}} \frac{e^{-2\sigma^2 t^2}}{1-\mathrm{erf}[\sqrt{2}\sigma t]}, \tag{22}$$

with $\mathrm{erf}(x)$ the error function. The FWHM γ used in the main text is related to the variance as $\gamma = 2\sqrt{2\ln 2}\sigma$.

The ideal Hamiltonian for the detector, emitter, and waveguide is given by

$$\begin{aligned}
\hat{H} &= \hat{H}_0 + \hat{H}_{\rm ideal} + \hat{H}_c, \\
\hat{H}_0 &= \sum_\nu \int_\Omega d\omega\, \hbar\omega \hat{b}^\dagger_{\nu,\omega}\hat{b}_{\nu,\omega}, \\
\hat{H}_{\rm ideal} &= \hbar g \sum_{\nu\mu} \int_{-z/2}^{z/2} dx\, \hat{b}^\dagger_\nu(x)\hat{b}_\mu(x)(\hat{a}^\dagger + \hat{a}), \\
\hat{H}_c &= \bar{\omega}\hat{c}^\dagger\hat{c} + \sqrt{\kappa_c(t)v}\left[\hat{b}^\dagger_+(x_0)\hat{c} + \mathrm{H.c.}\right].
\end{aligned} \tag{23}$$

Using this Hamiltonian and adding decay of the probe resonator, we write the corresponding Keldysh action following Ref. (*32*). As explained in the Supplementary Materials, do to this we take advantage of the fact that the action is quadratic in the fields $\hat{b}_\pm(x)$ and integrate out the waveguide degrees of freedom. The result is then expanded in a Taylor series in the interaction strength, which yields an effective Keldysh action for the emitter-resonator system. Finally, from that effective action, we find the equivalent master equation Eq. (6).

Detector response neglecting backaction

To help in building intuition for the detector's response to a single photon, it is useful to neglect backaction effects and any correlations between the emitter and detector. Under these approximations, upon tracing out the emitter from Eq. (6), we can replace the term $\mathrm{tr}_C\left[\hat{c}\hat{\rho}\hat{c}^\dagger\right]$ by the approximate expression $\langle\hat{c}^\dagger\hat{c}\rangle \otimes \hat{\rho}_A$, where $\mathrm{tr}_C\bullet$ is a partial trace over the emitter and $\hat{\rho}_A$ is the reduced state of the probe resonator. In this way, the reduced master equation for the probe resonator takes the form

$$\dot{\hat{\rho}}_A \simeq -i\left[g n_{\rm det}(t)(\hat{a}+\hat{a}^\dagger), \hat{\rho}_A\right] + \kappa_a \mathcal{D}[\hat{a}]\hat{\rho}_A. \tag{24}$$

The associated quantum Langevin equation is

$$\dot{\hat{a}} \simeq -ig n_{\rm det}(t) - \frac{\kappa_a}{2}\hat{a} + \sqrt{\kappa_a}\hat{a}_{\rm in}(t), \tag{25}$$

with $\hat{a}_{\rm in}(t)$ the input field which is in the vacuum state in the displaced frame, i.e. $\langle\hat{a}_{\rm in}(t)\rangle = 0$. The solution for the expectation value $\langle\hat{a}(t)\rangle$ is then given by

$$\langle\hat{a}(t)\rangle \simeq -ig\int_{t_0}^{t} dt' e^{-\kappa_a(t-t')/2} n_{\rm det}(t). \tag{26}$$

As expected, the number of photon in the metamaterial, $n_{\rm det}(t)$, leads to a displacement of the probe field. We have confirmed that for the parameters used in Fig. 4, the above approximate expression is indistinguishable from the solution found from the full Keldysh master equation [dotted lines in Fig. 4 (a,e)].

Detectors in series

We can generalize the above discussion to a situation where the metamaterial is divided into M equal subsections, individually coupled to a set of M independent and identical probe resonators. The interaction Hamiltonian then takes the form

$$\begin{aligned}
\hat{H}_{\rm ideal} = \hbar g \sum_{m=0}^{M-1} \sum_{\nu\mu} \int_{x_m-\Delta x/2}^{x_{m+\Delta x/2}} dx \\
\times \hat{b}^\dagger_\nu(x)\hat{b}_\mu(x)\left(\hat{a}^\dagger_m + \hat{a}_m\right),
\end{aligned} \tag{27}$$

with $x_m = -z/2 + \left(m+\frac{1}{2}\right)\Delta x$, $\Delta x = z/M$, and $[\hat{a}_m, \hat{a}^\dagger_n] = \delta_{mn}$. Defining the collective mode

$$\hat{a}_\Sigma = \frac{1}{\sqrt{M}}\sum_{m=0}^{M-1}\hat{a}_m, \tag{28}$$

satisfying $[\hat{a}_\Sigma, \hat{a}^\dagger_\Sigma] = 1$, and assuming that each probe resonator labeled by m couples identically with rate κ to a common input-output waveguide, leads to the quantum Langevin equation for the collective mode

$$\dot{\hat{a}}_\Sigma = \frac{i}{\hbar}[\hat{H}_{\rm ideal}, \hat{a}_\Sigma] - \frac{\kappa_\Sigma}{2}\hat{a}_\Sigma + \sqrt{\kappa_\Sigma}\hat{a}_{\rm in}(t), \tag{29}$$

where $\kappa_\Sigma = M\kappa$ and where we have taken the resonator frequencies to be identical. Under a similar set of approximations as above, we find

$$\dot{\hat{a}}_\Sigma \simeq -\frac{ig}{\sqrt{M}} n_{\rm det}(t) - \frac{\kappa_\Sigma}{2}\hat{a}_\Sigma + \sqrt{\kappa_\Sigma}\hat{a}_{\rm in}(t), \tag{30}$$

Comparing to Eq. (25) which was obtained for $M = 1$, we find a $\sqrt{M}$ reduction in the displacement. To compensate one could increase $g \to g\sqrt{M}$, but this leads to a breakdown of the assumption of negligible backaction. In summary the "giant probe" limit $M = 1$ is ideal.

Matrix Product State simulations The JTWPD is an open quantum many-body system with nonlocal interactions, and numerically simulating its time evolution poses an important challenge. Recently, approaches based on Matrix Product States (MPS) have been developed to simulate point-like scatterers interacting with one-dimensional waveguides (*25, 26*). Applying these ideas to the JTWPD, however, requires nontrivial extensions of the techniques in order to deal with the nonlocal interaction and the stochastic nature of the evolution in the presence of continuous homodyne detection. We outline here the main ideas behind the method we have developed, leaving further details to the Supplementary Materials.

To represent the system as an MPS, we discretize both time and space. In the following we only consider the right moving field in the waveguide. As long as the different parts of the waveguide are impedance matched and $g/\bar{\omega} \ll 1$, back scattering into the left-moving field is negligible and we can therefore drop it. Following (*25, 26*), we trotterize the time evolution operator

$$U(T) = \mathcal{T} e^{-i\int_0^T dt \hat{H}(t)} = \lim_{N_t\to\infty} \hat{U}_{N_t-1}\dots\hat{U}_1\hat{U}_0, \quad (31)$$

where $\hat{H}(t)$ is the Hamiltonian in the interaction picture, and $\hat{U}_i$ evolves the system for a small time t_i to $t_i + \Delta t$. We moreover similarly discretize the spatial integral for each $\hat{U}_i$

$$\hat{U}_i = \lim_{N_x\to\infty} \hat{U}_{i,N_x-1}\dots\hat{U}_{i,1}\hat{U}_{i,0}, \quad (32)$$

where

$$\hat{U}_{i,n} = e^{-\frac{i}{\hbar}\int_{t_i}^{t_i+\Delta t} dt \int_{x_n}^{x_n+\Delta x} dx \hat{\mathcal{H}}_{\rm int}(x,t) - \frac{i}{\hbar}\Delta t \hat{H}_r/N_x}, \quad (33)$$

and $\Delta x = v\Delta t$. We next make the approximations

$$\begin{aligned}
&\int_{t_i}^{t_i+\Delta t} dt \int_{x_n}^{x_n+\Delta x} dx \hat{b}_+^\dagger(x-vt)\hat{b}_+(x-vt)\hat{A}(x) \\
&\simeq \int_{t_i}^{t_i+\Delta t} dt \hat{b}_+^\dagger(x_n-vt)\int_{x_n}^{x_n+\Delta x} dx \hat{b}_+(x-vt_i)\hat{A}(x_n) \\
&= -\Delta t \hat{b}_{n-i}\hat{b}_{n-i}\hat{A}(x_n),
\end{aligned} \quad (34)$$

with $\hat{A}(x) = \chi(x)\left(\hat{a}^\dagger\hat{a} + \alpha^2\right) + g(x)\left(\hat{a}^\dagger + \hat{a}\right)$ and where, in the last line, we have defined

$$\hat{b}_n = \frac{1}{\sqrt{\Delta x}}\int_{x_n}^{x_n+\Delta x} dx \hat{b}_+(x). \quad (35)$$

For a photon that is not too broad in frequency, we can extend the integration limits in Eq. (4) and approximate

$$\hat{b}_+(x) \simeq \sqrt{\frac{1}{2\pi v}}\int_{-\infty}^{\infty} d\omega \hat{b}_{+\omega} e^{i\omega x/v}. \quad (36)$$

Since $[\hat{b}_{+\omega}, \hat{b}^\dagger_{+\omega'}] = \delta(\omega-\omega')$ this leads to $[\hat{b}_n, \hat{b}_m^\dagger] \simeq \delta_{nm}$, such that these discrete modes can be interpreted as harmonic oscillators.

As illustrated in Fig. 7, Eq. (33) thus suggests the following picture: In the ith time step, the probe resonator interacts with waveguide modes $\hat{b}_j$ with $-i \le j < N_x - i$. In the next time step, the waveguide modes are shifted one unit cell to the right relative to the probe, such that interaction is now with $-i-1 \le j < N_x - i - 1$, and so on. To model an incoming photon, we also include an emitter

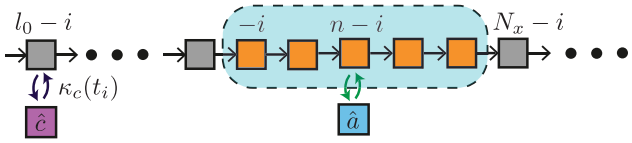

Figure 7: At the ith time step, the probe resonator ($\hat{a}$) interacts with oscillators labeled $-i \le j < N_x - i$, as indicated by the dashed box. An emitter ($\hat{c}$) decays with rate σ far to the left of the detector.

decaying at rate $\kappa_c(t_i)$ into the waveguide at site $l_0 - i$ with $l_0 < 0$ to the left of the detector.

This discretized system can be evolved using methods described in Ref. (*26*), with two important changes: 1) Within each time step the probe resonator interacts with multiple waveguide oscillators represented by the blue region in Fig. 7. We therefore perform a single time step by swapping (*33*) the MPS site corresponding to the probe resonator along the MPS, letting it interact with the waveguide modes one by one. 2) For $\kappa_a > 0$, the probe resonator is coupled to an additional bath describing the input-output fields $\hat{a}_{\rm in/out}(t)$, with $\hat{a}_{\rm out}(t)$ being continuously monitored by homodyne detection. To avoid representing these bath degrees of freedom explicitly, we replace the unitary evolution $e^{-i\hat{H}_r\Delta t}$ with a stochastic Schrödinger equation for the MPS integrated from t_i to $t_i + \Delta t$. For this, we use the usual stochastic Schrödinger equation for homodyne detection which can be integrated using standard numerical solvers for stochastic differential equations (*34*). Note that only a single site of the MPS is changed during this step. Further details are given in the Supplementary Materials.

Supplementary Materials

Supplementary material for this article is available at [attached pdf].

References

1. F. Helmer, M. Mariantoni, E. Solano, F. Marquardt, *Phys. Rev. A* **79**, 052115 (2009).
2. Y.-F. Chen, *et al.*, *Phys. Rev. Lett.* **107**, 217401 (2011).
3. S. R. Sathyamoorthy, *et al.*, *Phys. Rev. Lett.* **112**, 093601 (2014).
4. B. Fan, G. Johansson, J. Combes, G. Milburn, T. M. Stace, *Phys. Rev. B* **90**, 035132 (2014).
5. K. Koshino, Z. Lin, K. Inomata, T. Yamamoto, Y. Nakamura, *Phys. Rev. A* **93**, 023824 (2016).
6. K. Inomata, *et al.*, *Nature Comm.* **7**, 12303 (2016).
7. A. Narla, *et al.*, *Phys. Rev. X* **6**, 031036 (2016).
8. O. Kyriienko, A. S. Sørensen, *Phys. Rev. Lett.* **117**, 140503 (2016).

9. J. Leppäkangas, *et al.*, *Physical Review A* **97**, 013855 (2018).

10. S. Kono, K. Koshino, Y. Tabuchi, A. Noguchi, Y. Nakamura, *Nature Physics* **14**, 546 (2018).

11. J.-C. Besse, *et al.*, *Phys. Rev. X* **8**, 021003 (2018).

12. B. Royer, A. L. Grimsmo, A. Choquette-Poitevin, A. Blais, *Phys. Rev. Lett.* **120**, 203602 (2018).

13. R. Lescanne, *et al.*, *arXiv:1902.05102* (2019).

14. J. B. Spring, *et al.*, *Science* **339**, 798 (2013).

15. N. H. Nickerson, J. F. Fitzsimons, S. C. Benjamin, *Phys. Rev. X* **4**, 041041 (2014).

16. S. Lloyd, *Science* **321**, 1463 (2008).

17. S. K. Lamoreaux, K. A. van Bibber, K. W. Lehnert, G. Carosi, *Phys. Rev. D* **88**, 035020 (2013).

18. R. H. Hadfield, *Nature Photonics* **3**, 696 (2009).

19. J. H. Shapiro, *Phys. Rev. A* **73**, 062305 (2006).

20. J. H. Shapiro, M. Razavi, *New Journal of Physics* **9**, 16 (2007).

21. J. Gea-Banacloche, *Phys. Rev. A* **81**, 043823 (2010).

22. B. Fan, *et al.*, *Phys. Rev. Lett.* **110**, 053601 (2013).

23. C. Macklin, *et al.*, *Science* **350**, 307 (2015).

24. N. Didier, J. Bourassa, A. Blais, *Phys. Rev. Lett.* **115**, 203601 (2015).

25. A. L. Grimsmo, *Phys. Rev. Lett.* **115**, 060402 (2015).

26. H. Pichler, P. Zoller, *Phys. Rev. Lett.* **116**, 093601 (2016).

27. H. M. Wiseman, G. J. Milburn, *Quantum measurement and control* (Cambridge university press, 2009).

28. J. Koch, *et al.*, *Phys. Rev. A* **76**, 042319 (2007).

29. N. Frattini, *et al.*, *Applied Physics Letters* **110**, 222603 (2017).

30. G. Zhang, P. S. Mundada, A. A. Houck, *arXiv:1810.04182* (2018).

31. S. E. Nigg, *et al.*, *Phys. Rev. Lett* **108**, 240502 (2012).

32. L. M. Sieberer, M. Buchhold, S. Diehl, *Reports on Progress in Physics* **79**, 096001 (2016).

33. M. L. Wall, A. Safavi-Naini, A. M. Rey, *Phys. Rev. A* **94**, 053637 (2016).

34. P. E. Kloeden, E. Platen, *Numerical Solution of Stochastic Differential Equations* (Springer-Verlag Berlin Heidelberg, 1992).

35. U. Vool, M. Devoret, *International Journal of Circuit Theory and Applications* **45**, 897 (2017).

36. N. A. R. Bhat, J. E. Sipe, *Phys. Rev. A* **73**, 063808 (2006).

37. M. Dolfi, *et al.*, *Comp. Phys. Comm.* **185**, 3430 (2014).

38. U. Schollwöck, *Ann. Phys.* **326**, 96 (2011).

39. P. Z. C.W. Gardiner, *Quantum Noise: A Handbook of Markovian and Non-Markovian Quantum Stochastic Methods with Applications to Quantum Optics*, Springer Series in Synergetics (Springer, 2000), second edn.

40. Z. K. Minev, Catching and reversing a quantum jump mid-flight, Ph.D. thesis, Yale University (2019).

Acknowledgements

We thank J. Bourassa, T. Stace and J. Combes for valuable discussions. **Funding:** This work is supported by the Australian Research Council (ARC) via Centre of Excellence in Engineered Quantum Systems (EQUS) Project No. CE170100009 and a Discovery Early Career Researcher Award (DE190100380). Part of this work was supported by the Army Research Office under Grant no. W911NF-15-1-0421, NSERC and by the Canada First Research Excellence Fund. **Author contributions:** ALG and BR devised the project and performed the numerical and analytical analysis. All authors contributed to analyzing and interpreting the results, and to writing the manuscript. **Competing interests:** The authors declare that they have no competing interests. **Data and material availability:** All relevant data to support the conclusions are within the paper and its Supplementary Materials. The authors will make raw data available upon request at arne.grimsmo@sydney.edu.au.

3.3.3 Avenues de recherche

Une des avenues intéressantes de ce travail est l'utilisation des méthodes développées pour décrire le JWTPD à d'autres métamatériaux similaires, par exemple les amplificateurs JTWPA [141]. Par leur nature unidimensionnelle, ces métamatériaux sont difficiles à représenter numériquement et analytiquement, car il faut considérer un continuum de modes. Les travaux réalisés à ce jour [145, 149] négligent typiquement les interactions non linéaires et se cantonnent à des régimes où le champ de sortie est gaussien. Il serait intéressant de voir si la méthode d'intégrales de chemin Keldysh permet d'aller au-delà de ces analyses pour mieux caractériser des métamatériaux non linéaires.

Chapitre 4

Mesure de parité

4.1 Contexte

Considérant la fragilité des états quantiques, il est inévitable que l'information contenue dans un qubit physique, par exemple un transmon, soit éventuellement corrompue. Pour développer un ordinateur quantique universel, il est donc impératif de développer des stratégies afin de protéger l'information logique contre les interactions parasites avec l'environnement. Heureusement, le théorème du seuil [150, 151] nous certifie qu'il est possible de protéger l'information quantique contre les inévitables erreurs à condition que toutes les opérations de l'ordinateur quantique se fassent avec un taux d'erreur suffisamment bas, $p < p_{\text{seuil}}$. Afin d'obtenir cette protection, on utilise des codes de corrections d'erreur qui diminuent le taux d'erreur au prix de qubits et d'opérations additionnelles.

Dans l'article présenté à l'intérieur de ce chapitre, j'introduis une méthode qui pourrait aider à la fabrication d'un ordinateur quantique universel en diminuant le coût expérimental relié à la correction d'erreur. Bien que ces résultats s'appliquent à plusieurs codes de correction d'erreur, je ferai surtout référence au code de surface [152, 153, 154, 155] illustré à la figure 4.1. Ce code est particulièrement attrayant grâce à son seuil élevé, $p_{\text{seuil}} \approx 1\%$ [154], et à sa géométrie bidimensionnelle planaire.

Essentiellement, un code de correction d'erreur quantique protège l'information logique en l'encodant de manière redondante et non locale dans un ensemble de

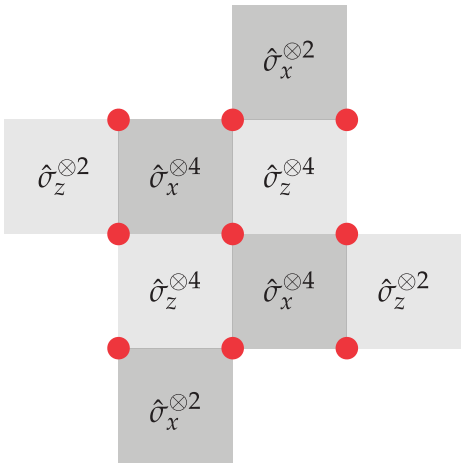

FIGURE 4.1 – Schéma du code de surface. Neuf qubits physiques (ronds rouges) encodent un qubit logique défini dans le sous-espace propre +1 des huit stabilisateurs (carrés gris). Ces stabilisateurs consistent en opérateurs $\hat{\sigma}_z^{\otimes n}$ (gris pâle) et $\hat{\sigma}_x^{\otimes n}$ (gris foncé) avec $n = 4$ à l'intérieur de la surface de qubits et $n = 2$ sur les bords.

qubits physiques. Par exemple, pour le code de surface illustré à la figure 4.1, un qubit logique est encodé dans un ensemble de $L \times L$ qubits physiques avec $L = 3$, où allonger L équivaut à augmenter la robustesse du qubit logique contre les erreurs locales. On définit l'espace logique du code comme le sous-espace correspondant à la valeur propre +1 d'un ensemble d'opérateurs multi qubits, appelés stabilisateurs [156], et on s'assure que le système est dans cet espace logique à partir d'une mesure des stabilisateurs. Pour le code de surface, ces stabilisateurs correspondent aux opérateurs $\hat{\sigma}_z^{\otimes n}$ (gris foncé), et $\hat{\sigma}_x^{\otimes n}$ (gris pâle). Après une erreur sur un qubit physique, le système sort du sous-espace logique et se retrouve dans l'espace propre -1 d'au moins un stabilisateur. En mesurant à répétition ces stabilisateurs, opération aussi appelée *mesure de parité*, il est possible de détecter et de corriger les erreurs avant que l'information logique ne soit corrompue.

Techniquement, une mesure de parité réfère seulement à un sous-ensemble des mesures de stabilisateurs, soit une mesure d'opérateurs de Pauli, $\hat{\sigma}_z^{\otimes n}$, révélant si le nombre de 1 est pair ou impair dans l'ensemble de n qubits. Par abus de langage, j'étends ici la définition de mesure de parité à toutes les mesures d'opérateurs de Pauli sur plusieurs qubits. Ceci est justifié par le fait que ces mesures peuvent être

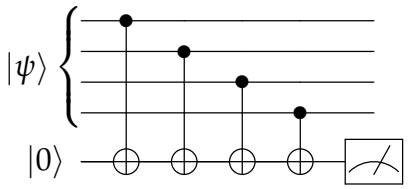

FIGURE 4.2 – Un qubit ancillaire préparé dans l'état $|0\rangle$ permet de mesurer la parité, $\hat{\sigma}_z^{\otimes 4}$, de l'état $|\psi\rangle$ à quatre qubits.

effectuées à partir d'une mesure $\hat{\sigma}_z^{\otimes n}$ combinée à des portes à un qubit.

Étant donné que les mesures de parité doivent se faire à intervalles réguliers, il est important qu'elles soient rapides et qu'elles aient une fidélité proche de l'unité. De plus, la mesure elle-même devrait éviter d'introduire des erreurs dans les qubits physiques et un état avec une parité initiale bien définie ne devrait pas être affecté par la mesure.

L'approche standard pour la mesure de parité est d'utiliser un qubit ancillaire préparé dans son état fondamental [46, 47, 48, 49, 51, 52]. En utilisant une série de portes logiques à deux qubits comme illustré sur la figure 4.2, il est possible d'encoder la valeur du stabilisateur dans l'état de ce qubit ancillaire qui est ensuite mesuré. Toutefois, cette approche nécessite une surcharge expérimentale considérable, car chaque stabilisateur requiert l'addition d'un qubit. Pour le code de surface, cela implique d'approximativement doubler le nombre de qubits à fabriquer, calibrer et contrôler ($9 \rightarrow 17$ qubits sur la figure 4.1). Par exemple, voici le bilan en matériel nécessaire à la mesure de parité indirecte démontrée par Takita *et al.* [51] :

— Un qubit ancillaire avec grand temps de cohérence
— Deux résonateurs de couplage entre les qubits
— Un résonateur de mesure pour le qubit ancillaire
— Un filtre Purcell pour le résonateur de mesure

Chaque mesure requiert aussi plusieurs portes à deux qubits qui allongent le temps nécessaire pour mesurer la parité en plus d'être une source additionnelle d'erreurs.

Une seconde approche à la mesure de parité est de mesurer directement celle-ci en couplant plusieurs qubits à un résonateur de mesure [53, 54, 55, 57, 157, 50]. En encodant directement la parité dans ce mode commun, la nécessité d'un qubit ancillaire et de portes à deux qubits disparaît, allégeant considérablement le coût

expérimental d'une telle mesure. Dans cette approche, le défi réside dans la conception d'une interaction effective globale entre l'ensemble des qubits et le résonateur. Typiquement, les mesures de parité directes se basent sur l'interaction dispersive qui, dans la situation où plusieurs qubits sont couplés au même résonateur, prend la forme

$$\hat{H} = \sum_j \chi_j \hat{\sigma}_{z,j} \hat{a}^\dagger \hat{a}. \tag{4.1}$$

En sondant la fréquence de résonance du résonateur à l'aide d'un pilotage bien choisi et en mesurant le champ de sortie, certaines propriétés de l'ensemble des qubits peuvent être mesurées. Crucialement, l'opérateur couplé au résonateur ne correspond pas à l'observable désirée, mais plutôt au poids de Hamming de l'état des qubits

$$\hat{M} = \bigotimes_j \hat{\sigma}_{z,j}. \tag{4.2}$$

Conséquemment, le champ de sortie n'est pas exactement un état binaire encodant l'observable 4.2, ce qui induit un déphasage parasite sur les qubits. En d'autres mots, il est difficile d'encoder *seulement* le bit d'information correspondant à l'observable 4.2 dans l'état du résonateur, et l'information acquise en plus de ce bit mène à du déphasage.

Par exemple, il est possible de réaliser une mesure de parité pour deux qubits à partir d'un protocole similaire à la mesure dispersive standard à un qubit [53, 54, 57]. Cette méthode consiste à sonder la fréquence du résonateur à l'aide d'une onde micro-onde à la fréquence nue du résonateur, ω_r. Dans le référentiel tournant à la fréquence du résonateur, cette situation est décrite par l'Hamiltonien

$$\hat{H} = \epsilon(\hat{a} + \hat{a}^\dagger) + \chi \sum_{j=1}^{2} \hat{\sigma}_{z,j} \hat{a}^\dagger \hat{a}, \tag{4.3}$$

où on suppose que le couplage dispersif entre les qubits et le résonateur est homogène, $\chi_1 = \chi_2 = \chi$ [1]. Comme illustré sur la figure 4.3a, la fréquence du résonateur peut prendre trois valeurs différentes, $\omega_r - 2\chi, \omega_r, \omega_r + 2\chi$, lorsque l'état des qubits est donné par $|00\rangle$, $\{|01\rangle, |10\rangle\}$, $|11\rangle$, respectivement. En prenant en compte

1. Notons que cette condition n'implique pas que les qubits aient les mêmes fréquences, seulement que la combinaison du couplage et de la fréquence, $\chi \approx g^2/(\omega_q - \omega_r)$, soit la même pour les deux qubits.

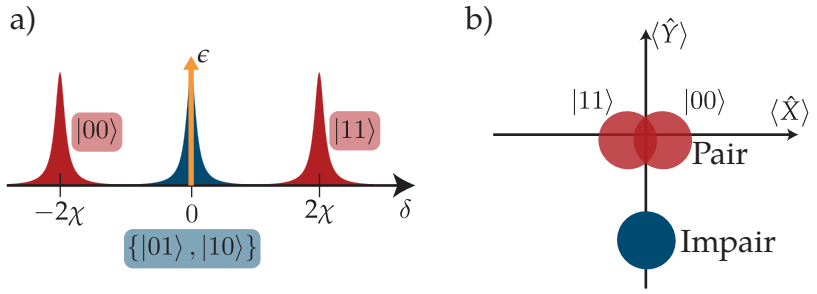

FIGURE 4.3 – Concept de la mesure de parité généralisant la mesure dispersive standard. a) Absorption du résonateur en fonction du décalage en fréquence entre le pilotage et la fréquence nue du résonateur, $\delta = \omega_d - \omega_r$. Lorsque le décalage dispersif des deux qubits est homogène, $\chi_1 = \chi_2$, la fréquence du résonateur peut prendre trois valeurs différentes. Une mesure de parité entre le sous-espace pair (rouge) et impair (bleu) s'effectue en pilotant le résonateur (flèche orange) à sa fréquence nue, $\delta = 0$. b) Espace de phase du résonateur. Lorsque les qubits sont dans l'espace impair, le champ du résonateur est fortement déplacé. Lorsque les qubits sont dans l'espace pair, le champ du résonateur est faiblement déplacé, avec une phase inverse entre l'état de résonateur associé à $|00\rangle$ et l'état associé à $|11\rangle$.

le pilotage linéaire, l'état du système combiné qubits-résonateur est donné par $|\psi\rangle = \sum_{ij} |ij\rangle \otimes |\alpha_{ij}\rangle$, où $i, j = \{0, 1\}$ notent les états de qubits et α_{ij} est l'état cohérent du résonateur associé à l'état ij des qubits. En pilotant le résonateur à la fréquence ω_r, le champ dans le résonateur a une grande amplitude seulement si les qubits se trouvent dans le sous-espace impair, $|\alpha_{01}| = |\alpha_{10}| \gg 1$, et une faible amplitude dans le sous-espace pair, $|\alpha_{00}| = |\alpha_{11}| \ll 1$, comme illustré sur la figure 4.3b. En mesurant le champ de sortie du résonateur avec une mesure homodyne ou hétérodyne, il est possible de distinguer cette différence d'amplitude, et par conséquent distinguer la parité de l'état des qubits avec un ratio signal sur bruit (SNR)

$$\text{SNR} \approx \sqrt{\kappa t} \left(\frac{2\epsilon}{\kappa} \right), \tag{4.4}$$

en supposant un état stationnaire et dans la limite où $2\chi \gg \kappa$.

Le problème avec cette méthode est que la phase des états α_{00} et α_{11} est différente, et le champ de sortie du résonateur encode de l'information sur l'état des qubits dans le sous-espace pair. Conséquemment, cette mesure de parité induit un déphasage

significatif à l'intérieur du sous-espace pair à un taux

$$\gamma_p \approx \kappa \left(\frac{\epsilon}{2\chi} \right)^2 . \tag{4.5}$$

En comparant les expressions pour le SNR (équation 4.4) et le taux de déphasage dans le sous-espace pair (équation 4.5), on remarque que tous deux sont directement reliés à l'amplitude du pilotage, ϵ. En particulier, le décalage dispersif, χ, est limité par des contraintes physiques et le taux de dissipation, κ, détermine le temps de mesure. Cette situation correspond à un cul-de-sac paramétrique et de nouvelles méthodes sont requises pour réaliser une mesure de parité sans introduire d'erreurs.

Il est possible d'éviter le déphasage dans l'espace pair, γ_p, en mesurant le champ de sortie avec un détecteur sensible seulement à l'amplitude du champ [22, 58], mais comme on l'a vu au chapitre précédent, la réalisation de ce type de détecteurs est un défi en soit. Une autre méthode est de réaliser une mesure homodyne du champ de sortie qui, en choisissant le bon axe de mesure, ne révèle pas d'information sur l'état des qubits dans l'espace pair (mesure de la quadrature Y sur la figure 4.3b). Dans cette situation, le déphasage γ_p se traduit par une phase aléatoire dans l'espace pair dont la valeur est encodée dans le champ de sortie du résonateur. En principe, il est possible de corriger cette phase en mesurant parfaitement le signal de sortie, soit en effectuant une mesure homodyne avec $\eta = 1$ [55, 56]. Finalement, il existe aussi d'autres propositions permettant de mitiger le déphasage induit par la mesure en complexifiant le montage [157, 158, 159, 160, 50].

Une autre limitation de la mesure de parité illustrée à la figure 4.3 est qu'il n'est pas évident de la généraliser à plus de deux qubits. Par conséquent, elle ne peut pas être utilisée dans un code de surface comme celui illustré sur la figure 4.1, où les mesures de parités à quatre qubits sont essentielles. Considérons un couplage dispersif entre quatre qubits et un résonateur, $\hat{H} = \chi \sum_{j=1}^{4} \hat{\sigma}_{z,j} \hat{a}^\dagger \hat{a}$. Lorsque les qubits sont dans un état impair, le résonateur est décalé de $\delta_\mathrm{i} = \pm 2\chi$, tandis qu'un état pair des qubits mène à un décalage de $\delta_\mathrm{p} = \pm 4\chi, 0$. Pour mesurer la parité des qubits, l'objectif est donc de distinguer entre δ_p et δ_i sans différencier les différents décalages à l'intérieur de ces sous-espace, ce qui est impossible avec un pilotage linéaire monochromatique.

Dans l'article présenté dans ce chapitre [59], je propose une méthode pour une mesure de parité directe où le SNR et le taux de déphasage peuvent être contrôlés indépendamment. En utilisant un résonateur non linéaire et un pilotage à deux photons, je montre qu'il est possible d'optimiser les paramètres du système pour obtenir à la fois un grand SNR et un faible taux de déphasage. De plus, j'introduis une méthode pour passer d'une mesure de parité à deux qubits vers une mesure de parité à quatre qubits, rendant cette proposition attrayante pour une implémentation du code de surface.

4.2 Article

J'ai développé l'idée originale pour cet article en collaboration avec Shruti Puri alors qu'elle était postdoctorante dans le groupe. J'ai ensuite fait les calculs numériques et analytiques nécessaires avec des apports de Shruti et Alexandre. Finalement, j'ai écrit l'article qui a été révisé par Shruti et Alexandre. Le matériel supplémentaire pour cet article, qui contient les calculs plus complexes, se trouve en annexe B.3.

Erratum

Il est mentionné dans l'article que le taux d'erreur obtenu pour le protocole de mesure est en dessous de la valeur seuil pour le code de surface. Cette affirmation est légèrement erronée, car les valeurs seuil pour le code de surface ont été calculées pour un canal de dépolarisation sans corrélations d'un qubit à l'autre. Dans le protocole proposé, les erreurs de déphasage sont corrélées à l'intérieur d'une même plaquette, ce qui pourrait changer la valeur seuil citée. De plus, dans le texte de la page 3, il est fait référence aux Lorentziennes de la figure 3A. Contrairement à ce qui est écrit, les états pairs sont associés à la couleur rouge et les états impairs à la couleur bleue.

Baptiste Royer, Shruti Puri et Alexandre Blais. Qubit parity measurement by parametric driving in circuit qed. *Sci. Adv.* **4**(11) (2018)

PHYSICS

Qubit parity measurement by parametric driving in circuit QED

Baptiste Royer[1]*, Shruti Puri[2], Alexandre Blais[1,3]

Multiqubit parity measurements are essential to quantum error correction. Current realizations of these measurements often rely on ancilla qubits, a method that is sensitive to faulty two-qubit gates and that requires notable experimental overhead. We propose a hardware-efficient multiqubit parity measurement exploiting the bifurcation dynamics of a parametrically driven nonlinear oscillator. This approach takes advantage of the resonator's parametric oscillation threshold, which depends on the joint parity of dispersively coupled qubits, leading to high-amplitude oscillations for one parity subspace and no oscillation for the other. We present analytical and numerical results for two- and four-qubit parity measurements, with high-fidelity readout preserving the parity eigenpaces. Moreover, we discuss a possible realization that can be readily implemented with the current circuit quantum electrodynamics (QED) experimental toolbox. These results could lead to substantial simplifications in the experimental implementation of quantum error correction and notably of the surface code.

INTRODUCTION

Quantum error correction (QEC) protects fragile quantum information from decoherence and will play a vital role in large-scale quantum computations. Typical QEC codewords are defined in a given eigenspace of multiple parity operators. When an error occurs, the state of the qubits leaves the codespace, something that is revealed by measuring the parity operators. Because these measurements have to be performed repeatedly, it is crucial that they be of high fidelity. Moreover, to avoid introducing errors, these measurements should leave the parity subspaces intact, that is, states within a given parity subspace should remain unperturbed by the measurement.

In practice, parity measurement strategies can be broadly classified as direct or indirect. The latter approach, used in recent experimental demonstrations of small-scale error correction (*1*–*3*), relies on a series of two-qubit entangling gates between the data qubits and an additional ancilla qubit that is subsequently measured (*1*–*7*). Drawbacks of this strategy are the accumulation of errors due to faulty two-qubit gates and the experimental overhead that could become an impediment to the implementation of larger QEC codes.

Faulty gates and overhead issues can be addressed by using direct parity measurements. The central idea there is to map the parity information onto the state of a common mode coupled to the data qubits and which is then measured. For example, a possible strategy to realize direct measurements of two-qubit parity in circuit quantum electrodynamics (QED) is to monitor the response of a resonator dispersively coupled to the qubits. In this situation, the frequency of the oscillator, and therefore its response to a drive, becomes dependent on the joint-qubit parity (*8*–*10*). A challenge with this method is to design and implement a protocol that preserves the parity eigenspaces. In other words, in an ideal parity measurement, the common mode and its environment should gain information only about which parity subspace (even or odd) the qubit state belongs to. Possible improvements to overcome this eigenspace dephasing were introduced in (*11*–*14*) but require quantum-limited amplifiers with unit efficiency (*11*, *12*) or high-efficiency single microwave photon detectors (*13*, *14*).

Here, we introduce a scheme for direct, high-fidelity parity measurements that leaves the parity subspaces intact. Our approach is based on dispersively coupling multiple qubits to a nonlinear resonator driven by a two-photon parametric pump. This situation leads to a qubit parity–dependent parametric oscillation threshold. When the qubits are in the even subspace, the amplitude of the two-photon drive is below the parametric oscillation threshold and the resonator state remains close to vacuum. On the other hand, in the odd subspace, the parametric drive is above threshold and the resonator bifurcates to a high-amplitude state. We show that, by monitoring the amplitude of the resonator output field with standard homodyne detection, it is possible to infer the parity of the qubit ensemble with high fidelity while preserving both even and odd parity subspaces. We show that the photon number in the high-amplitude state can be increased by reducing the resonator nonlinearity, leading to an increased signal-to-noise ratio (SNR) at constant eigenspace dephasing. These ideas are generalized to more than two qubits by using a multitone parametric drive targeting the multiple dispersive shifts corresponding to the same parity subspace.

These ideas can be applied to different types of qubits coupled to oscillators. For concreteness, here, we present a circuit QED implementation (*15*, *16*) based on transmon qubits (*17*) that can easily be implemented with the current circuit QED toolbox (*18*, *19*).

RESULTS AND DISCUSSION

Parametrically driven nonlinear resonator

Before introducing our proposal for multiqubit parity measurements, we present its main component: a resonator of frequency ω_r and Kerr nonlinearity K. In the presence of a resonant parametric two-photon drive $\mathcal{E}_p$ of frequency $\omega_p = 2\omega_r$ and in a frame rotating at ω_r, this system is described by the Hamiltonian ($\hbar = 1$)

$$\hat{H}_R = \frac{\mathcal{E}_p}{2}\left(\hat{a}\hat{a} + \hat{a}^\dagger\hat{a}^\dagger\right) - \frac{K}{2}\hat{a}^\dagger\hat{a}^\dagger\hat{a}\hat{a} \quad (1)$$

where $\hat{a}$ and $\hat{a}^\dagger$ denote the resonator's annihilation and creation operators, respectively. When the drive is turned off, $\mathcal{E}_p = 0$, the steady state of the system is the vacuum state. Below the parametric oscillation threshold, $\mathcal{E}_p < \kappa/2$, with κ the single-photon loss rate of the resonator, this system corresponds to the widely used Josephson parametric amplifier (JPA)

[1]Institut quantique and Département de Physique, Université de Sherbrooke, 2500 boulevard de l'Université, Sherbrooke, Québec J1K 2R1, Canada. [2]Department of Applied Physics, Yale University, P.O. Box 208284, New Haven, CT 06511, USA. [3]Canadian Institute for Advanced Research, Toronto, Ontario, Canada.
*Corresponding author. Email: baptiste.royer@usherbrooke.ca

(*19*) with a vacuum-squeezed steady state. Above $\mathcal{E}_p > \kappa/2$, this system bifurcates into one of two states of equal amplitude but opposite phases characterized by $\langle\hat{a}\rangle_{ss} = \pm\,\alpha_o$ with (*20*, *21*)

$$|\alpha_o| = \left(\frac{\mathcal{E}_p^2 - \kappa^2/4}{K^2}\right)^{1/4} \tag{2}$$

$$\theta_o \equiv \mathrm{Arg}[\alpha_o] = \frac{1}{2}\tan^{-1}\left(\frac{\kappa}{\sqrt{4\mathcal{E}_p^2 - \kappa^2}}\right) \tag{3}$$

Because both the Hamiltonian $\hat{H}_R$ and the dissipation are symmetric under the transformation $\hat{a} \rightarrow -\hat{a}$ (see Methods), in steady state, the resonator occupies either of the two states with equal probability, leading to a null average displacement of the resonator field. However, a single shot homodyne measurement of the resonator steady state will always reveal a large amplitude $|\alpha_o|$. Once the resonator has latched onto one of its two steady states, tunneling to the other is highly suppressed for large values of $|\alpha_o|$ (*21*–*23*). In the limit where the two-photon drive is well above the parametric oscillation threshold $\mathcal{E}_p \gg \kappa/2$, the two steady states are coherent states.

If the parametric drive is detuned such that $\omega_r - \omega_p/2 = \delta$, the system Hamiltonian becomes

$$\hat{H}_{R,\delta} = \delta\hat{a}^\dagger\hat{a} + \hat{H}_R \tag{4}$$

At large detunings $\delta^2 > \mathcal{E}_p^2 - \kappa^2/4$, the vacuum-squeezed state is a steady state of the system, with the squeezing axis governed by the sign of the detuning δ (*21*). The degree of squeezing decreases as the ratio $|\delta|/\mathcal{E}_p$ increases and, for $|\delta| \gg \mathcal{E}_p$, the steady state is very close to the vacuum state.

Two-qubit parity measurement

We now turn to the core of our proposal, first considering two-qubit parity measurements. More precisely, we aim to distinguish the odd subspace spanned by the two-qubit states $\{|01\rangle, |10\rangle\}$ from the even subspace spanned by $\{|00\rangle, |11\rangle\}$. To this end, we take two qubits dispersively coupled with equal strength χ to the parametrically driven nonlinear resonator. In a frame rotating at ω_r, this system is described by the Hamiltonian

$$\hat{H}_{2qb} = \chi(\hat{\sigma}_{z1} + \hat{\sigma}_{z2})\hat{a}^\dagger\hat{a} + \hat{H}_R \tag{5}$$

where $\hat{\sigma}_{zi}$ is the Pauli Z operator for the ith qubit. Under this dispersive coupling, the resonator frequency becomes qubit state dependent. We note that single-qubit readout in a similar setup was proposed in (*20*) and experimentally demonstrated in (*18*).

The above Hamiltonian, combined with the discussion of the previous section, immediately suggests an approach for multiqubit parity measurement. In Eq. 5, the qubits induce a dispersive shift of the resonator frequency that will change the parametric oscillation threshold of the two-photon pump in a parity-dependent manner. More precisely, if the state of the qubit lies in the odd subspace, $|\psi_o\rangle = c_{01}|01\rangle + c_{10}|10\rangle$, the two dispersive shifts cancel, as illustrated in Fig. 1A. With $\delta_o = 0$, the system then behaves as a resonantly driven nonlinear resonator. Consequently, in the odd subspace, the resonator bifurcates to a large-amplitude state, as illustrated in Fig. 1B. The combined qubit-resonator system thus evolves from the initial state, $|\Psi(0)\rangle = |\psi_o\rangle \otimes |0\rangle$, to one of the two steady states $|\Psi(t)\rangle = |\psi_o\rangle \otimes |\pm\alpha_o\rangle$. The phase of the oscillations, $\mathrm{Arg}[\langle\hat{a}\rangle_o] = \theta_o, \theta_o + \pi$, is independent of the state of the qubits within the odd subspace. In this situation, monitoring the output field of the resonator using standard homodyne measurement of the $X_{\theta_o} = \langle\hat{a}e^{-i\theta_o} + \hat{a}^\dagger e^{i\theta_o}\rangle$ quadrature reveals a large photon population in the resonator, $|\langle\hat{a}\rangle_o|^2 = |\alpha_o|^2$. Note that during the homodyne measurement, the field can, in principle, switch between the two steady states $\pm\alpha_o$, something that can reduce the measurement fidelity. However, these switching events are rare for large $|\alpha_o|$ (*21*–*23*).

On the contrary, in the even subspace, $|\psi_e\rangle = c_{00}|00\rangle + c_{11}|11\rangle$, the dispersive shifts of the two qubits add up and the two-photon drive is off-resonant by $\delta_e = \pm 2\chi$. For dispersive shifts $|2\chi| \gg \sqrt{\mathcal{E}_p^2 - \kappa^2/4}$ (*20*), the vacuum state remains a stable steady state even after activation of the two-photon drive, as schematically depicted in Fig. 1B. That is, the system remains in the initial state, $|\psi_e\rangle \otimes |0\rangle$. In this case, tracking the output of the resonator with homodyne measurement results in a null amplitude $|\langle\hat{a}\rangle_e| = 0$.

In practice, because the dispersive shifts are finite, the resonator state will deviate from vacuum when the qubits are in the even subspace and will become slightly vacuum squeezed under the action of the off-resonant two-photon drive. The axis of squeezing, schematically represented in the inset of Fig. 1B, depends on the sign of the parametric pump detuning and is therefore different for the two even states $|00\rangle$ and $|11\rangle$. This results in slow dephasing within the even parity subspace at rate $\gamma_e = \kappa(\mathcal{E}_p/2\chi)^2$ (see Methods). This dephasing can be made small by limiting the amplitude of the two-photon drive $\mathcal{E}_p/2\chi \ll 1$. Crucially, this does not limit the SNR of the measurement because $|\alpha_o|$ can be made large by reducing the resonator nonlinearity, K, as shown by Eq. 2. In other words, the measurement SNR and the eigenspace

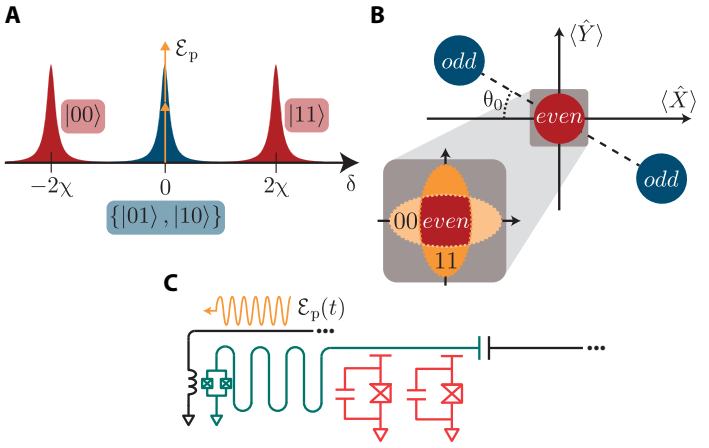

Fig. 1. Two-qubit parity measurement. (**A**) Qubit state–dependent frequency of the resonator. The parametric two-photon drive (orange) is resonant when the qubits are in the odd subspace, $\delta_o = 0$ (blue), and strongly detuned when the qubits are in the even subspace, $\delta_e = \pm 2\chi$ (red). (**B**) Resonator phase space under two-photon driving. In the odd subspace, the resonator bifurcates in either $\pm\alpha_o$ (blue), while in the even subspace, it stays close to vacuum (red). The qubit parity is inferred by monitoring the amplitude of the field leaking out of the resonator. Inset: In the qubit even subspace, fluctuations are increased in a qubit state–dependent quadrature, leading to slow dephasing inside the subspace. (**C**) Possible circuit QED realization of the two-qubit parity measurement. Transmon qubits (red) are capacitively coupled to an off-resonant, nonlinear resonator (green).

dephasing rate γ_e can be optimized separately. This is in stark contrast with schemes based on coherent drives where, for a fixed dispersive coupling χ, the eigenspace dephasing increases with the SNR (*8*, *9*, *11*).

To numerically evaluate the performance of this measurement scheme, we simulate the evolution generated by Eq. 5 under a stochastic master equation (see Methods) (*24*), which implicitly includes switching events between the two resonator steady states in the odd qubit parity subspace. We first compute 2000 trajectories where the qubits are initialized in the odd (even) subspace. For each trajectory, we integrate the resulting homodyne current and categorize it as odd (even) if the absolute value of the signal is above (below) an optimized threshold value. The resulting measurement fidelity $\mathcal{F}_m(\tau) = 1/2[P(e|e) + P(o|o)]$ is shown as a function of time in Fig. 2A. Starting at $\mathcal{F}_m(0) = 0.5$ corresponding to a random parity guess, the fidelity steadily increases toward 1. For the realistic parameters $K/\kappa = 0.175$, $\chi/\kappa = 25$, $\mathcal{E}_p/\kappa = 2.5$, and $\tau = 5/\kappa$, we find a large measurement fidelity $\mathcal{F}_m = 99.9\%$. In these simulations, the steady-state photon number (in the odd subspace) is set to $|\alpha_o|^2 \approx 14$, leading to a high SNR once the resonator reaches steady state. For these parameters, we observed no switching events between $\pm\alpha_o$ and, consequently, the measurement time is limited by the bifurcation time to the steady state, which scales as $\sim 1/(\mathcal{E}_p - \kappa/2)$ (see Methods). This could potentially be shortened by shaping the two-photon pulse $\mathcal{E}_p(t)$ or with further parameter optimization. Moreover, the measurement fidelity might be improved further by using more sophisticated signal analysis methods such as machine learning (*25*).

Starting with an unentangled superposition of the odd and even states, this parity measurement collapses the qubits to an entangled Bell state within one of the two subspaces. To study the creation of entanglement and assess eigenspace dephasing, we initialize the system in an unentangled state with both qubits in the +1 eigenstate of $\hat{\sigma}_x$ and the resonator in the vacuum state, $|++\rangle \otimes |0\rangle$. We again compute 2000 realizations of the evolution and register the qubit state conditioned on the measurement record, ρ_c. Figure 2B shows the concurrence of ρ_c as a function of the measurement time τ. From the initial unentangled state, the qubits are rapidly projected on one of the two parity subspaces, leading to a high concurrence at moderate times. At longer times, the concurrence conditioned on an odd parity measurement approaches unity and, in the even subspace, it slowly decreases due to the slow dephasing γ_e (not apparent on the scale of Fig. 2B). To study the properties of the measurement process only, we considered ideal qubits (T_1, $T_2 \to \infty$) and perfectly matched dispersive shifts. In practice, these imperfections will cause the concurrence to slowly decrease and, in the case of relaxation errors during the measurement (T_1), will decrease the measurement fidelity $\mathcal{F}_m$. Using realistic relaxation times for the qubits, $T_1 = 50\,\mu s$, we compute a measurement fidelity of 98.2% in $\tau = 1.56\,\mu s$ (see the Supplementary Materials).

After the measurement, the resonator is reset by turning off the two-photon drive and waiting for a few resonator lifetimes $1/\kappa$ or, alternatively, by adiabatically ramping down the parametric drive (*21*). Because the resonator ends up in a state close to a coherent state, this process can also be sped up using active reset techniques (*26*–*28*).

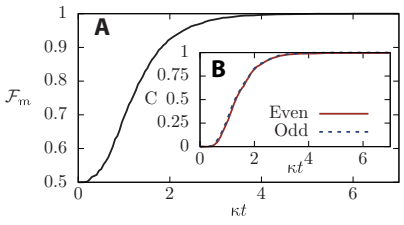

Fig. 2. Measurement fidelity and concurrence. (**A**) Measurement fidelity as a function of time. (**B**) Concurrence conditioned on the measurement record being even (red) or odd (blue). The parameters are $K/\kappa = 0.175$, $\chi/\kappa = 25$, and $\mathcal{E}_p/\kappa = 2.5$ for both panels.

Four-qubit parity measurement

We now turn to a generalization of the above approach to four qubits. This is motivated by the many QEC codes that require frequent parity measurements of more than two qubits. This is the case, for example, of the surface code that relies on four-qubit parity measurements (*29*). Because of the larger Hilbert space, it is now challenging to extract the measurement fidelity and study the entangle creation from numerical simulations. As a result, in this section, we focus on the underlying concepts and on analytical results.

Building on the results for the two-qubit scenario presented above, we now consider four qubits dispersively coupled to a single nonlinear resonator, where we aim to distinguish between two parity subspaces that are eightfold degenerate. In the even subspace, the dispersive shift can take three different values $\delta_e = 0, \pm 4\chi$ (blue Lorentzians), while in the odd subspace it can take two different values $\delta_o = \pm 2\chi$ (red Lorentzians), as schematically illustrated in Fig. 3A. Accordingly, a naive generalization of the two-qubit scheme presented above is to excite the resonator with a two-tone two-photon drive $\mathcal{E}_p^{(2\omega)}$ at frequencies $2(\omega_r \pm 2\chi)$, as shown by the two sets of orange double arrows in Fig. 3A. As in the two-qubit case, this two-tone drive leads to a situation where the parity information is encoded in the amplitude of the resonator field: A high amplitude corresponds to the odd subspace, and a null amplitude corresponds to the even subspace. When the two tones of the two-photon drive are of equal amplitude, the amplitude of the output field does not depend on the two possible dispersive shifts within the odd subspace $\delta_o = \pm 2\chi$. However, the frequency of the output field

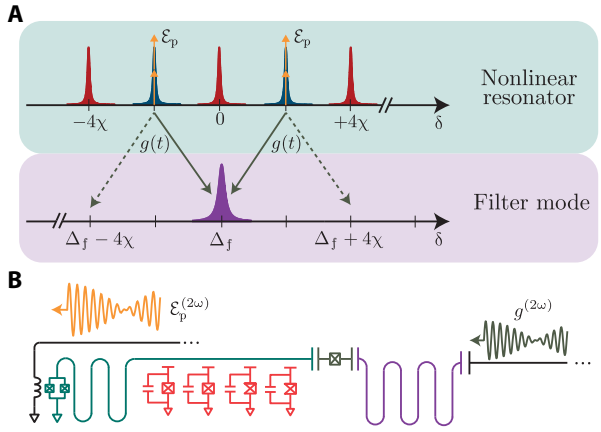

Fig. 3. Four-qubit parity measurement. (**A**) Top: Nonlinear resonator qubit state–dependent frequency. A two-tone two-photon drive $\mathcal{E}_p^{(2\omega)}$ is sent to the resonator at $\delta = \pm 2\chi$ (orange double arrows). Bottom: Resonator photons are converted to a filter frequency (purple) via a two-tone coupling modulation $g(t)$ (dark green). (**B**) Possible circuit QED realization. Transmon qubits (red) are capacitively coupled to a high-Q, nonlinear resonator (light green), which is coupled via a tunable coupler (dark green) to a low-Q filter mode (purple). A two-tone microwave drive on the nonlinear resonator (orange) induces the two-photon drive, while the coupling modulation is induced by the combination of a drive on the nonlinear resonator and a two-tone drive on the filter mode (dark green).

directly depends on δ_o, leading to fast dephasing inside the odd parity subspace at a rate $\gamma_o = \kappa|\alpha_o|^2$. A possible solution introduced for linear drive schemes (*13*) and also applicable here is to use such a two-tone drive $\mathcal{E}_p^{(2\omega)}$ in combination with a detector that is sensitive exclusively to the amplitude of the output field, that is, a broadband, high-efficiency photon detector. However, the realization of this type of detector in the microwave domain remains challenging. Alternative proposals also offer solutions to this frequency distinguishability problem but at the cost of higher experimental complexity (*13*, *30*–*33*).

Here, we introduce a simpler, hardware-efficient approach to four-qubit parity measurements where the nonlinear resonator is coupled to a low-Q "filter" resonator of frequency ω_f through a tunable coupling element. As we show, this effectively implements a "frequency erasure" channel that converts resonator photons at $\omega_r \pm 2\chi$ to a single frequency ω_f. As a result, only the parity information remains in the output field, that is, the output field contains no information about the different dispersive shifts δ_o within the odd subspace. Crucially, this allows us to infer multiqubit parity using standard homodyne detection without inducing dephasing within that subspace.

To implement this frequency erasure channel, we consider a two-tone modulation $g^{(2\omega)}$ of the resonator-filter coupling at frequencies $\Delta_f \pm 2\chi$, where $\Delta_f \equiv \omega_r - \omega_f$. This multitone coupling modulation is schematically illustrated in Fig. 3A (dark green arrows), where one modulation tone (full lines) brings the $\delta = \pm 2\chi$ resonator peaks (blue) in resonance with the filter mode (purple), while the other coupling modulation tone (dashed lines) is off-resonant by $\mp 4\chi$ and has only a small effect. Irrespective of the dispersive shift $\delta = \pm 2\chi$, resonator photons are then converted to a single frequency ω_f. In a frame rotating at $\omega_r \pm 2\chi$ for the resonator, ω_f for the filter resonator and neglecting for now off-resonant terms, the above situation is described by the Hamiltonian (see Methods)

$$\hat{H}_{4qb,o}^{(\pm 2\chi)} = \hat{H}_R + \frac{g}{2}\left[\hat{a}\hat{f}^\dagger + \hat{a}^\dagger\hat{f}\right] \quad (6)$$

where $\hat{f}$ and $\hat{f}^\dagger$ denote the annihilation and creation operators, respectively, of the filter mode.

Equation 6 crucially shows that the resonators' dynamics does not depend on the state of the qubits within the odd qubit subspaces, $\delta_o = \pm 2\chi$. Consequently, similar to the two-qubit case, four-qubit parity information can be inferred without eigenspace dephasing by monitoring the amplitude of the output field of the filter mode using homodyne detection.

Expanding further the simple analysis leading to Eq. 6 reveals that, in the odd parity subspace, the filter also emits in a qubit state–dependent sideband $\omega_f \pm 4\chi$, as illustrated by the dark green dashed lines in Fig. 3A. Consequently, a small portion of the "which-frequency" information is present in the output field, causing a slow dephasing at a rate $\gamma_o^{eff} = \kappa_{eff}|\alpha_o|^2/(1 + (8\chi/\kappa_f)^2)$ inside the odd subspace where $\kappa_{eff} = g^2/\kappa_f$ (see Methods). Taking a measurement time $\kappa_{eff}\tau = 5$, a steady-state photon number $|\alpha_o|^2 = 10$, and a ratio $\chi/\kappa_f = 20$, this leads to an approximate error probability $\gamma_o^{eff}\tau = 0.2\%$, which is below the threshold for QEC with the surface code (*34*). Internal photon loss of the nonlinear resonator at a rate κ_{int} will also induce dephasing inside the odd subspace at a rate $\gamma_o^{int} = \kappa_{int}|\alpha_o|^2$, something that should ideally be minimized.

The mechanism responsible for this frequency erasure is the alignment of one nonlinear resonator sideband with the filter frequency for all odd parity qubit states. In the approach described above, we proposed to activate these sidebands via a multitone modulation of the coupling between the nonlinear resonator and the filter. An alternative approach is to modulate the nonlinear resonator frequency. This leads to FM (frequency modulation) sidebands that can be used, for example, to perform entangling gates between superconducting qubits (*35*). Moreover, we considered above that all qubits had the same dispersive coupling χ to the nonlinear resonator. As long as the absolute value of the dispersive coupling stays homogeneous, its sign could vary among the qubits, $\chi \rightarrow -\chi$, with sole consequence to exchange even and odd in the discussion above. Last, an added advantage of introducing the filter mode is that it acts naturally as a Purcell filter for the qubits (*36*).

Circuit QED implementation

Realization of the above ideas is natural in different quantum systems, and as a concrete example, we now describe a possible circuit QED (*15*, *16*) implementation with transmon qubits (*17*). Figure 1C shows the circuit for a two-qubit parity measurement, where two transmon qubits (red) are capacitively coupled to a nonlinear quarter-wavelength resonator (green). Taking the transmons to be far detuned from the resonator, the qubit-resonator coupling takes the dispersive character shown in Eq. 5. The dispersive couplings χ are adjusted to be of equal magnitude, and we assume the transmon qubits to be detuned from each other to avoid qubit-qubit interaction mediated by the resonator. The resonator nonlinearity K is induced, in part, by a superconducting quantum interference device (SQUID) located at the end of the resonator and, in part, by the qubits. The two-photon drive is induced by modulating the SQUID's flux at twice the resonator frequency (orange). In short, the circuit that we propose consists of two transmon qubits dispersively coupled to a JPA parametrically driven above threshold and is well within reach of current experimental capabilities. Alternatively, the need for flux modulation can be removed by replacing the SQUID by a three-wave mixing element (*37*).

Figure 3B shows a possible implementation of the four-qubit parity measurement. Similarly to the two-qubit version, it consists of a nonlinear, quarter-wavelength coplanar resonator (green) capacitively coupled now to four transmon qubits (red). To erase the which-frequency information, the nonlinear resonator is coupled to a linear filter resonator (purple) by a tunable coupling element (dark green). Multiple circuits can be used to generate the necessary coupling modulation (*38*–*41*), and here, we follow (*41*). With this approach, the two-tone coupling modulation $g^{(2\omega)}$ is activated by driving the linear resonator (purple) with a three-tone coherent drive on the filter mode (dark green).

Surface code implementation

Figure 4 shows a schematic representation of what our proposed hardware-efficient implementation of the surface code could look like, here shown for nine qubits. Red circles represent data qubits, and nonlinear resonators are implemented using the circuit of Fig. 3B. Out-of-plane interconnects, represented by squares, allow us to address all elements in this planar architecture. Single-qubit readout is performed through the yellow resonators, and single-qubit control is performed through the brown lines. Light gray regions represent measurement of $\hat{\sigma}_z$ error syndromes, while dark gray regions represent measurement of $\hat{\sigma}_x$ error syndromes. The latter are realized by applying Hadamard gates before and after the parity measurement. In contrast to architectures based on indirect parity measurements requiring 17 qubits, only 9 data qubits are necessary here.

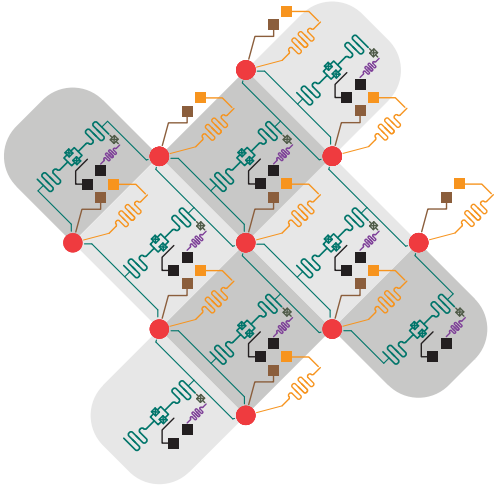

Fig. 4. Schematic for a possible circuit QED realization of the nine-qubit surface code. Qubits are represented by red circles, and out-of-plane interconnects are represented by squares. Single-qubit readout and control are achieved through the yellow resonators and brown lines, respectively. Parity measurements are performed using the circuit of Fig. 3B, here represented with half-wavelength nonlinear resonators. $\hat{\sigma}_z$ error syndromes are measured in light gray regions, while $\hat{\sigma}_x$ error syndromes are measured in dark gray regions.

To summarize, we have introduced a scheme for qubit parity readout exploiting the bifurcation dynamics of a nonlinear oscillator. For two qubits, this leads to a high-fidelity readout that preserves the parity eigenspaces. We also presented an extension of this scheme to the parity readout of four qubits using a multitone parametric drive in combination with a multitone modulation of the coupling between a nonlinear resonator and a filter mode. Both schemes have a simple circuit QED implementation that could be realized with current devices. This work paves the way for a hardware-efficient implementation of QEC codes such as the surface code in circuit QED.

METHODS

Stability of resonator vacuum state

When parametrically driven on resonance, the classical equations of motion for the field quadratures of the nonlinear resonator $x = \langle \hat{a} + \hat{a}^\dagger \rangle/2$ and $y = -i\langle \hat{a} - \hat{a}^\dagger \rangle/2$ are given by

$$\dot{x} = K(x^2 + y^2)y - \mathcal{E}_p y - \frac{\kappa}{2}x \tag{7}$$

$$\dot{y} = -K(x^2 + y^2)x - \mathcal{E}_p x - \frac{\kappa}{2}y \tag{8}$$

Computing the eigenvalues of the evolution matrix linearized around vacuum $(x, y) = (0, 0)$, we obtained $\lambda_\pm = \pm\mathcal{E}_p - \kappa/2$. Small fluctuations around vacuum will thus make the system leave this unstable point on a time scale given by $\lambda_+^{-1} = (\mathcal{E}_p - \kappa/2)^{-1}$.

Dephasing in the two-qubit parity measurement

In the odd qubit subspace, the dispersive shifts shown in Eq. 5 cancel out and the qubits decouple from the resonator. Consequently, there is no dephasing in that subspace. On the other hand, in the even subspace, the two-photon parametric drive leads to a qubit state–dependent resonator field. More precisely, and as schematically illustrated in the inset of Fig. 1B, when the dispersive shifts are much larger than the two-photon drive and the resonator decay rate, $4\chi \gg \mathcal{E}_p, \kappa$, the resonator field is in the slightly squeezed state $|re^{i\theta}\rangle$. The squeezing parameter is $r \approx \mathcal{E}_p/4\chi$, and the squeezing angle $\theta \approx 0$ or $\pi/2$ is qubit state dependent (*19*). The overlap of these squeezed pointer states is $\langle r|re^{i\pi/2}\rangle = 1/\sqrt{\cosh 2r}$. The corresponding measurement-induced dephasing in this subspace is then roughly given by $\gamma_e \sim \kappa(1 - \langle r|re^{i\pi/2}\rangle) \sim \kappa(\mathcal{E}_p/4\chi)^2$ for small r. A more rigorous derivation of this rate can be found in the Supplementary Materials.

Simulations

To model the back action of the homodyne measurement chain, we simulated multiple realizations of the evolution of the system under the stochastic master equation (*24*)

$$d\rho = -i[\hat{H}, \rho]dt + \kappa\mathcal{D}[\hat{a}]\rho dt + \sqrt{\kappa}\mathcal{H}[\hat{a}e^{-i\theta_o}]\rho dW \tag{9}$$

where $\mathcal{D}[\hat{a}]\bullet = \hat{a}\bullet\hat{a}^\dagger - 1/2\{\hat{a}^\dagger\hat{a}, \bullet\}$ is the dissipation superoperator and $\mathcal{H}[\hat{M}]\bullet = \hat{M}\bullet + \bullet\hat{M}^\dagger - \mathrm{Tr}[\hat{M}\bullet + \bullet\hat{M}^\dagger]\bullet$ is the homodyne measurement back-action superoperator. Moreover, dW is a Wiener increment, which has statistical properties $E[dW] = 0$, $E[dW^2] = dt$, with $E[\bullet]$ denoting the ensemble average. The results of Fig. 2 were obtained using Eq. 9 with the Hamiltonian Eq. 5. Equation 9 shows that the Hamiltonian and dissipation (first two terms) are symmetric under the transformation $\hat{a} \to -\hat{a}$. This symmetry is broken by the homodyne measurement back action (last term), that is, by conditioning the state on the measurement record. In other words, although the average displacement of the resonator is null, conditioning the state on the measurement record makes it collapse onto $\pm\alpha_o$.

The homodyne current resulting from the stochastic master equation is given by $j_h(t) = \sqrt{\kappa}\langle \hat{a}e^{-i\theta_o} + \hat{a}^\dagger e^{i\theta_o}\rangle + dW/dt$. For a given measurement time τ, the dimensionless integrated signal is given by $s(\tau) = \sqrt{\kappa}\int_0^\tau dt\, j_h(t)$.

To focus solely on the measurement scheme itself, we considered a homodyne measurement chain with unit efficiency. Because of the large number of photons in steady state, $|\alpha_o|^2$, the measurement time and fidelity are mostly limited by the bifurcation time. As a result, adding imperfections to the measurement line affects the measurement time in a negligible manner. Moreover, for the parameters considered in the main text, the output power to amplify is below the 1-dB compression point for state-of-the-art amplifiers (*42*).

Effective four-qubit Hamiltonian

As mentioned in the main text, we consider four qubits dispersively coupled to a nonlinear resonator under a two-tone two-photon drive $\mathcal{E}_p^{(2\omega)}(t) = \mathcal{E}_p\cos[2(\omega_r - 2\chi)t] + \mathcal{E}_p\cos[2(\omega_r + 2\chi)t]$. Coupling the nonlinear resonator to a harmonic filter through a two-tone modulation $g^{(2\omega)} = g\cos[(\Delta_f + 2\chi)t] + g\cos[(\Delta_f - 2\chi)t]$, this system is described by the Hamiltonian

$$\hat{H}_{4qb} = \omega_r\hat{a}^\dagger\hat{a} + \chi\sum_{i=1}^{4}\hat{\sigma}_{zi}\hat{a}^\dagger\hat{a} - \frac{K}{2}\hat{a}^\dagger\hat{a}^\dagger\hat{a}\hat{a} + \omega_f\hat{f}^\dagger\hat{f} + \mathcal{E}_p^{(2\omega)}(t)[\hat{a}\hat{a} + \hat{a}^\dagger\hat{a}^\dagger] + g^{(2\omega)}(t)[\hat{a}\hat{f}^\dagger + \hat{a}^\dagger\hat{f}] \tag{10}$$

For the circuit of Fig. 3, this two-tone coupling modulation is obtained by driving the filter mode with a three-tone linear drive at

frequencies $\omega_{d1}, \omega_{d2}, \omega_{d3}$. Setting $\omega_{d1} - \omega_{d2} = \Delta_f - 2\chi$ and $\omega_{d1} - \omega_{d3} = \Delta_f + 2\chi$ results in the desired two-tone modulation as well as AC-Stark shifts of the resonator and filter mode frequencies (see the Supplementary Materials).

To go from Eq. 9 to Eq. 6 of the main text, we restrict the qubit state to the one-excitation subspace spanned by $\{|0001\rangle, |0010\rangle, |0100\rangle, |1000\rangle\}$, leading to a dispersive shift $\delta_o = -2\chi$. We then go to a frame rotating at $\omega_r - 2\chi$ for the nonlinear resonator and at ω_f for the filter mode, and neglecting fast-rotating terms, $\hat{H}_{4qb}$ takes the form

$$\hat{H}_{4qb,o}^{(-2\chi)} = \frac{\mathcal{E}_p}{2}\left(\hat{a}\hat{a} - \frac{K}{2}\hat{a}^\dagger\hat{a}^\dagger\hat{a}\hat{a} + \hat{a}^\dagger\hat{a}^\dagger\right) + \frac{g}{2}\left[\hat{a}\hat{f}^\dagger + \hat{a}^\dagger\hat{f}\right] + \frac{\mathcal{E}_p}{2}\left[e^{i8\chi t}\hat{a}\hat{a} + e^{-i8\chi t}\hat{a}^\dagger\hat{a}^\dagger\right] + \frac{g}{2}\left[e^{i4\chi t}\hat{a}\hat{f}^\dagger + e^{-i4\chi t}\hat{a}^\dagger\hat{f}\right] \quad (11)$$

The first two terms correspond to the effective Hamiltonian Eq. 6. The third term is the off-resonant two-photon drive tone and has a small effect on the resonator. The fourth and final term leads to a small photon emission in the filter sideband $\omega_f - 4\chi$ and, consequently, to a dephasing rate $\kappa_{eff}|\alpha_o|^2/(1 + (8\chi/\kappa_f)^2)$ (see the Supplementary Materials). The effective Hamiltonian $\hat{H}_{4qb,o}^{(+2\chi)}$ in the three-excitation subspace with dispersive shift $\delta_o = 2\chi$ is obtained in the same way.

SUPPLEMENTARY MATERIALS

Supplementary material for this article is available at http://advances.sciencemag.org/cgi/content/full/4/11/eaau1695/DC1

Supplementary Text

Fig. S1. Schematic representation of the steady state of a parametrically driven nonlinear resonator in parameter space.

Fig. S2. Illustration of the resonator phase space when the qubits are in the even subspace.

Fig. S3. Illustration of the resonator phase space when the qubits are in the odd subspace.

Fig. S4. Possible circuit QED implementation of the two-qubit parity measurement.

Fig. S5. A possible circuit QED implementation for the four-qubit parity measurement.

Fig. S6. Fidelity of the two-qubit parity measurement as a function of measurement time for different decay times of the qubits.

References (*43*–*47*)

REFERENCES AND NOTES

1. R. Barends, J. Kelly, A. Megrant, A. Veitia, D. Sank, E. Jeffrey, T. C. White, J. Mutus, A. G. Fowler, B. Campbell, Y. Chen, Z. Chen, B. Chiaro, A. Dunsworth, C. Neill, P. O'Malley, P. Roushan, A. Vainsencher, J. Wenner, A. N. Korotkov, A. N. Cleland, J. M. Martinis, Superconducting quantum circuits at the surface code threshold for fault tolerance. *Nature* **508**, 500–503 (2014).
2. A. D. Córcoles, E. Magesan, S. J. Srinivasan, A. W. Cross, M. Steffen, J. M. Gambetta, J. M. Chow, Demonstration of a quantum error detection code using a square lattice of four superconducting qubits. *Nat. Commun.* **6**, 6979 (2015).
3. J. Kelly, R. Barends, A. G. Fowler, A. Megrant, E. Jeffrey, T. C. White, D. Sank, J. Y. Mutus, B. Campbell, Y. Chen, Z. Chen, B. Chiaro, A. Dunsworth, I.-C. Hoi, C. Neill, P. J. J. OMalley, C. Quintana, P. Roushan, A. Vainsencher, J. Wenner, A. N. Cleland, J. M. Martinis, State preservation by repetitive error detection in a superconducting quantum circuit. *Nature* **519**, 66–69 (2015).
4. W. Pfaff, T. H. Taminiau, L. Robledo, H. Bernien, M. Markham, D. J. Twitchen, R. Hanson, Demonstration of entanglement-by-measurement of solid-state qubits. *Nat. Phys.* **9**, 29–33 (2013).
5. J. M. Chow, J. M. Gambetta, E. Magesan, D. W. Abraham, A. W. Cross, B R Johnson, N. A. Masluk, C. A. Ryan, J. A. Smolin, S. J. Srinivasan, M. Steffen, Implementing a strand of a scalable fault-tolerant quantum computing fabric. *Nat. Commun.* **5**, 4015 (2014).
6. O.-P. Saira, J. P. Groen, J. Cramer, M. Meretska, G. de Lange, L. DiCarlo, Entanglement genesis by ancilla-based parity measurement in 2D circuit QED. *Phys. Rev. Lett.* **112**, 070502 (2014).
7. M. Takita, A. D. Córcoles, E. Magesan, B. Abdo, M. Brink, A. Cross, J. M. Chow, J. M. Gambetta, Demonstration of weight-four parity measurements in the surface code architecture. *Phys. Rev. Lett.* **117**, 210505 (2016).
8. C. L. Hutchison, J. M. Gambetta, A. Blais, F. K. Wilhelm, Quantum trajectory equation for multiple qubits in circuit QED: Generating entanglement by measurement. *Can. J. Phys.* **87**, 225–231 (2009).
9. K. Lalumière, J. M. Gambetta, A. Blais, Tunable joint measurements in the dispersive regime of cavity QED. *Phys. Rev. A* **81**, 040301 (2010).
10. D. Ristè, M. Dukalski, C. A. Watson, G. de Lange, M. J. Tiggelman, Ya. M. Blanter, K. W. Lehnert, R. N. Schouten, L. DiCarlo, Deterministic entanglement of superconducting qubits by parity measurement and feedback. *Nature* **502**, 350–354 (2013).
11. L. Tornberg, G. Johansson, High-fidelity feedback-assisted parity measurement in circuit QED. *Phys. Rev. A* **82**, 012329 (2010).
12. A. Frisk Kockum, L. Tornberg, G. Johansson, Undoing measurement-induced dephasing in circuit QED. *Phys. Rev. A* **85**, 052318 (2012).
13. L. C. G. Govia, E. J. Pritchett, B. L. T. Plourde, M. G. Vavilov, R. McDermott, F. K. Wilhelm, Scalable two- and four-qubit parity measurement with a threshold photon counter. *Phys. Rev. A* **92**, 022335 (2015).
14. P. Huembeli, S. E. Nigg, Towards a heralded eigenstate-preserving measurement of multi-qubit parity in circuit QED. *Phys. Rev. A* **96**, 012313 (2017).
15. A. Blais, R.-S. Huang, A. Wallraff, S. M. Girvin, R. J. Schoelkopf, Cavity quantum electrodynamics for superconducting electrical circuits: An architecture for quantum computation. *Phys. Rev. A* **69**, 062320 (2004).
16. A. Wallraff, D. I. Schuster, A. Blais, L. Frunzio, R.-S. Huang, J. Majer, S. Kumar, S. M. Girvin, R. J. Schoelkopf, Strong coupling of a single photon to a superconducting qubit using circuit quantum electrodynamics. *Nature* **431**, 162–167 (2004).
17. J. Koch, T. M. Yu, J. Gambetta, A. A. Houck, D. I. Schuster, J. Majer, A. Blais, M. H. Devoret, S. M. Girvin, R. J. Schoelkopf, Charge-insensitive qubit design derived from the Cooper pair box. *Phys. Rev. A* **76**, 042319 (2007).
18. P. Krantz, A. Bengtsson, M. Simoen, S. Gustavsson, V. Shumeiko, W. D. Oliver, C. M. Wilson, P. Delsing, J. Bylander, Single-shot read-out of a superconducting qubit using a Josephson parametric oscillator. *Nat. Commun.* **7**, 11417 (2016).
19. S. Boutin, D. M. Toyli, A. V. Venkatramani, A. W. Eddins, I. Siddiqi, A. Blais, Effect of higher-order nonlinearities on amplification and squeezing in Josephson parametric amplifiers. *Phys. Rev. Applied* **8**, 054030 (2017).
20. W. Wustmann, V. Shumeiko, Parametric resonance in tunable superconducting cavities. *Phys. Rev. B* **87**, 184501 (2013).
21. S. Puri, S. Boutin, A. Blais, Engineering the quantum states of light in a Kerr-nonlinear resonator by two-photon driving. *npj Quantum Inform.* **3**, 18 (2017).
22. B. Wielinga, G. J. Milburn, Quantum tunneling in a Kerr medium with parametric pumping. *Phys. Rev. A* **48**, 2494 (1993).
23. M. Marthaler, M. I. Dykman, Switching via quantum activation: A parametrically modulated oscillator. *Phys. Rev. A* **73**, 042108 (2006).
24. H. Wiseman, G. Milburn, *Quantum Measurement and Control* (Cambridge Univ. Press, 2010).
25. E. Magesan, J. M. Gambetta, A. D. Córcoles, J. M. Chow, Machine learning for discriminating quantum measurement trajectories and improving readout. *Phys. Rev. Lett.* **114**, 200501 (2015).
26. C. C. Bultink, M. A. Rol, T. E. O'Brien, X. Fu, B. C. S. Dikken, C. Dickel, R. F. L. Vermeulen, J. C. de Sterke, A. Bruno, R. N. Schouten, L. DiCarlo, Active resonator reset in the nonlinear dispersive regime of circuit QED. *Phys. Rev. Appl.* **6**, 034008 (2016).
27. D. T. McClure, H. Paik, L. S. Bishop, M. Steffen, J. M. Chow, J. M. Gambetta, Rapid driven reset of a qubit readout resonator. *Phys. Rev. Appl.* **5**, 011001 (2016).
28. S. Boutin, C. K. Andersen, J. Venkatraman, A. J. Ferris, A. Blais, Rapid driven reset of a qubit readout resonator. *Phys. Rev. A* **96**, 042315 (2017).
29. A. Kitaev, Fault-tolerant quantum computation by anyons. *Ann. Phys. Rehabil. Med.* **303**, 2–30 (2003).
30. D. P. DiVincenzo, F. Solgun, Multi-qubit parity measurement in circuit quantum electrodynamics. *New J. Phys.* **15**, 075001 (2013).
31. S. E. Nigg, S. M. Girvin, Stabilizer quantum error correction toolbox for superconducting qubits. *Phys. Rev. Lett.* **110**, 243604 (2013).
32. J. Z. Blumoff, K. Chou, C. Shen, M. Reagor, C. Axline, R. T. Brierley, M. P. Silveri, C. Wang, B. Vlastakis, S. E. Nigg, L. Frunzio, M. H. Devoret, L. Jiang, S. M. Girvin, R. J. Schoelkopf, Implementing and characterizing precise multiqubit measurements. *Phys. Rev. X* **6**, 031041 (2016).
33. B. Criger, A. Ciani, D. P. DiVincenzo, Multi-qubit joint measurements in circuit QED: Stochastic master equation analysis. *EPJ Quant. Technol.* **3**, 6 (2016).
34. R. Raussendorf, J. Harrington, K. Goyal, Topological fault-tolerance in cluster state quantum computation. *New J. Phys.* **9**, 199 (2007).

35. F. Beaudoin, M. P. da Silva, Z. Dutton, A. Blais, First-order sidebands in circuit QED using qubit frequency modulation. *Phys. Rev. A* **86**, 022305 (2012).
36. M. D. Reed, B. R. Johnson, A. A. Houck, L. DiCarlo, J. M. Chow, D. I. Schuster, L. Frunzio, R. J. Schoelkopf, Fast reset and suppressing spontaneous emission of a superconducting qubit. *Appl. Phys. Lett.* **96**, 203110 (2010).
37. N. E. Frattini, U. Vool, S. Shankar, A. Narla, K. M. Sliwa, M. H. Devoret, 3-wave mixing Josephson dipole element. *Appl. Phys. Lett.* **110**, 222603 (2017).
38. Y. Yin, Y. Chen, D. Sank, P. J. O'Malley, T. C. White, R. Barends, J. Kelly, E. Lucero, M. Mariantoni, A. Megrant, C. Neill, A. Vainsencher, J. Wenner, A. N. Korotkov, A. N. Cleland, J. M. Martinis, Catch and release of microwave photon states. *Phys. Rev. Lett.* **110**, 107001 (2013).
39. M. Pierre, I.-M. Svensson, S. R. Sathyamoorthy, G. Johansson, P. Delsing, Storage and on-demand release of microwaves using superconducting resonators with tunable coupling. *Appl. Phys. Lett.* **104**, 232604 (2014).
40. E. Flurin, N. Roch, J. D. Pillet, F. Mallet, B. Huard, Superconducting quantum node for entanglement and storage of microwave radiation. *Phys. Rev. Lett.* **114**, 090503 (2015).
41. W. Pfaff, C. J. Axline, L. D. Burkhart, U. Vool, P. Reinhold, L. Frunzio, L. Jiang, M. H. Devoret, R. J. Schoelkopf, Controlled release of multiphoton quantum states from a microwave cavity memory. *Nat. Phys.* **13**, 882–887 (2017).
42. C. Macklin, K. O'Brien, D. Hover, M. E. Schwartz, V. Bolkhovsky, X. Zhang, W. D. Oliver, I. Siddiqi, A near–quantum-limited Josephson traveling-wave parametric amplifier. *Science* **350**, 307–310 (2015).
43. C. Gardiner, P. Zoller, *Quantum Noise: A Handbook of Markovian and Non-Markovian Quantum Stochastic Methods with Applications to Quantum Optics* (Springer Series in Synergetics, Springer, 2004).
44. J. Gambetta, A. Blais, D. I. Schuster, A. Wallraff, L. Frunzio, J. Majer, M. H. Devoret, S. M. Girvin, R. J. Schoelkopf, Qubit-photon interactions in a cavity: Measurement-induced dephasing and number splitting. *Phys. Rev. A* **74**, 042318 (2006).
45. J. Gambetta, A. Blais, M. Boissonneault, A. A. Houck, D. I. Schuster, S. M. Girvin, Quantum trajectory approach to circuit QED: Quantum jumps and the Zeno effect. *Phys. Rev. A* **77**, 012112 (2008).
46. C. Rigetti, J. M. Gambetta, S. Poletto, B. L. T. Plourde, J. M. Chow, A. D. Córcoles, John A. Smolin, S. T. Merkel, J. R. Rozen, G. A. Keefe, M. B. Rothwell, M. B. Ketchen, M. Steffen, Superconducting qubit in a waveguide cavity with a coherence time approaching 0.1 ms. *Phys. Rev. B* **86**, 100506 (2012).
47. U. Vool, M. Devoret, Introduction to quantum electromagnetic circuits. *Int. J. Circ. Theor. App.* **45**, 897–934 (2017).

Acknowledgments: We thank A. Wallraff for discussions on Fig. 4. **Funding:** This research was undertaken thanks, in part, to funding from NSERC, the Canada First Research Excellence Fund, and the Vanier Canada Graduate Scholarships. S.P. acknowledges financial support by the National Science Foundation under grant no. DMR-1609326 and Army Research Office under grant no. W911NF1410011. **Author contributions:** B.R. performed the numerical simulations and analytical calculations with inputs from S.P. and A.B. B.R. wrote the manuscript with contributions from S.P. and A.B. A.B. supervised the work. **Competing interests:** The authors declare that they have no competing interests. **Data and materials availability:** All data needed to evaluate the conclusions in the paper are present in the paper and/or the Supplementary Materials. Additional data related to this paper may be requested from the authors.

Submitted 14 May 2018
Accepted 26 October 2018
Published 30 November 2018
10.1126/sciadv.aau1695

Citation: B. Royer, S. Puri, A. Blais, Qubit parity measurement by parametric driving in circuit QED. *Sci. Adv.* **4**, eaau1695 (2018).

4.2.1 Précisions sur l'article

La mesure de parité directe à quatre qubits que je propose nécessitant plus de matériel que la mesure de parité directe à deux qubits, il est utile de dresser le bilan du matériel nécessaire :

— Un résonateur non linéaire de mesure
— Un filtre pour le résonateur de mesure
— Un qubit pour le couplage variable entre les deux résonateurs précédents

L'avantage par rapport à la mesure indirecte réside ici dans l'élimination de deux résonateurs de couplage. De plus, le qubit supplémentaire permettant un couplage variable n'est jamais excité durant le protocole, enlevant la contrainte d'un grand temps de cohérence présente pour le qubit ancillaire de la mesure indirecte. La fonction du qubit de couplage est seulement d'ajouter une non-linéarité au circuit. Finalement, la mesure de parité directe ne requiert pas de portes à deux qubits, simplifiant grandement la calibration du système et rendant la protocole plus robuste aux erreurs. En effet, une erreur de porte à deux qubits dans une mesure de parité indirecte mène à un état erroné du qubit ancillaire, ce qui mène ultimement à des erreurs sur la mesure de parité et sur l'état des qubits de données. Au contraire, dans la mesure de parité directe, il y une résilience intrisèque à certaines erreurs. Par exemple, une légère erreur sur la longueur de l'impulsion de mesure aura peu d'effet sur la fidélité finale de la mesure.

Une autre façon de comprendre le protocole d'effacement de fréquence est de considérer tout le dispositif au-delà du résonateur non linéaire comme un instrument de mesure insensible au décalage en fréquence, $\delta_o = \pm 2\chi$. En effet, le pilotage à deux photons combiné au couplage dispersive mène à une intrication photons-qubits qu'il est impossible de défaire par une opération unitaire uniquement sur les photons. Cependant, en mesurant une observable bien choisie, il est possible de conserver les superpositions quantiques désirées. Dans le cas présent et lorsque les qubits sont dans un état impair, l'état du résonateur non linéaire est donné par un état cohérent $\left|\alpha\, e^{\pm i\delta_o t}\right\rangle$ et une mesure homodyne stroboscopique permet d'être sensible à l'amplitude α sans tenir compte de la phase additionnelle $\pm i\delta_o t$. L'effet du couplage variable est donc d'extraire les photons de manière stroboscopique, c'est-à-dire seulement aux temps où les états $\left|\alpha\, e^{\pm i\delta_o t}\right\rangle$ sont indistinguables.

4.3 Avenues de recherche

Une première option pour améliorer cette mesure de parité directe serait de trouver des stratégies pour l'accélerer. Par exemple, on pourrait optimiser la forme du pilotage à deux photons à l'aide d'outils numériques [161].

Ensuite, il serait intéressant d'étudier un système similaire avec un pilotage général à n photons plutôt qu'un pilotage à deux photons. Par exemple, considérons un résonateur non linéaire piloté par une pompe paramétrique à une fréquence $n\omega_r$ et décrit par l'Hamiltonien

$$\hat{H} = K_n \hat{a}^{\dagger n} \hat{a}^n + \epsilon_p (\hat{a}^{\dagger n} + \hat{a}^n). \tag{4.6}$$

Dans cette situation, les états stationnaires du résonateur correspondent à n états cohérents symétriques sous une rotation $\alpha \rightarrow \alpha\, e^{i2\pi/n}$ [162]. En suivant un raisonnement similaire à celui présenté dans l'article, il serait possible de réaliser une mesure de parité en tirant avantage d'un couplage dispersif induisant un désaccord entre le résonateur et la pompe conditionnel à l'état des qubits. Un projet intéressant pourrait être d'étudier ce type de dispositif pour la mesure de parité à deux qubits, en particulier obtenir des valeurs analytiques pour le déphasage dans l'espace propre pair et pour le temps de bifurcation. On peut cependant noter que l'analyse utilisée dans l'article principal pour obtenir un taux de déphasage analytique n'est pas directement transposable étant donné que l'Hamiltonien 4.6 n'est pas quadratique.

Une autre direction attrayante serait d'étudier les corrections à l'interaction dispersive dues au grand nombre de photons dans le résonateur durant la mesure [70]. Entre autres, il serait intéressant d'étudier les différences entre les mesures basées sur la bifurcation et la mesure dispersive standard à nombre de photons égal.

Finalement, j'ai présenté en détails comment la mesure de parité directe peut induire des erreurs de déphasage, $\hat{\sigma}_z$. En principe, les inversions de qubits, c'est-à-dire des erreurs de type $\hat{\sigma}_x$, sont absentes tant que l'Hamiltonien dispersif est valide. À l'inverse, pour la mesure de parité indirecte se basant sur un qubit ancillaire, les erreurs due à la mesure ne suivent pas de structure particulière. Il serait intéressant d'étudier plus en profondeur si ce modèle d'erreur biaisé [163] présente des

avantages vis-à-vis des la tolérance aux fautes [164, 165].

Chapitre 5

Intrication à distance

Ce chapitre présente les travaux que j'ai effectués en collaboration avec mes collègues de l'ETH Zürich. Plus précisément, j'ai effectué le support théorique accompagnant les expériences réalisées dans le groupe d'Andreas Wallraff. Je commence ce chapitre par décrire l'élément de base liant les différentes expériences, le couplage f0g1, puis je présente les trois articles résultants de cette collaboration [60, 63, 72]. Les deux premiers utilisent le même montage expérimental et montrent comment établir un canal de communication quantique entre deux nœuds distants. Le troisième article se base sur le montage d'un seul de ces deux nœuds et introduit une méthode pour réinitialiser rapidement un transmon.

5.1 Couplage f0g1

La méthode la plus simple pour faire interagir un transmon et un résonateur est de les coupler capacitivement comme illustré à la figure 2.3. Cependant, la valeur de la capacité étant donnée par une géométrie fixe, l'interaction transmon-résonateur résultante est, elle aussi, fixe. Pour certaines applications, par exemple l'émission contrôlée de photons [166], un couplage variable est nécessaire.

Pour obtenir ce couplage variable, une option est d'utiliser un transmon de fréquence adaptable, où la jonction Josephson est remplacée par une boucle SQUID

avec un flux modifiable, $\Phi_x(t)$. Pour activer l'interaction g, il suffit de varier la fréquence du transmon depuis une valeur de grand désaccord en fréquence, $|\Delta| = |\omega_r - \omega_q| \gg g$, vers la fréquence du résonateur, $\Delta = 0$ [83]. Cette méthode, simple en principe, n'est pas idéale pour plusieurs raisons. Tout d'abord, le fait de posséder une fréquence modifiable dégrade le temps de cohérence du transmon en raison du bruit de flux, surtout lorsque $\partial\omega_q/\partial\Phi_x \neq 0$, c'est-à-dire lorsque le transmon est loin de son point idéal de flux (*sweet spot*). De plus, en parcourant une grande gamme de fréquences pour arriver à la fréquence du résonateur, il existe un risque que le transmon soit momentanément en résonance avec des systèmes à deux niveaux présents dans l'environnement. Ce type d'interaction indésirable mène à une réduction du temps de vie des transmons [167]. Finalement, la réalisation d'impulsions DC rapides et précises est difficile à réaliser [168].

Une autre option pour obtenir un couplage variable est d'utiliser un coupleur ajustable dédié à cette tâche [169, 170, 171, 172, 173, 174] ou un qubit dont le couplage au résonateur peut être directement ajusté [175, 176]. Cependant, ces approches sont plus complexes à réaliser.

Le couplage f0g1 [166, 177, 178] est une alternative à ces méthodes et permet d'obtenir une interaction contrôlée entre un transmon et un résonateur sans variation de flux ni circuit additionnel. Se basant sur une transition de type Raman, cette interaction est compatible avec des transmons de fréquence fixe. D'autre part, avec cette approche, autant l'amplitude que la phase du couplage peuvent être contrôlées.

Considérons le montage illustré à la figure 5.1a représentant la situation de couplage dispersif typique entre un transmon (rouge) et un résonateur (vert). Le couplage f0g1 est induit par un pilotage du qubit (orange) à une fréquence $\omega_{f0g1} = \omega_{f0} - \omega_{g1}$, où ω_{f0} (ω_{g1}) est la fréquence de l'état $|f0\rangle$ ($|g1\rangle$). Comme son nom l'indique et tel qu'illustré à la figure 5.1b, ce couplage mène à une hybridation des états $|f0\rangle$ et $|g1\rangle$, une situation décrite par l'Hamiltonien

$$\hat{H}_{f0g1} = \tilde{g}\,|f0\rangle\langle g1| + \tilde{g}^*\,|g1\rangle\langle f0|\,. \tag{5.1}$$

Comme illustré schématiquement à la figure 5.1c, on peut comprendre le couplage f0g1 comme un processus de mélange à quatre ondes généré par la jonction Josephson du qubit piloté, où un photon de la pompe (orange) combiné à un photon du

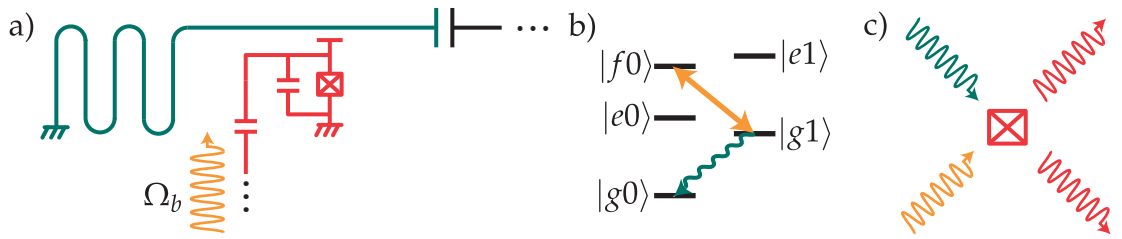

FIGURE 5.1 – a) Un transmon (rouge) est couplé dispersivement (équation 2.6) à un résonateur $\lambda/4$ (vert) lui-même couplé capacitivement à un port de sortie (noir). Un port capacitif permet de piloter (orange) le transmon à la différence de fréquence entre l'état $|f0\rangle$ et $|g1\rangle$. b) Niveaux d'énergies du système combiné transmon-résonateur. L'onde de pilotage induit un couplage entre les états $|f0\rangle$ et $|g1\rangle$ (ligne fléchée orange) et le faible facteur de qualité du résonateur mène à la perte de photons (ligne ondulée verte). c) Le couplage f0g1 est un processus de mélange à quatre ondes convertissant un photon de la pompe (orange) et un photon de résonateur (vert) en deux excitations de transmon (rouge).

résonateur (vert) sont convertis en deux excitations de qubits (rouge).

Dans le régime de faible amplitude de pilotage par rapport au désaccord entre le pilotage et le transmon, $\Omega_b \ll \omega_d - \omega_q$, le couplage f0g1 est donné par [177]

$$\tilde{g} = \frac{\Omega_b \alpha_q g}{\sqrt{2}\Delta(\Delta + \alpha_q)}. \tag{5.2}$$

Comme mentioné plus haut, l'amplitude et phase de $\tilde{g}$ sont déterminés par l'amplitude et la phase de l'impulsion de pilotage, Ω_b. Le calcul de cette relation est inclus en annexe C.1. Bien que la relation linéaire 5.2 capture le comportement qualitatif de $\tilde{g}$, l'accord quantitatif avec l'expérience n'est pas parfait. Cette différence est en partie due au pilotage de grande amplitude qui induit un décalage AC-Stark des niveaux d'énergie de l'ordre de $|\Omega_b|^2$, changeant de ce fait le désaccord effectif entre le transmon et le résonateur, $\Delta \to \Delta(\Omega_b)$. Une autre conséquence de ce décalage AC-Stark est le fait que la fréquence de pilotage doit être ajustée en fonction de l'amplitude de pilotage, $\omega_d \to \omega_d(\Omega_b)$.

Afin de bien modéliser la relation entre le couplage, l'amplitude de pilotage et le décalage AC-Stark, $\tilde{g}(\Omega_b)$ et $\omega_d(\Omega_b)$, on utilise une méthode numérique inspirée de Zeytinoğlu *et al.* [177]. Ainsi, pour chaque amplitude de pilotage, Ω_b, on

effectue une spectroscopie numérique en cherchant la fréquence de pilotage ω_d où l'on observe un anti-croisement entre les états $|f0\rangle$ et $|g1\rangle$. Plus précisément, on diagonalise numériquement l'Hamiltonien Jaynes-Cummings avec un terme de pilotage additionnel,

$$\hat{H} = (\omega_r - \omega_d)\hat{a}^\dagger\hat{a} + (\omega_q - \omega_d)\hat{b}^\dagger\hat{b} + g(\hat{a}^\dagger\hat{b} + \hat{a}\hat{b}^\dagger) + \frac{\alpha_q}{2}\hat{b}^\dagger\hat{b}^\dagger\hat{b}\hat{b} + \frac{\Omega_b}{2}(\hat{b} + \hat{b}^\dagger), \quad (5.3)$$

en faisant varier la fréquence de pilotage, ω_d. L'Hamiltonien 5.3 est exprimé dans le référentiel tournant à la fréquence ω_d. En supposant que la fréquence de pilotage est près de la fréquence ω_{f0g1}, les valeurs propres sont similaires aux valeurs propres d'un système à deux niveaux, $E_\pm = (\delta_d \pm \sqrt{4\tilde{g}^2 + \delta_d^2})/2$, où $\delta_d = \omega_d - \omega_{f0g1}$. Lorsque $\delta_d = 0$, les états propres sont $|\psi_\pm\rangle = (|f0\rangle \pm |g1\rangle)/\sqrt{2}$. Ainsi, à partir des états propres, $\{|\psi_i(\omega_d)\rangle\}$, et des valeurs propres, $\{\lambda_i(\omega_d)\}$, de l'Hamiltonien 5.3, on identifie l'amplitude du couplage et la bonne fréquence de pilotage à partir de la différence d'énergie entre les états $|\psi_\pm\rangle$,

$$|\tilde{g}| = \frac{1}{2}\min_{\omega_d} |\lambda_+(\omega_d) - \lambda_-(\omega_d)|. \quad (5.4)$$

Étant donné que le pilotage change la nature des états propres en plus d'ajouter un terme de couplage, $\tilde{g}$, il est important de bien identifier les états $|\psi_\pm\rangle$ (et leurs valeurs propres $\lambda_\pm$) parmi tous les états propres $\{|\psi_i\rangle\}$. À cette fin, on cherche les états $|\psi_i\rangle$ ayant un recouvrement maximal avec les états sans pilotage $|\psi_\pm(0)\rangle$,

$$\max_{\psi_i} |\langle\psi_i|\psi_\pm\rangle|. \quad (5.5)$$

Un exemple typique de calibration issue de cette procédure est illustré à la figure 5.2. La méthode expérimentale pour réaliser la calibration de $\tilde{g}(\Omega_b)$ et $\omega_d(\omega_b)$ est décrite dans l'article de la section 5.4.

Une des applications principales du couplage f0g1 est l'émission de photons avec une forme contrôlée [166]. Pour un résonateur de faible facteur de qualité, l'état $|g1\rangle$ relaxe vers l'état fondamental $|g0\rangle$ à un taux κ en émettant un photon. Pour émettre un photon de façon contrôlée, on peut ainsi préparer le transmon dans l'état $|f0\rangle$ et appliquer une impulsion Ω_b amenant le système vers l'état $|g1\rangle$. En contrôlant la forme temporelle du couplage f0g1, $\tilde{g}(t) \propto \Omega_b(t)$, il est possible de

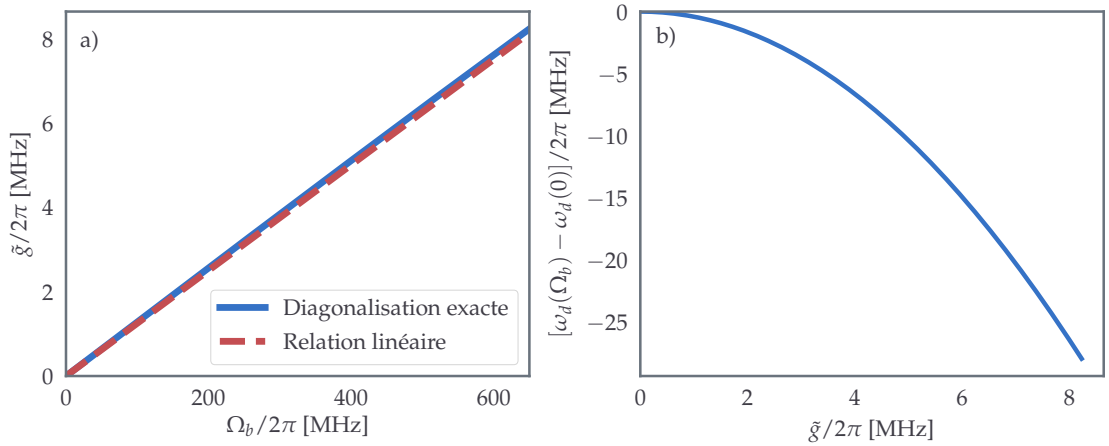

FIGURE 5.2 – Exemple de calibration pour le couplage f0g1. a) Couplage f0g1 en fonction de l'amplitude de pilotage, $\tilde{g}(\Omega_b)$. b) Décalage AC-Stark de la fréquence de pilotage en fonction de l'amplitude du couplage f0g1, $\omega_d(\Omega_b)$.

choisir la forme $\xi(t)$ du photon émis,

$$|1_\xi\rangle = \int dt\, \xi(t)\hat{a}^\dagger(t)\,|0\rangle\,, \tag{5.6}$$

où $|0\rangle$ est l'état vide de la ligne à transmission de sortie et $\hat{a}(t)$ l'opérateur de champ annihilant un photon au temps t ($[\hat{a}(t), \hat{a}^\dagger(t')] = \delta(t-t')$). L'enveloppe $\xi(t)$ du photon est normalisée, $\int_{-\infty}^{\infty} dt\,|\xi(t)|^2 = 1$. Le lien entre $\xi(t)$ et $\tilde{g}(t)$ est donné en annexe C.2. Une limitation de ce protocole est la largeur de bande maximale du photon donnée par le taux d'émission du résonateur, κ. En pratique, il est facile d'avoir des résonateurs avec un taux de dissipation dans la gamme de fréquence intéressante, $\kappa/2\pi \sim 10$ MHz, et cette limitation a peu d'impact.

5.2 Intrication à distance, encodage de Fock

5.2.1 Contexte

Une approche intéressante pour la réalisation d'un calcul quantique à grande échelle est l'architecture modulaire [179]. Dans cette approche, un calcul quantique est divisé en plusieurs parties effectuées sur des processeurs quantiques distincts. Chacun de ces processeurs étant de taille modeste, cette stratégie présente de nombreux avantages pratiques par rapport à la réalisation d'un seul grand processeur. Par exemple, on peut penser à la fabrication facilité des processeurs, à la calibration plus rapide des échantillons ou encore à une réduction globale de la diaphonie (*crosstalk*).

Afin que les différents processeurs puissent travailler de concert, un élément essentiel est un canal de communication quantique permettant d'intriquer les modules et de transférer des états quantiques [26, 27]. Avec mes collègues de l'ETH Zürich, nous avons réalisé une preuve de concept pour ces canaux quantiques. Plus précisément, nous avons réalisé un dispositif permettant à la fois de transférer un état quantique entre deux qubits distants et d'intriquer ces deux qubits. Une caractéristique importante de cette implémentation est qu'elle est déterministe, permettant de générer de l'intrication plus rapidement que les expériences précédentes avec les circuits supraconducteurs se basant sur des processus stochastiques [180, 38].

La méthode que nous avons choisie pour réaliser un transfert d'état quantique a été introduite par Cirac et Zoller [62] et utilise un photon unique pour transporter l'information d'un nœud à l'autre. Dans cette proposition et comme illustré à la figure 5.3, un état de qubit est converti en photon itinérant avant d'être absorbé au nœud récepteur. Considérons deux systèmes d'EDQc standard mis en cascade en supposant qu'on puisse contrôler la valeur du couplage. Comme illustré à la figure 5.3, une excitation initialement dans le qubit émetteur est transférée au résonateur en activant $g_1(t)$, puis un photon est émis du résonateur et dirigé vers le nœud récepteur. L'intuition cruciale de Cirac et Zoller est que le processus d'émission du photon est symétrique sous inversement du temps. Ainsi, il est possible d'absorber parfaitement un photon s'il est temporellement symétrique, $\xi(t) = \xi(-t)$, en utili-

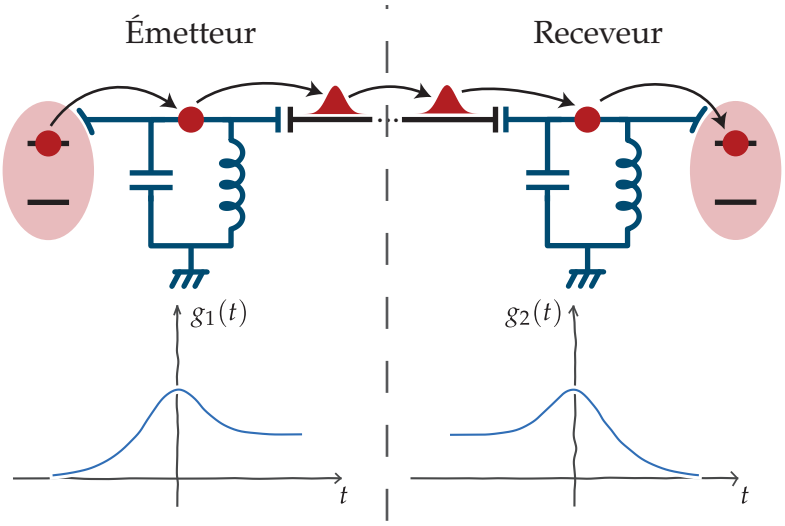

FIGURE 5.3 – Une excitation (point rouge) du qubit émetteur (système à deux niveaux, fond rouge) est transférée à un résonateur (bleu) en activant un couplage, $g_1(t)$. Le photon est ensuite émis dans un guide d'onde dirigée vers l'entrée d'un résonateur récepteur. En utilisant un couplage inversé, $g_2(t) = g_1(-t)$, on absorbe parfaitement le photon dans le qubit récepteur.

sant un couplage inversé en temps au nœud récepteur, $g_1(t) = g_2(-t)$. En utilisant un photon itinérant pour encoder l'information, il est donc possible de réaliser un transfert d'état quantique entre deux nœuds distants.

Comme mentionné dans la section précédente 5.1 et démontré par Pechal *et al.* [166], le couplage f0g1 permet d'émettre des photons en préparant le transmon dans l'état $|f\rangle$. Afin de réaliser un transfert d'état de qubit, défini dans le sous-espace $\{|g\rangle, |e\rangle\}$ des transmons, on peut donc suivre la méthode de Cirac et Zoller [62] en inversant la population des états $|e\rangle$ et $|f\rangle$,

$$\alpha |g\rangle + \beta |e\rangle \leftrightarrow \alpha |g\rangle + \beta |f\rangle . \tag{5.7}$$

Pour générer de l'intrication à distance, il suffit de suivre la même procédure que pour le transfert d'état, mais en préparant initialement le transmon émetteur dans l'état $(|e\rangle + |f\rangle)/\sqrt{2}$. Ainsi, après le protocole, les transmons se retrouvent dans un état intriqué

$$\frac{|e\rangle + |f\rangle}{\sqrt{2}} \otimes |g\rangle \rightarrow \frac{|eg\rangle + |gf\rangle}{\sqrt{2}}. \tag{5.8}$$

Un état de Bell $|\psi^+\rangle$ est obtenu après une inversion de population des états $|e\rangle$ et $|f\rangle$ du transmon récepteur.

Un choix intéressant pour la forme du photon est

$$\xi(t) = \frac{\sqrt{\kappa_{\text{eff}}}}{2\cosh(\kappa_{\text{eff}} t/2)}, \tag{5.9}$$

où $\kappa_{\text{eff}} \leq \kappa$. Ce choix est motivé par le fait que cette forme est symétrique, $\xi(t) = \xi(-t)$, et que dans la limite de temps longs, elle correspond à la dissipation standard d'un résonateur, $\lim_{t\to\infty} \xi(t) = \sqrt{\kappa_{\text{eff}}}\, e^{-\kappa_{\text{eff}} t/2}$. La forme du couplage f0g1, permettant d'émettre un photon de cette forme est donnée par

$$\tilde{g}(t) = \frac{\kappa_{\text{eff}}}{4\cosh(\kappa t/2)} \frac{1 - e^{\kappa t} + \frac{\kappa}{\kappa_{\text{eff}}}(1 + e^{\kappa t})}{\sqrt{\frac{\kappa}{\kappa_{\text{eff}}}(1 + e^{\kappa t}) - e^{\kappa t}}}, \tag{5.10}$$

où κ est le taux de dissipation du résonateur. Un désavantage de la forme 5.9 est qu'en principe son étendue est infinie. En pratique, on choisit de tronquer le photon à $t_{\text{max/min}} \approx \pm 3/\kappa_{\text{eff}}$, ce qui mène à une légère imperfection sur le transfert d'état. Dans l'expérience que nous avons réalisée, cette source d'erreur est petite par rapport à la décohérence des transmons et les pertes de photons dans le canal de transmission.

Notons que deux groupes de Yale ont publié des articles conceptuellement similaires au nôtre au même moment [181, 182]. Utilisant aussi le protocole de Cirac et Zoller, ces deux articles sont basés sur des cavités micro-ondes tridimensionnelles plutôt qu'une architecture planaire. De plus, au même moment, un groupe de Delft a démontré un protocole d'intrication à distance stochastique [183] améliorant les résultats précédents de Roch *et al.* [180]. On peut aussi souligner les travaux de Leung *et al.* [184] publiés peu après démontrant l'intrication de deux qubits distants sans utiliser de circulateur entre les deux noeuds.

5.2.2 Article

Pour cet article, j'ai effectué le travail de support théorique pour l'expérience qui a été réalisée à l'ETH Zürich dans le groupe d'Andreas Wallraff. Plus précisément,

j'ai réalisé une analyse approfondie du couplage f0g1, dont une version simplifiée est présentée en annexe C.1. De plus j'ai réalisé les simulations d'équation maîtresse permettant de comprendre et modéliser la dynamique du système. À ce sujet, on peut souligner l'accord remarquable entre l'expérience et les simulations numériques qui ont été effectuées sans aucun paramètres ajustables. Finalement, j'ai participé à la préparation du manuscrit en rédigeant la section *Master-equation simulation* (Méthodes) et en aidant à écrire l'article.

P. Kurpiers, P. Magnard, T. Walter, B. Royer, M. Pechal, J. Heinsoo, Y. Salathé, A. Akin, S. Storz, J. C. Besse, S. Gasparinetti, A. Blais et A. Wallraff. Deterministic quantum state transfer and remote entanglement using microwave photons. *Nature* **558**(7709), 264–267 (2018)

Deterministic Quantum State Transfer and Generation of Remote Entanglement using Microwave Photons

P. Kurpiers,[1,*] P. Magnard,[1,*] T. Walter,[1] B. Royer,[2] M. Pechal,[1] J. Heinsoo,[1] Y. Salathé,[1] A. Akin,[1] S. Storz,[1] J.-C. Besse,[1] S. Gasparinetti,[1] A. Blais,[2,3] and A. Wallraff[1]

[1] *Department of Physics, ETH Zürich, CH-8093 Zürich, Switzerland.*
[2] *Institut Quantique and Département de Physique, Université de Sherbrooke, Sherbrooke, Québec J1K 2R1, Canada*
[3] *Canadian Institute for Advanced Research, Toronto, Canada*

(Dated: December 25, 2017)

Sharing information coherently between nodes of a quantum network is at the foundation of distributed quantum information processing. In this scheme, the computation is divided into subroutines and performed on several smaller quantum registers connected by classical and quantum channels[1]. A direct quantum channel, which connects nodes deterministically, rather than probabilistically, is advantageous for fault-tolerant quantum computation because it reduces the threshold requirements and can achieve larger entanglement rates[2]. Here, we implement deterministic state transfer and entanglement protocols between two superconducting qubits[3] fabricated on separate chips. Superconducting circuits constitute a universal quantum node[4] capable of sending, receiving, storing, and processing quantum information[5–8]. Our implementation is based on an all-microwave cavity-assisted Raman process[9] which entangles or transfers the qubit state of a transmon-type artificial atom[10] to a time-symmetric itinerant single photon. We transfer qubit states at a rate of 50 kHz using the emitted photons which are absorbed at the receiving node with a probability of $98.1 \pm 0.1\%$ achieving a transfer process fidelity of $80.02 \pm 0.07\%$. We also prepare on demand remote entanglement with a fidelity as high as $78.9 \pm 0.1\%$. Our results are in excellent agreement with numerical simulations based on a master equation description of the system. This deterministic quantum protocol has the potential to be used as a backbone of surface code quantum error correction across different nodes of a cryogenic network to realize large-scale fault-tolerant quantum computation[11,12] in the circuit quantum electrodynamic (QED) architecture.

Remote entanglement has been realized probabilistically in heralded[13–17] and unheralded protocols[18–21] (see Appendix A for details). A fully deterministic entanglement protocol[22] utilizing a stationary atom coupled to a single mode cavity in remote quantum nodes is more challenging to realize[20]. This protocol uses a coherent drive to entangle the state of an atom with the field of the cavity. The cavity is coupled to a directional quantum channel into which the field is emitted as a time-symmetric single photon. This photon travels to the receiving node where it is ideally absorbed with unit probability, using a time reversed coherent drive (Fig. 1 a). In addition to establishing entanglement between the nodes, this direct transfer of quantum information naturally offers the possibility to transmit an arbitrary qubit state from one node to the other.

In our adaptation of this scheme (Fig. 1 b) to the circuit QED architecture, each quantum node is composed of a superconducting transmon qubit with transition frequency $\nu_{\mathrm{ge}}^{\mathrm{A}} = 6.343$ GHz ($\nu_{\mathrm{ge}}^{\mathrm{B}} = 6.093$ GHz) dispersively coupled to two coplanar microwave resonators, analogous to an atom in two cavities. One resonator is dedicated to dispersive qubit readout and the second one to excitation transfer. The transfer resonator of the two nodes have a matched frequency $\nu_{\mathrm{T}} = 8.400$ GHz and a large bandwidth $\kappa_{\mathrm{T}}/2\pi \sim 11$ MHz (see Appendix B). All resonators are coupled to a dedicated filter, to protect the qubits from Purcell decay[23–25]. An external coaxial line, bisected with a circulator, connects the transfer circuits of both nodes. With this setup, photons can be routed from node A to B, and from node B to a detection line. To generate a controllable light-matter interaction, we apply a coherent microwave tone to the transmon that induces an effective interaction $\tilde{g}(t)$ between states $|f,0\rangle$ and $|g,1\rangle$ with tunable amplitude and phase[9,26]. Here $|s,n\rangle$ denotes a Jaynes-Cummings dressed eigenstate with the transmon in state $|s\rangle$, where $|g\rangle$, $|e\rangle$ and $|f\rangle$ are its three lowest energy eigenstates, and $|n\rangle$ the Fock state of the transfer resonator. This interaction swaps an excitation from the transmon to the transfer resonator, which then couples to a mode propagating towards node B. By controlling $\tilde{g}(t)$ (see Appendix C), we shape the itinerant photon to have a time-reversal symmetric envelope $\phi(t) = \frac{1}{2}\sqrt{\kappa_{\mathrm{eff}}}\,\mathrm{sech}(\kappa_{\mathrm{eff}}t/2)$, with an adjustable photon bandwidth κ_{eff} limited only by κ_{T}. By inducing the reverse process $|f,0\rangle \leftrightarrow |g,1\rangle$ with the time reversed amplitude and phase profile of $\tilde{g}(t)$ we absorb the itinerant photon with the transmon at node B. Ideally, this procedure returns all photonic modes to their vacuum state.

To characterize the excitation transfer, we start by initializing the transmon in its ground state[27] followed by a sequence of two π-pulses ($\mathrm{R}_{\mathrm{ge}}^{\pi}$, $\mathrm{R}_{\mathrm{ef}}^{\pi}$), used to prepare the transmon at node B in state $|f,0\rangle$. Next, we induce the effective coupling $\tilde{g}(t)$ with a modulated drive $\mathrm{R}_{\mathrm{f0g1}}^{\tau}$ to

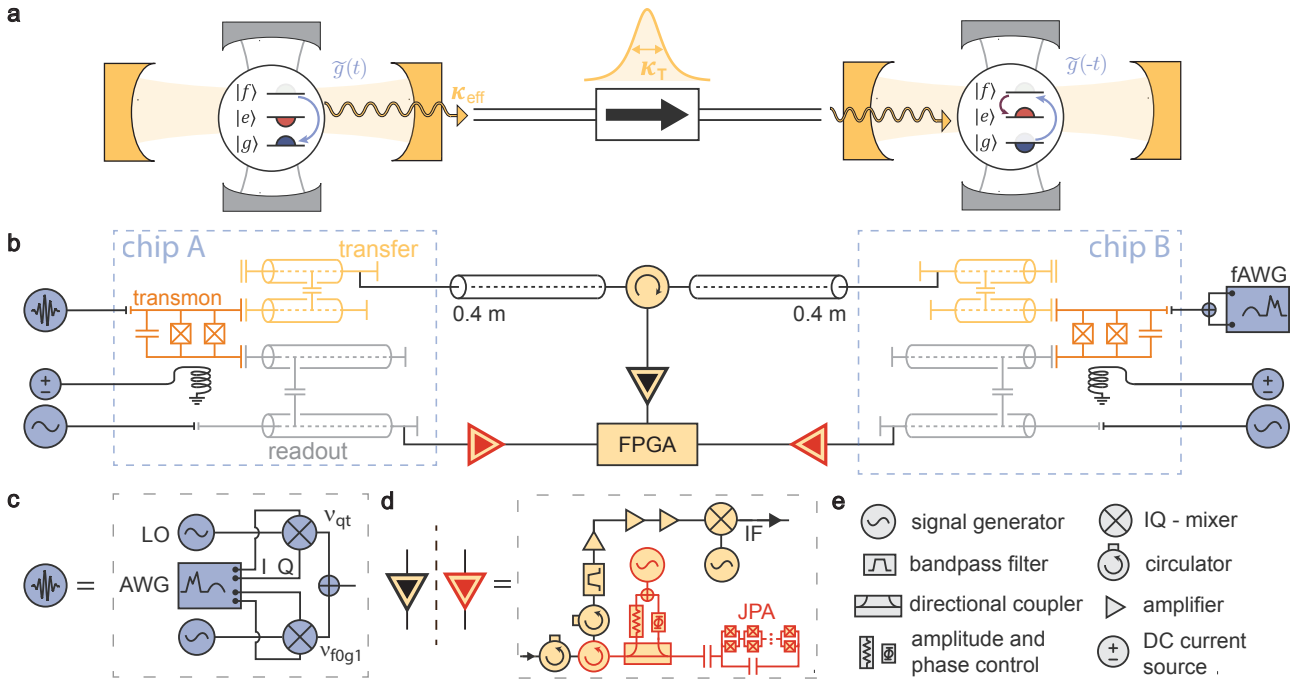

FIG. 1. **Schematic and measurement setup. a,** Quantum optical schematic of a deterministic unidirectional entanglement protocol between two cavity QED nodes of a quantum network. At the first node, a three level system is prepared in its second excited state $|f\rangle$ (grey half-circle) and coherently driven ($\tilde{g}(t)$, blue arrow) to $|g\rangle$ (blue half-circle) creating the transfer cavity field $|1\rangle$ (light yellow). The cavity field couples into the directional quantum channel with rate κ_{T} as a single photon wavepacket with an effective bandwidth κ_{eff} (yellow hyperbolic secant shape). In the second quantum node, the time reversed drive $\tilde{g}(-t)$ transfers the excitation from $|g\rangle$ to $|f\rangle$ in the presence of the transferred photon field $|1\rangle$. Finally, the protocol is completed with a transfer pulse between $|f\rangle$ and $|e\rangle$ (red half-circle) to return to the qubit subspace. Additionally, each three level system is coupled to a readout cavity (grey). **b,** Circuit QED implementation of the system depicted in **a**. At each node, a transmon (orange) is coupled to two $\lambda/4$ coplanar waveguide resonator and Purcell filter circuits[23], acting as the transfer (yellow) and readout (grey) cavities respectively. A directional quantum channel is realized using a semi-rigid coaxial cable and circulator connecting to the output port of the transfer circuit Purcell filter at each node. **c-e,** details of the circuit QED implementation. **c,** Combined qutrit (ν_{qt}) and $|f,0\rangle$ to $|g,1\rangle$ transition (ν_{f0g1}) microwave drive using single side-band modulation with in-phase (I) and quadrature (Q) mixers driven by a local oscillator (LO) and with an envelope defined by an arbitrary waveform generator (AWG) for node A. On node B these drives are directly synthesized by a fast AWG (fAWG) with 25 GS/s. **d,** Schematic of microwave detection lines (black). All detections lines consist of two isolators, a bandpass-filter, a cryogenic amplifier (HEMT) and two room-temperature amplifiers followed by a filter and analogue down-conversion to an intermediate frequency of 250 MHz. The down-converted signal is lowpass-filtered, digitized using an analogue-to-digital converter and recorded using a field-programmable gate array (FPGA). The readout lines include an additional Josephson parametric amplifier (JPA) circuit (red elements) between the first two isolators. The JPA is pumped by a signal generator and the reflected pump signal from the JPA is cancelled at a directional coupler using amplitude and phase (Φ) controlled destructive interference.

emit a symmetric photon[9] (Fig. 2 a). We vary the instantaneous frequency of $\mathrm{R}^{\tau}_{\mathrm{f0g1}}$, to compensate for the drive amplitude dependent ac-Stark shift of the $|f,0\rangle \leftrightarrow |g,1\rangle$ transition[27] (see Appendix C). Here, and in all following measurements, the population of the transmon states are extracted using single-shot readout with a correction to account for measurement errors (see Appendix D). The population of the three lowest levels of the transmon $P_{\mathrm{g,e,f}}$ is measured immediately after truncating the emission pulse $\mathrm{R}^{\tau}_{\mathrm{f0g1}}$ at time τ (see Fig. 2 b). In this way, we observe that the transmon smoothly evolves from $|f\rangle$ to $|g\rangle$ during the emission process. The emitting transmon eventually reaches a ground state population $P_{\mathrm{g}} = 95\%$ which puts an upper bound to the emission efficiency.

To verify that the emitted photon envelope has the targeted shape and bandwidth $\kappa_{\mathrm{eff}}/2\pi = 10.4$ MHz, we repeat the emission protocol with an initial transmon state $(|g\rangle + |f\rangle)/\sqrt{2}$ and measure the averaged electric field amplitude $\langle a_{\mathrm{out}}(t)\rangle \propto \phi(t)$ of the emitted photon state $(|0\rangle + |1\rangle)/\sqrt{2}$ using heterodyne detection[28] (Fig. 2 c). We prepare this photon state because of its non-zero average electric field[9]. Repeating the emission protocol from node A, leads to similar dynamics of the transmon population (see Fig. 2 e). The emitted photon state (Fig. 2 f) has, however, a lower integrated power $\int |\langle a_{\mathrm{out}}(t)\rangle|^2 dt$ compared to emission from node B, due to a loss of $23.0 \pm 0.5\%$ between the remote nodes (see Appendix E). The loss is extracted from the ratio of integrated pho-

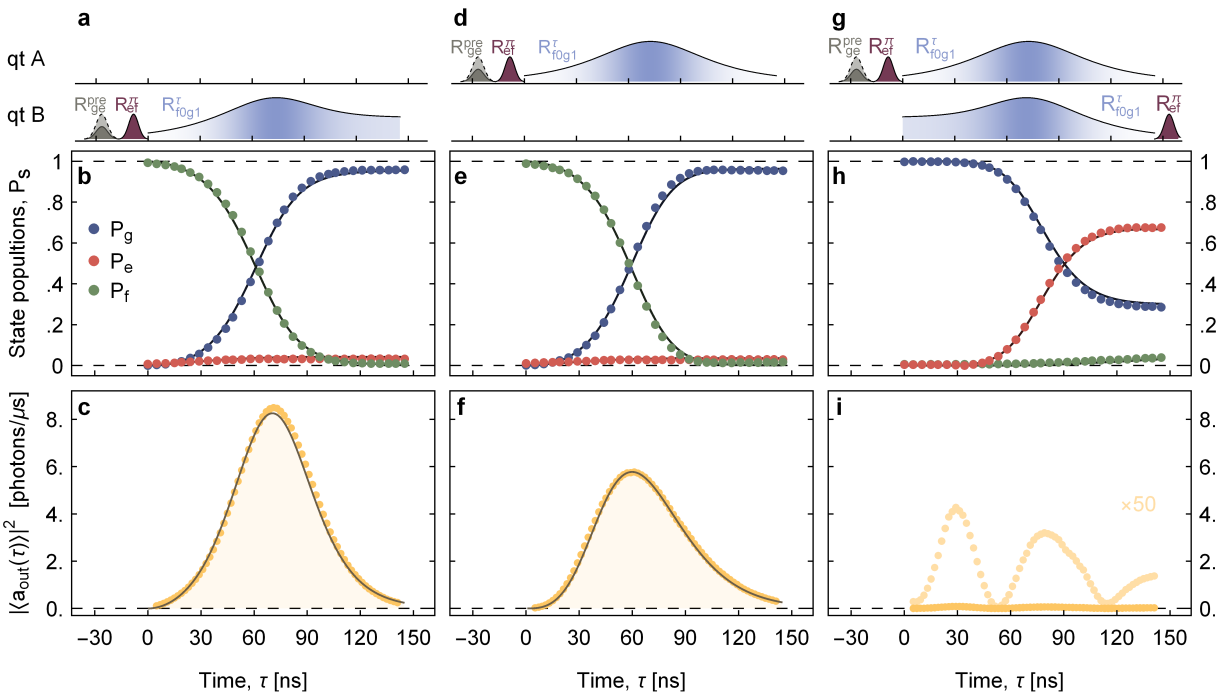

FIG. 2. **Emission, transfer and absorption of a single photon.** The transmon at node B (**a**) and node A (**d**) are prepared in the state $|f\rangle$ using Gaussian DRAG microwave pulses $\mathrm{R}^{\pi}_{\mathrm{ge}}$ and $\mathrm{R}^{\pi}_{\mathrm{ef}}$. We characterize (dots) the time dependence (τ) of the qutrit populations $\mathrm{P}_{\mathrm{g,e,f}}$ (**b**, **e**) while driving the $|f,0\rangle$ to $|g,1\rangle$ transition (f0g1). The phase (white-blue shading) of the f0g1 drive is modulated to compensated the drive-induced quadratic ac Stark shift. The mean field amplitude squared $|\langle \mathrm{a_{out}}(\tau)\rangle|^2$ of the travelling photons emitted from node B (**c**) and node A (**f**) is obtained for the emitted photon state $(|0\rangle+|1\rangle)/\sqrt{2}$. The effective photon bandwidths are $\kappa^{\mathrm{A}}_{\mathrm{eff}}/2\pi = 10.4\,\mathrm{MHz}$ and $\kappa^{\mathrm{B}}_{\mathrm{eff}}/2\pi = 10.6\,\mathrm{MHz}$. The solid lines in **b, c, e, f, h, and i** are results of master equation simulations (see text for details). The time dependence of $\mathrm{P_s}$ when executing the excitation transfer scheme (**g**) from qubit A to qubit B (**h**) are extracted simultaneously with the amplitude of the emitted field from node A. **i** shows the remaining $|\langle \mathrm{a_{out}}(\tau)\rangle|^2$ (light yellow x50) during the absorption process.

ton powers for emission from nodes B and A.The photon emitted from node A changes shape when it reflects off node B due to the response function of its transfer resonator before being detected.

Finally, we measure the population of transmon B during the absorption of a single-photon emitted from A. We apply a π-pulse on transmon B right before the measurement to map $|f\rangle$ to $|e\rangle$. The excited state population, shown in Fig. 2 h, smoothly rises before saturating at $P_{\mathrm{e}}^{\mathrm{sat}} = 67.6$ %. This saturation level defines the total excitation transfer efficiency from node A to B which is reached here in only 180 ns. From the ratio of the emitted photon integrated power in the absence (Fig. 2 i) or presence (Fig. 2 f) of the absorption pulse, the absorption efficiency is determined to be as high as 98%.

We perform master equation simulations (MES), shown as solid lines in Fig. 2, of the excitation transfer experiments, using the time offset between the nodes as the only adjustable parameter (see Appendix F). The excellent agreement between the MES and the data demonstrates a high level of control over the emission and absorption processes and an accurate understanding of the experimental imperfections. According to the MES these imperfections are accurately accounted for by decoherence and photon loss.

We demonstrate the use of the presented protocol to deterministically transfer an arbitrary qubit state from node A to node B. This is realized by preparing transmon B in state $|g\rangle$, applying a $\mathrm{R}^{\pi}_{\mathrm{ef}}$ on transmon A, followed by the emission/absorption pulse and finally a rotation $\mathrm{R}^{\pi}_{\mathrm{ef}}$ on transmon B. We characterize this quantum state transfer by reconstructing its process matrix χ with quantum process tomography (Fig. 3 b). We prepare all six mutually unbiased qubit basis-states[29] at node A, transfer them to node B, and reconstruct the transferred state using quantum state tomography (QST) (see Appendix G). The process fidelity is $\mathcal{F}_{\mathrm{p}} = \mathrm{Tr}(\chi\chi_{\mathrm{ideal}}) = 80.02 \pm 0.07\%$, well above the limit of 1/2 that could be achieved using local gates and classical communication only. The process matrix χ_{sim} calculated with the MES, depicted with red wire frames in Fig. 3 b, agrees well with the data, as suggested by the small trace distance $\sqrt{\mathrm{Tr}\left[(\chi-\chi_{\mathrm{sim}})^2\right]} = 0.014$.

Finally, we use the excitation transfer to deterministically generate an entangled state between nodes A and B. The protocol starts by preparing transmon A and B in states $(|e\rangle+|f\rangle)/\sqrt{2}$ and $|g\rangle$, respectively, and by applying the emission/absorption pulses followed by a ro-

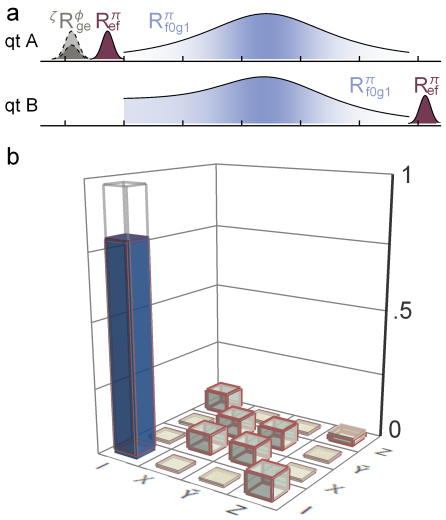

FIG. 3. **Quantum state transfer. a,** Pulse scheme used to characterize the qubit state transfer between the two nodes. We prepare six mutually unbiased input states with rotations ${}^{x}\mathrm{R}^{0}_{ge}$, ${}^{x}\mathrm{R}^{\pi/2}_{ge}$, ${}^{x}\mathrm{R}^{-\pi/2}_{ge}$, ${}^{y}\mathrm{R}^{\pi/2}_{ge}$, ${}^{y}\mathrm{R}^{-\pi/2}_{ge}$ and ${}^{x}\mathrm{R}^{\pi}_{ge}$ at node A (denoted by ${}^{\zeta}\mathrm{R}^{\phi}_{ge}$ where ζ is the rotation axis). **b,** We experimentally obtain (coloured bars) a process matrix with a fidelity of $\mathcal{F}_{\mathrm{p}} = 80.02 \pm 0.07\%$ relative to the ideal identity operation. The grey and red wire frames show the ideal and the master equation simulation of the absolute values of the process matrix, respectively. The trace distance between the measurement and the simulation is 0.014.

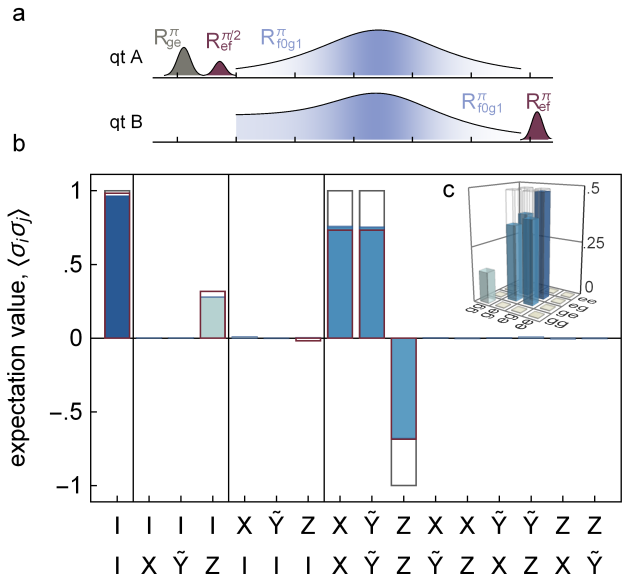

FIG. 4. **Remote entanglement generation. a,** Pulse scheme to generate deterministic remote entanglement between node A and B. **b,** Expectation values of two-qubit Pauli operators and **c,** reconstructed density matrix after execution of the remote entanglement protocol. **b,** The coloured bars indicate the measurement results, the ideal expectation values for the Bell state $|\psi^+\rangle = (|ge\rangle + |eg\rangle)/\sqrt{2}$ are shown in grey wire frames and the results of a master equation simulation in red. We calculate a fidelity of $F = 78.9 \pm 0.1\%$ well explained by the photon loss and decoherence.

tation R^{π}_{ef} on transmon B to generate the entangled Bell state $|\psi^+\rangle = (|e_A, g_B\rangle + |g_A, f_B\rangle)/\sqrt{2}$. As leakage to the $|f\rangle$ level at both nodes leads to errors in the two-qubit density matrix reconstruction, we measure the full two-qutrit state $\rho_{3\otimes3}$ using QST (see Appendix G). For illustration purposes, we display the two-qubit density matrix ρ_m (Fig. 4 b and c), consisting of the two-qubit elements of $\rho_{3\otimes3}$. We find a state fidelity compared to the ideal Bell state $\mathcal{F}^{s}_{|\psi^+\rangle} = \langle\psi^+|\rho_{\mathrm{m}}|\psi^+\rangle = 78.9 \pm 0.1\%$, and a concurrence $\mathcal{C}(\rho_{\mathrm{m}}) = 0.747 \pm 0.004$ (see Appendix H for a detailed discussion). The state ρ_{sim} calculated from the MES of the entanglement protocol (red wireframe in Fig. 4) results in a small trace distance $\sqrt{\mathrm{Tr}\left[(\rho_{\mathrm{m}} - \rho_{\mathrm{sim}})^2\right]} = 0.024$. The excellent agreement between the experimental and numerical results suggest that photon loss and finite coherence times of the transmons are the dominant sources of error, accounting for 12.5% and 11% infidelity, respectively.

Using transmons with relaxation and coherence times of $\mathrm{T}_{1ge} = \mathrm{T}_{2ge} = 30\,\mu$s, $\mathrm{T}_{1ef} = \mathrm{T}_{2ef} = 20\,\mu$s, and with an achievable 12% loss between the nodes, this protocol would allow deterministic generation of remote entangled states with fidelity 93%, at the threshold for surface code quantum error correction across different nodes[11,12,30,31]. In addition, the protocol can be extended to generate deterministic heralded remote entanglement, utilizing the three-level structure of the transmons and encoding quantum information in different time bins to detect photon loss events, which would extend its functionality for quantum network applications[4]. These perspectives indicate that the approach demonstrated here can serve as the basis for fault-tolerant quantum computation in the circuit QED architecture using distributed cryogenic nodes.

During writing of this manuscript we became aware of related work[32,33].

ACKNOWLEDGMENTS

This work is supported by the European Research Council (ERC) through the 'Superconducting Quantum Networks' (SuperQuNet) project, by the National Centre of Competence in Research 'Quantum Science and Technology' (NCCR QSIT), a research instrument of the Swiss National Science Foundation (SNSF), by ETH Zurich and NSERC, the Canada First Research Excellence Fund and the Vanier Canada Graduate Scholarships.

AUTHOR CONTRIBUTIONS

The experiment was designed and developed by P.K., T.W., P.M. and M.P. The samples were fabricated by J.-C.B., T.W. and S.G. The experiments were performed by P.K., P.M. and T.W. The data was analysed and interpreted by P.K., P.M., B.R., A.B. and A.W. The FPGA firmware and experiment automation was implemented by J.H., Y.S., A.A., S.S, P.M. and P.K. The master equation simulation were performed by B.R., M.P., P.M. and P.K. The manuscript was written by P.K., P.M., T.W., B.R. and A.W. All authors commented on the manuscript. The project was led by A.W.

Appendix A: Literature Overview

We provide an overview of remote entanglement experiments performed in a range of physical systems using several different schemes listed in the caption of Fig. 5.

Appendix B: Sample Parameters

The devices are identical to the one found in Ref. 23 with only minor parameter modifications. The $\lambda/4$ coplanar waveguide resonators and additional feed-lines are created from etched niobium on a sapphire substrate using standard photolithography techniques. We then define the transmon pads and junctions with electron-beam lithography and shadow evaporated aluminium with lift-off. We extract the parameters of the readout circuit

	Node A	Node B
ν_{R}	4.787 GHz	4.780 GHz
ν_{Rpf}	4.778 GHz	4.780 GHz
$\kappa_R/2\pi$	12.6 MHz	27.1 MHz
$\chi_R/2\pi$	5.8 MHz	11.6 MHz
ν_{T}	8.4005 GHz	8.4003 GHz
ν_{Tpf}	8.426 GHz	8.415 GHz
$\kappa_T/2\pi$	10.4 MHz	13.5 MHz
$\chi_T/2\pi$	6.3 MHz	4.7 MHz
ν_{ge}	6.343 GHz	6.096 GHz
α	-265 MHz	-308 MHz
$T_{1\mathrm{ge}}$	4.9 μs	4.6 μs
$T_{1\mathrm{ef}}$	1.6 μs	1.4 μs
$T_{2\mathrm{ge}}$	3.4 μs	2.6 μs
$T_{2\mathrm{ef}}$	2.1 μs	0.9 μs

TABLE I. Summary of device parameters for node A and B. With $\ell = \mathrm{R}, \mathrm{T}$, ν_ℓ is the frequency of the coupling resonator, $\nu_{\ell\mathrm{pf}}$ the frequency of the Purcell Filter, $\kappa_\ell/2\pi$ the effective decay rate of the coupled resonator to the external feed line and $\chi_\ell/2\pi$ the dispersive coupling strength of the transmon readout or transfer circuit, respectively.

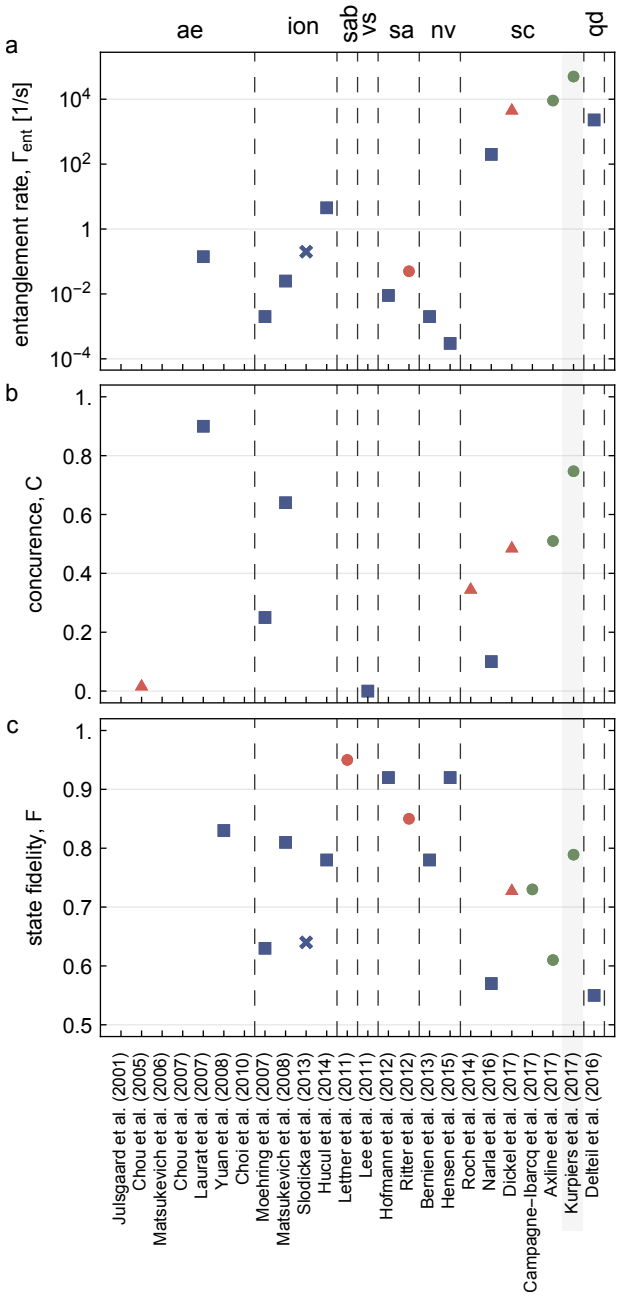

FIG. 5. **Overview of remote entanglement experiments.** **a,** entanglement rates **b,** concurrence, **c,** entangled state fidelity. The experiments are sorted by physical system: atomic ensembles (ae)[13,18,19,34–37], trapped ions (ion)[14,38–40], single atom - Bose Einstein condensate (sab)[41],vibrational state of diamonds (vs)[42], single atoms (sa)[15,20], nitrogen-vacancy (nv) center[16,43], superconducting circuits (sc)[21,32,33,44,45] and quantum dots (qd)[17]. The colours indicate probabilist unheralded (red), probabilist heralded (blue), deterministic unheralded (green) implementations. The plot markers indicate different schemes to realize the remote interaction: measurement induced (triangle), interference of two single photons on beam splitter (squares), single photon emission and detection (cross), direct transfer (pentagon), direct transfer with shaped photons (circles).

(grey Fig. 1 b) and transfer circuit (yellow Fig. 1 b), as well as the coupling strength of the transmon to these circuits, with fits to the transmission spectra of the respective Purcell filter when the transmon is prepared in its ground and excited state using the technique and model as discussed in Ref. 23. Furthermore, the anharmonicity, the energy relaxation times and the coherence times of the qutrits are found using Ramsey-type measurements. Finally, we used miniature superconducting coils to thread flux through the SQUID of each transmon to tune their frequencies such that their transfer circuit resonator had identical frequencies. All relevant device parameters are summarized in Table I.

Appendix C: Microwave Drive Schemes

We use resonant Gaussian-shaped DRAG[46,47] microwave pulses of length 19.8 ns and 16.8 ns for R^{π}_{ge} and R^{π}_{ef} in order to swap populations between the $|g\rangle$ and $|e\rangle$ state and the $|e\rangle$ and $|f\rangle$ state respectively. We extract an averaged Clifford-gate fidelity for the $|g\rangle$ and $|e\rangle$ pulses of more than 99.2% for both transmon qubits, from randomized benchmarking experiments[48].

We induce the effective coupling $\tilde{g}$ between states $|f,0\rangle$ and $|g,1\rangle$ by applying a microwave tone on the transmon with drive amplitude ϵ, at the resonance frequency of the transition $\nu^{A}_{f0g1} = 4.0219\,\text{GHz}$ and $\nu^{B}_{f0g1} = 3.4845\,\text{GHz}$. Following the procedure described in Refs. 27 and 9, we calibrate the ac Stark shift of the transmon levels induced by the $|f,0\rangle \leftrightarrow |g,1\rangle$ drive, and extract the linear relation between the drive amplitude ϵ and the effective coupling $\tilde{g}$ (see Fig. 6). We adjust the phase of ϵ based on the measured ac Stark shift in order to remain resonant with the driven transition. We calibrate our transmon drive lines to reach a maximum effective coupling $\tilde{g}^{A}/2\pi = 6.0\,\text{MHz}$ and $\tilde{g}^{B}/2\pi = 6.7\,\text{MHz}$ (Fig. 6 b).

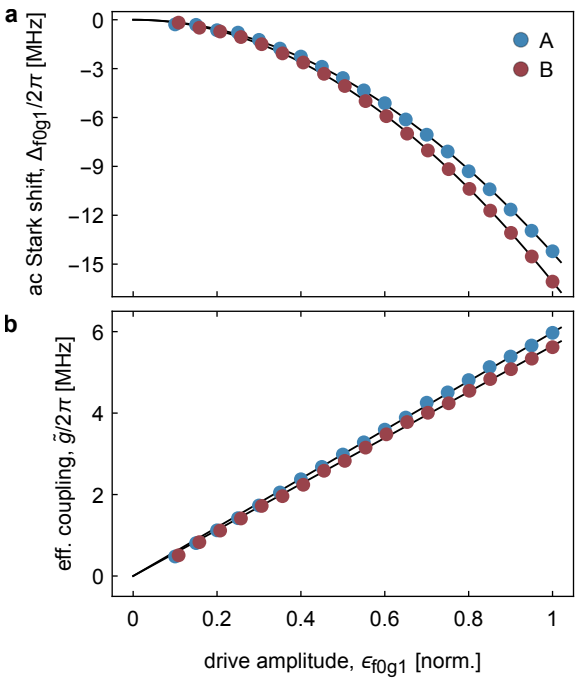

FIG. 6. **AC stark shift and Rabi rate of the $|f,0\rangle$ to $|g,1\rangle$ transition.** Measurement (dots) of the ac Stark shift $\Delta_{f0g1}/2\pi$ (**a**) and effective coupling $\tilde{g}/2\pi$ (**b**) of the $|f0\rangle$ to $|g1\rangle$ transition versus drive amplitude ϵ_{f0g1} for sample A and B. The solid lines in **a** (**b**) are quadratic (linear) fits to the data.

We generate photons with temporal shape $\phi(t) = \frac{1}{2}\sqrt{\kappa_{\text{eff}}}\,\text{sech}(\kappa_{\text{eff}}t/2)$ by resonantly driving the $|f,0\rangle \leftrightarrow |g,1\rangle$ transition with

$$\tilde{g}(t) = \frac{\kappa_{\text{eff}}}{4\cosh\frac{\kappa_{\text{eff}}t}{2}} \frac{1 - e^{\kappa_{\text{eff}}t} + (1 + e^{\kappa_{\text{eff}}t})\kappa_T/\kappa_{\text{eff}}}{\sqrt{(1 + e^{\kappa_{\text{eff}}t})\kappa_T/\kappa_{\text{eff}} - e^{\kappa_{\text{eff}}t}}}. \quad \text{(C1)}$$

where κ_T is the coupling of the transfer resonator to the coaxial line, and κ_{eff} is determined by the strength and duration of the transfer pulse, and is constrained by $\kappa_{\text{eff}} \leq \kappa_T$. The dynamics are well described by a two-level model with loss, captured by the non-Hermitian Hamiltonian

$$H = \begin{bmatrix} 0 & \tilde{g} \\ \tilde{g}^* & i\kappa/2 \end{bmatrix} \quad \text{(C2)}$$

which acts on states $|f,0\rangle$ and $|g,1\rangle$, analysed in a rotating frame. The non-Hermitian term $i\kappa/2$ accounts for photon emission, which brings the system to the dark state $|g,0\rangle$. One can show that using the effective coupling of Equation (C1) in the Hamiltonian (C2) leads to the emission of a single photon with the desired temporal shape.

Appendix D: Three-Level Single-Shot Readout

The state of transmon A (B) is read out with a gated microwave tone, with frequency $\nu^{A}_{d} = 4.778$ GHz ($\nu^{B}_{d} = 4.765$ GHz), applied to the input port of the Purcell filter. As depicted in Fig. 1 b, the output signal is routed through a set of two circulators and a combiner and then amplified at 10 mK with 22 (19.3) dB gain using a Josephson parametric amplifier (JPA). The JPA pump tone is 2 MHz detuned from the measurement signal and has a bandwidth of 18.3 (32) MHz. Using these JPAs we find a phase-preserving detection efficiency of $\eta_{2Q} = 0.61$ (0.60) for the full detection line.The signal is then further amplified by a high electron mobility transistor (HEMT) at 4 K and two low-noise amplifiers at room temperature. Next, the signal is analogue down-converted to 250 MHz, lowpass-filtered, digitized by an analog-to-digital converter and processed by a field-programmable gate array (FPGA). Within the FPGA, the data is digitally down-converted to DC and the corresponding I and Q quadratures values are recorded during a window of 256 ns in 8 ns time steps. The FPGA trigger is timed so that the measurement window starts with

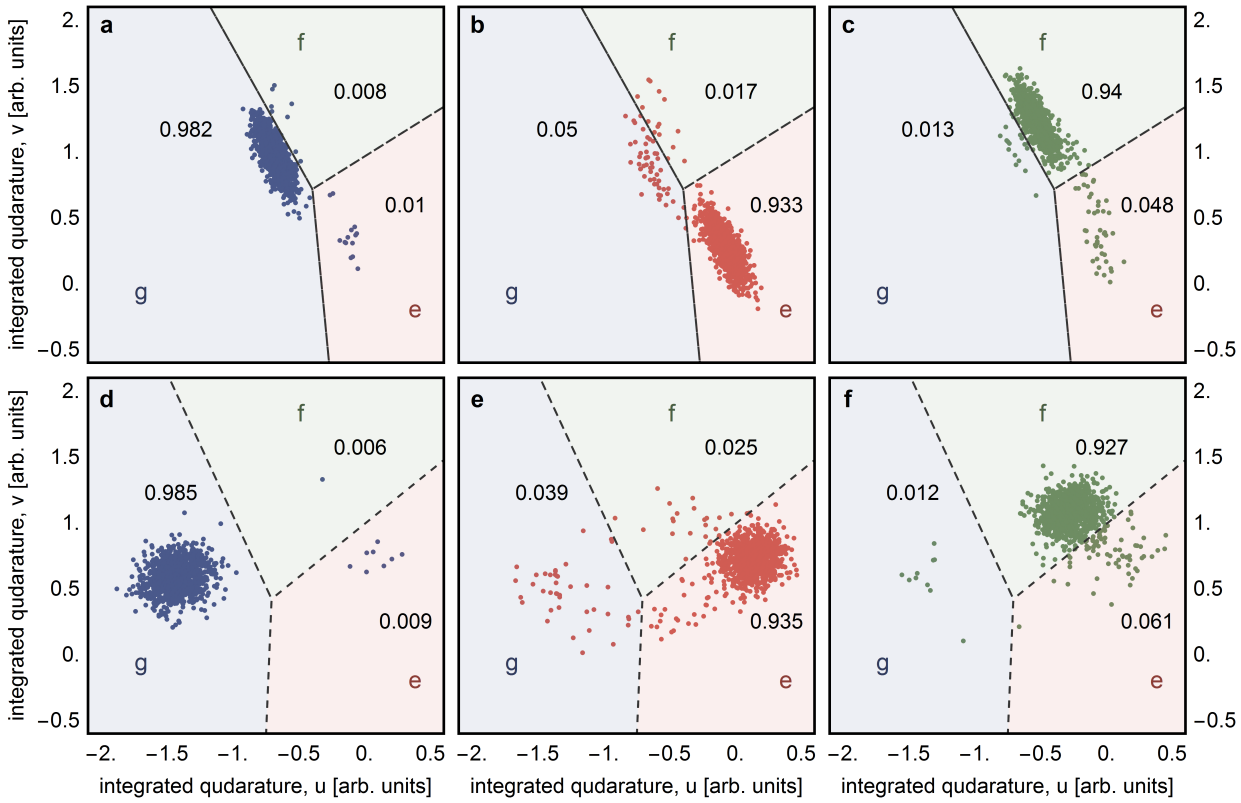

FIG. 7. **Qutrit single-shot readout characterization.** Scatter plot of the measured integrated quadrature values u, v for qutrit A (**a-c**) and B (**d-f**) when prepared in state $|g\rangle$ (blue), $|e\rangle$ (red), $|f\rangle$ (green), respectively. We plot only the first 1000 of the total 25000 repetitions for each state preparation experiment. The dashed lines are the qutrit state discrimination thresholds used to obtain the assignment probabilities (indicated numbers and also listed in Table II).

the rising edge of the measurement tone. We refer to a recording of the I and Q quadrature of a measurement tone as a readout trace, $S(t)$.

We prepare the transmon in state $|g\rangle$, $|e\rangle$ and $|f\rangle$, 25000 times each and record the single-shot traces. Each trace is then integrated in post-processing, with two weight functions $w_1(t)$ and $w_2(t)$, to obtain the integrated quadratures $u = \int S(t)w_1(t)dt$ and $v = \int S(t)w_2(t)dt$. The collected and integrated traces form three Gaussian shaped clusters in the u-v plane (Fig. 7), that correspond to the Gaussian probability distributions of the trace when the qutrit is prepared in one of the three eigenstates. We model the probability distribution (u, v) as a mixture of three Gaussian distributions, with density

$$f(\vec{x}) = \sum_s \frac{A_s}{2\pi\sqrt{|\Sigma|}} e^{-\frac{1}{2}(\vec{x}-\mu_s)^\top \cdot \Sigma^{-1} \cdot (\vec{x}-\mu_s)} \qquad \text{(D1)}$$

and estimate the parameters A_s, μ_s and Σ with likelihood maximization. Based on these parameters, we divide the u-v plane into three regions used to assign the result of the readout of the qutrit state (Fig. 7). If an integrated trace is in the region labelled s', we assign it state s'. By counting the number of traces prepared in state $|s\rangle$ and assigned the value s', we estimate the assignment probabilities $R_{ss'} = P(s'||s\rangle)$ (see Fig. 7). We optimize the measurement power and signal integration time in order to minimize the measurement error probability $\frac{1}{6}||I - R||_1$. The optimum occurs with the measurement time $t_m = 112$ ns and input power $P_{in} = -24$ dBm for qutrit A and $t_m = 216$ ns, $P_{in} = -25$ dBm for qutrit B. The total assignment error probability is approximately 5% for both qutrits as seen in the assignment probability matrix compiled in Table II. The probability $M_{s'}$ to assign value s' to a single shot measurement of a qutrit

	Qutrit A			Qutrit B			
	$\|g\rangle$	$\|e\rangle$	$\|f\rangle$	$\|g\rangle$	$\|e\rangle$	$\|f\rangle$	
g	98.2	5.0	1.3	98.5	3.9	1.2	g
e	1.0	93.3	4.8	0.9	93.5	6.1	e
f	0.8	1.7	94.0	0.6	2.5	92.7	f

TABLE II. Probabilities of identifying prepared input states (columns) as the indicated output states (rows) for qutrit A and B. The diagonal elements show correct identification, the off-diagonal elements misidentifications.

	$\|gg\rangle$	$\|ge\rangle$	$\|gf\rangle$	$\|eg\rangle$	$\|ee\rangle$	$\|ef\rangle$	$\|fg\rangle$	$\|fe\rangle$	$\|ff\rangle$
gg	96.8	3.9	1.1	4.9	0.2	0.1	1.2	0.0	0.0
ge	0.9	91.9	6.0	0.0	4.7	0.3	0.0	1.2	0.1
gf	0.6	2.5	91.1	0.0	0.1	4.6	0.0	0.0	1.2
eg	1.0	0.0	0.0	91.9	3.7	1.1	4.7	0.2	0.1
ee	0.0	0.9	0.1	0.8	87.3	5.7	0.0	4.5	0.3
ef	0.0	0.0	0.9	0.6	2.4	86.5	0.0	0.1	4.4
fg	0.8	0.0	0.0	1.6	0.1	0.0	92.5	3.7	1.1
fe	0.0	0.7	0.0	0.0	1.6	0.1	0.8	87.9	5.8
ff	0.0	0.0	0.7	0.0	0.0	1.6	0.6	2.4	87.1

TABLE III. Probabilities of identifying prepared input states (columns) as the indicated output states (rows) for all possible tuples of two-qutrit basis state $|g\rangle$, $|e\rangle$ and $|f\rangle$. The diagonal elements show correct identification, the off-diagonal elements misidentifications.

in state ρ is given by

$$M_{s'} = P(s'|\rho) = \sum_s P(s'||s\rangle) \cdot \rho_{ss} \tag{D2}$$

which can be expressed as $M = R \cdot \vec{\rho}_{\text{diag}}$ where $\vec{\rho}_{\text{diag}}$ is the vector consisting of the diagonal elements of ρ. The assignment probabilities M are typically estimated from assignment counts and a first approach to estimate $\vec{\rho}_{\text{diag}}$ is to equate $\vec{\rho}_{\text{diag}} = M$. This approach is sensitive to measurement errors, but insensitive to state preparation errors. Setting $\vec{\rho}_{\text{diag}} = R^{-1} \cdot M$ effectively accounts for the effect of single-shot readout error. However, this approach relies on the ability to estimate R precisely and thus is sensitive to state-preparation error. With transmon reset infidelities of approximately 0.2%[27], and single qubit gate errors of 0.6% (measured with randomized benchmarking), state preparation errors are expected to be lower than readout errors. For this reason, we chose to use the latter approach.

We note that the assignment probability matrix $R_{s_A s_B, s'_A s'_B} = P(s'_A s'_B| |s_A s_B\rangle) = P(s'_A| |s_A\rangle) \cdot P(s'_B| |s_B\rangle)$ can be obtained as the outer product of the single-qutrit assignment probability matrices (compiled in Table D) and that we can extend this formalism to correct for single-shot readout errors and extract the state populations of a two-qutrit system.

Appendix E: Loss Estimation

The loss on the printed circuit boards including connectors is measured to be $2.5 \pm 1\%$, of the coaxial cables of length 0.4 m (each $4.0 \pm 0.1\%$)[49] and information provided by the manufacturer for the microwave circulator ($13 \pm 2\%$).

Appendix F: Master Equation Simulation

We model the transmons as anharmonic oscillators with annihilation (creation) operators $\hat{b}_i$ ($\hat{b}_i^\dagger$)[10], where the subscript $i = A, B$ denotes the emitter and receiver samples, respectively. The transfer resonator annihilation (creation) operators are denoted $\hat{a}_i$ ($\hat{a}_i^\dagger$). Setting $\hbar = 1$, the driven Jaynes-Cummings Hamiltonian for sample i is given by

$$\begin{aligned}\hat{H}^i = &\omega_T^i \hat{a}_i^\dagger \hat{a}_i + \omega_{eg}^i \hat{b}_i^\dagger \hat{b}_i + \Omega^i(t)(\hat{b}_i + \hat{b}_i^\dagger) \\ &+ g_T^i(\hat{a}_i^\dagger \hat{b}_i + \hat{a}_i \hat{b}_i^\dagger) - \frac{E_C^i}{2} \hat{b}_i^\dagger \hat{b}_i^\dagger \hat{b}_i \hat{b}_i,\end{aligned} \tag{F1}$$

where g_T^i denotes the coupling between the transmon and the transfer resonator, E_C^i the charging energy of the transmon and $\Omega^i(t) = \Omega^i \cos[\omega_d^i t + \varphi^i(t)]$ is the amplitude of the microwave drive inducing the desired coupling $\tilde{g}(t)$. Since the readout resonators do not play a role in the photon transfer dynamics, they are omitted from the Hamiltonian and the static Lamb shifts they induce are implicitly included in the parameters.

In order to make the effective coupling $\tilde{g}(t)$ between the $|f,0\rangle$ and $|g,1\rangle$ states apparent and to simplify the simulations, we perform a series of unitary transformations on Equation (F1). First moving to a frame rotating at the drive frequency ω_d^i, we then perform a displacement transformation $\hat{b}_i \to \hat{b}_i - \beta^i$, $\hat{a}_i \to \hat{a}_i - \gamma^i$ and choose β^i, γ^i such that the amplitude of the linear drive terms is set to zero. Next, we perform a Bogoliubov transformation $\hat{b}_i \to \cos(\Lambda^i)\hat{b}_i - \sin(\Lambda^i)\hat{a}_i$, $\hat{a}_i \to \cos(\Lambda^i)\hat{a}_i + \sin(\Lambda^i)\hat{b}_i$, where $\tan(2\Lambda^i) = -2g_T^i/(\omega_T^i - \omega_{eg}^i + 2E_C^i|\beta^i|)$ and, neglecting small off-resonant terms, obtain the resulting effective Hamiltonian

$$\begin{aligned}\hat{H}_{\tilde{g}}^i = &\Delta_T^i \hat{a}_i^\dagger \hat{a}_i + \Delta_{eg}^i \hat{b}_i^\dagger \hat{b}_i + \frac{\alpha^i}{2} \hat{b}_i^\dagger \hat{b}_i^\dagger \hat{b}_i \hat{b}_i + \frac{K^i}{2} \hat{a}_i^\dagger \hat{a}_i^\dagger \hat{a}_i \hat{a}_i \\ &+ 2\chi_T^i \hat{a}_i^\dagger \hat{a}_i \hat{b}_i^\dagger \hat{b}_i + \frac{1}{\sqrt{2}}(\tilde{g} \hat{b}_i^\dagger \hat{b}_i^\dagger \hat{a}_i + \tilde{g}^* \hat{a}_i^\dagger \hat{b}_i \hat{b}_i),\end{aligned} \tag{F2}$$

where $\alpha^i = -E_C^i \cos^4 \Lambda$ is the transmon anharmonicity, $K^i = -E_C^i \sin^4 \Lambda^i$ is the qubit-induced resonator anharmonicity, $\chi_T^i = -E_C^i \cos^2 \Lambda^i \sin^2 \Lambda^i$ is the dispersive shift, $\Delta_T^i = \omega_T^i \cos^2 \Lambda^i + (\omega_{ge}^i - 2E_C^i|\beta^i|^2) \sin^2 \Lambda^i - g_T^i \sin 2\Lambda^i - \omega_d^i$ is the resonator-drive detuning and $\Delta_{eg}^i = \omega_{ge}^i - 2E_C^i|\beta^i|^2) \cos^2 \Lambda^i + \omega_T^i \sin^2 \Lambda^i + g_T^i \sin 2\Lambda^i - \omega_d^i$ is the qubit-drive detuning. In Equation (F2), the desired effective coupling $\tilde{g}^i = -E_C^i \beta^i \sqrt{2} \cos^2 \Lambda^i \sin \Lambda^i$ between the $|f,0\rangle$ and $|g,1\rangle$ states is now made explicit.

Finally, moving to a frame rotating at Δ_T^i for the resonator and $\Delta_{eg}^i + \alpha^i/2$ for the transmon qubits, the combined effective Hamiltonian of the two samples can be

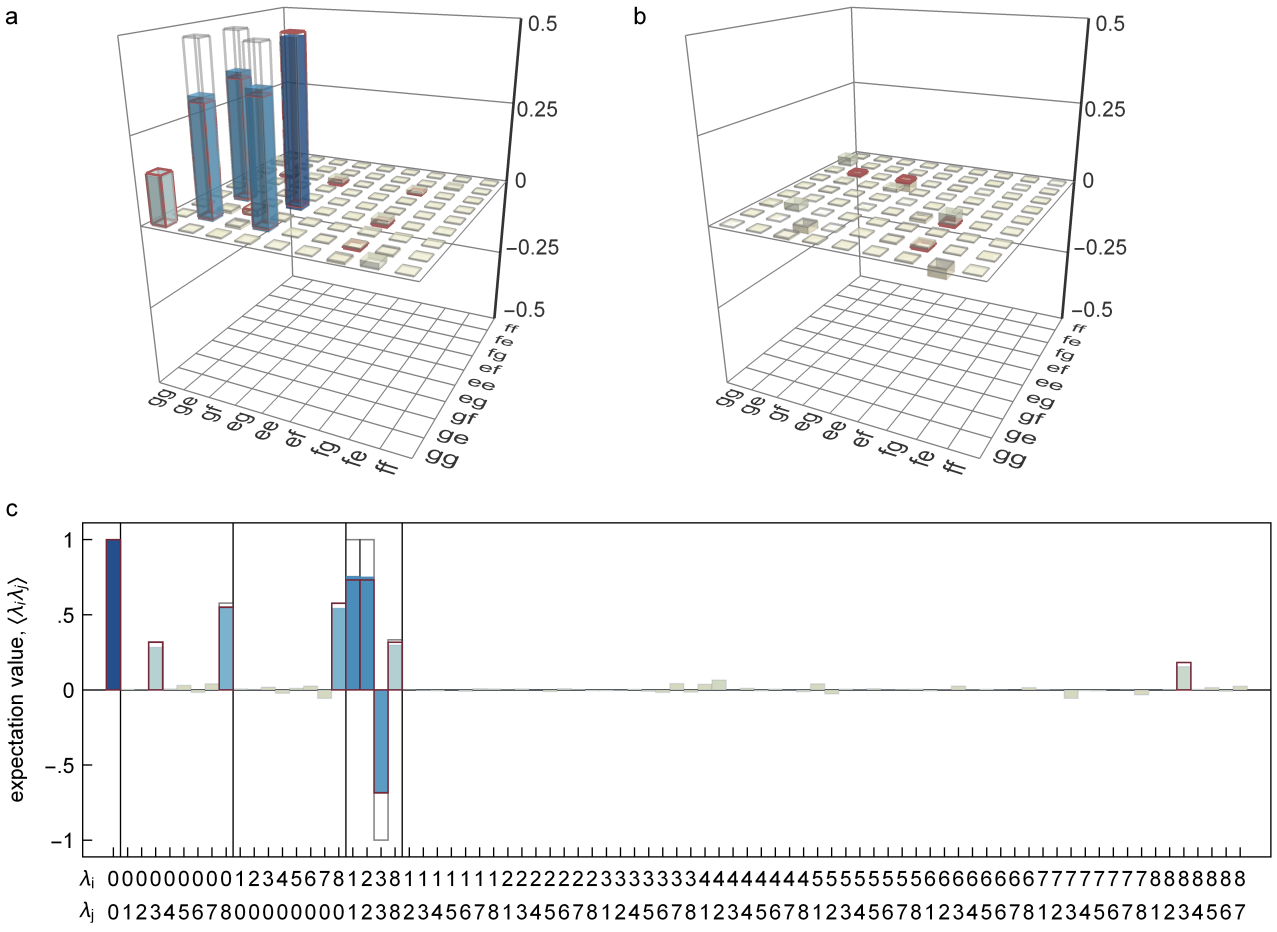

FIG. 8. **Characterization of a remotely entangled state.** We prepare a qubit-qubit entangled state between the distant quantum systems using the protocol described in the main text and perform two-qutrit state tomography: (**a**) real and (**b**) imaginary part of the density matrix and (**c**) expectation values of the Gell-Mann operators λ_k. The ideal Bell state $|\psi^+\rangle$ is depicted with grey wire frames. The numerical master equation simulation is depicted in red wire frames. λ_0 denotes the identity operation, $\lambda_{1,2,3}$ the Pauli matrices $\sigma^{ge}_{\mathrm{x,y,z}}$ in the qubit (ge) subspace, $\lambda_{4,5}$ correspond to $\sigma^{gf}_{\mathrm{x,y,z}}$, $\lambda_{6,7}$ to $\sigma^{ef}_{\mathrm{x,y,z}}$ and λ_8 is the diagonal matrix $(\sigma^{ge}_{\mathrm{z}} + 2\sigma^{ef}_{\mathrm{z}})/\sqrt{3}$. The trace distance between the measurement and the simulation is 0.027.

written as

$$\begin{aligned}\hat{H}_{eff} = \sum_{i=A,B} \Big\{ & -\frac{\alpha^i}{2}\hat{b}_i^\dagger\hat{b}_i + \frac{\alpha^i}{2}\hat{b}_i^\dagger\hat{b}_i^\dagger\hat{b}_i\hat{b}_i \\ & + \frac{K^i}{2}\hat{a}_i^\dagger\hat{a}_i^\dagger\hat{a}_i\hat{a}_i + 2\chi_T^i\hat{a}_i^\dagger\hat{a}_i\hat{b}_i^\dagger\hat{b}_i \\ & + \frac{1}{\sqrt{2}}\left[\tilde{g}^i(t)\hat{b}_i^\dagger\hat{b}_i^\dagger\hat{a}_i + \tilde{g}^i(t)^*\hat{a}_i^\dagger\hat{b}_i\hat{b}_i\right]\Big\} \\ & - i\frac{\sqrt{\kappa_T^A\kappa_T^B\eta_c}}{2}(\hat{a}_A\hat{a}_B^\dagger - \hat{a}_A^\dagger\hat{a}_B),\end{aligned} \tag{F3}$$

where η_c is the photon loss probability of the circulator between the two samples. Using this effective Hamiltonian, numerical results are obtained by integrating the master equation

$$\begin{aligned}\dot{\rho} = & -i[\hat{H}_{eff},\rho] \\ & + \kappa_T^A(1-\eta_c)\mathcal{D}[\hat{a}_A]\rho + \mathcal{D}[\sqrt{\kappa_T^A\eta_c}\hat{a}_A + \sqrt{\kappa_T^B}\hat{a}_B]\rho \\ & + \sum_{i=A,B}\Big\{\kappa_{int}^i\mathcal{D}[\hat{a}_i]\rho + \gamma_{1ge}^i\mathcal{D}\left[|g\rangle\langle e|_i\right]\rho \\ & \quad + \gamma_{1ef}^i\mathcal{D}\left[|e\rangle\langle f|_i\right]\rho\Big\} \\ & + \sum_{i=A,B}\Big\{\gamma_{\phi ge}^i\mathcal{D}\left[|e\rangle\langle e|_i - |g\rangle\langle g|_i\right]\rho \\ & \quad + \gamma_{\phi ef}^i\mathcal{D}\left[|f\rangle\langle f|_i - |e\rangle\langle e|_i\right]\rho\Big\},\end{aligned} \tag{F4}$$

where $\mathcal{D}[\hat{O}]\bullet = \hat{O}\bullet\hat{O}^\dagger - \{\hat{O}^\dagger\hat{O},\bullet\}/2$ denotes the dissipation super-operator, κ_{int}^i the internal decay rates of the resonators, $\gamma_{1nm}^i = 1/T_{1nm}^i$ the decay rates of the transmon qubits between the $|n\rangle_i, |m\rangle_i$ states and $\gamma_{\phi nm}^i = 1/2T_{1nm}^i - 1/T_{2nm}^i$ the dephasing rates between the $|n\rangle_i, |m\rangle_i$ states of the transmon qubits. The last

term in $\hat{H}_{eff}$ combined with the resonator dissipators in the second line of the master equation (F4), assure that the output of the emitter A is cascaded to the input of the receiver B[50,51] through a circulator with photon loss η_c.

Appendix G: Quantum State and Process Tomography

Quantum state tomography of a single qutrit is performed by measuring the qutrit state population with the single-shot readout method described in Appendix D, after applying the following tomography gates: ${}^{x}\mathrm{R}^{0}_{ge}$, ${}^{x}\mathrm{R}^{\pi/2}_{ge}$, ${}^{y}\mathrm{R}^{\pi/2}_{ge}$, ${}^{x}\mathrm{R}^{\pi}_{ge}$, ${}^{x}\mathrm{R}^{\pi/2}_{ef}$, ${}^{y}\mathrm{R}^{\pi/2}_{ef}$, $({}^{x}\mathrm{R}^{\pi}_{ge}\,{}^{x}\mathrm{R}^{\pi/2}_{ef})$, $({}^{x}\mathrm{R}^{\pi}_{ge}\,{}^{y}\mathrm{R}^{\pi/2}_{ef})$ and $({}^{x}\mathrm{R}^{\pi}_{ge}\,{}^{x}\mathrm{R}^{\pi}_{ef})$. The elements of the density matrix are then reconstructed with a maximum-likelihood method, assuming ideal tomography gates.

To extend this QST procedure to two-qutrit density matrices, we perform two local tomography gates (from the 81 pairs of gates that can be formed from the single-qutrit QST gates) on transmon A and B, before extracting the state populations using the two-qutrit single shot measurement method described in Appendix D.

To characterize the qubit state transfer from node A to node B we performed full quantum process tomography[52]. We prepare each of the six mutually unbiased qubit basis states $|g\rangle$, $|e\rangle$, $(|g\rangle+|e\rangle)/\sqrt{2}$, $(|g\rangle+i\,|e\rangle)/\sqrt{2}$, $(|g\rangle-|e\rangle)/\sqrt{2}$, $(|g\rangle-i\,|e\rangle)/\sqrt{2}$ [29], transfer the state to node B, then independently measure the three-level density matrix at node A and node B with QST. We obtain the process matrix through linear inversion, from these density matrices.

Appendix H: Two-Qutrit Entanglement

Due to a residual population of 3.5% of the $|f\rangle$ level of the transmons after the entanglement protocol, the entangled state cannot be rigorously described by a two-qubit density matrix. To be concise we represent the reconstructed two-qutrit entangled state $\rho_{3\otimes3}$ (Fig. 8) by a two-qubit density matrix ρ_{m}, that consists of the two-qubit elements of $\rho_{3\otimes3}$. This choice of reduction from a two-qutrit to a two-qubit density matrix conserves the state fidelity $\mathcal{F}^{s}_{|\psi^+\rangle}=\langle\psi^+|\rho_{\mathrm{m}}|\psi^+\rangle=\langle\psi^+|\rho_{3\otimes3}|\psi^+\rangle$, however, ρ_{m} has a non-unit trace. In addition, this reduction method gives a conservative estimate of the concurrence $\mathcal{C}(\rho_{\mathrm{m}})$, compared to a projection of $\rho_{3\otimes3}$ on the set of physical two-qubit density matrices. To thoroughly verify the three-level bipartite entanglement, we use the computable cross norm or realignment (CCNR) criterion[53], which is well defined for multi-level mixed entangled states. The CCNR criterion states that a state ρ must be entangled if $\mathrm{ccnr}=\sum_{\mathrm{k}}\lambda_{\mathrm{k}}>1$ with $\rho=\sum_{\mathrm{k}}\lambda_{\mathrm{k}}\mathrm{G}^{\mathrm{A}}_{\mathrm{k}}\otimes\mathrm{G}^{\mathrm{B}}_{\mathrm{k}}$ and $\mathrm{G}^{\mathrm{A(B)}}_{\mathrm{k}}$ being an orthonormal basis of the observable spaces of $\mathcal{H}^{\mathrm{A(B)}}$. We obtain $\mathrm{ccnr}=1.612\pm0.003$ with the measured entangled state $\rho_{3\otimes3}$, witnessing unambiguously the existence of entanglement of the prepared state.

---

* These authors contributed equally to this work.

[1] J. I. Cirac, A. K. Ekert, S. F. Huelga, and C. Macchiavello, Phys. Rev. A **59**, 4249 (1999).

[2] L. Jiang, J. M. Taylor, A. S. Sørensen, and M. D. Lukin, Phys. Rev. A **76**, 062323 (2007).

[3] A. Wallraff, D. I. Schuster, A. Blais, L. Frunzio, R.-S. Huang, J. Majer, S. Kumar, S. M. Girvin, and R. J. Schoelkopf, Nature **431**, 162 (2004).

[4] A. Reiserer and G. Rempe, Rev. Mod. Phys. **87**, 1379 (2015).

[5] C. Eichler, C. Lang, J. M. Fink, J. Govenius, S. Filipp, and A. Wallraff, Phys. Rev. Lett. **109**, 240501 (2012).

[6] B. R. Johnson, M. D. Reed, A. A. Houck, D. I. Schuster, L. S. Bishop, E. Ginossar, J. M. Gambetta, L. DiCarlo, L. Frunzio, S. M. Girvin, and R. J. Schoelkopf, Nat. Phys. **6**, 663 (2010).

[7] J. Wenner, Y. Yin, Y. Chen, R. Barends, B. Chiaro, E. Jeffrey, J. Kelly, A. Megrant, J. Mutus, C. Neill, P. OMalley, P. Roushan, D. Sank, A. Vainsencher, T. White, A. N. Korotkov, A. Cleland, and J. M. Martinis, Phys. Rev. Lett. **112**, 210501 (2014).

[8] L. DiCarlo, J. M. Chow, J. M. Gambetta, L. S. Bishop, B. R. Johnson, D. I. Schuster, J. Majer, A. Blais, L. Frunzio, S. M. Girvin, and R. J. Schoelkopf, Nature **460**, 240 (2009).

[9] M. Pechal, L. Huthmacher, C. Eichler, S. Zeytinoğlu, A. Abdumalikov Jr., S. Berger, A. Wallraff, and S. Filipp, Phys. Rev. X **4**, 041010 (2014).

[10] J. Koch, T. M. Yu, J. Gambetta, A. A. Houck, D. I. Schuster, J. Majer, A. Blais, M. H. Devoret, S. M. Girvin, and R. J. Schoelkopf, Phys. Rev. A **76**, 042319 (2007).

[11] A. G. Fowler, D. S. Wang, C. D. Hill, T. D. Ladd, R. Van Meter, and L. C. L. Hollenberg, Phys. Rev. Lett. **104**, 180503 (2010).

[12] C. Horsman, A. G. Fowler, S. Devitt, and R. V. Meter, New Journal of Physics **14**, 123011 (2012).

[13] C.-W. Chou, J. Laurat, H. Deng, K. S. Choi, H. de Riedmatten, D. Felinto, and H. J. Kimble, Science **316**, 1316 (2007), http://science.sciencemag.org/content/316/5829/1316.full.pdf.

[14] D. L. Moehring, P. Maunz, S. Olmschenk, K. C. Younge, D. N. Matsukevich, L. M. Duan, and C. Monroe, Nature **449**, 68 (2007).

[15] J. Hofmann, M. Krug, N. Ortegel, L. Gérard, M. Weber, W. Rosenfeld, and H. Weinfurter, Science **337**, 72 (2012).

[16] H. Bernien, B. Hensen, W. Pfaff, G. Koolstra, M. S. Blok, L. Robledo, T. H. Taminiau, M. Markham, D. J. Twitchen, L. Childress, and R. Hanson, Nature **497**, 86 (2013).

[17] A. Delteil, Z. Sun, W. Gao, E. Togan, S. Faelt, and A. Imamogglu, Nature Physics **12**, 218 (2016).

[18] B. Julsgaard, A. Kozhekin, and E. S. Polzik, Nature **413**, 400 (2001).
[19] D. N. Matsukevich, T. Chanelière, S. D. Jenkins, S.-Y. Lan, T. A. B. Kennedy, and A. Kuzmich, Phys. Rev. Lett. **96**, 030405 (2006).
[20] S. Ritter, C. Nolleke, C. Hahn, A. Reiserer, A. Neuzner, M. Uphoff, M. Mucke, E. Figueroa, J. Bochmann, and G. Rempe, Nature **484**, 195 (2012).
[21] N. Roch, M. E. Schwartz, F. Motzoi, C. Macklin, R. Vijay, A. W. Eddins, A. N. Korotkov, K. B. Whaley, M. Sarovar, and I. Siddiqi, Phys. Rev. Lett. **112**, 170501 (2014).
[22] J. I. Cirac, P. Zoller, H. J. Kimble, and H. Mabuchi, Phys. Rev. Lett. **78**, 3221 (1997).
[23] T. Walter, P. Kurpiers, S. Gasparinetti, P. Magnard, A. Potocnik, Y. Salathé, M. Pechal, M. Mondal, M. Oppliger, C. Eichler, and A. Wallraff, Phys. Rev. Applied **7**, 054020 (2017).
[24] M. D. Reed, B. R. Johnson, A. A. Houck, L. DiCarlo, J. M. Chow, D. I. Schuster, L. Frunzio, and R. J. Schoelkopf, Appl. Phys. Lett. **96**, 203110 (2010).
[25] E. Jeffrey, D. Sank, J. Y. Mutus, T. C. White, J. Kelly, R. Barends, Y. Chen, Z. Chen, B. Chiaro, A. Dunsworth, A. Megrant, P. J. J. O'Malley, C. Neill, P. Roushan, A. Vainsencher, J. Wenner, A. N. Cleland, and J. M. Martinis, Phys. Rev. Lett. **112**, 190504 (2014).
[26] S. Zeytinoglu, M. Pechal, S. Berger, A. A. Abdumalikov Jr., A. Wallraff, and S. Filipp, Phys. Rev. A **91**, 043846 (2015).
[27] P. Magnard, P. Kurpiers, B. Royer, T. Walter, J.-C. Besse, S. Gasparinetti, M. Pechal, A. Blais, and W. A., (in preparation) (2017).
[28] D. Bozyigit, C. Lang, L. Steffen, J. M. Fink, C. Eichler, M. Baur, R. Bianchetti, P. J. Leek, S. Filipp, M. P. da Silva, A. Blais, and A. Wallraff, Nat. Phys. **7**, 154 (2011).
[29] S. J. van Enk, N. Lütkenhaus, and H. J. Kimble, Phys. Rev. A **75**, 052318 (2007).
[30] S. Perseguers, G. J. L. Jr, D. Cavalcanti, M. Lewenstein, and A. Acn, Reports on Progress in Physics **76**, 096001 (2013).
[31] E. T. Campbell, B. M. Terhal, and C. Vuillot, Nature **549**, 172 (2017).
[32] P. Campagne-Ibarcq, E. Zalys-Geller, A. Narla, S. Shankar, P. Reinhold, L. D. Burkhart, C. J. Axline, W. Pfaff, L. Frunzio, R. J. Schoelkopf, and M. H. Devoret, arXiv:1712.05854 (2017).
[33] C. Axline, L. Burkhart, W. Pfaff, M. Zhang, K. Chou, P. Campagne-Ibarcq, P. Reinhold, L. Frunzio, S. M. Girvin, L. Jiang, M. H. Devoret, and R. J. Schoelkopf, arXiv:1712.05832 (2017).
[34] C. W. Chou, H. de Riedmatten, D. Felinto, S. V. Polyakov, S. J. van Enk, and H. J. Kimble, Nature (London) **438**, 828 (2005), arXiv:quant-ph/0510055.
[35] J. Laurat, K. S. Choi, H. Deng, C. W. Chou, and H. J. Kimble, Phys. Rev. Lett. **99**, 180504 (2007).
[36] Z.-S. Yuan, Y.-A. Chen, B. Zhao, S. Chen, J. Schmiedmayer, and J.-W. Pan, Nature **454**, 1098 (2008).
[37] K. S. Choi, A. Goban, S. B. Papp, S. J. van Enk, and H. J. Kimble, Nature **468**, 412 (2010).
[38] D. N. Matsukevich, P. Maunz, D. L. Moehring, S. Olmschenk, and C. Monroe, Phys. Rev. Lett. **100**, 150404 (2008).
[39] L. Slodička, G. Hétet, N. Röck, P. Schindler, M. Hennrich, and R. Blatt, Phys. Rev. Lett. **110**, 083603 (2013).
[40] D. Hucul, I. V. Inlek, G. Vittorini, C. Crocker, S. Debnath, S. M. Clark, and C. Monroe, Nature Physics **11**, 37 (2014).
[41] M. Lettner, M. Mücke, S. Riedl, C. Vo, C. Hahn, S. Baur, J. Bochmann, S. Ritter, S. Dürr, and G. Rempe, Phys. Rev. Lett. **106**, 210503 (2011).
[42] N. Lee, H. Benichi, Y. Takeno, S. Takeda, J. Webb, E. Huntington, and A. Furusawa, Science **332**, 330 (2011).
[43] B. Hensen, H. Bernien, A. E. Dreau, A. Reiserer, N. Kalb, M. S. Blok, J. Ruitenberg, R. F. L. Vermeulen, R. N. Schouten, C. Abellan, W. Amaya, V. Pruneri, M. W. Mitchell, M. Markham, D. J. Twitchen, D. Elkouss, S. Wehner, T. H. Taminiau, and R. Hanson, Nature **526**, 682 (2015).
[44] A. Narla, S. Shankar, M. Hatridge, Z. Leghtas, K. M. Sliwa, E. Zalys-Geller, S. O. Mundhada, W. Pfaff, L. Frunzio, R. J. Schoelkopf, and M. H. Devoret, Phys. Rev. X **6**, 031036 (2016).
[45] C. Dickel, J. J. Wesdorp, N. K. Langford, S. Peiter, R. Sagastizabal, A. Bruno, B. Criger, F. Motzoi, and L. DiCarlo, arXiv:1712.06141 (2017).
[46] F. Motzoi, J. M. Gambetta, P. Rebentrost, and F. K. Wilhelm, Phys. Rev. Lett. **103**, 110501 (2009).
[47] J. M. Gambetta, A. A. Houck, and A. Blais, Phys. Rev. Lett. **106**, 030502 (2011).
[48] J. M. Chow, J. M. Gambetta, L. Tornberg, J. Koch, L. S. Bishop, A. A. Houck, B. R. Johnson, L. Frunzio, S. M. Girvin, and R. J. Schoelkopf, Phys. Rev. Lett. **102**, 090502 (2009).
[49] P. Kurpiers, T. Walter, P. Magnard, Y. Salathe, and A. Wallraff, EPJ Quantum Technology **4**, 8 (2017).
[50] C. W. Gardiner, Physical Review Letters **70**, 2269 (1993).
[51] H. J. Carmichael, Physical Review Letters **70**, 2273 (1993).
[52] I. L. Chuang and M. A. Nielsen, J. Mod. Opt. **44**, 2455 (1997).
[53] O. Gühne and G. Tóth, Physics Reports **474**, 1 (2009).

5.2.3 Avenues de recherche

La majorité des sources erreurs présentes dans cette expérience sont d'origines purement expérimentales, par exemple les temps de cohérences des transmons. Cependant, quelques éléments théoriques pourraient être améliorés afin d'augmenter la fidélité du transfert d'information.

Tout d'abord, une difficulté dans la fabrication des échantillons pour cette expérience est la condition d'avoir deux résonateurs à la même fréquence. Après la publication de cet article, j'ai développé une forme d'impulsion permettant d'émettre un photon à une fréquence légèrement différente de la fréquence naturelle du résonateur, permettant ainsi de tolérer un léger désaccord entre les résonateurs émetteurs et récepteurs, voir annexe C.2.2. Cette impulsion améliorée se base sur le fait qu'il est possible de changer non seulement l'amplitude du couplage $f0g1$, mais aussi sa phase, $\tilde{g}(t) \rightarrow \tilde{g}(t)\, e^{i\phi(t)}$. Pour les expériences futures, il sera dorénavant possible de choisir les échantillons ayant les meilleurs temps de cohérence au lieu de ceux ayant des résonateurs de même fréquence.

Pour émettre des photons, il est important de contrôler précisément la forme du couplage f0g1, $\tilde{g}(t)$. La méthode présentée à la section 5.1 permet de caractériser précisément la relation entre l'amplitude du pilotage, Ω_b, et le couplage, $\tilde{g}$. Cependant, cette méthode suppose un état stationnaire du système, et donc la forme du couplage $\tilde{g}(t)$ est valide tant que le pilotage change de manière adiabatique. Il serait intéressant d'étudier des impulsions permettant de corriger les effets non adiabatiques, en utilisant par exemple des idées du pilotage quantique sans transition (*transitionless quantum driving, TQD*) [185]. Pour prendre avantage de ce genre de technique, il est cependant nécessaire d'aller au-delà de la formule linéaire, équation 5.2, et de développer une meilleure compréhension analytique du couplage $f0g1$.

Finalement, l'utilisation de meilleurs encodages qu'un état de Fock est une autre avenue de recherche intéressante. Par exemple, l'article suivant réalise une version simple de code de détection d'erreurs à partir d'un encodage temporel. Il serait intéressant d'étudier si d'autres encodages plus robustes sont envisegeables avec ce système.

5.3 Intrication à distance, encodage en temps

5.3.1 Contexte

Dans l'article de la section précédente, la source principale d'erreurs est la perte de photons dans le canal de transmission entre les deux nœuds, et le circulateur situé à cet endroit contribue en majeure partie à ces pertes. Bien qu'en principe il soit possible d'éliminer ce circulateur, il reste utile d'un point de vue pratique pour aider à thermaliser la ligne à transmission ainsi que pour caractériser les processus d'émission et absorption de photons. De plus, la ligne à transmission elle-même n'est pas parfaite et induit des pertes de photons. Pour ces raisons, la perte de photons micro-ondes en transmission apparaît comme une source d'erreur difficile à éradiquer complètement. Le développement de protocoles robustes par rapport à ce type d'erreur est donc une étape importante dans le développement de canaux de communication quantique à haute fidélité.

Dans le prochain article [63], on montre qu'un encodage temporel de l'information quantique permet de détecter les évènements où le photon est perdu en cours de transfert. Ainsi, seulement les expériences où un photon est transmis avec succès sont gardés et la perte de photons dégrade le taux de succès de la transmission plutôt que la fidélité de l'état final. Le principe de fonctionnement de ce code minimal de détection d'erreur est illustré à la figure 5.4. Au lien d'encoder l'information quantique dans une base de Fock, $\{|0\rangle, |1\rangle\}$, où une erreur n'est pas détectable, on encode l'information dans le temps d'arrivée du photon transmis, $\{|1_{t_a}\rangle, |1_{t_b}\rangle\}$. Ainsi, la perte d'un photon peut être détectée en effectuant une mesure distinguant la présence ou l'absence de photon au nœud récepteur sans discriminer le temps d'arrivée du photon.

Comme illustré à la figure 5.5, il est possible de réaliser ce type de mesure en exploitant le troisième niveau du transmon. Plus précisément, avec la bonne séquence d'impulsions, il est possible de transférer l'information du photon vers les deux premiers niveaux du transmon, $\alpha |1_{t_b}\rangle + \beta |1_{t_a}\rangle \rightarrow \alpha |g\rangle + \beta |e\rangle$, et de préparer le transmon dans l'état $|f\rangle$ lorsqu'aucun photon n'atteint le nœud récepteur. Ainsi, il est possible de certifier que le transfert d'état a été complété avec succès en effectuant

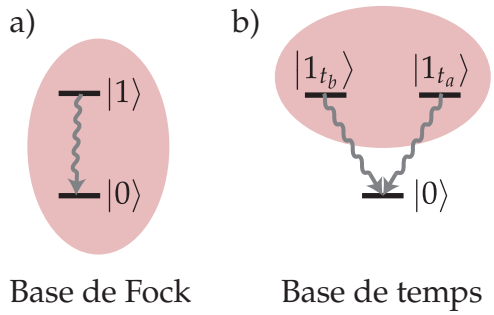

FIGURE 5.4 – a) Dans la base de Fock, la perte d'un photon (ligne ondulée grise) garde le système dans l'espace logique, $\{|0\rangle, |1\rangle\}$. Dans cette situation, il est impossible de détecter ou corriger l'erreur. b) Dans l'encodage en temps, la perte d'un photon mène le système en dehors du sous-espace logique. En mesurant si le système est dans le sous-espace $\{|1_{t_a}\rangle, |1_{t_b}\rangle\}$ ou dans l'état $|0\rangle$, il est possible de détecter la perte d'un photon sans détruire l'état quantique.

une mesure discriminant la population de l'état $|f\rangle$ de la population du sous-espace $\{|g\rangle, |e\rangle\}$. Ce type de mesure est en principe possible en ajustant le décalage dispersif du transmon avec un résonateur de mesure [186].

Il est important de souligner que le montage expérimental utilisé pour cette expérience est identique au montage utilisé pour l'encodage en base de Fock. Dans ce montage, la mesure du transmon récepteur est calibrée pour donner une réponse ternaire, c'est-à-dire une mesure distinguant les états $|g\rangle$, $|e\rangle$ et $|f\rangle$. Par conséquent, dans cette expérience, la mesure du transmon permettant de détecter la perte d'un photon détruit du même coup l'état quantique du qubit. La prochaine étape d'un point de vue expérimental est de fabriquer un nœud récepteur avec un second transmon servant à certifier que le transfert a eu lieu avec succès. Par exemple, la population de l'état f du premier transmon pourrait être convertie en population de l'état e du second à partir d'une impulsion « fgge », c'est-à-dire l'équivalent d'une impulsion f0g1 pour deux transmons ($0 \leftrightarrow g, 1 \leftrightarrow e$). Une fois cette conversion effectuée, une mesure dispersive standard du second transmon permet de certifier le transfert réussi du photon sans détruire l'état quantique du premier.

Un désavantage de l'encodage temporel est que la longueur totale du protocole est doublée par rapport à l'encodage en base de Fock, car l'émission de photons doit être répétée deux fois. La décohérence des transmons est donc plus néfaste pour

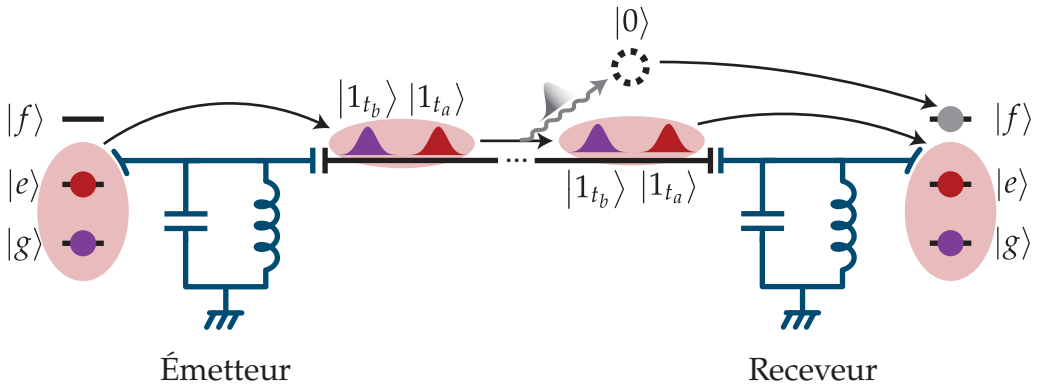

FIGURE 5.5 – L'état du qubit en converti en état de photon dans une base en temps, $\alpha|g\rangle + \beta|e\rangle \rightarrow \alpha|1_{t_b}\rangle + \beta|1_{t_a}\rangle$. En cas de perte de photon (ligne ondulée grise), le nœud récepteur reçoit un état $|0\rangle$ et le transmon est envoyé vers l'état $|f\rangle$.

l'encodage en temps que pour l'encodage de Fock, rendant l'encodage temporel attrayant seulement pour des systèmes où la perte de photons est la source d'erreur dominante. On peut cependant ajouter à cela que certains événements de relaxation des transmons sont équivalents à la perte d'un photon et peuvent donc être détectés.

5.3.2 Article

Comme pour l'article précédent, j'ai effectué le support théorique pour l'expérience effectuée à l'ETH Zürich. En particulier, j'ai réalisé les simulations d'équation maîtresse et les simulations d'équation maîtresse stochastique étudiant la robustesse du protocole par rapport à la relaxation des transmons. J'ai rédigé l'annexe A et participé à l'écriture du manuscrit.

Philipp Kurpiers, Marek Pechal, Baptiste Royer, Paul Magnard, Theo Walter, Johannes Heinsoo, Yves Salathé, Abdulkadir Akin, Simon Storz, Jean-Claude Besse, Simone Gasparinetti, Alexandre Blais et Andreas Wallraff. Quantum communication with time-bin encoded microwave photons. *arXiv e-prints* , arXiv:1811.07604 (2018)

Quantum communication with time-bin encoded microwave photons

P. Kurpiers,[1,*] M. Pechal,[2,*] B. Royer,[3] P. Magnard,[1] T. Walter,[1] J. Heinsoo,[1] Y. Salathé,[1] A. Akin,[1] S. Storz,[1] J.-C. Besse,[1] S. Gasparinetti,[1] A. Blais,[3,4] and A. Wallraff[1]

[1] *Department of Physics, ETH Zürich, CH-8093 Zürich, Switzerland*[†]
[2] *Department of Applied Physics and Ginzton Laboratory, Stanford University, Stanford CA 94305 USA*
[3] *Institut Quantique and Départment de Physique, Université de Sherbrooke, Sherbrooke, Québec J1K 2R1, Canada*
[4] *Canadian Institute for Advanced Research, Toronto, Canada*

(Dated: November 20, 2018)

Heralding techniques are useful in quantum communication to circumvent losses without resorting to error correction schemes or quantum repeaters. Such techniques are realized, for example, by monitoring for photon loss at the receiving end of the quantum link while not disturbing the transmitted quantum state. We describe and experimentally benchmark a scheme that incorporates error detection in a quantum channel connecting two transmon qubits using traveling microwave photons. This is achieved by encoding the quantum information as a time-bin superposition of a single photon, which simultaneously realizes high communication rates and high fidelities. The presented scheme is straightforward to implement in circuit QED and is fully microwave-controlled, making it an interesting candidate for future modular quantum computing architectures.

Engineering of large-scale quantum systems will likely require coherent exchange of quantum states between distant units. The concept of quantum networks has been studied theoretically [1–4] and substantial experimental efforts have been devoted to distribute entanglement over increasingly larger distances [5–15]. In practice, quantum links inevitably experience losses, which vary significantly between different architectures and may range from 2×10^{-4} dB/m in optical fibers [16] to 5×10^{-3} dB/m in superconducting coaxial cables and waveguides at cryogenic temperatures [17]. However, no matter which architecture is used, the losses over a sufficiently long link will eventually destroy the coherence of the transmitted quantum state, unless some measures are taken to mitigate these losses. Possible ways to protect the transmitted quantum information rely, for example, on using quantum repeaters [18, 19], error correcting schemes [20–22] or heralding protocols [23–26], which allow one to retransmit the information in case photon loss is detected.

Heralding protocols are particularly appealing for near-term scaling of quantum systems since they are implementable without a significant resource overhead and can provide deterministic remote entanglement at predetermined times [27]. In essence, these protocols rely on encoding the transmitted quantum information in a suitably chosen subspace S such that any error, which may be encountered during transmission, causes the system to leave this subspace. On the receiving end, a measurement which determines whether the system is in S but does not distinguish between individual states within S, can be used to detect if an error occurred. Crucially, when the transfer is successful, this protocol does not disturb the transmitted quantum information. As a counter example, a simple encoding as a superposition of the vacuum state $|0\rangle$ and the single photon Fock state $|1\rangle$ is not suitable to detect errors due to photon loss because the error does not cause a transition out of the encoding subspace $\{|0\rangle, |1\rangle\}$. For this reason, encodings using other degrees of freedom such as polarization [28, 29], angular momentum [30, 31], frequency [32], time-bin [33–36] or path [37, 38] are more common at optical frequencies. Heralding schemes have been used with superconducting circuits in the context of measurement based generation of remote entanglement [9, 39] and also using two-photon interference [40]. The more recent deterministic state transfer and remote entanglement protocols based on the exchange of shaped photon wave packets [13–15, 41] have to the best of our knowledge not yet been augmented using heralding protocols.

In this work, we propose and experimentally benchmark a method to transfer qubit states over a distance of approximately 0.9 m using a time-bin superposition of two propagating temporal microwave modes. Our experimental results show that the protocol leads to a significant performance improvement, which is, in our case, a reduction of the transfer process infidelity by a factor of approximately two assuming ideal qubit readout. The stationary quantum nodes are transmons [42] coupled to coplanar waveguide resonators. The two lowest energy eigenstates of the transmon, $|g\rangle$ and $|e\rangle$, form the qubit subspace S while the second excited state, $|f\rangle$, is used to detect potential errors. The multi-level nature of the transmon is also essential to the photon emission and reabsorption process, as described below. This technique can also be adapted to prepare entangled states of the qubit and the time-bin degree of freedom, making it suitable for heralded distribution of entanglement. Remarkably, it does not require any specialized components beyond the standard circuit QED setup with a transmon or any other type of non-linear multi-level system coupled to a resonator, such as capacitively shunted flux

* P.K. and M.P. contributed equally to this work.
† philipp.kurpiers@phys.ethz.ch, mpechal@stanford.edu, andreas.wallraff@phys.ethz.ch

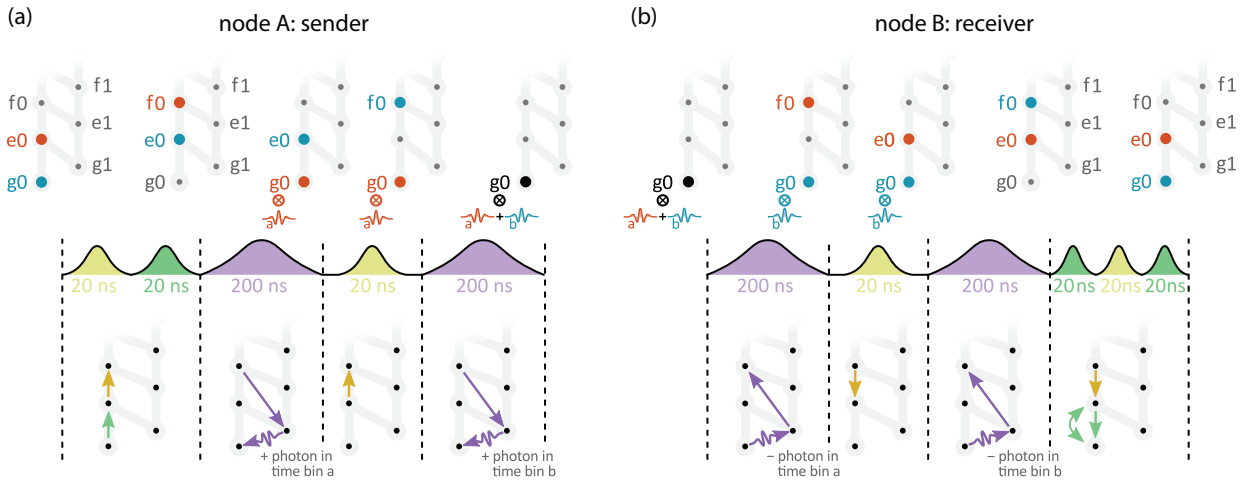

FIG. 1. Schematic representation of the pulse sequence implementing the time-bin encoding process at (a) the sender and (b) the receiver. In the level diagrams, the gray vertical lines represent Hamiltonian matrix elements due to microwave drive between transmon levels while the diagonal ones show the transmon-resonator coupling. (a) The qubit state is initially stored as a superposition of $|g0\rangle$ (blue dot) and $|e0\rangle$ (red dot). The first two pulses map this state to a superposition of $|e0\rangle$, $|f0\rangle$ and the third pulse transfers $|f0\rangle$ into $|g0\rangle$ while emitting a photon in time bin a (see red symbol for photon in mode a). Then, after $|e0\rangle$ is swapped to $|f0\rangle$, the last pulse again transfers $|f0\rangle$ into $|g0\rangle$ and emits a photon in time bin b. (b) Reversing the protocol we reabsorb the photon, mapping the time-bin superposition back onto a superposition of transmon states.

qubits [43], and can be implemented without frequency tunability.

Our time-bin encoding scheme is based on a technique for generating traveling microwave photons [44] via a Raman-type transition in the transmon-resonator system [45]. When the transmon is in its second excited state $|f\rangle$ and the resonator in the vacuum state $|0\rangle$, application of a strong microwave drive of appropriate frequency induces a second order transition from the initial state $|f0\rangle$ into the state $|g1\rangle$ where the transmon is in the ground state and the resonator contains a single photon. This photon is subsequently emitted into a waveguide coupled to the resonator, leaving the transmon-resonator system in its joint ground state. As the magnitude and phase of the coupling between $|f0\rangle$ and $|g1\rangle$ is determined by the amplitude and phase of the applied drive [44], the waveform of the emitted photon can be controlled by shaping the drive pulse. The same process applied in reverse can then be used to reabsorb the traveling photon by another transmon-resonator system [1, 14].

The process for transferring quantum information stored in the transmon into a time-bin superposition state consists of the steps illustrated in Fig. 1(a): The transmon qubit at node A is initially prepared in a superposition of its ground and first excited state, $\alpha|g\rangle + \beta|e\rangle$, and the resonator in its vacuum state $|0\rangle$. Next, two pulses are applied to transform this superposition into $\alpha|e\rangle + \beta|f\rangle$. Then, another pulse induces the transition from $|f0\rangle$ to $|g1\rangle$ as described above, which is followed by spontaneous emission of a photon from the resonator. The shape of the $|f0\rangle$-$|g1\rangle$ drive pulse is chosen such that the photon is emitted into a time-symmetric mode centered around time t_a. After this first step, the system is in the state $\alpha|e0\rangle \otimes |0\rangle + \beta|g0\rangle \otimes |1_a\rangle$, where $|0\rangle$ and $|1_a\rangle$ denote the vacuum state of the waveguide and the single-photon state in the time-bin mode a. Next, the population from state $|e\rangle$ is swapped into $|f\rangle$ and the photon emission process is repeated, this time to create a single photon in a time-bin mode b centered around time t_b. The resulting state of the system is $|g0\rangle \otimes (\alpha|1_b\rangle + \beta|1_a\rangle)$.

Because of time-reversal symmetry, a single photon, which is emitted by a transmon-resonator system into a propagating mode with a time-symmetric waveform, can be reabsorbed with high efficiency by another identical transmon-resonator system [1]. This absorption process is induced by a drive pulse obtained by time-reversing the pulse that led to the emission of the photon. By reversing both drive pulses in the time-bin encoding scheme, as illustrated in Fig. 1(b), an incoming single photon in the time-bin superposition state $\alpha|1_b\rangle + \beta|1_a\rangle$ will cause the receiving transmon-resonator system, initialized in $|g0\rangle$, to be driven to the state $\alpha|e0\rangle + \beta|g0\rangle$ as the photon is absorbed. Thus, this protocol transfers the qubit state encoded as a superposition of $|g\rangle$ and $|e\rangle$ from transmon A to transmon B. In short, the sequence is

$$\begin{aligned}
&\Big(\alpha|g\rangle_A + \beta|e\rangle_A\Big) \otimes |g\rangle_B \rightarrow \\
&|g\rangle_A \otimes \Big(\alpha|1_b\rangle + \beta|1_a\rangle\Big) \otimes |g\rangle_B \rightarrow \\
&|g\rangle_A \otimes \Big(\alpha|g\rangle_B + \beta|e\rangle_B\Big)
\end{aligned}$$

where we have omitted the states of the resonators and the propagating field whenever they are in their respective vacuum states.

An important property of this transfer protocol is its ability to detect photon loss in the communication chan-

nel. Indeed, if a photon is lost or not absorbed by the receiver, system B receives a vacuum state at its input instead of the desired single-photon state. This means that both absorption pulse sequences will leave transmon B in its ground state $|g\rangle$ which will be subsequently mapped into $|f\rangle$ by the final three pulses. By performing a quantum non-demolition measurement on the transmon which distinguishes between $|f\rangle$ and the subspace spanned by $|g\rangle$, $|e\rangle$, but does not measure within this subspace, we can detect the photon loss event without affecting the transmitted quantum information. Such a binary measurement of a qutrit state can, for example, be realized by suppressing the measurement-induced dephasing in the *ge* subspace using parametric amplification and feedback [46] or by engineering the dispersive shifts of two transmon states on the readout resonator to be equal [47]. The protocol also detects failures of the state transfer due to energy relaxation at certain times during the time-bin encoding protocol, e.g. if no photon is emitted from A due to decay to $|g\rangle$ before the first time bin. We discuss the detection of qutrit energy relaxation based on quantum trajectories in Appendix A.

We implemented this time-bin encoding protocol using the setup depicted in Fig. 2(a) (see Appendix B and Ref. [14] for details). We performed qutrit single-shot readout instead of the binary measurement at transmon B to characterize the quantum state transfer with process tomography. For that, we initialized both transmon qubits in their ground states [50, 51] and subsequently prepared the qubit at node A in one of the six mutually unbiased qubit basis states $|\psi_{\rm in}\rangle = \{|g\rangle, |e\rangle, |\pm\rangle = (|g\rangle \pm |e\rangle)/\sqrt{2}, |\pm i\rangle = (|g\rangle \pm i\,|e\rangle)/\sqrt{2}\}$ [52] [Fig. 2(b)]. We then ran the time-bin encoding and reabsorption protocol, as described above [Fig. 1] and implemented quantum state tomography at node B for all six input states. Directly after the tomography pulses, we read out the $|g\rangle$, $|e\rangle$ and $|f\rangle$ states of transmon B with single-shot readout using a Josephson parametric amplifier (JPA) [53] in the output line. For readout characterization, we extracted probabilities of correct assignment of state $|g\rangle$, $|e\rangle$ and $|f\rangle$ for transmon B of $P_{\rm g|g\rangle} = P(g|\,|g\rangle) = 98.5\%$, $P_{\rm e|e\rangle} = 92.3\%$ and $P_{\rm f|f\rangle} = 86.4\%$ (see also Appendix C). Based on these single-shot measurements, we postselected experimental runs in which transmon B is not measured in the $|f\rangle$ state keeping on average $P_{\rm suc}^{qst} = 64.6\%$ of the data, and transferring qubit states at a rate $\Gamma_{\rm qst}/2\pi = P_{\rm suc}^{\rm qst}\Gamma_{\rm exp}/2\pi \approx 32.3\,$kHz. Using the post-selected data, we reconstructed the density matrices $\rho_{\rm ps}$ of the qubit output state at node B based solely on the single-shot readout results and obtain the process matrix $\chi_{\rm ps}$ of the quantum state transfer. We compute an averaged state fidelity of $F_{\rm s}^{\rm ps} = {\rm avg}(\langle\psi_{\rm in}|\rho_{\rm ps}|\psi_{\rm in}\rangle) = 88.2 \pm 0.2\%$ and a process fidelity of $F_{\rm p}^{\rm ps} = {\rm tr}(\chi_{\rm ps}\chi_{\rm ideal}) = 82.3 \pm 0.2\%$ relative to the ideal input states $|\psi_{\rm in}\rangle$ and the ideal identity process, respectively.

To illustrate the detection of photon loss using the time-bin encoding protocol, we reconstructed all six qutrit density matrices ρ_{cor} of the output state at node B using the same dataset and correcting for measurement errors in the qutrit subspace [14, 54] (see Appendix C for

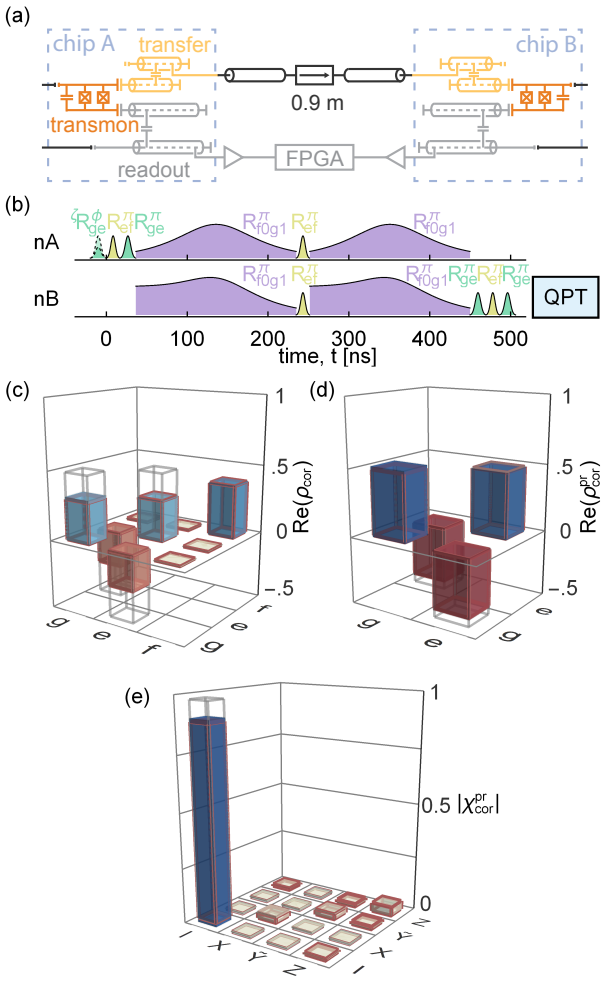

FIG. 2. (a) Simplified schematic of the circuit QED setup. At each of the nodes a transmon (orange) is capacitively coupled to two Purcell-filtered resonators which are used for readout (gray) and remote quantum communication (yellow). The directional quantum channel consists of a semi-rigid coaxial cable intersected by an isolator (see Ref. [14] for details). (b) Pulse scheme used to characterize the time-bin encoding protocol to transfer qubit states between two distant nodes using quantum process tomography (QPT). ${}^{\zeta}{\rm R}_{\rm ij}^{\phi}$ labels a Gaussian derivative removal by adiabatic gate (DRAG) microwave pulses [48, 49] for transmon transition ij = {ge, ef} or transmon-resonator transitions ij = f0g1 of angle $\phi = \{\pi/2, \pi\}$ around the rotation axis $\zeta = \{{\rm x}, {\rm y}\}$. If no axis is specified the pulses are around the x-axis. (c) Real part of the qutrit density matrix $\rho_{\rm cor}$ for the input state $|-\rangle = (|g\rangle - |e\rangle)/\sqrt{2}$ after the state transfer protocol reconstructed using measurement-error correction. The magnitude of each imaginary part is < 0.017. (d) Projection of $\rho_{\rm cor}$ (c) onto the *ge* subspace $\rho_{\rm cor}^{\rm pr}$ performed numerically which we use to reconstruct the process matrix $\chi_{\rm cor}^{\rm pr}$ (absolute value shown in (e)). The colored bars show the measurement results, the gray wire frames the ideal density or process matrix, respectively. The results of numerical master equation simulations are depicted as red wire frames.

details). These qutrit density matrices have a significant average population of level $|f\rangle$ of 39.1% indicating the detection of errors after the time-bin encoding protocol, which is compatible with $1 - P_{\rm suc}^{gst}$ of the post-selected analysis [Fig. 2(c)]. Next, we projected these density matrices numerically onto the qubit ge subspace $\rho_{cor}^{\rm pr}$ [Fig. 2(d)], simulating an ideal error detection and reconstructed the process matrix $\chi_{\rm cor}^{\rm pr}$ of the quantum state transfer [Fig. 2(e)]. In this way, we found an average state fidelity of $F_{\rm s}^{\rm cor} = {\rm avg}(\langle\psi_{\rm in}|\rho_{\rm cor}^{\rm pr}|\psi_{\rm in}\rangle) = 93.5 \pm 0.1\%$ and a process fidelity of $F_{\rm p}^{\rm cor} = {\rm tr}(\chi_{\rm cor}^{\rm pr}\chi_{\rm ideal}) = 90.3 \pm 0.2\%$ based on these measurement-corrected matrices. This analysis allowed us to compare the time-bin encoded protocol directly to a fully deterministic scheme without error mitigation, implemented in a similar setup [14], in which we obtained $F_{\rm p}^{\rm det} \approx 80\%$. This clearly shows the advantage of time-bin encoding to reduce the effect of photon loss. In addition, we analyzed the sources of infidelity by performing numerical master equation simulations (MES) of the time-bin encoding protocol which we compared to the measurement-error corrected density and process matrices. We find excellent agreement with the experimental results, indicated by a small trace distance ${\rm tr}\,|\chi_{\rm cor}^{\rm pr} - \chi_{\rm sim}|\,/2 = 0.03$ which is ideally 0 for identical matrices and 1 for orthogonal ones. The MES results indicate that approximately 5.5% of the infidelity can be attributed to $|f\rangle \rightarrow |e\rangle$ and $|e\rangle \rightarrow |g\rangle$ energy relaxation at both transmons during the protocol. Pure qutrit dephasing can explain the remaining infidelity.

In addition to a direct quantum state transfer, the generation of entanglement between distant nodes is a key task of quantum communication. Here, we use a simple modification of the state-transfer protocol to perform this task [Fig. 3(a)]. Both transmon-resonator systems are first initialized in their ground states. The first two pulses of the remote-entanglement protocol prepare transmon A in an equal superposition state $1/\sqrt{2}(|e\rangle + |f\rangle)$, followed by a pulse sequence which entangles the transmon state $|g\rangle$ and $|e\rangle$ with the time-bin qubit and maps the state of the time-bin qubit to transmon B. This process can be summarized as

$$\frac{1}{\sqrt{2}}\Big((|e\rangle_A + |f\rangle_A\Big) \otimes |g\rangle_B \rightarrow$$
$$\frac{1}{\sqrt{2}}\Big(|g\rangle_A \otimes |1_a\rangle + |e\rangle_A \otimes |1_b\rangle\Big) \otimes |g\rangle_B \rightarrow$$
$$\frac{1}{\sqrt{2}}\Big(|g\rangle_A \otimes |e\rangle_B + |e\rangle_A \otimes |g\rangle_B\Big)$$

and, in case of an error, transmon B ends up in state $|f\rangle_B$.

We performed post-selected experiments of the entanglement-generation protocol by selecting only experimental runs in which neither qutrit was measured in the $|f\rangle$ state using individual single-shot readout on both transmons. Under this condition, we retained $P_{\rm suc}^{\rm ent} \approx 61.5\%$ of the data and obtained a Bell state fidelity of $F_{\rm s}^{\rm ps} = \langle\psi^+|\rho_{\rm ps}|\psi^+\rangle = 82.3 \pm 0.4\%$ compared to an ideal Bell state $|\psi^+\rangle = (|g_A, e_B\rangle + |e_A, g_B\rangle)/\sqrt{2}$. In

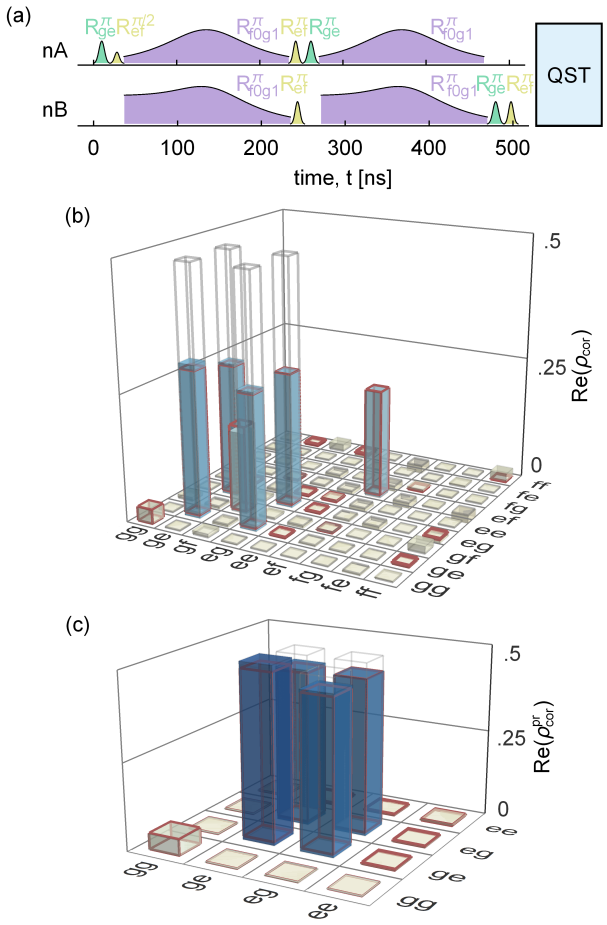

FIG. 3. (a) Pulse scheme for generating remote entanglement between nodes A and B (see text for details). (b) Real part of the two-qutrit density matrix $\rho_{\rm cor}$ reconstructed after execution of the time-bin remote entanglement protocol using measurement-error correction. The colored bars indicate the measurement results, the ideal expectation values for the Bell state $|\psi^+\rangle = (|g_A, e_B\rangle + |e_A, g_B\rangle)/\sqrt{2}$ are shown as gray wire frames and the results of a master equation simulation as red wire frames. The magnitude of the imaginary part of each element of the density matrix is < 0.024. (c) Numerical projection of the $\rho_{\rm cor}$ onto the ge subspace to obtain the two-qubit density matrix $\rho_{\rm cor}^{\rm pr}$ which is in excellent agreement with our MES (trace distance of 0.028).

these post-selected experiments, we generated entangled states at rate $\Gamma_{\rm ent}/2\pi = P_{\rm suc}^{\rm ent}\Gamma_{\rm exp}/2\pi \approx 30.8\,{\rm kHz}$. To benchmark this entanglement protocol, we used full two-qutrit state tomography of the transmons in which we corrected for measurement errors with the same data set. The reconstructed density matrix, shown in Fig. 3(c), displays a high population of the $|g_A, f_B\rangle$, $|e_A, f_B\rangle$ states, $P_{gf} = 16.0\%$ and $P_{ef} = 21.4\%$, and small population of $|f_A, g_B\rangle$, $|f_A, e_B\rangle$ and $|f_A, f_B\rangle$, $\sum_{i=\{g,e,f\}} P_{fi} = 2.7\%$, which indicates that photon loss is a significant source of error. We projected onto the ge qubit subspace numerically and obtained a two-qubit density matrix, Fig. 3(d), showing a fidelity of $F_{\rm s}^{\rm cor} = \langle\psi^+|\rho_{\rm cor}^{\rm pr}|\psi^+\rangle = 92.4 \pm 0.4\%$.

Comparing this state fidelity to the fully deterministic case, $F_{\mathrm{s}}^{\mathrm{det}} \approx 79\%$ [14], shows the potential of the proposed time-bin encoding protocol to generate remote entanglement independent of photon loss. Using a MES we attribute approximately 6.5% of the infidelity to energy relaxation and the rest to dephasing. As detailed in Appendix A, we performed a MES based on quantum trajectories and find that 64% of all decay events during the time-bin encoding protocol are detected. However, due to the additional time needed for performing the time-bin encoding protocol relative to the direct Fock-state encoding this protocol is affected more by pure qutrit dephasing.

In conclusion, we experimentally demonstrated a method for transferring a qubit state between a three-level superconducting quantum circuit and a time-bin superposition of a single propagating microwave photon. This type of encoding lends itself naturally to quantum communication protocols which allow detection of photon loss in the quantum link while maintaining a high communication rate. In our experiment, we have observed that the described protocol significantly improves the fidelity of transmitted quantum states and distributed Bell states between two distant transmon qubits when outcomes are post-selected on successful transmission of a photon. We also observed and analyzed the potential of the time-bin encoding protocol to detect errors due to energy relaxation of the qutrits during the protocol.

ACKNOWLEDGEMENTS

This work was supported by the European Research Council (ERC) through the 'Superconducting Quantum Networks' (SuperQuNet) project, by the National Centre of Competence in Research 'Quantum Science and Technology' (NCCR QSIT) a research instrument of the Swiss National Science Foundation (SNSF), by Baugarten Stiftung, by ETH Zürich Foundation, by ETH Zürich, by NSERC, the Canada First Research Excellence Fund, and by the Vanier Canada Graduate Scholarships. Marek Pechal was supported by the Early Postdoc Mobility Fellowship of the Swiss National Science Foundation (SNSF), and by the National Science Foundation (NSF) grant ECCS-1708734.

AUTHOR CONTRIBUTIONS

The time-bin encoding protocol was developed by M.P. and P.K. The experimental implementation was designed by P.K., P.M., T.W and M.P. The samples were fabricated by J.-C.B., T.W. and S.G. The experiments were performed by P.K. The data was analyzed and interpreted by P.K., M.P., B.R., A.B. and A.W. The FPGA firmware and experiment automation was implemented by J.H., Y.S., A.A., S.S, P.M. and P.K. The master equation simulation were performed by B.R., P.K and M.P. The manuscript was written by M.P., P.K., B.R., A.B. and A.W. All authors commented on the manuscript. The project was led by A.W.

Appendix A: Stochastic Master Equation Simulations

In order to investigate the robustness of the time-bin encoding protocol with respect to qutrit energy relaxation, we numerically study a fictitious experiment with the same device parameters in which we monitor quantum jumps from $|f\rangle \rightarrow |e\rangle$ and from $|e\rangle \rightarrow |g\rangle$ on qutrits A and B, conditioning the system state on the measurement record. We perform $N_{\mathrm{traj}} = 2000$ trajectories unraveled in the manner described above [55] and, for each realization for which a jump occurred, compute the probability that the error is detected at the end of the time-bin protocol. Fig. 4(b) and (c) show this heralding probability as a function of the time at which the jump occurred for the four energy relaxation processes, $|f\rangle_{\mathrm{n}} \rightarrow |e\rangle_{\mathrm{n}}$ and $|e\rangle_{\mathrm{n}} \rightarrow |g\rangle_{\mathrm{n}}$, $\mathrm{n} = \{\mathrm{A}, \mathrm{B}\}$. For some decay events, qutrit B ends in the $|f\rangle$ state and, consequently, the time-bin encoding protocol partially allows the heralding of qutrit relaxation.

For simplicity, Fig. 4(b) and (c) only show the cases where a single decay event occurred. Summing over all trajectories where one or more jumps are present, we can estimate the probability of an undetected decay event,

$$P_{\mathrm{undet}} = \frac{1}{N_{\mathrm{traj}}} \sum_{\mathrm{jump}} \left(1 - \mathrm{Tr}\left[|f\rangle \langle f|_B \, \rho_{\mathrm{jump}}(t_f)\right]\right),$$

where $\rho_{\mathrm{jump}}(t_f)$ is the state conditioned on the measurement record at the end of the protocol. For the entanglement generation protocol and the parameters of this experiment, we find that the probability of an undetected decay event is $P_{\mathrm{undet}} = 5.5\%$ which corresponds to $P_{\mathrm{undet}}/P_{\mathrm{jump}} = 35.7\%$ of trajectories where a jump occurred. Three types of decay events contribute the most to P_{undet}, as shown in Fig. 4(b) and (c). At node A, $|f\rangle_A \rightarrow |e\rangle_A$ jumps (light blue points) in the first time bin are generally not detected since this results in a photon being emitted in the second time bin, with qutrit B ending in $|e\rangle$. However, if there is also a photon loss event in the communication channel in the second time bin, then qutrit B ends in $|f\rangle$ and the combination of the two errors is detected. When the communication channel is perfect, this type of decay event is not detected. Second, $|e\rangle_A \rightarrow |g\rangle_A$ jumps (dark blue points) in the second time bin are generally not detected and there are two ways they can occur. If there are no other errors in the protocol, then qutrit B ends in $|g\rangle$ and the error is not detected. However, a $|e\rangle_A \rightarrow |g\rangle_A$ jump can also occur if there is a photon loss event in the first time bin. In that situation, qutrit B ends $|f\rangle$ and the error is detected. At node B, $|f\rangle_B \rightarrow |e\rangle_B$ jumps (beige points) in the second time bin are not detected since qutrit B ends in $|g\rangle$.

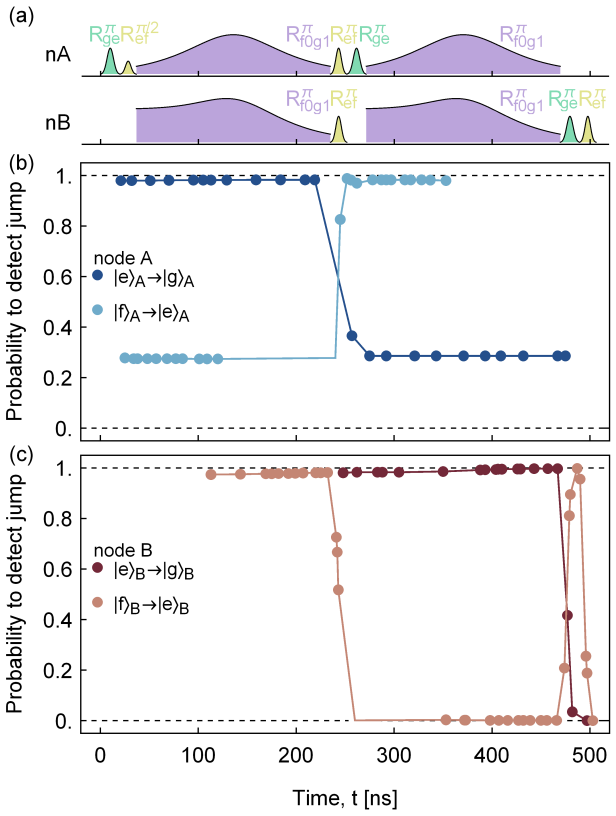

FIG. 4. (a) Pulse scheme for generating remote entanglement between node A and B. Probability that a quantum jump from $|f\rangle \rightarrow |e\rangle$ or $|e\rangle \rightarrow |g\rangle$ of the qutrit at node A (b) or node B (c) is detected during the time-bin remote entanglement protocol. The data is based on 2000 stochastic trajectories of a numerical master equation simulation (see Appendix A for details).

In contrast to energy relaxation, pure dephasing does not lead to direct changes in qutrit populations. Consequently, the time-bin encoding does not allow the heralding of phase errors.

Appendix B: Sample and Setup

The samples and setup are identical to the one of Ref. [14]. Up to an exchange of the cryogenic coaxial circulator (Raditek RADC-8-12-Cryo) in the connection between the two samples with a rectangular waveguide isolator (RADI-8.3-8.4-Cryo-WR90) which affected the bandwidth of the transfer resonators due to its different impedance. The device parameters are summarized in Table I.

quantity, symbol (unit)	Node A	Node B
readout resonator frequency, ν_{R} (GHz)	4.788	4.780
readout Purcell filter frequency, ν_{Rpf} (GHz)	4.778	4.780
readout resonator bandwidth, $\kappa_R/2\pi$ (MHz)	12.6	27.1
readout circuit dispersive shift, $\chi_R/2\pi$ (MHz)	5.8	11.6
transfer resonator frequency, ν_{T} (GHz)	8.400	8.400
transfer Purcell filter frequency, ν_{Tpf} (GHz)	8.426	8.415
transfer resonator bandwidth, $\kappa_T/2\pi$ (MHz)	7.4	12.6
transfer circuit dispersive shift, $\chi_T/2\pi$ (MHz)	6.3	4.7
qubit transition frequency, ν_{ge} (GHz)	6.343	6.098
transmon anharmonicity, α (MHz)	-265	-306
$\|f,0\rangle \leftrightarrow \|g,1\rangle$ transition frequency, ν_{f0g1} (GHz)	4.021	3.490
$\|f,0\rangle \leftrightarrow \|g,1\rangle$ max. eff. coupling, $\tilde{g}_{\mathrm{m}}/2\pi$ (MHz)	5.4	5.6
energy relaxation time on ge, $T_{1\mathrm{ge}}$ (μs)	5.0±0.4	4.5±0.2
energy relaxation time on ef, $T_{1\mathrm{ef}}$ (μs)	2.3±0.4	1.6±0.1
coherence time on ge, $T^{\mathrm{R}}_{2\mathrm{ge}}$ (μs)	7.7±0.5	5.7±0.2
coherence time on ef, $T^{\mathrm{R}}_{2\mathrm{ef}}$ (μs)	3.2±1.3	2.3±0.7

TABLE I. Device parameters for nodes A and B.

Appendix C: Qutrit single-shot readout and population extraction

We estimated the measurement assignment probabilities $P_{s'|s\rangle} = P(s'||s\rangle)$ by first assigning each trace prepared in state $|s\rangle$ to state s' obtained from a single-shot measurement and normalized the recorded counts. We summarized those normalized counts in a vector N^i_{B} for each measured trace i. To obtain the assignment probabilities matrix $R_{\mathrm{A}} = P_{\mathrm{A}}(s'_{\mathrm{A}}||s_{\mathrm{A}}\rangle) = (N_{\mathrm{A}}^{|g\rangle}, N_{\mathrm{A}}^{|e\rangle}, N_{\mathrm{A}}^{|f\rangle})$ and $R_{\mathrm{B}} = P_{\mathrm{B}}(s'_{\mathrm{B}}||s_{\mathrm{B}}\rangle$ for transmon A and B, we reset both transmons to their ground state, prepared them in either $|g\rangle$, $|e\rangle$ or $|f\rangle$ individually using DRAG microwave pulses and performed single shot readout for which we optimized the readout power and integration time [56] to minimize the sum of all measurement misidentifications (the off-diagonal elements of R) [14]. For the single-shot readout we used Josephson parametric amplifiers (JPAs) with a gains of 21 dB and 24 dB and bandwidths of 20 MHz and 28 MHz. We obtained the assignment probabilities matrix $R_{\mathrm{A}} =$

	$\|g\rangle$	$\|e\rangle$	$\|f\rangle$
g	97.8	2.7	2.9
e	0.7	93.8	3.7
f	1.5	3.5	93.4

for transmon A for a readout time of $t^{\mathrm{A}}_{\mathrm{r}} = 96$ ns and a state-dependent number of photons in the readout resonator $n^{\mathrm{A}}_{\mathrm{r}}$ of 0.5 to 2. For transmon B we computed $R_{\mathrm{B}} =$

	$\|g\rangle$	$\|e\rangle$	$\|f\rangle$
g	98.5	3.8	1.1
e	0.9	92.3	12.5
f	0.6	3.9	86.4

	gg	ge	gf	eg	ee	ef	fg	fe	ff
gg	0.027	-0.004i	0.007-0.007i	-0.001-0.011i	0	-0.001i	0	-0.003	0.002+0.002i
ge	0.004i	0.301	-0.005-0.024i	0.269	0.004i	-0.003+0.007i	-0.002-0.006i	-0.001	-0.001
gf	.007+0.007i	-0.005+0.024i	0.16	0.004+0.013i	-0.005+0.003i	-0.002-0.001i	0.001-0.002i	0.001+0.016i	0.014-0.004i
eg	-0.001+0.011i	0.269	0.004-0.013i	0.268	-0.001-0.001i	-0.003+0.008i	-0.007-0.010i	-0.001i	-0.006-0.004i
ee	0.	-0.004i	-0.005-0.003i	-0.001+0.001i	0.003	-0.008+0.011i	-0.003i	0.	0.001
ef	0.001i	-0.003-0.007i	-0.002+0.001i	-0.003-0.008i	-0.008-0.011i	0.214	-0.011+0.017i	0.001-0.001i	-0.016-0.007i
fg	0.	-0.002+0.006i	0.001+0.002i	-0.007+0.01i	0.003i	-0.011-0.017i	0.006	-0.001+0.001i	0.001+0.001i
fe	-0.003	-0.001	0.001-0.016i	0.001i	0.	0.001+0.001i	-0.001-0.001i	0.003	0.
ff	0.002-0.002i	-0.001	0.014+0.004i	-0.006+0.004i	0.001	-0.016+0.007i	0.001-0.001i	0.	0.018

TABLE II. Numerical values of the experimentally obtained density matrix elements of the two-transmon remote entangled state in a two-qutrit basis using the time-bin encoding. The real part of this density matrix is depicted as colored bars in Fig. 3(b).

for $t_{\rm r}^{\rm B} = 216\,$ns and $n_{\rm r}^{\rm B}$ between 0.2 and 0.5 used for characterizing the quantum state transfer protocol.

For two-qutrit states the assignment probability matrix $R_{\rm AB} = P_{\rm AB}(s'_{\rm A}, s'_{\rm B}|\,|s_{\rm A}, s_{\rm B}\rangle) = R_{\rm A} R_{\rm B}$ can be calculated using the outer product of the single-qutrit assignment probabilities matrices.

In the post-selected measurement analysis we discarded traces which were assigned to $s' = f$ in the single-shot measurement, keeping only the ge qubit subspace. We normalized the g, e counts and set the normalized counts equal to the populations of transmons in the qubit subspace. Based on these population we reconstructed the density matrices of the output states after the state-transfer or entanglement-generation protocol using a maximum-likelihood approach [57].

To reconstruct the full single-qutrit (two-qutrit) density matrices we inverted the assignment probability matrix $R_{\rm B}^{-1}$ ($R_{\rm AB}^{-1}$) and obtained the qutrit population for each measured trace $M_{\rm B}^i = R_{\rm B}^{-1} N_{\rm B}^i$ (two-qutrit correlations $C_{\rm AB} = R_{\rm AB}^{-1} N_{\rm AB}$). Applying $R_{\rm B}^{-1}$ ($R_{\rm AB}^{-1}$) is an advantage since we can prepare qutrit states with a higher fidelity than performing qutrit readout [14] because of an efficient reset [50] and high fidelity single qutrit pulses.

	I	X	$\tilde{\rm Y}$	Z
I	0.903	-0.003-0.002i	-0.004	0.007+0.005i
X	-0.003+0.002i	0.033	-0.007	0.001
$\tilde{\rm Y}$	-0.004	-0.007	0.027	-0.003+0.002i
Z	0.007-0.005i	0.001	-0.003-0.002i	0.037

TABLE III. Numerical values of the experimentally obtained process matrix elements of the qubit state transfer using the time-bin encoding protocol. The absolute value of this process matrix is depicted in Fig. 2(e) as colored bars.

Appendix D: Measurement data

The measurement results of the quantum process tomography used to characterize the state-transfer protocol and of the two-qutrit density matrix after the remote entanglement protocol are shown in Table II and Table III.

[1] J. I. Cirac, P. Zoller, H. J. Kimble, and H. Mabuchi, "Quantum state transfer and entanglement distribution among distant nodes in a quantum network," Phys. Rev. Lett. **78**, 3221–3224 (1997).

[2] L. Jiang, J. M. Taylor, A. S. Sørensen, and M. D. Lukin, "Distributed quantum computation based on small quantum registers," Phys. Rev. A **76**, 062323 (2007).

[3] H. J. Kimble, "The quantum internet," Nature **453**, 1023–1030 (2008).

[4] T. E. Northup and R. Blatt, "Quantum information transfer using photons," Nat Photon **8**, 356–363 (2014).

[5] C. W. Chou, H. de Riedmatten, D. Felinto, S. V. Polyakov, S. J. van Enk, and H. J. Kimble, "Measurement-induced entanglement for excitation stored in remote atomic ensembles," Nature **438**, 828–832 (2005).

[6] D. L. Moehring, P. Maunz, S. Olmschenk, K. C. Younge, D. N. Matsukevich, L. M. Duan, and C. Monroe, "Entanglement of single-atom quantum bits at a distance," Nature **449**, 68–71 (2007).

[7] X.-S. Ma, T. Herbst, T. Scheidl, D. Wang, S. Kropatschek, W. Naylor, B. Wittmann, A. Mech, J. Kofler, E. Anisimova, V. Makarov, T. Jennewein, R.t Ursin, and A. Zeilinger, "Quantum teleportation over 143 kilometres using active feed-forward," Nature **489**, 269–273 (2012).

[8] S. Ritter, C. Nolleke, C. Hahn, A. Reiserer, A. Neuzner, M. Uphoff, M. Mucke, E. Figueroa, J. Bochmann, and G. Rempe, "An elementary quantum network of single atoms in optical cavities," Nature **484**, 195–200 (2012).

[9] N. Roch, M. E. Schwartz, F. Motzoi, C. Macklin, R. Vijay, A. W. Eddins, A. N. Korotkov, K. B. Whaley, M. Sarovar, and I. Siddiqi, "Observation of measurement-induced entanglement and quantum trajectories of remote superconducting qubits," Phys. Rev. Lett. **112**, 170501 (2014).

[10] B. Hensen, H. Bernien, A. E. Dreau, A. Reiserer, N. Kalb, M. S. Blok, J. Ruitenberg, R. F. L. Vermeulen, R. N. Schouten, C. Abellan, W. Amaya, V. Pruneri, M. W. Mitchell, M. Markham, D. J. Twitchen, D. Elkouss, S. Wehner, T. H. Taminiau, and R. Hanson, "Loophole-free bell inequality violation using electron spins separated by 1.3 kilometres," Nature **526**, 682–686 (2015).

[11] J. Yin, Y. Cao, Y.-H. Li, S.-K. Liao, L. Zhang, J.-G. Ren, W.-Q. Cai, W.-Y. Liu, B. Li, H. Dai, G.-B. Li, Q.-M. Lu, Y.-H. Gong, Y. Xu, S.-L. Li, F.-Z. Li, Y.-Y. Yin, Z.-Q. Jiang, M. Li, J.-J. Jia, G. Ren, D. He, Y.-L. Zhou, X.-X. Zhang, N. Wang, X. Chang, Z.-C. Zhu, N.-L. Liu, Y.-A. Chen, C.-Y. Lu, R. Shu, C.-Z. Peng, J.-Y. Wang, and J.-W. Pan, "Satellite-based entanglement distribution over 1200 kilometers," Science **356**, 1140–1144 (2017).

[12] A. Delteil, Z. Sun, S. Fält, and A. Imamoğlu, "Realization of a cascaded quantum system: Heralded absorption of a single photon qubit by a single-electron charged quantum dot," Phys. Rev. Lett. **118**, 177401 (2017).

[13] P. Campagne-Ibarcq, E. Zalys-Geller, A. Narla, S. Shankar, P. Reinhold, L. Burkhart, C. Axline, W. Pfaff, L. Frunzio, R. J. Schoelkopf, and M. H. Devoret, "Deterministic remote entanglement of superconducting circuits through microwave two-photon transitions," Phys. Rev. Lett. **120**, 200501 (2018).

[14] P. Kurpiers, P. Magnard, T. Walter, B. Royer, M. Pechal, J. Heinsoo, Y. Salathé, A. Akin, S. Storz, J.-C. Besse, S. Gasparinetti, A. Blais, and A. Wallraff, "Deterministic quantum state transfer and remote entanglement using microwave photons," Nature **558**, 264–267 (2018).

[15] C. Axline, L. Burkhart, W. Pfaff, M. Zhang, K. Chou, P. Campagne-Ibarcq, P. Reinhold, L. Frunzio, S. M. Girvin, L. Jiang, M. H. Devoret, and R. J. Schoelkopf, "On-demand quantum state transfer and entanglement between remote microwave cavity memories," Nature Physics **14**, 705–710 (2018).

[16] G. P. Agrawal, *Fiber-Optic Communication Systems*, 4th ed. (John Wiley & Sons, 2011).

[17] P. Kurpiers, T. Walter, P. Magnard, Y. Salathe, and A. Wallraff, "Characterizing the attenuation of coaxial and rectangular microwave-frequency waveguides at cryogenic temperatures," EPJ Quantum Technology **4**, 8 (2017).

[18] H.-J. Briegel, W. Dür, J. I. Cirac, and P. Zoller, "Quantum repeaters: The role of imperfect local operations in quantum communication," Phys. Rev. Lett. **81**, 5932–5935 (1998).

[19] S. Muralidharan, L. Li, J. Kim, N. Lütkenhaus, M. D. Lukin, and L. Jiang, "Optimal architectures for long distance quantum communication," Scientific Reports (2016).

[20] P. W. Shor, "Scheme for reducing decoherence in quantum computer memory," Phys. Rev. A **52**, R2493–R2496 (1995).

[21] S. L. Braunstein and H. J. Kimble, "Teleportation of continuous quantum variables," Phys. Rev. Lett. **80**, 869–872 (1998).

[22] S. Lloyd and J.-J. E. Slotine, "Analog quantum error correction," Phys. Rev. Lett. **80**, 4088–4091 (1998).

[23] P. Maunz, S. Olmschenk, D. Hayes, D. N. Matsukevich, L.-M. Duan, and C. Monroe, "Heralded quantum gate between remote quantum memories," Phys. Rev. Lett. **102**, 250502 (2009).

[24] J. Hofmann, M. Krug, N. Ortegel, L. Gérard, M. Weber, W. Rosenfeld, and H. Weinfurter, "Heralded entanglement between widely separated atoms," Science **337**, 72–75 (2012).

[25] I. Usmani, C. Clausen, F. Bussieres, N. Sangouard, M. Afzelius, and N. Gisin, "Heralded quantum entanglement between two crystals," Nature Photonics **6**, 234 (2012).

[26] H. Bernien, B. Hensen, W. Pfaff, G. Koolstra, M. S. Blok, L. Robledo, T. H. Taminiau, M. Markham, D. J. Twitchen, L. Childress, and R. Hanson, "Heralded entanglement between solid-state qubits separated by three metres," Nature **497**, 86–90 (2013).

[27] P. C. Humphreys, N. Kalb, J. P. J. Morits, R. N. Schouten, R. F. L. Vermeulen, D. J. Twitchen, M. Markham, and R. Hanson, "Deterministic delivery of remote entanglement on a quantum network," Nature **558**, 268 (2018).

[28] K. Mattle, H. Weinfurter, P. G. Kwiat, and A. Zeilinger, "Dense coding in experimental quantum communication," Phys. Rev. Lett. **76**, 4656–4659 (1996).

[29] N. A. Peters, J. T. Barreiro, M. E. Goggin, T.-C. Wei, and P. G. Kwiat, "Remote state preparation: Arbitrary remote control of photon polarization," Phys. Rev. Lett. **94**, 150502 (2005).

[30] G. Molina-Terriza, J. P. Torres, and L. Torner, "Twisted photons," Nature Physics **3**, 305 (2007).

[31] A. M. Yao and M. J. Padgett, "Orbital angular momentum: origins, behavior and applications," Adv. Opt. Photon. **3**, 161–204 (2011).

[32] J. M. Lukens and P. Lougovski, "Frequency-encoded photonic qubits for scalable quantum information processing," Optica **4**, 8–16 (2017).

[33] J. Brendel, N. Gisin, W. Tittel, and H. Zbinden, "Pulsed energy-time entangled twin-photon source for quantum communication," Phys. Rev. Lett. **82**, 2594–2597 (1999).

[34] I. Marcikic, H. de Riedmatten, W. Tittel, H. Zbinden, M. Legré, and N. Gisin, "Distribution of time-bin entangled qubits over 50 km of optical fiber," Phys. Rev. Lett. **93**, 180502 (2004).

[35] B. Brecht, Dileep V. Reddy, C. Silberhorn, and M. G. Raymer, "Photon temporal modes: A complete framework for quantum information science," Phys. Rev. X **5**, 041017 (2015).

[36] C. M. Lee and M. J. Hoban, "Towards device-independent information processing on general quantum networks," Phys. Rev. Lett. **120**, 020504 (2018).

[37] P. Kok, H. Lee, and J. P. Dowling, "Creation of large-photon-number path entanglement conditioned on photodetection," Phys. Rev. A **65**, 052104 (2002).

[38] J. C. F. Matthews, A. Politi, D. Bonneau, and J. L. O'Brien, "Heralding two-photon and four-photon path entanglement on a chip," Phys. Rev. Lett. **107**, 163602 (2011).

[39] C. Dickel, J. J. Wesdorp, N. K. Langford, S. Peiter, R. Sagastizabal, A. Bruno, B. Criger, F. Motzoi, and L. DiCarlo, "Chip-to-chip entanglement of transmon qubits using engineered measurement fields," Phys. Rev. B **97**, 064508 (2018).

[40] A. Narla, S. Shankar, M. Hatridge, Z. Leghtas, K. M. Sliwa, E. Zalys-Geller, S. O. Mundhada, W. Pfaff, L. Frunzio, R. J. Schoelkopf, and M. H. Devoret, "Robust concurrent remote entanglement between two superconducting qubits," Phys. Rev. X **6**, 031036 (2016).

[41] N. Leung, Y. Lu, S. Chakram, R. K. Naik, N. Earnest, R. Ma, K. Jacobs, A. N. Cleland, and D. I. Schuster, "Deterministic bidirectional communication and remote entanglement generation between superconducting quantum processors," arXiv:1804.02028 (2018).

[42] J. Koch, T. M. Yu, J. Gambetta, A. A. Houck, D. I. Schuster, J. Majer, A. Blais, M. H. Devoret, S. M. Girvin, and R. J. Schoelkopf, "Charge-insensitive qubit design derived from the Cooper pair box," Phys. Rev. A **76**, 042319 (2007).

[43] Y. Yan, Z. Lü, H. Zheng, and Y. Zhao, "Exotic fluorescence spectrum of a superconducting qubit driven simultaneously by longitudinal and transversal fields," Phys. Rev. A **93**, 033812 (2016).

[44] M. Pechal, L. Huthmacher, C. Eichler, S. Zeytinoğlu, A. A. Abdumalikov Jr., S. Berger, A. Wallraff, and S. Filipp, "Microwave-controlled generation of shaped single photons in circuit quantum electrodynamics," Phys. Rev. X **4**, 041010 (2014).

[45] S. Zeytinoğlu, M. Pechal, S. Berger, A. A. Abdumalikov Jr., A. Wallraff, and S. Filipp, "Microwave-induced amplitude- and phase-tunable qubit-resonator coupling in circuit quantum electrodynamics," Phys. Rev. A **91**, 043846 (2015).

[46] G. de Lange, D. Riste, M. J. Tiggelman, C. Eichler, L. Tornberg, G. Johansson, A. Wallraff, R. N. Schouten, and L. DiCarlo, "Reversing quantum trajectories with analog feedback," Phys. Rev. Lett. **112**, 080501– (2014).

[47] M. Jerger, P. Macha, A. R. Hamann, Y. Reshitnyk, K. Juliusson, and A. Fedorov, "Realization of a binary-outcome projection measurement of a three-level superconducting quantum system," Phys. Rev. Applied **6**, 014014 (2016).

[48] F. Motzoi, J. M. Gambetta, P. Rebentrost, and F. K. Wilhelm, "Simple pulses for elimination of leakage in weakly nonlinear qubits," Phys. Rev. Lett. **103**, 110501 (2009).

[49] J. M. Gambetta, A. A. Houck, and Alexandre Blais, "Superconducting qubit with Purcell protection and tunable coupling," Phys. Rev. Lett. **106**, 030502 (2011).

[50] P. Magnard, P. Kurpiers, B. Royer, T. Walter, J.-C. Besse, S. Gasparinetti, M. Pechal, J. Heinsoo, S. Storz, A. Blais, and A. Wallraff, "Fast and unconditional all-microwave reset of a superconducting qubit," Phys. Rev. Lett. **121**, 060502 (2018).

[51] D.J. Egger, M. Werninghaus, M. Ganzhorn, G. Salis, A. Fuhrer, P. Müller, and S. Filipp, "Pulsed reset protocol for fixed-frequency superconducting qubits," Phys. Rev. Applied **10**, 044030 (2018).

[52] S. J. van Enk, N. Lütkenhaus, and H. J. Kimble, "Experimental procedures for entanglement verification," Phys. Rev. A **75**, 052318 (2007).

[53] C. Eichler, Y. Salathe, J. Mlynek, S. Schmidt, and A. Wallraff, "Quantum-limited amplification and entanglement in coupled nonlinear resonators," Phys. Rev. Lett. **113**, 110502 (2014).

[54] M. Steffen, M. Ansmann, R. C. Bialczak, N. Katz, E. Lucero, R. McDermott, M. Neeley, E. M. Weig, A. N. Cleland, and J. M. Martinis, "Measurement of the entanglement of two superconducting qubits via state tomography," Science **313**, 1423–1425 (2006).

[55] H. P. Breuer and F. Petruccione, *The theory of open quantum systems* (Oxford University Press, 2002).

[56] T. Walter, P. Kurpiers, S. Gasparinetti, P. Magnard, A. Potočnik, Y. Salathé, M. Pechal, M. Mondal, M. Oppliger, C. Eichler, and A. Wallraff, "Rapid, high-fidelity, single-shot dispersive readout of superconducting qubits," Phys. Rev. Applied **7**, 054020 (2017).

[57] J. A. Smolin, J. M. Gambetta, and G. Smith, "Efficient method for computing the maximum-likelihood quantum state from measurements with additive gaussian noise," Phys. Rev. Lett. **108**, 070502 (2012).

5.3.3 Précisions sur l'article

Pour le premier article (encodage de Fock), la probabilité d'effectuer avec succès le transfert d'un photon a été mesurée à $P_{\mathrm{e}}^{\mathrm{sat}} = 67,5\%$. Pour le transfert d'état avec l'encodage temporel, cette probabilité est un peu plus faible, $P_{\mathrm{suc}}^{\mathrm{qst}} = 64,6\%$. Cette différence peut être expliquée par le fait qu'en pratique, les échantillons utilisés pour les deux protocoles sont différents. Finalement, pour le protocole d'intrication avec l'encodage temporel, la probabilité de succès est encore plus faible, $P_{\mathrm{suc}}^{\mathrm{ent}} = 61,5\%$. La différence avec le protocole de transfert d'état est qu'ici la mesure est conditionnée sur la mesure des deux qubits dans le sous-espace de calcul $\{|g\rangle, |e\rangle\}$, rejetant les données lorsqu'un des deux qubits est mesuré l'état $|f\rangle$.

5.4 Initialisation de qubits

Malgré que l'article suivant ne traite pas d'intrication à distance, j'ai choisi de l'inclure dans ce chapitre car le montage expérimental est similaire aux deux expériences précédentes. En résumé, on choisit ici d'interpréter le couplage f0g1 non pas comme un processus émettant un photon, mais comme un mécanisme retirant deux excitations du transmon.

5.4.1 Contexte

Pour réaliser un calcul quantique, il est crucial de connaître précisément l'état initial des qubits. De plus, plusieurs protocoles de correction d'erreur nécessitent l'utilisation de qubits ancillaires qui doivent constamment être réinitialisés dans leur état fondamental. Par conséquent, l'initialisation de qubits est un élément important de l'ordinateur quantique. Le protocole d'initialisation présenté dans le prochain article tire avantage du couplage f0g1 et fonctionne de la manière suivante. Le transmon est piloté par deux ondes, une à la fréquence f0g1 et l'autre à la fréquence entre les états $|e\rangle$ et $|f\rangle$ (voir figure 5.6). Ainsi, une excitation initialement dans l'état $|e0\rangle$ est transférée à l'état $|f0\rangle$, puis à l'état $|g1\rangle$. La relaxation naturelle du résonateur ramène ensuite le système vers son état fondamental, $|g0\rangle$. On peut interpréter la

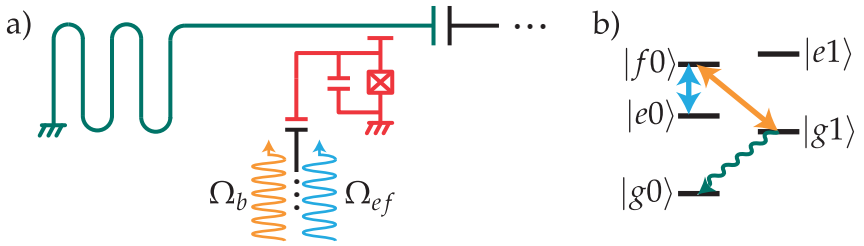

FIGURE 5.6 – a) Circuit pour l'initialisation de qubit. Le qubit est piloté par deux ondes, une à la fréquence ω_{f0g1} (orange) et une à la fréquence ω_{ef} (bleu). b) Niveaux d'énergie du système transmon-résonateur. Lorsque le transmon est initialement dans son état excité $|e\rangle$, les pilotages (bleu et orange) combinés à la dissipation du résonateur (ligne ondulée verte) ramènent le transmon vers son état fondamental, $|e0\rangle \rightarrow |f0\rangle \rightarrow |g1\rangle \rightarrow |g0\rangle$.

combinaison des pilotages $f0g1$ et ef comme un couplage vers un bain à température nulle qui refroidit naturellement le transmon vers son état fondamental.

Un avantage de ce protocole est qu'il est passif, c'est-à-dire ne requiert pas l'application d'une impulsion de rétroaction sur le système basée sur le résultat d'une mesure. L'absence de rétroaction simplifie le montage expérimental, mais surtout la réinitialisation du transmon n'est pas limitée par la fidélité de la mesure. Un autre avantage de cette méthode est le niveau $|f\rangle$ qui est lui aussi réinitialisé par cette méthode, rendant ce protocole plus robuste contre la fuite vers les niveaux supérieurs.

Le montage expérimental de cette expérience correspond au nœud émetteur pour les deux articles précédents [1]. Dans ce montage, le transmon est couplé à deux résonateurs, un pour la mesure et un pour la réinitialisation. Il est important de souligner qu'un seul de ces résonateurs est nécessaire à la réinitialisation du transmon.

1. De manière équivalente, le nœud récepteur aurait pu être utilisé. Le nœud émetteur a été choisi pour le meilleur temps de cohérence du transmon.

5.4.2 Article

Comme dans les deux articles précédents, j'ai réalisé les simulations d'équation maîtresse pour cette expérience. J'ai aussi participé à la rédaction du manuscrit.

P. Magnard, P. Kurpiers, B. Royer, T. Walter, J.-C. Besse, S. Gasparinetti, M. Pechal, J. Heinsoo, S. Storz, A. Blais et A. Wallraff. Fast and unconditional all-microwave reset of a superconducting qubit. *Phys. Rev. Lett.* **121**, 060502 (2018)

Fast and Unconditional All-Microwave Reset of a Superconducting Qubit

P. Magnard,[1,*] P. Kurpiers,[1] B. Royer,[2] T. Walter,[1] J.-C. Besse,[1] S. Gasparinetti,[1] M. Pechal,[1] J. Heinsoo,[1] S. Storz,[1] A. Blais,[2,3] and A. Wallraff[1]

[1]*Department of Physics, ETH Zürich, CH-8093 Zürich, Switzerland*

[2]*Institut Quantique and Département de Physique, Université de Sherbrooke, Sherbrooke, Québec J1K 2R1, Canada*

[3]*Canadian Institute for Advanced Research, Toronto, Ontario M5G IZ8, Canada*

(Received 17 April 2018; published 7 August 2018)

Active qubit reset is a key operation in many quantum algorithms, and particularly in quantum error correction. Here, we experimentally demonstrate a reset scheme for a three-level transmon artificial atom coupled to a large bandwidth resonator. The reset protocol uses a microwave-induced interaction between the $|f,0\rangle$ and $|g,1\rangle$ states of the coupled transmon-resonator system, with $|g\rangle$ and $|f\rangle$ denoting the ground and second excited states of the transmon, and $|0\rangle$ and $|1\rangle$ the photon Fock states of the resonator. We characterize the reset process and demonstrate reinitialization of the transmon-resonator system to its ground state in less than 500 ns and with 0.2% residual excitation. Our protocol is of practical interest as it has no additional architectural requirements beyond those needed for fast and efficient single-shot readout of transmons, and does not require feedback.

DOI: 10.1103/PhysRevLett.121.060502

The efficient initialization of a set of qubits into their ground state is one of the DiVincenzo criteria for quantum information processing [1]. Initialization is also critical for the implementation of error correction codes [2–4] to reset ancilla qubits on demand to a fiducial state in short time and with high fidelity. For this reason, qubit reset procedures have been implemented for a wide range of physical quantum computation platforms [5–9], including superconducting qubits for which we discuss the most common approaches below [10–19].

Reset for superconducting qubits is commonly realized using the outcome of a strong projective measurement to either herald the ground state [13] or deterministically prepare it using feedback [14–17]. Measurement-induced state mixing limits the achievable single-shot readout fidelity and the performance of this approach [16,20,21]. In addition, measurement-induced mixing constrains the quantum-nondemolition nature of dispersive readout giving rise to leakage out of the qubit subspace [16,22], which is particularly detrimental to quantum error correction [23].

Alternatively, qubit reset can be achieved by coupling the qubit excited state to a cold and rapidly decaying quantum system. Such driven reset schemes [10,11,18,24,25] make use of ideas related to dissipation engineering [26–29]. In one variant of this approach [11], the qubit is quickly tuned into resonance with a Purcell filtered, large-bandwidth, resonator using magnetic flux. The qubit then quickly thermalizes to its ground state due to Purcell decay, the rate of which can be adjusted, on-demand, by 3 orders of magnitude. The flux pulses employed in this scheme require careful calibration, they may affect subsequent gates by bleedthrough and neighboring qubits through cross talk [30].

An all-microwave reset protocol utilizing the qubit-state-dependent response of a resonator [18] avoids the use of flux tuning and its potentially detrimental effects. This protocol [18] has minimal hardware requirements, only a single resonator, but requires a cavity linewidth κ smaller than the dispersive interaction strength χ limiting both the speed of the reset process and the readout if the same resonator is used [31,32].

In this work, we demonstrate an alternative all-microwave reset protocol of a three-level transmon coupled to a resonator with no constraint on κ. Driving the transmon simultaneously with two coherent tones forms a Λ system in the Jaynes-Cumming ladder [33] and unconditionally transfers any excitation in the two lowest excited states of the transmon to a single photon emitted to the environment, thus resetting the transmon qutrit on demand. This protocol outperforms existing measurement-based and all-microwave driven reset schemes in speed and fidelity [34], populates the resonator with one photon at most, and can be extended to other types of superconducting qubits. In addition, this protocol is of practical interest as it is optimized when the resonator is designed for rapid and high-fidelity transmon readout [32].

The device used in our experiment and schematically illustrated in Fig. 1(a), uses a transmon qubit [35,36] (orange), with transition frequency $\omega_{ge}/2\pi = 6.343$ GHz, anharmonicity $\alpha/2\pi = -265$ MHz and energy relaxation time $T_1 = 5.5$ μs. We control the qubit state with microwave pulses up-converted from an arbitrary waveform

generator (AWG), applied to the transmon through a dedicated drive line. To perform the reset, the transmon is capacitively coupled with rate $g_r/2\pi = 335$ MHz to a resonator of frequency $\omega_r/2\pi = 8.400$ GHz, resulting in a dispersive interaction with rate $\chi_r/2\pi = -6.3$ MHz (light blue). The reset resonator is connected through a Purcell-filter resonator to cold 50 Ω loads with an effective coupling $\kappa/2\pi = 9$ MHz. This resonator can, in principle, be used for transmon readout. However, in the present work, to decouple the reset from its characterization process, we read out the transmon with a dedicated, Purcell-filtered resonator (light green). We present further details about the sample in the Supplemental Material [34].

We read out the transmon state using a gated drive applied to the input port of the readout resonator at a frequency optimized for qutrit readout [37]. The signal scattered off the readout resonator is amplified at $T_{\mathrm{BT}} = 10$ mK by a Josephson parametric amplifier [38,39]. The signal is then amplified at 4 K with high electron mobility transistors, down-converted using an I-Q mixer, digitized using an analog-to-digital converter, digitally down-converted and processed using a field programmable gate array.

The reset concept, illustrated in Fig. 1(b), is based on a cavity-assisted Raman transition between $|f,0\rangle$ and $|g,1\rangle$ [33,40,41]. Here, $|s,n\rangle$ denotes the tensor product of the transmon in state $|s\rangle$, with its three lowest energy eigenstates $|g\rangle$, $|e\rangle$, and $|f\rangle$, and the reset resonator in the n photon Fock state $|n\rangle$. By simultaneously driving the $|f,0\rangle \leftrightarrow |g,1\rangle$ ($f0$-$g1$) transition and the $|e,0\rangle \leftrightarrow |f,0\rangle$ (e-f) transition, the population is transferred from the qutrit excited states, $|e,0\rangle$ and $|f,0\rangle$, to the state $|g,1\rangle$. The system then rapidly decays to the target dark state $|g,0\rangle$ by photon emission at rate κ, effectively resetting the qutrit to its ground state.

We model the dynamics of the reset by the non-Hermitian Hamiltonian

$$H/\hbar = \begin{bmatrix} -\delta_{ef} & \Omega_{ef} & 0 \\ \Omega_{ef}^{*} & 0 & \tilde{g} \\ 0 & \tilde{g}^{*} & -\delta_{f0g1} - i\kappa/2 \end{bmatrix}, \qquad (1)$$

acting on the states $|e,0\rangle$, $|f,0\rangle$, and $|g,1\rangle$. Here, the non-Hermitian term $-i\kappa/2$ accounts for the photon emission process, and Ω_{ef} and $\tilde{g}$ are the e-f and $f0$-$g1$ drive-induced Rabi rates, respectively. Because the $f0$-$g1$ drive acts on a second order transition, it requires a high amplitude V_{f0g1} and induces significant ac Stark shifts $\bar{\Delta}_{ef}$ and $\bar{\Delta}_{f0g1}$ of the e-f and $f0$-$g1$ transitions [40]. In Hamiltonian (1), δ_{ef} and δ_{f0g1} denote the detuning of the drives from their respective ac Stark shifted transitions. Therefore, gaining experimental control over the reset drive parameters requires us to characterize the dependence of $\bar{\Delta}_{ef}$ and $\bar{\Delta}_{f0g1}$ on V_{f0g1} as well as the relation between the drive amplitudes and their corresponding Rabi rates.

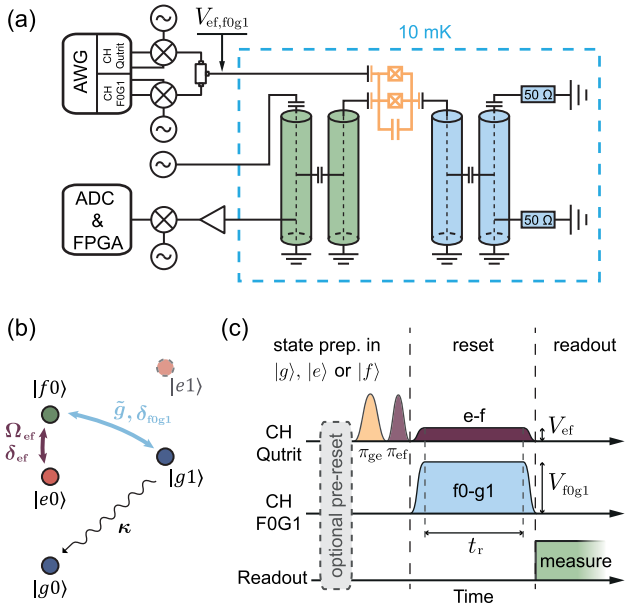

FIG. 1. (a) Simplified schematic of the experimental setup. A transmon (orange) is coupled to two Purcell-filtered resonators. The readout resonator (green) is connected to room temperature electronics (description in the main text), while the reset resonator (blue) is connected to two 50 Ω loads thermalized at base temperature. (b) Jaynes-Cummings ladder diagram of the transmon-reset resonator energy levels. The purple and light blue arrows represent the e-f and $f0$-$g1$ pulsed coherent drives, respectively, and the black arrow labeled κ illustrates the resonator decay process. (c) Illustration of the pulse schemes used to test the reset protocol. We initialize the qutrit to its ground state passively or optionally with an unconditional reset, then prepare the desired state $|g\rangle$, $|e\rangle$, or $|f\rangle$ with control pulses (labeled π_{ge} and π_{ef}). We reset the qutrit by simultaneously applying flattop e-f (purple) and $f0$-$g1$ (light blue) pulses for a reset time t_r. The resulting qutrit state is then measured by applying a microwave tone to the readout resonator (green).

First, we determine the ac Stark shift $\bar{\Delta}_{f0g1}$. We initialize the transmon in $|g\rangle$, then apply a sequence of two π pulses (π_{ge}, π_{ef}) to prepare the system in $|f,0\rangle$ [Fig. 1(c)]. We apply a flattop $f0$-$g1$ pulse of carrier frequency ν_{f0g1}, amplitude V_{f0g1} and duration t_r and read out the resulting transmon state populations. Here and in all calibration measurements, the populations $P_{g,e,f}$ of the transmon qutrit are extracted by comparing the averaged signal transmitted through the readout resonator to reference traces [37]. We repeat the process varying ν_{f0g1} and V_{f0g1}, while keeping $V_{f0g1}t_r$ fixed to obtain comparable Rabi angles for the rotations induced by the $f0$-$g1$ drive. For a given value of V_{f0g1}, we fit the dependence of P_g on ν_{f0g1} to a Gaussian whose center yields the ac Stark shifted frequency, at which the population transfer from $|f,0\rangle$ to $|g,1\rangle$ is maximized [Fig. 2(a)]. The ac Stark shift $\bar{\Delta}_{f0g1}$ extracted in this way shows a quadratic dependence on V_{f0g1} [blue diamonds in Fig. 2(b)].

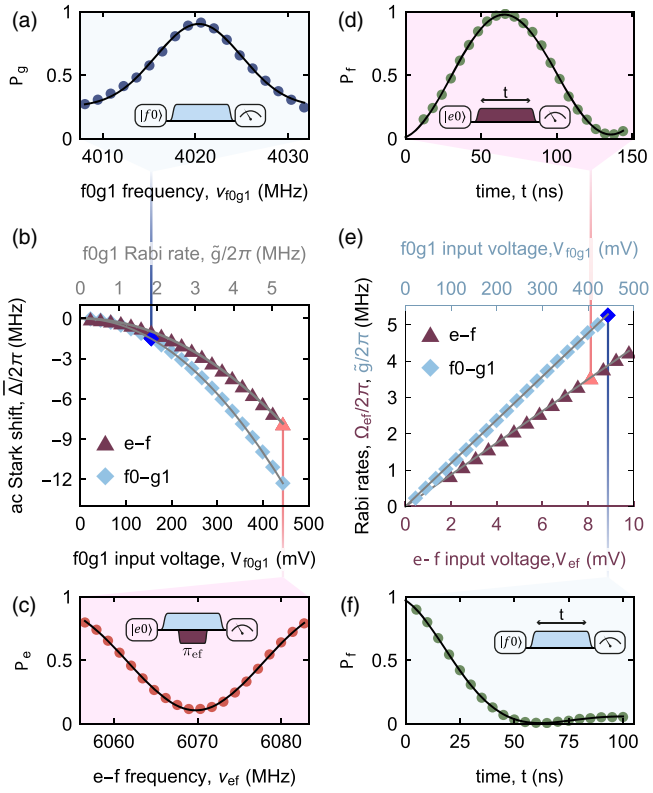

FIG. 2. (a) Population P_g vs the frequency ν_{f0g1} of a flattop $f0$-$g1$ pulse, of amplitude V_{f0g1}, applied to the qutrit initially prepared in $|f,0\rangle$. (b) Measured ac Stark shifts $\bar{\Delta}_{f0g1}$ and $\bar{\Delta}_{ef}$ of the $f0$-$g1$ (blue diamonds) and e-f (purple triangles) transitions, vs amplitude V_{f0g1} of the f0-g1 drive. The solid lines are quadratic fits to the data. (c) Population P_e vs frequency ν_{ef} of a flattop e-f π pulse applied on the qutrit, initially prepared in state $|e,0\rangle$, in the presence of a continuous $f0$-$g1$ drive of amplitude V_{f0g1}. (d) Population P_f vs duration t of a resonant flattop e-f pulse, of amplitude $V_{ef} = 8$ mV. (e) Extracted Rabi rates Ω_{ef} and $\tilde{g}$, of the e-f (purple triangles) and $f0$-$g1$ (blue diamonds) drives versus their amplitude, V_{ef} and V_{f0g1}. The solid lines are linear fits. (f) Population P_f vs duration t of a resonant square $f0$-$g1$ pulse, of amplitude $V_{f0g1} = 444$ mV. The pulse schemes used to acquire the data shown in panels (a), (c), (d), and (f) are shown as insets, with the $f0$-$g1$ and e-f pulse envelopes represented in blue and purple, respectively. The solid lines in (a) and (c) are fits to Gaussians. The solid lines in (c) and (f) are fits to Rabi oscillation models described in Ref. [34].

To determine $\bar{\Delta}_{ef}$, we prepare the system in $|e,0\rangle$ and apply a short square e-f π pulse of frequency ν_{ef} in the presence of a continuous, resonant f0-g1 drive of amplitude V_{f0g1}. For each V_{f0g1}, we extract the ac Stark shifted frequency of the e-f transition by finding the minimum of P_e vs ν_{ef} with a fit to a Gaussian [Fig. 2(c)]. As before, we observe a quadratic dependence of $\bar{\Delta}_{ef}$ on V_{f0g1} [purple triangles in Fig. 2(b)].

Finally, we perform resonant Rabi oscillation measurements on the e-f and $f0$-$g1$ transitions to extract the linear relation between the drive amplitudes V_{ef} and V_{f0g1}, and their corresponding Rabi rates [34] [Figs. 2(d)–2(f)]. The Rabi oscillations between $|f,0\rangle$ and $|g,1\rangle$ are damped due to the spontaneous decay from $|g,1\rangle$ to $|g,0\rangle$ [Fig. 2(f)].

In all the following experiments, we adjust the drive frequencies such that $\delta_{ef} = \delta_{f0g1} = 0$ to reset the transmon, leaving only $\tilde{g}$ and Ω_{ef} as tunable parameters. From Eq. (1), we derive the time dependence of the population

$$P^H_{s|s_0}(t) = \left|\sum\nolimits_k \langle s|\hat{A}_k|s_0\rangle e^{-i\lambda_k t}\right|^2 \tag{2}$$

of state $|s\rangle \in \{|e,0\rangle, |f,0\rangle, |g,1\rangle\}$ during the reset. Here, $|s_0\rangle$ is the initial state of the system, λ_k are the eigenvalues of Hamiltonian (1) and $\hat{A}_k$ are operators that depend only on Hamiltonian (1) [34]. These populations oscillate at rates $2\mathrm{Re}(\lambda_k)$ and decay exponentially at rates $2|\mathrm{Im}(\lambda_k)|$. As the smallest decay rate dominates at long reset times, we define the reset rate as $\Gamma \equiv \min[2|\mathrm{Im}(\lambda_k)|]$. The reset can be operated in two regimes [34]. In the low drive-power region hatched in Fig. 3(a), the eigenvalues λ_k are purely imaginary: the reset is in an overdamped regime where the qutrit excited populations decay with no oscillation. When crossing the critical damping boundary, two eigenvalues abruptly display a finite real part and the reset enters an underdamped, oscillatory regime. The reset rate Γ is bounded by its maximum value $\kappa/3$, which it reaches on a line in parameter space, defining an optimal branch (solid red line in Fig. 3). The optimal branch intersects the critical-damping boundary at an exceptional point (black cross in Fig. 3) where all three eigenvalues are identical [42]. At this point, the reset has maximum rate and displays no oscillations. For a given $\tilde{g}$, there is a unique value of Ω_{ef} maximizing the reset rate to $\Gamma_{\max}(\tilde{g})$. The parameter configuration then lies on the critical-damping boundary if $\tilde{g}$ is below its value at the exceptional point

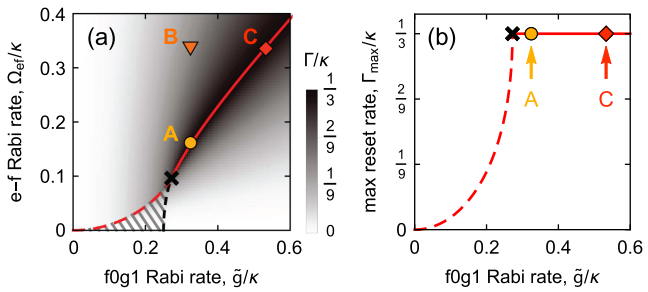

FIG. 3. (a) Calculated reset rate Γ/κ, vs Rabi rates $\tilde{g}/\kappa$ and Ω_{ef}/κ. The overdamped parameter region is hatched. The red line shows the values of Ω_{ef} maximizing Γ as a function of $\tilde{g}$, and corresponds to the optimal branch where it is solid. (b) Maximized reset rate $\Gamma_{\max}/\kappa$ vs $\tilde{g}/\kappa$ [we follow the red line from (a)]. In (a) and (b), the parameter configurations A, B, and C at which the reset dynamic was probed (see main text and Fig. 4) are indicated with colored symbols and the exceptional point is represented by a black cross.

$\tilde{g}_{\rm ep} = \sqrt{2/27}\kappa$ (red dashed line in Fig. 3), and on the optimal branch otherwise. As $\tilde{g}$ goes below $\tilde{g}_{\rm ep}$, $\Gamma_{\rm max}(\tilde{g})$ abruptly drops [Fig. 3(b)]. Therefore, the ability to drive the $f0$-$g1$ transition with $\tilde{g} > \tilde{g}_{\rm ep}$ is crucial to achieve fast reset.

We probed the reset dynamics at the three parameter configurations labeled A, B, and C in Fig. 3(a). We initialize the transmon in $|e,0\rangle$ or $|f,0\rangle$, apply the reset drive pulses for a time t_r, and then readout the transmon with single-shot measurements, as illustrated in Fig. 1(c). Utilizing the single-shot statistics, we correct for the qutrit state assignment errors, to determine the population of the qutrit with systematic errors below 0.3% [34]. We first probed the reset in configuration A ($\Omega_{ef}/2\pi = 1.5$ MHz, $\tilde{g}/2\pi = 2.9$ MHz), which is on the optimal branch and is the closest to the exceptional point. During the reset, the transmon state oscillates between $|g\rangle$, $|e\rangle$, and $|f\rangle$ while rapidly decaying to $|g\rangle$ on a timescale of 300 ns, independent of the initial state [Figs. 4(a) and 4(b)]. The excited population $P_{\rm exc} = P_e + P_f$ drops to below 1% without displaying any oscillations [Fig. 4(c)]. The reset dynamics calculated from Eq. (2) is in excellent agreement with the data, as shown by the solid lines in Figs. 4(a) and 4(b). When increasing the e-f drive to $\Omega_{ef}/2\pi = 3$ MHz (B), the decaying state $|g,1\rangle$ is populated earlier. As a result, we observe that $P_{\rm exc}$ drops faster initially but at a slower rate at longer times since configuration B is not on the optimal branch [Fig. 4(c)]. Because this parameter set realizes the underdamped regime, $P_{\rm exc}$ displays oscillatory features. Configuration C ($\Omega_{ef}/2\pi = 3$ MHz, $\tilde{g}/2\pi = 4.8$ MHz) is on the optimal branch and has higher drive rates than configuration A. Therefore, $P_{\rm exc}$ drops faster initially, and with the same long-time rate, leading to a more efficient reset. In this configuration, $P_{\rm exc}$ drops below 1% in only 280 ns, and below measurement errors (~0.3%) in steady state [Fig. 4(c)], outperforming all existing measurement-based and microwave-driven reset schemes by an order of magnitude [34].

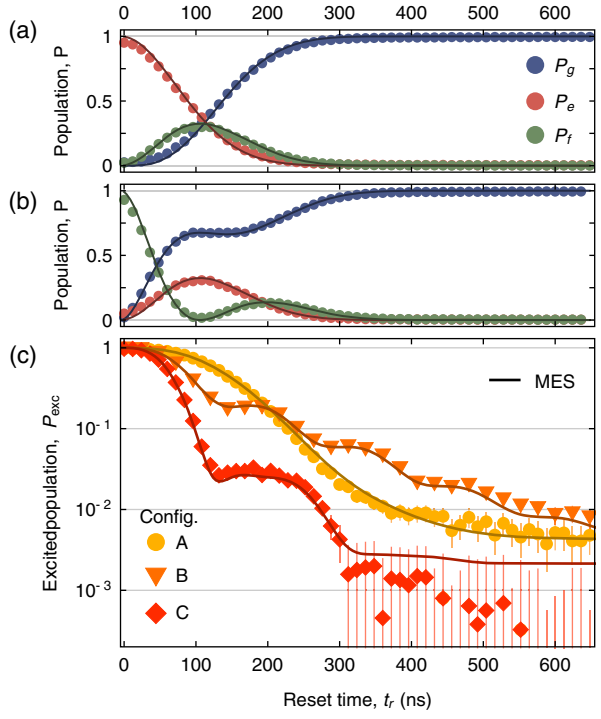

FIG. 4. Qutrit populations $P_{g,e,f}$ vs reset time t_r with reset parameters in configuration A (see main text), and (a) system initialized in $|e,0\rangle$ or (b) in $|f,0\rangle$. The solid lines in (a) and (b) are calculated from Eq. (2). (c) Excited population $P_{\rm exc}$ as a function of reset time t_r, when the qutrit is initialized in $|e,0\rangle$, shown for reset parameter configurations A, B, and C. The solid lines are calculated from a master equation simulation.

At long reset times, $P_{\rm exc}$ saturates to a nonzero steady-state value $P_{\rm exc}^{\rm sat}$ because of transmon rethermalization. To fully capture the role of decoherence and rethermalization during the reset, we perform master equation simulations using only parameters extracted from independent measurements [34]. The numerical simulations are in excellent agreement with the data for all probed reset parameter configurations [solid lines in Fig. 4(c)] and yield $P_{\rm exc}^{\rm sat} = 0.2\%$ for configuration C, suggesting that the $P_{\rm exc}^{\rm sat}$ achievable in our experiment is limited by transmon rethermalization. In this case, the excited population saturates at $P_{\rm exc}^{\rm sat} = k_\uparrow \tau$, where $k_\uparrow \simeq n_{\rm th}/T_1$ is the rethermalization rate, with $n_{\rm th}$ the excited population at thermal equilibrium, and $\tau = \int_0^\infty [P_{e|e}^H + P_{f|e}^H](t)dt$ [34]. Therefore, faster drops of $P_{\rm exc}$, obtained by increasing the drive rates along the optimal branch, result in lower steady-state excited populations [Fig. 4(c)]. Other limitations, such as residual driving of the g-e transition by the e-f drive, and finite temperature of the resonator, are negligible for the presented parameters [34].

High transmon anharmonicity α combined with large transmon-resonator coupling g allows for reaching larger Ω_{ef} and $\tilde{g}$ without driving unwanted transitions [40]. Driving the reset at higher Rabi rates, we can reach the optimal branch, where $\Gamma = \kappa/3$, for larger values of κ. As a result, increasing g, α, and κ maximizes Γ and optimizes the reset. Increasing these parameters also optimizes speed and fidelity of qubit readout without degrading the coherence and thermalization of the qubit, if Purcell filters are used [32,34]. Therefore, our reset protocol performs best with a resonator designed for optimal readout. As an illustration, using the results of the present work, we calculate that implementing this reset protocol with the readout resonator of Ref. [32] would reset the qutrit below $P_{\rm exc} = 0.1\%$ in 83 ns, and to a steady-state value $P_{\rm exc}^{\rm sat} = 1.6 \times 10^{-4}$ in 200 ns, provided that the $f0$-$g1$ Rabi rate exceeds $\sqrt{2/27}\kappa \simeq 2\pi \times 10$ MHz.

In conclusion, we have demonstrated an unconditional all-microwave protocol to reset the state of a three-level transmon below 1% excitation in less than 280 ns. This reset

scheme does neither require feedback, nor qubit tunability, not does it constrain device parameters or populate the readout resonator with a large number of photons. Furthermore, the protocol can conveniently be integrated in an architecture where the qubits are coupled to high bandwidth, Purcell-filtered resonators, in order to perform rapid and high-fidelity quantum manipulations [43] and readout [32,44]. However, in a multiqubit system, the protocol's need for high $f0$-$g1$ drive power increases the sensitivity to cross talk and can cause spurious driving of two-qubit transitions. Addressing these concerns in scaled up circuits will require improved shielding of drive lines, and careful selection of resonator and qubit frequencies. We did not observe any degradation of qubit coherence and operation fidelity in the presence of the reset drive tones [43], but a systematic study of these effects constitutes valuable future work.

We thank Christian Kraglund Andersen for helpful discussions. This work is supported by the European Research Council (ERC) through the "Superconducting Quantum Networks" (SuperQuNet) project, by National Centre of Competence in Research "Quantum Science and Technology" (NCCR QSIT), a research instrument of the Swiss National Science Foundation (SNSF), by the Office of the Director of National Intelligence (ODNI), Intelligence Advanced Research Projects Activity (IARPA), via the U.S. Army Research Office Grant No. W911NF-16-1-0071, NSERC, the Canada First Research Excellence Fund and the Vanier Canada Graduate Scholarships and by ETH Zurich. The views and conclusions contained herein are those of the authors and should not be interpreted as necessarily representing the official policies or endorsements, either expressed or implied, of the ODNI, IARPA, or the U.S. Government. The U.S. Government is authorized to reproduce and distribute reprints for Governmental purposes notwithstanding any copyright annotation thereon.

*Corresponding author.
pmagnard@phys.ethz.ch

[1] D. P. DiVincenzo, Fortschr. Phys. **48**, 771 (2000).
[2] P. Schindler, J. T. Barreiro, T. Monz, V. Nebendahl, D. Nigg, M. Chwalla, M. Hennrich, and R. Blatt, Science **332**, 1059 (2011).
[3] M. D. Reed, L. DiCarlo, S. E. Nigg, L. Sun, L. Frunzio, S. M. Girvin, and R. J. Schoelkopf, Nature (London) **482**, 382 (2012).
[4] J. Chiaverini, D. Leibfried, T. Schaetz, M. Barrett, R. Blakestad, J. Britton, W. Itano, J. Jost, E. Knill, C. Langer, R. Ozeri, and D. Wineland, Nature (London) **432**, 602 (2004).
[5] C. Monroe, D. M. Meekhof, B. E. King, S. R. Jefferts, W. M. Itano, D. J. Wineland, and P. Gould, Phys. Rev. Lett. **75**, 4011 (1995).
[6] F. Jelezko, T. Gaebel, I. Popa, A. Gruber, and J. Wrachtrup, Phys. Rev. Lett. **92**, 076401 (2004).
[7] J. M. Elzerman, R. Hanson, L. H. W. van Beveren, L. M. K. Vandersypen, and L. P. Kouwenhoven, Nature (London) **430**, 431 (2004).
[8] M. V. G. Dutt, L. Childress, L. Jiang, E. Togan, J. Maze, F. Jelezko, A. S. Zibrov, P. R. Hemmer, and M. D. Lukin, Science **316**, 1312 (2007).
[9] L. J. Rogers, K. D. Jahnke, M. H. Metsch, A. Sipahigil, J. M. Binder, T. Teraji, H. Sumiya, J. Isoya, M. D. Lukin, P. Hemmer, and F. Jelezko, Phys. Rev. Lett. **113**, 263602 (2014).
[10] S. O. Valenzuela, W. D. Oliver, D. M. Berns, K. K. Berggren, L. S. Levitov, and T. P. Orlando, Science **314**, 1589 (2006).
[11] M. D. Reed, B. R. Johnson, A. A. Houck, L. DiCarlo, J. M. Chow, D. I. Schuster, L. Frunzio, and R. J. Schoelkopf, Appl. Phys. Lett. **96**, 203110 (2010).
[12] M. Mariantoni, H. Wang, T. Yamamoto, M. Neeley, R. C. Bialczak, Y. Chen, M. Lenander, E. Lucero, A. D. O'Connell, D. Sank, M. Weides, J. Wenner, Y. Yin, J. Zhao, A. N. Korotkov, A. N. Cleland, and J. M. Martinis, Science **334**, 61 (2011).
[13] J. E. Johnson, C. Macklin, D. H. Slichter, R. Vijay, E. B. Weingarten, J. Clarke, and I. Siddiqi, Phys. Rev. Lett. **109**, 050506 (2012).
[14] D. Ristè, J. G. van Leeuwen, H.-S. Ku, K. W. Lehnert, and L. DiCarlo, Phys. Rev. Lett. **109**, 050507 (2012).
[15] D. Ristè, C. C. Bultink, K. W. Lehnert, and L. DiCarlo, Phys. Rev. Lett. **109**, 240502 (2012).
[16] P. Campagne-Ibarcq, E. Flurin, N. Roch, D. Darson, P. Morfin, M. Mirrahimi, M. H. Devoret, F. Mallet, and B. Huard, Phys. Rev. X **3**, 021008 (2013).
[17] Y. Salathé, P. Kurpiers, T. Karg, C. Lang, C. K. Andersen, A. Akin, S. Krinner, C. Eichler, and A. Wallraff, Phys. Rev. Applied **9**, 034011 (2018).
[18] K. Geerlings, Z. Leghtas, I. M. Pop, S. Shankar, L. Frunzio, R. J. Schoelkopf, M. Mirrahimi, and M. H. Devoret, Phys. Rev. Lett. **110**, 120501 (2013).
[19] D. J. Egger, M. Ganzhorn, G. Salis, A. Fuhrer, P. Mueller, and S. Filipp, arXiv:1802.08980.
[20] M. Boissonneault, J. M. Gambetta, and A. Blais, Phys. Rev. A **79**, 013819 (2009).
[21] D. H. Slichter, R. Vijay, S. J. Weber, S. Boutin, M. Boissonneault, J. M. Gambetta, A. Blais, and I. Siddiqi, Phys. Rev. Lett. **109**, 153601 (2012).
[22] D. Sank, Z. Chen, M. Khezri, J. Kelly, R. Barends, B. Campbell, Y. Chen, B. Chiaro, A. Dunsworth, A. Fowler *et al.*, Phys. Rev. Lett. **117**, 190503 (2016).
[23] A. G. Fowler, Phys. Rev. A **88**, 042308 (2013).
[24] M. Grajcar, S. H. W. van der Ploeg, A. Izmalkov, E. Il'ichev, H.-G. Meyer, A. Fedorov, A. Shnirman, and G. Schön, Nat. Phys. **4**, 612 (2008).
[25] D. Basilewitsch, R. Schmidt, D. Sugny, S. Maniscalco, and C. P. Koch, New J. Phys. **19**, 113042 (2017).
[26] K. W. Murch, U. Vool, D. Zhou, S. J. Weber, S. M. Girvin, and I. Siddiqi, Phys. Rev. Lett. **109**, 183602 (2012).
[27] S. P. Premaratne, F. C. Wellstood, and B. S. Palmer, Phys. Rev. A **96**, 043858 (2017).
[28] K. Y. Tan, M. Partanen, R. E. Lake, J. Govenius, S. Masuda, and M. Möttönen, Nat. Commun. **8**, 15189 (2017).

[29] Y. Liu, S. Shankar, N. Ofek, M. Hatridge, A. Narla, K. M. Sliwa, L. Frunzio, R. J. Schoelkopf, and M. H. Devoret, Phys. Rev. X **6**, 011022 (2016).
[30] J. Kelly, R. Barends, B. Campbell, Y. Chen, Z. Chen, B. Chiaro, A. Dunsworth, A. G. Fowler, I.-C. Hoi, E. Jeffrey, A. Megrant, J. Mutus, C. Neill, P. J. J. O'Malley, C. Quintana, P. Roushan, D. Sank, A. Vainsencher, J. Wenner, T. C. White *et al.*, Phys. Rev. Lett. **112**, 240504 (2014).
[31] J. Gambetta, W. A. Braff, A. Wallraff, S. M. Girvin, and R. J. Schoelkopf, Phys. Rev. A **76**, 012325 (2007).
[32] T. Walter, P. Kurpiers, S. Gasparinetti, P. Magnard, A. Potocnik, Y. Salathé, M. Pechal, M. Mondal, M. Oppliger, C. Eichler, and A. Wallraff, Phys. Rev. Applied **7**, 054020 (2017).
[33] M. Pechal, L. Huthmacher, C. Eichler, S. Zeytinoğlu, A. A. Abdumalikov Jr., S. Berger, A. Wallraff, and S. Filipp, Phys. Rev. X **4**, 041010 (2014).
[34] See Supplemental Material at http://link.aps.org/supplemental/10.1103/PhysRevLett.121.060502 for an overview and comparison to prior art, for details about the sample fabrication and parameters, for details about the fit functions for the calibration procedure, for a derivation of the reset operating regimes, for a description of the readout method, for a discussion of the limitations of the reset, and for a description of the master equation simulations.
[35] J. Koch, T. M. Yu, J. Gambetta, A. A. Houck, D. I. Schuster, J. Majer, A. Blais, M. H. Devoret, S. M. Girvin, and R. J. Schoelkopf, Phys. Rev. A **76**, 042319 (2007).
[36] J. A. Schreier, A. A. Houck, J. Koch, D. I. Schuster, B. R. Johnson, J. M. Chow, J. M. Gambetta, J. Majer, L. Frunzio, M. H. Devoret, S. M. Girvin, and R. J. Schoelkopf, Phys. Rev. B **77**, 180502 (2008).
[37] R. Bianchetti, S. Filipp, M. Baur, J. M. Fink, C. Lang, L. Steffen, M. Boissonneault, A. Blais, and A. Wallraff, Phys. Rev. Lett. **105**, 223601 (2010).
[38] B. Yurke, M. L. Roukes, R. Movshovich, and A. N. Pargellis, Appl. Phys. Lett. **69**, 3078 (1996).
[39] C. Eichler and A. Wallraff, Eur. Phys. J. Quantum Technology **1**, 2 (2014).
[40] S. Zeytinoğlu, M. Pechal, S. Berger, A. A. Abdumalikov Jr., A. Wallraff, and S. Filipp, Phys. Rev. A **91**, 043846 (2015).
[41] S. Gasparinetti, S. Berger, A. A. Abdumalikov, M. Pechal, S. Filipp, and A. J. Wallraff, Sci. Adv. **2**, e1501732 (2016).
[42] W. D. Heiss, J. Phys. A **37**, 2455 (2004).
[43] P. Kurpiers, P. Magnard, T. Walter, B. Royer, M. Pechal, J. Heinsoo, Y. Salathé, A. Akin, S. Storz, J.-C. Besse, S. Gasparinetti, A. Blais, and A. Wallraff, Nature (London) **558**, 264 (2018).
[44] J. Heinsoo, C. K. Andersen, S. K. A. Remm, T. Walter, Y. Salathé, S. Gasparinetti, J.-C. Besse, A. Potočnik, C. Eichler, and A. Wallraff, arXiv:1801.07904.

Chapitre 6

Conclusion

Dans cette thèse, j'ai présenté mes travaux de doctorat organisés en trois chapitres. Tout d'abord, j'ai décrit mes travaux sur la détection de photons micro-ondes uniques (chapitre 3), où je propose deux concepts de détecteurs promettant une grande efficacité et ne détruisant pas le photon à détecter. Le premier détecteur (section 3.2) se base sur l'absorption d'un photon dans un ensemble de transmons inhomogènes, alors que le second (section 3.3) se base sur la propagation du photon dans un métamatériau unidimensionnel. Le second détecteur promet une large bande de détection tandis que le premier est plus simple à réaliser. La réalisation expérimentale de ces propositions permettrait d'ajouter une pièce importante dans la boîte à outils de l'optique quantique micro-onde : c'est le défi que nous sommes actuellement en train de relever avec mes collègues du groupe d'Irfan Siddiqi de l'université de Berkeley en Californie.

Ensuite, j'ai introduit une méthode pour effectuer une mesure de parité avec un faible coût expérimental (chapitre 4), une opération essentielle pour les codes de correction d'erreurs quantiques. En utilisant astucieusement un résonateur non linéaire excité à l'aide d'un pilotage à deux photons, j'ai montré comment mesurer directement la parité d'un ensemble de qubits sans induire trop de déphasage dans les sous-espaces de parités pairs et impairs. De plus, j'ai introduit une méthode permettant d'augmenter le nombre de qubits mesurés de deux à quatre. Ces travaux pourraient aider à la réalisation d'un ordinateur quantique universel tolérant aux fautes.

Par la suite, j'ai présenté les travaux que j'ai effectués en collaboration avec le groupe expérimental d'Andreas Wallraff de l'ETH Zürich (chapitre 5). Dans le premier article de cette série (section 5.2), nous avons réalisé le premier transfert déterministe d'état quantique entre deux qubits supraconducteurs distants [1]. Avec le même montage expérimental et une modification mineure au protocole de transfert d'état quantique, nous avons aussi généré des états intriqués entre les deux qubits distants. Le deuxième article (section 5.3) s'attaque à la perte de photons durant le transfert entre les deux qubits. À l'aide d'un code de détection d'erreur basé sur un encodage temporel du photon émis, il est possible de certifier que le transfert du photon a été effectué avec succès et ainsi augmenter la fidélité du transfert d'état quantique ou de l'état intriqué. Ces deux expériences représentent une étape importante vers la réalisation d'une architecture modulaire pour l'ordinateur quantique, où un calcul est effectué sur plusieurs petits processeurs quantiques distincts. Le troisième et dernier article de cette collaboration (section 5.4) introduit une méthode pour initialiser rapidement des transmons dans leur état fondamental. L'avantage de cette méthode est qu'elle ne nécessite pas de rétroaction ni d'impulsion de flux et qu'elle peut être utilisée avec les montages standards d'électrodynamique en circuit.

Plusieurs avenues de recherches en continuation de mes travaux ont été mentionnées dans cette thèse. Je résume ici les perspectives qui sont, à mon avis, les plus excitantes. Pour les deux versions du détecteur de photons présentées au chapitre 3, la présence de plusieurs modes d'absorption implique que le système peut absorber plus d'un photon. Il serait judicieux d'analyser ce cas de figure plus en profondeur pour déterminer si ces détecteurs peuvent résoudre le nombre de photons d'un signal. Ensuite, un projet intéressant serait d'étudier les conséquences du modèle de bruit biaisé pour la mesure de parité introduite au chapitre 4. En particulier, il serait intéressant de déterminer si cette mesure de parité permet une meilleure tolérance aux fautes par rapport à une mesure de parité indirecte où, à priori, il n'y a pas de structure à exploiter dans le modèle d'erreurs. Finalement, une piste de recherche attrayante pour la collaboration avec l'ETH Zürich présentée au chapitre 5 serait d'améliorer la forme des impulsions pour l'émission de photons uniques. Plus précisément, une meilleure compréhension analytique du couplage f0g1 pourrait permettre d'annuler certains effets diabatiques à l'aide de techniques comme le

1. Simultanément avec deux groupes de Yale.

pilotage quantique sans transition (*TQD*).

Annexe A

Porte à deux qubits longitudinale

Un des premiers projet que j'ai mené à terme pendant ma thèse concerne les portes à deux qubits [187]. Plus particulièrement, j'ai travaillé sur une porte logique se basant sur le couplage longitudinal, c'est-à-dire un couplage qubit-résonateur prenant la forme

$$\hat{H} = g_z \hat{\sigma}_z (\hat{a} + \hat{a}^\dagger). \tag{A.1}$$

Par souci de longueur, j'ai choisi de ne pas incorporer cet article dans le texte principal.

Baptiste Royer, Arne L. Grimsmo, Nicolas Didier et Alexandre Blais. Fast and high-fidelity entangling gate through parametrically modulated longitudinal coupling. *Quantum* **1**, 11 (2017)

Fast and High-Fidelity Entangling Gate through Parametrically Modulated Longitudinal Coupling

Baptiste Royer[1], Arne L. Grimsmo[1], Nicolas Didier[2 3], and Alexandre Blais[1 4]

[1]Institut quantique and Départment de Physique, Université de Sherbrooke, 2500 boulevard de l'Université, Sherbrooke, Québec J1K 2R1, Canada

[2]Current address: Rigetti Quantum Computing, 775 Heinz Avenue, Berkeley, California 94710, USA.

[3]QUANTIC team, Inria Paris, 2 rue Simone Iff, 75012 Paris, France

[4]Canadian Institute for Advanced Research, Toronto, Canada

May 11, 2017

We investigate an approach to universal quantum computation based on the modulation of longitudinal qubit-oscillator coupling. We show how to realize a controlled-phase gate by simultaneously modulating the longitudinal coupling of two qubits to a common oscillator mode. In contrast to the more familiar transversal qubit-oscillator coupling, the magnitude of the effective qubit-qubit interaction does not rely on a small perturbative parameter. As a result, this effective interaction strength can be made large, leading to short gate times and high gate fidelities. We moreover show how the gate infidelity can be exponentially suppressed with squeezing and how the entangling gate can be generalized to qubits coupled to separate oscillators. Our proposal can be realized in multiple physical platforms for quantum computing, including superconducting and spin qubits.

Introduction—A widespread strategy for quantum information processing is to couple the dipole moment of multiple qubits to common oscillator modes, the latter being used to measure the qubits and to mediate long-range interactions. Realizations of this idea are found in Rydberg atoms [1], superconducting qubits [2] and quantum dots [3] amongst others. With the dipole moment operator being off-diagonal in the qubit's eigenbasis, this type of *transversal* qubit-oscillator coupling leads to hybridization of the qubit and oscillator degrees of freedom. In turn, this results in qubit Purcell decay [4] and to qubit readout that is not truly quantum non-demolition (QND) [5]. To minimize these problems, the qubit can be operated at a frequency detuning from the oscillator that is large with respect to the transverse coupling strength g_x. This interaction then only acts perturbatively, taking a dispersive character [1]. While it has advantages, this perturbative character also results in slow oscillator-mediated qubit entangling gates [6–8].

Rather than relying on the standard transversal coupling, $H_x = g_x(\hat{a}^\dagger + \hat{a})\hat{\sigma}_x$, an alternative approach is to use a longitudinal interaction, $H_z = g_z(\hat{a}^\dagger + \hat{a})\hat{\sigma}_z$ [9–14]. Since H_z commutes with the qubit's bare Hamiltonian the qubit is not dressed by the oscillator. Purcell decay is therefore absent [10, 11] and qubit readout is truly QND [13]. The absence of qubit dressing also allows for scaling up to a lattice of arbitrary size with strictly local interactions [11].

By itself, longitudinal interaction however only leads to a vanishingly small qubit state-dependent displacement of the oscillator field of amplitude $g_z/\omega_r \ll 1$, with ω_r the oscillator frequency. In Ref. [13], it was shown that modulating g_z at the oscillator frequency ω_r activates this interaction leading to a large qubit state-dependent oscillator displacement and to fast QND qubit readout. In this paper, we show how the same approach can be used, together with single qubit rotations, for universal quantum computing by introducing a fast and high-fidelity controlled-phase gate based on longitudinal coupling. The two-qubit logical operation relies on parametric modulation of a longitudinal qubit-oscillator coupling, inducing an effective $\hat{\sigma}_z\hat{\sigma}_z$ interaction between qubits coupled to the same mode. A similar gate was first studied in Ref. [10] in the presence of an additional dispersive interaction $\chi\hat{a}^\dagger\hat{a}\hat{\sigma}_z$ and a cavity drive. We show that, with a purely longitudinal interaction excluding the former term, the gate fidelity can be improved exponentially using squeezing. We moreover show that the gate can be performed remotely on qubits coupled to separate but interacting oscillators. The latter allows for a modular architecture that relaxes design constraints and avoids spurious interactions while maintaining minimal circuit complexity [11, 14, 15].

In contrast to two-qubit gates based on a transversal interaction [6, 7], this proposal does not rely on strong qubit-oscillator detuning and is not based on a perturbative argument. As a result, the longitudinally mediated $\hat{\sigma}_z\hat{\sigma}_z$ interaction is valid for all qubit, oscillator and modulation parameters and does not result in unwanted residual terms in the Hamiltonian. For this reason, in the ideal case where the interaction is purely longitudinal (i.e. described by H_z), there are no fundamental bounds on gate infidelity or gate time and both can in principle be made arbitrarily small simultaneously.

Similarly to other oscillator-mediated gates, loss from the oscillator during the gate leads to gate infidelity. This can be minimized by working with high-Q oscillators something that is, however, in contradiction with the requirements for fast qubit readout [2]. We solve this dilemma by exploiting quantum bath engineering, using squeezing at the oscillator input. By appropriately choosing the squeezed quadrature, we show how 'which-qubit-state' information carried by the photons leaving the oscillator can be erased. This leads to an exponential improvement in gate fidelity with squeezing strength.

Oscillator mediated qubit-qubit interaction—Following Ref. [13], we consider two qubits coupled to a single harmonic mode via their $\hat{\sigma}_z$ degree of freedom. Allowing for a time-dependent coupling, the Hamiltonian reads ($\hbar = 1$)

$$\begin{aligned}\hat{H}(t) = \omega_r\hat{a}^\dagger\hat{a} + \tfrac{1}{2}\omega_{a1}\hat{\sigma}_{z1} + \tfrac{1}{2}\omega_{a2}\hat{\sigma}_{z2} \\ + g_1(t)\hat{\sigma}_{z1}\,(\hat{a}^\dagger + \hat{a}) + g_2(t)\hat{\sigma}_{z2}\,(\hat{a}^\dagger + \hat{a}).\end{aligned} \tag{1}$$

In this expression, ω_r and ω_{ai} are the frequencies of the oscillator and of the i^{th} qubit, respectively, while $g_i(t)$ are the corresponding longitudinal coupling strengths.

For constant couplings, $g_i(t) = g_i$, the longitudinal interaction only leads to a displacement of order $\sim g_i/\omega_r$, which is vanishingly small for typical parameters. This interaction can be rendered resonant by modulating $g_i(t)$ at the oscillator frequency leading to a large qubit-state dependent displacement of the oscillator state. Measurement of the oscillator by homodyne detection can then be used for fast QND qubit readout [13]. Consequently, modulating the coupling at the oscillator frequency rapidly dephases the qubits. To keep dephasing to a minimum, we instead use an off-resonant modulation of $g_i(t)$ at a frequency ω_m detuned from ω_r by many oscillator linewidths κ: $g_i(t) = g_i\cos(\omega_m t)$, where $g_{1,2}$ are constant real amplitudes [10].

The oscillator-mediated qubit-qubit interaction can be made more apparent by applying a polaron transformation $\hat{U}(t) = \exp[\sum_{i=1,2}\alpha_i(t)\hat{\sigma}_{zi}\hat{a}^\dagger - \text{H.c.}]$ with an appropriate choice of $\alpha_i(t)$ (see supplemental material). Doing this, we find in the polaron frame the simple Hamiltonian

$$\hat{H}_{\text{pol}}(t) = \omega_r\hat{a}^\dagger\hat{a} + J_z(t)\hat{\sigma}_{z1}\hat{\sigma}_{z2}. \tag{2}$$

The full expression for the $\hat{\sigma}_z\hat{\sigma}_z$-coupling strength $J_z(t)$ is given in the supplemental material. In the following we will, however, assume two conditions on the total gate time, t_g, such that this expression simplifies greatly. For $\delta t_g = n \times 2\pi$ and $\omega_m t_g = m \times \pi$, with n and m integers, we can replace $J_z(t)$ by

$$\bar{J}_z = -\frac{g_1 g_2}{2}\left[\frac{1}{\delta} + \frac{1}{\omega_r + \omega_m}\right], \tag{3}$$

where $\delta \equiv \omega_r - \omega_m$ is the modulation drive detuning.

By modulating the coupling for a time $t_g = \theta/4|\bar{J}_z|$, evolution under Eq. (2) followed by single qubit Z-rotations leads to the entangling controlled-phase gate $U_{CP}(\theta) = \text{diag}[1, 1, 1, \text{e}^{i\theta}]$. Since $U_{CP}(\pi)$ together with single qubit rotations forms a universal set [16], we only consider this gate from now on.

Note that the conditions on the gate time used in Eq. (3) are not necessary for the validity of Eq. (2), and the gate can be realized without these assumptions. However, as we will discuss below, these conditions are important for optimal gate performance: They ensure that the oscillator starts and ends in the vacuum state, which implies that the gate does not need to be performed adiabatically. Finally, not imposing the second constraint, $\omega_m t_g = m \times \pi$, only introduces fast rotating terms to Eq. (3) which we find to have negligible effect for the parameters used later in this paper. In other words, this constraint can be ignored under a rotating-wave approximation.

The above situation superficially looks similar to controlled-phase gates based on transversal coupling and strong oscillator driving [6, 17, 18]. There are, however, several key differences. With transversal coupling, the $\hat{\sigma}_z\hat{\sigma}_z$ interaction is derived using perturbation theory and is thus only approximately valid for small $g_x/\{\Delta, \delta_{\text{d}}\}$, with Δ the qubit-oscillator detuning and δ_{d} the oscillator-drive detuning. For the same reason, it is also only valid for small photon numbers $n \ll n_{\text{crit}} = \Delta^2/4g_x^2$ [6]. Moreover, this interaction is the result of a fourth order process in $g_x/\{\Delta, \delta_{\text{d}}\}$, leading to slow gates. Because of the breakdown of the dispersive approximation, attempts to speed up the gate by decreasing the detunings or increasing the drive amplitude have resulted in low gate fidelities [7]. In contrast, with longitudinal coupling, the $\hat{\sigma}_z\hat{\sigma}_z$ interaction conveniently scales as $\sim g_1 g_2/\delta$, *i.e.* it scales as a second-order process in $g_{1,2}/\delta$, but the exact nature of the transformation means that there are no higher order terms. Consequently, Eq. (2) is valid for any value of $g_{1,2}/\delta$, independent of the oscillator photon number.

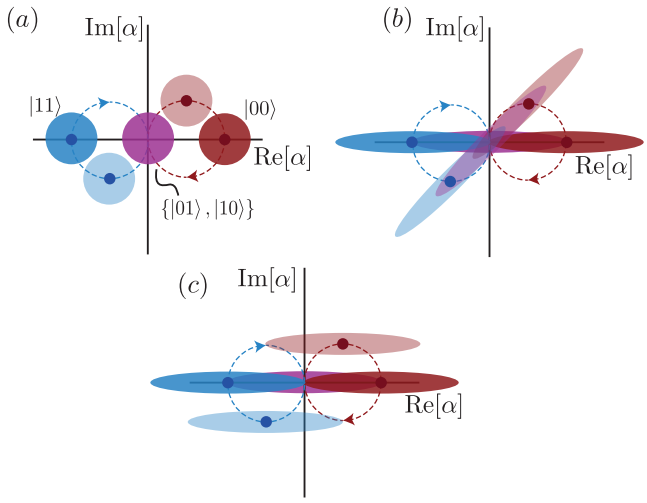

Figure 1: Schematic illustration, in a frame rotating at ω_r, of the qubit-state dependent oscillator field in phase space for $g_1 = g_2$ starting and ending in the vacuum state (purple). The oscillator's path for $|00\rangle$ ($|11\rangle$) is shown by the dashed red (blue) line. The qubit-state dependent oscillator state is shown in light ($t = t_g/4$) and dark colors ($t = t_g/2$). The oscillator's state associated to $\{|01\rangle, |10\rangle\}$ stays in the vacuum state for the duration of the gate (purple). (a) No squeezing. (b,c) Squeezing can help in erasing the which-qubit-state information.

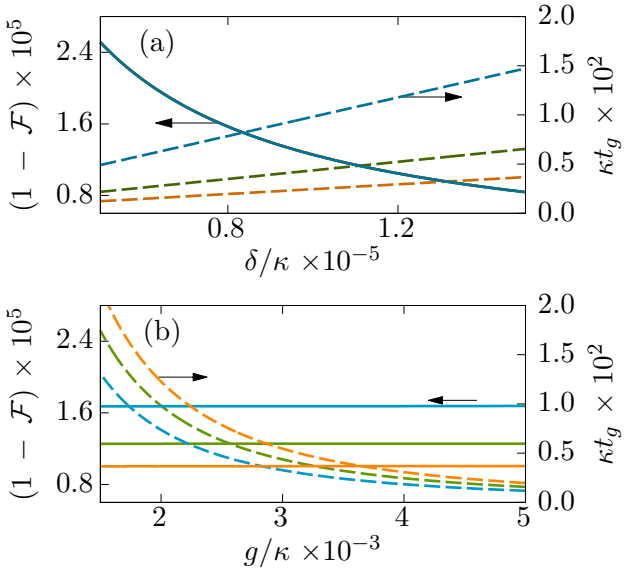

Figure 2: Average gate infidelity $1-\mathcal{F}$ (full line) and gate time (dashed lines) of $U_{CP}(\pi)$ as a function of (a) detuning and (b) coupling strength. In panel (a) $g/\kappa \times 10^{-3}$ is fixed at 2 (blue), 3 (green), 4 (orange). Note that the corresponding three infidelity curves are indistinguishable on this scale. In panel (b) $\delta/\kappa \times 10^{-5}$ is fixed at 0.75 (blue), 1 (green), 1.25 (orange).

As will become clear later, this implies that the gate time and the gate infidelity can be decreased simultaneously. Finally, with longitudinal coupling, there is no constraint on the qubit frequencies, in contrast with usual oscillator-induced phase gates where the detuning between qubits should preferably be small.

Oscillator-induced qubit dephasing—Fig. 1 illustrates, for $g_1 = g_2$, the mechanism responsible for the qubit-qubit interaction. Under longitudinal coupling, the oscillator field is displaced in a qubit-state dependent way, following the dashed lines in Fig. 1(a) (Panels (b) and (c) will be discussed later). This conditional displacement leads to a non-trivial qubit phase accumulation. This schematic illustration also emphasizes the main cause of gate infidelity for this type of controlled-phase gate, irrespective of its longitudinal or transversal nature: Photons leaking out from the oscillator during the gate carry information about the qubit state, leading to dephasing.

A quantitative understanding of the gate infidelity under photon loss can be obtained by deriving a master equation for the joint qubit-oscillator system. While general expressions are given in the supplemental material, to simplify the discussion we assume here that $g_1 = g_2 \equiv g$. Following the standard approach [19], the Lindblad master equation in the polaron frame reads

$$\begin{aligned}\dot{\rho}(t) = &-i[\hat{H}_{\rm pol}, \rho(t)] + \kappa\mathcal{D}[\hat{a}]\rho(t) \\ &+ \Gamma[1-\cos(\delta t)]\mathcal{D}[\hat{\sigma}_{z1}+\hat{\sigma}_{z2}]\rho(t),\end{aligned} \tag{4}$$

where κ is photon decay rate and $\mathcal{D}[x]$ denotes the usual dissipation super-operator $\mathcal{D}[x]\bullet = x\bullet x^\dagger - \frac{1}{2}\{x^\dagger x, \bullet\}$. The last term of Eq. (4) corresponds to a dephasing channel with rate $\Gamma = 2\kappa(g/2\delta)^2$. Since $\hat{H}_{\rm pol}$ does not generate qubit-oscillator entanglement during the evolution, we can ensure that in this frame, gate-induced dephasing only happens due to the last term in Eq. (4) with rate Γ, by imposing that the initial and final polaron transformations also do not lead to qubit-oscillator entanglement. This translates to the condition $\alpha_i(0) = \alpha_i(t_g) = 0$ and is realized for $\delta t_g = n \times 2\pi$, which is the constraint mentioned earlier (neglecting fast-rotating terms related to the second constraint $\omega_m t_g = m \times \pi$). More intuitively, it amounts to completing n full circles in Fig. 1, the oscillator ending back in its initial unentangled state. Note that these conclusions remain unchanged if the oscillator is initially in a coherent state. As a result, there is no need for the oscillator to be empty at the start of the gate [10].

Based on the dephasing rate Γ and on the gate time t_g, a simple estimate for the scaling of the gate infi-

delity is $1-\mathcal{F} \sim \Gamma \times t_g \sim \kappa/\delta$ [1]. A key observation is that this gate error is independent of g, while the gate time scales as $t_g \sim \delta/g^2$. Both the gate time and the error can therefore, in principle, be made arbitrarily small simultaneously. This scaling of the gate error and gate time is confirmed by the numerical simulations of Fig. 2, which shows the dependence of the gate infidelity [20] on detuning δ and coupling strength g, as obtained from numerical integration of Eq. (4). The expected increase in both fidelity (full lines) and gate time (dashed lines) with increasing detuning δ are apparent in panel (a). In addition, panel (b) confirms that, to a very good approximation, the fidelity is independent of g (full lines) while the gate time decreases as $t_g \sim 1/g^2$ (dashed lines).

This oscillator-induced phase gate can be realized in a wide range of physical platforms where longitudinal coupling is possible. Examples include spin qubits in inhomogeneous magnetic field [21], singlet-triplet spin qubits [22], flux qubits capacitively coupled to a resonator [11] and transmon-based superconducting qubits [10, 13, 14]. The parameters used in Fig. 2 have been chosen following the latter references. In particular, taking $\kappa/2\pi = 0.05$ MHz [23], $g/2\pi = 60$ MHz [13] and $\delta/2\pi = 537$ MHz results in a very short gate time of $t_g = 37$ ns with an average gate infidelity as small as 1×10^{-4}. Taking into account finite qubit lifetimes $T_1 = 30\,\mu$s and $T_2 = 20\,\mu$s [24], we find that the infidelity is increased to $\sim 10^{-3}$ (see supplemental material). In other words, the gate fidelity is limited by the qubit's natural decoherence channels with these parameters. For a comparison with transversal resonator-induced phase gate, see the supplemental material.

A crucial feature of this gate is that the circular path followed by the oscillator field in phase space maximizes qubit-state dependent phase accumulation while minimizing dephasing, allowing for high gate fidelities. In contrast to [10], this relies on the assumption that there is no dispersive interaction of the form $\chi\hat{a}^\dagger\hat{a}\hat{\sigma}_z$ in Eq. (1). Furthermore, we show below that this also allows for exponential improvement in gate fidelity with squeezing. It is therefore desirable to minimize, or avoid completely, dispersive coupling in experimental implementations [2].

Improved fidelity with squeezing— As discussed above, for fixed g and δ the fidelity increases with decreasing κ. A small oscillator decay rate κ, however, comes at the price of longer measurement time if the same oscillator is to be used for readout [13]. This problem can be solved by sending squeezed radiation to the oscillator's readout port. As schematically illustrated in Fig. 1, by orienting the squeezing axis with the direction of the qubit-dependent displacement of the oscillator state, the which-path information carried by the photons leaving the oscillator can be erased. By carefully choosing the squeezing angle and frequency, it is thus possible to improve the gate performance without reducing κ. We now show two different approaches to realize this, referring the reader to the supplemental material for technical details.

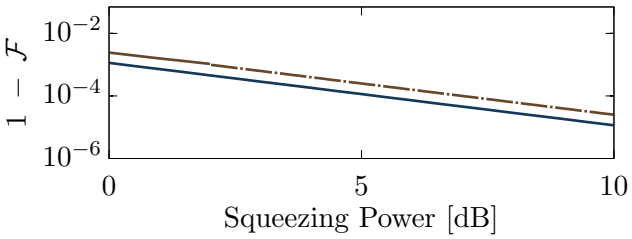

Figure 3: Average gate infidelity $1-\mathcal{F}$ squeezing power. Parameters are $\delta/2\pi = 0.6$ GHz, $g/2\pi = 60$ MHz, $t_g = 42.7$ ns, $\kappa/2\pi = 1$ MHz. In brown, rotating squeezing angle as illustrated in Fig. 1(b). In dark blue, squeezing at ω_r as illustrated in Fig. 1(c), and $\kappa(\omega_m) = 0$ simulating a filter reducing the density of modes to zero at ω_m.

A first approach is to send broadband two-mode squeezed vacuum at the input of the oscillator, where the squeezing source is defined by a pump frequency $\omega_p = (\omega_r + \omega_m)/2$ and a squeezing spectrum with large degree of squeezing at ω_r and ω_m. A promising source of this type of squeezing is the recently developed Josephson travelling wave amplifiers [25, 26]. With such a squeezed input field, a coherent state of the oscillator becomes a squeezed state with a squeezing angle that rotates at a frequency $\delta/2$. As illustrated in Fig. 1(b), this is precisely the situation where the anti-squeezed quadrature and the displacement of the oscillator's state are aligned at all times. This leads to an exponential decrease in dephasing rate

$$\Gamma(r) \sim \mathrm{e}^{-2r}\Gamma(0), \tag{5}$$

with r the squeezing parameter. This reduction in dephasing rate leads to the exponential improvement in gate fidelity with squeezing power shown by the brown line in Fig. 3(c). An interesting feature in this Figure is that increasing κ by 2 orders of magnitude to allow for fast measurement [13], leads to the same $\sim 10^{-5}$ gate infidelity obtained above without squeezing here using only ~6 dB of squeezing. Since numerical simulations are intractable for large amount of squeezing, we depict the infidelity obtained from a master equation simulation by a solid line and the expected infidelity from

[1] Note that $1-\mathcal{F}$ refers only to the error due to photon decay, excluding the qubits natural T_1 and T_2 times.

[2] In the proposal of Ref. [13], this can be done by reducing the participation ratio, η, such that $\chi \lesssim \kappa$

analytical calculations by a dash-dotted line.

An alternative solution is to use broadband squeezing centered at the oscillator's frequency, *i.e.* a squeezing source defined by a pump frequency $\omega_p = \omega_r$. As illustrated in Fig. 1(c), using this type of input leads to a squeezing angle that is constant in time in a frame rotating at ω_r. With this choice, information about the qubits' state contained in the $\hat{a}^\dagger + \hat{a}$ quadrature of the field is erased while information in the $i(\hat{a}^\dagger - \hat{a})$ quadrature is amplified (cf. Fig. 1). By itself, this does not lead to a substantial fidelity improvement. However, a careful treatment of the master equation shows that Eq. (5) can be recovered by adding a filter reducing the density of modes at ω_m to zero at the output port of the oscillator (see supplemental material). Filters of this type are routinely used experimentally to reduce Purcell decay of superconducting qubits [27, 28]. As illustrated by the dark blue line in Fig. 3(c), using single-mode squeezing at ω_r and a filter at the modulation frequency, we recover the same exponential improvement found with two-mode squeezing, Eq. (5), in addition to a factor of two decrease in gate infidelity without squeezing.

Interestingly, rotating the squeezing axis by $\pi/2$ when squeezing at the oscillator frequency helps in distinguishing the different oscillator states and has been shown to lead to an exponential increase in the signal-to-noise ratio for qubit readout [13]. In practice, the difference between performing a two-qubit gate and a measurement is thus the parametric modulation frequency (off-resonant for the gate and on resonance for measurement) and the choice of squeezing axis.

We note that Eq. (5) was derived from a master equation treatment under the standard secular approximation [29], which is not valid at high squeezing powers (here, $\gtrsim$ 10 dB, see supplemental material). At such high powers, the frequency dependence of κ together with other imperfections are likely to be relevant.

Scalability—So far we have focused on two qubits coupled to a single common oscillator. As shown by Billangeon *et al.* [11], longitudinal coupling of several qubits to separate oscillators that are themselves coupled transversely has favorable scaling properties. Circuits implementing this idea were also proposed by Richer *et al.* [14]. Interestingly, the gate introduced in this paper can also be implemented in such an architecture. Consider two qubits interacting with distinct, but coupled, oscillators with the corresponding Hamiltonian [11]

$$\begin{aligned}\hat{H}_{ab} = {} & \omega_a \hat{a}^\dagger \hat{a} + \omega_b \hat{b}^\dagger \hat{b} + \tfrac{1}{2}\omega_{a1}\hat{\sigma}_{z1} + \tfrac{1}{2}\omega_{a2}\hat{\sigma}_{z2} \\ & + g_1(t)\hat{\sigma}_{z1}\,(\hat{a}^\dagger + \hat{a}) + g_2(t)\hat{\sigma}_{z2}\,(\hat{b}^\dagger + \hat{b}) \\ & - g_{ab}(\hat{a}^\dagger - \hat{a})(\hat{b}^\dagger - \hat{b}).\end{aligned} \tag{6}$$

In this expression, $\hat{a}$, $\hat{b}$ label the mode of each oscillator of respective frequencies $\omega_{a,b}$, and g_{ab} is the oscillator-oscillator coupling. As above, $g_{1,2}(t)$ are modulated at the same frequency ω_m, corresponding to the detunings $\delta_a \equiv \omega_a - \omega_m$ and $\delta_b \equiv \omega_b - \omega_m$. Following the same procedure as above and performing a rotating-wave approximation for simplicity, we find a Hamiltonian in the polaron frame of the same form as Eq. (2), but now with a modified $\hat{\sigma}_z\hat{\sigma}_z$ interaction strength

$$\bar{J}_z = \frac{1}{2}\frac{g_1 g_2 g_{ab}}{\bar{\delta}^2 - g_{ab}^2(1+\zeta^2)}, \tag{7}$$

where $\bar{\delta} = (\delta_a + \delta_b)/2$ and $\zeta = (\omega_b - \omega_a)/(2g_{ab})$. This implementation allows for a modular architecture, where each unit cell is composed of a qubit and coupling oscillators, used for both readout and entangling gates. Such a modular approach can relax design constraints and avoids spurious interactions with minimal circuit complexity [11, 14, 15].

Conclusion—We have proposed a controlled-phase gate based on purely longitudinal coupling of two qubits to a common oscillator mode. The key to activating the qubit-qubit interaction is a parametric modulation of the qubit-oscillator coupling at a frequency far detuned from the oscillator. The gate infidelity and gate time can in principle be made arbitrarily small simultaneously, in stark contrast to the situation with transversal coupling. We have also shown how the gate fidelity can be exponentially increased using squeezing and that it is independent of qubit frequencies. The gate can moreover be performed remotely in a modular architecture based on qubits coupled to separate oscillators. Together with the fast, QND and high-fidelity measurement scheme presented in Ref. [13], this makes a platform based on parametric modulation of longitudinal coupling a promising path towards universal quantum computing in a wide variety of physical realizations.

Acknowledgments

We thank J. Bourassa, D. Poulin and S. Puri for useful discussions. This work was supported by the Army Research Office under Grant No. W911NF-14-1-0078 and NSERC. This research was undertaken thanks in part to funding from the Canada First Research Excellence Fund and the Vanier Canada Graduate Scholarships.

References

[1] S. Haroche and J.-M. Raimond, *Exploring the Quantum: Atoms, Cavities, and Photons* (Oxford University Press, Oxford, 2006).

[2] A. Blais, R.-S. Huang, A. Wallraff, S. M. Girvin, and R. J. Schoelkopf, Phys. Rev. A **69**, 062320 (2004).

[3] A. Imamoglu, D. D. Awschalom, G. Burkard, D. P. DiVincenzo, D. Loss, M. Sherwin, and A. Small, Phys. Rev. Lett. **83**, 4204 (1999).

[4] A. A. Houck, J. A. Schreier, B. R. Johnson, J. M. Chow, J. Koch, J. M. Gambetta, D. I. Schuster, L. Frunzio, M. H. Devoret, S. M. Girvin, and R. J. Schoelkopf, Phys. Rev. Lett. **101**, 080502 (2008).

[5] M. Boissonneault, J. M. Gambetta, and A. Blais, Phys. Rev. A **79**, 013819 (2009).

[6] A. Blais, J. Gambetta, A. Wallraff, D. I. Schuster, S. M. Girvin, M. H. Devoret, and R. J. Schoelkopf, Phys. Rev. A **75**, 032329 (2007).

[7] J. M. Chow, J. M. Gambetta, A. W. Cross, S. T. Merkel, C. Rigetti, and M. Steffen, New Journal of Physics **15**, 115012 (2013).

[8] H. Paik, A. Mezzacapo, M. Sandberg, D. T. McClure, B. Abdo, A. D. Córcoles, O. Dial, D. F. Bogorin, B. L. T. Plourde, M. Steffen, A. W. Cross, J. M. Gambetta, and J. M. Chow, Phys. Rev. Lett. **117**, 250502 (2016).

[9] A. J. Kerman and W. D. Oliver, Phys. Rev. Lett. **101**, 070501 (2008).

[10] A. J. Kerman, New Journal of Physics **15**, 123011 (2013).

[11] P.-M. Billangeon, J. S. Tsai, and Y. Nakamura, Phys. Rev. B **91**, 094517 (2015).

[12] P.-M. Billangeon, J. S. Tsai, and Y. Nakamura, Phys. Rev. B **92**, 020509 (2015).

[13] N. Didier, J. Bourassa, and A. Blais, Phys. Rev. Lett. **115**, 203601 (2015).

[14] S. Richer and D. DiVincenzo, Phys. Rev. B **93**, 134501 (2016).

[15] T. Brecht, W. Pfaff, C. Wang, Y. Chu, L. Frunzio, M. H. Devoret, and R. J. Schoelkopf, Npj Quantum Information **2**, 16002 EP (2016).

[16] M. Nielsen and I. Chuang, *Quantum Computation and Quantum Information*, Cambridge Series on Information and the Natural Sciences (Cambridge University Press, 2000).

[17] A. W. Cross and J. M. Gambetta, Phys. Rev. A **91**, 032325 (2015).

[18] S. Puri and A. Blais, Phys. Rev. Lett. **116**, 180501 (2016).

[19] C. Gardiner and P. Zoller, *Quantum Noise: A Handbook of Markovian and Non-Markovian Quantum Stochastic Methods with Applications to Quantum Optics*, Springer Series in Synergetics (Springer, 2004).

[20] M. A. Nielsen, Physics Letters A **303**, 249 (2002).

[21] F. Beaudoin, D. Lachance-Quirion, W. A. Coish, and M. Pioro-Ladrière, Nanotechnology **27**, 464003 (2016).

[22] P.-Q. Jin, M. Marthaler, A. Shnirman, and G. Schön, Phys. Rev. Lett. **108**, 190506 (2012).

[23] A. Bruno, G. de Lange, S. Asaad, K. L. van der Enden, N. K. Langford, and L. DiCarlo, Applied Physics Letters **106**, 182601 (2015).

[24] A. D. Corcoles, E. Magesan, S. J. Srinivasan, A. W. Cross, M. Steffen, J. M. Gambetta, and J. M. Chow, Nat Commun **6** (2015).

[25] C. Macklin, K. O'Brien, D. Hover, M. E. Schwartz, V. Bolkhovsky, X. Zhang, W. D. Oliver, and I. Siddiqi, Science **350**, 307 (2015).

[26] T. White, J. Mutus, I.-C. Hoi, R. Barends, B. Campbell, Y. Chen, Z. Chen, B. Chiaro, A. Dunsworth, E. Jeffrey, *et al.*, Applied Physics Letters **106**, 242601 (2015).

[27] M. D. Reed, B. R. Johnson, A. A. Houck, L. DiCarlo, J. M. Chow, D. I. Schuster, L. Frunzio, and R. J. Schoelkopf, Applied Physics Letters **96**, 203110 (2010).

[28] N. T. Bronn, Y. Liu, J. B. Hertzberg, A. D. Córcoles, A. A. Houck, J. M. Gambetta, and J. M. Chow, Applied Physics Letters **107** (2015).

[29] H. Breuer and F. Petruccione, *The Theory of Open Quantum Systems* (OUP Oxford, 2007).

Supplemental Material for "Fast and High-Fidelity Entangling Gate through Parametrically Modulated Longitudinal Coupling"

Baptiste Royer[1], Arne L. Grimsmo[1], Nicolas Didier[2], and Alexandre Blais[1 3]

[1]Institut quantique and Département de Physique, Université de Sherbrooke, 2500 boulevard de l'Université, Sherbrooke, Québec J1K 2R1, Canada

[2]Centre de Recherche Inria de Paris, 2 rue Simone Iff, 75012 Paris, France

[3]Canadian Institute for Advanced Research, Toronto, Canada

May 9, 2017

This supplemental material is organized as follows: In Sect. 1 we derive a general master equation for two qubits coupled to a single oscillator that is itself coupled to an external bath. We then use this result to study three cases: a standard bath at zero temperature, a bath that is two-mode squeezed at the modulation and oscillator frequency and a bath that is squeezed at the oscillator frequency. In Sect. 2 we give more information about possible physical implementations. In Sect. 3 we show how the gate can be realized for qubits that are in separate, but coupled, oscillators. In Sect. 4 we give more details about the numerical simulations, followed by a comparison with a transversal resonator-induced phase gate in Sect. 5 and finally in Sect. 6 we derive an error bound for the secular approximation made in deriving the master equation.

1 Derivation of the master equation

In this section, we follow the procedure outlined in the main paper, taking damping of the oscillator into account. We start with the full Hamiltonian of two qubits longitudinally coupled to an oscillator, and a bath coupled to the oscillator ($\hbar = 1$),

$$\hat{H} = \hat{H}_0 + \hat{H}_{qr} + \hat{H}_{rf}, \tag{S1}$$

$$\hat{H}_0 = \omega_r \hat{a}^\dagger \hat{a} + \tfrac{1}{2}\omega_{a1}\hat{\sigma}_{z1} + \tfrac{1}{2}\omega_{a2}\hat{\sigma}_{z2} + \int_0^\infty d\omega\, \omega \hat{b}_\omega^\dagger \hat{b}_\omega, \tag{S2}$$

$$\hat{H}_{qr} = g_1(t)\hat{\sigma}_{z1}\,(\hat{a}^\dagger + \hat{a}) + g_2(t)\hat{\sigma}_{z2}\,(\hat{a}^\dagger + \hat{a}), \tag{S3}$$

$$\hat{H}_{rf} = \int_0^\infty \frac{\mathrm{d}\omega}{\sqrt{2\pi}} \sqrt{\kappa(\omega)}(\hat{a} + \hat{a}^\dagger)(\hat{b}_\omega + \hat{b}_\omega^\dagger), \tag{S4}$$

where $\hat{H}_{qr}$ is the qubit-oscillator coupling Hamiltonian and $\hat{H}_{rf}$ is the oscillator-bath coupling Hamiltonian. $\hat{b}_\omega$ ($\hat{b}_\omega^\dagger$) is a bath mode annihilation (creation) operator, satisfying the commutation relation $[\hat{b}_\omega, \hat{b}_{\omega'}^\dagger] = \delta(\omega - \omega')$, and $\kappa(\omega)$ is the damping rate of the oscillator at frequency ω. We assume the form $g_1(t) = g_1 \cos(\omega_m t)$, $g_2(t) = g_2 \cos(\omega_m t + \phi)$ for the qubit-oscillator couplings, with $\phi = 0$ and the modulation frequency far from the oscillator frequency $\delta \equiv \omega_r - \omega_m$. Setting $\phi = \pi$ leads to a very similar derivation, with ultimately a sign difference in the $\hat{\sigma}_{z1}\hat{\sigma}_{z2}$ interaction and allowing us to choose between a ferromagnetic or an antiferromagnetic interaction.

Following the approach outlined in the paper, we first go to a polaron frame by applying the unitary transformation

$$\hat{\mathbf{U}}(t) = \exp\left[(\alpha_1\hat{\sigma}_{z1} + \alpha_2\hat{\sigma}_{z2})\,\hat{a}^\dagger - (\alpha_1^*\hat{\sigma}_{z1} + \alpha_2^*\hat{\sigma}_{z2})\,\hat{a}\right], \tag{S5}$$

with

$$\alpha_j(t) = \frac{g_j}{2}\left(\frac{\mathrm{e}^{-i\omega_m t} - \mathrm{e}^{-i\omega_r t}}{\delta} + \frac{\mathrm{e}^{i\omega_m t} - \mathrm{e}^{-i\omega_r t}}{\omega_r + \omega_m}\right), \tag{S6}$$

leading to the transformed Hamiltonian

$$\begin{aligned}\hat{H}_{\mathrm{pol}} &= \hat{\mathbf{U}}^\dagger \hat{H} \hat{\mathbf{U}} - i\hat{\mathbf{U}}^\dagger \dot{\hat{\mathbf{U}}} \\ &= \omega_r \hat{a}^\dagger \hat{a} + J_z(t)\hat{\sigma}_{z1}\hat{\sigma}_{z2} + \tfrac{1}{2}\omega_{a1}\hat{\sigma}_{z1} + \tfrac{1}{2}\omega_{a2}\hat{\sigma}_{z2} \\ &\quad + \int_0^\infty \frac{\mathrm{d}\omega}{\sqrt{2\pi}}\sqrt{\kappa(\omega)}(\hat{a} + \hat{a}^\dagger)(\hat{b}_\omega \mathrm{e}^{-i\omega t} + \hat{b}_\omega^\dagger \mathrm{e}^{i\omega t}) \\ &\quad - \int_0^\infty \frac{\mathrm{d}\omega}{\sqrt{2\pi}}\sqrt{\kappa(\omega)}(\hat{\mathcal{O}}\mathrm{e}^{-i\omega_m t} + \hat{\mathcal{O}}\mathrm{e}^{i\omega_m t})(\hat{b}_\omega \mathrm{e}^{-i\omega t} + \hat{b}_\omega^\dagger \mathrm{e}^{i\omega t}) \\ &\quad + \int_0^\infty \frac{\mathrm{d}\omega}{\sqrt{2\pi}}\sqrt{\kappa(\omega)}(\hat{\mathcal{O}}\mathrm{e}^{-i\omega_r t} + \hat{\mathcal{O}}\mathrm{e}^{i\omega_r t})(\hat{b}_\omega \mathrm{e}^{-i\omega t} + \hat{b}_\omega^\dagger \mathrm{e}^{i\omega t}).\end{aligned} \tag{S7}$$

To simplify expressions, we have defined a two-qubit operator

$$\hat{\mathcal{O}} \equiv \frac{g_1\hat{\sigma}_{z1} + g_2\hat{\sigma}_{z2}}{2}\left(\frac{1}{\delta} + \frac{1}{\omega_r + \omega_m}\right) \equiv \frac{g_1\hat{\sigma}_{z1} + g_2\hat{\sigma}_{z2}}{2\tilde{\delta}}, \tag{S8}$$

with $\tilde{\delta} = [1/\delta + 1/(\omega_r + \omega_m)]^{-1}$, and the qubit-qubit coupling strength

$$\begin{aligned}J_z(t) = &-\frac{g_1 g_2}{2\delta}\left\{1 - \cos(\delta t) - \cos[(\omega_m + \omega_r)t] + \frac{2\omega_r}{\omega_r + \omega_m}\cos(2\omega_m t)\right\} \\ &- \frac{g_1 g_2}{2(\omega_m + \omega_r)}\left\{1 - \cos(\delta t) - \cos[(\omega_m + \omega_r)t]\right\}.\end{aligned} \tag{S9}$$

It is important to note that, up to this point, all transformations performed are exact. Also, we have specifically chosen $\alpha(t)$ in such a way that at all times the oscillator's state is vacuum in the polaron frame: We will use this fact later in the discussion.

In practice Eq. (S9) can be simplified greatly if we impose the two conditions $\delta t_g = 2n\pi$, $2\omega_m t_g = 2m\pi$ on the modulation parameters, with n and m integers. In this case, all the cosine terms in Eq. (S9) average to zero and can be dropped exactly. We can thus use

$$J_z(t) = \bar{J}_z = -\frac{g_1 g_2}{2\tilde{\delta}} \qquad \text{for } \delta t_g = n \times 2\pi, \quad \omega_m t_g = m \times \pi. \tag{S10}$$

We emphasize that in the main paper we used $\bar{J}_z$ for the qubit-qubit coupling to simplify the discussion, but in general there is no obstacle to keeping the full form of $J_z(t)$, Eq. (S9). In the numerical results presented, we always use the full form.

To derive the Lindblad Master equation, we transform to the interaction picture with the unitary transformation

$$\hat{U}_I = \exp\left\{-i\int_0^t \mathrm{d}s\,[H_0 + J_z(s)\hat{\sigma}_{z1}\hat{\sigma}_{z2}]\right\}, \tag{S11}$$

leading to

$$\begin{aligned}\hat{H}^I_{\mathrm{pol}} = &\int_0^\infty \frac{\mathrm{d}\omega}{\sqrt{2\pi}}\sqrt{\kappa(\omega)}\left[(\hat{a} + \hat{\mathcal{O}})\mathrm{e}^{-i\omega_r t} + (\hat{a}^\dagger + \hat{\mathcal{O}})\mathrm{e}^{i\omega_r t}\right](\hat{b}_\omega \mathrm{e}^{-i\omega t} + \hat{b}_\omega^\dagger \mathrm{e}^{i\omega t}) \\ &- \int_0^\infty \frac{\mathrm{d}\omega}{\sqrt{2\pi}}\sqrt{\kappa(\omega)}(\hat{\mathcal{O}}\mathrm{e}^{-i\omega_m t} + \hat{\mathcal{O}}\mathrm{e}^{i\omega_m t})(\hat{b}_\omega \mathrm{e}^{-i\omega t} + \hat{b}_\omega^\dagger \mathrm{e}^{i\omega t}).\end{aligned} \tag{S12}$$

This expression can be simplified by defining $\hat{B}(t) \equiv \int_0^\infty d\omega\ (\hat{b}_\omega \mathrm{e}^{-i\omega t} + \hat{b}_\omega^\dagger \mathrm{e}^{i\omega t})$ and assuming that $\kappa(\omega)$ is independent of frequency close to ω_m and ω_r according to the usual Markov approximation [S1]. Defining $\kappa(\omega_m) \equiv \kappa_m$ and $\kappa(\omega_r) \equiv \kappa_r$, we can write

$$\hat{H}^I_{\mathrm{pol}} = \sqrt{\frac{\kappa_r}{2\pi}}\left[(\hat{a} + \hat{\mathcal{O}})\mathrm{e}^{-i\omega_r t} + (\hat{a}^\dagger + \hat{\mathcal{O}})\mathrm{e}^{i\omega_r t}\right]\hat{B}(t) - \sqrt{\frac{\kappa_m}{2\pi}}(\hat{\mathcal{O}}\mathrm{e}^{-i\omega_m t} + \hat{\mathcal{O}}\mathrm{e}^{i\omega_m t})\hat{B}(t) \tag{S13}$$

$$= \sum_n \sqrt{\frac{\kappa_n}{2\pi}}(\hat{\mathcal{C}}_n \mathrm{e}^{-i\omega_n t} + \hat{\mathcal{C}}_n^\dagger \mathrm{e}^{i\omega_n t})\hat{B}(t), \tag{S14}$$

where $n = r, m$ and $\hat{\mathcal{C}}_r \equiv \hat{a} + \hat{\mathcal{O}}, \hat{\mathcal{C}}_m \equiv -\hat{\mathcal{O}}$.

Using this result and following the standard approach [S1], we find a Born-Markov master equation

$$\dot{\rho}(t) = -\int_0^\infty d\tau \ \mathrm{Tr}_f\{[\hat{H}^I_{\mathrm{pol}}(t), [\hat{H}^I_{\mathrm{pol}}(t-\tau), \rho(t)\otimes\rho_f]]\}, \tag{S15}$$

where $\rho(t)$ is the density matrix of the qubit-oscillator system and ρ_f the density matrix of the oscillator's bath. Using Eq. (S13) and defining $S(t,\omega) \equiv \int_0^\infty d\tau \ \langle \hat{B}(t-\tau)\hat{B}(t)\rangle \mathrm{e}^{-i\omega\tau}$, $S^*(t,\omega) \equiv \int_0^\infty d\tau \ \langle \hat{B}(t)\hat{B}(t-\tau)\rangle \mathrm{e}^{i\omega\tau}$ results in

$$\begin{aligned}
\dot{\rho}(t) = \sum_{n,n'} & -i[\Delta(\omega_n, -\omega_{n'}, t)\hat{\mathcal{C}}_n\hat{\mathcal{C}}_{n'}, \rho(t)] + \Gamma(\omega_n, -\omega_{n'}, t)\mathcal{D}[\hat{\mathcal{C}}_n, \hat{\mathcal{C}}_{n'}]\rho(t) \\
& -i[\Delta(-\omega_n, \omega_{n'}, t)\hat{\mathcal{C}}^\dagger_n\hat{\mathcal{C}}^\dagger_{n'}, \rho(t)] + \Gamma(-\omega_n, \omega_{n'}, t)\mathcal{D}[\hat{\mathcal{C}}^\dagger_n, \hat{\mathcal{C}}^\dagger_{n'}]\rho(t) \\
& -i[\Delta(-\omega_n, -\omega_{n'}, t)\hat{\mathcal{C}}^\dagger_n\hat{\mathcal{C}}_{n'}, \rho(t)] + \Gamma(-\omega_n, -\omega_{n'}, t)\mathcal{D}[\hat{\mathcal{C}}^\dagger_n, \hat{\mathcal{C}}_{n'}]\rho(t) \\
& -i[\Delta(\omega_n, \omega_{n'}, t)\hat{\mathcal{C}}_n\hat{\mathcal{C}}^\dagger_{n'}, \rho(t)] + \Gamma(\omega_n, \omega_{n'}, t)\mathcal{D}[\hat{\mathcal{C}}_n, \hat{\mathcal{C}}^\dagger_{n'}]\rho(t),
\end{aligned} \tag{S16}$$

where

$$\mathcal{D}[\hat{x}, \hat{y}]\bullet = \hat{x}\bullet\hat{y} - \frac{1}{2}\{\hat{y}\hat{x}, \bullet\}, \tag{S17}$$

$$\Gamma(\omega_n, \omega_{n'}, t) = \frac{\sqrt{\kappa_n\kappa_{n'}}}{2\pi}[S(t,\omega_{n'}) + S^*(t,\omega_n)]\mathrm{e}^{-i(\omega_n-\omega_{n'})t}, \tag{S18}$$

$$\Delta(\omega_n, \omega_{n'}, t) = \frac{i}{2}\frac{\sqrt{\kappa_n\kappa_{n'}}}{2\pi}[S(t,\omega_{n'}) - S^*(t,\omega_n)]\mathrm{e}^{-i(\omega_n-\omega_{n'})t}. \tag{S19}$$

The last two equations correspond to the dissipation rates Γ and the lamb shifts Δ. To get an explicit form for $S(t,\omega)$, we consider a squeezed bath at a pump frequency ω_p [S1],

$$\langle \hat{b}_{\omega_1}\hat{b}_{\omega_2}\rangle = M(\omega_1)\delta(\omega_1+\omega_2-2\omega_p), \tag{S20}$$

$$\langle \hat{b}^\dagger_{\omega_1}\hat{b}^\dagger_{\omega_2}\rangle = M^*(\omega_1)\delta(\omega_1+\omega_2-2\omega_p), \tag{S21}$$

$$\langle \hat{b}^\dagger_{\omega_1}\hat{b}_{\omega_2}\rangle = N(\omega_1)\delta(\omega_1-\omega_2), \tag{S22}$$

$$\langle \hat{b}_{\omega_1}\hat{b}^\dagger_{\omega_2}\rangle = [N(\omega_1)+1]\delta(\omega_1-\omega_2). \tag{S23}$$

Using these expressions in $S(t,\omega)$, we get two different expressions for $\omega > 0$ and $\omega < 0$

$$S(t,\omega>0) = \pi\left[M(\omega)\mathrm{e}^{-i2\omega_p t} + N(\omega) + 1\right], \tag{S24}$$

$$S(t,\omega<0) = \pi\left[M^*(\omega)\mathrm{e}^{i2\omega_p t} + N(\omega)\right]. \tag{S25}$$

Neglecting fast rotating terms in the usual secular approximation [S2], the dissipation rates take the form

$$\Gamma(\omega_n, -\omega_{n'}, t) = \frac{\sqrt{\kappa_n\kappa_{n'}}}{2}[M^*(\omega_n) + M^*(\omega_{n'})]\mathrm{e}^{-i(\omega_{n'}+\omega_n-2\omega_p)t}, \tag{S26}$$

$$\Gamma(-\omega_n, \omega_{n'}, t) = \frac{\sqrt{\kappa_n\kappa_{n'}}}{2}[M(\omega_n) + M(\omega_{n'})]\mathrm{e}^{i(\omega_{n'}+\omega_n-2\omega_p)t}, \tag{S27}$$

$$\Gamma(-\omega_n, -\omega_{n'}, t) = \frac{\sqrt{\kappa_n\kappa_{n'}}}{2}[N(\omega_{n'}) + N(\omega_n)]\mathrm{e}^{i(\omega_n-\omega_{n'})t}, \tag{S28}$$

$$\Gamma(\omega_n, \omega_{n'}, t) = \frac{\sqrt{\kappa_n\kappa_{n'}}}{2}[N(\omega_{n'}) + N(\omega_n) + 2]\mathrm{e}^{-i(\omega_n-\omega_{n'})t}, \tag{S29}$$

and the lamb shifts

$$\Delta(\omega_n, -\omega_{n'}, t) = \frac{i\sqrt{\kappa_n\kappa_{n'}}}{4}[M^*(\omega_{n'}) - M^*(\omega_n)]\mathrm{e}^{-i(\omega_n+\omega_{n'}-2\omega_p)t}, \tag{S30}$$

$$\Delta(-\omega_n, \omega_{n'}, t) = \frac{i\sqrt{\kappa_n\kappa_{n'}}}{4}[M(\omega_{n'}) - M(\omega_n)]\mathrm{e}^{i(\omega_n+\omega_{n'}-2\omega_p)t}, \tag{S31}$$

$$\Delta(-\omega_n, -\omega_{n'}, t) = \frac{i\sqrt{\kappa_n\kappa_{n'}}}{4}[N(\omega_{n'}) - N(\omega_n)]\mathrm{e}^{i(\omega_n-\omega_{n'})t}, \tag{S32}$$

$$\Delta(\omega_n, \omega_{n'}, t) = \frac{i\sqrt{\kappa_n\kappa_{n'}}}{4}[N(\omega_{n'}) - N(\omega_n)]\mathrm{e}^{-i(\omega_n-\omega_{n'})t}. \tag{S33}$$

See Sect. 6 for a discussion on the validity of the secular approximation here. In the next sections we consider three relevant cases: A) No squeezing: $N(\omega) = M(\omega) = 0$, B) squeezing at $\omega_p = (\omega_m + \omega_r)/2$ and C) squeezing at $\omega_p = \omega_r$ with a filter at ω_m: $\kappa_m \to 0$.

1.1 No squeezing

The first case is a bath at zero temperature, corresponding to $M(\omega) = N(\omega) = 0$. The generalization to a finite temperature bath is simply obtained by setting $N(\omega) \neq 0$. The master equation Eq. (S16) then reduces to the Lindblad form

$$\dot{\rho}(t) = \mathcal{D}[\sqrt{\kappa_r}(\hat{a} + \hat{\mathcal{O}}) - \sqrt{\kappa}_m \mathrm{e}^{i\delta t}\hat{\mathcal{O}}]\rho(t). \tag{S34}$$

where $\mathcal{D}[\hat{x}]\bullet = \hat{x} \bullet \hat{x}^\dagger - \frac{1}{2}\{\hat{x}^\dagger\hat{x}, \bullet\} = \mathcal{D}[\hat{x}, \hat{x}^\dagger]\bullet$ is the usual dissipation superoperator. In this frame, the oscillator starts and stays in vacuum which means that the terms $\mathcal{D}[a, \hat{\mathcal{O}}]\rho(t)$ and $\mathcal{D}[\hat{\mathcal{O}}, \hat{a}^\dagger]\rho(t)$ will be zero at all times. We can thus rewrite the equation in a way that makes the qubit dephasing rate explicit

$$\dot{\rho}(t) = \kappa_r \mathcal{D}[\hat{a}]\rho(t) + [\kappa_r + \kappa_m - 2\sqrt{\kappa_r \kappa_m}\cos(\delta t)]\mathcal{D}[\hat{\mathcal{O}}]\rho(t). \tag{S35}$$

Moving out of the interaction picture and setting $g_1 = g_2 \equiv g$, $\kappa_r = \kappa_m \equiv \kappa$, $1/\tilde{\delta} \approx 1/\delta$ for simplicity, we recover Eq. (4) of the main paper. We also see from this equation that we can use a filter at the modulation frequency to lower the dephasing rate. Setting $\kappa_m \to 0$, we get $\Gamma = \kappa(g/2\delta)^2$ which is on average a factor two decrease over the initial dephasing rate.

1.2 Squeezing at the average frequency

The second case we consider is a bath with a broadband squeezing spectrum centred at the average of the oscillator and modulation frequency $\omega_p = (\omega_r + \omega_m)/2$. We assume a flat squeezing spectrum over the relevant bandwidth such that $M \equiv M(\omega_m) = M(\omega_r)$ and $N \equiv N(\omega_m) = N(\omega_r)$. In the limit of perfect squeezing, we can write $M = \sqrt{N(N+1)}\mathrm{e}^{2i\theta}$ with θ the squeezing angle and $N = \sinh^2 r$ with r the squeezing parameter. As explained in the main paper, the condition on θ is that the anti-squeezed quadrature is aligned with the displacement direction at all time. Note that here we set the displacement direction by fixing the phase reference of the first qubit modulation drive, so that θ is also referenced to the modulation. Setting $\theta = 0$ and assuming a flat spectrum in the output field density of modes $\kappa_r = \kappa_m \equiv \kappa$, we get after some algebra that Eq. (S16) can be written in Lindblad form

$$\dot{\rho}(t) = \kappa\, \mathcal{D}\left[\cosh(r)\hat{a}\mathrm{e}^{-\frac{i\delta t}{2}} + \sinh(r)\hat{a}^\dagger \mathrm{e}^{\frac{i\delta t}{2}} - i\mathrm{e}^{-r}\sin\left(\frac{\delta t}{2}\right)\hat{\mathcal{O}}\right]\rho(t). \tag{S36}$$

The last term in the dissipation operator clearly shows that phase information is completely hidden at high squeezing power. Assuming that the squeezing interaction has been turned on long before the gate, the oscillator starts in a squeezed vacuum state ($\alpha_j(0) = 0$ in Eq. (S5)). In the polaron frame, the oscillator is at all times in a squeezed vacuum state, which means that the dephasing rate is given by the prefactor in front of the qubit ($\hat{\mathcal{O}}$) operator

$$\Gamma = 2\kappa\left(\frac{g}{2\tilde{\delta}}\right)^2 [1 - \cos(\delta t)]\mathrm{e}^{-2r}, \tag{S37}$$

for $g_1 = g_2 \equiv g$.

This equation indicates that we dephasing can be reduced exponentially for arbitrarily high squeezing levels r, but one must keep in mind the approximations that were made in order to get the final master equation Eq. (S36). In particular, we neglected fast-rotating terms in the secular approximation when calculating the dephasing rates of the master equation, Eq. (S26). Since N and M grow exponentially with squeezing power, there will be a point where the secular approximation is no longer valid. In general the error made due to the secular approximation can be upper bounded by

$$\varepsilon_{\text{secular}} \lesssim \frac{2}{3}\left[2\kappa\left(\frac{g}{2\tilde{\delta}}\right)^2 \mathrm{e}^{2r}\right]^2 t_g \frac{2\pi}{(2\omega_m)}, \tag{S38}$$

following the approach outlined in Sect. 6. The physical intuition behind this error bound is that the real path in phase space of the oscillator, given by $\alpha(t)$ in Eq. (S6), is not a perfect circle due to the fast rotating terms. Thus, the anti-squeezed quadrature cannot be aligned with the displacement at all times and small deviations from the circle will eventually lead to an increase in dephasing at very high squeezing power.

For the parameters used in Fig. 2 (c) of the main paper, $\delta/(2\pi) = 0.6$ GHz, $g/(2\pi) = 60$ MHz, $t_g = 42.7$ ns, $\kappa/(2\pi) = 1.0$ MHz and $\omega_r/(2\pi) = 10$ GHz, the right-hand side of Eq. (S38) evaluates

to $\sim 10^{-5}$ for $S = 10$ dB of squeezing. Hence we expect that we cannot be confident about a gate error smaller than this number based on evaluating Eq. (S36) with this set of parameters. The curve in Fig. 3 of the paper is only shown for values of S smaller than this bound.

We also assumed an equal squeezing spectrum and equal decay rates at the two frequencies ω_r and ω_m. It is not shown in Eq. (S36), but a discrepancy in the decay rates and/or squeezing spectrum will lead to an additional dephasing that grows exponentially with squeezing.

1.3 Squeezing at the oscillator frequency

The third case we consider is a bath squeezed at the resonator frequency, $\omega_p = \omega_r$. We set $N(\omega_m) = M(\omega_m) = 0$ and define $M \equiv M(\omega_r)$, $N \equiv N(\omega_r)$, which corresponds to a squeezing spectrum much larger than κ_r, but much narrower than δ. Furthermore, we will assume a filter at the oscillator's output so that $\kappa_m = 0$, leading to

$$\dot{\rho}(t) = \kappa_r(N+1)\mathcal{D}[\hat{a}+\hat{\mathcal{O}}]\rho(t) + \kappa_r N\hat{\mathcal{D}}[\hat{a}^\dagger+\hat{\mathcal{O}}]\rho(t) + \kappa_r M\mathcal{S}[\hat{a}^\dagger+\hat{\mathcal{O}}]\rho(t) + \kappa_r M^*\mathcal{S}[\hat{a}+\hat{\mathcal{O}}]\rho(t). \tag{S39}$$

In this expression, $\mathcal{S}[\hat{x}]\bullet = \hat{x}\bullet\hat{x} - \frac{1}{2}\{\hat{x}\hat{x},\bullet\} = \mathcal{D}[\hat{x},\hat{x}]\bullet$ is a squeezing superoperator. The gain in fidelity appears when we rewrite this in Lindblad form and set $\theta = \pi/2$

$$\dot{\rho}(t) = \kappa_r\mathcal{D}[\cosh(r)\hat{a} - \sinh(r)\hat{a}^\dagger + \mathrm{e}^{-r}\hat{\mathcal{O}}]\rho(t). \tag{S40}$$

The dephasing rate is then exponentially reduced

$$\Gamma = \kappa_r\left(\frac{g}{2\tilde{\delta}}\right)^2\mathrm{e}^{-2r}, \tag{S41}$$

for $g_1 = g_2 \equiv g$. Phase information is completely hidden for large squeezing.

Since this equation is derived the same way as Eq. (S36), this exponential gain also has a confidence bound similar to Eq. (S38). We also note that adding filter this way does no contradict the Markov approximation made earlier. As long as the filter's bandwith is smaller than δ, making the Markov approximation here amounts to assuming that the bath density of modes is constant around each frequency in play (ω_r and ω_m).

2 Examples of physical implementation

In this section we give a very brief summary of how we can achieve a longitudinal coupling modulation in various platforms, as well as references on how to perform single qubit control.

Transmons—More details about transmons longitudinally-coupled to resonators can be found in [S3–S5]. Arbitrary single qubit $X = \hat{\sigma}_x$ and $Y = \hat{\sigma}_y$ rotations can be performed in the standard way by applying a microwave drive at a side gate voltage. Fidelities for these gates are now above 99.9% [S6]. The longitudinal coupling $g_z(t)$ can be modulated via an AC flux drive $\Phi_x(t)$ in the middle of the qubit squid loop: The frequency and the amplitude of the coupling modulation are then directly related to the frequency and amplitude of the flux drive.

Flux qubits—In this implementation, for which more details can be found in Ref. [S7], X and Y single-qubit gates can be realized via modulation of the flux inside the qubit loop with over 99.8% fidelity [S8]. Modulation of the longitudinal coupling can be realized via modulation of the reduced gate charge on the superconducting island.

Spin qubits—As discussed in more details in [S9], in this implementation the longitudinal coupling could be modulated by controlling the inter-dot tunnelling. Single-qubit gates with average fidelities of 99.6% have been demonstrated [S10].

Singlet-triplet spin qubits—For this implementation, single qubit operations with 99% have been demonstrated [S11]. Similar to the previous implementation, longitudinal coupling to a resonator can be modulated through the inter-dot tunnelling [S12].

3 Coupled oscillators

In this section we derive the effective $\hat{\sigma}_z\hat{\sigma}_z$-coupling induced when the two qubits are in different but coupled oscillators. Similar to the single oscillator case, both couplings are modulated at the same

frequency ω_m. The Hamiltonian corresponding to this situation with capacitively coupled oscillators is

$$\hat{H} = \omega_a \hat{a}^\dagger \hat{a} + \omega_b \hat{b}^\dagger \hat{b} + \tfrac{1}{2}\omega_{a1}\hat{\sigma}_{z1} + \tfrac{1}{2}\omega_{a2}\hat{\sigma}_{z2} + g_1(t)\hat{\sigma}_{z1}\,(\hat{a}^\dagger + \hat{a}) + g_2(t)\hat{\sigma}_{z2}\,(\hat{b}^\dagger + \hat{b}) - g_{ab}(\hat{a}^\dagger - \hat{a})(\hat{b}^\dagger - \hat{b}). \tag{S42}$$

Following the same approach as in the single oscillator case, we first move to a frame rotating at ω_m for both oscillators and ω_{ai} for the respective qubits. To simplify the discussion, we also perform a rotating wave approximation and neglect fast-rotating terms leading to

$$\hat{H}_R = \delta_a \hat{a}^\dagger \hat{a} + \delta_b \hat{b}^\dagger \hat{b} + \frac{g_1}{2}\hat{\sigma}_{z1}\,(\hat{a}^\dagger + \hat{a}) + \frac{g_2}{2}\hat{\sigma}_{z2}\,(\hat{b}^\dagger + \hat{b}) + g_{ab}(\hat{a}^\dagger \hat{b} + \hat{a}\hat{b}^\dagger). \tag{S43}$$

The second step is to diagonalize the oscillator part of the Hamiltonian $\hat{H}_r = \delta_a \hat{a}^\dagger \hat{a} + \delta_b \hat{b}^\dagger \hat{b} + g_{ab}(\hat{a}^\dagger \hat{b} + \hat{a}\hat{b}^\dagger)$ and to express the longitudinal coupling in terms of the resulting hybridized modes. For this purpose, we define the eigenmode operators

$$\hat{c} = \cos\xi\,\hat{a} + \sin\xi\,\hat{b}, \tag{S44}$$

$$\hat{d} = -\sin\xi\,\hat{a} + \cos\xi\,\hat{b}, \tag{S45}$$

where $\tan 2\xi = 2g_{ab}/(\omega_a - \omega_b)$. Expressing the Hamiltonian Eq. (S43) in terms of these eigenmodes yields

$$\hat{H}_R = \delta_c \hat{c}^\dagger \hat{c} + \delta_d \hat{d}^\dagger \hat{d} + \left\{ \frac{1}{2}\left[g_1 \cos\xi\,\hat{\sigma}_{z1} + g_2 \sin\xi\,\hat{\sigma}_{z2}\right]\hat{c}^\dagger + \frac{1}{2}\left[-g_1 \sin\xi\,\hat{\sigma}_{z1} + g_2 \cos\xi\,\hat{\sigma}_{z2}\right]\hat{d}^\dagger + \text{H.c.} \right\}, \tag{S46}$$

where the detunings are

$$\delta_c = \frac{\delta_a + \delta_b}{2} + \frac{g_{ab}}{\sin 2\xi}, \qquad \delta_d = \frac{\delta_a + \delta_b}{2} - \frac{g_{ab}}{\sin 2\xi}. \tag{S47}$$

Following the same approach as in Sect. 1 we finally apply the unitary transformation

$$\hat{U}_D = \mathrm{e}^{\hat{\mathcal{O}}_c \hat{c}^\dagger - \hat{\mathcal{O}}_c^\dagger \hat{c}} \mathrm{e}^{\hat{\mathcal{O}}_d \hat{d}^\dagger - \hat{\mathcal{O}}_d^\dagger \hat{d}} \equiv \hat{U}_c \hat{U}_d, \tag{S48}$$

with $\hat{\mathcal{O}}_c = (g_1 \cos\xi\,\hat{\sigma}_{z1} + g_2 \sin\xi\,\hat{\sigma}_{z2})/2\delta_c$ and $\hat{\mathcal{O}}_d = (-g_1 \sin\xi\,\hat{\sigma}_{z1} + g_2 \cos\xi\,\hat{\sigma}_{z2})/2\delta_d$. Because $[\hat{U}_c, \hat{U}_d] = 0$, the transformation does not generate a coupling between the eigenmodes. The resulting Hamiltonian is then

$$\hat{H}_{\text{pol}} = \delta_c \hat{c}^\dagger \hat{c} + \delta_d \hat{d}^\dagger \hat{d} + J_z(t)\hat{\sigma}_{z1}\hat{\sigma}_{z2}, \tag{S49}$$

with the $\hat{\sigma}_z\hat{\sigma}_z$-coupling strength

$$\bar{J}_z = \frac{\delta_c - \delta_d}{\delta_c \delta_d}\frac{g_1 g_2}{4}\sin 2\xi. \tag{S50}$$

Defining $\bar{\delta} = (\delta_a + \delta_b)/2$ and $\zeta = 1/\tan 2\xi$, we can write this as

$$\bar{J}_z = \frac{1}{2}\frac{g_1 g_2 g_{ab}}{\bar{\delta}^2 - g_{ab}^2(1+\zeta^2)} \tag{S51}$$

corresponding to the result stated in the main paper.

4 Details on the simulations

To calculate the average gate fidelity, we compare full master equation simulations to the ideal channel $\mathcal{U}_{CZ}\bullet = \hat{U}_{CZ}\,\bullet\,\hat{U}_{CZ}^\dagger$ with $\hat{U}_{CZ} = \mathrm{diag}[1,1,1,-1] = \hat{U}_{CP}(\pi)$. The master equation is defined over the system oscillator-qubit and we therefore eliminate the oscillator degree of freedom. We define the channel $\mathcal{E}_{q_1 q_2}$ acting on the qubits as

$$\mathcal{E}_{q_1 q_2}(\bullet) = \mathcal{T}_r\,\mathcal{U}_D^\dagger\,\mathcal{U}_I^\dagger\,\mathcal{E}^{t_g}\,\mathcal{U}_I\,\mathcal{U}_D\,\mathcal{S}\left(|0\rangle\langle 0|_r \otimes \bullet\right), \tag{S52}$$

where the superoperator $\mathcal{T}_r\bullet \equiv \mathrm{Tr}_r(\bullet)$ is the trace over the oscillator degree of freedom and the superoperators $\mathcal{U}_D\bullet \equiv \hat{\mathbf{U}}\,\bullet\,\hat{\mathbf{U}}^\dagger$, $\mathcal{U}_D^\dagger\bullet \equiv \hat{\mathbf{U}}^\dagger\,\bullet\,\hat{\mathbf{U}}$ are the unitary displacement transformations defined in Eq. (S5). We also defined the interaction picture superoperators $\mathcal{U}_I\bullet \equiv \hat{U}_I\,\bullet\,\hat{U}_I^\dagger$ and $\mathcal{U}_I^\dagger\bullet \equiv \hat{U}_I^\dagger\,\bullet\,\hat{U}_I$

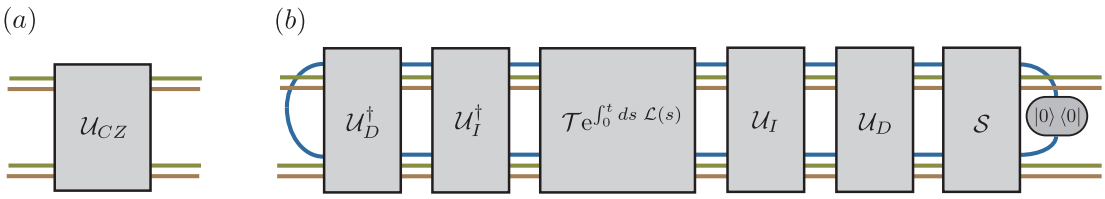

Figure S1: Tensor representation of the CZ gate supermatrix [S13]. Here the blue lines represent the oscillator degree of freedom and the green (brown) lines represent the first (second) qubit. (a) Ideal controlled-Z channel. (b) Simulated quantum channel over two qubits. We project onto an initial vacuum state of the oscillator at the beginning (right) and trace over the oscillator degree of freedom at the end (left). The superoperator $\mathcal{T}e^{\bullet}$ denotes the time-ordering exponential.

with $\hat{U}_I$ defined in Eq. (S11). The squeezing superoperator is given by $\mathcal{S} \equiv \hat{\mathbf{S}}(re^{2i\theta})^\dagger \bullet \hat{\mathbf{S}}(re^{2i\theta})$ with the standard definition $\hat{\mathbf{S}}(re^{2i\theta}) = \exp\left[re^{-2i\theta}\hat{a}^2/2 - \text{H.c.}\right]$.

Finally, $\mathcal{E}^{t_g}$ is the oscillator-qubit channel calculated from numerical integration of the differential equation

$$\dot{\mathcal{E}}^t = \mathcal{L}\mathcal{E}^t. \tag{S53}$$

where $\mathcal{L}$ is a Liouvillian derived in Sect. 1. If we impose the initial condition $\mathcal{E}^0 = \text{Id}$, then $\mathcal{E}^t$ denotes the channel resulting from evolution under the Liouvillian $\mathcal{L}$ for a time t. This whole procedure is illustrated in terms of tensor diagrams in Fig. S1 [S13].

In the case where we include intrinsic qubit decay and dephasing, we add additional terms to the calculated Liouvillian

$$\dot{\rho}(t) = \mathcal{L}'\rho(t) = \mathcal{L}\rho(t) + \sum_i \gamma_1^{(i)}\mathcal{D}[\hat{\sigma}_{-i}]\rho(t) + \gamma_\phi^{(i)}\mathcal{D}[\hat{\sigma}_{zi}]\rho(t), \tag{S54}$$

where the decay rates are given by $\gamma_1^{(i)} = 1/T_1^{(i)}$, $1/T_2^{(i)} = \gamma_\phi^{(i)} + \gamma_1^{(i)}/2$.

Although we take the oscillator to initially be in a vacuum squeezed state in our numerical calculations, we emphasize that any initial displacement could have been added without change to the resulting fidelity.

Knowing the effective channel over two qubits, the average gate fidelity $\mathcal{F}$ is obtained by averaging over all two-qubit initial states according to the uniform (Haar) measure [S14].

$$\mathcal{F} = \int d\psi \langle\psi|U_{CZ}^\dagger \mathcal{E}_{q_1 q_2}(|\psi\rangle\langle\psi|)U_{CZ}|\psi\rangle. \tag{S55}$$

The simulations were performed using QuTiP [S15].

5 Comparison with transverse resonator-induced phase gate

In the main Paper, we present a numerical example for the gate time and gate fidelity using $\kappa/2\pi = 0.05$ MHz [S16], $g/2\pi = 60$ MHz [S3] and $\delta/2\pi = 537$ MHz. This results in a very short gate time of $t_g = 37$ ns with an average gate infidelity as small as 1×10^{-4}. Taking into account finite qubit lifetimes $T_1 = 30\,\mu$s and $T_2 = 20\,\mu$s [S6], we find that the infidelity is increased to $\sim 10^{-3}$. As also pointed out in the Paper, the gate fidelity is limited by the qubit's natural decoherence channels with these parameters.

For the same value of κ and typical circuit QED parameters, ideal simulations (excluding T_1 and T_2) of a transversal resonator-induced phase (RIP) gates yield a gate fidelity of 4×10^{-4} for a gate time of 200 ns [S17]. Thus, comparing to a transversal RIP gate with parameters from Ref. [S17], the scheme introduced here, with the representative choice of parameters used in the previous paragraph, exhibits a factor 4 improvement in fidelity and a factor 5 improvement in gate time. Since a transversal RIP gate depends on a different set of parameters (in particular there is a strong dependence on resonator-qubit detuning), the use of optimal control would allow the comparison of best-case performance for the gate proposed in this paper and transversal RIP gates. The large improvement we find for typical parameter choices and un-optimized pulse shapes, however, suggests that very substantial improvements are possible in practice.

6 Error bound for rotating terms in the master equation

In this section, we estimate an upper bound on the error made by neglecting fast-rotating terms in the master equation. More precisely, we want to estimate where the secular approximation made in Eqs. (S26) to (S33) is no longer valid. We will follow closely the supplemental material of [S18], where a similar question was addressed for unitary evolution.

We start with a general Lindbladian $\mathcal{L}(t) = \mathcal{L}_0 + \gamma(t)\mathcal{L}_1$ and we will assume that $\mathcal{L}_0, \mathcal{L}_1$ do not depend on time and that $\gamma(t)$ is some fast-oscillating function. In particular, we are interested in the case where

$$\int_0^{\Delta t} dt\ \gamma(t) = 0, \tag{S56}$$

with Δt the smallest time increment for which Eq. (S56) is respected. In our case, we have $\Delta t \sim 2\pi/(2\omega_m)$.

The problem we address is the following: What is the error we make when we replace $\mathcal{L}(t)$ by

$$\mathcal{L}_{av} \equiv \frac{1}{\Delta t}\int_0^{\Delta t} dt\mathcal{L}(t) = \mathcal{L}_0. \tag{S57}$$

In other words, what is the error we make by doing a Suzuki-Trotter decomposition and at each time step we replace the linbladian by its average. We define an average channel $\mathcal{E}_{av}(t) \equiv \mathrm{e}^{\mathcal{L}_{av}t}$, which replaces the full evolution channel $\mathcal{E}(t) = \mathcal{T}\mathrm{e}^{\int_0^t ds\ \mathcal{L}(s)}$. To estimate the error for a single time step, we look at the norm of the superoperator $X(\Delta t) \equiv \mathbb{I} - \mathcal{E}_{av}^{-1}(\Delta t)\mathcal{E}(\Delta t)$. Knowing that $X(0) = 0$, we write

$$\begin{aligned} X(\Delta t) &= \int_0^{\Delta t} ds\ \dot{X}(s) \\ &= -\int_0^{\Delta t} ds\ \dot{\mathcal{E}}_{av}^{-1}(s)\mathcal{E}(s) + \mathcal{E}_{av}^{-1}(s)\dot{\mathcal{E}}(s) \\ &= \int_0^{\Delta t} ds\ \mathcal{E}_{av}^{-1}(s)\mathcal{L}_{av}\mathcal{E}(s) - \mathcal{E}_{av}^{-1}(s)\mathcal{L}(s)\mathcal{E}(s) \end{aligned} \tag{S58}$$

where we used the differential equation for the channel $\dot{\mathcal{E}} = \mathcal{L}\mathcal{E}$ and we directly differentiated $\dot{\mathcal{E}}_{av}^{-1} = \partial_t(\mathrm{e}^{-\mathcal{L}_{av}t}) = -\mathcal{E}_{av}^{-1}\mathcal{L}_{av}$. We replace $\mathcal{L}_{av}$ by its explicit expression Eq. (S57) and change the integration variables to get

$$X(\Delta t) = \frac{1}{\Delta t}\int_0^{\Delta t} ds\ \int_0^{\Delta t} d\tau\ \mathcal{E}_{av}^{-1}(s)\mathcal{L}(\tau)\mathcal{E}(s) - \mathcal{E}_{av}^{-1}(\tau)\mathcal{L}(\tau)\mathcal{E}(\tau). \tag{S59}$$

We now evaluate the norm and use the triangle inequality to get

$$\|X(\Delta t)\| \leqslant \frac{1}{\Delta t}\int_0^{\Delta t} ds\ \int_0^{\Delta t} d\tau\ \left\|\mathcal{E}_{av}^{-1}(\tau)\mathcal{L}(\tau)\left[\mathcal{E}(s) - \mathcal{E}(\tau)\right]\right\| + \left\|\left[\mathcal{E}_{av}^{-1}(s) - \mathcal{E}_{av}^{-1}(\tau)\right]\mathcal{L}(\tau)\mathcal{E}(\tau)\right\|. \tag{S60}$$

We know that a physical channel is norm contractive and we will choose a norm respecting $\|\mathcal{E}\| \leq 1$ so that we can use the Schwartz inequality and write

$$\|X(\Delta t)\| \leqslant \frac{\|\mathcal{L}\|}{\Delta t}\int_0^{\Delta t} ds\ \int_0^{\Delta t} d\tau\ \left\|\mathcal{E}_{av}^{-1}(\tau)\right\|\|\mathcal{E}(s) - \mathcal{E}(\tau)\| + \left\|\mathcal{E}_{av}^{-1}(s) - \mathcal{E}_{av}^{-1}(\tau)\right\|, \tag{S61}$$

where we defined $\|\mathcal{L}\| = \max_s \|\mathcal{L}(s)\|$. The first term in the integral is upper bounded by

$$\begin{aligned} \|\mathcal{E}(s) - \mathcal{E}(\tau)\| &= \left\|\int_s^{\tau} dt\ \dot{\mathcal{E}}(t)\right\| \\ &= \left\|\int_{\tau}^{s} dt\ \mathcal{L}(t)\mathcal{E}(t)\right\| \\ &\leqslant \|\mathcal{L}\|\,|s - \tau|, \end{aligned} \tag{S62}$$

and the second term by

$$\begin{aligned}\left\|\mathcal{E}_{av}^{-1}(s)-\mathcal{E}_{av}^{-1}(\tau)\right\| &= \left\|\int_s^\tau dt\ \dot{\mathcal{E}}_{av}^{-1}(t)\right\| \\ &= \left\|\mathcal{L}_{av}\int_s^\tau dt\ \mathcal{E}_{av}^{-1}(t)\right\| \\ &\leqslant \|\mathcal{L}\|\left\|\mathcal{E}_{av}^{-1}(\Delta t)\right\||s-\tau|.\end{aligned} \tag{S63}$$

In the last line we used that fact that if a physical channel contracts the norm, then its inverse must necessarily increase it which means that for $t_1 > t_2$ we have $\left\|\mathcal{E}^{-1}(t_1)\right\| \geq \left\|\mathcal{E}^{-1}(t_2)\right\|$ Putting back Eqs. (S62) and (S63) into Eq. (S61), we get

$$\begin{aligned}\|X(\Delta t)\| &\leqslant \frac{2\|\mathcal{L}\|^2}{\Delta t}\left\|\mathcal{E}_{av}^{-1}(\Delta t)\right\|\int_0^{\Delta t} ds\int_0^{\Delta t} d\tau\ |s-\tau| \\ &\leqslant \frac{2}{3}\|\mathcal{L}\|^2\Delta t^2\left\|\mathcal{E}_{av}^{-1}(\Delta t)\right\| \\ &\lesssim \frac{2}{3}\|\mathcal{L}\|^2\Delta t^2.\end{aligned} \tag{S64}$$

In general, the norm of the average inverse channel can be large, but in our specific case Δt is much smaller than any evolution time scale of the average channel, which means that we can approximate $\left\|\mathcal{E}_{av}^{-1}(\Delta t)\right\| \approx 1$. Knowing the error made for each Δt step, we get an upper bound for the full evolution

$$\|X(t_g)\| \lesssim \frac{2}{3}\|\mathcal{L}\|^2 t_g\Delta t. \tag{S65}$$

We add that in order to apply this bound in a meaningful way, the operators inside $\mathcal{L}$ should be bounded, which is not the case for the oscillator operators $\hat{a}, \hat{a}^\dagger$. However, using a Bogoliubov transformation followed by the steps used to go from Eq. (S34) to Eq. (S35) we can express the master equations Eqs. (S36) and (S40) in a form similar to Eq. (S35) where we can trace out the harmonic oscillator. That way, the bound Eq. (S65) can be applied on an effective two-qubit master equation where all the operators are bounded.

References

[S1] C. Gardiner and P. Zoller, *Quantum Noise: A Handbook of Markovian and Non-Markovian Quantum Stochastic Methods with Applications to Quantum Optics*, Springer Series in Synergetics (Springer, 2004).

[S2] H. Breuer and F. Petruccione, *The Theory of Open Quantum Systems* (OUP Oxford, 2007).

[S3] N. Didier, J. Bourassa, and A. Blais, Phys. Rev. Lett. **115**, 203601 (2015).

[S4] S. Richer and D. DiVincenzo, Phys. Rev. B **93**, 134501 (2016).

[S5] A. J. Kerman, New Journal of Physics **15**, 123011 (2013).

[S6] A. D. Corcoles, E. Magesan, S. J. Srinivasan, A. W. Cross, M. Steffen, J. M. Gambetta, and J. M. Chow, Nat Commun **6** (2015).

[S7] P.-M. Billangeon, J. S. Tsai, and Y. Nakamura, Phys. Rev. B **92**, 020509 (2015).

[S8] S. Gustavsson, O. Zwier, J. Bylander, F. Yan, F. Yoshihara, Y. Nakamura, T. P. Orlando, and W. D. Oliver, Phys. Rev. Lett. **110**, 040502 (2013).

[S9] F. Beaudoin, D. Lachance-Quirion, W. A. Coish, and M. Pioro-Ladrière, Nanotechnology **27**, 464003 (2016).

[S10] K. Takeda, J. Kamioka, T. Otsuka, J. Yoneda, T. Nakajima, M. R. Delbecq, S. Amaha, G. Allison, T. Kodera, S. Oda, and S. Tarucha, Science Advances **2** (2016).

[S11] J. M. Nichol, L. A. Orona, S. P. Harvey, S. Fallahi, G. C. Gardner, M. J. Manfra, and A. Yacoby, ArXiv e-prints (2016), arXiv:1608.04258 [cond-mat.mes-hall] .

[S12] P.-Q. Jin, M. Marthaler, A. Shnirman, and G. Schön, Phys. Rev. Lett. **108**, 190506 (2012).

[S13] C. J. Wood, J. D. Biamonte, and D. G. Cory, Quantum Information & Computation **15** (2015).

[S14] M. A. Nielsen, Physics Letters A **303**, 249 (2002).

[S15] J. Johansson, P. Nation, and F. Nori, Computer Physics Communications **184**, 1234 (2013).

[S16] A. Bruno, G. de Lange, S. Asaad, K. L. van der Enden, N. K. Langford, and L. DiCarlo, Applied Physics Letters **106**, 182601 (2015).

[S17] S. Puri and A. Blais, Phys. Rev. Lett. **116**, 180501 (2016).

[S18] D. Poulin, A. Qarry, R. Somma, and F. Verstraete, Phys. Rev. Lett. **106**, 170501 (2011).

Annexe B

Matériel Supplémentaire

Cette annexe contient le matériel supplémentaire de chacun des articles.

B.1 Détecteur de photon version discrète

Supplemental Material for "Itinerant microwave photon detector"

Baptiste Royer,[1] Arne L. Grimsmo,[1,2] Alexandre Choquette-Poitevin,[1] and Alexandre Blais[1,3]

[1] *Institut quantique and Département de Physique, Université de Sherbrooke, 2500 boulevard de l'Université, Sherbrooke, Québec J1K 2R1, Canada*
[2] *Centre for Engineered Quantum Systems, School of Physics, The University of Sydney, Sydney NSW 2006, Australia*
[3] *Canadian Institute for Advanced Research, Toronto, Canada*

This supplemental information is organized as follow. In Section I we describe how to compute the shape of an output photon reflected off an ensemble of inhomogeneous modes. The Hamiltonian of the proposed circuit implementation is derived in Sect. II while Sect. III shows that the circuit Hamiltonian is a good approximation of Eq. (4) of the main Letter. Finally, more informations about the numerical simulations are given in Sect. IV and in Sect. V we highlight some of the challenges in the realization of our scheme for large N.

I. SHAPE OF REFLECTED PHOTON

In this section, we derive the expression for the shape of a single photon reflected off an ensemble of N modes used to produce Fig. 3 of the main text. In this analysis, we set the measurement back-action from the measurement resonator to zero ($g_z = 0$). This considerably simplifies the calculation and allows us to focus on the photon trapping properties of the system.

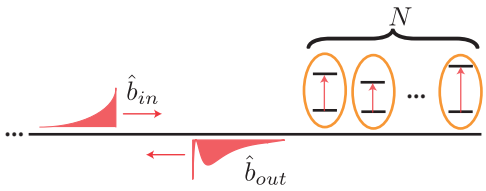

FIG. S1. We consider an ensemble of N modes with different frequencies coupled to a single waveguide, here reprensented as an ensemble of two-level systems without loss of generality. We want to compute the output photon shape $\langle \hat{b}^\dagger_{out}\hat{b}_{out}(t)\rangle$ as a function of the input photon shape $\langle \hat{b}^\dagger_{in}\hat{b}_{in}(t)\rangle$.

Qubit j, of transition frequency frequency ω_{Bj}, is described by its lowering $\hat{b}_j$ and raising $\hat{b}^\dagger_j$ operators. Using this notation, the starting point of our analysis are the standard input-output relations, expressed here in a frame rotating at the average qubit frequency $\omega_B = \sum_j \omega_{Bj}/N$ [S1]

$$\hat{b}_{out} = -i\sum_j \sqrt{\kappa_{Bj}}\hat{b}_j + \hat{b}_{in}, \tag{S1}$$

$$\dot{\hat{b}}_j = -i\Delta_j\hat{b}_j - \frac{\kappa_{Bj}}{2}\hat{b}_j - i\sqrt{\kappa_{Bj}}\hat{b}_{in}, \tag{S2}$$

where $\hat{b}_{in}, \hat{b}_{out}$ are respectively the input and ouput fields. For simplicity, we assume that the coupling of each absorber to the input waveguide is identical, $\kappa_{Bj} = \kappa_B/N$. We rewrite Eq. (S2) in matrix form by defining the column vector $\mathbf{b}^T \equiv (\hat{b}_1\, \hat{b}_2 \ldots \hat{b}_N)$ and the matrix $\Delta \equiv \mathrm{diag}[\vec{\Delta}]$ with $\vec{\Delta} \equiv (\Delta_1\, \Delta_2 \ldots \Delta_N)$,

$$\dot{\mathbf{b}} = -i\Delta\mathbf{b} - \frac{\kappa_B}{2}P_+\mathbf{b} - i\sqrt{\kappa_B}\hat{b}_{in}\mathbf{e}_+, \tag{S3}$$

where $\mathbf{e}_+^T = 1/\sqrt{N} \times (1\,1 \ldots 1)$ is the unit vector corresponding to the bright mode $\hat{b}_+ = 1/\sqrt{N}\sum_j \hat{b}_j$ and $P_+ = \mathbf{e}_+\mathbf{e}_+^\dagger$ is the projector on the subspace spanned by that vector.

It is useful to perform a change of basis, introducing $\tilde{\mathbf{b}} = \mathrm{U}\mathbf{b}$ with $\mathrm{U}_{jk} = \frac{1}{\sqrt{N}}\exp\left(\frac{jk2\pi}{N}\right)$, such that the dissipative terms take a diagonal form

$$\dot{\tilde{\mathbf{b}}} = -i\tilde{\Delta}\tilde{\mathbf{b}} - \frac{\kappa_B}{2}\widetilde{P}_0\tilde{\mathbf{b}} - i\sqrt{\kappa_B}\hat{b}_{in}\tilde{\mathbf{e}}_0, \tag{S4}$$

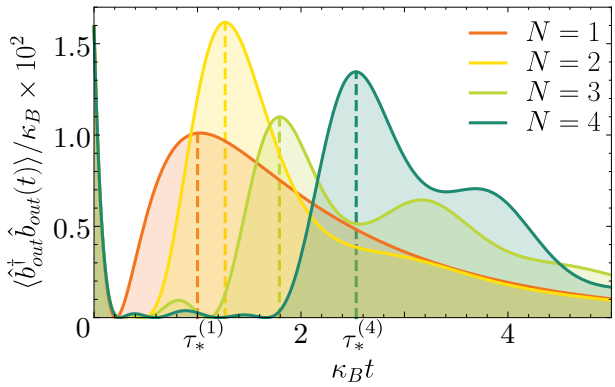

FIG. S2. Output photon shape for different number of absorbers. Here, the input photon shape is a decaying exponential $\langle \hat{b}^\dagger_{in} \hat{b}_{in}(t) \rangle = \kappa_C e^{-\kappa_C t}$ with $\kappa_C/\kappa_B = 0.1$ and, for multiple absorbers, we set detunings to $\vec{\Delta}^{(2)}/\kappa_B = (0.55, -0.55)$, $\vec{\Delta}^{(3)}/\kappa_B = (0.7, -0.7, 0)$ and $\vec{\Delta}^{(4)}/\kappa_B = (0.7, -0.7, 0.23, -0.23)$.

where $U\mathbf{e}_+ = \tilde{\mathbf{e}}_0$, $\tilde{P}_0 \equiv U P_+ U^\dagger$ and $\tilde{\Delta} \equiv U \Delta U^\dagger$. Projecting on the bright and dark subspaces, this leads to the two coupled Langevin equations

$$\begin{aligned} \dot{\hat{\tilde{b}}}_0 &= -i\tilde{\mathbf{e}}_0^\dagger \tilde{\Delta} \tilde{P}_D \tilde{\mathbf{b}}_D - i\tilde{\mathbf{e}}_0^\dagger \tilde{\Delta} \tilde{\mathbf{e}}_0 \hat{\tilde{b}}_0 - \frac{\kappa_B}{2} \hat{\tilde{b}}_0 - i\sqrt{\kappa_B} \hat{b}_{in}, \\ \dot{\tilde{\mathbf{b}}}_D &= -i\tilde{P}_D \tilde{\Delta} \tilde{P}_D \tilde{\mathbf{b}}_D - i\tilde{P}_D \tilde{\Delta} \tilde{\mathbf{e}}_0 \hat{\tilde{b}}_0, \end{aligned} \tag{S5}$$

where we have defined $\hat{\tilde{b}}_0 \equiv \tilde{\mathbf{e}}_0^\dagger \tilde{\mathbf{b}}$ and $\tilde{\mathbf{b}}_D \equiv \tilde{P}_D \tilde{\mathbf{b}}$.

These equations can be solved in Laplace space using the identity $\mathcal{L}[\dot{f}(t)] = s\mathcal{L}[f(t)] - f(0)$, where $\mathcal{L}[f(t)] = \int_0^\infty dt\, e^{-st} f(t)$. Indeed, defining $\tilde{B}_k(s) \equiv \mathcal{L}\left[\hat{\tilde{b}}_k\right]$, we get

$$\tilde{\mathbf{B}}_D(s) = (s + i\tilde{P}_D \tilde{\Delta} \tilde{P}_D)^{-1} \tilde{\mathbf{b}}_D(0) - i(s + i\tilde{P}_D \tilde{\Delta} \tilde{P}_D)^{-1} \tilde{P}_D \tilde{\Delta} \tilde{\mathbf{e}}_0 \tilde{B}_0(s). \tag{S6}$$

Taking the absorbers to initially be in their ground state, we set $\tilde{\mathbf{b}}_D(0) = 0$ and use the last equation together with Eq. (S5) to solve for $\tilde{B}_0(s)$. To simplify the notation, we define $\delta(s, \Delta) \equiv -i\tilde{\mathbf{e}}_0^\dagger \tilde{\Delta} \tilde{P}_D (s + i\tilde{P}_D \tilde{\Delta} \tilde{P}_D)^{-1} \tilde{P}_D \tilde{\Delta} \tilde{\mathbf{e}}_0$ and find

$$\tilde{B}_0(s) = \frac{-i\sqrt{\kappa_B}}{s + i\tilde{\mathbf{e}}_0^\dagger \tilde{\Delta} \tilde{\mathbf{e}}_0 + i\delta(s, \Delta) + \frac{\kappa_B}{2}} B_{in}(s). \tag{S7}$$

To obtain the shape of the output photon, we replace this result in the Laplace transform of Eq. (S1) and perform the inverse Laplace transform to find

$$\hat{b}_{out}(t) = \mathcal{L}^{-1}\left[\left(1 - \frac{\kappa_B}{s + i\tilde{\mathbf{e}}_0^\dagger \tilde{\Delta} \tilde{\mathbf{e}}_0 + i\delta(s, \Delta) + \frac{\kappa_B}{2}} \right) B_{in}(s) \right]. \tag{S8}$$

Figure S2 was calculated by performing the inverse laplace transform numerically. In our model, the input photon comes from an additional mode with decay rate κ_C and initialized in the one photon Fock state $|1\rangle$, such that $B_{in}(s) = \hat{b}_{in}(0)\sqrt{\kappa_C}/(s + \kappa_C/2)$ with $\langle \hat{b}^\dagger_{in} \hat{b}_{in}(0) \rangle = 1$.

To illustrate the increasing trapping time with ensemble size, Fig. S2 shows the shape of the signal photon after re-emission from the detector, $\langle \hat{b}^\dagger_{out} \hat{b}_{out}(t) \rangle$. In the single absorber case $N = 1$ (orange), the photon is absorbed and then re-emitted after a time $\tau_*^{(1)} = 1/\kappa_B$ (dashed orange line). The output photon number also shows, at short times $< 0.2/\kappa_B$, a $\sim 4\%$ component that is directly reflected by the absorber. On the other hand, for $N > 1$ the detunings $\vec{\Delta}$ were optimized such that the photon is re-emitted after an increased time $\tau_*^{(N)} = 1/\kappa_B + \tau_{trap}^{(N)}$ (dashed vertical lines), clearly showing the trapping effect. Also as expected, the photon number at the output is conserved $\int_0^\infty dt\, \langle \hat{b}^\dagger_{out} \hat{b}_{out}(t) \rangle = 1$, corresponding to a non-destructive process. Moreover, because the collective absorption rate has been scaled such that it does not depend on

ensemble size, the small, immediate reflection of about $\sim 4\%$ at short times is identical for all values of N in Fig. S2. Since this component will not lead to a detectable signal in mode A, an upper bound of the quantum efficiency can be obtained from $\eta_{max} \simeq 1 - \int_0^{0.2/\kappa_B} dt\, \langle \hat{b}_{out}^\dagger \hat{b}_{out}(t)\rangle \simeq 96\%$, for these parameters. The value of this upper bound is linked to the choice of both detector and signal photon parameters and could be improved upon further optimization.

II. CIRCUIT DESIGN

In the following two sections, we derive the Hamiltonian Eq. (4) of the main Letter starting from the circuit illustrated in Fig. S3. In this section, we start from the circuit Lagrangian and perform a Legendre transform to obtain the circuit Hamiltonian. Then, in Sect. III, we show how the circuit Hamiltonian Eq. (S16) approximates the desired Hamiltonian.

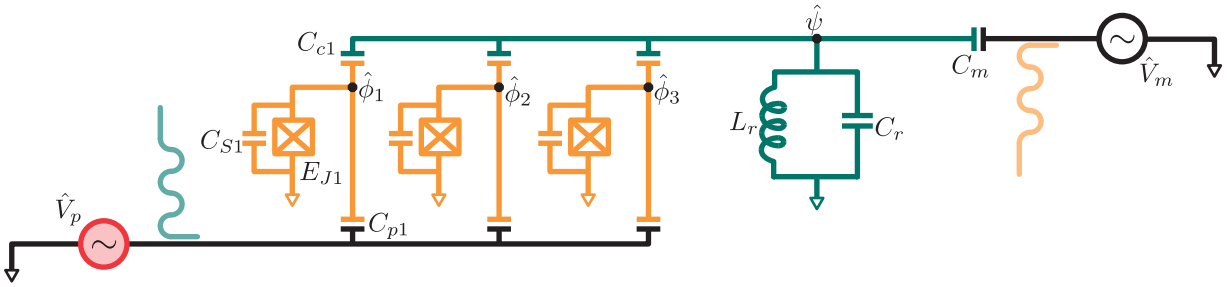

FIG. S3. Circuit design realising the desired Hamiltonian Eq. (4) of the main Letter for $N = 3$. The absorber qubits are in orange ($\hat{\phi}_j$), the measurement resonator is in green ($\hat{\psi}$) and the red voltage $\hat{V}_p$ represents the input photon. The two wavy lines coming out of the transmission lines represent purcell filters that prevent leakage of the modes in the wrong port. The light green purcell filter should thus be at ω_r and the light orange one at ω_B.

Following standard circuit quantization techniques [S2], the Lagrangian for the circuit illustrated in Fig. S3 takes the form

$$\begin{aligned}\hat{L} =& \frac{C_r\dot{\hat{\psi}}^2}{2} - \frac{\hat{\psi}^2}{2L_r} + \frac{C_m}{2}(\dot{\hat{\psi}} - \dot{\hat{V}}_m)^2 \\ &+ \sum_{j=1}^{N} \frac{C_{cj}}{2}(\dot{\hat{\phi}}_j - \dot{\hat{\psi}})^2 + \frac{C_{Sj}}{2}\dot{\hat{\phi}}_j^2 + \frac{C_{pj}}{2}(\dot{\hat{\phi}}_j - \dot{\hat{V}}_p)^2 + E_{Jj}\cos\left(\frac{2\pi}{\Phi_0}\hat{\phi}_j\right).\end{aligned} \tag{S9}$$

Here, $\hat{\psi}$ represents the readout resonator (mode A) while the $\hat{\phi}_n$ are the qubit phases. It is useful to express the Lagrangian in matrix form with $\vec{\varphi}^T = (\hat{\psi}\,\hat{\phi}_1 \ldots \hat{\phi}_N)$, $\hat{L} = \frac{1}{2}\dot{\vec{\varphi}}^T C \dot{\vec{\varphi}} + \vec{v}^T\dot{\vec{\varphi}} - V(\vec{\varphi})$, $V(\vec{\varphi}) = \hat{\psi}^2/2L_r - \sum_j E_{Jj}\cos(2\pi\hat{\phi}_j/\Phi_0)$ and

$$C = \begin{pmatrix} C_r + C_m & -C_{c1} & -C_{c2} & \ldots & -C_{cN} \\ -C_{c1} & C_{S1} + C_{c1} + C_{p1} & 0 & \ldots & 0 \\ -C_{c2} & 0 & C_{S2} + C_{c2} + C_{p2} & \ldots & 0 \\ \vdots & \vdots & \vdots & \ddots & \vdots \\ -C_{cN} & 0 & 0 & \ldots & C_{SN} + C_{cN} + C_{pN} \end{pmatrix}, \tag{S10}$$

$$\vec{v} = \begin{pmatrix} -C_m\hat{V}_m \\ -C_{p1}\hat{V}_p \\ -C_{p2}\hat{V}_p \\ \ldots \\ -C_{pN}\hat{V}_p \end{pmatrix}. \tag{S11}$$

Using this notation, the Hamiltonian is obtained by inverting the capacitance matrix

$$\hat{H} = \frac{1}{2}\vec{q}^T C^{-1}\vec{q} - \vec{v}^T C^{-1}\vec{q} + V(\vec{\varphi}), \tag{S12}$$

where the conjugated variable are given by $\vec{q} = \partial\hat{L}/\partial\dot{\vec{\varphi}} \equiv (\hat{q}_\psi\ \hat{q}_1\ \ldots\ \hat{q}_N)$. Below, we will refer to the element ij of the inverse of the capacitance matrix as $[C^{-1}]_{ij}$, with the index 0 refering to the resonator degree of freedom.

Because a measurement drive is always present on the resonator, it is useful to make the displacement $\hat{V}_m \to V_m(t) + \hat{V}_m$ to separate the classical and the quantum part. For the resonator, we introduce the annihilation and creation operators $\hat{a}, \hat{a}^\dagger$ through

$$\hat{\psi} = \sqrt{\frac{\hbar Z_r}{2}}(\hat{a} + \hat{a}^\dagger), \qquad \hat{q}_\psi = -i\sqrt{\frac{\hbar}{2Z_r}}(\hat{a} - \hat{a}^\dagger), \tag{S13}$$

where $Z_r = \sqrt{L_r[C^{-1}]_{00}}$ is the impedance of the measurement resonator. Moreover, we cast the qubits degree of freedom in the form of a truncated Duffing oscillator with M levels, writing the transition operator of the j^{th} qubit from the n^{th} to the m^{th} level $\hat{\sigma}^{(j)}_{m,n} = |m\rangle\langle n|_j$,

$$\begin{aligned}
\hat{\phi}_j &= \sqrt{\frac{1}{2}}\left(\frac{\hbar}{2e}\right)\left(\frac{2E_{Cj}}{E_{Jj}}\right)^{1/4}\sum_{m=0}^{M-1}\sqrt{m+1}(\hat{\sigma}^{(j)}_{m,m+1} + \hat{\sigma}^{(j)}_{m+1,m}),\\
\hat{q}_j &= -ie\sqrt{2}\left(\frac{E_{Jj}}{8E_{Cj}}\right)^{1/4}\sum_{m=0}^{M-1}\sqrt{m+1}(\hat{\sigma}^{(j)}_{m,m+1} - \hat{\sigma}^{(j)}_{m+1,m}),
\end{aligned} \tag{S14}$$

where $E_{Cj} = [C^{-1}]_{jj}e^2/2$ is the charging energy of the j^{th} qubit. Finally, we introduce the field operators of the measurement transmission line, $\hat{a}_\omega$, and of the input transmission line, $\hat{b}_\omega$, such that

$$\hat{V}_m = \frac{-i}{2}\sqrt{\frac{\hbar Z_m}{\pi}}\int_0^\infty d\omega\,\sqrt{\omega}(\hat{a}_\omega - \hat{a}^\dagger_\omega), \qquad \hat{V}_p = \frac{-i}{2}\sqrt{\frac{\hbar Z_p}{\pi}}\int_0^\infty d\omega\,\sqrt{\omega}(\hat{b}_\omega - \hat{b}^\dagger_\omega). \tag{S15}$$

In these expressions, Z_m, Z_p are respectively the impedance of the measurement and input transmission line. These field operators obey the commutation relations $[\hat{a}_\omega, \hat{a}^\dagger_{\omega'}] = \delta(\omega - \omega')$ and $[\hat{b}_\omega, \hat{b}^\dagger_{\omega'}] = \delta(\omega - \omega')$.

Using Eqs. (S13) to (S15) in Eq. (S12), and performing the standard rotating-wave approximation (RWA) and Born-Markov approximations, the system plus transmission lines Hamiltonian can be expressed as ($\hbar = 1$)

$$\begin{aligned}
\hat{H} = {}& \omega_r\hat{a}^\dagger\hat{a} - i\epsilon(t)(\hat{a} - \hat{a}^\dagger) + \sqrt{\frac{\kappa_A}{2\pi}}\int_0^\infty d\omega\,(\hat{a}^\dagger\hat{a}_\omega + \hat{a}\hat{a}^\dagger_\omega) + \int_0^\infty d\omega\,\omega\hat{a}^\dagger_\omega\hat{a}_\omega + \int_0^\infty d\omega\,\omega\hat{b}^\dagger_\omega\hat{b}_\omega\\
&+ \sum_{j=1}^{N}\sum_{m=0}^{M-1}\left[\omega_{Bj,m}\hat{\sigma}^{(j)}_{m,m} + g_{j,m}(\hat{\sigma}^{(j)}_{m+1,m}\hat{a} + \hat{\sigma}^{(j)}_{m,m+1}\hat{a}^\dagger) + \int_0^\infty d\omega\,\sqrt{\frac{\kappa_{Bj,m}}{2\pi}}(\hat{\sigma}^{(j)}_{m+1,m}\hat{b}_\omega + \hat{\sigma}^{(j)}_{m,m+1}\hat{b}^\dagger_\omega)\right]\\
&+ \sum_{i>j=1}^{N}\sum_{m=0}^{M-1} J_{ij,m}(\hat{\sigma}^{(i)}_{m+1,m}\hat{\sigma}^{(j)}_{m,m+1} + \hat{\sigma}^{(j)}_{m+1,m}\hat{\sigma}^{(j)}_{m,m+1}).
\end{aligned} \tag{S16}$$

In this expressions, the resonator parameters are given by

$$\omega_r = \sqrt{\frac{[C^{-1}]_{00}}{L_r}}, \qquad \epsilon(t) = C_m[C^{-1}]_{00}\frac{1}{\sqrt{2\hbar Z_r}} \times V_m(t), \qquad \kappa_A = C_m[C^{-1}]_{00}\frac{Z_m\omega_r}{4Z_r}. \tag{S17}$$

We assume that the qubits are in the transmon regime $E_{Jj} \gg E_{Cj}$ and use the results from Ref. [S3] to

obtain the Hamiltonian parameters, which we recall here for completeness

$$\begin{aligned}
\omega_{Bj,m} &= \left[-E_{Jj} + \sqrt{8E_{Jj}E_{Cj}}\left(m+\frac{1}{2}\right) - \frac{E_{Cj}}{12}(6m^2+6m+3)\right]/\hbar, \\
\kappa_{Bj,m} &= C_{pj}\left(\sum_{k=1}^{N}[C^{-1}]_{jk}\right)\frac{\pi Z_p}{R_K}\sqrt{\frac{E_{Jj}}{2E_{Cj}}}(\omega_{Bj,m+1}-\omega_{Bj,m})(m+1), \\
g_{j,m} &= [C^{-1}]_{0j}\left(\frac{E_{Jj}}{2E_{Cj}}\right)^{1/4}\sqrt{\frac{\pi}{R_K Z_r}}\sqrt{m+1}, \\
J_{ij,m} &= [C^{-1}]_{ij}\left(\frac{E_{Ji}}{2E_{Ci}}\right)^{1/4}\left(\frac{E_{Jj}}{2E_{Cj}}\right)^{1/4}\frac{\pi}{R_K}(m+1),
\end{aligned} \tag{S18}$$

where $R_K = h/e^2$ is the resistance quantum. In order to tune *in-situ* the Josephson energy of the junctions, each junction can be replaced by a SQUID, making the Josephson energy dependant on a tunable external flux, $E_{Jj} \to E_{Jj}(\Phi_{ext,j})$.

In the regime where ω_r is far detuned from $\omega_{Bj,1} - \omega_{Bj,0}$, the two first lines of Eq. (S16) correspond to the desired Hamiltonian and, in Sect. III, we show how this Hamiltonian implements the model presented in the Letter. The third line of Eq. (S16) represents a spurious direct coupling between the qubits where the couplings $J_{ij,m}$ are small for the range of parameters used here. Finally, a more complete calculation show that a small spurious coupling between the resonator and the input line voltage is present. This leads to a small, unwanted, decay of the resonator field in the input transmission line. This decay can be negated using a Purcell filter, as illustrated by the light green resonator in Fig. S3. Similarly, a small coupling appears between the qubits and the measurement transmission line, leading to decay of the qubits in the measurement transmission line. This can also be mitigated using a Purcell filter (light orange in Fig. S3).

We note that Eqs. (S1) and (S2) are recovered under a two-level approximation, setting $g_{j,0} = 0$ and identifying $\hat{b}_j = \hat{\sigma}^{(j)}_{0,1}$, $\kappa_{Bj} = \kappa_{Bj,0}$, $\omega_{Bj} = \omega_{Bj,1} - \omega_{Bj,0}$.

III. DISPERSIVE TRANSFORMATION

In this section, we show how the circuit Hamiltonian Eq. (S16) approximates the desired Hamiltonian, Eq. (4) of the main Letter. First, following standard treatment [S1], the bath degrees of freedom, $\hat{a}_\omega$ and $\hat{b}_\omega$, can be eliminated from Eq. (S16) to obtain the master equation

$$\dot{\rho} = -i[\hat{H}^{ME}, \rho] + \sum_i \mathcal{D}[\hat{L}_i]\rho, \tag{S19}$$

where

$$\begin{aligned}
\hat{H}^{ME} =& \omega_r \hat{a}^\dagger\hat{a} - i\epsilon(t)(\hat{a}-\hat{a}^\dagger) + \sum_{j=1}^{N}\sum_{m=0}^{M-1}\left[\omega_{Bj,m}\hat{\sigma}^{(j)}_{m,m} + g_{j,m}(\hat{\sigma}^{(j)}_{m+1,m}\hat{a} + \hat{\sigma}^{(j)}_{m,m+1}\hat{a}^\dagger)\right] \\
&+ \sum_{i>j=1}^{N}\sum_{m=0}^{M-1} J_{ij,m}(\hat{\sigma}^{(i)}_{m+1,m}\hat{\sigma}^{(j)}_{m,m+1} + \hat{\sigma}^{(j)}_{m+1,m}\hat{\sigma}^{(j)}_{m,m+1}), \\
\hat{L}_1 =& \sqrt{\kappa_A}\hat{a}, \\
\hat{L}_2 =& \sum_{j=1}^{N}\sum_{m=0}^{M}\sqrt{\kappa_{Bjm}}\hat{\sigma}^{(j)}_{m,m+1}.
\end{aligned} \tag{S20}$$

The first jump operator $\hat{L}_1$ corresponds to the resonator decay into the measurement transmission line while the second jump operator $\hat{L}_2$ to decay of the transmons into the input transmission line. For simplicity, below we assume identical couplings between the transmons and the resonator $g_{j,m} \equiv g_m \,\forall\, j$ as well as identical transmon-transmon couplings $J_{ij,m} \equiv J_m \,\forall\, i,j$. Assuming large detuning between the transmons and the measurement resonator, we eliminate their Jaynes-Cummings-like coupling with a Schrieffer-Wolf transformation $\hat{H}^{SW} = \hat{U}^{SW}\hat{H}(\hat{U}^{SW})^\dagger$ with

$$\hat{U}^{SW} = \exp\left[\sum_{m=0}^{M-1}\frac{g_m}{\bar{\omega}_{B(m+1)} - \bar{\omega}_{Bm} - \omega_r}\left(\hat{a}\hat{\sigma}^{(+)}_{m+1,m} - \hat{a}^\dagger\hat{\sigma}^{(+)}_{m,m+1}\right)\right]. \tag{S21}$$

In this expression, we have introduced $\bar{\omega}_{Bm} \equiv \sum_j \omega_{Bj,m}/N$, the average energy of the m^{th} level, and defined $\hat{\sigma}^{(+)}_{m,n} \equiv \sum_j \hat{\sigma}^{(j)}_{m,n}$.

In addition to assuming large transmon-resonator detuning, $|g_m| \ll |\bar{\omega}_{B(m+1)} - \bar{\omega}_{Bm} - \omega_r|$, we set the inhomogeneity of the qubits to be small compared with the resonator-transmon coupling, $|(\omega_{Bj(m+1)} - \omega_{Bjm}) - (\bar{\omega}_{B(m+1)} - \bar{\omega}_{Bm})| \ll |g| \; \forall \; j$. Moreover, we set the decay rates of all transmons equal and, without loss of generality, we scale their value with the total number N of transmons : $\kappa_{Bj,m} = \kappa_{Bm}/N$. Keeping terms to order g_m^2/Δ_{mn}, where $\Delta_{mn} \equiv \bar{\omega}_{Bm} - \bar{\omega}_{Bn} - \omega_r$, we then find the transformed Hamiltonian

$$\begin{aligned}
\hat{H}^{SW} =& \omega_r \hat{a}^\dagger \hat{a} - i\epsilon(t)(\hat{a} - \hat{a}^\dagger) + \sum_{j=1}^{N}\sum_{m=0}^{M} \omega_{Bj,m}\hat{\sigma}^{(j)}_{m,m} + i\epsilon(t)\sum_m \frac{g_m}{\Delta_{m+1,m}}(\hat{\sigma}^{(+)}_{m,m+1} - \hat{\sigma}^{(+)}_{m+1,m}) \\
&+ \sum_m \frac{g_m^2}{\Delta_{m+1,m}}\hat{\sigma}^{(+)}_{m+1,m}\hat{\sigma}^{(+)}_{m,m+1} - \frac{g^2}{\Delta_0}\hat{a}^\dagger\hat{a}\hat{\sigma}^{(+)}_{0,0} + \sum_{mj}\left(\frac{g_m^2}{\Delta_{m+1,m}} - \frac{g_{m+1}^2}{\Delta_{m+2,m+1}}\right)\hat{a}^\dagger\hat{a}\hat{\sigma}^{(j)}_{m+1,m+1} \\
&+ \sum_{m=0}^{M-2} g_m g_{m+1}\left(\frac{1}{\Delta_{m+2,m+1}} - \frac{1}{\Delta_{m+1,m}}\right)\left(\hat{a}\hat{a}\hat{\sigma}^{(+)}_{m+2,m} + \hat{a}^\dagger\hat{a}^\dagger\hat{\sigma}^{(+)}_{m,m+2}\right) \\
&+ \sum_m J_m \hat{\sigma}^{(+)}_{m+1,m}\hat{\sigma}^{(+)}_{m,m+1}
\end{aligned} \tag{S22}$$

and the transformed Lindbladians

$$\begin{aligned}
\hat{L}_1^{SW} =& \sqrt{\kappa_A}\hat{a} - \sqrt{\kappa_A}\sum_m \frac{g_m}{\Delta_{m+1,m}}\hat{\sigma}^{(+)}_{m,m+1}, \\
\hat{L}_2^{SW} =& \sum_m \sqrt{\frac{\kappa_{Bm}}{N}}\hat{\sigma}^{(+)}_{m,m+1} - \sum_{mj}\sqrt{\frac{\kappa_{Bm}}{N}}\frac{g_m}{\Delta_{m+1,m}}\hat{a}(\hat{\sigma}^{(+)}_{m+1,m+1} - \hat{\sigma}^{(+)}_{m,m}) \\
&- \sum_m \sqrt{\frac{\kappa_{Bm}}{N}}\frac{g_m}{\Delta_{m+1,m}}\hat{a}^\dagger(\hat{\sigma}^{(+)}_{m,m+2} - \hat{\sigma}^{(+)}_{m-1,m+1}).
\end{aligned} \tag{S23}$$

A few key observations can significantly reduce the complexity of the above expressions. First, we set the resonator drive at the (pulled) resonator frequency, which means that the induced drive on the transmons is far off-resonant and thus negligible. Second, we consider that a single photon with carrier frequency $\bar{\omega}_{B1} - \bar{\omega}_{B0}$ is sent to the transmons, justifying a two-level approximation for the transmons. In this situation, we can neglect the small, and off-resonant, two-photon transitions. Finally, we note that we neglected a small renormalization of the transmon frequencies $\omega_{Bj,m} - J_m \approx \omega_{Bj,m}$. Defining the normalized modes $\hat{b}_j \equiv \hat{\sigma}^{(j)}_{0,1}$, $\hat{b}_+ \equiv \hat{\sigma}^{(+)}_{0,1}/\sqrt{N}$, the excitation number $\hat{N}_B \equiv \hat{\sigma}^{(+)}_{1,1}$ and using the identity $\hat{\sigma}^{(j)}_{0,0} = 1 - \hat{\sigma}^{(j)}_{1,1}$, the above expressions take the simplified form

$$\hat{H}^{SW} = \tilde{\omega}_r\hat{a}^\dagger\hat{a} - i\epsilon(t)(\hat{a} - \hat{a}^\dagger) + \sum_{j=1}^{N}\omega_{Bj}\hat{b}_j^\dagger\hat{b}_j + N(\chi_{1,0} + J_0)\hat{b}_+^\dagger\hat{b}_+ + 2\left(\chi_{1,0} - \frac{\chi_{2,1}}{2}\right)\hat{N}_B\hat{a}^\dagger\hat{a} \tag{S24}$$

and

$$\begin{aligned}
\hat{L}_1^{SW} =& \sqrt{\kappa_A}\hat{a} - \sqrt{\kappa_A}\frac{g\sqrt{N}}{\Delta_{1,0}}\hat{b}_+, \\
\hat{L}_2^{SW} =& \sqrt{\kappa_B}\hat{b}_+ - \sqrt{\kappa_B}\frac{g\sqrt{N}}{\Delta_{1,0}}\hat{a}\left(\frac{2\hat{N}_B}{N} - 1\right),
\end{aligned} \tag{S25}$$

where $\chi_{n,m} \equiv g_m^2/\Delta_{n,m}$, $\tilde{\omega}_r \equiv \omega_r - N\chi_{1,0}$ and $\omega_{Bj} \equiv \omega_{Bj1} - \omega_{Bj0}$. We note that here the $\hat{b}$ operators were defined as two-level operators, but since we work in the single excitation subspace (the transmons are excited by a single photon) we can equivalently think of them as ladder operators.

Using these simplified expressions, we now go to a rotating frame for both the resonator and the transmons using the transformation

$$\hat{U}_{rot} = \exp\left\{-it\left[\tilde{\omega}_r\hat{a}^\dagger\hat{a} + [\omega_B + 2\chi(\epsilon/\kappa_A)^2]\hat{N}_B\right]\right\}, \tag{S26}$$

where $\omega_B = \sum_j(\omega_{Bj1} - \omega_{Bj0})/N$ and $\chi \equiv \chi_{1,0} - \chi_{2,1}/2$. Then we take $\epsilon(t) = \epsilon\cos(\tilde{\omega}_r t)$ and neglect fast-rotating terms at $2\tilde{\omega}_r$. Finally, we notice that both jump operators $\hat{L}_1^{SW}, \hat{L}_2^{SW}$ contain terms that rotate a different frequencies. Using the rotating-wave approximation, we neglect the cross terms in the Lindbladian and write

$$\hat{H}_{rot}^{SW} = -i\frac{\epsilon}{2}(\hat{a} - \hat{a}^\dagger) + \sum_{j=1}^{N}\Delta_j\hat{b}_j^\dagger\hat{b}_j + \Delta_+\hat{b}_+^\dagger\hat{b}_+ + 2\chi\hat{N}_B\hat{a}^\dagger\hat{a} - 2\chi\left(\frac{\epsilon}{\kappa_A}\right)^2\hat{N}_B, \tag{S27}$$

together with

$$\begin{aligned}
\hat{L}_1^{SW} =& \sqrt{\kappa_A}\hat{a},\\
\hat{L}_2^{SW} =& \sqrt{\kappa_B}\hat{b}_+,\\
\hat{L}_3^{SW} =& \sqrt{\kappa_A}\frac{g\sqrt{N}}{\Delta_{1,0}}\hat{b}_+,\\
\hat{L}_4^{SW} =& \sqrt{\kappa_B}\frac{g\sqrt{N}}{\Delta_{1,0}}\hat{a}\left(\frac{2\hat{N}_B}{N} - 1\right),
\end{aligned} \tag{S28}$$

where $\Delta_j \equiv \omega_{Bj1} - \omega_{Bj0} - \omega_B$ and $\Delta_+ = N(\chi_{1,0} + J_0)$. The decay operator $\hat{L}_3^{SW}$ corresponds to a Purcell decay of the bright mode into the measurement transmission line. As already mentioned, this type of decay can be mitigated using standard Purcell filter techniques where the density of states at the transmons frequency is depleted in the measurement transmission line, as illustrated in light orange in Fig. S3. Similarly, $\hat{L}_4^{SW}$ corresponds to a Purcell decay of the measurement resonator into the input transmission line and can also be mitigated by adding another Purcell filter (light green, Fig. S3), depleting the density of states at the resonator frequency in the input transmission line.

Long after the activation of the resonator drive, but before the arrival of a signal photon, the transmons are in their ground state and the resonator is in a coherent steady state $\langle\hat{a}\rangle = \alpha = -\epsilon/\kappa_A$. Following the absorption of a signal photon by the transmons, we are interested in the displacement of the resonator with respect to the average value α. Using a displacement transformation $\hat{H}_\chi^D = \hat{D}(\alpha)\hat{H}_{rot}^{SW}\hat{D}^\dagger(\alpha)$, with $\hat{D}(\alpha)\hat{a}\hat{D}^\dagger(\alpha) = \hat{a} - \alpha$, we find the desired Hamiltonian

$$\hat{H}_\chi^D = g_z\hat{N}_B(\hat{a} + \hat{a}^\dagger) + \sum_{j=1}^{N}\Delta_j\hat{b}_j^\dagger\hat{b}_j + 2\chi\hat{N}_B\hat{a}^\dagger\hat{a} + \Delta_+\hat{b}_+^\dagger\hat{b}_+, \tag{S29}$$

and jump terms

$$\begin{aligned}
\hat{L}_1^D =& \sqrt{\kappa_A}\hat{a},\\
\hat{L}_2^D =& \sqrt{\kappa_B}\hat{b}_+,
\end{aligned} \tag{S30}$$

where $g_z = 2\chi\alpha$.

The ideal situation for photodection is to work at large α and small χ. In other words, the ideal situation is reached for a very small dispersive shift probed using a large amplitude coherent state. However, the dispersive transformation is only valid at small photon number $|\alpha|^2 \ll n_{crit}$, limiting the maximal g_z/χ ratio. Another effect that can in principle significantly reduce the quantum efficiency of the detector is the qubit-induced resonator Kerr non-linearity. At modest N and large detunings, this non-linearity is very small $K = 2N\chi g_0^2/\Delta_{1,0}^2$ and numerical simulations including this effect showed no deviations from the results presented in the main Letter.

IV. DETAILS ON THE NUMERICAL SIMULATIONS

In this section, we present details concerning the numerical trajectory simulations.

A. Filtering

As mentionned in the main Letter, the output current is convolved with a filter

$$\bar{J}_{hom}(t) = \int_t^{t+T} d\tau\, J_{hom}(\tau) f(\tau - t), \tag{S31}$$

choosing T so that $f(t > T) \to 0$. As in Ref. [S4], we choose the filter of the same form as the average displacement value computed using a standard master equation simulation. This can be done by, for example, omitting the stochastic part of the stochastic master equation Eq. (2) of the main Letter (by taking $\eta_h = 0$). We denote $y_{av}(t)$ the average displacement calculated this way.

Without loss of generality, we choose to scale the filter so that, at any fixed time, the vacuum noise corresponds to a normal distribution of variance one

$$f(t) = \frac{y_{av}(t)}{\int_0^T d\tau\, y_{av}(\tau)^2}. \tag{S32}$$

This allows to compare the thresholds Y_{thr} for different sets of parameters in a meaningful way.

For high thresholds, the dark count rates are very small and it becomes too numerically expensive to precisely calculate them using trajectories. We therefore derive an approximate analytical formula to compute the dark count rate for high thresholds. First, in the case where there is no signal photon, the homodyne current is given by

$$\bar{J}^0_{hom}(t) = \int_t^{\infty} d\tau\, f(\tau - t)\xi(\tau), \tag{S33}$$

where $\xi(t)$ is a random variable with statistical properties $E[\xi(t)] = 0$, $E[\xi(t)\xi(t')] = \delta(t - t')$ and the upper bound of the integral has been taken to infinity since $f(t > T) \approx 0$. Due to the above normalization of the filter, the probability that the vacuum signal is above the threshold at any time is given by

$$P(\bar{J}^0_{hom}(t) > Y_{thr}) = \frac{\mathrm{Erfc}(Y_{thr}/\sqrt{2})}{2}. \tag{S34}$$

We define the two-time correlation function for the vacuum homodyne signal

$$C^{(2)}(\tau) = \frac{E[\bar{J}^0_{hom}(0)\bar{J}^0_{hom}(\tau)]}{\int_{-\infty}^{\infty} d\tau'\, E[\bar{J}^0_{hom}(0)\bar{J}^0_{hom}(\tau')]}, \tag{S35}$$

normalized so that $\int_{\infty}^{\infty} d\tau\, C^{(2)}(\tau) = 1$. Using this correlation function, we estimate that the correlation time τ_{corr} for the vacuum homodyne current is given by

$$\tau_{corr} = \frac{1}{2}\int_{-\infty}^{\infty} d\tau\, \tau^2 C^{(2)}(\tau). \tag{S36}$$

For a given threshold, the dark count rate can thus be estimated to be

$$\Gamma_{dark} = \frac{P(\bar{J}^0_{hom}(t) > Y_{thr})}{\tau_{corr}}. \tag{S37}$$

In brief, we assume that the dark count rate is given by the probability of a false positive at any time divided by the correlation time of the signal. Figure S4 shows that the estimate Eq. (S37) (dashed lines) approximates well the dark count rate calculated from trajectories (full lines) for moderate dark count rates $5 \times 10^{-5} < \Gamma_{dark} < 10^{-3}$. For smaller dark count rates $\Gamma_{dark} < 5 \times 10^{-5}$, the full lines are unreliable because there are not enough trajectories to calculate precisely the dark count rate. For higher dark count rates $\Gamma_{dark} > 10^{-3}$ the estimate Eq. (S37) is no longer valid: the threshold is so low that the signal can stay above threshold for longer than τ_{corr}. Using Eq. (S37) thus leads to an overestimation of the dark count rate.

B. Simulations parameters

Tables I and II summarize the parameters used to produce Fig. 3 of the main Letter and Fig. S4. Figure S5 shows the filtered homodyne current for the ideal model Eq. (3) of the main Letter while Fig. S6 shows trajectory results for the more realistic model Eq. (S29).

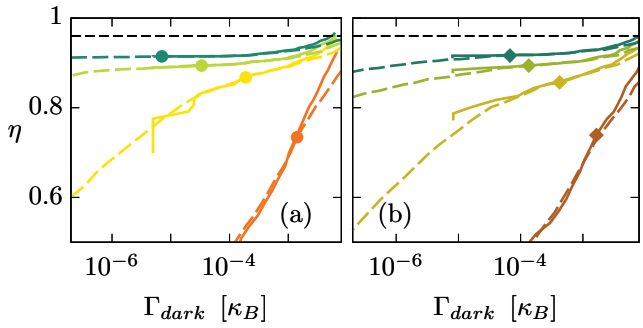

FIG. S4. Efficiency as a function of the dark count rate for the ideal (a) and realistic (b) models. The dark count rate was calculated using trajectories without a signal photon (full lines) and using Eq. (S37) (dashed lines). The points show where the fidelity is maximized.

N	κ_A	κ_C	g_z	$\vec{\Delta}$	Y_{thr}
1	0.2	0.1	1	(0)	2.2
2	0.2	0.1	0.6	(0.55 -0.55)	2.9
3	0.2	0.1	0.5	(0.7 -0.7 0)	3.4
4	0.2	0.1	0.4	(0.7 -0.7 0.23 -0.23)	3.8

TABLE I. Parameters used in the ideal model simulations (Eq. (3) of the main Letter). Here, κ_A, κ_C, g_z and $\vec{\Delta}$ are in units of κ_B.

N	$\kappa_A/2\pi$ [MHz]	$\kappa_{Bi}/2\pi$ [MHz]	$\kappa_C/2\pi$ [MHz]	$g_z/2\pi$ [MHz]	$\chi/2\pi$ [MHz]	$\Delta_+/2\pi$ [MHz]	$\vec{\Delta}/2\pi$ [MHz]	Y_{thr}
1	2	10	1	10	1	1	(0)	2.1
2	2	5	1	6	0.6	1.2	(4.9 -6.1)	2.7
3	2	3.33	1	5	0.5	1.5	(7 -7 0)	3.0
4	2	2.5	1	4	0.4	1.6	(6.6 -7.4 2.3 -2.3)	3.2

TABLE II. Parameters used in the simulations for the more realistic model, Eq. (S29). In all cases, we set intrinsic decoherence times at $T_1 = 30\ \mu s$ and $T_2 = 30\ \mu s$.

V. LIMITS ON THE NUMBER OF ARTIFICIAL ATOMS

As the number of artificial atoms in the ensemble, N, is increased, the ideal model studied in the main Letter might become more difficult to realize because of spurious interactions. In this section, we describe three such effects.

First, in order to form dark states, the size of the artificial atoms should be small compared to the photon wavelength. Moreover, the photon travel time between the artificial atoms (in the input waveguide) should be negligible compared to the other system evolution timescales. Because artificial atoms have a finite size, this imposes an upper bound on N over which non-Markovian effects will have to be taken into account.

Second, for the particular implementation studied here, each transmon adds to the resonator nonlinearity $K \propto N$ and to the bright state frequency shift $\Delta_+ \propto N$ (see Sect. III). For large N, this might significantly reduce the quantum efficiency of the detector.

Third, the present schemes assumes that the coherence times T_1, T_2 of the artificial atoms are long compared to the trapping time of the photon. For modest $N \lesssim 4$ and typical transmon decoherence times $T_1 = T_2 = 30\,\mu s$, this does not impact the quantum efficiency of the detector in a significant way. For large N, finite relaxation times, T_1, will lead to the loss of signal photons in the ensemble. Moreover, dephasing errors will limit the coherent transfer of a signal photon from the bright to the dark states and, as a result, limit the trapping properties of the ensemble. Finally, in order to fix the collective asborption rate of the ensemble κ_B, we assumed that the individual linewidth of the artificial atoms scaled as $\kappa_{Bi} = \kappa_B/N$. Since the linewidth of individual artificial atoms is limited by their T_2 time, this will eventually impose a limit on

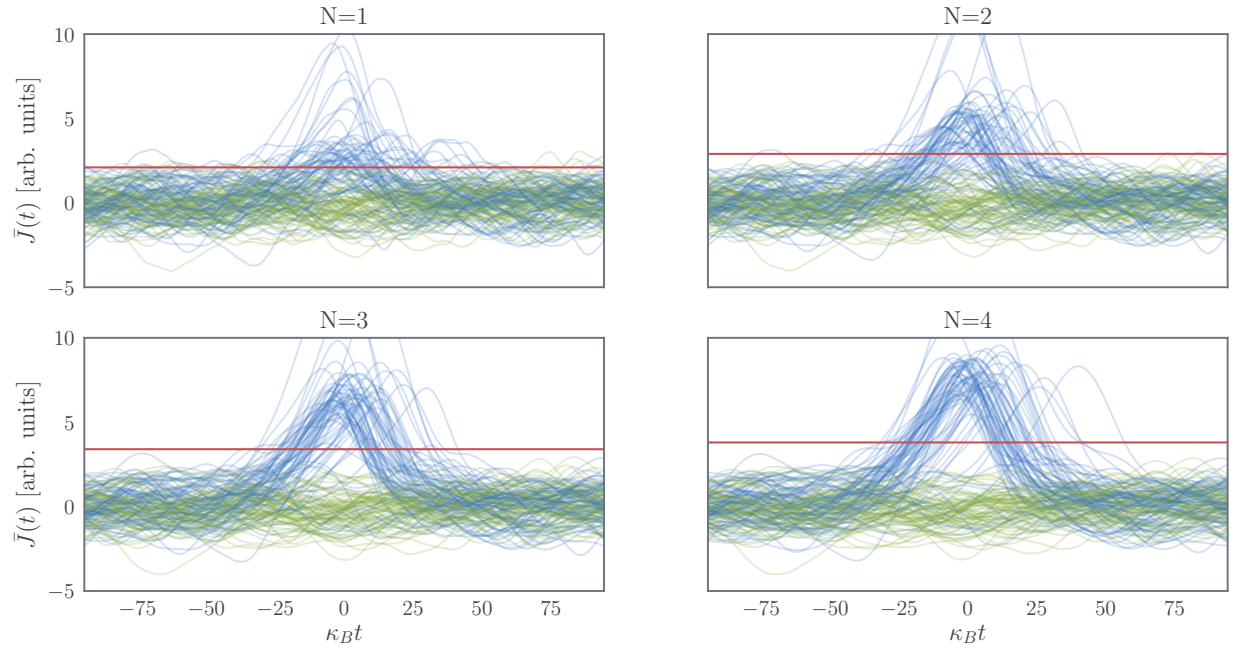

FIG. S5. Filtered homodyne current from 75 trajectories of the ideal model for different number of absorbers with (blue) and without (green) a signal photon. The parameters for each panel are found in Tab. I and the threshold leading to the optimal fidelity is showned in red. The time reference $\kappa_B t = 0$ has been chosen arbitrarily.

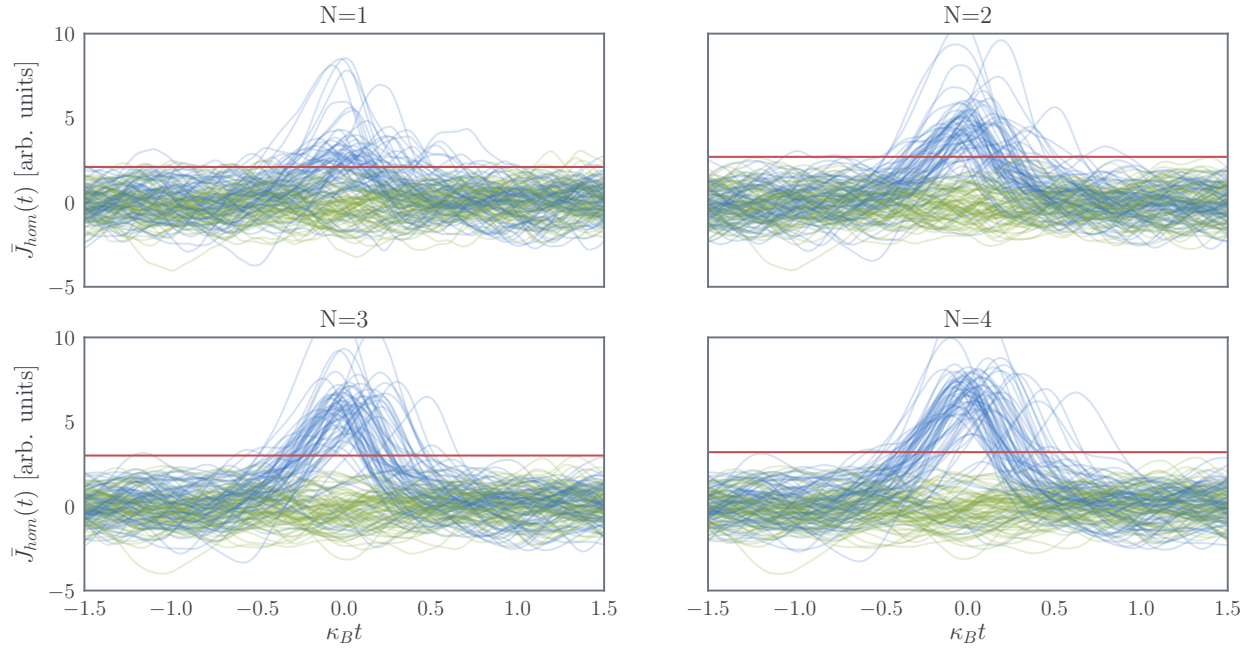

FIG. S6. Filtered homodyne current from 75 trajectories of the realistic model for different number of absorbers with (blue) and without (green) a signal photon. The parameters for each panel are found in Tab. II and the threshold leading to the optimal fidelity is showned in red. The time reference $\kappa_B t = 0$ has been chosen arbitrarily.

the minimal linewidth achievable.

[S1] C. Gardiner and P. Zoller, *Quantum Noise: A Handbook of Markovian and Non-Markovian Quantum Stochastic Methods with Applications to Quantum Optics*, Springer Series in Synergetics (Springer, 2004).
[S2] U. Vool and M. Devoret, International Journal of Circuit Theory and Applications **45**, 897 (2017).
[S3] J. Koch, T. M. Yu, J. Gambetta, A. A. Houck, D. I. Schuster, J. Majer, A. Blais, M. H. Devoret, S. M. Girvin, and R. J. Schoelkopf, Phys. Rev. A **76**, 042319 (2007).
[S4] B. Fan, G. Johansson, J. Combes, G. J. Milburn, and T. M. Stace, Phys. Rev. B **90**, 035132 (2014).

B.2 Détecteur de photon version continue

Supplementary Materials: Quantum metamaterial for non-destructive microwave photon counting

May 6, 2019

Contents

1 Josephson Travelling Wave Photodetector Hamiltonian

1.1 Diagonalization of coupled resonator array

Before deriving the Hamiltonian of the full coupled metamaterial-detector system depicted in Fig. 2 of the main paper, it is useful to first recall the basic structure of a chain of N coupled LC oscillators, forming the backbone of the metamaterial. The Hamiltonian of the generic array of inductively and capacitively coupled LC oscillators illustrated in Fig. S1 is

$$\hat{H}_{\text{array}} = \sum_{n=-N/2}^{N/2-1} \left\{ \frac{\hat{q}_n^2}{2C_0} + \frac{\hat{\phi}_n^2}{2L_0} + \frac{C_{\text{nn}}}{2C_0^2}\left(\hat{q}_{n-1}\hat{q}_n + \hat{q}_n\hat{q}_{n+1}\right) - \frac{1}{2L_{\text{nn}}}\left(\hat{\phi}_{n-1}\hat{\phi}_n + \hat{\phi}_n\hat{\phi}_{n+1}\right) \right\}, \quad (1)$$

where ϕ_n and $\hat{q}_n$ are the canonical flux and charge variables, respectively, of the nth oscillator satisfying $[\hat{\phi}_n, \hat{q}_n] = i\hbar$ [1]. Here, $C_0 = C_g + 2C_{\text{nn}}$ and $L_0 = (L_g^{-1} + 2L_{\text{nn}}^{-1})^{-1}$ are the total capacitance and inductance of the LCs, while C_{nn} and L_{nn} are the coupling capacitances and inductances.

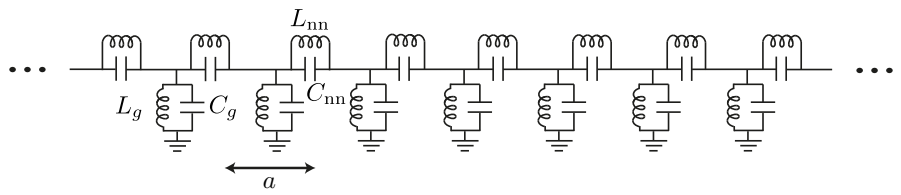

Figure S1: Array of identical LC resonators with inductive and capacitive nearest neighbor couplings. Of particular interest are the two cases 1) **Capacitive coupling:** $L_{\rm nn} \to \infty$ and $0 \ll C_{\rm nn} < C_g$. 2) **Inductive coupling:** $L_g = \infty$, $L_{\rm nn}^{-1} \gg 0$, and $C_{\rm nn} \simeq 0$. The latter corresponds to a standard lumped element representation of a linear waveguide, with no infrared cut-off in the thermodynamics limit.

It is convenient to introduce the Fourier transformed variables

$$\hat{\phi}_n = \frac{1}{\sqrt{N}} \sum_r \hat{\phi}_r e^{ik_r x_n}, \tag{2}$$

$$\hat{q}_n = \frac{1}{\sqrt{N}} \sum_r \hat{q}_r e^{ik_r x_n}, \tag{3}$$

where $r = -N/2, \ldots, N/2-1$, $k_r = 2\pi r/Na$ and $x_n = na$ with a the unit cell distance defined in Fig. S1. Note that $\hat{\phi}_{-r} = \hat{\phi}_r^\dagger$, and similarly for $\hat{q}_{-r}$. Using these new variables, $\hat{H}_{\rm array}$ takes the simpler form

$$\hat{H}_{\rm array} = \sum_{r=-N/2}^{N/2-1} \left\{ \frac{1}{2C_r} \hat{q}_r \hat{q}_{-r} + \frac{1}{2L_r} \hat{\phi}_r \hat{\phi}_{-r} \right\}, \tag{4}$$

where $C_r = C_0 \left[1 + C_{\rm nn}/C_0 \cos(k_r a)\right]^{-1}$ and $L_r = L_0 \left[1 - L_0/L_{\rm nn} \cos(k_r a)\right]^{-1}$. Using ladder operators satisfying $[\hat{b}_r, \hat{b}_q^\dagger] = \delta_{rq}$ and chosen such that

$$\hat{\phi}_r = \sqrt{\frac{\hbar Z_r}{2}} \left(\hat{b}_r + \hat{b}_{-r}^\dagger \right), \tag{5}$$

$$\hat{q}_r = -i \sqrt{\frac{\hbar}{2Z_r}} \left(\hat{b}_r - \hat{b}_{-r}^\dagger \right), \tag{6}$$

where $Z_r = \sqrt{L_r/C_r}$, the array Hamiltonian takes the diagonal form

$$\hat{H}_{\rm array} = \sum_r \hbar \omega_r \hat{b}_r^\dagger \hat{b}_r, \tag{7}$$

with the dispersion relation

$$\omega_r = \sqrt{\frac{1}{C_r L_r}} = \omega_0 \sqrt{\left[1 + \frac{C_{\rm nn}}{C_0} \cos(k_r a)\right] \left[1 - \frac{L_0}{L_{\rm nn}} \cos(k_r a)\right]}, \tag{8}$$

where $\omega_0 = \sqrt{1/C_0 L_0}$.

Note that the telegrapher model for a waveguide is found from setting $C_{\rm nn} = 0$, $L_g = 0$ and $L_{\rm nn} = 2L_0$, leading to $\omega_r = \sqrt{\frac{2}{C_0 L_0}} |\sin(k_r a/2)|$ and $Z_r = \sqrt{\frac{L_0}{2C_0}} \frac{1}{|\sin(k_r a/2)|}$. In this particular situation, there is no infrared cut-off in the limit $N \to \infty$ where k_r becomes a continuous variable, $k_r \to k \in [0, 2\pi)$.

Another situation of interest is when the LCs are weakly coupled. Assuming capacitive coupling $C_{\rm nn} \ll C_0$ and taking $L_0/L_{\rm nn} = 0$ for simplicity, leads to

$$\omega_r \simeq \omega_0 + 2J \cos(k_r a), \tag{9}$$

where $\omega_0 = 1/\sqrt{C_0 L_0}$ and $J = \omega_0 C_{\rm nn}/2C_0$. In this situation, there is low- and high-frequency cut-offs, $\omega_0 - 2J < \omega_r < \omega_0 + 2J$, which holds in the $N \to \infty$ limit. The group velocity in the array is furthermore

$$\frac{\partial \omega_r}{\partial k_r} = -2Ja\sin(k_r a). \tag{10}$$

The dispersion relation is approximately linear around $k_r a = \pm\pi/2$, where $\omega_r = \omega_0$ and $\partial\omega_r/\partial k_r = \mp 2Ja$ (the sign corresponding to left- and right moving fields). In the large N limit, the LC array thus behaves as a waveguide with cut-off frequencies $\omega_0 \pm 2J = \omega_0(1 \pm C_{\rm nn}/C_0)$, and an approximately linear dispersion relation with speed of light

$$v = 2Ja = \frac{C_{\rm nn}}{C_0}\omega_0 a, \tag{11}$$

for frequencies $\omega \simeq \omega_0$.

1.1.1 Impedance matching

Besides the speed of light, a linear waveguide is described by its characteristic impedance. The effective characteristic impedance of the oscillator array close to ω_0 can be found by noting that the flux at position $x_n = na$ is

$$\begin{aligned}\hat{\phi}_{\rm array}(x_n) \equiv \hat{\phi}_n &= \sum_{r=-N/2}^{N/2+1} \sqrt{\frac{\hbar Z_r}{2N}}\left(\hat{b}_r + \hat{b}^\dagger_{-r}\right) e^{ik_r x_n} \\ &= \sum_{r=-N/2}^{N/2+1} \sqrt{\frac{\hbar}{2z\omega_0 C_0/a}}\left(\hat{b}_r + \hat{b}^\dagger_{-r}\right) e^{ik_r x_n}.\end{aligned} \tag{12}$$

This should be compared to the flux of a linear transmission line of finite length $-z/2 < x < z/2$ with $z = Na$, capacitance $c_{\rm tml} = C_{\rm tml}/a$, and inductance $l_{\rm tml} = L_{\rm tml}/a$ per unit length which takes the form

$$\hat{\phi}_{\rm tml}(x) = \sum_{r=-\infty}^{\infty} \sqrt{\frac{\hbar}{2z\omega_r c}}\left(\hat{c}_r + \hat{c}^\dagger_{-r}\right) e^{ik_r x}, \tag{13}$$

with $|k_r| = \omega_r/v_{\rm tml}$ and $v_{\rm tml} = 1/\sqrt{cl}$. The characteristic impedance for the transmission line is defined as $Z_{\rm tml} = \sqrt{l_{\rm tml}/c_{\rm tml}}$. Hence, comparing Eq. (12) and Eq. (13), we see that

$$c_{\rm array} \equiv \frac{C_0}{a}, \tag{14}$$

plays the role of capacitance to ground per unit cell for the array, again for frequencies $\omega_r \simeq \omega_0$. An effective characteristic impedance for the array around this frequency can be read off from the relation

$$Z_{\rm array} \equiv \frac{a}{C_0 v} = \frac{C_0}{C_{\rm nn}}\sqrt{\frac{L_0}{C_0}} = \frac{C_0}{C_{\rm nn}} Z_0, \tag{15}$$

where $Z_0 = \sqrt{L_0/C_0}$ is the characteristic impedance of a single LC oscillator. We generically want to use $C_{\rm nn}/C_0 < 1$, which means that Z_0 has to be reduced correspondingly to achieve the desired impedance matching with input/output lines. By comparison with a conventional transmission line, we can also define an effective inductance per unit cell for the array

$$l_{\rm array} \equiv \frac{Z_{\rm array}}{v} = \left(\frac{C_0}{C_{\rm nn}}\right)^2 \frac{L_0}{a}. \tag{16}$$

With this definition $Z_{\rm array} = \sqrt{l_{\rm array}/c_{\rm array}}$.

1.1.2 Modifications due to coupling circuitry

The JTWPD is based on coupling an array of LC oscillators as described in the previous section to a probe resonator, via an array of Josephson junctions, as illustrated in Fig. S2. Following the standard approach, we diagonalize a linearized version of this system, replacing the Josephson junctions by linear inductances $L_J = \phi_0^2/E_J$, in terms of a set of spatial mode functions. For frequencies close to the localized junction modes the system no longer supports traveling waves. However, as long as the system is probed away from such resonances, and in the band of frequency where the dispersion relation of the LC array is linear $\omega \simeq \omega_0$, we expect the system to behave as a waveguide.

In fact, as long as the coupling capacitances denoted $C_{c,n}$ in Fig. S2 are sufficiently small compared to all the other relevant capacitances, the presence of the coupling circuit to the resonator has a minimal effect on the properties of the LC array. This can be seen from the fact that the impedance of the circuit coupling each unit cell of the LC array to ground is given by

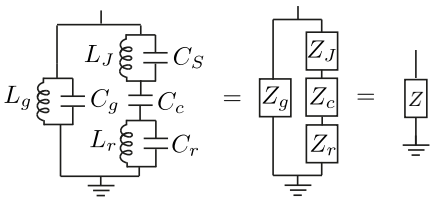

Here, $Z_g^{-1}(\omega) = i\omega C_g\left(1+\omega_g^2/\omega^2\right)$ with $\omega_g = 1/\sqrt{C_g L_g}$ is the impedance of one of the LC oscillators of the array, $Z_J^{-1}(\omega) = i\omega C_S\left(1+\omega_J^2/\omega^2\right)$ with $\omega_J = 1/\sqrt{C_S L_J}$ the impedance of the linearized capacitively shunted coupling junction, $Z_c^{-1}(\omega) = i\omega C_c$ the impedance of the coupling capacitance C_c, and $Z_r(\omega) = i\omega C_r\left(1+\omega_r^2/\omega^2\right)$ the impedance of the probe resonator treated here in a single mode approximation for simplicity. The total admittance to ground can therefore be expressed as

$$\begin{aligned} Z^{-1}(\omega) &= i\omega C_g\left(1-\frac{\omega_g^2}{\omega^2}\right) + i\omega C_c\left[1+\frac{C_c}{C_S}\left(1-\frac{\omega_J^2}{\omega^2}\right)^{-1}+\frac{C_c}{C_r}\left(1-\frac{\omega_r^2}{\omega^2}\right)^{-1}\right]^{-1} \\ &\simeq i\omega C_g\left(1-\frac{\omega_g^2}{\omega^2}\right) + i\omega C_c \\ &\simeq i\omega C_g\left(1-\frac{\omega_g^2}{\omega^2}\right), \end{aligned} \tag{17}$$

where the first approximation holds for $C_c \ll C_S, C_r$ and the last approximation for $C_c \ll C_g$. Thus, as long as the coupling capacitance, C_c, is small compared to the other capacitances, the presence of the coupling junctions has a minimal influence on the behaviour of the waveguide. We can then use the results of the previous section for a coupled LC array without major modifications. In particular, we can assume that the center frequency where the dispersion relation of the array is approximately linear, is approximately given by the bare resonance frequency of the LCs in the array ω_0 .

1.2 Detector-Metamaterial Hamiltonian

The JTWPD design illustrated in Fig. S2 is one possible realization of this device. In particular, other coupling schemes, such as to a 3D cavity rather than 2D resonator are possible without significant changes. Furthermore, although we mostly focus on a homogeneous transmission line with nominally identical circuit elements, the approach taken in this section can also be used in the presence of disorder.

To find a Hamiltonian for the metamaterial, we follow a black-box quantization approach and divide the Hamiltonian in a linear and a non-linear contribution

$$\hat{H} = \hat{H}_{\rm lin} + \hat{H}_{\rm nl}, \tag{18}$$

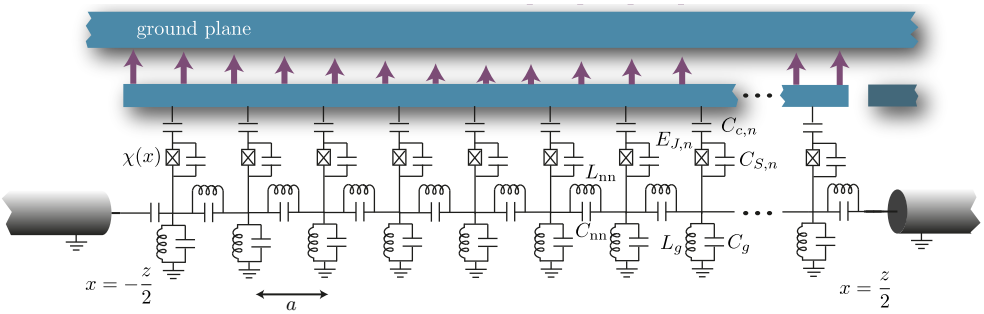

Figure S2: The detector consists of three parts. 1) A linear chain of coupled LC oscillators forms the backbone of the detector, and serves effectively as a linear waveguide over some frequency range. 2) A transmission line resonator (blue) serves as a probe system. 3) The probe (resonator) is coupled to the waveguide (LC chain) via an array of Josephson junctions (vertical junctions in the figure).

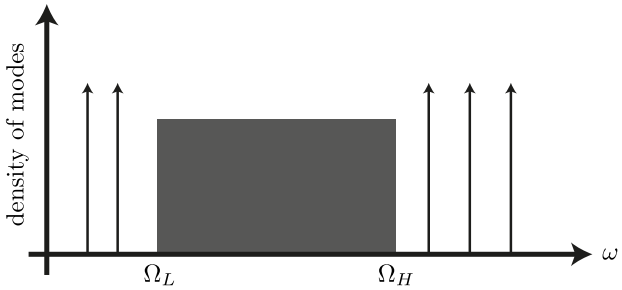

Figure S3: Schematic illustration of generic spectrum consisting of both discrete and continuum modes.

where $\hat{H}_{\rm lin}$ is the Hamiltonian of the linearized system which includes all capacitances, inductances and the linear inductance of all Josephson junction [2].

Whether we are considering a 2D or 3D setup, the Hamiltonian $\hat{H}_{\rm lin}$ can be diagonalized using of a set of eigenmodes with, in general, both discrete and continuous contributions [3]

$$\hat{H}_{\rm lin} = \sum_m \hbar\omega_m \hat{a}_m^\dagger \hat{a}_m + \sum_\nu \int_{\Omega_L}^{\Omega_H} d\omega \hbar\omega \hat{b}_{\nu\omega}^\dagger \hat{b}_{\nu\omega}, \tag{19}$$

where $0 \leq \Omega_L < \Omega_H \leq \infty$ are low and high frequency cut-offs for the continuous part of the spectrum. The index ν is used to label degenerate modes (e.g. left- and right-movers). A generic eigenspectrum is illustrated in Fig. S3. In the case of interest, the continuum modes are associated to the metamaterial waveguide at the bottom of Fig. S2, treated here in the continuum limit, and the discrete spectrum is associated to the probe resonator. Note, however, that since we are dealing with eigenmodes of the full system, the different parts of the setup are hybridized.

Following Ref. [3] and using the displacement and magnetic fields as canonical fields, we can write (in the Schrödinger picture)

$$\hat{\mathbf{D}}(\mathbf{r}) = \sum_m \left[\mathbf{D}_m(\mathbf{r})\hat{a}_m + \text{H.c.}\right] + \sum_\nu \int_{\Omega_L}^{\Omega_H} d\omega \left[\mathbf{D}_{\nu\omega}(\mathbf{r})\hat{b}_{\nu\omega} + \text{H.c.}\right], \tag{20a}$$

$$\hat{\mathbf{B}}(\mathbf{r}) = \sum_m \left[\mathbf{B}_m(\mathbf{r})\hat{a}_m + \text{H.c.}\right] + \sum_\nu \int_{\Omega_L}^{\Omega_H} d\omega \left[\mathbf{B}_{\nu\omega}(\mathbf{r})\hat{b}_{\nu\omega} + \text{H.c.}\right], \tag{20b}$$

where $\mathbf{r} = (x, y, z)$. The $\mathbf{D}_m$'s and $\mathbf{B}_m$'s are mode functions satisfying appropriate normalization and orthogonality conditions, and can be found numerically [3]. The quantized modes satisfy

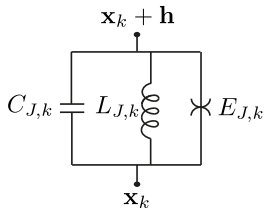

Figure S4: Representation of a Josephson junction in terms of capacitive, and linear and and non-linear inductive elements.

$[\hat{a}_m, \hat{a}_n^\dagger] = \delta_{mn}$ and $[\hat{b}_{\nu\omega}, \hat{b}_{\mu\omega'}^\dagger] = \delta_{\nu\mu}\delta(\omega - \omega')$. We assume here that the electric field is related to the displacement field as $\hat{\mathbf{D}}(\mathbf{r}) = \varepsilon\hat{\mathbf{E}}(\mathbf{r})$ with $\varepsilon(\mathbf{r})$ the permittivity of the material. This relation only holds if dispersion and absorption is negligible [3].

In the lumped element limit, we separate the k'th junction into capacitive, linear inductive and non-linear inductive elements as illustrated in Fig. S4 where the spider symbol represents the non-linear potential of the Josephson junction [2]. To express the non-linear part of the Hamiltonian we first need to find the dimensionless flux across the junction located at $\mathbf{x}_k$, defined as $\hat{\varphi}_{J,k}(t) = (1/\phi_0)\int_{-\infty}^{t} dt' V_k(t')$ with $V_k(t)$ the branch voltage $V_k(t) = \int_{\mathbf{x}_k}^{\mathbf{x}_k+\mathbf{h}} d\mathbf{l}\cdot\hat{\mathbf{E}}(\mathbf{r}) = \int_{\mathbf{x}_k}^{\mathbf{x}_k+\mathbf{h}} d\mathbf{l}\cdot\hat{\mathbf{D}}(\mathbf{r})/\varepsilon(\mathbf{r})$ and $\phi_0 = \Phi_0/2\pi = \hbar/2e$ the reduced flux quantum [1]. From Eq. (20), the flux across the Josephson junction takes the form (in the Schrödinger picture)

$$\hat{\varphi}_{J,k} = \sum_m \left[\varphi_m(x_k)\hat{a}_m + \text{H.c.}\right] + \sum_\nu \int_{\Omega_L}^{\Omega_H} d\omega \left[\varphi_{\nu\omega}(x_k)\hat{b}_{\nu\omega} + \text{H.c.}\right], \tag{21}$$

where $\varphi_m(x_k) = (i/\phi_0)\int_{\mathbf{x}_k}^{\mathbf{x}_k+\mathbf{h}} d\mathbf{l}\cdot\mathbf{D}_m(\mathbf{r})/(\omega_m\varepsilon)$ and $\varphi_{\nu\omega}(x_k) = (i/\phi_0)\int_{\mathbf{x}_k}^{\mathbf{x}_k+\mathbf{h}} d\mathbf{l}\cdot\mathbf{D}_{\nu\omega}(\mathbf{r})/(\omega\varepsilon)$ are discrete and continuum flux mode functions, respectively. It is also convenient to introduce rescaled mode functions via

$$\varphi_m(x_k) \equiv \frac{1}{\phi_0}\sqrt{\frac{\hbar Z_m}{2}}u_m(x_k) = \sqrt{\frac{4\pi Z_m}{R_K}}u_m(x_k),, \tag{22}$$

$$\varphi_{\nu\omega}(x_k) \equiv \frac{1}{\phi_0}\sqrt{\frac{\hbar Z_{\text{tml}}}{4\pi\omega}}u_{\nu\omega}(x_k) = \sqrt{\frac{2Z_{\text{tml}}}{R_K\omega}}u_{\nu\omega}(x_k), \tag{23}$$

where Z_m is the characteristic impedance of the m'th mode, Z_{tml} the characteristic impedance of the transmission line and $R_K = h/e^2$ the quantum of resistance, while $|u_m(x)| \leq 1$ and $|u_{\nu\omega}(x)| \leq 1$ are unit less mode functions.[1] In the absence of disorder and with linear dispersion over the relevant frequency range of the transmission line, we can use

$$u_{\pm\omega}(x) = e^{\pm i\omega x/v}, \tag{24}$$

with v the speed of light and Z_{tml} the characteristic impedance of the transmission line.

Moreover, to lowest order the nonlinear Hamiltonian can be expressed as

$$\hat{H}_{\text{nl}} = -\sum_{k=0}^{N-1}\frac{E_{J,k}}{24}\hat{\varphi}_{J,k}^4, \tag{25}$$

where $E_{J,k}$ is the Josephson energy of the kth junction. Using Eq. (21) this can be expressed as

$$\begin{aligned}\hat{H}_{\text{nl}} = &\sum_m\left[\hbar\Delta_m\hat{a}_m^\dagger\hat{a}_m + \frac{\hbar K}{2}(\hat{a}_m^\dagger)^2\hat{a}_m^2\right] + \sum_{m>n}\chi_{m,n}\hat{a}_m^\dagger\hat{a}_m\hat{a}_n^\dagger\hat{a}_n \\ &+ \hbar\sum_m\sum_{\nu\mu}\sum_{k=0}^{N-1} a\,\chi_m(x_k)\hat{a}_m^\dagger\hat{a}_m\hat{b}_\nu^\dagger(x_k)\hat{b}_\mu(x_k) \\ &+ \sum_\nu\int_{\Omega_L}^{\Omega_H} d\omega\hbar\Delta_{\nu\omega}\hat{b}_{\nu\omega}^\dagger\hat{b}_{\nu\omega},\end{aligned} \tag{26}$$

[1] In the notation of Ref. [2], $\mathcal{Z}_m^{\text{eff}} = Z_m u(x_k)$ is the effective impedance of mode m as seen from the kth junction.

where fast rotating terms have been dropped, and cross- and self-Kerr couplings between continuum modes have been neglected based on the assumption that the photon number in the transmission line is locally very low. The x-dependent photon annihilation operators in the second term of $\hat{H}_{\rm nl}$ are defined as

$$\hat{b}_\nu(x) = \sqrt{\frac{\bar{\omega}}{2\pi v}} \int_{\Omega_L}^{\Omega_H} \frac{d\omega}{\sqrt{\omega}} u_{\nu\omega}(x) \hat{b}_{\nu\omega}, \tag{27}$$

where $\bar{\omega}$ is the carrier frequency of the incoming photon introduced here for later convenience and v the speed of light. The coefficients in Eq. (26) are given by $\Delta_m = \frac{1}{2}\sum_n \chi_{m,n}$, $K_m = \chi_{m,m}/2$ and

$$\hbar\chi_{m,n} = -\sum_k E_{J,k} |\varphi_m(x_k)|^2 |\varphi_n(x_k)|^2 = -\sum_k E_{J,k} \frac{(4\pi)^2 Z_m Z_n}{R_K^2} |u_m(x_k)|^2 |u_n(x_k)|^2, \tag{28}$$

$$\hbar\chi_m(x_k) = -\frac{v E_{J,k}}{a\bar{\omega}} \frac{(4\pi)^2 Z_m Z_{\rm tml}}{R_K^2} |u_m(x_k)|^2, \tag{29}$$

where in the last expression we used Eq. (24).

Finally, taking the continuum limit, $\sum_{k=0}^{N-1} a \to \int_{-z/2}^{z/2} dx$, we find for the total Hamiltonian

$$\begin{aligned} \hat{H} = &\sum_m \hbar\tilde{\omega}_m \hat{a}_m^\dagger \hat{a}_m + \sum_\nu \int_{\tilde{\Omega}_{L,\nu}}^{\tilde{\Omega}_{H,\nu}} d\omega \hbar\omega \hat{b}_{\nu\omega}^\dagger \hat{b}_{\nu\omega} + \frac{\hbar}{2} \sum_{mn} \chi_{m,n} \hat{a}_m^\dagger \hat{a}_m \hat{a}_n^\dagger \hat{a}_n \\ &+ \hbar \sum_m \sum_{\nu\mu} \int_{-z/2}^{z/2} dx \chi_m(x) \hat{a}_m^\dagger \hat{a}_m \hat{b}_\nu^\dagger(x) \hat{b}_\mu(x), \end{aligned} \tag{30}$$

where $\tilde{\omega}_m = \omega_m + \Delta_m$, $\tilde{\Omega}_{L/H,\nu} = \Omega_{L/H} + \Delta_{\nu\Omega_{L/H}}$ and we have relabelled $b_{\nu(\omega-\Delta_{\nu\omega})} \to \hat{b}_{\nu\omega}$. Because the shifted frequencies are those that are measured in practice, we drop the tildes from now on.

The Hamiltonian used in the main paper is found from Eq. (30) by taking the single-mode approximation for the probe resonator, including only one term from the sum over m, and adding a drive term for this resonator mode. An important aspect of our proposal is that the resonator mode in question lies outside the continuum part of the spectrum, $\omega_r \notin [\Omega_L, \Omega_H]$. This choice helps in minimizing hybridization of the probe mode and the continuum, something which would otherwise lead to loss of resonator photons via the waveguide.

1.3 The Kerr non-linear resonator

Under a single-mode approximation for the resonator, and including a drive term, the resonator-Hamiltonian is

$$\hat{H}_r/\hbar = \omega_r \hat{a}^\dagger \hat{a} + \frac{K}{2} \left(\hat{a}^\dagger\right)^2 \hat{a}^2 + \left(\varepsilon e^{-i\omega_d t} \hat{a}^\dagger + \text{H.c.}\right), \tag{31}$$

where $K \equiv K_m = \chi_{m,m}/2$ with m the resonator mode in question, ε is the drive strength and ω_d the drive frequency. Also taking damping into account through a master equation we have

$$\dot{\rho} = -\frac{i}{\hbar}[\hat{H}, \rho] + \kappa_a \mathcal{D}[\hat{a}_0]\rho, \tag{32}$$

where $\mathcal{D}[\hat{x}]\rho \equiv \hat{x}\rho\hat{x}^\dagger - \frac{1}{2}\hat{x}^\dagger\hat{x}\rho - \frac{1}{2}\rho\hat{x}^\dagger\hat{x}$. Moving first to a frame rotating at the drive frequency ω_d, and subsequently doing a displacement transformation $\hat{a} \to \hat{a} + \alpha$ we can write a Hamiltonian in the new frame

$$\hat{H}_r'/\hbar = (\delta + 2K|\alpha|^2)\hat{a}^\dagger\hat{a} + \frac{K}{2}\left(\hat{a}^\dagger\right)^2 \hat{a}^2, \tag{33}$$

where $\delta = \omega_r - \omega_d$, while the master equation retains its original form, with α chosen to satisfy

$$(\delta + K|\alpha|^2)\alpha - \frac{i\kappa_a}{2}\alpha + \varepsilon = 0. \tag{34}$$

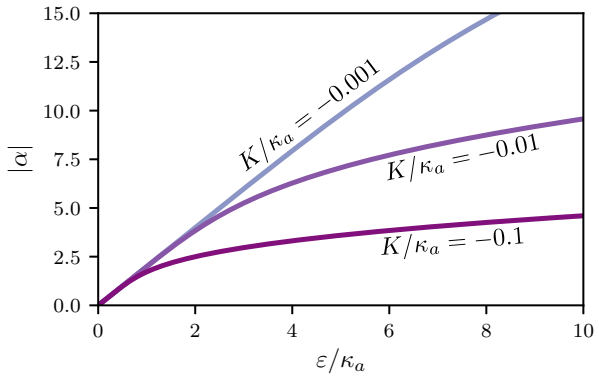

Figure S5: Displacement of a Kerr non-linear resonator driven at the shifted resonance $\omega_d = \omega_0 + 2K|\alpha|^2$ as a function of drive strength, for three different values of K/κ_a.

We wish to drive the resonator on resonance, taking the dynamic frequency shift due to the Kerr non-linearity into account, and consequently choose ω_d such that $\delta = -2K|\alpha|^2$. $\hat{H}_r'$ then reduces to

$$\hat{H}_r' = \frac{\hbar K}{2}\left(\hat{a}^\dagger\right)^2 \hat{a}^2. \tag{35}$$

while the non-linear equation for α becomes

$$K|\alpha|^2\alpha + \frac{i\kappa_a}{2}\alpha = \varepsilon. \tag{36}$$

For $K|\alpha|^2 \ll \kappa_a$ the solution is approximately $\alpha = -2i\varepsilon/\kappa_a$ and the steady state of the resonator is to a good approximation the coherent state $|\alpha\rangle$. In the opposite limit, however, the solution goes like $|\alpha| \sim (\varepsilon/K)^{1/3}$, and the steady state is highly non-Gaussian due to the non-linear Hamiltonian $\hat{H}_r'$. The solution for $|\alpha|$ for different values of K/κ_a is shown in Fig. S5.

1.4 Cancelling the Kerr non-linearity

Due to the large number of Josephson junctions coupled to the readout resonator in our proposal, the Kerr non-linearity of the resonator might become too large and reduce the fidelity of the detector. This effect can be mitigated by noting that the Kerr non-linearity K is always negative [c.f. Eq. (28)]. One can therefore balance it out by introducing an additional positive Kerr non-linearity. One possible source of positive Kerr non-linearity is a single transmon in the so-called straddling regime coupled to the readout resonator [4]. The straddling regime is defined to be when the resonator frequency lies between the $|g\rangle \leftrightarrow |e\rangle$ and the $|e\rangle \leftrightarrow |f\rangle$ transition frequencies, $\omega_{fe} < \omega_r < \omega_{eg}$. Figure S6 shows the Kerr non-linearity, K_s, due to a single transmon coupled to a single resonator mode in the vicinity of the upper boundary of the straddling regime. These results were calculated using the full cosine potential for the transmon, *i.e.*, without expanding the non-linearity in powers of the superconducting phase. Depending on the coupling strength between the transmon and the resonator, the figure shows that it is possible to have positive Kerr non-linearities from the kHz range to several MHz. By using a tunable transmon, one can thus attempt to cancel out the total Kerr non-linearity $K + K_s \simeq 0$.

2 Design details

In this section we consider the design illustrated in Fig. S2 in more detail. We assume that the nearest neighbor coupling is purely capacitive ($L_{\rm nn} \to \infty$). We investigate values for circuit parameters necessary to achieve high detector performance with this design. The purpose of the section is to illustrate typical parameter ranges needed and elucidate the role played by different circuit parameters, rather than give a detailed, quantitative analysis for a particular parameter

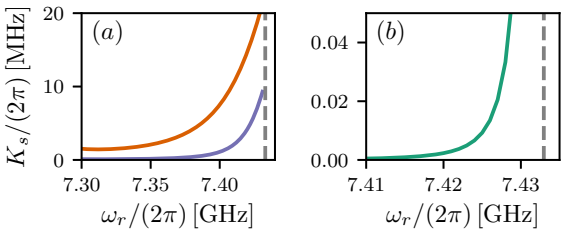

Figure S6: Kerr non-linearity for a resonator coupled to a transmon in the straddling regime as a function of resonator frequency. The transmon parameters are $E_J = 25$ GHz, $E_C = 300$ MHz, and the dashed gray line in the figure marks the transition frequency for the two lowest energylevels of the transmon. The orange line in panel (a) is for a transmon-resonator coupling strength of $g/(2\pi) = 25$ MHz, the purple line for $g/(2\pi) = 12$ MHz and panel (b) is for $g/(2\pi) = 1.3$ MHz.

set. We therefore make the simplifying assumption of neglecting spatial dependence of parameters. We emphasize that this is done only for simplicity, as we have shown that the detector is in fact robust to spatial parameter variations.

2.1 Number of unit cells needed

As we have shown in the main paper, the key figure of merit for the detector is

$$g\tau = \frac{2gz}{v} = 2\alpha \times \frac{\chi z}{v}, \tag{37}$$

where α is the displacement of the resonator, χ is the cross-Kerr shift per unit cell, $z = Na$ is the detector length and v the speed of light, We are here neglecting the spatial dependence of $\chi = \chi(x_n)$ for simplicity. Moreover, in contrast to the numerical results presented in the main paper we here assume that the detector is operated in reflection mode, *i.e.*, the waveguide is ended by an open at $x = z/2$, such that the total interaction time is $\tau = 2z/v$.

Using Eqs. (28) and (29) it is convenient to re-express the dimensionless quantity $\frac{Z_r}{R_K}|u|^2$ with $u \equiv u(x_n)$ the resonator mode-function as

$$\frac{Z_r}{R_K}|u|^2 = \frac{\alpha}{|g\tau|} \times \frac{|K|}{\bar{\omega}} \times \frac{4Z_{\rm tml}}{R_K}. \tag{38}$$

Using this in Eq. (29) we have

$$|g\tau| = 2\alpha \times \frac{\sqrt{N|K|E_J/\hbar}}{\bar{\omega}} \frac{8\pi Z_{\rm tml}}{R_K}. \tag{39}$$

where we recall that N is the total number of unit cells and $\bar{\omega}$ is the center frequency of the incoming photon. This expression can be inverted to give the necessary number of unit cells N to reach a certain value of $|g\tau|$

$$N = \frac{1}{2}\left(\frac{|g\tau|}{\alpha}\frac{R_K}{8\pi Z_{\rm tml}}\right)^2 \frac{\bar{\omega}^2}{|K|E_J/\hbar}. \tag{40}$$

In Fig. S7 the number of unit cells, Eq. (40), necessary to reach $g\tau$ in the range 1–3 is shown as a function of $Z_{\rm tml}$ for a representative choice of parameters: $I_c = 5\,\mu$A (with $E_J = \phi_0 \times I_c$), $\bar{\omega}/(2\pi) = 5$ GHz, $\alpha = 5$ and $|K|/(2\pi) = 200$ kHz (solid lines) or $|K|/(2\pi) = 30$ kHz (dashed lines). Recent experiments with Josephson travelling wave parametric amplifiers (JTWPAs) have demonstrated metamaterials of similar complexity to what is required here with $N \sim 2000$ unit cells [5]. Fig. S7 shows that reaching values $g\tau = 2$–3, necessary for reaching fidelities close to one, are likely out of reach for a $Z_{\rm tml} = 50\ \Omega$ transmission line, as it would require a prohibitively

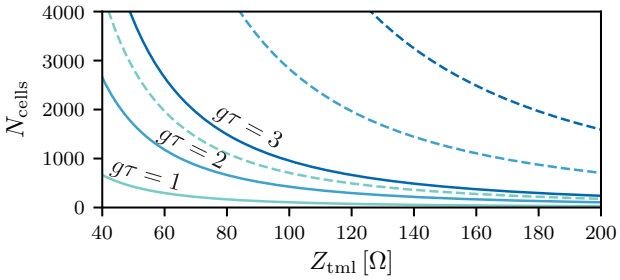

Figure S7: Number of unit cells, N, vs the impedance of the LC array, Z_{tml}, necessary to reach a certain value of $g\tau$, for $|K|/(2\pi) = 200$ kHz (solid lines) and $|K|/(2\pi) = 30$ kHz (dashed lines), and other parameters as given in the text.

large number of unit cells. However, with a modest increase in impedance, the figure shows that $N \sim 2000$ is sufficient. In applications where matching to a $50\,\Omega$ environment is less important, Z_{tml} can be increased even further relaxing the constraint on other parameters. Otherwise low-loss impedance transformers can be used to couple to $50\,\Omega$ input/output transmission lines.

2.2 Controlling the Kerr nonlinearity

The nonlinearity of the detector characterized by the cross-Kerr coupling between the metamaterial and the probe, $\chi(x)$, as well as the probe's self-Kerr K, is controlled by the junction parameters $E_{J,n}$, $C_{S,n}$ as well as the coupling capacitance $C_{c,n}$ between the junctions and the probe, c.f. Fig. S2. As can be seen from Eqs. (28) and (29), the non-linearities depend on the dimensionless number $\sqrt{Z_r/R_K}u_r(x_n)$, with $u_r(x)$ a dressed resonator mode function. Alternatively, from Eq. (22), this quantity can be directly related to $\varphi_r(x_n)$, the dimensionless magnitude of the zero-point fluctuations of the resonator mode as seen by the junction located at x_n. Accurately determining the zero-point fluctuations $\varphi_r(x_n)$ can be complicated for a complex geometry such as the JTWPA, but the problem can in principle be addressed using commercial numerical software such as finite element solvers [6].

To get a rough estimate for how the non-linearity depends on the circuit parameters, we estimate the contribution to the self-Kerr from a single unit cell of the metamaterial, *i.e.*, we consider the circuit

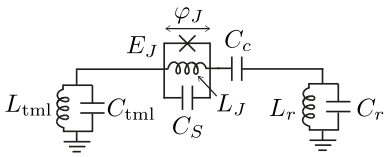

where in this simplified model we use a lumped element LC oscillator $\{L_r, C_r\}$ to represent the probe resonator, and another lumped element LC oscillator $\{L_{\text{tml}}, C_{\text{tml}}\}$ to represent the vacuum fluctuations of the transmission line with characteristic impedance $Z_{\text{tml}} = \sqrt{L_{\text{tml}}/C_{\text{tml}}}$ biasing the junction. Moreover, the spider symbol represent the non-linear part of the circuit, corresponding to a Hamiltonian potential term $\hat{H}_{\text{nl}} = -E_J\left(\cos\hat{\varphi}_J + \hat{\varphi}_J^2/2\right) \simeq -E_J\hat{\varphi}_J^4/24$, and $L_J = \phi_0^2/E_J = \phi_0/I_c$ is the linear inductance due to the Josephson junction. By diagonalizing the linear part of the circuit we can write

$$\begin{aligned}\hat{H} &\simeq \sum_m \hbar\omega_m \hat{a}_m^\dagger \hat{a}_m - \frac{E_J}{24}\left(\sum_m \varphi_m(\hat{a}_m^\dagger + \hat{a}_m)\right)^4 \\ &\simeq \sum_m \left[\hbar(\omega_m + \Delta_m)\hat{a}_m^\dagger\hat{a}_m + \frac{\hbar K_m}{2}(\hat{a}_m^\dagger)^2\hat{a}_m^2\right] + \sum_{m>n}\hbar\chi_{m,n}\hat{a}_m^\dagger\hat{a}_m\hat{a}_n^\dagger\hat{a}_n,\end{aligned} \tag{41}$$

with $m = \{\text{tml}, J, r\}$ running over three dressed modes, corresponding to the tml LC, the junction mode and the probe LC. In this expression $\Delta_m = \frac{1}{2}\sum_n \chi_{m,n}$, $K_m = \chi_{m,m}/2$ and $\hbar\chi_{m,m}/2 =$

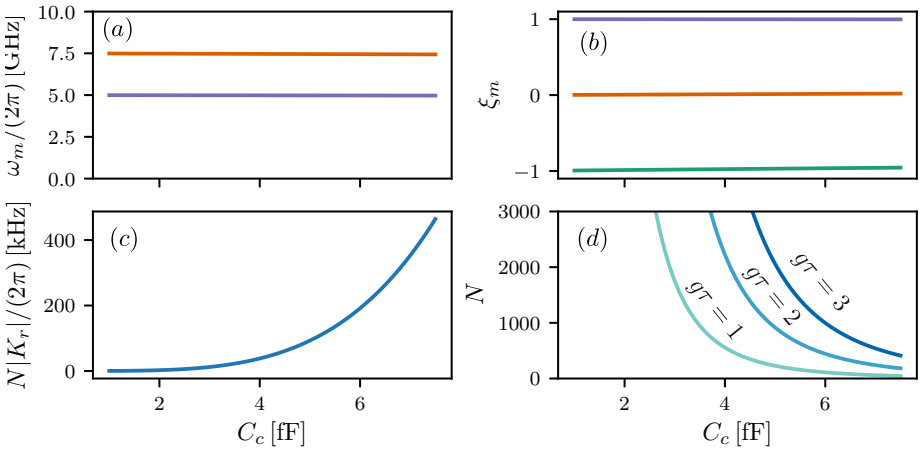

Figure S8: Properties of the normal modes as C_c is varied. (a) Dressed probe resonator (orange) and tml (blue) frequencies. (b) Zero-point vacuum fluctuations normalized by bare charecteristic zero-point fluctuations $\xi_m = \varphi_m/\varphi_{m,0}$, for the resonator (orange), tml LC (blue) and junction mode (green). (c) Self-Kerr of the probe resonator mode multiplied by $N = 2000$. (d) Number of unit cells needed to reach $g\tau = 1$–3 using the self-Kerr $K = NK_r$ extracted from panel (c).

$-E_J\varphi_m^2\varphi_n^2$. We find the normal mode frequencies ω_m and the dimensionless zero-point fluctuations φ_m by a standard numerical diagonalization of the linear part of the circuit, which allows us to extract the non-linearities $\chi_{m,m}$.

In Fig. S8 we show properties of the dressed normal modes as the small coupling capaitance C_c is varied in the range 1–7 fF, with the other parameter set to

$$\omega_{\rm tml}/(2\pi) = 5 \text{ GHz}, \quad Z_{\rm tml} = \sqrt{\frac{L_{\rm tml}}{C_{\rm tml}}} = 50\,\Omega, \tag{42}$$

$$\omega_r/(2\pi) = 7.5 \text{ GHz}, \quad Z_r = \sqrt{\frac{L_r}{C_r}} = 50\,\Omega, \tag{43}$$

$$I_c = 5\,\mu\text{A}, \quad C_S = 50 \text{ fF}. \tag{44}$$

Here $\omega_{\rm tml} = 1/\sqrt{C_{\rm tml}L_{\rm tml}}$ and $\omega_r = 1/\sqrt{C_rL_r}$ are bare frequencies. Figure S8 (a) show the corresponding dressed frequencies as C_c is varied. As this plot shows, the dressed frequencies hardly change from their bare values for the range of coupling capacitance considered. Note that there is also a third junction mode at a much higher frequency, not shown in the figure. Panel (b) of the figure show the zero-point vacuum fluctuations $\xi_m = \varphi_m/\varphi_{m,0}$ normalized by the characteristic "bare" zero-point vacuum fluctuations of each mode

$$\varphi_{m,0} = \frac{1}{\phi_0}\sqrt{\frac{\hbar Z_m}{2}}, \tag{45}$$

with $Z_J = \sqrt{L_J/C_S}$ for the junction mode. The dressed zero-point fluctuations of the tml- and the junction mode biasing the Josephson junction are close to their maximal value, corresponding to the galvanic coupling of these two modes. The dressed zero-point fluctuations of the probe resonator biasing the junciton is however much smaller, corresponding to the small capacitive coupling of this mode to the junction.

In Fig. S8 (c) we show the extracted self-Kerr non-linearity of the resonator $|K_r|$ due to the single junction, multiplied by $N = 2000$ as a representative number of unit cells for the metamaterial. This gives a rough estimate for the total self-Kerr non-linearity of the resonator. Although we do not expect this estimate to particularly accurate, these results show that the Kerr non-linearity can easily be tuned in the range 10–400 kHz by adjusting the small coupling capacitance C_c, keeping all other parameters fixed. Finally panel (d) shows the number of unit cells N from Eq. (40) needed to reach $g\tau = 1$–3 using the extracted value $K = NK_r$ for the total Kerr non-linearity.

2.3 Detection time

The interaction time is set by the number of unit cells, the center frequency ω_0 of the LC array and the capacitance ratio $C_{\rm nn}/C_0$, c.f Sec. 1.1. For $N = 2000$ unit cells, $C_{\rm nn}/C_0 = 0.1$ and $\omega_0/(2\pi) = 5$ GHz we have

$$\tau = \frac{2z}{v} = 2N \times \frac{C_0}{C_{\rm nn}} \frac{1}{\omega_0} = 1.3\,\mu\text{s}. \tag{46}$$

The numerical results of the main paper indicates a detetion time of about 3τ, *i.e.*, in the μs range. A typical photon dimensionless photon width of $\gamma\tau = 2$–6 as used in the numerical simulations in the main paper thus corresponds to $\gamma/(2\pi) = 0.25$–0.75 Mhz. We emphasize that the detection fidelity improves with *increasing* γ. It is therefore encouraging that very high detection fidelities are found for such narrow photons.

In the numerical simulations presented in the main paper we used a resonator decay rate such that $\kappa_\tau = 1.0$, which for the present parameter set corresponds to

$$\kappa_a\tau = 1.0 \Rightarrow \kappa_a/(2\pi) = 0.13 \text{ MHz}. \tag{47}$$

With such a small value for κ_a it is necessary to reduce the total self-Kerr nonlinearity $K_{\rm tot} = K + K_s$ of the resonator, using *e.g.* the approach discussed in Sec. 1.4. Alternatively, it might be beneficial to increase κ_a to the range $\kappa_a/(2\pi) = 1$–10 MHz, thus correspondingly increasing $\kappa\tau$. Unfortunately we found it numerically too challenging to simulate this regime of larger κ_a, due to need for correspondingly smaller time steps needed. Based on a simplified model, we expect the SNR to increase with κ_a at short times, and go down as $1/\sqrt{\kappa_a}$ for large $\kappa_a\tau$ [7]. An order of magnitude increase in κ_a might therefore lead to a decrease of about a factor of three in the SNR, which compares to reducing g from say $g\tau = 3$ to $g\tau = 1$.

2.4 Alternative design

Figure S9 shows an alternative design for the JTWPD. In this design, the "backbone" of the detector is a a linear chain of galvanically coupled inductors, $L_{\rm nn}$, with capacitance C_g to ground per unit cell. This would in itself form a linear waveguide with impedance $Z_{\rm tml} = \sqrt{L_{\rm nn}/C_g}$ and speed of light $v = a/\sqrt{L_{\rm nn}C_g}$, and no frequency cut-offs. However, as described in the main paper, it is advantageous to have a low-frequency cut-off for two reasons: It shunts the detector from thermal low-frequency photons, and by placing the resonator below a cut-off we can minimize loss of resonator via the metamaterial. We therefore introduce to the design a shunt inductor L_g to ground in each unit cell. This gives a low-frequency cut-off

$$\Omega_L = \frac{1}{\sqrt{C_g L_g}}. \tag{48}$$

This design has both advantages and disadvantages. The main advantage is the potentially large bandwidth. The main disadvantage, however, is that achieving a frequency cutoff $\omega_L/(2\pi) < 10$ GHz requires very large shunt inductors L_g. For example, a $Z_{\rm tml} = 50\,\Omega$ waveguide with a capacitance to ground of $C_g = 50$ fF would require a shunt inductance $L_g = 5$ nH to have a cut-off frequency of $\Omega_L = 10$ GHz. Unless an alternative method can be devised to achieve a low-frequency cut-off we therefore consider this design less practical than the design presented in Sec. 2.

3 Keldysh path-integral treatment

To study the scaling of the detector back-action, we integrate out the waveguide part of the system using Keldysh field theory. This allows us to derive an effective Keldysh action describing the evolution of the measurement resonator when a photon travels through the nonlinear waveguide. As we show, this effective Keldysh action indicates that

1. The relevant small parameter for the measurement back-actio is g/σ, with σ^2 the variance of an incoming Gaussian photon.

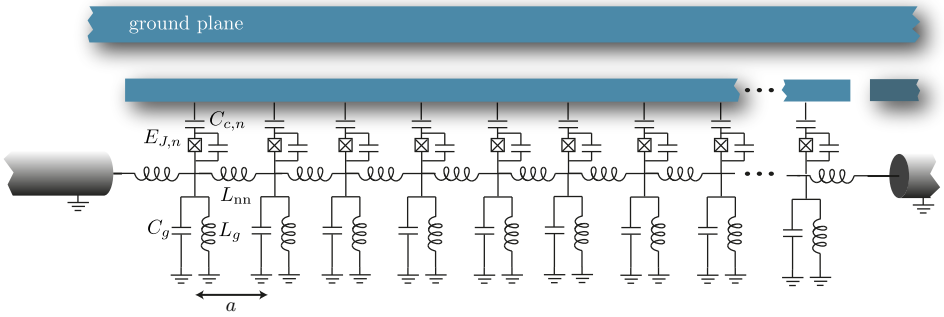

Figure S9: Alternative design.

2. Back-scattering of the signal photons due to measurement back-action are suppressed when the local coupling strength is small in front of the photon carrier frequency, $g/\bar{\omega} \ll 1$.

Moreover, from the effective action, we derive an equivalent master equation that can be used to perform numerical simulations.

3.1 Keldysh action for the emitter-waveguide-probe system

Recall the Hamiltonian for the interacting system in the rotating frame for the resonator

$$\begin{aligned} \hat{H} &= \hat{H}_0 + \hat{H}_{\rm int}, \\ \hat{H}_0 &= \sum_\nu \int_\Omega d\omega\, \hbar\omega \hat{b}^\dagger_{\nu,\omega}\hat{b}_{\nu,\omega}, \\ \hat{H}_{\rm ideal} &= \hbar g \sum_{\nu,\mu} \int_{-z/2}^{z/2} dx\, \hat{b}^\dagger_\nu(x)\hat{b}_\mu(x)(\hat{a}^\dagger + \hat{a}), \end{aligned} \tag{49}$$

where

$$\hat{b}_\nu(x) = \sqrt{\frac{\bar{\omega}}{2\pi v}} \int_\Omega \frac{d\omega}{\sqrt{\omega}} \hat{b}_{\nu\omega} e^{\nu i\omega x/v}. \tag{50}$$

In order to simplify the calculation and focus solely on the part of the interaction that induces a displacement in the measurement resonator, we have here set $K = \chi(x) = 0$ and $g(x) = g$ in the Hamiltonian above, as discussed in the main text. In this section, we will use the convention $\hbar = 1$ for brievity and, to avoid ambiguousness with the $\pm$ notation from the upper and lower branches of the Keldysh contour, use the $\nu = R, L$ subscripts for right- and left-moving fields, respectively.

Instead of directly considering a signal photon on the waveguide, we add the fictitious emitter of such a photon far away from the nonlinear waveguide at the initial position $x_0 \ll -z/2$ and consider that this emitter is only coupled to the right-moving modes. This is modeled by a combined emitter-waveguide-resonator Hamiltonian [8] in the rotating wave approximation

$$\begin{aligned} \hat{H} &= \hat{H}_0 + \hat{H}_{\rm ideal} + \hat{H}_c, \\ \hat{H}_c &= \omega_c \hat{c}^\dagger\hat{c} + \sqrt{\kappa_c(t)v} \int dx\, \delta(x - x_0) \left[\hat{b}^\dagger_R(x)\hat{c} + \hat{c}^\dagger \hat{b}_R(x)\right], \end{aligned} \tag{51}$$

where $\kappa_c(t)$ is the coupling of the emitter to the waveguide and ω_c is the frequency of the emitter. In principle, any photon shape can be modeled this way and we follow the main text by considering a photon of carrier frequency $\omega_c = \bar{\omega}$ with a Gaussian envelope of linewidth σ,

$$\xi(t) = \left(\frac{2\sigma^2}{\pi}\right)^{1/4} e^{-i\omega_c t} e^{-\sigma^2(t+x_0/v)^2}, \tag{52}$$

with x_0 the initial position of the signal photon. Here, we simulate such a photon wavepacket by initializing the emitter in the $|1\rangle$ photon Fock state and choosing [9]

$$\kappa_c(t) = \sqrt{\frac{8\sigma^2}{\pi}} \frac{e^{-2\sigma^2 t^2}}{\mathrm{erfc}(\sqrt{2}\sigma t)}. \tag{53}$$

Note that Eq. (52) corresponds to the amplitude of the photon wavepacket as a function of time at the fixed waveguide position $x = 0$. Since we consider a waveguide without dispersion, the amplitude of the wavepacket as a function of both time and position is easily calculated, $\xi(x,t) = \xi(t - x/v)$.

Following Ref. [10], we write the Keldysh action for the combined emitter-waveguide-resonator system

$$\begin{aligned} S[a,b,c] = & \int dt\, a_+^* \partial_t a_+ - a_-^* \partial_t a_- + c_+^* \partial_t c_+ - c_-^* \partial_t c_- \\ & + \int dt dx\, b_+(x)^* \partial_t b_+(x) - b_-(x)^* \partial_t b_-(x) - i\mathcal{L}(a,b,c), \\ \mathcal{L}(a,b,c) = & -i(H_+ - H_-) + \kappa_a \left[a_+ a_-^* - \frac{1}{2}\left(a_+^* a_+ + a_-^* a_- \right) \right] \end{aligned} \tag{54}$$

where the arguments of S and $\mathcal{L}$ have been shortened to $\psi \leftrightarrow \psi_+^*, \psi_+, \psi_-^*, \psi_-$, with $\psi = a, b, c$. The Hamiltonian part $H_\pm$ is found by writing Eq. (51) in a normal-ordered form and replacing each operator by the corresponding variable $\hat{\psi} \to \psi_\pm$. Unless otherwise noted, we will keep the time dependence of variables implicit to make the notation more compact. Performing the Keldysh rotation $\psi_{cl} = (\psi_+ + \psi_-)/\sqrt{2}$ and $\psi_q = (\psi_+ - \psi_-)/\sqrt{2}$, we write the action as

$$S[a,b,c] = \int dt\, \mathbf{a}^\dagger \mathrm{G}_a^{-1} \mathbf{a} + \mathbf{c}^\dagger \mathrm{G}_c^{-1} \mathbf{c} + \int dt dx\, \mathbf{b}^\dagger \left[\mathrm{G}_b^{-1} - \mathrm{V} \right] \mathbf{b} + \mathbf{b}^\dagger \mathbf{j} + \mathbf{j}^\dagger \mathbf{b}, \tag{55}$$

where the dependence on x was made implicit in the second part to make the notation more compact and we defined the vectors

$$\begin{aligned} \mathbf{a} &= \begin{pmatrix} a_{cl} \\ a_q \end{pmatrix}, \quad \mathbf{c} = \begin{pmatrix} c_{cl} \\ c_q \end{pmatrix} \\ \mathbf{b} &= \begin{pmatrix} b_{R,cl}(x) \\ b_{R,q}(x) \\ b_{L,cl}(x) \\ b_{L,q}(x) \end{pmatrix}, \quad \mathbf{j} = -\delta(x - x_0)\sqrt{\kappa_c(t) v} \begin{pmatrix} c_q \\ c_{cl} \\ 0 \\ 0 \end{pmatrix}. \end{aligned} \tag{56}$$

We also defined

$$\begin{aligned} \mathrm{G}_a^{-1} &= \begin{pmatrix} 0 & i\partial_t - i\kappa_a/2 \\ i\partial_t + i\kappa_a/2 & i\kappa_a \end{pmatrix}, \\ \mathrm{G}_b^{-1} &= \begin{pmatrix} \mathrm{G}_{b,R}^{-1} & 0_{2\times 2} \\ 0_{2\times 2} & \mathrm{G}_{b,L}^{-1} \end{pmatrix}, \\ \tilde{G}_{b,\nu}^{-1}(k) &= \begin{pmatrix} 0 & i\partial_t - \nu v k - i\eta \\ i\partial_t - \nu v k + i\eta & i\eta \end{pmatrix}, \\ \mathrm{G}_c^{-1} &= \begin{pmatrix} 0 & i\partial_t - \omega_c - i\eta \\ i\partial_t - \omega_c + i\eta & i\eta \end{pmatrix}, \\ \mathrm{V} &= \begin{pmatrix} \mathrm{W} & \mathrm{W} \\ \mathrm{W} & \mathrm{W} \end{pmatrix}, \\ \mathrm{W} &= g\, \theta(x + z/2)\theta(z/2 - x) \begin{pmatrix} X_q & X_{cl} \\ X_{cl} & X_q \end{pmatrix}, \\ X_{cl/q} &\equiv (a_{cl/q} + a_{cl/q}^*)/\sqrt{2}, \end{aligned} \tag{57}$$

where η is there for regularization and the limit $\eta \to 0$ is implicit. In Eq. (55), we expressed the waveguide's field inverse Green's function in position space instead of momentum as the interaction term V is local in space. However, it is easier to solve for the free field Green's function in momentum, so we will perform the Fourier transform back to position space after finding $\tilde{G}_{b,\nu}(k)$.

3.2 Tracing out the waveguide

The partition function associated with the action Eq. (55) is given by

$$Z = \int \mathcal{D}[a,b,c] e^{iS[a,b,c]}. \tag{58}$$

It is useful to point out two properties of the Keldysh action Eq. (55). First, it is quadratic in the waveguide field $b(x)$ and second, the coupling between the emitter and the waveguide acts as a source term for $b(x)$. Using these properties and the Gaussian integral identity,

$$\int D[z,z^*]e^{i\int_{t,t'}\ \psi^\dagger(t)G^{-1}(t,t')\psi(t')+\psi^\dagger(t)j(t)+j^\dagger(t)\psi(t)} = \frac{e^{-i\int_{t,t'}\ j^\dagger(t)G(t,t')j(t')}}{\det G^{-1}}, \tag{59}$$

we can integrate out exactly the waveguide field,

$$Z = \int \mathcal{D}[a,c]e^{iS[a,c]-i\int_{\mathrm{x_1x_2}}\mathbf{j}^\dagger(\mathrm{x_1})[\mathrm{G_b^{-1}-V}]^{-1}(\mathrm{x_1,x_2})\mathbf{j}(\mathrm{x_2})}, \tag{60}$$

where the determinant denominator is canceled by a factor in the integration measure $\mathcal{D}[b]$. We also used the shorthand notation $\mathrm{x}\equiv x,t$ for compactness. From the partition function Eq. (60), it is natural to define an effective action for the emitter-resonator system,

$$S_{\mathrm{eff}}[a,c] = -\int d\mathrm{x_1x_2}\,\mathbf{j}^\dagger(\mathrm{x_1})[\mathrm{G_b^{-1}-V}]^{-1}(\mathrm{x_1,x_2})\mathbf{j}(\mathrm{x_2}) + \int dt\,\mathbf{a}^\dagger\mathrm{G_a^{-1}}\mathbf{a}+\mathbf{c}^\dagger\mathrm{G_c^{-1}}\mathbf{c}. \tag{61}$$

This effective action is not very useful in its present form as (1), it is nonlocal in time and (2), we don't have an exact expression for $[\mathrm{G_b^{-1}-V}]^{-1}$. To remediate to this situation, we use perturbation theory and expand $(1-\mathrm{G_bV})^{-1}$ as a Taylor series in $\mathrm{G_bV}$, assuming that the linewidth of the photon is large compared to the coupling strength g,

$$\begin{aligned} S_{\mathrm{eff}}[a,c] &\approx -\sum_n \int d\mathrm{x_1x_2x_3}\,\mathbf{j}^\dagger(\mathrm{x_1})[\mathrm{G_bV}]^n(\mathrm{x_1,x_2})\mathrm{G_b}(\mathrm{x_2,x_3})\mathbf{j}(\mathrm{x_3}) + \int dt\,\mathbf{a}^\dagger\mathrm{G_a^{-1}}\mathbf{a}+\mathbf{c}^\dagger\mathrm{G_c^{-1}}\mathbf{c}, \\ &\equiv \sum_n S_{\mathrm{eff}}^{(n)} + \int dt\,\mathbf{a}^\dagger\mathrm{G_a^{-1}}\mathbf{a}+\mathbf{c}^\dagger\mathrm{G_c^{-1}}\mathbf{c}. \end{aligned} \tag{62}$$

More precisely, any point in the waveguide will interact for a time $\sim 1/\sigma$ with the photon, and, consequently, the expansion is valid as long as $g/\sigma < 1$. Note that this expansion relies on the fact that the signal photon has a finite width and Eq. (62) is thus not valid for a general incoming signal. Before evaluating the effective action at various orders, we compute the waveguide Green's function in momentum space

$$\tilde{G}_{b,\nu}(k,t_1,t_2) = e^{-i\nu vk(t_1-t_2)}\begin{pmatrix} 1 & \theta(t_1-t_2) \\ -\theta(t_2-t_1) & 0 \end{pmatrix}. \tag{63}$$

Formally, the right-moving (left-moving) fields are defined only on the positive (negative) wavevectors. Here, we will make the assumption that the coupling to the waveguide is small, $\kappa_c \ll \omega_c$ and, consequently, only wavevectors around $k_c = \omega_c/v$ will contribute to the effective action. Note that this assumption was already used earlier to write the Hamiltonian in the rotating wave approximation for the emitter-waveguide coupling, Eq. (51). In practice, this means that for both right- and left-moving fields we extend the wavevector integral to the whole real line. Using the above approximation and Eq. (63), we can write the Green's function in position space

$$\begin{aligned} \mathrm{G}_{b,\nu}(x_1,x_2,t_1,t_2) &= \frac{-i}{2\pi}\int_0^\infty dk\, e^{i\nu k(x_1-x_2)}e^{-ivk(t_1-t_2)}\begin{pmatrix} 1 & \theta(t_1-t_2) \\ -\theta(t_2-t_1) & 0 \end{pmatrix} \\ &\approx \frac{-i}{2\pi}\int_{-\infty}^\infty dk\, e^{i\nu k(x_1-x_2)}e^{-ivk(t_1-t_2)}\begin{pmatrix} 1 & \theta(t_1-t_2) \\ -\theta(t_2-t_1) & 0 \end{pmatrix} \\ &= -i\delta[v(t_1-t_2)-\nu(x_1-x_2)]\begin{pmatrix} 1 & \theta(t_1-t_2) \\ -\theta(t_2-t_1) & 0 \end{pmatrix} \\ &\equiv \begin{pmatrix} \mathrm{G}_{b,\nu}^K & \mathrm{G}_{b,\nu}^R, \\ \mathrm{G}_{b,\nu}^A & 0 \end{pmatrix}, \\ \mathrm{G}_b &= \begin{pmatrix} \mathrm{G}_{b,R} & 0_{2\times 2} \\ 0_{2\times 2} & \mathrm{G}_{b,L} \end{pmatrix}, \end{aligned} \tag{64}$$

with the useful identity $\mathrm{G}_{b,\nu}^K = \mathrm{G}_{b,\nu}^R - \mathrm{G}_{b,\nu}^A$ [10] and the convention $\theta(0) = 1/2$. Since the Green's function depends only on the space and time difference, we will use the shorter notation $\mathrm{G}_b(x_1,x_2,t_1,t_2) = \mathrm{G}_{b,\nu}(x_1-x_2,t_1-t_2)$.

3.3 Zeroth order

Using Eqs. (62) and (64), we compute the zeroth order term of the effective action,

$$\begin{aligned}
S_{\text{eff}}^{(0)} &= -\int dx_1 dx_2 dt_1 dt_2 \mathbf{j}^\dagger(x_1,t_1)\mathrm{G}_b(x_1-x_2,t_1-t_2)\mathbf{j}(x_2,t_2),\\
&= -v\int dx_1 dt_1 dx_2 dt_2\, \delta(x_1-x_0)\delta(x_2-x_0)\sqrt{\kappa_c(t_1)\kappa_c(t_2)}\\
&\times \tilde{\mathbf{c}}^\dagger(t_1)\mathrm{G}_{b,R}(x_1-x_2,t_1-t_2)\tilde{\mathbf{c}}(t_2),\\
&= iv\int dt_1 dt_2\, \delta(vt_1-vt_2)\sqrt{\kappa_c(t_1)\kappa_c(t_2)}\times \tilde{\mathbf{c}}^\dagger(t_1)\begin{pmatrix}1 & \theta(t_1-t_2)\\ -\theta(t_2-t_1) & 0\end{pmatrix}\tilde{\mathbf{c}}(t_2),\\
&= i\int dt\,\kappa_c(t)\left[c_q^*(t)c_q(t)-\frac{1}{2}c_q^*(t)c_{cl}(t)+\frac{1}{2}c_{cl}^*(t)c_q(t)\right]
\end{aligned} \tag{65}$$

where we defined $\tilde{\mathbf{c}}^\dagger = (c_q^*\ c_{cl}^*)$ and used the identity $\delta(\alpha t) = \delta(t)/|\alpha|$. $S_{\text{eff}}^{(0)}$ corresponds to the decay of the emitter into the waveguide and we include this term into the bare action for the emitter,

$$\mathrm{G}_c^{-1} \to \begin{pmatrix}0 & i\partial_t-\omega_c-i\kappa_c/2\\ i\partial_t-\omega_c+i\kappa_c/2 & i\kappa_c\end{pmatrix}. \tag{66}$$

Note that keeping the full Green's function for the waveguide field instead of extending the wavevector integral in Eq. (64) would have resulted in an additional renormalization of the emitter frequency ω_c.

3.4 First order

The first term of the effective action is given by

$$\begin{aligned}
S_{\text{eff}}^{(1)} =& -\int dx_1 dx_2 dx_3 dt_1 dt_2 dt_3\, \mathbf{j}^\dagger(x_1,t_1)\mathrm{G}_b(x_1-x_2,t_1-t_2)\mathrm{V}(x_2,t_2)\mathrm{G}_b(x_2-x_3,t_2-t_3)\mathbf{j}(x_3,t_3),\\
=& \frac{1}{v}\int dx_2 dt_2\,\kappa_c\left(t_2+\frac{x_0-x_2}{v}\right)\tilde{\mathbf{c}}^\dagger\left(t_2+\frac{x_0-x_2}{v}\right)\begin{pmatrix}1 & \theta(x_0-x_2)\\ -\theta(x_2-x_0) & 0\end{pmatrix}\mathrm{W}(x_2,t_2)\\
&\times\begin{pmatrix}1 & \theta(x_2-x_0)\\ -\theta(x_0-x_2) & 0\end{pmatrix}\tilde{\mathbf{c}}\left(t_2+\frac{x_0-x_2}{v}\right),
\end{aligned} \tag{67}$$

where we used the identity $\theta(\alpha t) = \theta(t)$ for $\alpha > 0$. Here, we know that the integral in position is non-zero only when $x_2 > x_0$ since we placed the emitter before the nonlinear waveguide, $x_0 < -z/2$. As a result, we can evaluate the Heaviside functions (in position) in the equation above,

$$S_{\text{eff}}^{(1)} = -\frac{2g}{v}\int dt\int_{-z/2}^{z/2} dx\,\kappa_c\left(t+\frac{x_0-x}{v}\right)\times c_-^*\left(t+\frac{x_0-x}{v}\right)X_q(t)c_+\left(t+\frac{x_0-x}{v}\right). \tag{68}$$

We then use the fact that we know, by construction, the solution for the time evolution of the emitter, $\sqrt{\kappa_c(t)}c(t) = \xi(t-x_0/v)$. Using this, we replace $\sqrt{\kappa_c(t+\Delta t)}c(t+\Delta t) = \sqrt{\kappa_c(t)}c(t)\times \xi(t-x_0/v+\Delta t)/\xi(t-x_0/v)$ in the equation above. We carry out the integration in position and arrive at a first order effective action that is local in time

$$S_{\text{eff}}^{(1)} = -g\int dt\, c_-^*(t)\,X_q(t)c_+(t)\,\frac{\kappa_c(t)}{\sigma}\sqrt{\frac{\pi}{2}}e^{\tilde{t}^2}\left\{\mathrm{erf}(\tilde{t}+\tilde{t}_0+\tilde{z}/2)-\mathrm{erf}\left(\tilde{t}+\tilde{t}_0-\tilde{z}/2\right)\right\}, \tag{69}$$

where we defined $\tilde{t}\equiv\sqrt{2}\sigma t$, $\tilde{t}_0\equiv\sqrt{2}\sigma x_0/v$ and $\tilde{z}\equiv\sqrt{2}\sigma z/v$. The above action is equivalent to a term in the master equation [10]

$$S_{\text{eff}}^{(1)} \sim \mathcal{L}^{(1)}(\rho) = -ig\frac{\mathrm{erf}(\tilde{t}+\tilde{t}_0+\tilde{z}/2)-\mathrm{erf}\left(\tilde{t}+\tilde{t}_0-\tilde{z}/2\right)}{\mathrm{erfc}(\tilde{t})}\left[\hat{c}(\hat{a}+\hat{a}^\dagger)\rho\hat{c}^\dagger-\hat{c}\rho\hat{c}^\dagger(\hat{a}+\hat{a}^\dagger)\right], \tag{70}$$

which corresponds to a drive term on the measurement resonator with an proportional to the probability of the photon being in the nonlinear waveguide at time t. We can write the above equation as a Hamiltonian-like term in the master equation

$$\begin{aligned}\mathcal{L}^{(1)}(\rho) &= -i\left[g\eta_{\rm det}(t)(\hat{a}+\hat{a}^\dagger), \frac{2\hat{c}\rho\hat{c}^\dagger}{\mathrm{erfc}(\tilde{t})}\right], \\ \eta_{\rm det}(t) &\equiv \frac{1}{2}\left[\mathrm{erf}(\tilde{t}_+) - \mathrm{erf}\left(\tilde{t}_-\right)\right],\end{aligned} \tag{71}$$

where we defined $\tilde{t}_\pm \equiv \tilde{t} + \tilde{t}_0 \pm \tilde{z}/2$ to further simplify the notation.

3.5 Second order

We now evaluate the second order term of the effective action,

$$\begin{aligned}S^{(2)}_{\rm eff} = &-\int d\mathrm{x}_1 d\mathrm{x}_2 d\mathrm{x}_3 d\mathrm{x}_4\, \tilde{\mathbf{c}}^\dagger(\mathrm{x}_1)\mathrm{G}_{b,R}(\mathrm{x}_1-\mathrm{x}_2)\mathrm{W}(\mathrm{x}_2) \\ &\times[\mathrm{G}_{b,R}(\mathrm{x}_2-\mathrm{x}_3)+\mathrm{G}_{b,L}(\mathrm{x}_2-\mathrm{x}_3)]\mathrm{W}(\mathrm{x}_3)\mathrm{G}_{b,R}(\mathrm{x}_3-\mathrm{x}_4)\tilde{\mathbf{c}}(\mathrm{x}_4).\end{aligned} \tag{72}$$

In this second order term, we see that there is the possibility of backscattering of the photon due to the appearance of the left-moving field Green's function, $\mathrm{G}_{b,L}$. In order to make the equations more manageable, we split the effective action in two, $S^{(2)}_{\rm eff} \equiv S^{(2)}_{{\rm eff},R} + S^{(2)}_{{\rm eff},L}$, and evaluate the terms one at a time. First, we consider the "forward-scattering" part, $S^{(2)}_{{\rm eff},R}$,

$$\begin{aligned}S^{(2)}_{{\rm eff},R} = &-\int d\mathrm{x}_1 d\mathrm{x}_2 d\mathrm{x}_3 d\mathrm{x}_4\, \tilde{\mathbf{c}}^\dagger(\mathrm{x}_1)\mathrm{G}_{b,R}(\mathrm{x}_1-\mathrm{x}_2)\mathrm{W}(\mathrm{x}_2)\mathrm{G}_{b,R}(\mathrm{x}_2-\mathrm{x}_3)\mathrm{W}(\mathrm{x}_3)\mathrm{G}_{b,R}(\mathrm{x}_3-\mathrm{x}_4)\tilde{\mathbf{c}}(\mathrm{x}_4), \\ = &\frac{-2ig^2}{v}\int d\mathrm{x}_2 d\mathrm{x}_3 \sqrt{\kappa_c\left(t_2+\frac{x_0-x_2}{v}\right)\kappa_c\left(t_3+\frac{x_0-x_3}{v}\right)}c^*_-\left(t_2+\frac{x_0-x_2}{v}\right)c_+\left(t_3+\frac{x_0-x_3}{v}\right) \\ &\times\delta[v(t_2-t_3)-(x_2-x_3)]\begin{pmatrix}X_q(t_2) & X_{cl}(t_2)\end{pmatrix}\begin{pmatrix}\theta(t_2-t_3)+\theta(t_3-t_2) & \theta(t_2-t_3)\\ -\theta(t_3-t_2) & 0\end{pmatrix}\begin{pmatrix}X_q(t_3)\\ X_{cl}(t_3)\end{pmatrix}, \\ = &\frac{-2ig^2\sqrt{2}}{v}\int d\mathrm{x}_2 d\mathrm{x}_3 \sqrt{\kappa_c\left(t_2+\frac{x_0-x_2}{v}\right)\kappa_c\left(t_3+\frac{x_0-x_3}{v}\right)}c^*_-\left(t_2+\frac{x_0-x_2}{v}\right)c_+\left(t_3+\frac{x_0-x_3}{v}\right) \\ &\times\delta[v(t_2-t_3)-(x_2-x_3)]\left[X_q(t_2)X_+(t_3)\theta(t_2-t_3)-X_-(t_2)X_q(t_3)\theta(t_3-t_2)\right], \\ = &\frac{-2ig^2\sqrt{2}}{v^2}\int_{-z/2}^{z/2} dx_2 dx_3 \\ &\times\left\{\int dt_2\,\kappa_c\left(t_2+\frac{x_0-x_2}{v}\right)c^*_-c_+\left(t_2+\frac{x_0+x_2}{v}\right)X_q(t_2)X_+\left(t_2-\frac{x_2-x_3}{v}\right)\theta(x_2-x_3)\right. \\ &\left.-\int dt_3\,\kappa_c\left(t_3+\frac{x_0-x_3}{v}\right)c^*_-c_+\left(t_3+\frac{x_0-x_3}{v}\right)X_-\left(t_3+\frac{x_2-x_3}{v}\right)X_q(t_3)\theta(x_3-x_2)\right\}.\end{aligned} \tag{73}$$

Similar as above, we use $\sqrt{\kappa_c(t+\Delta t)}c(t+\Delta t) = \sqrt{\kappa_c(t)}c(t)\times\xi(t-x_0/v+\Delta t)/\xi(t-x_0/v)$ to replace the time dependance of the emitter variable. Moreover, because of the simple form of Eq. (51), the correlations in the resonator quadrature coupled to the waveguide are given by $X(t)X(t+\Delta t) = X^2(t)e^{-\kappa_a|\Delta t|/2}$. We remark that this simplification is possible only because we assumed $\chi = K = 0$ in the starting point of this derivation, Eq. (49). However, our result remains approximately correct in the limit of small spurious nonlinearities where $\chi, K \ll g, \sigma$. Using these properties and relabeling the integration variables, we find

$$\begin{aligned}S^{(2)}_{{\rm eff},R} &= \frac{-4ig^2}{v^2}\int dt\,\kappa_c(t)c^*_-c_+(t)X^2_q(t)\int_{-z/2}^{z/2} dx_2 dx_3\, e^{-2\sigma^2\left[\frac{(x_0-x_2)^2}{v^2}+2\frac{(x_0-x_2)}{v}t\right]}e^{\frac{-\kappa_a(x_2-x_3)}{2v}}\theta(x_2-x_3), \\ &= \frac{-4ig^2}{\kappa_a}\int dt\, c^*_-c_+(t)X^2_q(t)\frac{\kappa_c(t)}{\sigma}\sqrt{\frac{\pi}{2}} \\ &\quad\times\left\{e^{\tilde{t}^2}\left[\mathrm{erf}(\tilde{t}_+)-\mathrm{erf}\left(\tilde{t}_-\right)\right]+e^{(\tilde{\kappa}_a-\tilde{t})^2-\tilde{\kappa}_a(2\tilde{t}_0+\tilde{z})}\left[\mathrm{erf}(\tilde{\kappa}_a-\tilde{t}_+)-\mathrm{erf}\left(\tilde{\kappa}_a-\tilde{t}_-\right)\right]\right\},\end{aligned} \tag{74}$$

where we defined $\tilde{\kappa}_a \equiv \kappa_a/(4\sqrt{2}\sigma)$. We can write the effective action Eq. (74) as an equivalent term in the master equation

$$S^{(2)}_{\text{eff},R} \sim \mathcal{L}^{(2)}(\rho) = \frac{2\Gamma(t)}{\text{erfc}(\tilde{t})}\left[\hat{c}(\hat{a}+\hat{a}^\dagger)\rho\hat{c}^\dagger(\hat{a}+\hat{a}^\dagger) - \frac{1}{2}\hat{c}\rho\hat{c}^\dagger(\hat{a}+\hat{a}^\dagger)^2 - \frac{1}{2}(\hat{a}+\hat{a}^\dagger)^2\hat{c}\rho\hat{c}^\dagger\right], \tag{75}$$

where

$$\Gamma(t) \equiv \frac{2g^2}{\kappa_a}\left\{\left[\text{erf}(\tilde{t}_+) - \text{erf}\left(\tilde{t}_-\right)\right] + e^{(\tilde{\kappa}_a-\tilde{t})^2-\tilde{t}^2-\tilde{\kappa}_a(2\tilde{t}_0+\tilde{z})}\left[\text{erf}(\tilde{\kappa}_a-\tilde{t}_+) - \text{erf}\left(\tilde{\kappa}_a-\tilde{t}_-\right)\right]\right\}. \tag{76}$$

We can write the above equation as a dissipator-like term

$$\mathcal{L}^{(2)}(\rho) = \Gamma(t)\mathcal{D}[\hat{a}+\hat{a}^\dagger]\frac{2\hat{c}\rho\hat{c}^\dagger}{\text{erfc}(\tilde{t})}. \tag{77}$$

We now turn to the "backscattering" part of the effective second order action, $S^{(2)}_{\text{eff},L}$. Using a similar procedure as above, we obtain

$$\begin{aligned}
S^{(2)}_{\text{eff},L} =& -\int d\text{x}_1 d\text{x}_2 d\text{x}_3 d\text{x}_4\, \tilde{\mathbf{c}}^\dagger(\text{x}_1)\text{G}_{b,R}(\text{x}_1-\text{x}_2)\text{W}(\text{x}_2)\text{G}_{b,L}(\text{x}_2-\text{x}_3)\text{W}(\text{x}_3)\text{G}_{b,R}(\text{x}_3-\text{x}_4)\tilde{\mathbf{c}}(\text{x}_4),\\
=& \frac{ig^2\sqrt{2}}{v}\int d\text{x}_2 d\text{x}_3 \sqrt{\kappa_c\left(t_2+\frac{x_0-x_2}{v}\right)\kappa_c\left(t_3+\frac{x_0-x_3}{v}\right)}c^*_-\left(t_2+\frac{x_0-x_2}{v}\right)c_+\left(t_3+\frac{x_0-x_3}{v}\right)\\
&\times\delta[v(t_2-t_3)+(x_2-x_3)]\left[X_q(t_2)X_+(t_3)\theta(t_2-t_3) - X_-(t_2)X_q(t_3)\theta(t_3-t_2)\right],\\
=& \frac{-ig^2\sqrt{2}}{v^2}\int_{-z/2}^{z/2} dx_2 dx_3 \left\{\int dt_3 \sqrt{\kappa_c\left(t_3-\frac{2x_2-x_3-x_0}{v}\right)\kappa_c\left(t_3+\frac{x_0-x_3}{v}\right)}\theta(x_2-x_3)\right.\\
&\times c^*_-\left(t_3-\frac{2x_2-x_3-x_0}{v}\right)c_+\left(t_3+\frac{x_0-x_3}{v}\right)X_q(t_3)X_+\left(t_3-\frac{x_2-x_3}{v}\right)\\
&-\int dt_2\sqrt{\kappa_c\left(t_2+\frac{x_0-x_2}{v}\right)\kappa_c\left(t_2-\frac{2x_3-x_2-x_0}{v}\right)}\theta(x_3-x_2)\\
&\left.\times c^*_-\left(t_2+\frac{x_0-x_2}{v}\right)c_+\left(t_2-\frac{2x_3-x_2-x_0}{v}\right)X_-\left(t_2+\frac{x_2-x_3}{v}\right)X_q(t_2)\right\},\\
=& \frac{-ig^2\sqrt{2}}{v^2}\int dt\, X_q(t)c^*_-(t)c_+(t)\kappa_c(t)\int_{-z/2}^{z/2} dx_2 dx_3\,\theta(x_2-x_3)e^{-2\sigma^2\left[\frac{(x_3-x_0)^2}{v^2}+\frac{(2x_2-x_3-x_0)^2}{v^2}-4\frac{(x_2-x_0)}{v}t\right]}\\
&\times e^{-\kappa_a(x_2-x_3)/2v}\left\{X_+(t)e^{-2i\omega_c(x_2-x_3)/v} - X_-(t)e^{2i\omega_c(x_2-x_3)/v}\right\},
\end{aligned} \tag{78}$$

The two integrals in position can easily be evaluated, but the exact form is lengthy and does not yield much insight, so we will not report it here. However, due to the fast-oscillating integrand, we see that

$$S^{(2)}_{\text{eff},L} \propto \frac{g}{2\omega_c}, \tag{79}$$

and, consequently, we can safely neglect backscattering for small couplings, $g \ll \omega_c$. This is easily understood if we consider that a backscattering event creates a momentum shift in the photon of $2\omega_c/v$, something that must be compensated by the interaction, g.

3.6 Effective emitter-probe master equation

To summarize, we can write an effective master equation for the emitter-resonator system in a Linblad-like form,

$$\begin{aligned}
\dot{\rho} =& \kappa_a\mathcal{D}[\hat{a}]\rho + \kappa_c(t)\mathcal{D}[\hat{c}]\rho - i\left[g\eta_{\text{det}}(t)(\hat{a}+\hat{a}^\dagger), \frac{\hat{c}\rho\hat{c}^\dagger}{\langle\hat{c}^\dagger\hat{c}\rangle}\right] + \Gamma(t)\mathcal{D}[\hat{a}+\hat{a}^\dagger]\frac{\hat{c}\rho\hat{c}^\dagger}{\langle\hat{c}^\dagger\hat{c}\rangle}\\
&+\mathcal{O}\left(\frac{g^3}{\sigma^3}\right)+\mathcal{O}\left(\frac{g}{2\omega_c}\right).
\end{aligned} \tag{80}$$

Note that small parameter in the expansion is g/σ only in the limit $\kappa_a \to 0$. Otherwise, the small parameter in the expansion is a non-trivial combination of g, κ_a and σ.

In writing Eq. (80), we have used that, by construction, $\kappa_c(t)\langle\hat{c}^\dagger\hat{c}\rangle(t) = |\xi(t-t_0)|^2$, so that using Eq. (53) we have $\langle\hat{c}^\dagger\hat{c}\rangle(t) = \frac{1}{2}\operatorname{erfc}(\tilde{t})$. We recognize the state $\hat{c}\rho\hat{c}^\dagger/\langle\hat{c}^\dagger\hat{c}\rangle$ as the normalized state of the system, conditioned on the photon having left the emitter. We, moreover, have the following more intuitive forms for the coefficients η_{det} and $\Gamma(t)$:

$$\eta_{\text{det}}(t) = \frac{1}{v}\int_{-z/2}^{z/2} dx \left|\xi\left(t - \frac{x}{v}\right)\right|^2, \tag{81}$$

$$\Gamma(t) = \frac{4g^2}{\kappa_a v}\int_{-z/2}^{z/2} dx \left[1 - e^{-\frac{\kappa_a}{2v}(x+z/2)}\right]\left|\xi\left(t - \frac{x}{v}\right)\right|^2. \tag{82}$$

In the limit $\kappa_a \to 0$ the coefficient $\Gamma(t)$ reduces to

$$\begin{aligned}\lim_{\kappa_a\to 0}\Gamma(t) &= \frac{2g^2}{v}\int_{-z/2}^{z/2}\frac{dx}{v}\,(x+z/2)\left|\xi\left(t-\frac{x}{v}\right)\right|^2, \\ &= \frac{g^2}{\sqrt{2\pi}\sigma}\left\{e^{-\tilde{t}_+^2} - e^{-\tilde{t}_-^2} + \pi\tilde{t}_+\left[\operatorname{erf}(\tilde{t}_+) - \operatorname{erf}(\tilde{t}_-)\right]\right\}.\end{aligned} \tag{83}$$

4 Matrix Product State simulations

To validate the performance of the detector in numerical simulations, we represent the state of the metamaterial as a Matrix Product State (MPS) [11]. Recall that the interacting system is described by a Hamiltonian

$$\hat{H} = \hat{H}_r + \hat{H}_0 + \hat{H}_{\text{int}}, \tag{84}$$

where we are now working in the displaced and rotating frame for the probe resonator, defined in the main text, such that

$$\hat{H}_r = \frac{\hbar K}{2}\left(\hat{a}^\dagger\right)^2\hat{a}^2, \tag{85}$$

$$\hat{H}_0 = \sum_\nu \int_\Omega d\omega \hbar\omega \hat{b}^\dagger_{\nu\omega}\hat{b}_{\nu\omega}, \tag{86}$$

and

$$\begin{aligned}\hat{H}_{\text{int}} = \hbar\sum_{\nu\mu}\int_{-z/2}^{z/2} dx \chi(x)\hat{b}^\dagger_\nu(x)\hat{b}_\mu(x)\left(\hat{a}^\dagger\hat{a} + \alpha^2\right) \\ + \hbar\sum_{\nu\mu}\int_{-z/2}^{z/2} dx g(x)\hat{b}^\dagger_\nu(x)\hat{b}_\mu(x)\left(\hat{a}^\dagger + \hat{a}\right)\end{aligned} \tag{87}$$

where

$$\hat{b}_\nu(x) = \sqrt{\frac{\bar{\omega}}{2\pi v}}\int_\Omega \frac{d\omega}{\sqrt{\omega}}\hat{b}_{\nu\omega}e^{\nu i\omega x/v}. \tag{88}$$

In the following we present an approach based on discretizing both space and time, to efficiently represent the state of the system as an MPS. A main additional simplification that is made in this section is that we only treat the right-moving field $\nu = +$ for the waveguide. This simplification is justified based on the Keldysh analysis which shows that backscattering is suppressed by $g/\bar{\omega}$.

Returning to Eq. (87), we note that the interaction becomes in a rotating frame defined with respect to $\hat{H}_0$

$$\hat{H}_{\text{int}}(t) = \hbar\int_0^z dx \hat{b}^\dagger_+(x-vt)\hat{b}_+(x-vt)\left[\chi(x)\left(\hat{a}^\dagger\hat{a} + \alpha^2\right) + g(x)\left(\hat{a}^\dagger + \hat{a}\right)\right], \tag{89}$$

where we now only treat the right-moving $\mu = +$ field and we shift the x-axis by $z/2$ in this section for later notational convenience. Following [12, 13], we trotterize the time-evolution

$$U(T) = \mathcal{T}e^{-\frac{i}{\hbar}\int_0^T dt\hat{H}(t)} = \lim_{N_t\to\infty}\hat{U}_{N_t-1}\ldots\hat{U}_1\hat{U}_0, \tag{90}$$

where

$$\hat{U}_i = e^{-\frac{i}{\hbar}\int_{t_i}^{t_i+\Delta t} dt \hat{H}(t)}, \tag{91}$$

for $i = 0, \ldots, N_t - 1$, $\Delta t = T/N_t$ and $t_i = i\Delta t$. We can, moreover, do a similar discretization of the spatial integral for each $\hat{U}_i$

$$\hat{U}_i = \lim_{N_x \to \infty} \hat{U}_{i,N_x-1} \ldots \hat{U}_{i,1}\hat{U}_{i,0}, \tag{92}$$

where

$$\hat{U}_{i,n} = e^{-\frac{i}{\hbar}\int_{t_i}^{t_i+\Delta t} dt \int_{x_n}^{x_n+\Delta x} dx \hat{\mathcal{H}}_{\text{int}}(x,t) - \frac{i}{\hbar}\Delta t \hat{H}_r/N_x}, \tag{93}$$

where $n = 0, \ldots N_x - 1$, we choose $\Delta x = z/N_x = v\Delta t$, and $x_n = n\Delta x$ and the Hamiltonian density $\hat{\mathcal{H}}_{\text{int}}(x,t)$ is

$$\hat{\mathcal{H}}_{\text{int}}(x,t) = \hat{b}_+^\dagger(x - vt)\hat{b}_+(x - vt)\hat{A}(x), \tag{94}$$

where we have defined $\hat{A}(x) = \chi(x)\left(\hat{a}^\dagger\hat{a} + \alpha^2\right) + g(x)\left(\hat{a}^\dagger + \hat{a}\right)$ for notational convenience. For sufficiently small Δt and Δx, we now make the approximations

$$\begin{aligned} &\int_{t_i}^{t_i+\Delta t} dt \int_{x_n}^{x_n+\Delta x} dx \hat{b}_+^\dagger(x - vt)\hat{b}_+(x - vt)\hat{A}(x) \\ &\simeq \int_{t_i}^{t_i+\Delta t} dt \hat{b}_+^\dagger(x_n - vt) \int_{x_n}^{x_n+\Delta x} dx \hat{b}_+(x - vt_i)\hat{A}(x_n) \\ &= -\Delta t \hat{b}_{n-i}\hat{b}_{n-i}\hat{A}(x_n). \end{aligned} \tag{95}$$

where in the last line we have defined

$$\hat{b}_n = \frac{1}{\sqrt{\Delta x}} \int_{x_n}^{x_n+\Delta x} dx \hat{b}_+(x). \tag{96}$$

When the incoming photon has a narrow width concentrated around $\omega = \bar{\omega}$ we can approximate

$$\hat{b}_+(x) = \sqrt{\frac{1}{2\pi v}} \int_{-\infty}^{\infty} d\omega \hat{b}_{\nu\omega} e^{i\omega x/v}, \tag{97}$$

such that $[\hat{b}_+(x), \hat{b}_+(y)^\dagger] = \delta(x - y)$, and consequently $[\hat{b}_n, \hat{b}_m^\dagger] = \delta_{mn}$.

The interaction Eq. (95) suggests the following picture, illustrated in Fig. S10: At time $t = 0$, the probe resonator (denoted $\hat{a}$ in the figure) interacts with a subset of oscillators $\hat{b}_n$ with $n = 0, \ldots, N_x - 1$, for a short time Δt. In the next time step, the interaction is instead with oscillators labeled $n = -1, \ldots, N_x - 2$, which we can think of as resulting from shifting all the waveguide oscillators one unit cell to the right. The waveguide thus appears as a "conveyor belt" of oscillators moving past the probe, where for each time step the probe interacts with the subset $-i, \ldots, N_x - 1 - i$. We now furthermore have a natural representation of the system as an MPS. Each oscillator b_n represents a site in the MPS, and the probe resonator is a special site which needs to be swapped along the MPS interacting with sites $n = -i, \ldots, N_x - 1 - i$ for each time step i. To simulate an incoming photon we also include an emitter at a site $l = l_0 - i - 1$ with $l_0 \leq 0$ (*i.e.*, the emitter is to the left of the detector), interacting with site $l_0 - i$ through an interaction

$$\hat{U}_{\text{emitter}} = e^{\sqrt{\Delta t}\sqrt{\kappa_c(t_i)}(\hat{c}\hat{b}_{l_0-i}^\dagger - \text{H.c.})}, \tag{98}$$

where $\hat{c}$ is the annihilation operator for the emitter, initialized in Fock state $|1\rangle$, and $\kappa_c(t)$ the decay rate determining the shape of the incoming photon (see Refs. [12, 13] for a derivation). Note that the emitter is swapped one site to the left in the MPS for each time step.

To model a non-zero measurement rate $\kappa_a > 0$, we must include the interaction to a bath in the resonator Hamiltonian $\hat{H}_r$. The total time-evolution for the resonator for a small time step Δt can be written

$$\hat{U}_{i,n} \simeq \hat{U}_{i,n}^{\text{int}}(\Delta t/2)\hat{U}_r(\Delta t)\hat{U}_{i,n}^{\text{int}}(\Delta t/2), \tag{99}$$

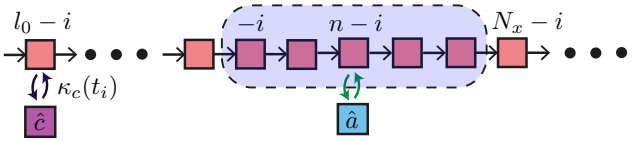

Figure S10: At the ith time step, the probe resonator ($\hat{a}$) interacts with oscillators labelled $-i, \ldots N_x - 1 - i$, as indicated by the dashed box. The interaction with the oscillator labeled $n - i$, for $n = 0, \ldots N_x - 1$ is described by the interaction operator $\hat{A}(x_n)$. In the next time step, all the waveguide oscillators are shifted one cell to the right, such that the interaction is with $-(i+1), \ldots, N_x - 1 - (i+1)$. To perform one time step we swap the MPS site corresponding to S along the chain letting it interact with the sites $-i, \ldots, N_x - 1$ one by one. A single photon is released by an emitter ($\hat{c}$) interacting with site $l_0 - i$ in the i time step.

where $\hat{U}_{i,n}^{\rm int}(\Delta t) = e^{-i\int_{t_i}^{t_i+\Delta t} dt \int_{x_n}^{x_n+\Delta x} dx \hat{\mathcal{H}}_{\rm int}(x,t)}$ and $\hat{U}_r(\Delta t) = e^{-i\Delta t \hat{H}_r}$. To model a homodyne measurement of the resonator's outputfield without explicitly including the bath degrees of freedom, we replace the unitary evolution $\hat{U}_r(\Delta t)$ by a stochastic Schrödinger equation integrated from t_i to $t_i + \Delta t$

$$d|\psi_{\rm MPS}\rangle = D_1|\psi_{\rm MPS}\rangle\, dt + D_2|\psi_{\rm MPS}\rangle\, dW(t), \tag{100}$$

where $dW(t)$ is a real Wiener increment and (see Chapter 7 of [14])

$$D_1|\psi\rangle = -\frac{i}{\hbar}\hat{H}_r|\psi\rangle + \frac{\kappa_a}{2}\left(\langle \hat{a}_\theta + \hat{a}_\theta^\dagger\rangle \hat{a}_\theta - \hat{a}_\theta^\dagger \hat{a}_\theta - \frac{1}{4}\langle \hat{a}_\theta + \hat{a}_\theta^\dagger\rangle^2\right)|\psi\rangle, \tag{101}$$

$$D_2|\psi\rangle = \sqrt{\kappa_a}\left(\hat{a}_\theta - \frac{1}{2}\langle \hat{a}_\theta + \hat{a}_\theta^\dagger\rangle\right)|\psi\rangle, \tag{102}$$

with $\hat{a}_\theta = e^{-i\theta}\hat{a}$ and $\langle \hat{A}\rangle = \langle\psi|\hat{A}|\psi\rangle$. Homodyne measurement of the $\hat{y}$-quadrature corresponds to $\theta = \pi/2$. A variety of numerical methods can be used to integrate the stochastic differential equation Eq. (100) from time t to $t + \Delta t$. We experimented with the order 0.5 Euler scheme and the order 1.0 Platen scheme given in [14], as well as an implicit order 1.5 Taylor method found in [15] [Chapter 12.2, Eq. (2.18), $\alpha = 0.5$]. We found the implicit scheme to be most stable and the results presented in the main paper were generated with this method. The homodyne current is given by $J_{\rm hom}(t) = \sqrt{\kappa_a}\langle \hat{a}_\theta + \hat{a}_\theta^\dagger\rangle + \xi(t)$ where $\xi(t) = dW(t)/dt$. This current is then integrated over a measurement window $0 < t < \tau_m$ with a filter function, as explained in the main text.

References

[1] U. Vool, M. Devoret, *International Journal of Circuit Theory and Applications* **45**, 897 (2017).

[2] S. E. Nigg, *et al.*, *Phys. Rev. Lett* **108**, 240502 (2012).

[3] N. A. R. Bhat, J. E. Sipe, *Phys. Rev. A* **73**, 063808 (2006).

[4] J. Koch, *et al.*, *Phys. Rev. A* **76**, 042319 (2007).

[5] C. Macklin, *et al.*, *Science* **350**, 307 (2015).

[6] Z. K. Minev, Catching and reversing a quantum jump mid-flight, Ph.D. thesis, Yale University (2019).

[7] N. Didier, J. Bourassa, A. Blais, *Phys. Rev. Lett.* **115**, 203601 (2015).

[8] P. Z. C.W. Gardiner, *Quantum Noise: A Handbook of Markovian and Non-Markovian Quantum Stochastic Methods with Applications to Quantum Optics*, Springer Series in Synergetics (Springer, 2000), second edn.

[9] J. E. Gough, M. R. James, H. I. Nurdin, J. Combes, *Phys. Rev. A* **86**, 043819 (2012).

[10] L. M. Sieberer, M. Buchhold, S. Diehl, *Reports on Progress in Physics* **79**, 096001 (2016).

[11] U. Schollwöck, *Ann. Phys.* **326**, 96 (2011).

[12] A. L. Grimsmo, *Phys. Rev. Lett.* **115**, 060402 (2015).

[13] H. Pichler, P. Zoller, *Phys. Rev. Lett.* **116**, 093601 (2016).

[14] H.-P. Breuer, F. Petruccione, *The theory of open quantum systems* (Oxford University Press on Demand, 2002).

[15] P. E. Kloeden, E. Platen, *Numerical Solution of Stochastic Differential Equations* (Springer-Verlag Berlin Heidelberg, 1992).

B.3 Mesure de parité

Science Advances
AAAS

advances.sciencemag.org/cgi/content/full/4/11/eaau1695/DC1

Supplementary Materials for

Qubit parity measurement by parametric driving in circuit QED

Baptiste Royer*, Shruti Puri, Alexandre Blais

*Corresponding author. Email: baptiste.royer@usherbrooke.ca

Published 30 November 2018, *Sci. Adv.* **4**, eaau1695 (2018)
DOI: 10.1126/sciadv.aau1695

This PDF file includes:

I. PARAMETRICALLY DRIVEN NONLINEAR RESONATOR

We give a summary of the different steady-states of a Kerr nonlinear resonator under two-photon driving as a function of the system parameters. The Hamiltonian of the parametrically driven nonlinear resonator is

$$\hat{H}_{R,\delta} = \delta \hat{a}^\dagger \hat{a} + \frac{\mathcal{E}_p}{2}(\hat{a}\hat{a} + \hat{a}^\dagger \hat{a}^\dagger) - \frac{K}{2}\hat{a}^\dagger \hat{a}^\dagger \hat{a}\hat{a}, \tag{S1}$$

where $\delta = \omega_r - \omega_p/2$ is the resonator-pump detuning, $\mathcal{E}_p$ is the two-photon pump amplitude and K is the resonator nonlinearity. Single photon damping at a rate κ is also taken into account. Figure S1 illustrates the different resonator steady-states, which are separated in three regions of the parameter space [20]. First, when the two-photon drive is below the parametric oscillation threshold, $|\mathcal{E}_p| < \sqrt{\delta^2 + (\kappa/2)^2}$, the resonator has a steady-state centered at the origin. When the resonator nonlinearity K can be neglected, this steady-state is characterized by the average values [43]

$$\begin{aligned} \langle \hat{a}^\dagger \hat{a} \rangle &= \frac{\mathcal{E}_p^2}{2(\delta^2 + \kappa^2/4 - \mathcal{E}_p^2)} \\ \langle \hat{a}\hat{a} \rangle &= \frac{-\mathcal{E}_p(\delta + i\kappa/2)}{2(\delta^2 + \kappa^2/4 - \mathcal{E}_p^2)} \end{aligned} \tag{S2}$$

Here, we are only interested in configurations far from the parametric oscillation threshold where the above average values are very small. Consequently, the effect of the nonlinearity in this regime is negligible. The effect of the nonlinearity on the resonator field in the regime close to the parametric oscillation threshold

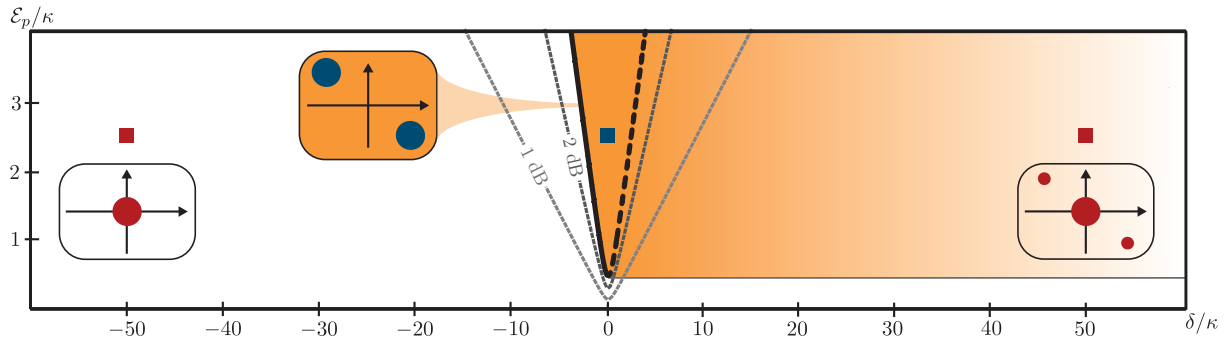

Fig. S1. Schematic representation of the steady-state of a parametrically driven nonlinear resonator in parameter space. In the white region, the resonator has a single steady-state centered at the origin. In the middle light orange region, the system has two high-amplitude steady-states. In the shaded region there are three steady-state: two high amplitude states and one state centered at the origin. The blue square indicates the configuration corresponding to parity measurement in the odd subspace, $\mathcal{E}_p/\kappa = 2.5, \delta = 0$. On the other hand, the red squares indicate the configurations in the even subspace, $\mathcal{E}_p = 2.5, \delta/\kappa = 50, \chi < 0$. The dashed gray lines correspond to 1 and 2 dB of squeezing and illustrate that for the dispersive shifts $2|\chi|/\kappa = 50$ that are considered, the level of squeezing is minimal.

was investigated in Ref. [19]. In the white region of Fig. S1, the steady-state described by Eq. (S2) is unique. On the other hand, when the two-photon drive is above the parametric oscillation threshold $|\mathcal{E}_p| \geq \sqrt{\delta^2 + (\kappa/2)^2}$, the vacuum state becomes unstable and two new steady-states appear with average photon number

$$\langle \hat{a}^\dagger \hat{a} \rangle = \frac{\delta + \sqrt{\mathcal{E}_p^2 - (\kappa/2)^2}}{K} \tag{S3}$$

In the resonant case $\delta = 0$, this expression corresponds to Eq. (2) of the main text. This bistable region is illustrated in orange and enclosed in the parabolic full and dashed black lines in Fig. S1. Finally, when $\mathcal{E}_p > \kappa/2$ (full gray horizontal line) and $\delta > \sqrt{\mathcal{E}_p^2 - (\kappa/2)^2}$ (black dashed parabolic line), both the low-amplitude steady-state described by Eq. (S2) and the two high-amplitude states described by Eq. (S3) coexist [20]. This tristable region is shaded in light orange in Fig. S1.

As discussed in the main text, in the dispersive regime with two transmon qubits, the resonator frequency is shifted by $\pm 2\chi$ if the qubits are in the even parity subspace $\{|00\rangle, |11\rangle\}$ and remains unshifted in the odd subspace $\{|10\rangle, |01\rangle\}$. This parity-dependent frequency shift leads to an effective detuning δ with the two-photon drive that is illustrated by the blue (odd parity) and red (even parity) squares in Fig. S1. This observation is the basis for the parity measurement: even qubit parity corresponds to a low-amplitude state of the nonlinear resonator while odd qubit parity to a large amplitude state. Because the state $|00\rangle$ state places the nonlinear resonator in the tri-stability region (right red square), the resonator state can in principle tunnel from the low-amplitude state to a high-amplitude state, something that reduces the measurement fidelity and increases eigenspace dephasing in the even subspace. In practice, however, these tunneling events are highly suppressed for large dispersive shifts that we are considering, $|2\chi| \gg \mathcal{E}_p$, and can be safely neglected. Finally, we note that the overall situation described here remains unchanged in the four-qubit case and the same intuition therefore applies.

II. DEPHASING RATES

In this section, we derive explicitly the qubit dephasing rates induced by the parity measurements for the different cases studied in the main text.

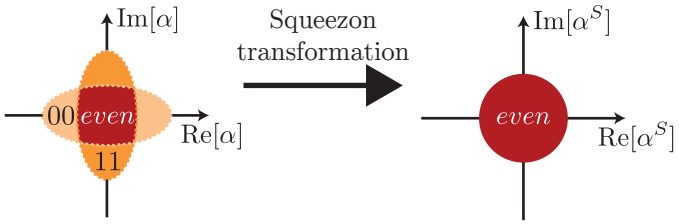

Fig. S2. Illustration of the resonator phase space when the qubits are in the even subspace. A "squeezon" transformation allows to compute the solution to the master equation in a frame where the dynamics are easier to solve.

A. Two Qubits

The master equation for two qubits dispersively coupled to a parametrically drive nonlinear resonator is given by ($\hbar = 1$)

$$\dot{\varrho} = -i\left[\chi(\hat{\sigma}_{z1}+\hat{\sigma}_{z2})\hat{a}^\dagger\hat{a} + \frac{\mathcal{E}_p}{2}(\hat{a}\hat{a}+\hat{a}^\dagger\hat{a}^\dagger) - \frac{K}{2}\hat{a}^\dagger\hat{a}^\dagger\hat{a}\hat{a}, \varrho\right] + \kappa\mathcal{D}[\hat{a}]\varrho \tag{S4}$$

where ϱ is the combined qubits-resonator density matrix. When the qubits are in the odd subspace spanned by $\{|01\rangle, |10\rangle\}$, the above master equation reduces to

$$\dot{\varrho}_\mathrm{o} = -i\left[\frac{\mathcal{E}_p}{2}(\hat{a}\hat{a}+\hat{a}^\dagger\hat{a}^\dagger) - \frac{K}{2}\hat{a}^\dagger\hat{a}^\dagger\hat{a}\hat{a}, \varrho_\mathrm{o}\right] + \kappa\mathcal{D}[\hat{a}]\varrho_\mathrm{o} \tag{S5}$$

where $\varrho_{\mathrm{o(e)}}$ is the qubit-resonator density matrix projected in the odd (even) qubit subspace. Since the above equation does not depend on the qubits state within the odd subspace, it is clear that the odd qubit states remain unperturbed by the measurement. In other words, there is no measurement-induced dephasing within the odd subspace.

The situation is more complicated in the even subspace spanned by $\{|00\rangle, |11\rangle\}$. In a frame rotating at ω_r, the system in this subspace is described by the Hamiltonian

$$\hat{H}_{2qb,\mathrm{e}} = 2\chi\hat{\tau}_z\hat{a}^\dagger\hat{a} + \frac{\mathcal{E}_p}{2}(\hat{a}\hat{a}+\hat{a}^\dagger\hat{a}^\dagger) - \frac{K}{2}\hat{a}^\dagger\hat{a}^\dagger\hat{a}\hat{a} \tag{S6}$$

where we have defined $\hat{\tau}_z \equiv |11\rangle\langle 11| - |00\rangle\langle 00|$. Taking into account single photon loss at a rate κ, the combined qubits-resonator density matrix ϱ_e evolves according to the master equation

$$\dot{\varrho}_\mathrm{e} = -i[\hat{H}_{2qb,\mathrm{e}}, \varrho_\mathrm{e}] + \kappa\mathcal{D}[\hat{a}]\varrho_\mathrm{e} \tag{S7}$$

Following the general approach of Ref. [44, 45], to find an expression for the measurement-induced dephasing rate in the even subspace we derive a reduced master equation for the qubit by first moving to a frame where the drive is absent. For a linear cavity and drive, this is realized with a polaron transformation, a qubit-state dependent displacement of the cavity field. In the presence of a two-photon drive, we rather introduce a "squeezon" transformation corresponding to a qubit-state dependent squeezing operation on the resonator field. As schematically illustrated in Fig. S1, this transformation is chosen such as to lead to the same resonator state irrespective of the qubit state inside in the even subspace. In this new frame the dynamics is simplified and the measurement-induced dephasing rate easier to evaluate. This unitary transformation

$$\hat{S} = |00\rangle\langle 00| \otimes \mathrm{e}^{-\frac{r}{2}\hat{a}\hat{a}+\frac{r}{2}\hat{a}^\dagger\hat{a}^\dagger} + |11\rangle\langle 11| \otimes \mathrm{e}^{\frac{r}{2}\hat{a}\hat{a}-\frac{r}{2}\hat{a}^\dagger\hat{a}^\dagger} \tag{S8}$$

is chosen such that $\hat{a}^S \equiv \hat{S}^\dagger\hat{a}\hat{S} = \cosh r\hat{a} - \hat{\tau}_z \sinh r\hat{a}^\dagger$, with r the squeezing parameter. For the two-qubit parity measurement, we assume the dispersive shift to be much bigger than the two-photon drive, $2\chi \gg \mathcal{E}_p$, which means that the degree of squeezing is very small. Consequently, the photon population induced by the parametric drive is also very small and the nonlinearity K of the resonator can be safely neglected. In the squeezon frame, the master equation governing the evolution of the density matrix $\varrho_\mathrm{e}^S \equiv \hat{S}^\dagger\varrho_\mathrm{e}\hat{S}$ is given by

$$\dot{\varrho}_\mathrm{e}^S = -i[\hat{H}_{2qb,\mathrm{e}}^S, \varrho_\mathrm{e}^S] + \kappa\mathcal{D}[\hat{a}^S]\varrho_\mathrm{e}^S \tag{S9}$$

with the Hamiltonian

$$\begin{aligned}\hat{H}^S_{2qb,\mathrm{e}} &\equiv \hat{S}^\dagger \hat{H}_{2qb,\mathrm{e}} \hat{S} \\ &\approx (2\chi\cosh 2r - \mathcal{E}_p \sinh 2r)\hat{\tau}_z \hat{a}^\dagger \hat{a} + \left(\frac{\mathcal{E}_p}{2}\cosh 2r - \chi \sinh 2r\right)(\hat{a}\hat{a} + \hat{a}^\dagger \hat{a}^\dagger) \\ &\quad + \left(2\chi \sinh^2 r - \frac{\mathcal{E}_p}{2}\sinh 2r\right)\hat{\tau}_z \\ &= 2\tilde{\chi}\hat{\tau}_z \hat{a}^\dagger \hat{a} + B\hat{\tau}_z\end{aligned} \tag{S10}$$

where we have defined $2\tilde{\chi} \equiv 2\chi\cosh 2r - \mathcal{E}_p \sinh 2r$, $B \equiv 2\chi \sinh^2 r - \mathcal{E}_p/2 \sinh 2r$ to simplify the notation and set $\tanh 2r = \mathcal{E}_p/2\chi$ in order to cancel the two-photon drive. Moreover, in this frame, single-photon loss leads to the dissipators

$$\begin{aligned}\mathcal{D}[\hat{a}^S]\varrho^S_{\mathrm{e}} &= \mathcal{D}[\hat{a}\cosh r - \hat{\tau}_z \hat{a}^\dagger \sinh r]\varrho^S_{\mathrm{e}} \\ &\approx (1 + n_{th})\mathcal{D}[\hat{a}]\varrho^S_{\mathrm{e}} + n_{th}\mathcal{D}[\hat{\tau}_z \hat{a}^\dagger]\varrho^S_{\mathrm{e}}\end{aligned} \tag{S11}$$

where we have defined the effective thermal photon number in the squeezon frame $n_{th} \equiv \sinh^2 r \approx (\mathcal{E}_p/4\chi)^2$ and neglected fast oscillating terms.

The reduced master equation for the qubit density matrix ρ_{e} is obtained by moving back to the lab frame and by tracing over the resonator

$$\rho_{\mathrm{e}} = \mathrm{Tr}_r[\hat{S}\varrho^S_{\mathrm{e}}\hat{S}^\dagger] \tag{S12}$$

Following [44], we express the combined qubits-resonator density matrix using the positive P representation [43]

$$\varrho^S_{\mathrm{e}} = \sum_{ij=00,11} \int d^2\alpha \int d^2\beta\, P_{i,j}(\alpha,\beta) \frac{|\alpha\rangle\langle\beta^*|}{\langle\beta^*|\alpha\rangle} \otimes |i\rangle\langle j| \tag{S13}$$

Back in the lab frame, the reduced qubit density matrix is then given by

$$\rho_{\mathrm{e}} = \sum_{i=00,11} \int d^2\alpha \int d^2\beta\, P_{i,i}(\alpha,\beta)|i\rangle\langle i| + \int d^2\alpha \int d^2\beta\, [\lambda(\alpha,\beta)|11\rangle\langle 00| + \lambda^*(\alpha,\beta)|00\rangle\langle 11|] \tag{S14}$$

where we have defined

$$\lambda(\alpha,\beta) \equiv P_{11,00}(\alpha,\beta)\frac{\langle\beta^*|\mathrm{e}^{r\hat{a}\hat{a} - r\hat{a}^\dagger\hat{a}^\dagger}|\alpha\rangle}{\langle\beta^*|\alpha\rangle} \tag{S15}$$

Differential equation for the $P_{i,j}(\alpha,\beta)$ are obtained by using the correspondence rules [43]

$$\begin{aligned}\hat{a}\varrho &\leftrightarrow \alpha P \\ \hat{a}^\dagger\varrho &\leftrightarrow (\beta - \partial_\alpha)P \\ \varrho\hat{a}^\dagger &\leftrightarrow \beta P \\ \varrho\hat{a} &\leftrightarrow (\alpha - \partial_\beta)P\end{aligned} \tag{S16}$$

taking the usual assumption that the P function vanishes at infinity. The equations for the qubits diagonal elements $\dot{\rho}_{00,00} = \dot{\rho}_{11,11} = 0$ are easily solved in steady-state using a thermal state *ansatz* with average photon number n_{th}. On the other hand, the equation for the off-diagonal element $P_{11,00}$ reads

$$\begin{aligned}\dot{P}_{11,00} = \Big\{&-2i\tilde{\chi}(2\alpha\beta - \partial_\alpha\alpha - \partial_\beta\beta) - 2iB + \frac{\kappa}{2}(\partial_\alpha\alpha + \partial_\beta\beta) \\ &-\kappa n_{th}\left[2\alpha\beta - 2(\partial_\alpha\alpha + \partial_\beta\beta) + 2 + \partial_\alpha\partial_\beta\right]\Big\} P_{11,00}\end{aligned} \tag{S17}$$

where we have defined $\partial_\gamma \equiv \partial/\partial\gamma$ ($\gamma = \alpha, \beta$). To solve the above equation, we use the transformation [46]

$$P(\alpha,\beta) \equiv \int d^2a \int d^2b\, \bar{P}(a,b)\mathrm{e}^{i(a\alpha + b\beta)} \tag{S18}$$

for which, using integration by part, we find the identities

$$\begin{aligned}\alpha P(\alpha,\beta) &\to i\partial_a \bar{P}(a,b)\\ \partial_\alpha P(\alpha,\beta) &\to ia\bar{P}(a,b)\\ \partial_\alpha \alpha P(\alpha,\beta) &\to -a\partial_a \bar{P}(a,b)\end{aligned} \tag{S19}$$

leading to the differential equation

$$\begin{aligned}\dot{\bar{P}}_{11,00} = \Big\{&-2i\tilde{\chi}(-2\partial_a\partial_b + a\partial_a + b\partial_b) - 2iB - \frac{\kappa}{2}(a\partial_a + b\partial_b)\\ &+2\kappa n_{th}\left[\partial_a\partial_b - (a\partial_a + b\partial_b) - 1 + ab/2\right]\Big\}\bar{P}_{11,00}\end{aligned} \tag{S20}$$

Since the equation for $\bar{P}$ is quadratic, it can be solved with a Gaussian function and we take the *ansatz*

$$\bar{P}_{11,00}(a,b) = \mathrm{e}^{\mu}\mathrm{e}^{ia\bar{\alpha}+ib\bar{\beta}-\frac{a^2X+b^2Y}{2}-abZ} \tag{S21}$$

where the variables $\bar{\alpha},\bar{\beta},X,Y,Z$ define the resonator field and μ is a prefactor that set the phase and amplitude of the qubit density matrix off-diagonal elements ρ_{e}. Replacing this ansatz in Eq. (S20) leads to

$$\begin{aligned}\dot{\mu} &= -4i\tilde{\chi}(Z+\bar{\alpha}\bar{\beta}) - 2iB - 2\kappa n_{th}(Z+\bar{\alpha}\bar{\beta}+1)\\ i\dot{\bar{\alpha}} &= 2\tilde{\chi}[2(\bar{\alpha}Z+\bar{\beta}X)+\bar{\alpha}] - i\kappa\bar{\alpha}/2 - 2i\kappa n_{th}[\bar{\alpha}Z+\bar{\beta}X+\bar{\alpha}]\\ i\dot{\bar{\beta}} &= 2\tilde{\chi}[2(\bar{\beta}Z+\bar{\alpha}Y)+\bar{\beta}] - i\kappa\bar{\beta}/2 - 2i\kappa n_{th}[\bar{\beta}Z+\bar{\alpha}Y+\bar{\beta}]\\ -\dot{X}/2 &= 2i\tilde{\chi}(2XZ+X) + \kappa X/2 + 2\kappa n_{th}(XZ+X)\\ -\dot{Y}/2 &= 2i\tilde{\chi}(2YZ+Y) + \kappa Y/2 + 2\kappa n_{th}(YZ+Y)\\ -\dot{Z} &= 4i\tilde{\chi}(XY+Z^2+Z) + \kappa Z + 2\kappa n_{th}(XY+Z^2+2Z+1/2)\end{aligned} \tag{S22}$$

For simplicity, we derive an equation for μ when the resonator has reached steady-state, *i.e.* we will neglect the resonator transient dynamics and set $\dot{X}=\dot{Y}=\dot{Z}=\dot{\bar{\alpha}}=\dot{\bar{\beta}}=0$. We easily find the steady-state solutions $X=Y=\bar{\alpha}=\bar{\beta}=0$. Discarding the unphysical solution for Z and expanding the physical solution to first order in n_{th} and $\kappa/4\tilde{\chi}$, we find

$$Z \approx -in_{th}\frac{\kappa}{4\tilde{\chi}} \tag{S23}$$

Replacing this into the equation for μ and again keeping terms to first order in $n_{th},\kappa/4\tilde{\chi}$, we find

$$\dot{\mu} = -\kappa n_{th} - 2iB \tag{S24}$$

Using the *ansatz* for $\bar{P}_{11,00}$, we find an equation of motion for the off-diagonal elements of the reduced qubit density matrix

$$\begin{aligned}\dot{\rho}_{11,00} &= \int d^2\alpha \int d^2\beta \frac{\langle\beta^*|\mathrm{e}^{r\hat{a}\hat{a}-r\hat{a}^\dagger\hat{a}^\dagger}|\alpha\rangle}{\langle\beta^*|\alpha\rangle}\int d^2a\int d^2b\,\mathrm{e}^{i(a\alpha+b\beta)}\dot{\bar{P}}_{11,00}(a,b)\\ &= \dot{\mu}\times\int d^2\alpha \int d^2\beta \frac{\langle\beta^*|\mathrm{e}^{r\hat{a}\hat{a}-r\hat{a}^\dagger\hat{a}^\dagger}|\alpha\rangle}{\langle\beta^*|\alpha\rangle}\int d^2a\int d^2b\,\mathrm{e}^{i(a\alpha+b\beta)}\bar{P}_{11,00}(a,b)\\ &= \dot{\mu}\times\rho_{11,00}\end{aligned} \tag{S25}$$

This finally allows us to write an effective master equation for the reduced qubits density matrix which takes the form

$$\dot{\rho} = -i[B\hat{\tau}_z,\rho] + \frac{\gamma_{\mathrm{e}}}{2}\mathcal{D}[\hat{\tau}_z]\rho \tag{S26}$$

with

$$\begin{aligned}\gamma_{\mathrm{e}} \equiv \kappa n_{th} &\approx \kappa\left(\frac{\mathcal{E}_p}{4\chi}\right)^2\\ B &\approx -\frac{\mathcal{E}_p^2}{4\chi}\end{aligned} \tag{S27}$$

In the even subspace, the qubits thus accumulate a deterministic phase $\phi = Bt$ that can be corrected with single qubit Z rotations at the end of the measurement. As discussed in the main text, the qubits also suffer from dephasing at a rate γ_{e}. This rate matches with the one derived in the main text in a more intuitive way.

B. Four Qubits

1. Without Filter

We now consider a situation where four qubits are dispersively coupled to a nonlinear resonator in the presence of a two-tone, two-photon parametric drive. This situation is described by the rotating frame Hamiltonian

$$\hat{H}_{4qb,wf} = \chi \sum_{i=1}^{4} \hat{\sigma}_{zi}\hat{a}^\dagger\hat{a} + \frac{\mathcal{E}_p}{2}(\mathrm{e}^{-i4\chi t} + \mathrm{e}^{i4\chi t})\left[\hat{a}^\dagger\hat{a}^\dagger + \hat{a}\hat{a}\right] - \frac{K}{2}\hat{a}^\dagger\hat{a}^\dagger\hat{a}\hat{a} \tag{S28}$$

and the master equation

$$\dot{\varrho} = -i[\hat{H}_{4qb,wf}, \varrho] + \kappa\mathcal{D}[\hat{a}]\varrho \tag{S29}$$

where ϱ is the combined qubits-resonator density matrix. In contrast to the previous subsection, here we are interested in deriving a rate γ_o for dephasing within the odd qubit subspace, where there is no squeezing and the resonator bifurcates to states that are close to coherent states. To simplify the calculations, we take the qubits state to be within the odd subspace which is a sum of the subspace $\mathcal{H}_-$ spanned by $\{|0001\rangle, |0010\rangle, |0100\rangle, |1000\rangle\}$ with associated projector $\hat{\Pi}_-$ and the subspace $\mathcal{H}_+$ spanned by $\{|0111\rangle, |1011\rangle, |1101\rangle, |1110\rangle\}$ with associated projector $\hat{\Pi}_+$. From Eq. (S28), we see that in a given subspace $\mathcal{H}_\pm$ one parametric drive will be on resonance while the other, far detuned, will have a minimal effect if $\mathcal{E}_p/8\chi \ll 1$. Following the intuition from the two-qubit case, the combined qubit-resonator system will thus evolve to a state close to

$$|\psi_\mathrm{o}\rangle \otimes |0\rangle \to c_+|\psi_+\rangle \otimes |\pm\alpha_\mathrm{o}\mathrm{e}^{-i2\chi t}\rangle + c_-|\psi_-\rangle \otimes |\pm\alpha_\mathrm{o}\mathrm{e}^{i2\chi t}\rangle \tag{S30}$$

where $c_\pm|\psi_\pm\rangle \equiv \hat{\Pi}_\pm|\psi_\mathrm{o}\rangle$ and α_o is given by Eq. (2) of the main text. To compute the dephasing rate γ_o, we first perform a Polaron transformation that unentangles the system and brings the resonator to a vacuum state [45]. Then, we use the simple form of the dynamics in the Polaron frame to trace out the resonator, which allows us to write an effective master equation for the qubits where the dephasing is made explicit. This procedure is therefore similar to the previous section Sect. II A, but uses a qubit-state dependent displacement transformation instead of a qubit-state dependent squeezing transformation. Moreover, similarly to the previous section, we aim to derive a qubit dephasing rate once the resonator has reached the steady-state Eq. (S30) and we do not consider the transient dynamics.
Projecting the initial Hamiltonian Eq. (S28) onto the odd qubit subspace yields

$$\hat{H}_{4qb,wf,\mathrm{o}} = 2\chi\hat{\tau}_z\hat{a}^\dagger\hat{a} + \mathcal{E}_p\cos(4\chi t)\left[\hat{a}^\dagger\hat{a}^\dagger + \hat{a}\hat{a}\right] - \frac{K}{2}\hat{a}^\dagger\hat{a}^\dagger\hat{a}\hat{a} \tag{S31}$$

where $\hat{\tau}_z \equiv \hat{\Pi}_+ - \hat{\Pi}_-$. We perform a Polaron transformation $\hat{P} = \hat{\Pi}_+\hat{D}(\alpha_+) + \hat{\Pi}_-\hat{D}(\alpha_-)$, where $\hat{D}(\alpha) = \exp[\alpha\hat{a}^\dagger - \alpha^*\hat{a}]$ is the displacement operator for the resonator, $\hat{D}^\dagger(\alpha)\hat{a}\hat{D}(\alpha) = \hat{a} + \alpha$. In order to unentangle the qubits and the resonator, we choose $\alpha_\pm = \alpha_\mathrm{o}\mathrm{e}^{\mp i2\chi t}$, leading to the master equation

$$\dot{\varrho}_\mathrm{o}^P = -i[\hat{H}_\mathrm{o}^P, \varrho_\mathrm{o}^P] + \kappa\mathcal{D}[\hat{a}]\varrho_\mathrm{o}^P + \kappa|\delta_\alpha|^2\mathcal{D}[\hat{\tau}_z]\varrho_\mathrm{o}^P + \kappa\delta_\alpha^*\hat{a}[\varrho_\mathrm{o}^P, \hat{\tau}_z] + \kappa\delta_\alpha[\hat{\tau}_z, \varrho_\mathrm{o}^P]\hat{a}^\dagger \tag{S32}$$

with

$$\begin{aligned}\hat{H}_\mathrm{o}^P = {} & 2\chi\hat{a}^\dagger\hat{a}\hat{\tau}_z - \frac{K}{2}\hat{a}^\dagger\hat{a}^\dagger\hat{a}\hat{a} + 2\chi|\alpha_\mathrm{o}|^2\hat{\tau}_z - 2K|\alpha_\mathrm{o}|^2\hat{a}^\dagger\hat{a} \\ & + \hat{\Pi}_+\left\{\frac{\mathcal{E}_p}{2}\alpha_\mathrm{o}\mathrm{e}^{-6i\chi t}\hat{a} + \left(\frac{i\kappa}{4}\frac{\alpha_\mathrm{o}^*}{\alpha_\mathrm{o}}\mathrm{e}^{4i\chi t} + \frac{\mathcal{E}_p}{2}\mathrm{e}^{-4i\chi t}\right)\hat{a}^2 - K\alpha_\mathrm{o}^*\mathrm{e}^{2i\chi t}\hat{a}^\dagger\hat{a}^2\right\} + h.c. \\ & + \hat{\Pi}_-\left\{\frac{\mathcal{E}_p}{2}\alpha_\mathrm{o}\mathrm{e}^{6i\chi t}\hat{a} + \left(\frac{i\kappa}{4}\frac{\alpha_\mathrm{o}^*}{\alpha_\mathrm{o}}\mathrm{e}^{-4i\chi t} + \frac{\mathcal{E}_p}{2}\mathrm{e}^{4i\chi t}\right)\hat{a}^2 - K\alpha_\mathrm{o}^*\mathrm{e}^{-2i\chi t}\hat{a}^\dagger\hat{a}^2\right\} + h.c.\end{aligned} \tag{S33}$$

where we have defined the displacement difference $\delta_\alpha \equiv (\alpha_+ - \alpha_-)/2 = -i\alpha_\mathrm{o}\sin(2\chi t)$, $\varrho_\mathrm{o}^P = \hat{P}^\dagger\varrho_\mathrm{o}\hat{P}$ is the combined resonator-qubits density matrix in the Polaron frame and $\hat{H}_\mathrm{o}^P = \hat{P}^\dagger\hat{H}_{4qb,wf,\mathrm{o}}\hat{P} - i\hat{P}^\dagger\dot{\hat{P}}$ is the Hamiltonian in the Polaron frame. In the master equation Eq. (S32), we see a dephasing term proportional

to κ (third term) appearing because of the phase difference between the displacements $\alpha_\pm$, $\delta_\alpha \neq 0$. In other words, photons leaving the resonator carry information about the qubits state, which in turn induces dephasing. The last two terms of Eq. (S32) have a minimal effect since the resonator state remains close to vacuum in the Polaron frame [45]. In the Hamiltonian Eq. (S33), we see that the displacement of the resonator state induces an additional frequency shift of both the qubits and resonator (last two terms of the first line). Finally, the last two lines of this Hamiltonian consist of off-resonant and small terms that have a small effect on the resonator state [21]. We can thus approximate Eqs. (S32) and (S33) with

$$\dot{\varrho}_{\rm o}^P = -i[2\chi\hat{a}^\dagger\hat{a}\hat{\tau}_z - \frac{K}{2}\hat{a}^\dagger\hat{a}^\dagger\hat{a}\hat{a} + 2\chi|\alpha_{\rm o}|^2\hat{\tau}_z - 2K|\alpha_{\rm o}|^2\hat{a}^\dagger\hat{a}, \varrho_{\rm o}^P] + \kappa\mathcal{D}[\hat{a}]\varrho_{\rm o}^P + \kappa|\delta_\alpha|^2\mathcal{D}[\hat{\tau}_z]\varrho_{\rm o}^P \tag{S34}$$

In the Polaron frame, the evolution of the density matrix $\varrho_{\rm o}^P$ can be calculated easily since the resonator remains in a vacuum state. To obtain a reduced master equation for the qubits density matrix $\rho_{\rm o}$ in the original frame, we trace out the resonator after performing the inverse Polaron transformation

$$\rho_{\rm o} = {\rm Tr}_r[\hat{P}\varrho_{\rm o}^P\hat{P}^\dagger] \tag{S35}$$

Following Ref. [45], we express $\varrho_{\rm o}^P$ in the Polaron frame in the Fock basis

$$\varrho_{\rm o}^P = \sum_{i,j=-,+}\sum_{n,m=0}^{\infty}\varrho_{i,j,n,m}^P|\psi_i,n\rangle\langle\psi_j,m| \tag{S36}$$

and, using Eq. (S35), we write the reduced qubit density matrix as

$$\rho_{\rm o} = \sum_n \varrho_{-,-,n,n}|\psi_-\rangle\langle\psi_-| + \varrho_{+,+,n,n}|\psi_+\rangle\langle\psi_+| + \sum_{n,m}\lambda_{n,m,m,n}|\psi_+\rangle\langle\psi_-| + \lambda^*_{m,n,n,m}|\psi_-\rangle\langle\psi_+| \tag{S37}$$

where

$$\lambda_{n,m,p,q} \equiv \varrho^P_{+,-,n,m}d_{p,q}{\rm e}^{-i{\rm Im}[\alpha_-\alpha_+^*]} \tag{S38}$$

$$d_{p,q} = \langle p|\hat{D}(2\delta_\alpha)|q\rangle \tag{S39}$$

In the absence of qubit relaxation, the diagonal elements of the above expressions are simply

$$\dot{\rho}_{i,i} = \sum_n \varrho^P_{i,i,n,n} = 0 \tag{S40}$$

On the other hand, the derivative of the off-diagonal elements λ are given by

$$\begin{aligned}\dot{\lambda}_{n,m,p,q} = {}& \dot{\varrho}^P_{n,m,+,-}d_{p,q}{\rm e}^{-i{\rm Im}[\alpha_-\alpha_+^*]} - i\partial_t({\rm Im}[\alpha_-\alpha_+])\lambda_{n,m,p,q} \\ & + 2\dot{\delta}_\alpha\sqrt{p}\lambda_{n,m,p-1,q} - 2\dot{\delta}^*_\alpha\sqrt{q}\lambda_{n,m,p,q-1} - \partial_t(\delta_\alpha\delta^*_\alpha)\lambda_{n,m,p,q}\end{aligned} \tag{S41}$$

Since the resonator remains in a vacuum state in the Polaron frame, only the $\lambda_{0,0,0,0}$ element is populated [45], leading to

$$\dot{\rho}_{+,-} = \dot{\lambda}_{0,0,0,0} = \left[-2\kappa\sin^2(2\chi t)|\alpha_{\rm o}|^2 - i4\chi|\alpha_{\rm o}|^2 - i4\chi|\alpha_{\rm o}|^2\cos(4\chi t) - \chi|\alpha_{\rm o}|^2\sin(4\chi t)\right]\lambda_{0,0,0,0}. \tag{S42}$$

Assuming that the total measurement time is much larger than the timescale set by the dispersive shift $\tau_m \gg 2\pi/\chi$, the above equation can be replaced by its average over one period $2\pi/4\chi$, leading to the reduced master equation for the qubits

$$\dot{\rho}_{\rm o} = -i[2\chi|\alpha_{\rm o}|^2\hat{\tau}_z, \rho_{\rm o}] + \kappa|\alpha_{\rm o}|^2\mathcal{D}[\hat{\sigma}_z]\rho_{\rm o}/2 \tag{S43}$$

As discussed in the main text, the qubits suffer from fast dephasing $\gamma_{\rm o} = \kappa|\alpha_{\rm o}|^2$, motivating the need for improvements on this simple set-up.

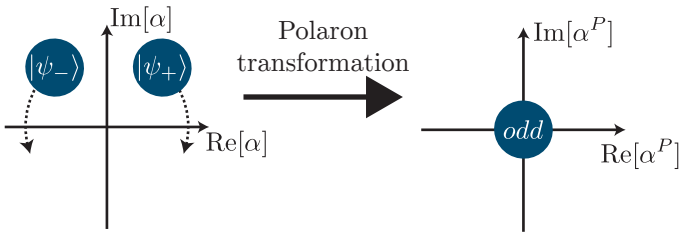

Fig. S3. Illustration of the resonator phase space when the qubits are in the odd subspace. A Polaron transformation allows to compute the solution to the master equation in a frame where the dynamics are easier to solve.

2. *With Filter*

In contrast to the previous section, we now consider that the nonlinear resonator is coupled to a harmonic mode, acting as a filter, through a two-tone modulated coupling element $g^{(2\omega)}(t) = g\cos[(\Delta_f + 2\chi)t] + g\cos[(\Delta_f - 2\chi)t]$. In a frame rotating a ω_r (ω_f) for the nonlinear resonator (filter) and taking the qubits state within the odd subspace, this situation is described by the Hamiltonian

$$\hat{H}_{4qb,\mathrm{o}} = 2\chi\hat{\tau}_z\hat{a}^\dagger\hat{a} + \mathcal{E}_p\cos(4\chi t)\left[\hat{a}^\dagger\hat{a}^\dagger + \hat{a}\hat{a}\right] - \frac{K}{2}\hat{a}^\dagger\hat{a}^\dagger\hat{a}\hat{a} + g\cos(2\chi t)(\hat{a}^\dagger\hat{f} + \hat{a}\hat{f}^\dagger) \tag{S44}$$

and the master equation

$$\dot{\varrho}_\mathrm{o} = -i[\hat{H}_{4qb,\mathrm{o}}, \varrho_\mathrm{o}] + \kappa_f\mathcal{D}[\hat{f}]\varrho_\mathrm{o} + \kappa_{int}\mathcal{D}[\hat{a}]\varrho_\mathrm{o} \tag{S45}$$

where κ_f is the single photon loss rate of the filter mode and κ_{int} is the internal single photon loss rate of the nonlinear resonator. Following the previous section, we start by applying a Polaron transformation on both the nonlinear resonator and the harmonic filter mode $\hat{P} = \hat{\Pi}_+\hat{D}_A(\alpha_+)\hat{D}_f(\beta_+) + \hat{\Pi}_-\hat{D}_A(\alpha_-)\hat{D}_f(\beta_-)$, where

$$\beta_\pm = \frac{-ig\alpha_\mathrm{o}}{\kappa_f}\left(1 + \frac{\mathrm{e}^{\mp i4\chi t}}{1 \mp i8\chi/\kappa_f}\right) \tag{S46}$$

$$\delta_\beta \equiv \frac{\beta_+ - \beta_-}{2} = \frac{g\alpha_\mathrm{o}}{\kappa_f}\left(\frac{-\sin(4\chi t) + 8\chi/\kappa_f\cos(4\chi t)}{1 + (8\chi/\kappa_f)^2}\right) \tag{S47}$$

The equations for $\beta_\pm(t)$ correspond to the assymptotic solutions for $\langle\hat{f}\rangle(t)$ when taking $\langle\hat{a}\rangle = \alpha_\mathrm{o}\mathrm{e}^{\mp i2\chi t}$. In the Polaron frame, the master equation is given by

$$\begin{aligned}\dot{\varrho}^P_\mathrm{o} =& -i[\hat{H}^P_{4qb,\mathrm{o}}, \varrho^P_\mathrm{o}] + \kappa_f\mathcal{D}[\hat{f}]\varrho^P_\mathrm{o} + \kappa_{int}\mathcal{D}[\hat{a}]\varrho^P_\mathrm{o} + (\kappa_f|\delta_\beta|^2 + \kappa_{int}|\delta_\alpha|^2)\mathcal{D}[\hat{\tau}_z]\varrho^P_\mathrm{o} \\ &+ \kappa_f\delta^*_\beta\hat{f}[\varrho^P_\mathrm{o}, \hat{\tau}_z] + \kappa_B\delta_\beta[\hat{\tau}_z, \varrho^P_\mathrm{o}]\hat{f}^\dagger + \kappa_{int}\delta^*_\alpha\hat{a}[\varrho^P_\mathrm{o}, \hat{\tau}_z] + \kappa_{int}\delta_\alpha[\hat{\tau}_z, \varrho^P_\mathrm{o}]\hat{a}^\dagger\end{aligned} \tag{S48}$$

with

$$\begin{aligned}\hat{H}^P_{4qb,\mathrm{o}} =& 2\chi\hat{a}^\dagger\hat{a}\hat{\tau}_z - \frac{K}{2}\hat{a}^\dagger\hat{a}^\dagger\hat{a}\hat{a} + 2\chi|\alpha_\mathrm{o}|^2\hat{\tau}_z - 2K|\alpha_\mathrm{o}|^2\hat{a}^\dagger\hat{a} + g\cos(2\chi t)(\hat{a}^\dagger\hat{f} + \hat{f}\hat{a}^\dagger) \\ &+ \hat{\Pi}_+\left\{\left[\frac{\mathcal{E}_p}{2}\alpha_\mathrm{o}\mathrm{e}^{-6i\chi t} + \frac{i\kappa_{eff}}{2}\alpha^*_\mathrm{o}\left(\mathrm{e}^{-2i\chi t} + \mathrm{e}^{4i\chi t}\frac{1}{1 + i8\chi/\kappa_f}\right)\right]\hat{a}\right. \\ &\left. + \left(\frac{i\kappa_{eff}}{4}\frac{\alpha^*_\mathrm{o}}{\alpha_\mathrm{o}}\mathrm{e}^{4i\chi t} + \frac{\mathcal{E}_p}{2}\mathrm{e}^{-4i\chi t}\right)\hat{a}^2 - K\alpha^*_\mathrm{o}\mathrm{e}^{2i\chi t}\hat{a}^\dagger\hat{a}^2\right\} + h.c. \\ &+ \hat{\Pi}_-\left\{\left[\frac{\mathcal{E}_p}{2}\alpha_\mathrm{o}\mathrm{e}^{6i\chi t} + \frac{i\kappa_{eff}}{2}\alpha^*_\mathrm{o}\left(\mathrm{e}^{2i\chi t} + \mathrm{e}^{-4i\chi t}\frac{1}{1 - i8\chi/\kappa_f}\right)\right]\hat{a}\right. \\ &\left. + \left(\frac{i\kappa_{eff}}{4}\frac{\alpha^*_\mathrm{o}}{\alpha_\mathrm{o}}\mathrm{e}^{-4i\chi t} + \frac{\mathcal{E}_p}{2}\mathrm{e}^{4i\chi t}\right)\hat{a}^2 - K\alpha^*_\mathrm{o}\mathrm{e}^{-2i\chi t}\hat{a}^\dagger\hat{a}^2\right\} + h.c.\end{aligned} \tag{S49}$$

where we have defined $\kappa_{eff} \equiv g^2/\kappa_f + \kappa_{int}$. Similarly to the no filter case analyzed in the previous section, the two resonator modes remain close to a vacuum state in the Polaron frame, which means that the second

line in Eq. (S48) has a minimal effect and can be neglected [45]. Moreover, the last four lines of $\hat{H}^P_{4qb,\mathrm{o}}$ are neglected because they consist of small and rotating terms, only inducing small fluctuations. We thus approximate the master equation Eq. (S48) to

$$\begin{aligned}\dot{\varrho}^P_{\mathrm{o}} =& -i\left[2\chi\hat{a}^\dagger\hat{a}\hat{\tau}_z - \frac{K}{2}\hat{a}^\dagger\hat{a}^\dagger\hat{a}\hat{a} + 2\chi|\alpha_{\mathrm{o}}|^2\hat{\tau}_z - 2K|\alpha_{\mathrm{o}}|^2\hat{a}^\dagger\hat{a} + g\cos(2\chi t)(\hat{a}^\dagger\hat{f} + \hat{f}\hat{a}^\dagger), \varrho^P_{\mathrm{o}}\right] \\ &+ \kappa_f\mathcal{D}[\hat{f}]\varrho^P_{\mathrm{o}} + (\kappa_f|\delta_\beta|^2 + \kappa_{int}|\delta_\alpha|^2)\mathcal{D}[\hat{\tau}_z]\varrho^P_{\mathrm{o}} + \kappa_{int}\mathcal{D}[\hat{a}]\varrho^P_{\mathrm{o}}\end{aligned} \tag{S50}$$

The reduced state of the effective qubit in the lab frame is given by

$$\rho_{\mathrm{o}} = \mathrm{Tr}_r[\hat{P}\varrho^P_{\mathrm{o}}\hat{P}^\dagger] \tag{S51}$$

where we write the state in the Polaron frame as

$$\varrho^P_{\mathrm{o}} = \sum_{n,m,l,k=0}^{\infty}\sum_{i,j=-,+}\varrho^P_{i,j,n,m,l,k}|\psi_i,n,l\rangle\langle\psi_j,m,k| \tag{S52}$$

with n,m (l,k) referring to the nonlinear resonator (filter mode) Fock states. The reduced qubit density matrix ρ_{o} is thus given by

$$\rho_{\mathrm{o}} = \sum_{n,l}\varrho_{-,-,n,n,l,l}|\psi_-\rangle\langle\psi_-| + \varrho_{+,+,n,n,l,l}|\psi_+\rangle\langle\psi_+| + \sum_{n,m}\lambda_{n,m,m,n,l,k,k,l}|\psi_+\rangle\langle\psi_-| + \lambda^*_{m,n,n,m,l,k,k,l}|\psi_-\rangle\langle\psi_+| \tag{S53}$$

where

$$\lambda_{n,m,p,q,k,l,r,s} = \varrho^P_{+,-,n,m,k,l}d^\alpha_{p,q}\mathrm{e}^{-i\mathrm{Im}[\alpha_-\alpha^*_+]}d^\beta_{r,s}\mathrm{e}^{-i\mathrm{Im}[\gamma_-\gamma^*_+]} \tag{S54}$$

$$d^\alpha_{p,q} \equiv \langle p|D(2\delta_\alpha)|q\rangle \tag{S55}$$

$$d^\beta_{r,s} \equiv \langle r|D(2\delta_\beta)|s\rangle \tag{S56}$$

The equations of motion of the reduced qubit diagonal elements are simply

$$\dot{\rho}_{i,i} = \sum_{n,l}\varrho^P_{i,i,n,n,l,l} = 0 \tag{S57}$$

On the other hand, the equation of motion for the qubits off-diagonal elements is more complex and given by

$$\begin{aligned}\dot{\lambda}_{n,m,p,q,k,l,r,s} =& \dot{\varrho}^P_{+,-,n,m,k,l}d^\alpha_{p,q}\mathrm{e}^{-i\mathrm{Im}[\alpha_-\alpha^*_+]}d^\beta_{r,s}\mathrm{e}^{-i\mathrm{Im}[\gamma_-\gamma^*_+]} \\ &- i\partial_t(\mathrm{Im}[\alpha_-\alpha_+])\lambda_{n,m,p,q,k,l,r,s} + \dot{\delta}_\alpha\sqrt{p}\lambda_{n,m,p-1,q,k,l,r,s} \\ &- \dot{\delta}^*_\alpha\sqrt{a}\lambda_{n,m,p,q-1,k,l,r,s} - 2\partial_t(\delta_\alpha\delta^*_\alpha)\lambda_{n,m,p,q,k,l,r,s} \\ &- i\partial_t(\mathrm{Im}[\beta_-\beta_+])\lambda_{n,m,p,q,k,l,r,s} + \dot{\delta}_\beta\sqrt{r}\lambda_{n,m,p,q,k,l,r-1,s} \\ &- \dot{\delta}^*_\beta\sqrt{s}\lambda_{n,m,p,q,k,l,r,s-1} - 2\partial_t(\delta_\beta\delta^*_\beta)\lambda_{n,m,p,q,k,l,r,s}\end{aligned} \tag{S58}$$

Similarly to the previous section, we use the fact that in the Polaron frame, both nonlinear resonator and filter remain in a vacuum state. Consequently, only the $\lambda_{0,0,0,0,0,0,0,0}$ element is populated [45]. Averaging the resulting equation over one period $2\pi/4\chi$, we get the equation

$$\dot{\rho}_{+,-} = \dot{\lambda}_{0,0,0,0,0,0,0,0} = \left[-\gamma^{eff}_{\mathrm{o}} - i4\chi|\alpha_{\mathrm{o}}|^2\right]\lambda_{0,0,0,0,0,0,0,0} \tag{S59}$$

where we have defined

$$\gamma^{eff}_{\mathrm{o}} \equiv \kappa_{eff}|\alpha_{\mathrm{o}}|^2\frac{1}{1+(8\chi/\kappa_f)^2} + \kappa_{int}|\alpha_{\mathrm{o}}|^2 \tag{S60}$$

Using these results, we finally obtain the reduced qubit master equation

$$\dot{\rho}_{\rm o} = -i[2\chi|\alpha_{\rm o}|^2\hat{\tau}_z, \rho_{\rm o}] + \gamma_{\rm o}^{eff}\mathcal{D}[\hat{\tau}_z]\rho_{\rm o}/2 \tag{S61}$$

This expression is the same as found in Eq. (S43) without the filter mode, but now with a renormalized decay rate $\gamma_{\rm o}^{eff}$. Here, dephasing can be kept under control by designing the system such that $8\chi/\kappa_f \gg 1$ and by reducing the internal photon loss rate of the nonlinear resonator, κ_{int}, as much as possible. Moreover, the deterministic phase proportional to $4\chi|\alpha_{\rm o}|^2$ accumulated inside this subspace can be corrected by setting the measurement time so that the phase is an integer multiple of 2π or, alternatively, with a series of single-qubit phase gates.

We mention that, although the phase of the resonator after the bifurcation ($\theta_{\rm o}$ or $\theta_{\rm o}+\pi$) does not depend on the qubits state, this phase is always the same in both odd qubit subspaces, $\mathcal{H}_\pm$. With both resonator modes starting in vacuum, the state of the combined system approximately evolves to

$$\begin{aligned}|\psi_{\rm o}\rangle_q|0\rangle_r|0\rangle_f \rightarrow\ & c_+|\psi_+\rangle_q(|\alpha_{\rm o}e^{-i2\chi t}\rangle_r|\beta\rangle_f + |-\alpha_{\rm o}e^{-i2\chi t}\rangle_r|-\beta\rangle_f) \\ & + c_-|\psi_-\rangle_q(|\alpha_{\rm o}e^{i2\chi t}\rangle_r|\beta\rangle_f + |-\alpha_{\rm o}e^{i2\chi t}\rangle_r|-\beta\rangle_f)\end{aligned} \tag{S62}$$

where $\beta \approx -ig\alpha_{\rm o}/\kappa_f$ (see Eq. (S46)) and q, r, f denote the qubits, nonlinear resonator and filter systems, respectively. Measuring the output of the filter mode projects the state of the filter onto $\pm\beta$, leading to a combined system state

$$|\psi_{\rm o}\rangle_q|0\rangle_r|0\rangle_f \rightarrow \left(c_+|\psi_+\rangle_q| \pm \alpha_{\rm o}e^{-i2\chi t}\rangle_r + c_-|\psi_-\rangle_q| \pm \alpha_{\rm o}e^{i2\chi t}\rangle_r\right)|\pm\beta\rangle_f \tag{S63}$$

As the equation above indicates, the measurement back-action on the filter leads to a situation where the initial nonlinear resonator phase ($\theta_{\rm o}$ or $\theta_{\rm o}+\pi$) is always the same in both odd qubit subspace $\mathcal{H}_\pm$.

III. CIRCUIT QED IMPLEMENTATION

In this section, we show how the circuits illustrated in Figs. S4 and S5 implement respectively the Hamiltonians Eqs. (5) and (10) of the main text.

A. Two qubits

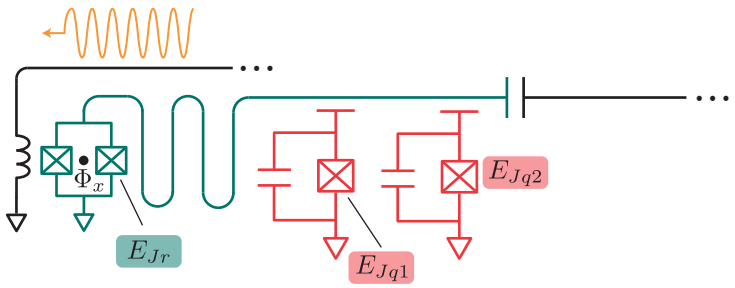

Fig. S4. Possible circuit QED implementation of the two-qubit parity measurement. Two transmon qubit (red) are dispersively coupled to a nonlinear resonator (green). The nonlinear resonator is ended by a SQUID loop threaded by a modulated flux $\Phi_x(t)$. For simplicity, we consider two identical Josephson junctions of energy E_{Jr} for the resonator SQUID loop. We denote the Josephson energy of the two transmon qubits by E_{Jq1}, E_{Jq2} respectively.

Using standard circuit quantization techniques [47] and expanding the qubits Josephson junctions potential to fourth order, one finds that the circuit illustrated in Fig. S4 is well described by the Hamiltonian ($\hbar = 1$)

$$\hat{H} = \omega_0\hat{a}^\dagger\hat{a} - E_{Jr}\cos\left[\frac{\Phi_x(t)}{2\Phi_0}\right]\cos(\hat{\varphi}_r) - E_{Jr}J_0(\delta f)\cos F\frac{\hat{\varphi}_r^2}{2} + \sum_{i=1}^{2}\left[\omega_{qi}\hat{b}_i^\dagger\hat{b}_i - \frac{E_{Jqi}}{24}\hat{\varphi}_{qi}^4 + g_i(\hat{a}\hat{b}_i^\dagger + \hat{a}^\dagger\hat{b}_i)\right] \tag{S64}$$

where ω_0, ω_{qi} are the bare frequencies of the resonator and transmon qubits respectively, Φ_0 is the quantum of flux, $\hat{\varphi}_r = \Phi_{zpf,r}(\hat{a} + \hat{a}^\dagger)/\Phi_0$ is the dimensionless phase difference across the resonator junctions, $J_n(x)$ is the n^{th} Bessel function of the first kind and g_i is the coupling strength between the resonator and the i^{th} qubit. We take a flux modulation of the form $\Phi_x(t)/2\Phi_0 \equiv F + \delta f \cos(\omega_p t)$ where $F, \delta f$ are the dimensionless amplitude of the static and modulated part of the flux and ω_p is the modulation frequency. We use the Jacobi-Anger expansion to express the second term of Eq. (S64) as

$$E_{Jr}\cos(F + \delta f \cos\omega_p t) = \sum_n E_{Jr}^{(n)} \cos(n\omega_p t) \tag{S65}$$

where we have defined

$$\begin{aligned} E_{Jr}^{(0)} &\equiv E_{Jr} J_0(\delta f)\cos(F) \\ E_{Jr}^{(2n-1)} &\equiv 2E_{Jr}(-1)^n J_{2n-1}(\delta f)\sin(F) \\ E_{Jr}^{(2n)} &\equiv 2E_{Jr}(-1)^n J_{2n}(\delta f)\cos(F) \end{aligned} \tag{S66}$$

Diagonalizing the static quadratic part of the Hamiltonian, we get

$$\hat{\tilde{H}} \approx \tilde{\omega}_0 \hat{a}^\dagger \hat{a} - \sum_n E_{Jr}^{(n)} \cos(n\omega_p t)\cos(\hat{\tilde{\varphi}}_r) - E_{Jr}^{(0)} \frac{\hat{\tilde{\varphi}}_r^2}{2} + \sum_i \tilde{\omega}_{qi} \hat{b}_i^\dagger \hat{b}_i - \frac{E_{Jqi}}{24} \hat{\tilde{\varphi}}_{qi}^4 \tag{S67}$$

where $\hat{\tilde{\varphi}}_r = \phi_{r,r}(\hat{a} + \hat{a}^\dagger) + \sum_i \phi_{r,qi}(\hat{b}_i + \hat{b}_i^\dagger), \hat{\tilde{\varphi}}_{qi} = \phi_{qi,r}(\hat{a} + \hat{a}^\dagger) + \sum_j \phi_{qi,qj}(\hat{b}_j + \hat{b}_j^\dagger)$. $\phi_{n,m}$ denotes the dimensionless zero point fluctuations of the flux of mode m across the junction of n and $\tilde{\omega}_0, \tilde{\omega}_{qi}$ denote the renormalized frequencies of the resonator and transmon qubits respectively. Here, we take a small flux modulation amplitude $\delta f \ll 1$ and use the fact that $J_n(\delta f) \approx (\delta f/2)^n/n!$ to keep only the first two terms in the sum of harmonics Eq. (S65). Expanding the resonator junction potential to fourth order, we get

$$\hat{\tilde{H}} \approx \tilde{\omega}_r \hat{a}^\dagger \hat{a} - E_{Jr}^{(0)} \frac{\hat{\tilde{\varphi}}_r^4}{24} + E_{Jr}^{(1)} \cos(\omega_p t) \frac{\hat{\tilde{\varphi}}_r^2}{2} + \sum_i \tilde{\omega}_{qi} \hat{b}_i^\dagger \hat{b}_i - \frac{E_{Jqi}}{24} \hat{\tilde{\varphi}}_{qi}^4 \tag{S68}$$

Expanding $\hat{\tilde{\varphi}}_r, \hat{\tilde{\varphi}}_{qi}$ and neglecting fast-rotating terms taking into account that we will take the flux modulation frequency at twice the resonator frequency $\omega_p = 2\omega_r$, we get

$$\begin{aligned} \hat{\tilde{H}} \approx\ & (\tilde{\omega}_0 - K + \sum_i \chi_i)\hat{a}^\dagger \hat{a} - \frac{K}{2}\hat{a}^\dagger \hat{a}^\dagger \hat{a}\hat{a} + \mathcal{E}_p \cos(\omega_p t)(\hat{a}\hat{a} + \hat{a}^\dagger \hat{a}^\dagger) \\ & + \sum_i (\tilde{\omega}_{qi} + \alpha_{qi} + \chi_i + \chi_{q1,q2})\hat{b}_i^\dagger \hat{b}_i + \frac{\alpha_{qi}}{2}\hat{b}_i^\dagger \hat{b}_i^\dagger \hat{b}_i \hat{b}_i + 2\chi_i \hat{b}_i^\dagger \hat{b}_i \hat{a}^\dagger \hat{a} + 2\chi_{q1,q2}\hat{b}_1^\dagger \hat{b}_1 \hat{b}_2^\dagger \hat{b}_2, \end{aligned} \tag{S69}$$

where $K \equiv E_{Jr}^{(0)}\phi_{r,r}^4/2 + \sum_i E_{Jqi}\phi_{qi,r}^4/2$ is the resonator nonlinearity, $\alpha_{qi} \equiv -E_{Jr}^{(0)}\phi_{r,qi}^4/2 - \sum_j E_{Jqi}\phi_{qj,qi}^4/2$, $\chi_i \equiv -E_{Jr}^{(0)}\phi_{r,r}^2\phi_{r,qi}^2/2 - E_{Jqi}\phi_{qi,r}^2\phi_{qi,qi}^2/2$ are the nonlinearity and dispersive shift of the i^{th} transmon qubit respectively and $\mathcal{E}_p \equiv -E_{Jr}^{(1)}\phi_{r,r}^2/2$ is the two-photon parametric pump amplitude. Here, the qubit-qubit cross-Kerr terms $\chi_{q1,q2} = -E_{Jq1}\phi_{q1,q2}^2\phi_{q1,q1}^2/2 - E_{Jq2}\phi_{q2,q2}^2\phi_{q2,q1}^2/2$ are small and can be safely neglected. Projecting the transmons onto the qubit subspace $\{|0\rangle, |1\rangle\}$, we get

$$\hat{\tilde{H}} = \omega_r \hat{a}^\dagger \hat{a} - \frac{K}{2}\hat{a}^\dagger \hat{a}^\dagger \hat{a}\hat{a} + \mathcal{E}_p \cos(\omega_p t)(\hat{a}\hat{a} + \hat{a}^\dagger \hat{a}^\dagger) + \sum_i \frac{\tilde{\omega}'_{qi}}{2}\hat{\sigma}_{zi} + \chi_i \hat{a}^\dagger \hat{a}\hat{\sigma}_{zi} \tag{S70}$$

where we have defined $\omega_r \equiv \tilde{\omega}_0 + K + \sum_i \chi_i$, $\tilde{\omega}'_{qi} \equiv \tilde{\omega}_{qi} + \alpha_{qi} + \chi_i + \chi_{q1,q2}$. We take identical dispersive shifts $\chi_1 = \chi_2 \equiv \chi$ and, as mentioned previously, choose a flux modulation frequency $\omega_p = 2\omega_r$. After going to a frame rotating at ω_r and neglecting fast-rotating terms, we get the Hamiltonian Eq. (5) of the main text

$$\hat{H}_{2qb} = \chi(\hat{\sigma}_{z1} + \hat{\sigma}_{z2})\hat{a}^\dagger \hat{a} + \frac{\mathcal{E}_p}{2}(\hat{a}\hat{a} + \hat{a}^\dagger \hat{a}^\dagger) - \frac{K}{2}\hat{a}^\dagger \hat{a}^\dagger \hat{a}\hat{a} \tag{S71}$$

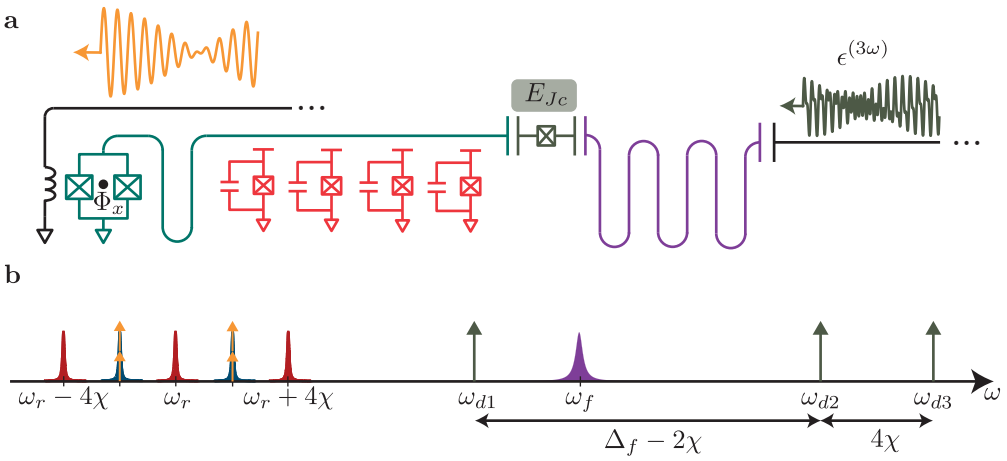

Fig. S5. A possible circuit QED implementation for the four-qubit parity measurement. **a** Possible circuit QED implementation for the 4 qubits parity measurement. Four transmon qubits (red) are dispersively coupled to a nonlinear resonator (green). The nonlinear resonator is ended by a SQUID loop threaded by a modulated flux $\Phi_x(t)$. The nonlinear resonator is capacitively coupled to a transmon mode (dark green) which in turn is capacitively coupled to a filter mode (purple). For simplicity, we consider two identical Josephson junctions of energy E_{Jr} for the resonator SQUID loop. We denote the Josephson energy of the transmon qubits by E_{Jqi} and the Josephson energy of the coupler transmon mode (dark green) is denoted E_{Jc}. Finally, a multi-tone, linear microwave drive (dark green) is applied at the input of the filter mode. **b** Illustration of the different frequencies involved in the four-qubit parity measurement. The different possible resonator frequencies when the qubits are in the even (odd) subspace are indicated by the red (blue) Lorentzians and the filter mode frequency is indicated by the purple Lorentzian. The two sets of orange double arrows indicate the parametric two-photon drive on the nonlinear resonator and the three single arrows in dark green indicate the multi-tone coherent drive on the filter mode. The drive frequencies ω_{di} are chosen such that $\omega_{d2} - \omega_{d1} = \omega_f - \omega_r - 2\chi$ and $\omega_{d3} - \omega_{d1} = \omega_f - \omega_r + 2\chi$.

B. Four Qubits

Following a procedure similar to the previous section, the Hamiltonian describing Fig S5**a** is

$$\begin{aligned}\hat{H} = \tilde{\omega}_a \hat{a}^\dagger \hat{a} - E_{Jr} \cos\left[\frac{\Phi_x(t)}{2\Phi_0}\right] \cos(\hat{\tilde{\varphi}}_r) - E_{Jr}^{(0)} \frac{\hat{\tilde{\varphi}}_r^2}{2} \\ + \sum_i \tilde{\omega}_{qi} \hat{b}_i^\dagger \hat{b}_i - \frac{E_{Jqi}}{24} \hat{\tilde{\varphi}}_{qi}^4 + \tilde{\omega}_c \hat{c}^\dagger \hat{c} - \frac{E_{Jc}}{24} \hat{\tilde{\varphi}}_c^4 + \tilde{\omega}_f \hat{f}^\dagger \hat{f} + \epsilon^{(3\omega)}(t)(\hat{f} + \hat{f}^\dagger)\end{aligned} \tag{S72}$$

where the static, quadratic, part of the Hamiltonian has already been diagonalized. Here, the transmon coupler mode (filter mode) annihilation and creation operators are denoted $\hat{c}, \hat{c}^\dagger$ ($\hat{f}, \hat{f}^\dagger$) and the phase across the junction j is denoted by $\hat{\tilde{\varphi}}_j = \sum_{\alpha=a,c,f} \phi_{j,\alpha}(\hat{\alpha} + \hat{\alpha}^\dagger) + \sum_i \phi_{j,qi}(\hat{b}_i + \hat{b}_i^\dagger)$.

1. *Flux modulation*

We take a two-tone flux modulation $\Phi_x(t)/2\Phi_0 = F + \delta f_1 \cos(\omega_{p1} t) + \delta f_2 \cos(\omega_{p2} t)$. Moreover, we take small, equal modulation amplitudes for both flux modulation tones $\delta f_1 = \delta f_2 \equiv \delta f \ll 1$, leading to the first order expansion in δf

$$\cos[F + \delta f \cos(\omega_{p1} t) + \delta f \cos(\omega_{p2} t)] \approx \cos(F) J_0(\delta f)^2 - 2\sin(F) J_0(\delta f) J_1(\delta f)[\cos(\omega_{p1} t) + \cos(\omega_{p2} t)] \tag{S73}$$

To simplify the notation, we define $E_{Jr}^{(0)} \equiv E_{Jr} J_0(\delta f)^2 \cos(F)$ and $E_{Jr}^{(1)} \equiv -2E_{Jr} J_0(\delta f) J_1(\delta f) \sin(F)$. The two-tone two-photon drive is thus given by $\mathcal{E}_p^{(2\omega)}(t) = \mathcal{E}_p \cos(\omega_{p1} t) + \mathcal{E}_p \cos(\omega_{p2} t)$, where $\mathcal{E}_p = -E_{Jr}^{(1)} \phi_{r,r}^2/2$. As schematically illustrated by the two sets of orange double arrows in Fig. S5**b**, we choose the flux modulation frequencies $\omega_{p1} = 2(\omega_r - 2\chi)$ and $\omega_{p2} = 2(\omega_r + 2\chi)$.

2. Coupling Modulation

In order to induce the desired two-tone coupling modulation between the filter mode and the nonlinear resonator, we take a three-tone drive on the filter mode $\epsilon^{(3\omega)}(t) = \sum_{i=1}^{3} \epsilon_i \cos(\omega_{di} t)$. In Ref. [41], a coupling between two modes was induced by driving each mode with a single-tone drive. Here, in contrast, we avoid the use of a direct drive on the nonlinear resonator as this would induce dephasing of the qubits state. Consequently, we consider a multi-tone drive that displaces the filter mode only. To understand the effect of this drive on the system, we perform the displacement transformation $\hat{f} \to \hat{f} + \sum_{i=1}^{3} \xi_i e^{-i\omega_{di} t}$, where the displacements are given by

$$\xi_i = \frac{\epsilon_i}{\Delta_i + i\kappa_f/2} \tag{S74}$$

with the detunings $\Delta_i \equiv \omega_{di} - \omega_f$. Since the filter mode is only coupled to the coupler mode, we neglect the fluctuations of the filter normal mode across the junctions of the resonator and the data qubits, $\phi_{r,f} = \phi_{qi,f} \approx 0$. Under the displacement transformation, the nonlinear term coming from the coupler transmon mode goes to

$$-\frac{E_{Jc}}{24}\hat{\varphi}_c^4 \to -\frac{E_{Jc}}{24}\left[\sum_{\alpha=a,c,f} \phi_{c,\alpha}(\hat{\alpha} + \hat{\alpha}^\dagger) + \phi_{c,f}\sum_{i=1}^{3}(\xi_i e^{-i\omega_{di}t} + \xi_i^* e^{i\omega_{di}t})\right]^4 \tag{S75}$$

where we neglected the contributions of the data qubits normal mode to the zero point fluctuations around the coupler transmon junction, $\phi_{c,qi} \approx 0$. Keeping only the non-rotating, energy-conserving terms, we expand Eq. (S75) to

$$\begin{aligned} &-\frac{E_{Jc}}{24}\left[\sum_{\alpha=a,c,f} \phi_{c,\alpha}(\hat{\alpha} + \hat{\alpha}^\dagger)\right]^4 \\ &\quad - E_{Jc}\phi_{c,f}^2|\xi|^2 \sum_{\alpha=a,c,f} \phi_{c,\alpha}^2 \hat{\alpha}^\dagger\hat{\alpha} \\ &\quad - \frac{E_{Jc}\phi_{c,f}^2}{2}\sum_{i>j}\sum_{\alpha\neq\beta=a,c,f} \phi_{c,\alpha}\phi_{c,\beta}\xi_i\xi_j \cos[(\omega_{di} - \omega_{dj})t]\hat{\alpha}^\dagger\hat{\beta} \end{aligned} \tag{S76}$$

where we have defined $|\xi|^2 \equiv \sum_i |\xi_i|^2$. The first line here corresponds to the static nonlinearity induced by the junction. The second line corresponds to an AC-stark shift of the different modes. The third line is the desired coupling modulation and, to make it resonant (in the odd data qubit subspace), we choose the drive frequencies so that $\omega_{d1} - \omega_{d2} = \omega_r - \omega_f - 2\chi$, $\omega_{d1} - \omega_{d3} = \omega_r - \omega_f + 2\chi$. Note that here $\omega_{r/f}$ have to be adjusted with the induced AC-Stark shift, something that can be done by adjusting the drive frequencies ω_{di} with the drive power. We then define $g^{(2\omega)}(t) \equiv g\cos[(\omega_{d1} - \omega_{d2})t] + g\cos[(\omega_{d1} - \omega_{d3})t]$, where $g \equiv -E_{Jc}\phi_{c,f}^3\phi_{c,a}\xi_1\xi_2/2$. In order to make the coupling strength of equal amplitude for both modulation frequencies, the displacements associated with the drives at frequencies ω_{d2}, ω_{d3} should be of equal magnitude $\xi_2 = \xi_3$.

3. Final Hamiltonian

Replacing Eqs. (S73) and (S76) in Eq. (S72) and neglecting fast-rotating terms, we get

$$\begin{aligned} \hat{H}' \approx\ & \omega_a'\hat{a}^\dagger\hat{a} + \mathcal{E}_p^{(2\omega)}(t)\left[\hat{a}\hat{a} + \hat{a}^\dagger\hat{a}^\dagger\right] + \omega_c'\hat{c}^\dagger\hat{c} + \omega_f'\hat{f}^\dagger\hat{f} + g^{(2\omega)}(t)\left[\hat{a}\hat{f}^\dagger + \hat{a}^\dagger\hat{f}\right] + \sum_i \omega_{qi}'\hat{b}_i^\dagger\hat{b}_i \\ &+ \sum_{\alpha=a,c,f,qi} \frac{\chi_{\alpha,\alpha}}{2}\hat{\alpha}^\dagger\hat{\alpha}^\dagger\hat{\alpha}\hat{\alpha} + \sum_{\beta>\alpha=a,c,f,qi} \chi_{\alpha,\beta}\hat{\alpha}^\dagger\hat{\alpha}\hat{\beta}^\dagger\hat{\beta} \end{aligned} \tag{S77}$$

where $\chi_{\alpha,\alpha} = -\sum_\beta E_{J\beta}\phi_{\beta,\alpha}^4/2$, $\chi_{\alpha,\beta} = -\sum_\gamma E_{J\gamma}\phi_{\gamma,\alpha}^2\phi_{\gamma,\beta}^2$ and $E_{Ja} \equiv E_{Jr}^{(0)}$. The nonlinear resonator nonlinearity is given by $K = -\chi_{a,a}$ while the dispersive coupling of the qubits is given by $\chi_i = \chi_{a,qi}/2$.

We now project the data qubits onto the $\{|0\rangle, |1\rangle\}$ subspace. Moreover, since the transmon coupler mode remains in its ground state and does not play a direct role in the dynamics, it can be removed from the Hamiltonian, leading to an expression close to Eq. (10) of the main text

$$\begin{aligned}\hat{H}_{4qb} = \omega_r \hat{a}^\dagger \hat{a} - \frac{K}{2}\hat{a}^\dagger\hat{a}^\dagger\hat{a}\hat{a} + \mathcal{E}_p^{(2\omega)}(t)\left[\hat{a}\hat{a} + \hat{a}^\dagger\hat{a}^\dagger\right] + \sum_i \frac{\omega_{qi}}{2}\hat{\sigma}_{zi} + \chi\sum_{i=1}^{4}\hat{\sigma}_{zi}\hat{a}^\dagger\hat{a} \\ + \omega_f \hat{f}^\dagger\hat{f} + g^{(2\omega)}(t)\left[\hat{a}\hat{f}^\dagger + \hat{a}^\dagger\hat{f}\right] + \frac{K_f}{2}\hat{f}^\dagger\hat{f}^\dagger\hat{f}\hat{f} + \chi_{a,f}\hat{a}^\dagger\hat{a}\hat{f}^\dagger\hat{f}\end{aligned} \tag{S78}$$

The last two terms of the above equation lead to small spurious effects and are a biproduct of this particular implementation. However, they are typically very small [41] and their main effect is a small shift of the modes frequencies, something that can be compensated by adjusting the frequencies of the different drives. We note that the photon number inside the filter mode is lower than in the nonlinear resonator by a factor $\sim (g/\kappa_f)^2$ (see Eq. (S46)). The last two terms of Eq. (S78) will, however, change the behavior of the system as the photon number inside both modes is increased further. For example, these terms cannot be neglected when considering parameters leading to a photon number similar to what was demonstrated in the experiment of Krantz *et al.* [18].

IV. MEASUREMENT FIDELITY WITH QUBIT DECAY

As mentioned in the main text, a finite qubit decoherence time reduces the measurement fidelity. For the two-qubit parity measurement and resonator parameters similar to those used in Fig. 2 of the main text, Fig. S6 shows the measurement fidelity as a function of the measurement time for different qubit decoherence times T_1. Single qubit decay events change the parity of the qubit ensemble which, in turn, changes the steady state of the resonator. As a result, more noise is introduced in the resonator as the measurement time is increased and, at some time τ_{max}, the measurement fidelity reaches a maximum. In Fig. S6, τ_{max} is indicated by a solid point and depends on the coherence time of the qubits. Integrating the signal beyond that point introduces more noise and does not increase the fidelity for the simple filter function used in this analysis. To remediate to this situation, we choose to set $\mathcal{F}_m(\tau > \tau_{max}) \equiv \mathcal{F}_m(\tau_{max})$ in Fig. S6. Note that this could potentially be improved using different filter functions or machine learning [25]. For $T_1 = 25$ μs, we find a fidelity of 96.8% for $\tau_{max} = 1.56$ μs. For $T_1 = 50$ μs, we find a fidelity of 98.2% for $\tau_{max} = 1.56$ μs and, for $T_1 = 100$ μs, we find a fidelity of 99.1% for $\tau_{max} = 2.12$ μs. These results were obtained from integration of the stochastic master equation Eq. (9) of the main text with added qubit decay superoperators

$$d\rho = -i[\hat{H}, \rho]dt + \kappa\mathcal{D}[\hat{a}]\rho\, dt + \sqrt{\kappa}\mathcal{H}[\hat{a}\mathrm{e}^{-i\theta_\circ}]\rho\, dW + \sum_i \frac{1}{T_1}\mathcal{D}[\hat{\sigma}_{-i}]\rho\, dt \tag{S79}$$

The measurement fidelity in Fig. S6 was calculated from twice 2000 realizations of the above equation with the qubits initially in the odd and even subspaces.

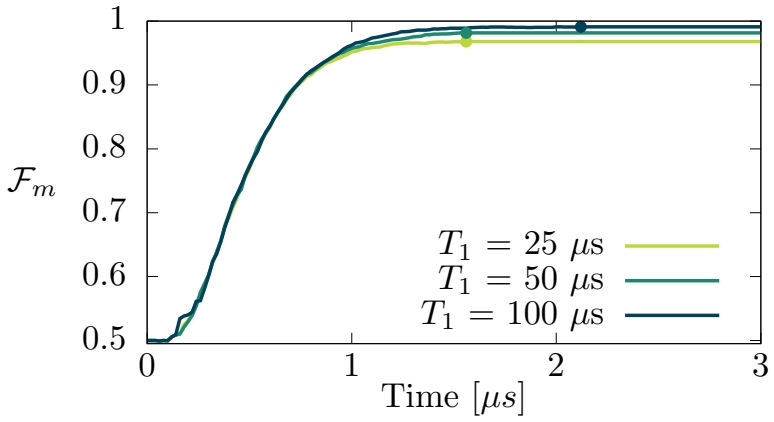

Fig. S6. Fidelity of the two-qubit parity measurement as a function of measurement time for different decay times of the qubits, $T_1 = 25\ \mu$s (light green), $T_1 = 50\ \mu$s (dark green) and $T_1 = 100\ \mu$s (blue). The parameters are $K/\kappa = 0.175$, $\chi/\kappa = 25$, $\mathcal{E}_p/\kappa = 2.5$ and $\kappa/2\pi = 0.4$ MHz.

B.4 Initialisation de Qubit

Fast and Unconditional All-Microwave Reset of a Superconducting Qubit
Supplemental Material

S1. PERFORMANCE OF RESET PROTOCOLS FOR SUPERCONDUCTING QUBITS.

We compare experimental implementations of superconducting qubit reset protocols by two performance metrics, the reset rate Γ and the residual excited state population $P_{\rm exc}^{\rm sat}$ (Fig. S1). $P_{\rm exc}^{\rm sat}$ is obtained at the end of the reset procedure (measurement-based and π-pulse-based reset) or at steady-state (microwave and flux driven reset), corresponding in all cases to the lowest residual excitation reached. For driven reset protocols, Γ is defined as the rate at which the qubit approaches the ground state. For measurement and π-pulse based protocols, Γ satisfies $P_{\rm exc}^{\rm sat} = e^{-\Gamma t_p}$, where t_p is the total protocol duration.

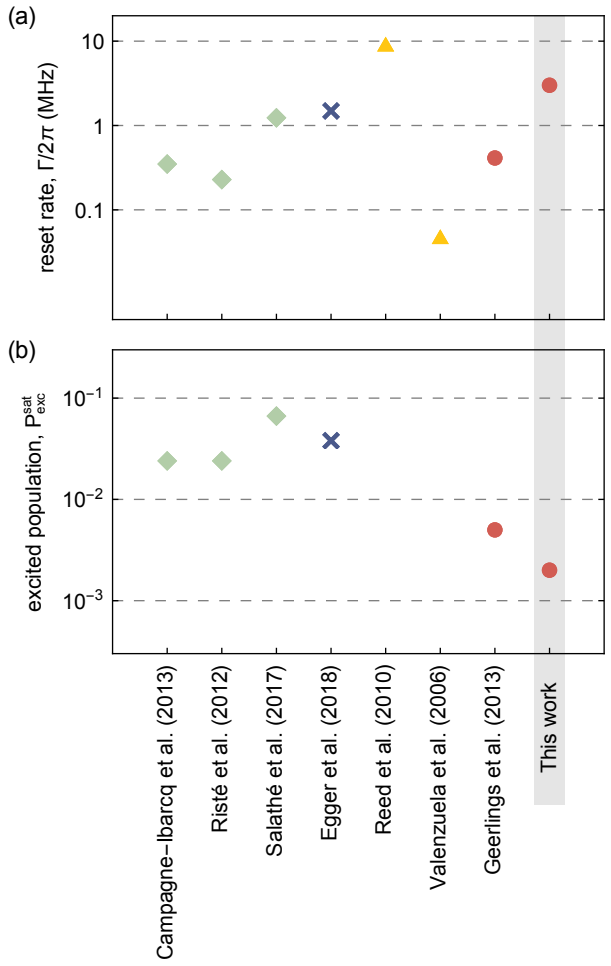

FIG. S1. Experimentally achieved reset rates Γ (a) and residual excited state populations $P_{\rm exc}^{\rm sat}$ (b) of selected implementations of superconducting qubit reset protocols based on: qubit measurement and feedback control (green squares) [S1–S3], sequential π-pulses to a dissipative state (blue cross) [S4], qubit frequency tuning via flux pulses (yellow triangles) [S5, S6] and all-microwave drive induced dissipation (red circles) [S7].

In a recent demonstration of a similar protocol, a transmon coupled to a low-Q cavity is reset by applying a sequence of π-pulses on the e-f and f0-g1 transitions [S4]. For a given sample, this alternative scheme leads to a faster reset. As an example, with our sample it is possible to apply e-f and f0-g1 π-pulses in 15 ns and 60 ns, respectively. This would lead to a reset protocol of 75 ns duration plus a photon leakage time $5/\kappa = 90$ ns to empty the cavity. However, unlike our unconditional driven protocol, the reset fidelity is limited by transmon coherence and the π-pulse fidelities. This leads to a reset level $P_{\rm exc}^{\rm sat}$ an order of magnitude higher than in the present work.

S2. SAMPLE PARAMETERS

The sample design is similar to the one used in Ref. [S8]. We etch the $\lambda/4$ coplanar waveguide resonators and feed-lines from a thin niobium film on a sapphire substrate using standard photolithography techniques. The transmon capacitor pads and Josephson junctions are fabricated using electron-beam lithography and shadow evaporation of aluminum. The parameters of the readout circuit (green elements in Fig.1a) and reset circuit (blue elements in Fig.1a) are obtained from fits to the

$\omega_{\rm ge}/2\pi$	6.343 GHz		
$\alpha/2\pi$	-265 MHz		
$n_{\rm th}$	17 %		
$T_1^{\rm ge}$	5.5 μs	$T_1^{\rm ef}$	2.1 μs
$T_2^{\rm ge}$	7.6 μs	$T_2^{\rm ef}$	4.2 μs
$T_2^{*\rm ge}$	3.5 μs	$T_2^{*\rm ef}$	2.0 μs
$\chi_m/2\pi$	-5.8 MHz	$\chi_r/2\pi$	-6.3 MHz
$g_{\rm m}/2\pi$	210 MHz	$g_{\rm r}/2\pi$	335 MHz
$\omega_m/2\pi$	4.787 GHz	$\omega_r/2\pi$	8.400 GHz
$\omega_{PFm}/2\pi$	4.778 GHz	$\omega_{PFr}/2\pi$	8.443 GHz
$Q_{\rm PFm}$	91	$Q_{\rm PFr}$	60
$J_{\rm m}/2\pi$	13.6 MHz	$J_{\rm r}/2\pi$	20.9 MHz
$\kappa_m/2\pi$	12.6 MHz	$\kappa/2\pi$	9.0 MHz

TABLE I. Sample parameters: From time resolved Ramsey measurements we extract the ge transition frequency $\omega_{\rm ge}/2\pi$, and the anharmonicity $\alpha/2\pi$. From resonator transmission spectroscopy we obtain the frequencies, quality factors and couplings of the measurement (m) and reset (r) resonators: Purcell filter frequency $\omega_{\rm PF_{m,r}}/2\pi$, resonator frequency $\omega_{\rm m,r}/2\pi$, quality factor of the Purcell filter $Q_{\rm PF_{m,r}}$ and the coupling rate of the resonator to Purcell filter $J_{\rm m,r}/2\pi$. We obtain the dispersive shifts $\chi_{\rm m,r}/2\pi$ by performing resonator spectroscopy with the qutrit initially prepared in $|g\rangle$, $|e\rangle$ and $|f\rangle$. The coherence times of the qutrit are extracted from time resolved measurements.

transmission spectrum of the respective Purcell filter using the technique and model discussed in Ref. [S8] and are listed in Table I. We extract the coupling strength of the transmon to both circuits using the same fitting procedure while preparing the transmon in its ground or excited state. The transition frequency $\omega_{\rm ge}/2\pi$, the anharmonicity α and the coherence times $T^{\rm R}_{\rm 2ge}$, $T^{\rm R}_{\rm 2ef}$ are measured using Ramsey-type measurements. The energy decay time $\mathrm{T}_1^{\rm ge}$ ($\mathrm{T}_1^{\rm ef}$) is extracted from an exponential fit to the measured time dependence of the populations when preparing the qubit in ether $|e\rangle$ or $|f\rangle$. The population $n_{\rm th}$ of state $|e\rangle$ in thermal equilibrium is extracted with the Rabi population measurement (RPM) method introduced in Ref. [S7]. We used a miniature superconducting coil to thread flux through the SQUID of the transmon to tune $\omega_{\rm ge}/2\pi$.

S3. RABI RATE EXTRACTION

In the fourth calibration step discussed in the main text, to measure the linear relation between the drive rate $\tilde{g}$ and drive amplitude $V_{\rm f0g1}$, we perform Rabi oscillation measurements (Fig. 2d and f). To analyze these oscillations, we use a two-level model with loss described by the non-Hermitian Hamiltonian

$$H_{\rm f0g1} = \begin{bmatrix} i\gamma/2 & \tilde{g} \\ \tilde{g}^* & i\kappa/2 \end{bmatrix}, \tag{S1}$$

which acts on states $|f,0\rangle$ and $|g,1\rangle$, analyzed in a rotating frame. The non-Hermitian terms $i\kappa/2$ and $i\gamma/2$ account for photon emission and transmon decay from $|f\rangle$ to $|e\rangle$, which bring the system to the dark states $|g,0\rangle$ and $|e,0\rangle$, respectively. Based on this model we derive an analytical expression for the $|f\rangle$ state population as a function of time

$$P_{\rm f}(t) = \mathrm{e}^{-\frac{(\kappa+\gamma)}{2}\mathrm{t}} \left| \cosh\left(\frac{\Omega \mathrm{t}}{2}\right) + \frac{\kappa-\gamma}{2\Omega}\sinh\left(\frac{\Omega \mathrm{t}}{2}\right)\right|^2, \tag{S2}$$

where $\Omega = \sqrt{-(2\tilde{g})^2 + (\kappa-\gamma)^2/4}$ is real positive or imaginary depending on the drive rate $\tilde{g}$. Using $P_{\rm f}(t)$ we obtain the fit function

$$f_{\tilde{\rm g}}(t) = \lambda P_{\rm f}(t-t_0) + \mu, \tag{S3}$$

where the parameters λ and μ account for potential state preparation and measurement (SPAM) errors and the parameter t_0 accounts for the fact that the gaussian rising and falling edges of the flat top f0-g1 pulse drive the f0-g1 transition for a finite time. For each drive amplitude $V_{\rm f0g1}$, we obtain Rabi oscillation data which we fit with Eq. (S3). To reduce the number of free parameters, we fit all data sets simultaneously and constrain λ, μ, t_0 and κ to be the the same for all sets as these parameters are expected to be independent of $V_{\rm f0g1}$.

In the second calibration step discussed in the main text, we measure the linear dependence of the drive rate $\Omega_{\rm ef}$ on the drive amplitude $V_{\rm ef}$, by performing Rabi oscillation measurements (Fig. 2b and d). We fit the time-dependence of the population $P_{\rm e}$ with the function

$$f_{\Omega_{\rm ef}}(t) = \frac{1}{2}\mathrm{e}^{-\gamma_{\rm a}\mathrm{t}^*}\left(1-\mathrm{e}^{-\gamma_{\rm b}\mathrm{t}^*}\cos\left(\frac{\Omega_{\rm ef}\mathrm{t}^*}{2}\right)\right), \tag{S4}$$

where $t^* = t - t_0$ offsets the time t by t_0 to account for the fact that the rising and falling edges of the e-f pulse drive the e-f transition for a finite time. The fit parameters γ_a and γ_b account for transmon relaxation to $|g\rangle$ and decoherence in the $\{|e\rangle, |f\rangle\}$ subspace, respectively. We verified numerically that Eq. (S4) is a good approximation of the time dependence of $P_{\rm e}$ during e-f Rabi oscillations and that it yields an unbiased estimate of $\Omega_{\rm ef}$, by comparing it to the result of a master equation simulation. Similarly to the f0-g1 Rabi rate calibration, we simultaneously fit the Rabi oscillation data sets obtained for all probed $V_{\rm ef}$, constraining the fit parameter t_0, γ_a and γ_b to be the the same for all sets.

S4. RESET OPERATING REGIMES

The discussion about the reset operating regimes is based on Eq. (2) in the main text. To derive this equation, we start with the expression for the population

$$P^{\rm H}_{\rm s|s_0}(t) = \left|\langle s|\, e^{-iHt}\,|s_0\rangle\right|^2,$$

of state $|s\rangle \in \{|e,0\rangle, |f,0\rangle, |g,1\rangle\}$, where s_0 is the initial state. We introduce the diagonalization matrix

$$T = \sum_k |\lambda_k\rangle\langle k|,$$

where $|\lambda_k\rangle$ are the eigenvectors of H and the vectors $|k\rangle$ form an orthonormal basis in which $D = T^{-1}\cdot H\cdot T$ is diagonal. Note that, since H is non-Hermitian, its eigenvectors $|\lambda_k\rangle$ are not orthogonal and T is not unitary. We then obtain

$$\begin{aligned} P^{\rm H}_{\rm s|s_0}(t) &= \left|\langle s|\, T e^{-iDt} T^{-1}\,|s_0\rangle\right|^2 \\ &= \left|\sum_{jklm}\langle s|\, T_{jk}\,|j\rangle\langle k|\, e^{-iDt} T^{-1}_{lm}\,|l\rangle\langle m|s_0\rangle\right|^2 \\ &= \left|\sum_k \langle s|\left(\sum_{jm} T_{jk}T^{-1}_{km}\,|j\rangle\langle m|\right)|s_0\rangle\, e^{-i\lambda_k t}\right|^2. \end{aligned}$$

We recover Eq. (2) by defining

$$\hat{A}_k = \sum_{jm} T_{jk}T^{-1}_{km}\,|j\rangle\langle m|.$$

As discussed in the main text, we can define operating regimes of the reset by studying the eigenvalues λ_k of Hamiltonian (1). We set $\delta_{\rm ef} = \delta_{\rm f0g1} = 0$, both to simplify

the analysis and to ensure that the full three-level transmon is reset. To reduce the notations, we tackle an equivalent problem and solve for the eigenvalues $\Lambda_k = i2\lambda_k/\kappa$ of the renormalized Hamiltonian

$$\tilde{H} = \begin{bmatrix} 0 & \sqrt{\Omega} & 0 \\ -\sqrt{\Omega} & 0 & \sqrt{G} \\ 0 & -\sqrt{G} & -1 \end{bmatrix}, \tag{S5}$$

where the dimensionless drive powers $\Omega = (2\Omega_{\rm ef}/\kappa)^2$ and $G = (2\tilde{g}/\kappa)^2$ are real and positive. Hamiltonian (S5) has the characteristic polynomial

$$\mathrm{P}_{\tilde{\mathrm{H}}}(\mathrm{X}) = \mathrm{X}^3 + \mathrm{X}^2 + (\mathrm{G}+\Omega)\mathrm{X} + \Omega, \tag{S6}$$

whose roots are the eigenvalues Λ_k. The discriminants of this cubic equation are

$$\Delta_0 = 1 - 3(G+\Omega), \tag{S7}$$
$$\Delta_1 = 2 - 9(G-2\Omega). \tag{S8}$$

Note that Δ_0 is a linear function of $G+\Omega$, so $(-\Delta_0)$ indicates the amount of total drive power. Conversely, Δ_1 indicates the level of asymmetry between the power of the two drives. Defining the sub-roots

$$C^{\pm} = \sqrt[3]{\frac{\Delta_1 \pm \sqrt{\Delta_1^2 - 4\Delta_0^3}}{2}}, \tag{S9}$$

we find the expression for the eigenvalues

$$\Lambda_k = -\frac{1}{3}\left(1 + \xi^k C^+ + \xi^{-k} C^-\right), \tag{S10}$$

where $k \in \{-1, 0, 1\}$, and $\xi^k = \exp\left[i2\pi k/3\right]$ are the cubic roots of unity. A consequence of Eq. (S10) is that the reset rate is bounded by $\Gamma/\kappa \equiv \min|\mathrm{Re}(\Lambda_k)| \leq 1/3$. We can distinguish three cases based on the sign of $\Delta_1^2 - 4\Delta_0^3$.

Under-damped regime: $\Delta_1^2 > 4\Delta_0^3$. In this case, the sub-roots C^+ and C^- are real and distinct from each other. Therefore, the eigenvalues Λ_k are complex, with a non-zero imaginary part: the populations display oscillations during the reset. Depending on the sign of Δ_1, we have

$$\Gamma/\kappa = \begin{cases} \frac{1}{3}\left[1 - \frac{1}{2}\left(C^+ + C^-\right)\right] < \frac{1}{3} & \text{, if } \Delta_1 > 0 \\ \frac{1}{3}\left[1 + \left(C^+ + C^-\right)\right] < \frac{1}{3} & \text{, if } \Delta_1 < 0 \\ \frac{1}{3} & \text{, if } \Delta_1 = 0. \end{cases} \tag{S11}$$

The reset rate is thus maximized ($\Gamma = \kappa/3$) only when the drives are strong enough ($\Delta_0 \leq 0$) and well balanced ($\Delta_1 = 0$). The conditions $\Delta_0 \leq 0$ and $\Delta_1 = 0$ define the optimal branch (solid red line in Fig. 3a).

Over-damped regime: $\Delta_1^2 < 4\Delta_0^3$. In this low power regime (Δ_0 has to be positive), C^+ and C^- are complex conjugates of each other. As a result, all eigenvalues Λ_k are purely real and the qutrit populations show no oscillatory features during the reset. In this regime, the reset rate can be expressed as

$$\Gamma/\kappa = \frac{1}{3}\left[1 - \sqrt{\Delta_0}\left(\cos\frac{\theta}{3} + \sqrt{3}\sin\frac{\theta}{3}\right)\right],$$

where $\theta = \arccos(\Delta_1/2\Delta_0^{3/2})$ is the argument of $(C^+)^3$, and ranges from 0 to π. Because $\Delta_0 > 0$, we have the strict inequality $\Gamma < \kappa/3$, which means that the optimal branch does not cross the over-damped region.

Critical-damping: $\Delta_1^2 = 4\Delta_0^3$. When this equality holds, we have $C^+ = C^- = \sqrt[3]{\Delta_1/2} = \sqrt{\Delta_0}$, and the eigenvalues are real. We parametrize the critical damping equality by introducing the variable $\beta = \sqrt[3]{\Delta_1/2}$. We then have $\Delta_0 = \beta^2$ and $C^{\pm} = \beta$, which leads to

$$\Gamma/\kappa = \begin{cases} \frac{1}{3}\left(1 - \beta\right) & \text{, if } \beta \geq 0 \\ \frac{1}{3}\left(1 + 2\beta\right) & \text{, otherwise.} \end{cases} \tag{S12}$$

Inverting Eqs. (S7) and (S8) we obtain a parametrization of the critical damping boundary region

$$G(\beta) = \frac{8}{27}(1 - \frac{3}{4}\beta^2 - \frac{1}{4}\beta^3),$$
$$\Omega(\beta) = \frac{1}{27}(1 - 3\beta^2 + 2\beta^3),$$

where β ranges from $-1/2$ to 1, to keep Γ, G and Ω positive.

For $\beta = 0$, we have $\Gamma = \kappa/3$. This point is an exceptional point, where all eigenvalues are identical (Eq. (S10) with $C^{\pm} = 0$) and the eigenvectors coalesce [S9]. This point ($G = 8/27$ and $\Omega = 1/27$, or equivalently, $\tilde{g} = \tilde{g}_{\rm ep} = \sqrt{2/27}\kappa$ and $\Omega_{\rm ef} = \Omega_{\rm ef,ep} = \sqrt{1/108}\kappa$) is the only one that maximizes Γ without displaying oscillatory features of the populations.

For a given value of G, there is a unique $\Omega^{\rm opt}$ that maximizes the reset rate to $\Gamma_{\rm max}(G)$. For $G \geq 8/27$, according to Eq. (S11), the reset rate is maximized by chosing Ω such that $\Delta_1 = 0$. Using Eq. (S8), we find that $\Omega_{\rm opt}(G) = G/2 - 1/9$. The parameters are then on the optimal branch and $\Gamma_{\rm max}(G) = \kappa/3$. For $G < 8/27$, the reset rate is maximized by chosing Ω such that $\Delta_1^2 = 4\Delta_0^3$ (critical damping) and $\Delta_1 > 0$ (upper branch). This can be proven by showing that $\partial_\Omega \Gamma \geq 0$ in the over-damped region, and that $\partial_\Omega\Gamma$ and Δ_1 have opposite signs in the under-damped region. Using these results, we obtain

$$\Gamma_{\rm max}(G) = \frac{2}{3}\left[1 - \cos\left(\frac{1}{3}\arccos\left(1 - \frac{27G}{4}\right)\right)\right].$$

The derivative of $\Gamma_{\rm max}$ diverges as $G \to 8/27$ from the left side (Fig. 3b). If one cannot drive the f0-g1 transition with enough power to get $G > 8/27$, or equivalently $\tilde{g} > \sqrt{2/27}\kappa$, $\Gamma_{\rm max}$ is abruptly reduced. To obtain a fast reset, one should therefore target a value of κ that is as high as possible within the limit that $\kappa < \tilde{g}_{\rm max}\sqrt{27/2} \simeq 3.67\tilde{g}_{\rm max}$, where $\tilde{g}_{\rm max}$ is the maximum f0-g1 drive rate experimentally achievable, without driving unwanted transitions [S10]. This ensures that the maximum reset rate $\Gamma = \kappa/3$ is high and always attainable.

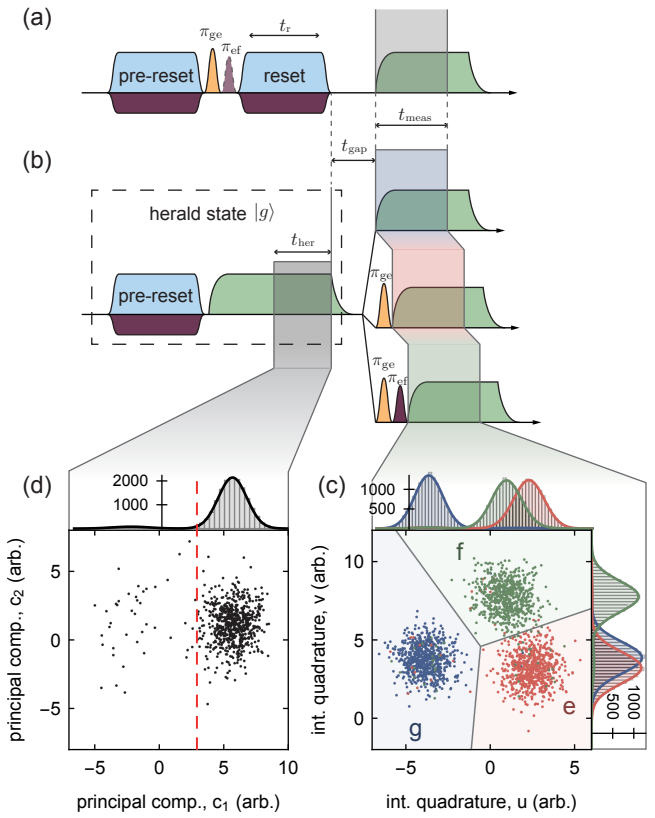

FIG. S2. (a) Schematic of the pulse scheme used to test the unconditional reset protocol. (b) Schematic of the pulse scheme used to record reference single-shot counts. (c) Subset of 500 reference traces displayed in the u-v plane, when the qutrit is prepared in state $|g\rangle$ (blue dots), $|e\rangle$ (red dots) or $|f\rangle$ (green dots). The assignment regions labeled g, e and f are shaded in blue, red and green, respectively, and are separated by a gray line at their boundaries. (d) Sub-sample of 1000 traces acquired during the pre-selection pulse, projected in the principal component plane c_1-c_2. Here c_1 and c_2 are the two first principal components of the set of traces. The red dashed line indicates the threshold for selection/rejection of traces. The plots on the top or right axes of (c) and (d) show histogram counts of the traces. The solid lines in these plots correspond to the density of the marginal probability distributions of the traces, scaled to match the histograms.

S5. SINGLE-SHOT READOUT

To study the reset dynamics (Fig. 4), we pre-reset the transmon with an unconditional reset, and prepare it in state $|e,0\rangle$ or $|f,0\rangle$ with a sequence of π-pulses (Fig. S2a). Next, we apply the reset pulses for a duration t_r and apply a microwave tone at the readout resonator to readout the transmon. We record the I and Q quadratures of the readout signal for a duration of $t_m = 120$ ns starting at the rising edge of the readout tone. We refer to each recorded readout signal as a single-shot trace S.

To define an assignment rule which discriminates the transmon state based on a single-shot trace, we collect

	$\|g\rangle$	$\|e\rangle$	$\|f\rangle$
g	98.2	2.5	2.4
e	0.9	95.7	4.6
f	0.9	1.8	93.0

TABLE II. Reference assignment probability matrix of identifying prepared states (columns) as the measured states (rows). The diagonal elements show correct identification, the off-diagonal elements misidentifications.

reference sets of 40000 single-shot traces obtained with the transmon initialized in states $|g\rangle$, $|e\rangle$ or $|f\rangle$. State initialization is performed using a pre-selection readout pulse that heralds the transmon in its ground state (details discussed later in this section) followed by control π-pulses to prepare states $|e\rangle$ and $|f\rangle$ (Fig. S2b). We integrate each reference single-shot trace with weight functions w_1 and w_2, to calculate the integrated quadratures $u = \int_0^{t_m} S(t)w_1(t)dt$ and $v = \int_0^{t_m} S(t)w_2(t)dt$, in post-processing. We choose w_1 and w_2 such that they maximize the distinguishability between the three qutrit states. For each prepared state $|p\rangle$, the set of integrated traces $\vec{x} = (u, v)$ forms three clusters in the u-v plane (Fig. S2c) following a trimodal Gaussian distribution of mixture density

$$f_p(\vec{x}) = \sum_s \frac{A_{s,p}}{2\pi\sqrt{|\Sigma|}} e^{-\frac{1}{2}(\vec{x}-\mu_s)^\top \cdot \Sigma^{-1} \cdot (\vec{x}-\mu_s)}. \quad \text{(S13)}$$

We extract the parameters $A_{s,p}$, Σ and μ_s with maximum likelihood estimation. Based on these parameters, we define regions in the u-v plane used to assign the result of the readout trace: if an integrated trace $\vec{x}_i$ is in the region labeled m, we assign it state m (Fig. S2c). By counting the number of traces assigned the value m when the qutrit was prepared in state $|s\rangle$, we estimate the elements $R_{m,s} = p(m||s\rangle)$ of the reference assignment probability matrix R (see Table II).

To extract the qutrit state populations $P = (P_g, P_e, P_f)$ after a reset of duration t_r, we also repeat the scheme illustrated in Fig. S2a 40000 times, and record single-shot traces for each run. As for the reference sets, the assignment probability M_m is estimated by counting the number of traces assigned the value m and follows

$$M_m = p(m|P) = \sum_s R_{m,s} \cdot P_s, \quad \text{(S14)}$$

which can be expressed as $M = R \cdot P$. A simple approach to estimate the population P of the qutrit is to set $P = M$. This approach is, however, sensitive to assignment errors due to readout imperfections: $P = M$ holds true only if $R_{m,s} = \delta_{m,s}$. To account for readout errors, we invert Eq. (S14) and set $P = R^{-1} \cdot M$. However, this procedure relies on the accurate characterization of R, which is sensitive to errors in state-preparation for the reference trace sets. The qutrit therefore needs to be initialized in $|g\rangle$ before applying the reference readout tone, with a residual excitation that can be

bounded, and that is ideally smaller than that of the unconditional reset protocol presented in this manuscript. As mentioned earlier in this section, to do so, we pre-reset the transmon with our protocol, then herald the ground state of the transmon with a pre-selection readout pulse (Fig. S2b). We record single-shot traces during the last 72 ns of the pre-selection pulse t_{her}. The pre-selection traces form two clusters, corresponding to ground and excited traces, that are maximally separated along their first principal component axis (Fig. S2c). We model the distribution of the first principal component c_1 of the traces with a bimodal Gaussian distribution and extract its parameters with maximum-likelihood estimation. Based on this model, we calculate a threshold value c_{thr} such that $p(c_1 > c_{\mathrm{thr}}|\mathrm{exc}) = 10^{-5}$. Selecting only traces with $c_1 > c_{\mathrm{thr}}$ heralds the ground state of the transmon. On the set of selected traces, the residual excitation of the transmon at the rising edge of the reference readout tone is therefore dominated by transmon thermalization, which occurs at rate $k_\uparrow/2\pi = 5\,\mathrm{kHz}$ in our sample. We use the same waiting time t_{gap} between initialization and readout to characterize the unconditional reset dynamics (Fig. S2a) and the reference trace set (Fig. S2b). As a result, thermalization occuring during this time can be seen as a source of readout error, which is compensated for. State preparation errors are then mostly explained by transmon thermalization occuring during the pre-selection, which we can bound by $k_\uparrow t_{\mathrm{her}} \simeq 0.25\%$.

In conclusion, the corrected single-shot readout method we developed suffers from state preparation error resulting in a systematic under-estimation of the extracted populations, bounded by 0.25%. This residual error is small compared to the populations extracted during the unconditional reset for most measured points (Fig. 4c); this readout method is therefore suitable for the analysis presented here.

S6. LIMITATIONS OF THE RESET PROTOCOL

The steady-state excited population $P_{\mathrm{exc}}^{\mathrm{sat}}$ which can be reached with the unconditional reset is constrained by three effects: transmon rethermalization, finite temperature of the reset resonator, and off-resonant driving of the g-e transition with the e-f drive. These constraints are quantitatively modelled in our master equation simulation, but they can also be discussed qualitatively to understand their effects on the performance.

The effective temperatures of superconducting qubits are typically higher than the base temperature of the dilution refrigerator T_{BT}, which implies that the thermal excitation rate $k_\uparrow$ of the qubit is higher than expected from T_{BT} [S11]. At equilibrium, thermalization competes against decay and the qubit has an equilibrium excited population $n_{\mathrm{th}} \simeq k_\uparrow T_1$ (in the limit where $n_{\mathrm{th}} \ll 1$). Similarly, for the unconditional reset protocol, the competition between thermalization and reset rate yields the steady-state excitation population $P_{\mathrm{ecx}}^{\mathrm{sat}} \sim k_\uparrow/\Gamma$. We model thermal excitations as quantum jumps to derive an analytical expression for $P_{\mathrm{ecx}}^{\mathrm{sat}}$. In steady state, the probability of a transmon rethermalization event (jump from $|g\rangle$ to $|e\rangle$) occurring between times $-t$ and $-t+dt$ is $(1-P_{\mathrm{ecx}}^{\mathrm{sat}})k_\uparrow dt \simeq k_\uparrow d\tau$. If such an event happens at time $-t$, the excited population a time 0 is $[P_{\mathrm{e|e}}^{\mathrm{H}} + P_{\mathrm{f|e}}^{\mathrm{H}}](t)$ as defined from Eq. (2) (main text). Integrating over all possible time windows for a rethermalization jump to occur, we obtain $P_{\mathrm{ecx}}^{\mathrm{sat}} = \int_0^{+\infty}[P_{\mathrm{e|e}}^{\mathrm{H}} + P_{\mathrm{f|e}}^{\mathrm{H}}](t)k_\uparrow dt = k_\uparrow\tau$, which tends towards $k_\uparrow/\Gamma$ for large drive rates. Using this method, we calculate $P_{\mathrm{ecx}}^{\mathrm{sat}} = 0.26\%$, 0.46% and 0.34% for configuration A, B and C, respectively. The close agreement of the calculated $P_{\mathrm{ecx}}^{\mathrm{sat}}$ with its measured and simulated values for all parameter configurations further supports our interpretation that transmon rethermalization is the dominant factor limiting the final population after reset.

In the level diagram of Fig. 1b, the black arrow labelled κ, connecting $|g,1\rangle$ to $|g,0\rangle$ represents the decay of the reset resonator. A finite temperature T_{rr} of the reset resonator can be accounted for by a transition in the opposite direction with rate $\kappa \cdot \exp[-\hbar\omega_{\mathrm{r}}/\mathrm{k_b T_{rr}}]$. If the unconditional reset is dominated by this rate, the entropy of the transmon and of the resonator equalize and the temperature of the transmon reaches $T_{\mathrm{rr}}\omega_{\mathrm{ge}}/\omega_{\mathrm{r}}$ in steady-state.

Driving the e-f transition during unconditional reset broadens also the g-e transition. The e-f drive, being detuned from the g-e transition by approximately the anharmonicity α of the transmon, also drives the g-e transition which leads to e-f drive induced thermalization. A trade-off between speed and reset fidelity has to be made when this effect is limiting.

The parameters we chose to optimize the reset are not the cause for the relatively large rethermalization rate $k_\uparrow/2\pi \simeq 5\,\mathrm{kHz}$ measured in our sample ($n_{\mathrm{th}} = 17\,\%$ and $T_1 = 5.5\,\mu s$). Indeed, Purcell decay through both resonators would allow for relaxation times up to $T_1^{\mathrm{Purcell}} = 370\,\mu s$ [S12]. In addition, we observed thermal excitation levels as low as $n_{\mathrm{th}} = 0.3\,\%$ in a sample with similar design and parameters in previous work [S8]. Therefore, with improved fabrication processes we expect to be able to decrease the rethermalization rate down to $k_\uparrow/2\pi \simeq 0.2\,\mathrm{kHz}$ ($n_{\mathrm{th}} < 5\,\%$ and $T_1 \sim 30\,\mu s$). With such a rate, transmon rethermalization would not limit the reset any more and we expect to reach saturation levels as low as $P_{\mathrm{ecx}}^{\mathrm{sat}} = 2 \times 10^{-4}$ with the current sample parameters.

S7. MASTER EQUATION SIMULATION

To model the transmon qutrit reset process numerically, we start with the Hamiltonian of a transmon dispersively coupled to a high bandwidth resonator. We add the two drive-induced couplings required for the unconditional reset protocol, *i.e.* a Rabi drive between the $|e\rangle, |f\rangle$

states of the transmon combined with an effective coupling $\tilde{g}$ between the $|f,0\rangle, |g,1\rangle$ states of the transmon-resonator system [S10, S13]. We represent the transmon as an anharmonic oscillator with annihilation and creation operators $\hat{b}$, $\hat{b}^\dagger$ [S14] which we truncate at the second excited state $|f\rangle$ and denote the annihilation and creation operators of the reset resonator $\hat{a}$ and $\hat{a}^\dagger$, respectively. In a frame rotating at ω_r for the resonator and $\omega_{ge} + \alpha/2$ for the transmon, the transmon-resonator system is described by the Hamiltonian

$$\begin{aligned}\hat{H} = & -\frac{\alpha}{2}\hat{b}^\dagger\hat{b} + \frac{\alpha}{2}\hat{b}^\dagger\hat{b}^\dagger\hat{b}\hat{b} + 2\chi_r\hat{a}^\dagger\hat{a}\hat{b}^\dagger\hat{b} \\ & + \frac{\tilde{g}}{\sqrt{2}}(\hat{b}^\dagger\hat{b}^\dagger\hat{a} + \hat{a}^\dagger\hat{b}\hat{b}) + \frac{\Omega_{\rm ef}}{\sqrt{2}}(\hat{b}\,\mathrm{e}^{i\alpha t/2} + \hat{b}^\dagger\mathrm{e}^{-i\alpha t/2}),\end{aligned} \tag{S15}$$

where α is the transmon anharmonicity, χ_r the dispersive coupling strength between the transmon and the resonator, and $\Omega_{\rm ef}$ is the Rabi rate between the $|e\rangle, |f\rangle$ states of the transmon. The readout resonator is omitted from the Hamiltonian since it does not affect the reset process and the induced static Lamb shifts are implicitly included in the parameters.

Numerical results are obtained by initializing the sytem in the $|e,0\rangle$ state and integrating the master equation

$$\begin{aligned}\dot{\rho} = & -i[\hat{H},\rho] \\ & + \kappa\mathcal{D}[\hat{a}]\rho + \kappa_{\rm int}\mathcal{D}[\hat{a}]\rho \\ & + \gamma_{1ge}(1+n_{\rm th})\mathcal{D}\left[|g\rangle\langle e|\right]\rho + \gamma_{1ge}n_{\rm th}\mathcal{D}\left[|e\rangle\langle g|\right]\rho \\ & + \gamma_{1ef}(1+n_{\rm th})\mathcal{D}\left[|e\rangle\langle f|\right]\rho + \gamma_{1ef}n_{\rm th}\mathcal{D}\left[|f\rangle\langle e|\right]\rho \\ & + \frac{\gamma_{\phi\rm ge}}{2}\mathcal{D}\left[|e\rangle\langle e| - |g\rangle\langle g|\right]\rho \\ & + \frac{\gamma_{\phi\rm ef}}{2}\mathcal{D}\left[|f\rangle\langle f| - |e\rangle\langle e|\right]\rho,\end{aligned} \tag{S16}$$

where $\mathcal{D}[\hat{O}]\bullet = \hat{O}\bullet\hat{O}^\dagger - \{\hat{O}^\dagger\hat{O},\bullet\}/2$ denotes the dissipation super-operator, $\kappa_{\rm int}$ the internal decay rate of the resonator, $\gamma_{1nm} = 1/T_{1nm}$ the decay rates of the transmon between the $|n\rangle, |m\rangle$ states, $\gamma_{\phi\rm nm} = 1/2T_1^{\rm nm} - 1/T_2^{\rm nm}$ the dephasing rates between the $|n\rangle, |m\rangle$ states of the transmon and $n_{\rm th}$ the thermal population of the transmon qubit in steady state.

[S1] D. Ristè, J. G. van Leeuwen, H.-S. Ku, K. W. Lehnert, and L. DiCarlo, Phys. Rev. Lett. **109**, 050507 (2012).

[S2] P. Campagne-Ibarcq, E. Flurin, N. Roch, D. Darson, P. Morfin, M. Mirrahimi, M. H. Devoret, F. Mallet, and B. Huard, Phys. Rev. X **3**, 021008 (2013).

[S3] Y. Salathé, P. Kurpiers, T. Karg, C. Lang, C. K. Andersen, A. Akin, S. Krinner, C. Eichler, and A. Wallraff, Phys. Rev. Applied **9**, 034011 (2018).

[S4] D. J. Egger, M. Ganzhorn, G. Salis, A. Fuhrer, P. Mueller, and S. Filipp, ArXiv:1802.08980 (2018), arXiv:1802.08980 [quant-ph].

[S5] S. O. Valenzuela, W. D. Oliver, D. M. Berns, K. K. Berggren, L. S. Levitov, and T. P. Orlando, Science **314**, 1589 (2006), http://www.sciencemag.org/content/314/5805/1589.full.pdf.

[S6] M. D. Reed, B. R. Johnson, A. A. Houck, L. DiCarlo, J. M. Chow, D. I. Schuster, L. Frunzio, and R. J. Schoelkopf, Appl. Phys. Lett. **96**, 203110 (2010).

[S7] K. Geerlings, Z. Leghtas, I. M. Pop, S. Shankar, L. Frunzio, R. J. Schoelkopf, M. Mirrahimi, and M. H. Devoret, Phys. Rev. Lett. **110**, 120501 (2013).

[S8] T. Walter, P. Kurpiers, S. Gasparinetti, P. Magnard, A. Potocnik, Y. Salathé, M. Pechal, M. Mondal, M. Oppliger, C. Eichler, and A. Wallraff, Phys. Rev. Applied **7**, 054020 (2017).

[S9] W. D. Heiss, Journal of Physics A: Mathematical and General **37**, 2455 (2004).

[S10] S. Zeytinoğlu, M. Pechal, S. Berger, A. A. Abdumalikov Jr., A. Wallraff, and S. Filipp, Phys. Rev. A **91**, 043846 (2015).

[S11] X. Y. Jin, A. Kamal, A. P. Sears, T. Gudmundsen, D. Hover, J. Miloshi, R. Slattery, F. Yan, J. Yoder, T. P. Orlando, S. Gustavsson, and W. D. Oliver, Phys. Rev. Lett. **114**, 240501 (2015).

[S12] E. A. Sete, J. M. Martinis, and A. N. Korotkov, Phys. Rev. A **92**, 012325 (2015).

[S13] M. Pechal, L. Huthmacher, C. Eichler, S. Zeytinoğlu, A. A. Abdumalikov Jr., S. Berger, A. Wallraff, and S. Filipp, Phys. Rev. X **4**, 041010 (2014).

[S14] J. Koch, T. M. Yu, J. Gambetta, A. A. Houck, D. I. Schuster, J. Majer, A. Blais, M. H. Devoret, S. M. Girvin, and R. J. Schoelkopf, Phys. Rev. A **76**, 042319 (2007).

Annexe C

Compléments sur les travaux avec ETH Zürich

C.1 Relation linéaire pour le couplage f0g1

Dans cette section je présente une méthode pour calculer la relation linéaire du couplage f0g1, équation 5.2. L'Hamiltonien de départ pour ce système est l'Hamiltonien Jaynes-Cummings, équation 2.5, avec un terme de pilotage,

$$\hat{H} = \omega_r \hat{a}^\dagger \hat{a} + \omega_q \hat{b}^\dagger \hat{b} + g(\hat{a}^\dagger \hat{b} + \hat{a}\hat{b}^\dagger) + \frac{\alpha_q}{2}\hat{b}^\dagger \hat{b}^\dagger \hat{b}\hat{b} + \Omega_b(t)(\hat{b} + \hat{b}^\dagger), \tag{C.1}$$

avec $\Omega_b(t) = \Omega_b \cos(\omega_d t + \phi)$. Pour éliminer la dépendance temporelle de cet Hamiltonien, on se place dans un référentiel tournant à la fréquence de pilotage, ω_d. Après une approximation séculaire, on obtient

$$\hat{H}' \approx \Delta_r \hat{a}^\dagger \hat{a} + \Delta_q \hat{b}^\dagger \hat{b} + g(\hat{a}^\dagger \hat{b} + \hat{a}\hat{b}^\dagger) + \frac{\alpha_q}{2}\hat{b}^\dagger \hat{b}^\dagger \hat{b}\hat{b} + \frac{\Omega_b}{2}(\hat{b}\, e^{i\phi} + \hat{b}^\dagger\, e^{-i\phi}), \tag{C.2}$$

où on définit $\Delta_r = \omega_r - \omega_d$, $\Delta_q = \omega_q - \omega_d$. Pour éliminer le terme linéaire, on effectue une transformation de déplacement $\hat{b} \to \hat{b} + \beta, \hat{a} \to \hat{a} + \alpha$,

$$\begin{aligned}
\hat{H}'' =& \Delta_r \hat{a}^\dagger \hat{a} + (\Delta_q + 2\alpha_q|\beta|^2)\hat{b}^\dagger \hat{b} + g(\hat{a}^\dagger \hat{b} + \hat{a}\hat{b}^\dagger) + \frac{\alpha_q}{2}\hat{b}^\dagger \hat{b}^\dagger \hat{b}\hat{b} \\
&+ \hat{a}\,(\Delta_r \alpha^* + g\beta^*) + h.c. \\
&+ \hat{b}\left(\frac{\Omega_b}{2}\, e^{i\phi} + \Delta_q \beta^* + g\alpha^* + \alpha_q|\beta|^2\beta^*\right) + h.c. \\
&+ \alpha_q \beta \hat{b}^\dagger \hat{b}^\dagger \hat{b} + \alpha_q \beta^* \hat{b}^\dagger \hat{b}\hat{b} + \frac{\alpha_q}{2}(\beta^{*2}\hat{b}\hat{b} + \beta^2 \hat{b}^\dagger \hat{b}^\dagger).
\end{aligned} \tag{C.3}$$

On choisit ensuite α et β de façon à éliminer les termes linéaires,

$$0 = \Delta_r \alpha^* + g\beta^*, \tag{C.4}$$

$$0 = \frac{\Omega_b}{2} e^{i\phi} + \Delta_q \beta^* + g\alpha^* + \alpha_q |\beta|^2 \beta^*. \tag{C.5}$$

En pratique, on considère des amplitudes de pilotage de l'ordre du désaccord entre la fréquence de pilotage et le transmon, $\Omega_b \sim \Delta_q$. Conséquemment, on approxime $\alpha \approx 0$ et

$$\beta \approx \frac{\Omega_b}{2\Delta_q}, \tag{C.6}$$

ce qui donne un Hamiltonien

$$\begin{aligned} \hat{H}'' =& \Delta_r \hat{a}^\dagger \hat{a} + (\Delta_q + 2\alpha_q |\beta|^2) \hat{b}^\dagger \hat{b} + g(\hat{a}^\dagger \hat{b} + \hat{a}\hat{b}^\dagger) + \frac{\alpha_q}{2} \hat{b}^\dagger \hat{b}^\dagger \hat{b}\hat{b} \\ &+ \alpha_q \beta \hat{b}^\dagger \hat{b}^\dagger \hat{b} + \alpha_q \beta^* \hat{b}^\dagger \hat{b}\hat{b} + \frac{\alpha_q}{2} (\beta^{*2} \hat{b}\hat{b} + \beta^2 \hat{b}^\dagger \hat{b}^\dagger). \end{aligned} \tag{C.7}$$

On élimine ensuite le terme d'interaction, g, à l'aide d'une transformation de Bogoliubov $\hat{a} \to \cos(\Lambda)\hat{a} + \sin(\Lambda)\hat{b}$, $\hat{b} \to \cos(\Lambda)\hat{b} - \sin(\Lambda)\hat{a}$. En négligeant tous les termes tournants, on obtient

$$\begin{aligned} \hat{H}''' \approx& \left[\Delta_r \cos^2\Lambda + (\Delta_q + 2\alpha_q|\beta|^2)\sin^2\Lambda - 2g\cos\Lambda\sin\Lambda\right] \hat{a}^\dagger\hat{a} \\ &+ \left[(\Delta_q + 2\alpha_q|\beta|^2)\cos^2\Lambda + \Delta_r \sin^2\Lambda + 2g\cos\Lambda\sin\Lambda\right] \hat{b}^\dagger\hat{b} \\ &+ \left[g\cos 2\Lambda + \frac{1}{2}(\Delta_r - \Delta_q - 2\alpha_q|\beta|^2)\sin 2\Lambda\right] (\hat{a}^\dagger\hat{b} + \hat{a}\hat{b}^\dagger) \\ &+ \frac{1}{2}\alpha_q \sin^4\Lambda \hat{a}^\dagger\hat{a}^\dagger\hat{a}\hat{a} + \frac{1}{2}\alpha_q\cos^4\Lambda \hat{b}^\dagger\hat{b}^\dagger\hat{b}\hat{b} + 2\alpha_q\cos^2\Lambda\sin^2\Lambda \hat{a}^\dagger\hat{a}\hat{b}^\dagger\hat{b} \\ &+ \alpha_q\cos^2\Lambda\sin\Lambda(\beta\hat{b}^\dagger\hat{b}^\dagger\hat{a} + \beta^*\hat{a}^\dagger\hat{b}\hat{b}). \end{aligned} \tag{C.8}$$

Le terme de couplage linéaire disparaît en choisissant

$$\tan 2\Lambda = \frac{2g}{\Delta + 2\alpha_q|\beta|^2}, \tag{C.9}$$

où $\Delta \equiv \omega_r - \omega_q$ est le désaccord entre le résonateur et le transmon. Dans le régime dispersif $g \ll \Delta$ et négligeant les corrections dues au décalage AC-stark, on a

$$\Lambda \approx \frac{g}{\Delta}. \tag{C.10}$$

On obtient donc finalement la forme désirée de l'Hamiltonien,

$$\hat{H}''' = \Delta_1'\hat{a}^\dagger\hat{a} + \Delta_2'\hat{b}^\dagger\hat{b} + \frac{K}{2}\hat{a}^\dagger\hat{a}^\dagger\hat{a}\hat{a} + \frac{\alpha_q'}{2}\hat{b}^\dagger\hat{b}^\dagger\hat{b}\hat{b} + \chi\hat{a}^\dagger\hat{a}\hat{b}^\dagger\hat{b} + (\tilde{g}\hat{b}^\dagger\hat{b}^\dagger\hat{a} + \tilde{g}^*\hat{a}^\dagger\hat{b}\hat{b})/\sqrt{2}, \tag{C.11}$$

où l'on a définit les variables simplifiées

$$\Delta_r' = \Delta_r\cos^2\Lambda + (\Delta_q + 2\alpha_q|\beta|^2)\sin^2\Lambda - g\sin 2\Lambda, \tag{C.12}$$
$$\Delta_q' = (\Delta_q + 2\alpha_q|\beta|^2)\cos^2\Lambda + \Delta_r\sin^2\Lambda + g\sin 2\Lambda, \tag{C.13}$$
$$K = \alpha_q\sin^4\Lambda, \tag{C.14}$$
$$\alpha_q' = \alpha_q\cos^4\Lambda, \tag{C.15}$$
$$\chi = 2\alpha_q\cos^2\Lambda\sin^2\Lambda, \tag{C.16}$$
$$\tilde{g} = \alpha_q\beta\cos^2\Lambda\sin\Lambda\sqrt{2}. \tag{C.17}$$

Pour que l'interaction correspondant au dernier terme de $\hat{H}'''$ soit résonante, la relation à respecter pour la fréquence de pilotage est

$$0 = 2\Delta_q' + \alpha_q - \Delta_r'. \tag{C.18}$$

Au premier ordre en g/Δ, on obtient

$$\omega_d \approx 2\omega_q + \alpha_q - \omega_r + \alpha_q 4|\beta|^2. \tag{C.19}$$

À l'aide de cette équation et de la relation C.6, on obtient une valeur linéaire approximative pour le déplacement β,

$$\beta \approx \frac{\Omega_b\, e^{i\phi}}{2(\Delta + \alpha_q)}. \tag{C.20}$$

Au premier ordre en g/Δ, on obtient donc finalement la relation linéaire 5.2,

$$\tilde{g} = \Omega_b\, e^{i\phi}\frac{\alpha_q g}{\sqrt{2}\Delta(\Delta + \alpha_q)}. \tag{C.21}$$

Cette démarche montre aussi que la fréquence de pilotage dépend de l'amplitude de pilotage,

$$\omega_d(\Omega_b) - \omega_d(0) \propto \Omega_b^2. \tag{C.22}$$

Notons que le terme dispersif obtenu à l'équation C.16 ne correspond pas à la valeur observée en pratique. Pour obtenir la bonne expression, il faut tenir compte d'une correction due aux niveaux supérieurs du transmon. Dans ce contexte, cela se traduit par une transformation Schrieffer-Wolff [188, 189] éliminant le terme

proportionnel à $\hat{a}^\dagger\hat{b}^\dagger\hat{b}\hat{b} + \hat{b}^\dagger\hat{b}^\dagger\hat{b}\hat{a}$ que nous avons ici simplement laissé tomber.

Bien que l'équation C.19 capture le comportement qualitatif du décalage AC-stark, elle ne mène pas à un bon accord quantitatif à cause des nombreuses approximations faites pour y arriver. Pour obtenir un bon accord avec l'expérience, on utilise plutôt la méthode numérique présentée à la section 5.1.

C.2 Relation entre couplage et photon émis

Dans cette section, je montre comment calculer la forme du couplage f0g1 nécessaire, $\tilde{g}(t)$, pour émettre un photon de forme $\xi(t)$. La sous-section C.2.1 traite du cas où l'on cherche à émettre un photon à la fréquence du résonateur. Ce calcul est fortement inspiré de la thèse de Marek Pechal [190]. La sous-section suivante C.2.2 montre plutôt comment il est possible d'émettre un photon à une fréquence légèrement différente de la fréquence du résonateur.

C.2.1 Photon à la fréquence du résonateur

Pour simplifier la notation, on utilise un modèle effectif à deux niveaux avec les relations d'équivalence $|0\rangle \leftrightarrow |f0\rangle$ et $|1\rangle \leftrightarrow |g1\rangle$. La perte d'un photon fait sortir de ce sous-espace, menant à un état non normalisé dont la norme est reliée à la forme du photon. La figure C.1 illustre cette situation.

Dans ce sous-espace, l'Hamiltonien effectif non hermitique de départ est donné par

$$\hat{H}_{\text{eff}} = -i\frac{\kappa}{2}\,|1\rangle\langle 1| + \tilde{g}(t)(|1\rangle\langle 0| + |0\rangle\,1), \tag{C.23}$$

et on calcule l'évolution d'un état à partir de l'équation de Schrödinger,

$$|\dot{\psi}(\tau)\rangle = -i\hat{H}_{\text{eff}}\,|\psi(\tau)\rangle\,. \tag{C.24}$$

L'Hamiltonien C.23 est exprimé dans le référentiel tournant à la fréquence du résonateur, ω_r. On suppose que l'état initial est $|\psi(0)\rangle = |0\rangle$ et en utilisant la relation d'entrée-sortie, équation 2.22, on trouve que la fonction d'onde du photon émis est donnée par

$$\tilde{\xi}(\tau) = \sqrt{\kappa}\langle 1|\psi(\tau)\rangle. \tag{C.25}$$

La fréquence porteuse de ce photon est celle du référentiel tournant, c'est-à-dire

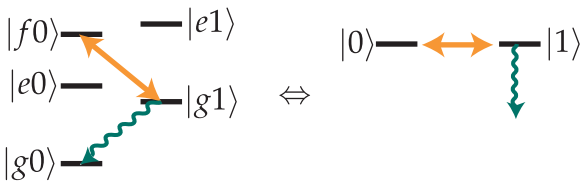

FIGURE C.1 – Au lieu de considérer le système complet, représenté à gauche, on prend un modèle effectif à deux niveaux, représenté à droite. La forme du photon émis est reliée à la norme de l'état dans ce modèle simple.

la fréquence du résonateur, ω_r. On calcule aisément à l'aide des équations C.24 et C.25 que la norme de l'état $|\psi\rangle$ est directement reliée à la forme du photon émis,

$$\partial_t \langle\psi|\psi\rangle = -|\xi(\tau)|^2. \tag{C.26}$$

Il est utile de définir un état normalisé

$$|\bar{\psi}\rangle \equiv \frac{|\psi\rangle}{\sqrt{\langle\psi|\psi\rangle}}, \tag{C.27}$$

respectant la relation

$$\sqrt{\kappa}\langle 1|\bar{\psi}(\tau)\rangle = \frac{\xi(\tau)}{\sqrt{1-\int_{t_i}^{\tau} dt|\xi(t)|^2}}, \tag{C.28}$$

et dont on peut calculer l'évolution temporelle à l'aide de l'équation

$$\left|\dot{\bar{\psi}}(\tau)\right\rangle = -i\left(\hat{H}_{\text{eff}} + i\frac{\kappa}{2}\left|\langle 1|\bar{\psi}(\tau)\rangle\right|^2\right)|\bar{\psi}(\tau)\rangle\,. \tag{C.29}$$

On paramétrise cet état,

$$|\bar{\psi}\rangle = \cos(\theta/2)\,|0\rangle + \sin(\theta/2)\,|1\rangle\,, \tag{C.30}$$

où l'angle de mélange θ est déterminé par la forme du photon, équation C.28. À l'aide de cette paramétrisation et de l'équation C.29, on calcule une équation différentielle pour θ,

$$\dot{\theta}/2 = i\tilde{g} - \frac{\kappa}{4}\sin(\theta). \tag{C.31}$$

La forme du couplage est donc donnée par

$$\tilde{g}(t) = -i\frac{\dot{\theta}}{2} - i\frac{\kappa}{4}\sin(\theta). \tag{C.32}$$

Par exemple, pour obtenir un photon de forme

$$\xi(t) = \frac{-i\sqrt{\kappa_{\text{eff}}}}{2\cosh(\kappa_{\text{eff}}t/2)}, \tag{C.33}$$

avec une largeur de bande effective $\kappa_{\text{eff}} < \kappa$, on doit appliquer un couplage

$$\tilde{g}(t) = \frac{\kappa_{\text{eff}}}{4\cosh(\kappa t/2)} \frac{1 - \mathrm{e}^{\kappa t} + \frac{\kappa}{\kappa_{\text{eff}}}(1 + \mathrm{e}^{\kappa t})}{\sqrt{\frac{\kappa}{\kappa_{\text{eff}}}(1 + \mathrm{e}^{\kappa t}) - \mathrm{e}^{\kappa t}}}. \tag{C.34}$$

C.2.2 Photon désaccordé du résonateur

Dans certaines situations, il est utile d'émettre un photon à une fréquence légèrement différente de celle du résonateur. Ceci est possible en modifiant la forme du couplage calculée à la sous-section précédente. On démarre avec un Hamiltonien similaire à l'équation C.23, mais en se plaçant dans un référentiel tournant à une fréquence $\omega = \omega_r + \delta$ et en ajoutant la possibilité de contrôler la phase du couplage f0g1,

$$\hat{H}_{\text{eff}} = \left(\delta - i\frac{\kappa}{2}\right)|1\rangle\langle 1| + \tilde{g}(t)(\,\mathrm{e}^{i\phi(t)}\,|1\rangle\,\langle 0| + \,\mathrm{e}^{-i\phi(t)}\,|0\rangle\,\langle 1|). \tag{C.35}$$

Il est important de noter que dans ce référentiel, une phase stable $\dot{\phi} = 0$ implique le pilotage f0g1 se fait à une fréquence $\omega_d = \omega_{f0g1} + \delta$.

On utilise ensuite une démarche similaire à la sous-section précédente en définissant un état normalisé $|\bar{\psi}\rangle$. Cependant, afin de prendre en compte l'accumulation de phase due au désaccord δ, on utilise la paramétrisation donnée par

$$|\bar{\psi}\rangle \equiv \,\mathrm{e}^{i\alpha}\cos(\theta/2)\,|0\rangle + \sin(\theta/2)\,|1\rangle\,. \tag{C.36}$$

L'angle de mélange, $0 \leq \theta < \pi$, est fixé par la forme du photon, équation C.28, alors que le paramètre α doit être calculé. À partir de l'équation C.29 et de cette

paramétrisation, on obtient deux équations différentielles complexes,

$$i\dot{\alpha}\cos\left(\frac{\theta}{2}\right) - \sin\left(\frac{\theta}{2}\right)\frac{\dot{\theta}}{2} = -i\tilde{g}\,e^{i(\phi-\alpha)}\sin\left(\frac{\theta}{2}\right) + \frac{\kappa}{2}\sin^2\left(\frac{\theta}{2}\right)\cos\left(\frac{\theta}{2}\right),$$
$$\cos\left(\frac{\theta}{2}\right)\frac{\dot{\theta}}{2} = i\tilde{g}\,e^{i(\phi-\alpha)}\cos\left(\frac{\theta}{2}\right) + \left(i\delta - \frac{\kappa}{2}\right)\sin\left(\frac{\theta}{2}\right) + \frac{\kappa}{2}\sin^3\left(\frac{\theta}{2}\right). \tag{C.37}$$

En séparant les parties réelles et imaginaires de ces équations, on obtient trois relations indépendantes,

$$\dot{\alpha} = -\tilde{g}\cos(\phi-\alpha)\tan(\theta/2), \tag{C.38}$$
$$\delta\tan(\theta/2) = -\tilde{g}\cos(\phi-\alpha), \tag{C.39}$$
$$\dot{\theta} = -2\tilde{g}\sin(\phi-\alpha) - \frac{\kappa}{2}\sin(\theta). \tag{C.40}$$

On détermine α à partir des équations C.38 et C.39,

$$\dot{\alpha} = \delta\tan^2(\theta/2). \tag{C.41}$$

Étant donné la paramétrisation C.36 et le fait que $\theta(0) = 0$, la phase initiale $\alpha(0)$ ajoute une phase globale au problème et peut donc être choisie de manière arbitraire. À partir des équations C.39 et C.40, on obtient la solution pour l'amplitude du couplage,

$$\tilde{g} = \sqrt{\frac{(\dot{\theta} + \kappa/2\sin\theta)^2}{4} + \delta^2\tan^2(\theta/2)}. \tag{C.42}$$

Finalement, on utilise C.39 pour trouver la phase du couplage,

$$\phi = \alpha - \arccos\left(\frac{-\delta\tan(\theta/2)}{\tilde{g}}\right), \tag{C.43}$$

où il est important de choisir la branche de la fonction arccos pour que les solutions $\tilde{g}, \tilde{\phi}, \alpha$ soient consistantes entre elles.

Bibliographie

[1] Y. Nakamura, Yu. A. Pashkin et J. S. Tsai. Coherent control of macroscopic quantum states in a single-cooper-pair box. *Nature* **398**, 786 EP – (1999). [cf. p. 1]

[2] J. E. Mooij, T. P. Orlando, L. Levitov, Lin Tian, Caspar H. van der Wal et Seth Lloyd. Josephson persistent-current qubit. *Science* **285**(5430), 1036–1039 (1999). [cf. p. 1]

[3] D. Vion, A. Aassime, A. Cottet, P. Joyez, H. Pothier, C. Urbina, D. Esteve et M. H. Devoret. Manipulating the quantum state of an electrical circuit. *Science* **296**(5569), 886–889 (2002). [cf. p. 1]

[4] Alexandre Blais, Ren-Shou Huang, Andreas Wallraff, S. M. Girvin et R. J. Schoelkopf. Cavity quantum electrodynamics for superconducting electrical circuits : An architecture for quantum computation. *Phys. Rev. A* **69**, 062320 (2004). [cf. p. 1, 2, 10, 11]

[5] A. Wallraff, D. I. Schuster, A. Blais, L. Frunzio, R. S. Huang, J. Majer, S. Kumar, S. M. Girvin et R. J. Schoelkopf. Strong coupling of a single photon to a superconducting qubit using circuit quantum electrodynamics. *Nature* **431**(7005), 162–167 (2004). [cf. p. 1, 10]

[6] M. H. Devoret et R. J. Schoelkopf. Superconducting circuits for quantum information : An outlook. *Science* **339**(6124), 1169–1174 (2013). [cf. p. 1]

[7] Io-Chun Hoi, C M Wilson, Göran Johansson, Joel Lindkvist, Borja Peropadre, Tauno Palomaki et Per Delsing. Microwave quantum optics with an artificial atom in one-dimensional open space. *New J. Phys.* **15**(2), 025011 (2013). [cf. p. 1]

[8] C. Lang, C. Eichler, L. Steffen, J. M. Fink, M. J. Woolley, A. Blais et A. Wallraff. Correlations, indistinguishability and entanglement in hong–ou–mandel experiments at microwave frequencies. *Nat. Phys.* **9**, 345 EP – (2013). [cf. p. 1]

[9] Arjan F. van Loo, Arkady Fedorov, Kevin Lalumière, Barry C. Sanders, Alexandre Blais et Andreas Wallraff. Photon-mediated interactions between distant artificial atoms. *Science* **342**(6165), 1494–1496 (2013). [cf. p. 1, 2, 14, 17]

[10] Y. Nakamura et T. Yamamoto. Breakthroughs in photonics 2012 : Breakthroughs in microwave quantum photonics in superconducting circuits. *IEEE Photonics Journal* **5**(2), 0701406–0701406 (2013). [cf. p. 1]

[11] Richard Bradley, John Clarke, Darin Kinion, Leslie J Rosenberg, Karl van Bibber, Seishi Matsuki, Michael Mück et Pierre Sikivie. Microwave cavity searches for dark-matter axions. *Rev. Mod. Phys.* **75**, 777–817 (2003). [cf. p. 1]

[12] B. M. Brubaker, L. Zhong, Y. V. Gurevich, S. B. Cahn, S. K. Lamoreaux, M. Simanovskaia, J. R. Root, S. M. Lewis, S. Al Kenany, K. M. Backes, I. Urdinaran, N. M. Rapidis, T. M. Shokair, K. A. van Bibber, D. A. Palken, M. Malnou, W. F. Kindel, M. A. Anil, K. W. Lehnert et G. Carosi. First results from a microwave cavity axion search at 24 μeV. *Phys. Rev. Lett.* **118**, 061302 (2017). [cf. p. 1]

[13] L. Zhong, S. Al Kenany, K. M. Backes, B. M. Brubaker, S. B. Cahn, G. Carosi, Y. V. Gurevich, W. F. Kindel, S. K. Lamoreaux, K. W. Lehnert, S. M. Lewis, M. Malnou, R. H. Maruyama, D. A. Palken, N. M. Rapidis, J. R. Root, M. Simanovskaia, T. M. Shokair, D. H. Speller, I. Urdinaran et K. A. van Bibber. Results from phase 1 of the haystac microwave cavity axion experiment. *Phys. Rev. D* **97**, 092001 (2018). [cf. p. 1]

[14] Pieter Kok, W. J. Munro, Kae Nemoto, T. C. Ralph, Jonathan P. Dowling et G. J. Milburn. Linear optical quantum computing with photonic qubits. *Rev. Mod. Phys.* **79**, 135–174 (2007). [cf. p. 2]

[15] Nicolas Gisin, Grégoire Ribordy, Wolfgang Tittel et Hugo Zbinden. Quantum cryptography. *Rev. Mod. Phys.* **74**, 145–195 (2002). [cf. p. 2]

[16] T. Walter, P. Kurpiers, S. Gasparinetti, P. Magnard, A. Potočnik, Y. Salathé, M. Pechal, M. Mondal, M. Oppliger, C. Eichler et A. Wallraff. Rapid high-fidelity single-shot dispersive readout of superconducting qubits. *Phys. Rev. Appl.* **7**, 054020 (2017). [cf. p. 2, 31]

[17] Robert H. Hadfield. Single-photon detectors for optical quantum information applications. *Nat Photon* **3**(12), 696–705 (2009). [cf. p. 2, 30, 33]

[18] Justin B. Spring, Benjamin J. Metcalf, Peter C. Humphreys, W. Steven Kolthammer, Xian-Min Jin, Marco Barbieri, Animesh Datta, Nicholas Thomas-Peter, Nathan K. Langford, Dmytro Kundys, James C. Gates, Brian J. Smith, Peter G. R. Smith et Ian A. Walmsley. Boson sampling on a photonic chip. *Science* **339**(6121), 798–801 (2013). [cf. p. 2]

[19] Luke C. G. Govia, Emily J. Pritchett, Canran Xu, B. L. T. Plourde, Maxim G. Vavilov, Frank K. Wilhelm et R. McDermott. High-fidelity qubit measurement with a microwave-photon counter. *Phys. Rev. A* **90**, 062307 (2014). [cf. p. 2]

[20] G. Oelsner, C. K. Andersen, M. Rehák, M. Schmelz, S. Anders, M. Grajcar, U. Hübner, K. Mølmer et E. Il'ichev. Detection of weak microwave fields with an underdamped josephson junction. *Phys. Rev. Appl.* **7**, 014012 (2017). [cf. p. 2, 34, 35]

[21] O. Astafiev, A. M. Zagoskin, A. A. Abdumalikov, Yu. A. Pashkin, T. Yamamoto, K. Inomata, Y. Nakamura et J. S. Tsai. Resonance fluorescence of a single artificial atom. *Science* **327**(5967), 840–843 (2010). [cf. p. 2, 14]

[22] Luke C. G. Govia, Emily J. Pritchett, B. L. T. Plourde, Maxim G. Vavilov, R. McDermott et Frank K. Wilhelm. Scalable two- and four-qubit parity measurement with a threshold photon counter. *Phys. Rev. A* **92**, 022335 (2015). [cf. p. 2, 4, 69]

[23] S. Pirandola, B. R. Bardhan, T. Gehring, C. Weedbrook et S. Lloyd. Advances in photonic quantum sensing. *Nature Photonics* **12**(12), 724–733 (2018). [cf. p. 2]

[24] Huaixiu Zheng, Matti Silveri, R. T. Brierley, S. M. Girvin et K. W. Lehnert. Accelerating dark-matter axion searches with quantum measurement technology. *arXiv e-prints* , arXiv:1607.02529 (2016). [cf. p. 2, 32]

[25] Jean Olivier Simoneau, Stéphane Virally, Christian Lupien et Bertrand Reulet. Photon-pair shot noise in electron shot noise. *Phys. Rev. B* **95**, 060301 (2017). [cf. p. 2]

[26] J. I. Cirac, A. K. Ekert, S. F. Huelga et C. Macchiavello. Distributed quantum computation over noisy channels. *Phys. Rev. A* **59**, 4249–4254 (1999). [cf. p. 2, 4, 86]

[27] Liang Jiang, Jacob M. Taylor, Anders S. Sørensen et Mikhail D. Lukin. Distributed quantum computation based on small quantum registers. *Phys. Rev. A* **76**, 062323 (2007). [cf. p. 2, 4, 86]

[28] Naomi H. Nickerson, Joseph F. Fitzsimons et Simon C. Benjamin. Freely scalable quantum technologies using cells of 5-to-50 qubits with very lossy and noisy photonic links. *Phys. Rev. X* **4**, 041041 (2014). [cf. p. 2]

[29] C. Gardiner et P. Zoller. *Quantum Noise : A Handbook of Markovian and Non-Markovian Quantum Stochastic Methods with Applications to Quantum Optics*. Springer Series in Synergetics. Springer, (2004). https://books.google.ca/books?id=a_xsT8oGhdgC. [cf. p. 3, 12, 20, 22, 24]

[30] G. Romero, J. J. García-Ripoll et E. Solano. Microwave photon detector in circuit qed. *Phys. Rev. Lett.* **102**, 173602 (2009). [cf. p. 3, 34, 35]

[31] Ferdinand Helmer, Matteo Mariantoni, Enrique Solano et Florian Marquardt. Quantum nondemolition photon detection in circuit qed and the quantum zeno effect. *Phys. Rev. A* **79**, 052115 (2009). [cf. p. 3, 31, 34]

[32] B. Peropadre, G. Romero, G. Johansson, C. M. Wilson, E. Solano et J. J. García-Ripoll. Approaching perfect microwave photodetection in circuit qed. *Phys. Rev. A* **84**, 063834 (2011). [cf. p. 3, 34, 35]

[33] Kazuki Koshino, Kunihiro Inomata, Tsuyoshi Yamamoto et Yasunobu Nakamura. Implementation of an impedance-matched Λ system by dressed-state engineering. *Phys. Rev. Lett.* **111**, 153601 (2013). [cf. p. 3, 31, 34]

[34] Sankar R. Sathyamoorthy, L. Tornberg, Anton F. Kockum, Ben Q. Baragiola, Joshua Combes, C. M. Wilson, Thomas M. Stace et G. Johansson. Quantum nondemolition detection of a propagating microwave photon. *Phys. Rev. Lett.* **112**, 093601 (2014). [cf. p. 3, 31, 34, 38]

[35] Bixuan Fan, Göran Johansson, Joshua Combes, G. J. Milburn et Thomas M. Stace. Nonabsorbing high-efficiency counter for itinerant microwave photons. *Phys. Rev. B* **90**, 035132 (2014). [cf. p. 3, 34, 38]

[36] Kazuki Koshino, Zhirong Lin, Kunihiro Inomata, Tsuyoshi Yamamoto et Yasunobu Nakamura. Dressed-state engineering for continuous detection of itinerant microwave photons. *Phys. Rev. A* **93**, 023824 (2016). [cf. p. 3, 34]

[37] Y.-F. Chen, D. Hover, S. Sendelbach, L. Maurer, S. T. Merkel, E. J. Pritchett, F. K. Wilhelm et R. McDermott. Microwave photon counter based on josephson junctions. *Phys. Rev. Lett.* **107**, 217401 (2011). [cf. p. 3, 34, 35]

[38] A. Narla, S. Shankar, M. Hatridge, Z. Leghtas, K. M. Sliwa, E. Zalys-Geller, S. O. Mundhada, W. Pfaff, L. Frunzio, R. J. Schoelkopf et M. H. Devoret. Robust concurrent remote entanglement between two superconducting qubits. *Phys. Rev. X* **6**, 031036 (2016). [cf. p. 3, 34, 86]

[39] Kunihiro Inomata, Zhirong Lin, Kazuki Koshino, William D. Oliver, Jaw-Shen Tsai, Tsuyoshi Yamamoto et Yasunobu Nakamura. Single microwave-photon detector using an artificial lambda-type three-level system. *Nat. Commun.* **7**, 12303 EP – (2016). [cf. p. 3, 34, 35]

[40] Baptiste Royer, Arne L. Grimsmo, Alexandre Choquette-Poitevin et Alexandre Blais. Itinerant microwave photon detector. *Phys. Rev. Lett.* **120**, 203602 (2018). [cf. p. 3, 34]

[41] John Preskill. Quantum Computing in the NISQ era and beyond. *Quantum* **2**, 79 (2018). [cf. p. 3]

[42] Peter W. Shor. Scheme for reducing decoherence in quantum computer memory. *Phys. Rev. A* **52**, R2493–R2496 (1995). [cf. p. 3]

[43] Andrew Steane. Multiple-particle interference and quantum error correction. *Proceedings of the Royal Society of London. Series A: Mathematical, Physical and Engineering Sciences* **452**(1954), 2551–2577 (1996). [cf. p. 3]

[44] Barbara M. Terhal. Quantum error correction for quantum memories. *Rev. Mod. Phys.* **87**, 307–346 (2015). [cf. p. 3]

[45] Earl T. Campbell, Barbara M. Terhal et Christophe Vuillot. Roads towards fault-tolerant universal quantum computation. *Nature* **549**, 172 EP – (2017). [cf. p. 3]

[46] M. D. Reed, L. DiCarlo, S. E. Nigg, L. Sun, L. Frunzio, S. M. Girvin et R. J. Schoelkopf. Realization of three-qubit quantum error correction with superconducting circuits. *Nature* **482**, 382 EP – (2012). [cf. p. 4, 66]

[47] J. Kelly, R. Barends, A. G. Fowler, A. Megrant, E. Jeffrey, T. C. White, D. Sank, J. Y. Mutus, B. Campbell, Yu Chen, Z. Chen, B. Chiaro, A. Dunsworth, I. C. Hoi, C. Neill, P. J. J. O'Malley, C. Quintana, P. Roushan, A. Vainsencher, J. Wenner, A. N. Cleland et John M. Martinis. State preservation by repetitive error

detection in a superconducting quantum circuit. *Nature* **519**, 66 EP – (2015). [cf. p. 4, 66]

[48] D. Ristè, S. Poletto, M. Z. Huang, A. Bruno, V. Vesterinen, O. P. Saira et L. DiCarlo. Detecting bit-flip errors in a logical qubit using stabilizer measurements. *Nat. Commun.* **6**, 6983 EP – (2015). [cf. p. 4, 66]

[49] A. D. Corcoles, Easwar Magesan, Srikanth J. Srinivasan, Andrew W. Cross, M. Steffen, Jay M. Gambetta et Jerry M. Chow. Demonstration of a quantum error detection code using a square lattice of four superconducting qubits. *Nat Commun* **6** (2015). [cf. p. 4, 66]

[50] J. Z. Blumoff, K. Chou, C. Shen, M. Reagor, C. Axline, R. T. Brierley, M. P. Silveri, C. Wang, B. Vlastakis, S. E. Nigg, L. Frunzio, M. H. Devoret, L. Jiang, S. M. Girvin et R. J. Schoelkopf. Implementing and characterizing precise multiqubit measurements. *Phys. Rev. X* **6**, 031041 (2016). [cf. p. 4, 48, 66, 69]

[51] Maika Takita, A. D. Córcoles, Easwar Magesan, Baleegh Abdo, Markus Brink, Andrew Cross, Jerry M. Chow et Jay M. Gambetta. Demonstration of weight-four parity measurements in the surface code architecture. *Phys. Rev. Lett.* **117**, 210505 (2016). [cf. p. 4, 66]

[52] Christian Kraglund Andersen, Ants Remm, Stefania Balasiu, Sebastian Krinner, Johannes Heinsoo, Jean-Claude Besse, Mihai Gabureac, Andreas Wallraff et Christopher Eichler. Entanglement Stabilization using Parity Detection and Real-Time Feedback in Superconducting Circuits. *arXiv e-prints* , arXiv:1902.06946 (2019). [cf. p. 4, 66]

[53] Chantal L. Hutchison, J. M. Gambetta, Alexandre Blais et F. K. Wilhelm. Quantum trajectory equation for multiple qubits in circuit qed : Generating entanglement by measurementthis paper was presented at the theory canada 4 conference, held at centre de recherches mathématiques, montréal, québec, canada on 4–7 june 2008. *Canadian Journal of Physics* **87**(3), 225–231 (2009). [cf. p. 4, 66, 67]

[54] Kevin Lalumière, J. M. Gambetta et Alexandre Blais. Tunable joint measurements in the dispersive regime of cavity qed. *Phys. Rev. A* **81**, 040301 (2010). [cf. p. 4, 66, 67]

[55] L. Tornberg et G. Johansson. High-fidelity feedback-assisted parity measurement in circuit qed. *Phys. Rev. A* **82**, 012329 (2010). [cf. p. 4, 66, 69]

[56] A. Frisk Kockum, L. Tornberg et G. Johansson. Undoing measurement-induced dephasing in circuit qed. *Phys. Rev. A* **85**, 052318 (2012). [cf. p. 4, 69]

[57] D. Ristè, M. Dukalski, C. A. Watson, G. de Lange, M. J. Tiggelman, Ya. M. Blanter, K. W. Lehnert, R. N. Schouten et L. DiCarlo. Deterministic entanglement of superconducting qubits by parity measurement and feedback. *Nature* **502**, 350 EP – (2013). [cf. p. 4, 66, 67]

[58] Patrick Huembeli et Simon E. Nigg. Towards a heralded eigenstate-preserving measurement of multi-qubit parity in circuit qed. *Phys. Rev. A* **96**, 012313 (2017). [cf. p. 4, 69]

[59] Baptiste Royer, Shruti Puri et Alexandre Blais. Qubit parity measurement by parametric driving in circuit qed. *Sci. Adv.* **4**(11) (2018). [cf. p. 4, 70]

[60] P. Kurpiers, P. Magnard, T. Walter, B. Royer, M. Pechal, J. Heinsoo, Y. Salathé, A. Akin, S. Storz, J. C. Besse, S. Gasparinetti, A. Blais et A. Wallraff. Deterministic quantum state transfer and remote entanglement using microwave photons. *Nature* **558**(7709), 264–267 (2018). [cf. p. 4, 12, 81]

[61] H. J. Kimble. The quantum internet. *Nature* **453**, 1023 EP – (2008). [cf. p. 4]

[62] J. I. Cirac, P. Zoller, H. J. Kimble et H. Mabuchi. Quantum state transfer and entanglement distribution among distant nodes in a quantum network. *Phys. Rev. Lett.* **78**, 3221–3224 (1997). [cf. p. 5, 86, 87]

[63] Philipp Kurpiers, Marek Pechal, Baptiste Royer, Paul Magnard, Theo Walter, Johannes Heinsoo, Yves Salathé, Abdulkadir Akin, Simon Storz, Jean-Claude Besse, Simone Gasparinetti, Alexandre Blais et Andreas Wallraff. Quantum communication with time-bin encoded microwave photons. *arXiv e-prints* , arXiv:1811.07604 (2018). [cf. p. 5, 81, 102]

[64] David P. DiVincenzo. The physical implementation of quantum computation. *Fortschritte der Physik* **48**(9-11), 771–783 (2000). [cf. p. 5]

[65] J. E. Johnson, C. Macklin, D. H. Slichter, R. Vijay, E. B. Weingarten, John Clarke et I. Siddiqi. Heralded state preparation in a superconducting qubit. *Phys. Rev. Lett.* **109**, 050506 (2012). [cf. p. 5]

[66] D. Ristè, J. G. van Leeuwen, H.-S. Ku, K. W. Lehnert et L. DiCarlo. Initialization by measurement of a superconducting quantum bit circuit. *Phys. Rev. Lett.* **109**, 050507 (2012). [cf. p. 5]

[67] D. Ristè, J. G. van Leeuwen, H.-S. Ku, K. W. Lehnert et L. DiCarlo. Initialization by measurement of a superconducting quantum bit circuit. *Phys. Rev. Lett.* **109**, 050507 (2012). [cf. p. 5]

[68] P. Campagne-Ibarcq, E. Flurin, N. Roch, D. Darson, P. Morfin, M. Mirrahimi, M. H. Devoret, F. Mallet et B. Huard. Persistent control of a superconducting qubit by stroboscopic measurement feedback. *Phys. Rev. X* **3**, 021008 (2013). [cf. p. 5]

[69] Yves Salathé, Philipp Kurpiers, Thomas Karg, Christian Lang, Christian Kraglund Andersen, Abdulkadir Akin, Sebastian Krinner, Christopher Eichler et Andreas Wallraff. Low-latency digital signal processing for feedback and feedforward in quantum computing and communication. *Phys. Rev. Appl.* **9**, 034011 (2018). [cf. p. 5]

[70] Maxime Boissonneault, J. M. Gambetta et Alexandre Blais. Dispersive regime of circuit qed : Photon-dependent qubit dephasing and relaxation rates. *Phys. Rev. A* **79**, 013819 (2009). [cf. p. 5, 79]

[71] D. H. Slichter, R. Vijay, S. J. Weber, S. Boutin, M. Boissonneault, J. M. Gambetta, A. Blais et I. Siddiqi. Measurement-induced qubit state mixing in circuit qed from up-converted dephasing noise. *Phys. Rev. Lett.* **109**, 153601 (2012). [cf. p. 5]

[72] P. Magnard, P. Kurpiers, B. Royer, T. Walter, J.-C. Besse, S. Gasparinetti, M. Pechal, J. Heinsoo, S. Storz, A. Blais et A. Wallraff. Fast and unconditional all-microwave reset of a superconducting qubit. *Phys. Rev. Lett.* **121**, 060502 (2018). [cf. p. 5, 81]

[73] Steven Girvin. *Circuit QED : Superconducting Qubits Coupled to Microwave Photons*. Oxford University Press, (2011). [cf. p. 7, 26]

[74] Uri Vool et Michel Devoret. Introduction to quantum electromagnetic circuits. *International Journal of Circuit Theory and Applications* **45**(7), 897–934 (2017). [cf. p. 7]

[75] Jens Koch, Terri M. Yu, Jay Gambetta, A. A. Houck, D. I. Schuster, J. Majer, Alexandre Blais, M. H. Devoret, S. M. Girvin et R. J. Schoelkopf. Charge-insensitive qubit design derived from the cooper pair box. *Phys. Rev. A* **76**, 042319 (2007). [cf. p. 7, 8, 9]

[76] J. Clarke et A.I. Braginski. *The SQUID Handbook : Fundamentals and Technology of SQUIDs and SQUID Systems*. Number v. 1 in The SQUID Handbook. Wiley, (2004). https://books.google.ca/books?id=MF3xAAAAMAAJ. [cf. p. 8]

[77] Georg Duffing. *Erzwungene schwingungen bei veränderlicher eigenfrequenz und ihre technische bedeutung*. Braunschweig, F. Vieweg & Sohn, (1918). [cf. p. 9]

[78] M.A. Nielsen et I.L. Chuang. *Quantum Computation and Quantum Information*. Cambridge Series on Information and the Natural Sciences. Cambridge University Press, (2000). https://books.google.ca/books?id=65FqEKQOfP8C. [cf. p. 9, 19, 20, 23]

[79] F. Motzoi, J. M. Gambetta, P. Rebentrost et F. K. Wilhelm. Simple pulses for elimination of leakage in weakly nonlinear qubits. *Phys. Rev. Lett.* **103**, 110501 (2009). [cf. p. 10]

[80] E. T. Jaynes et F. W. Cummings. Comparison of quantum and semiclassical radiation theories with application to the beam maser. *Proceedings of the IEEE* **51**(1), 89–109 (1963). [cf. p. 11]

[81] E. M. Purcell, H. C. Torrey et R. V. Pound. Resonance absorption by nuclear magnetic moments in a solid. *Phys. Rev.* **69**, 37–38 (1946). [cf. p. 12]

[82] Daniel Kleppner. Inhibited spontaneous emission. *Phys. Rev. Lett.* **47**, 233–236 (1981). [cf. p. 12]

[83] M. D. Reed, B. R. Johnson, A. A. Houck, L. DiCarlo, J. M. Chow, D. I. Schuster, L. Frunzio et R. J. Schoelkopf. Fast reset and suppressing spontaneous emission of a superconducting qubit. *Appl. Phys. Lett.* **96**(20), 203110 (2010). [cf. p. 12, 82]

[84] R. Bianchetti, S. Filipp, M. Baur, J. M. Fink, C. Lang, L. Steffen, M. Boissonneault, A. Blais et A. Wallraff. Control and tomography of a three level superconducting artificial atom. *Phys. Rev. Lett.* **105**, 223601 (2010). [cf. p. 12]

[85] Kôdi Husimi. Some formal properties of the density matrix. *Proceedings of the Physico-Mathematical Society of Japan. 3rd Series* **22**(4), 264–314 (1940). [cf. p. 13]

[86] Kevin Lalumière, Barry C. Sanders, A. F. van Loo, A. Fedorov, A. Wallraff et A. Blais. Input-output theory for waveguide qed with an ensemble of inhomogeneous atoms. *Phys. Rev. A* **88**, 043806 (2013). [cf. p. 14, 17]

[87] Kevin Lalumière. *Électrodynamique quantique en guide d'onde*. Thèse de Doctorat, Université de Sherbrooke, (2015). [cf. p. 14, 26]

[88] R. H. Dicke. Coherence in spontaneous radiation processes. *Phys. Rev.* **93**, 99–110 (1954). [cf. p. 15]

[89] Anton Frisk Kockum, Per Delsing et Göran Johansson. Designing frequency-dependent relaxation rates and lamb shifts for a giant artificial atom. *Phys. Rev. A* **90**, 013837 (2014). [cf. p. 17]

[90] Tommaso Tufarelli, M. S. Kim et Francesco Ciccarello. Non-markovianity of a quantum emitter in front of a mirror. *Phys. Rev. A* **90**, 012113 (2014). [cf. p. 17]

[91] H.P. Breuer, F. Petruccione et S.P.A.P.F. Petruccione. *The Theory of Open Quantum Systems*. Oxford University Press, (2002). https://books.google.ca/books?id=0Yx5VzaMYm8C. [cf. p. 18]

[92] C. W. Gardiner. Driving a quantum system with the output field from another driven quantum system. *Phys. Rev. Lett.* **70**, 2269–2272 (1993). [cf. p. 21]

[93] H. J. Carmichael. Quantum trajectory theory for cascaded open systems. *Phys. Rev. Lett.* **70**, 2273–2276 (1993). [cf. p. 21]

[94] Ananda Roy et Michel Devoret. Introduction to parametric amplification of quantum signals with josephson circuits. *Comptes Rendus Physique* **17**(7), 740 – 755 (2016). Quantum microwaves / Micro-ondes quantiques. [cf. p. 23]

[95] H.M. Wiseman et G.J. Milburn. *Quantum Measurement and Control*. Cambridge University Press, (2010). https://books.google.ca/books?id=ZNjvHaH8qA4C. [cf. p. 25]

[96] John F. Cochran et D. E. Mapother. Superconducting transition in aluminum. *Phys. Rev.* **111**, 132–142 (1958). [cf. p. 26]

[97] J. Wenner, Yi Yin, Erik Lucero, R. Barends, Yu Chen, B. Chiaro, J. Kelly, M. Lenander, Matteo Mariantoni, A. Megrant, C. Neill, P. J. J. O'Malley, D. Sank,

A. Vainsencher, H. Wang, T. C. White, A. N. Cleland et John M. Martinis. Excitation of superconducting qubits from hot nonequilibrium quasiparticles. *Phys. Rev. Lett.* **110**, 150502 (2013). [cf. p. 26]

[98] P. J. de Visser, D. J. Goldie, P. Diener, S. Withington, J. J. A. Baselmans et T. M. Klapwijk. Evidence of a nonequilibrium distribution of quasiparticles in the microwave response of a superconducting aluminum resonator. *Phys. Rev. Lett.* **112**, 047004 (2014). [cf. p. 26]

[99] X. Y. Jin, A. Kamal, A. P. Sears, T. Gudmundsen, D. Hover, J. Miloshi, R. Slattery, F. Yan, J. Yoder, T. P. Orlando, S. Gustavsson et W. D. Oliver. Thermal and residual excited-state population in a 3d transmon qubit. *Phys. Rev. Lett.* **114**, 240501 (2015). [cf. p. 26]

[100] K. Serniak, M. Hays, G. de Lange, S. Diamond, S. Shankar, L. D. Burkhart, L. Frunzio, M. Houzet et M. H. Devoret. Hot nonequilibrium quasiparticles in transmon qubits. *Phys. Rev. Lett.* **121**, 157701 (2018). [cf. p. 26]

[101] D. I. Schuster, A. A. Houck, J. A. Schreier, A. Wallraff, J. M. Gambetta, A. Blais, L. Frunzio, J. Majer, B. Johnson, M. H. Devoret, S. M. Girvin et R. J. Schoelkopf. Resolving photon number states in a superconducting circuit. *Nature* **445**, 515 EP – (2007). [cf. p. 27]

[102] Sébastien Gleyzes, Stefan Kuhr, Christine Guerlin, Julien Bernu, Samuel Deléglise, Ulrich Busk Hoff, Michel Brune, Jean-Michel Raimond et Serge Haroche. Quantum jumps of light recording the birth and death of a photon in a cavity. *Nature* **446**, 297 EP – (2007). [cf. p. 27]

[103] B. R. Johnson, M. D. Reed, A. A. Houck, D. I. Schuster, Lev S. Bishop, E. Ginossar, J. M. Gambetta, L. DiCarlo, L. Frunzio, S. M. Girvin et R. J. Schoelkopf. Quantum non-demolition detection of single microwave photons in a circuit. *Nat. Phys.* **6**, 663 EP – (2010). [cf. p. 27]

[104] W. H. Zurek. Pointer basis of quantum apparatus : Into what mixture does the wave packet collapse ? *Phys. Rev. D* **24**, 1516–1525 (1981). [cf. p. 27]

[105] B. Misra et E. C. G. Sudarshan. The zeno's paradox in quantum theory. *J. Math. Phys.* **18**(4), 756–763 (1977). [cf. p. 29]

[106] K. Kraus. Measuring processes in quantum mechanics i. continuous observation and the watchdog effect. *Foundations of Physics* **11**(7), 547–576 (1981). [cf. p. 29]

[107] P. Facchi et S. Pascazio. Quantum zeno subspaces. *Phys. Rev. Lett.* **89**, 080401 (2002). [cf. p. 29]

[108] Easwar Magesan, Jay M. Gambetta, A. D. Córcoles et Jerry M. Chow. Machine learning for discriminating quantum measurement trajectories and improving readout. *Phys. Rev. Lett.* **114**, 200501 (2015). [cf. p. 31, 47]

[109] Jean-Claude Besse, Simone Gasparinetti, Michele C. Collodo, Theo Walter, Philipp Kurpiers, Marek Pechal, Christopher Eichler et Andreas Wallraff. Single-shot quantum nondemolition detection of individual itinerant microwave photons. *Phys. Rev. X* **8**, 021003 (2018). [cf. p. 31, 32, 34]

[110] S. Kono, K. Koshino, Y. Tabuchi, A. Noguchi et Y. Nakamura. Quantum non-demolition detection of an itinerant microwave photon. *Nat. Phys.* **14**(6), 546–549 (2018). [cf. p. 32, 34]

[111] Raphaël Lescanne, Samuel Deléglise, Emanuele Albertinale, Ulysse Réglade, Thibault Capelle, Edouard Ivanov, Thibaut Jacqmin, Zaki Leghtas et Emmanuel Flurin. Detecting itinerant microwave photons with engineered nonlinear dissipation. *arXiv e-prints* , arXiv:1902.05102 (2019). [cf. p. 32, 34, 35]

[112] Bastian Hacker, Stephan Welte, Severin Daiss, Armin Shaukat, Stephan Ritter, Lin Li et Gerhard Rempe. Deterministic creation of entangled atom–light schrödinger-cat states. *Nature Photonics* **13**(2), 110–115 (2019). [cf. p. 32]

[113] Oleksandr Kyriienko et Anders S. Sørensen. Continuous-wave single-photon transistor based on a superconducting circuit. *Phys. Rev. Lett.* **117**, 140503 (2016). [cf. p. 34, 35]

[114] Clement H. Wong et Maxim G. Vavilov. Quantum efficiency of a single microwave photon detector based on a semiconductor double quantum dot. *Phys. Rev. A* **95**, 012325 (2017). [cf. p. 34, 35]

[115] Juha Leppäkangas, Michael Marthaler, Dibyendu Hazra, Salha Jebari, Romain Albert, Florian Blanchet, Göran Johansson et Max Hofheinz. Multiplying and detecting propagating microwave photons using inelastic cooper-pair tunneling. *Phys. Rev. A* **97**, 013855 (2018). [cf. p. 34, 35]

[116] A. Opremcak, I. V. Pechenezhskiy, C. Howington, B. G. Christensen, M. A. Beck, E. Leonard, J. Suttle, C. Wilen, K. N. Nesterov, G. J. Ribeill, T. Thorbeck, F. Schlenker, M. G. Vavilov, B. L. T. Plourde et R. McDermott. Measurement of a superconducting qubit with a microwave photon counter. *Science* **361**(6408), 1239–1242 (2018). [cf. p. 34, 35]

[117] K. Inomata, K. Koshino, Z. R. Lin, W. D. Oliver, J. S. Tsai, Y. Nakamura et T. Yamamoto. Microwave down-conversion with an impedance-matched ■ system in driven circuit qed. *Phys. Rev. Lett.* **113**, 063604 (2014). [cf. p. 35]

[118] Kazuki Koshino, Kunihiro Inomata, Zhirong Lin, Yasunobu Nakamura et Tsuyoshi Yamamoto. Theory of microwave single-photon detection using an impedance-matched Λ system. *Phys. Rev. A* **91**, 043805 (2015). [cf. p. 35]

[119] Bixuan Fan, Anton F. Kockum, Joshua Combes, Göran Johansson, Io-chun Hoi, C. M. Wilson, Per Delsing, G. J. Milburn et Thomas M. Stace. Breakdown of the cross-kerr scheme for photon counting. *Phys. Rev. Lett.* **110**, 053601 (2013). [cf. p. 35, 50]

[120] Xufeng Zhang, Chang-Ling Zou, Na Zhu, Florian Marquardt, Liang Jiang et Hong X. Tang. Magnon dark modes and gradient memory. *Nat. Commun.* **6**, 8914 EP – (2015). [cf. p. 37]

[121] A. G. Anderson, R. L. Garwin, E. L. Hahn, J. W. Horton, G. L. Tucker et R. M. Walker. Spin echo serial storage memory. *J. Appl. Phys.* **26**(11), 1324–1338 (1955). [cf. p. 37]

[122] S. Arnold, C. T. Liu, W. B. Whitten et J. M. Ramsey. Room-temperature microparticle-based persistent spectral hole burning memory. *Opt. Lett.* **16**(6), 420–422 (1991). [cf. p. 37]

[123] Lene Vestergaard Hau, S. E. Harris, Zachary Dutton et Cyrus H. Behroozi. Light speed reduction to 17 metres per second in an ultracold atomic gas. *Nature* **397**(6720), 594–598 (1999). [cf. p. 37]

[124] A. L. Alexander, J. J. Longdell, M. J. Sellars et N. B. Manson. Photon echoes produced by switching electric fields. *Phys. Rev. Lett.* **96**, 043602 (2006). [cf. p. 37]

[125] B. Kraus, W. Tittel, N. Gisin, M. Nilsson, S. Kröll et J. I. Cirac. Quantum memory for nonstationary light fields based on controlled reversible inhomogeneous broadening. *Phys. Rev. A* **73**, 020302 (2006). [cf. p. 37]

[126] Hugues de Riedmatten, Mikael Afzelius, Matthias U. Staudt, Christoph Simon et Nicolas Gisin. A solid-state light–matter interface at the single-photon level. *Nature* **456**, 773 EP – (2008). [cf. p. 37]

[127] Morgan P. Hedges, Jevon J. Longdell, Yongmin Li et Matthew J. Sellars. Efficient quantum memory for light. *Nature* **465**, 1052 EP – (2010). [cf. p. 37]

[128] M. Hosseini, B. M. Sparkes, G. Campbell, P. K. Lam et B. C. Buchler. High efficiency coherent optical memory with warm rubidium vapour. *Nat. Commun.* **2**, 174 EP – (2011). [cf. p. 37]

[129] Brian Julsgaard, Cécile Grezes, Patrice Bertet et Klaus Mølmer. Quantum memory for microwave photons in an inhomogeneously broadened spin ensemble. *Phys. Rev. Lett.* **110**, 250503 (2013). [cf. p. 37]

[130] Nicolas Didier, Jérôme Bourassa et Alexandre Blais. Fast quantum nondemolition readout by parametric modulation of longitudinal qubit-oscillator interaction. *Phys. Rev. Lett.* **115**, 203601 (2015). [cf. p. 38]

[131] J. S. Lundeen, A. Feito, H. Coldenstrodt-Ronge, K. L. Pregnell, Ch. Silberhorn, T. C. Ralph, J. Eisert, M. B. Plenio et I. A. Walmsley. Tomography of quantum detectors. *Nat. Phys.* **5**, 27 EP – (2008). [cf. p. 48]

[132] Lijian Zhang, Hendrik B. Coldenstrodt-Ronge, Animesh Datta, Graciana Puentes, Jeff S. Lundeen, Xian-Min Jin, Brian J. Smith, Martin B. Plenio et Ian A. Walmsley. Mapping coherence in measurement via full quantum tomography of a hybrid optical detector. *Nature Photonics* **6**, 364 EP – (2012). [cf. p. 48]

[133] M. A. Castellanos-Beltran et K. W. Lehnert. Widely tunable parametric amplifier based on a superconducting quantum interference device array resonator. *Appl. Phys. Lett.* **91**(8), 083509 (2007). [cf. p. 49]

[134] T. Yamamoto, K. Inomata, M. Watanabe, K. Matsuba, T. Miyazaki, W. D. Oliver, Y. Nakamura et J. S. Tsai. Flux-driven josephson parametric amplifier. *Appl. Phys. Lett.* **93**(4), 042510 (2008). [cf. p. 49]

[135] N. Bergeal, F. Schackert, M. Metcalfe, R. Vijay, V. E. Manucharyan, L. Frunzio, D. E. Prober, R. J. Schoelkopf, S. M. Girvin et M. H. Devoret. Phase-preserving amplification near the quantum limit with a josephson ring modulator. *Nature* **465**, 64 EP – (2010). [cf. p. 49]

[136] M. Hatridge, R. Vijay, D. H. Slichter, John Clarke et I. Siddiqi. Dispersive magnetometry with a quantum limited squid parametric amplifier. *Phys. Rev. B* **83**, 134501 (2011). [cf. p. 49]

[137] J. Y. Mutus, T. C. White, E. Jeffrey, D. Sank, R. Barends, J. Bochmann, Yu Chen, Z. Chen, B. Chiaro, A. Dunsworth, J. Kelly, A. Megrant, C. Neill, P. J. J. O'Malley, P. Roushan, A. Vainsencher, J. Wenner, I. Siddiqi, R. Vijay, A. N. Cleland et John M. Martinis. Design and characterization of a lumped element single-ended superconducting microwave parametric amplifier with on-chip flux bias line. *Appl. Phys. Lett.* **103**(12), 122602 (2013). [cf. p. 49]

[138] Christopher Eichler et Andreas Wallraff. Controlling the dynamic range of a josephson parametric amplifier. *EPJ Quantum Technology* **1**(1), 2 (2014). [cf. p. 49]

[139] J. Y. Mutus, T. C. White, R. Barends, Yu Chen, Z. Chen, B. Chiaro, A. Dunsworth, E. Jeffrey, J. Kelly, A. Megrant, C. Neill, P. J. J. O'Malley, P. Roushan, D. Sank, A. Vainsencher, J. Wenner, K. M. Sundqvist, A. N. Cleland et John M. Martinis. Strong environmental coupling in a josephson parametric amplifier. *Appl. Phys. Lett.* **104**(26), 263513 (2014). [cf. p. 49]

[140] C. Eichler, Y. Salathe, J. Mlynek, S. Schmidt et A. Wallraff. Quantum-limited amplification and entanglement in coupled nonlinear resonators. *Phys. Rev. Lett.* **113**, 110502 (2014). [cf. p. 49]

[141] C. Macklin, K. O'Brien, D. Hover, M. E. Schwartz, V. Bolkhovsky, X. Zhang, W. D. Oliver et I. Siddiqi. A near-quantum-limited josephson traveling-wave parametric amplifier. *Science* **350**(6258), 307–310 (2015). [cf. p. 49, 63]

[142] Jeffrey H. Shapiro. Single-photon kerr nonlinearities do not help quantum computation. *Phys. Rev. A* **73**, 062305 (2006). [cf. p. 50]

[143] Jeffrey H Shapiro et Mohsen Razavi. Continuous-time cross-phase modulation and quantum computation. *New J. Phys.* **9**(1), 16–16 (2007). [cf. p. 50]

[144] Julio Gea-Banacloche. Impossibility of large phase shifts via the giant kerr effect with single-photon wave packets. *Phys. Rev. A* **81**, 043823 (2010). [cf. p. 50]

[145] Arne L. Grimsmo et Alexandre Blais. Squeezing and quantum state engineering with josephson travelling wave amplifiers. *npj Quantum Information* **3**(1), 20 (2017). [cf. p. 52, 63]

[146] A. Kamenev. *Field Theory of Non-Equilibrium Systems*. Cambridge University Press, (2014). https://books.google.ca/books?id=uwuxjwEACAAJ. [cf. p. 52]

[147] L M Sieberer, M Buchhold et S Diehl. Keldysh field theory for driven open quantum systems. *Reports on Progress in Physics* **79**(9), 096001 (2016). [cf. p. 52]

[148] Arne L. Grimsmo, Baptiste Royer, John Mark Kreikebaum, Kevin O'Brien, Irfan Siddiqi et Alexandre Blais. Quantum metamaterial for nondestructive microwave photon counting. In preparation, (2019). [cf. p.]

[149] M. Houde, L. C. G. Govia et A. A. Clerk. Loss asymmetries in quantum travelling wave parametric amplifiers. *arXiv e-prints* , arXiv:1809.07418 (2018). [cf. p. 63]

[150] Emanuel Knill, Raymond Laflamme et Wojciech H. Zurek. Resilient quantum computation : error models and thresholds. *Proceedings of the Royal Society of London. Series A: Mathematical, Physical and Engineering Sciences* **454**(1969), 365–384 (1998). [cf. p. 64]

[151] Dorit Aharonov et Michael Ben-Or. Fault-Tolerant Quantum Computation With Constant Error Rate. *arXiv e-prints* , quant–ph/9906129 (1999). [cf. p. 64]

[152] A.Yu. Kitaev. Fault-tolerant quantum computation by anyons. *Annals of Physics* **303**(1), 2 – 30 (2003). [cf. p. 64]

[153] R Raussendorf, J Harrington et K Goyal. Topological fault-tolerance in cluster state quantum computation. *New J. Phys.* **9**(6), 199–199 (2007). [cf. p. 64]

[154] Robert Raussendorf et Jim Harrington. Fault-tolerant quantum computation with high threshold in two dimensions. *Phys. Rev. Lett.* **98**, 190504 (2007). [cf. p. 64]

[155] Austin G. Fowler, Ashley M. Stephens et Peter Groszkowski. High-threshold universal quantum computation on the surface code. *Phys. Rev. A* **80**, 052312 (2009). [cf. p. 64]

[156] Daniel Gottesman. *Stabilizer codes and quantum error correction*. Thèse de Doctorat, California Institute of Technology, (1997). [cf. p. 65]

[157] Simon E. Nigg et S. M. Girvin. Stabilizer quantum error correction toolbox for superconducting qubits. *Phys. Rev. Lett.* **110**, 243604 (2013). [cf. p. 66, 69]

[158] David P DiVincenzo et Firat Solgun. Multi-qubit parity measurement in circuit quantum electrodynamics. *New J. Phys.* **15**(7), 075001 (2013). [cf. p. 69]

[159] L. Tornberg, Sh. Barzanjeh et David P. DiVincenzo. Stochastic-master-equation analysis of optimized three-qubit nondemolition parity measurements. *Phys. Rev. A* **89**, 032314 (2014). [cf. p. 69]

[160] Ben Criger, Alessandro Ciani et David P. DiVincenzo. Multi-qubit joint measurements in circuit qed : stochastic master equation analysis. *EPJ Quantum Technology* **3**(1), 6 (2016). [cf. p. 69]

[161] Samuel Boutin, Christian Kraglund Andersen, Jayameenakshi Venkatraman, Andrew J. Ferris et Alexandre Blais. Resonator reset in circuit qed by optimal control for large open quantum systems. *Phys. Rev. A* **96**, 042315 (2017). [cf. p. 79]

[162] Shruti Puri, Samuel Boutin et Alexandre Blais. Engineering the quantum states of light in a kerr-nonlinear resonator by two-photon driving. *npj Quantum Information* **3**(1), 18 (2017). [cf. p. 79]

[163] Shruti Puri, Alexander Grimm, Philippe Campagne-Ibarcq, Alec Eickbusch, Kyungjoo Noh, Gabrielle Roberts, Liang Jiang, Mazyar Mirrahimi, Michel H. Devoret et Steven M. Girvin. Stabilized Cat in Driven Nonlinear Cavity : A Fault-Tolerant Error Syndrome Detector. *arXiv e-prints* , arXiv:1807.09334 (2018). [cf. p. 79]

[164] Panos Aliferis et John Preskill. Fault-tolerant quantum computation against biased noise. *Phys. Rev. A* **78**, 052331 (2008). [cf. p. 80]

[165] Paul Webster, Stephen D. Bartlett et David Poulin. Reducing the overhead for quantum computation when noise is biased. *Phys. Rev. A* **92**, 062309 (2015). [cf. p. 80]

[166] M. Pechal, L. Huthmacher, C. Eichler, S. Zeytinoğlu, A. A. Abdumalikov, S. Berger, A. Wallraff et S. Filipp. Microwave-controlled generation of shaped single photons in circuit quantum electrodynamics. *Phys. Rev. X* **4**, 041010 (2014). [cf. p. 81, 82, 84, 87]

[167] William D. Oliver et Paul B. Welander. Materials in superconducting quantum bits. *MRS Bulletin* **38**(10), 816–825 (2013). [cf. p. 82]

[168] J. Kelly, R. Barends, B. Campbell, Y. Chen, Z. Chen, B. Chiaro, A. Dunsworth, A. G. Fowler, I.-C. Hoi, E. Jeffrey, A. Megrant, J. Mutus, C. Neill, P. J. J. O'Malley, C. Quintana, P. Roushan, D. Sank, A. Vainsencher, J. Wenner, T. C. White, A. N. Cleland et John M. Martinis. Optimal quantum control using randomized benchmarking. *Phys. Rev. Lett.* **112**, 240504 (2014). [cf. p. 82]

[169] Matteo Mariantoni, Frank Deppe, A. Marx, R. Gross, F. K. Wilhelm et E. Solano. Two-resonator circuit quantum electrodynamics : A superconducting quantum switch. *Phys. Rev. B* **78**, 104508 (2008). [cf. p. 82]

[170] R. C. Bialczak, M. Ansmann, M. Hofheinz, M. Lenander, E. Lucero, M. Neeley, A. D. O'Connell, D. Sank, H. Wang, M. Weides, J. Wenner, T. Yamamoto, A. N. Cleland et J. M. Martinis. Fast tunable coupler for superconducting qubits. *Phys. Rev. Lett.* **106**, 060501 (2011). [cf. p. 82]

[171] Yu Chen, C. Neill, P. Roushan, N. Leung, M. Fang, R. Barends, J. Kelly, B. Campbell, Z. Chen, B. Chiaro, A. Dunsworth, E. Jeffrey, A. Megrant, J. Y. Mutus, P. J. J.

O'Malley, C. M. Quintana, D. Sank, A. Vainsencher, J. Wenner, T. C. White, Michael R. Geller, A. N. Cleland et John M. Martinis. Qubit architecture with high coherence and fast tunable coupling. *Phys. Rev. Lett.* **113**, 220502 (2014). [cf. p. 82]

[172] David C. McKay, Stefan Filipp, Antonio Mezzacapo, Easwar Magesan, Jerry M. Chow et Jay M. Gambetta. Universal gate for fixed-frequency qubits via a tunable bus. *Phys. Rev. Appl.* **6**, 064007 (2016). [cf. p. 82]

[173] Marco Roth, Marc Ganzhorn, Nikolaj Moll, Stefan Filipp, Gian Salis et Sebastian Schmidt. Analysis of a parametrically driven exchange-type gate and a two-photon excitation gate between superconducting qubits. *Phys. Rev. A* **96**, 062323 (2017). [cf. p. 82]

[174] Yulin Wu, Li-Ping Yang, Ming Gong, Yarui Zheng, Hui Deng, Zhiguang Yan, Yanjun Zhao, Keqiang Huang, Anthony D. Castellano, William J. Munro, Kae Nemoto, Dong-Ning Zheng, C. P. Sun, Yu-xi Liu, Xiaobo Zhu et Li Lu. An efficient and compact switch for quantum circuits. *npj Quantum Information* **4**(1), 50 (2018). [cf. p. 82]

[175] J. M. Gambetta, A. A. Houck et Alexandre Blais. Superconducting qubit with purcell protection and tunable coupling. *Phys. Rev. Lett.* **106**, 030502 (2011). [cf. p. 82]

[176] S. J. Srinivasan, A. J. Hoffman, J. M. Gambetta et A. A. Houck. Tunable coupling in circuit quantum electrodynamics using a superconducting charge qubit with a v-shaped energy level diagram. *Phys. Rev. Lett.* **106**, 083601 (2011). [cf. p. 82]

[177] S. Zeytinoğlu, M. Pechal, S. Berger, A. A. Abdumalikov, A. Wallraff et S. Filipp. Microwave-induced amplitude- and phase-tunable qubit-resonator coupling in circuit quantum electrodynamics. *Phys. Rev. A* **91**, 043846 (2015). [cf. p. 82, 83]

[178] Simone Gasparinetti, Simon Berger, Abdufarrukh A. Abdumalikov, Marek Pechal, Stefan Filipp et Andreas J. Wallraff. Measurement of a vacuum-induced geometric phase. *Sci. Adv.* **2**(5) (2016). [cf. p. 82]

[179] C. Monroe, R. Raussendorf, A. Ruthven, K. R. Brown, P. Maunz, L.-M. Duan et J. Kim. Large-scale modular quantum-computer architecture with atomic memory and photonic interconnects. *Phys. Rev. A* **89**, 022317 (2014). [cf. p. 86]

[180] N. Roch, M. E. Schwartz, F. Motzoi, C. Macklin, R. Vijay, A. W. Eddins, A. N. Korotkov, K. B. Whaley, M. Sarovar et I. Siddiqi. Observation of measurement-induced entanglement and quantum trajectories of remote superconducting qubits. *Phys. Rev. Lett.* **112**, 170501 (2014). [cf. p. 86, 88]

[181] Christopher J. Axline, Luke D. Burkhart, Wolfgang Pfaff, Mengzhen Zhang, Kevin Chou, Philippe Campagne-Ibarcq, Philip Reinhold, Luigi Frunzio, S. M. Girvin, Liang Jiang, M. H. Devoret et R. J. Schoelkopf. On-demand quantum

state transfer and entanglement between remote microwave cavity memories. *Nat. Phys.* **14**(7), 705–710 (2018). [cf. p. 88]

[182] P. Campagne-Ibarcq, E. Zalys-Geller, A. Narla, S. Shankar, P. Reinhold, L. Burkhart, C. Axline, W. Pfaff, L. Frunzio, R. J. Schoelkopf et M. H. Devoret. Deterministic remote entanglement of superconducting circuits through microwave two-photon transitions. *Phys. Rev. Lett.* **120**, 200501 (2018). [cf. p. 88]

[183] C. Dickel, J. J. Wesdorp, N. K. Langford, S. Peiter, R. Sagastizabal, A. Bruno, B. Criger, F. Motzoi et L. DiCarlo. Chip-to-chip entanglement of transmon qubits using engineered measurement fields. *Phys. Rev. B* **97**, 064508 (2018). [cf. p. 88]

[184] N. Leung, Y. Lu, S. Chakram, R. K. Naik, N. Earnest, R. Ma, K. Jacobs, A. N. Cleland et D. I. Schuster. Deterministic bidirectional communication and remote entanglement generation between superconducting qubits. *npj Quantum Information* **5**(1), 18 (2019). [cf. p. 88]

[185] M V Berry. Transitionless quantum driving. *Journal of Physics A: Mathematical and Theoretical* **42**(36), 365303 (2009). [cf. p. 101]

[186] Markus Jerger, Pascal Macha, Andrés Rosario Hamann, Yarema Reshitnyk, Kristinn Juliusson et Arkady Fedorov. Realization of a binary-outcome projection measurement of a three-level superconducting quantum system. *Phys. Rev. Appl.* **6**, 014014 (2016). [cf. p. 103]

[187] Baptiste Royer, Arne L. Grimsmo, Nicolas Didier et Alexandre Blais. Fast and high-fidelity entangling gate through parametrically modulated longitudinal coupling. *Quantum* **1**, 11 (2017). [cf. p. 126]

[188] J. M. Luttinger et W. Kohn. Motion of electrons and holes in perturbed periodic fields. *Phys. Rev.* **97**, 869–883 (1955). [cf. p. 203]

[189] J. R. Schrieffer et P. A. Wolff. Relation between the anderson and kondo hamiltonians. *Phys. Rev.* **149**, 491–492 (1966). [cf. p. 203]

[190] Marek Pechal. *Microwave photonics in superconducting circuits*. Thèse de Doctorat, ETH Zürich, (2016). [cf. p. 204]